



HAL
open science

Binary neutron star mergers in the multi-messenger era: very high energy afterglows and progenitor evolutionary tracks

Clément Pellouin

► To cite this version:

Clément Pellouin. Binary neutron star mergers in the multi-messenger era: very high energy afterglows and progenitor evolutionary tracks. Astrophysics [astro-ph]. Sorbonne Université, 2023. English. NNT: 2023SORUS370 . tel-04347622

HAL Id: tel-04347622

<https://theses.hal.science/tel-04347622v1>

Submitted on 15 Dec 2023

HAL is a multi-disciplinary open access archive for the deposit and dissemination of scientific research documents, whether they are published or not. The documents may come from teaching and research institutions in France or abroad, or from public or private research centers.

L'archive ouverte pluridisciplinaire **HAL**, est destinée au dépôt et à la diffusion de documents scientifiques de niveau recherche, publiés ou non, émanant des établissements d'enseignement et de recherche français ou étrangers, des laboratoires publics ou privés.



Sorbonne Université – École doctorale d’Astronomie et d’astrophysique d’Île-de-France

COALESCENCES DE BINAIRES D’ÉTOILES À NEUTRONS À L’ÈRE DE
L’ASTRONOMIE MULTI-MESSAGERS : RÉMANENCES À TRÈS HAUTE ÉNERGIE
ET VOIES D’ÉVOLUTION DES PROGÉNITEURS

thèse de doctorat présentée par

M. CLÉMENT PELLOUIN

préparée

À L’INSTITUT D’ASTROPHYSIQUE DE PARIS

sous la direction de

PROF. FRÉDÉRIC DAIGNE ET DR. IRINA DVORKIN

en vue d’obtenir le grade de

DOCTEUR ÈS SCIENCES DE SORBONNE UNIVERSITÉ,
SPÉCIALITÉ ASTRONOMIE ET ASTROPHYSIQUE.

Présentée et soutenue publiquement le 8 septembre 2023, devant un jury composé de :

MARIE-CHRISTINE ANGININ	Professeure des universités Sorbonne Université	Présidente du jury
MARICA BRANCHESI	Professor Gran Sasso Science Institute	Rapportrice
BENOIT CERUTTI	Chargé de recherche CNRS Institut de Planétologie et d’Astrophysique de Grenoble	Rapporteur
EHUD NAKAR	Professor Tel Aviv University	Examinateur
ASTRID LAMBERTS	Chargée de recherche CNRS Observatoire de la Côte d’Azur	Examinatrice
FRÉDÉRIC DAIGNE	Professeur des universités Sorbonne Université	Directeur de thèse
IRINA DVORKIN	Maître de conférences Sorbonne Université	Invitée (co-encadrante de thèse)

*Binary Neutron Star Mergers in the Multi-Messenger Era:
Very High Energy Afterglows and Progenitor Evolutionary Tracks*
Clément Pellouin, December 2023.

Psyyyyyy-yi-yi!
– Psyduck.

Remerciements

Le présent document est la concrétisation de trois années de travail de thèse l'IAP, qui furent particulièrement intenses, animées, et certainement inoubliables. Malgré l'apparente austérité que la rigueur scientifique impose à cette thèse, j'aimerais profiter de ces quelques lignes pour rendre hommage à toutes celles et tous ceux qui m'ont accompagné durant ces années. La liste est longue, vais-je réussir à être concis ?

Tout d'abord, je tiens à remercier Frédéric et Irina, qui ont encadré mon travail au quotidien. Votre aide chaque jour, votre patience, votre disponibilité, votre rigueur scientifique et surtout votre bienveillance constante ont été plus que précieuses dans l'accomplissement de mon travail et mon développement scientifique, et ces quelques mots ne sauraient rendre hommage à toute l'énergie que vous avez dédié à cette thèse, en particulier pour la relecture de ce manuscrit. Je vous en suis extrêmement reconnaissant.

Je veux remercier aussi toutes les personnes qui ont constitué l'environnement scientifique de cette thèse, à commencer par Robert, à la fois expert des sursauts gamma et source intarissable d'anecdotes farfelues. Merci à Raphaël, tu as été mon mentor dès 2019 lorsque je suis arrivé en stage dans l'équipe, puis en première année de thèse alors que tu finissais la tienne. Merci enfin à tous les locataires du troisième étage pour votre accueil : Nikos, Elisabeth, Yohan, Patrick, Pasquier, Jean-Philippe, sans oublier Jean-Grégoire, Mike, Filip pour les discussions fructueuses, Filippo, Marco, David et Jingwei ! Je remercie tout particulièrement le personnel administratif de l'IAP pour votre aide au quotidien, et notamment Valérie Bona et Isabelle Guillerme pour votre réactivité impressionnante. Merci à la direction, à Valérie de Lapparent, à Christophe Gobet, et à Christophe Pichon et Stéphane Rouberol pour l'accès au centre de calcul infinity du laboratoire sans lequel une partie des résultats présentés ici n'auraient jamais pu être obtenus. Un merci tout particulier à Clotilde Laigle pour avoir accepté d'être ma marraine de thèse et être toujours une oreille attentive. A l'IAP j'ai eu la chance de rencontrer un autre Clément, absolument génial : merci pour ton écoute. Merci aussi à Hakim de me permettre d'avoir confiance sur mon niveau au ping-pong. Je remercie l'Initiative Physique des Infinis de Sorbonne Université qui a financé cette thèse, ainsi que l'Ecole Doctorale Astronomie et Astrophysique d'Île-de-France pour le temps consacré à toutes les doctorantes et tous les doctorants.

Je souhaite ensuite remercier tous les membres du jury pour vos questions lors de la soutenance, et en particulier les rapporteurs, Marica et Benoît, pour le soin prêté à la lecture de cette thèse. Je suis fier d'avoir présenté ce travail devant des pairs d'une telle valeur. Une partie du travail réalisé dans cette thèse utilise COSMIC : je remercie toutes les personnes impliquées dans ce projet pour la mise à disposition d'un tel outil de manière publique, et plus particulièrement Katie Breivik pour avoir été disponible pour répondre à mes questions.

Dans un autre registre, j'ai eu l'occasion d'enseigner durant ces trois années de thèse, ce qui a été une expérience particulièrement enrichissante. Merci à Pacôme pour la gestion du cours de modélisation numérique en physique, qui m'a conféré une grande autonomie et même permis d'être une véritable star de YouTube. Merci aussi à celles et ceux rencontrés lors du concours Ma Thèse en 180s pour les moments joyeux et animés passés ensemble lors de la préparation du concours et de l'audition ! Merci à Claudine pour tes précieux conseils sur la prise de parole en public qui sont utiles

bien au-delà du monde académique. Je veux aussi saluer la team Cargèse, vous êtes incroyables.

Il faut maintenant que je parle de tous les autres doctorants de l'IAP, avec qui on a tant partagé pendant ces trois années, et qui forment cette espère de grande famille. J'espère qu'un jour deviendra pérenne le jeu du sachet de thé sur la terrasse, auquel Pierre (tu comptes comme un doctorant), Eduardo ou Alexandre vous êtes adonnés avec passion. Je suis heureux d'être resté vivant malgré les combats de nerf réguliers, et il est probable que les bières du Lakanal, de l'Irishman, du Relax ou du café Paulette (hem) y ont bien aidé. Différents camarades de bureaux se sont succédés : tout à commencé sous la coupole, bureau 308, en compagnie de Louis, puis au bureau 318 en compagnie de Simonono, auquel s'est joint Léonard. Avec Simon, on a vite compris qu'on formerait un duo de choc, vite rejoint par Valentinanana et Aline : le début de nombreuses guignoleries ensemble. Merci à tous les trois pour les restos thai, pour les sketches et débats incessants, et bien plus ! Merci Mike pour les parties de basket-bureau et tes goûts musicaux au top ; Pierre pour ta présence inévitable et indispensable à l'IAP ; Emilie pour les parties de tarot ; Julien pour ton incroyable capacité à dire n'importe quoi tout en étant sérieux ; Axel pour les fous rires ; Amaury pour ta gentillesse si caractéristique ; Louise pour ton humour qui me fait mourir de rire ; Quentin pour les traquenards au Lakanal ; Denis pour tes blagues douteuses. La liste est longue, tant j'ai passé des moments mémorables avec vous entre randonnées, escalade ou pauses café un peu trop longues. Merci donc aussi à François, Lukas, Lucas, Eduardo, Marko, Virginia, Warren, Alexandre, Iver, Louis, Etienne, Nai, David, Alice, Emma, Mathieu, Simon, Tianxiang, Chi An, Marie, Hugo, Ira, Marion. Pour finir, je voudrais remercier de tout mon cœur Aline. Tu as illuminé ma thèse par ta présence. Merci pour ta personnalité rayonnante, ta gentillesse sans limite, ton sourire et ta confiance. Surtout ne change rien.

La vie en thèse ne se limite pas aux seuls murs du laboratoire, et pour égayer le reste du temps de mes journées, j'ai pu compter sur les meilleures colocataires du monde. Merci à Yann et Victor qui ont partagé notre toit la première année, marquée par les dahls de lentilles et le yoga. Mais merci surtout à Johanna et Inès pour ces trois et deux années incroyables, à se raconter toute notre vie et discuter principalement debout dans le couloir pendant des heures (pourquoi s'installer confortablement). Ces trois années de thèse seront à jamais associées à vous qui avez partagé mon quotidien, et j'ai toujours été très heureux de rentrer le soir pour vous retrouver (peu de chances de se voir le matin). Merci aussi à Mathieu pour avoir permis des sessions de jeux tous les jeudis avec Maxime, Johanna et Thibault. Merci à Alicia pour le triple séjour de télétravail à la montagne, à mon frère dalton Erwan de partager le même chemin que moi en astrophysique (j'espère qu'on se reverra encore de nombreuses années) et plus généralement à toutes les personnes que j'ai pu voir à Paris pendant la thèse ou que j'aurais pu oublier ici.

Un travail de thèse équilibré n'est sûrement pas possible sans des fondations solides comme un roc. C'est pourquoi je veux remercier tout le boulo-drome qui m'accompagne dans mes folies depuis au minimum dix ans, et même depuis plus de vingt ans pour certains. C'est fou de se dire qu'on a traversé toutes ces années ensemble. Pouvoir revenir aux sources est toujours utile dans les moments moins faciles, merci d'être toujours là.

Enfin, je souhaite conclure cette longue série de remerciements par remercier infiniment toute ma famille. En particulier mes parents : vous m'avez soutenu depuis toujours, et une fraction significative de l'accomplissement de cette thèse vous revient aussi, à vous, pour toute l'éducation que vous m'avez donnée et l'environnement sain dans lequel j'ai grandi. Merci aussi à Mathieu et Victor, il est difficile d'espérer avoir des petits frères plus adorables que vous. Merci enfin aux papis et mamies, aux oncles et tantes et aux cousines.

Comme vous l'avez constaté, je n'ai pas brillé par ma concision. J'espère que cela traduit l'importance que chacun d'entre vous avez eu pendant cette thèse.

Acknowledgments

The present document is the culmination of three years of doctoral work at IAP, which were particularly intense, lively, and certainly unforgettable. Despite the scientific rigor imposed for such a document, I would like, in the following few lines, to pay tribute to all those who accompanied me during these years. The list is long; can I manage to be concise?

First and foremost, I would like to thank Frédéric and Irina, who supervised my work on a daily basis. Your help every day, your patience, your availability, your scientific rigor, and above all, your constant kindness have been more than precious in the accomplishment of my work and my scientific development. These few words cannot fully express the tribute to all the energy you dedicated to this thesis, especially for reviewing this manuscript. I am extremely grateful to you.

I also want to thank all the people who constituted the scientific environment of this thesis, starting with Robert, both an expert in gamma-ray bursts and an endless source of crazy anecdotes. Thanks to Raphaël, you were my mentor since 2019 when I joined the team for an internship, and in the first year of the thesis as you finished yours. Finally, thanks to all the occupants of the third floor for being so welcoming: Nikos, Elisabeth, Yohan, Patrick, Pasquier, Jean-Philippe, but also Jean-Grégoire, Mike, Filip for the fruitful discussions, Filippo, Marco, David, and Jingwei! I especially thank the administrative staff of IAP for your daily assistance, in particular Valérie Bona and Isabelle Guillerme for your impressive responsiveness. Thanks to the direction, to Valérie de Lapparent, to Christophe Gobet, and to Christophe Pichon and Stéphane Rouberol for granting the access to the laboratory’s infinity computing center, without which some of the results presented here could never have been obtained. A special thanks to Clotilde Laigle for accepting to be my “marraine de thèse” and always being an attentive ear. At IAP, I had the chance to meet another Clément, absolutely fantastic: thanks for your listening. Also, thanks to Hakim for allowing me to have confidence in my table tennis skills. I acknowledge funding support from the Initiative Physique des Infinis (IPI), a research training program of the IDEX SUPER at Sorbonne University, which funded this thesis, as well as the Doctoral School of Astronomy and Astrophysics of Île-de-France for the time dedicated to all doctoral students.

I would like to thank all the members of the jury for your questions during the defence, and especially the rapporteurs, Marica and Benoît, for the care given to the reading of this thesis. I am proud to have presented this work in front of peers of such value. Part of the work done in this thesis uses COSMIC: I thank all the people involved in this project for making such a tool publicly available, and especially Katie Breivik for being available to answer my questions.

On another note, I had the opportunity to teach during these three years of PhD, which was a particularly enriching experience. Thanks to Pacôme for managing the course on numerical modelling in physics, which gave me great autonomy and even allowed me to be a true YouTube star. Also, thanks to those I met during the *Ma Thèse en 180s* competition for the joyful and lively moments spent together during the preparation of the competition and the audition! Thanks to Claudine for your valuable advice on public speaking, which is useful far beyond the academic world. I also want to greet the Cargèse team, you are amazing.

Now I have to talk about all the other PhD students at IAP, with whom we shared so much during these three years and who form this kind of big family. I hope that one day the game of

tea bags on the terrace, in which Pierre (you count as a PhD student), Eduardo, or Alexandre passionately indulged, will become permanent. I am happy to have stayed alive despite the regular nerf battles, and it is likely that the beers from Lakanal, Irishman, Relax, or Café Paulette (hem) helped a lot. Different office mates have succeeded each other: it all started under the dome, office 308, in the company of Louis, then in office 318 with Simononono, joined by Léonard. With Simon, we quickly understood that we would form a dynamic duo, quickly joined by Valentinana and Aline: the beginning of many antics together. Thanks to all three of you for Thai restaurants, for sketches and endless debates, and much more! Thanks Mike for the office basketball games and your top-notch musical tastes; Pierre for your inevitable and indispensable presence at IAP; Emilie for tarot games; Julien for your incredible ability to say crazy things while being serious; Axel for the laughs; Amaury for your characteristic kindness; Louise for your humor that makes me die laughing; Quentin for the ambushes at Lakanal; Denis for your dubious jokes. The list is long, as I have had memorable moments with you between hikes, climbing, or overly long coffee breaks. So, thanks also to François, Lukas, Lucas, Eduardo, Marko, Virginia, Warren, Alexandre, Iver, Louis, Etienne, Nai, David, Alice, Emma, Mathieu, Simon, Tianxiang, Chi An, Marie, Hugo, Ira, Marion. Finally, I want to thank Aline with all my heart. You illuminated my thesis with your presence. Thank you for your radiant personality, boundless kindness, smile, and trust. Please don't change anything.

Thesis life is not limited to the laboratory walls alone, and to brighten the rest of my day, I could count on the best roommates in the world. Thanks to Yann and Victor who shared our roof the first year, marked by lentil dahls and yoga. But especially, thanks to Johanna and Inès for these incredible three and two years, telling each other our entire lives and mainly discussing standing in the hallway for hours (why sit comfortably). These three years of the thesis will forever be associated with you, who shared my daily life, and I have always been very happy to come home in the evening to see you again (not much chance of seeing each other in the morning). Thanks also to Mathieu for allowing game sessions every Thursday with Maxime, Johanna, and Thibault. Thanks to Alicia for the triple mountain stay, to my brother Dalton Erwan for sharing the same path as me in astrophysics (I hope we will see each other for many more years), and more generally to all the people I have seen in Paris during the thesis or that I may have forgotten here.

A balanced thesis work is surely not possible without solid foundations. That's why I want to thank the entire boudrome that has accompanied me for at least ten years, and even more than twenty years for some. It's crazy to think that we've been through all these years together. Being able to go back to the source is always useful in less easy moments, thank you for always being there.

Finally, I want to conclude this long series of thanks by thanking my family infinitely. Especially my parents: you have supported me forever, and a significant fraction of the achievement of this thesis also belongs to you, for all the education you gave me and the healthy environment in which I grew up. Thanks also to Mathieu and Victor, it is difficult to hope for more adorable little brothers than you. Finally, thanks to my grandparents, uncles and aunts, and cousins.

As you have noticed, I have not shone with my conciseness. I hope that this reflects the importance that each of you has had during this thesis.

Résumé Court – Abstract

Résumé court

En 2017, l'ère de l'astronomie multi-messagers avec les ondes gravitationnelles s'est ouverte avec la détection de la coalescence d'un système binaire d'étoiles à neutrons – baptisée GW 170817 – et de ses contreparties électromagnétiques : un sursaut gamma court et sa rémanence multi-longueurs d'onde, ainsi qu'une kilonova. Bien que de telles détections multi-messagers soient encore rares, d'autres coalescences ont été détectées par les interféromètres à ondes gravitationnelles et aident à mieux comprendre la population d'objets compacts en coalescence. Cette thèse de doctorat vise à exploiter les observations multi-messagers de coalescences d'étoiles à neutrons de deux manières. J'ai développé un nouveau modèle réaliste pour l'émission de la rémanence des sursauts gamma provenant de la décélération de jets structurés latéralement. Dans ce modèle, la population d'électrons accélérés au choc rayonne par effet synchrotron et via des diffusions Compton inverse de ces mêmes photons synchrotron dans les régimes Thomson et Klein-Nishina. Ce modèle a été utilisé pour ajuster les données d'observation de GW 170817 et prédire son flux à très haute énergie. Ces travaux montrent que le pic d'émission est au moins deux ordres de grandeur inférieur à la limite supérieure observée. Nous fournissons également des contraintes sur les conditions d'observabilité d'événements similaires par les instruments à très haute énergie actuels et futurs. Ce modèle a également été utilisé pour analyser les premières observations de la rémanence du GRB 221009A, le sursaut gamma le plus brillant jamais observé. Cette rémanence remet en question dans ce cas le modèle le plus simple dans lequel le rayonnement est émis par un jet conique est sans structure, observé dans l'axe. Une approche complémentaire à la modélisation des contreparties électromagnétiques des événements individuels consiste à modéliser statistiquement la population sous-jacente. J'ai étudié la population de systèmes binaires d'étoiles à neutrons en utilisant un modèle de synthèse de population, COSMIC, et j'ai découvert que la voie évolutive dominante des progéniteurs de tels systèmes évolue avec le redshift. En particulier, ces travaux ont mis en avant qu'une voie évolutive dans laquelle l'une des étoiles à neutrons de la binaire est produite par l'effondrement d'une naine blanche qui grossit par accrétion peut être dominante à haut redshift. Une telle évolution produit des binaires à courte séparation et pourrait donc contribuer à une population qui coalesce dans des environnements plus denses, et dont la rémanence est également plus susceptible d'être détectée à très haute énergie. Ces populations simulées d'étoiles binaires à neutrons ont également été utilisées pour étudier le bruit de fond stochastique des ondes gravitationnelles. En conclusion, cette thèse a conduit au développement de nouveaux modèles et méthodes qui sont bien adaptés à la recherche future dans le contexte florissant de l'astronomie multi-messagers.

Abstract

In 2017, the multi-messenger astronomy era with gravitational waves was opened with the detection of a binary neutron star merger – GW 170817 – and its electromagnetic counterparts: a short gamma-ray burst and its multi-wavelength afterglow, and a kilonova. Though such multi-messenger detections are still currently rare, more mergers have been detected by gravitational wave interferometers and provide insights into the population of merging binaries. This doctoral thesis aims to leverage multi-messenger observations of binary neutron star mergers in two ways. I developed a new realistic model for gamma-ray burst afterglow emission from the deceleration of laterally-structured jets. The population of shock-accelerated electrons radiates via synchrotron and synchrotron self-Compton diffusions in the Thomson and Klein-Nishina regimes. This model has been used to fit the observational data of GW 170817 and predict its very high energy flux. We find that the emission peak is at least two orders of magnitude below the observational upper limit. We provide constraints on the observability conditions by current and future very high energy instruments for similar events. This model was also used to analyse the early afterglow observations of GRB 221009A, the brightest gamma-ray burst ever observed. This afterglow challenges the simplest model where radiation is emitted by a top-hat jet observed on-axis. A complementary approach to the modelling of the electromagnetic counterparts of *single* events is to model the *population* statistically. I studied the population of binary neutron stars using a population synthesis model, COSMIC, and uncovered that the dominant evolutionary track of binary neutron star progenitors evolves with redshift. In particular, it is found that an evolutionary track with an accretion-induced collapse of the primary into a neutron star may be dominant at high redshifts. Such an evolutionary track produces short-separation binaries and could therefore contribute to a population of mergers in higher-density environments, the afterglow of which is also more likely to be detected at very high energy. These simulated populations of binary neutron stars have also been used to study the stochastic gravitational wave background. Overall, this thesis has led to the development of new models and methods that are well adapted for future research in the blossoming context of multi-messenger astronomy.

Résumé étendu

Partie I : Contexte et plan de la thèse

L'astronomie transitoire, qui s'intéresse aux phénomènes les plus variables dans l'Univers connaît un fort essor, en particulier en ce qui concerne les phénomènes observés à très haute énergie ou *via* l'astronomie multi-messagers (Chap. 1). Ces phénomènes présentent un intérêt scientifique particulier puis qu'ils permettent d'étudier des sources qui sont typiquement associées avec des phénomènes violents et fortement énergétiques. Phénomènes emblématiques de cette astronomie transitoire, les sursauts gamma sont des événements extrêmement brillants en rayons gamma, dont l'émission dite «prompte» est produite par un mécanisme de dissipation interne de l'énergie dans un éjecta ultra-relativiste (facteur de Lorentz $\Gamma \sim 100$). Leur durée varie entre quelques centaines de millisecondes et quelques dizaines de secondes. Depuis 1998, plus de 3000 sursauts gamma ont été observés, et leur durée apparaît bimodale (Chap. 1) : les sursauts longs (de durée supérieure à 2s) sont associés à l'effondrement de certaines étoiles massives (collapsars), tandis que les sursauts courts sont généralement associés à la coalescence de deux étoiles à neutrons. Les étoiles à neutrons sont les résidus de l'évolution d'étoiles massives et sont particulièrement compactes. Lorsqu'elles se trouvent en système binaire à des séparations faibles, elles sont de particulièrement bonnes sources d'ondes gravitationnelles, qui dissipent une partie de l'énergie orbitale du système et permettent sa coalescence. Au moment de la coalescence, une partie de la matière constituant les deux étoiles à neutrons est éjectée et produit différentes émissions lumineuses transitoires de plusieurs manières (Chap. 2). Une partie de l'éjecta, dans les régions équatoriales, est le siège de la synthèse des éléments chimiques les plus lourds par le processus de capture rapide des neutrons (*r-process*) par les noyaux de fer. Les isotopes ainsi créés, particulièrement instables, libèrent une partie de leur énergie par décroissance radioactive, ce qui chauffe l'éjecta et produit une source thermique détectable entre l'infrarouge proche et l'ultraviolet pendant plusieurs jours à plusieurs semaines : la kilonova. Une autre partie de la matière éjectée est accélérée à une vitesse ultra-relativiste et est le siège de l'émission prompte du sursaut gamma. Elle est ensuite suivie d'une émission «rémanente», due à l'accélération et au rayonnement non-thermique d'électrons à l'arrière du choc relativiste produit par la décélération du jet dans le milieu interstellaire. Cette émission est observable à partir des bandes radio et jusqu'aux rayons X.

Le travail de thèse présenté ici s'inscrit plus spécifiquement dans le sillage de la détection le 17 août 2017 de l'événement GW 170817, la première coalescence d'étoiles à neutrons détectée en ondes gravitationnelles. Un suivi multi-longueurs d'onde de grande précision a révélé une grande diversité de contreparties électromagnétiques : un sursaut gamma, une kilonova et l'émission rémanente, en faisant de fait le premier événement multi-messagers en ondes gravitationnelles (Chap. 2). La plupart des prédictions théoriques étaient attendues et se sont vues confirmées par cette détection, mais un certain nombre de différences notables ont été relevées. Le sursaut gamma court associé, GRB 170817A, était très faiblement lumineux malgré la faible distance à la source (40 Mpc), ce qui a été interprété comme l'émission liée au *shock breakout* : la sortie du choc relativiste de l'éjecta dynamique dans lequel il se propage initialement (Chap. 4). L'émission rémanente, au lieu d'être initialement très lumineuse puis de décroître, a d'abord suivi une phase d'augmentation lente de

luminosité jusqu'à atteindre un pic après une centaine de jours, avant de décroître. Cette émission rémanente était toujours détectée quatre ans après l'événement. Ces caractéristiques inhabituelles s'expliquent par une observation de côté, ce que confirme également l'analyse des données en ondes gravitationnelles. Ceci est très différent des cas habituels où les sursauts gamma et émissions rémanentes observées jusqu'alors provenaient de sources à des distances cosmologiques et imposaient une vue de face du fait de la focalisation relativiste du rayonnement. Les observations de l'émission rémanente de GW 170817 ont motivé le développement de nouveaux modèles plus précis prenant en compte les effets liés à l'angle de vue et à la présence d'une structure latérale autour de la partie centrale du jet, comme discuté dans le Chap. 4. Le travail présenté dans la première partie de cette thèse (Partie II) concerne la construction d'un tel modèle et une étude de GW 170817 avec ce même modèle, en l'étendant pour la première fois à l'émission à très haute énergie.

Ceci est motivé par un autre développement observationnel récent, la détection de quelques sursauts gamma à très haute énergie (photons d'énergie ~ 1 TeV), tels que GRB 190114C ou GRB 221009A (Chap. 4). Ces détections sont particulièrement intéressantes car à de telles énergies, elles sondent d'autres processus d'émission lors de la rémanence. Les photons de plus basses énergies sont émis par effet synchrotron, tandis qu'au TeV, un modèle prometteur est la diffusion Compton inverse des photons synchrotrons sur la population source d'électrons (*Synchrotron Self-Compton*, SSC). Comme nous le montrons dans le Chap. 6, un intérêt de ces sursauts détectés à très haute énergie est qu'ils sont de bons candidats pour survenir dans des milieux à haute densité (voir aussi Chap. 3). Dans le cas des sursauts courts associés aux coalescences d'étoiles à neutrons, ils peuvent être des traceurs indirects de systèmes binaires aux temps de coalescence très courts qui ont peu de temps pour migrer en dehors des zones plus denses de formation stellaire. D'autres éléments supportent l'existence de systèmes aux temps de coalescence courts, comme la distribution des positions des sursauts courts dans leurs galaxies hôtes avec une queue de distribution à faible séparation du centre galactique. Certaines étoiles de faible métallicité ont un taux élevé d'éléments produits par le r -process. Sous l'hypothèse que la formation de ces éléments a majoritairement lieu lors de coalescences d'étoiles à neutrons, cela requiert un moyen d'enrichir le milieu interstellaire en éléments produits par le r -process alors que les produits de l'évolution stellaire sont présents en faible quantité. Cela est possible si une partie des binaires a un temps de coalescence très court.

Une approche complémentaire est donc d'étudier la population de systèmes binaires d'étoiles à neutrons, qui commence à être caractérisée par les campagnes successives d'observation en ondes gravitationnelles (Chap. 3). Les trois premières campagnes d'observation des interféromètres LIGO et Virgo ont permis de contraindre le taux de coalescences de binaires d'étoiles à neutrons dans l'Univers local, et de futurs instruments permettront de suivre son évolution avec le redshift. La deuxième partie du travail présenté dans cette thèse (Partie III) concerne donc l'étude de la population de binaires d'étoiles à neutrons, et en particulier l'évolution des étoiles parentes qui permet la formation de binaires à faible séparation. Nous identifions une nouvelle voie d'évolution impliquant la formation intermédiaire d'une naine blanche, qui permet la formation de telles binaires à faible temps de coalescence.

Partie II : L'émission rémanente de jets structurés à très haute énergie

Pour étudier l'émission rémanente d'événements individuels et déduire des observations multi-longueurs d'onde leurs propriétés physiques, j'ai développé un modèle de rémanence qui s'articule autour de plusieurs points, et que je détaille au Chap. 5. Ce modèle de rémanence, pensé pour limiter le temps de calcul, allie pour la première fois la présence d'une structure latérale et l'émission à très haute énergie. L'émission est produite par une population d'électrons accélérés à l'arrière d'un choc relativiste fort produit par la décélération du jet dans le milieu interstellaire. Le jet est latéralement structuré : la densité d'énergie initiale et le facteur de Lorentz initial du choc décroissent avec θ , l'angle avec l'axe du jet. Le milieu interstellaire peut avoir un profil de vent (dans le cas où le

progéniteur est un collapsar) ou de densité constante (pour les coalescences). Le jet décélère dans ce milieu extérieur, et nous suivons cette décélération de manière cohérente dans les trois régimes successifs : phase initiale sans décélération (*coasting phase*), régime auto-similaire de décélération (Blandford & McKee) et régime newtonien. L'expansion latérale du jet, importante dans le régime newtonien, n'est pas prise en compte dans le modèle. L'accélération des électrons et l'amplification du champ magnétique est paramétrisée de manière simple avec des paramètres de microphysique qui traduisent la fraction d'énergie injectée dans chacun des deux processus. Nous incluons un paramètre important pour l'émission à très haute énergie, qui définit la fraction d'électrons accélérés. A chaque instant, les électrons accélérés sont injectés en loi de puissance. Les processus radiatifs à l'origine de l'émission lumineuse sont traités avec grand détail dans ce modèle. Les électrons émettent à basse énergie par le processus synchrotron, et les photons ainsi créés peuvent interagir avec les électrons source par diffusion Compton inverse. Cette diffusion peut s'effectuer dans deux régimes : Thomson, dans lequel la section efficace d'interaction et l'énergie du photon après diffusion sont constantes, et Klein-Nishina, dans lequel elles décroissent exponentiellement. Pour la population de photons et d'électrons entre lesquelles les diffusions SSC ont lieu, cela implique différents régimes possibles en fonction de la prédominance de l'un ou l'autre des régimes pour la population. Dans le contexte de notre modèle, qui se veut analytique afin de permettre un temps de calcul numérique rapide, nous détaillons une méthode de détermination des formes spectrales pour le régime synchrotron auto-cohérent, qui prend en compte les diffusions SSC. Le spectre synchrotron reste donc en lois de puissance brisées, comme proposé en 2009 par Nakar et collaborateurs, et l'émission SSC est calculée de manière analytique. La production de paires par les photons de très haute énergie est également prise en compte. Enfin, nous calculons les quantités observées à partir de l'émissivité locale du jet, en prenant en compte les surfaces de temps d'arrivées égaux et les effets de relativité restreinte. Nous validons la normalisation de notre modèle en le comparant à d'autres modèles couramment utilisés dans la communauté, tel que **afterglowpy**.

L'inclusion de la structure latérale et de la possibilité d'angles de vue élevés permet de modéliser l'émission rémanente de GW 170817 et de comprendre la montée lente de la courbe de lumière et le pic tardif, respectivement. La contribution SSC permet de modéliser l'émission à très haute énergie, utile notamment dans l'analyse de sursauts tels que GRB 221009A. Nous employons ce modèle pour analyser la rémanence de GW 170817 en ajustant les observations et limites supérieures multi-longueurs d'onde à l'aide d'une exploration de l'espace des paramètres par MCMC (Markov Chain Monte Carlo). Les résultats sont présentés au Chap. 6. Nous comparons trois modèles dans lesquels il n'y a pas d'émission SSC, une émission SSC seulement en régime Thomson, une émission SSC prenant en compte le régime Klein-Nishina. Les paramètres sont compatibles avec ceux trouvés dans la littérature, et nous constatons que l'émission SSC à très haute énergie au pic de la rémanence est bien plus faible que la limite supérieure obtenue par H.E.S.S., malgré une forte dispersion du modèle au TeV du fait de l'absence de données à ajuster. Nous étudions les conditions qui auraient permis la détection d'un événement similaire au TeV avec les instruments actuels et futurs tel que le CTAO, en nous concentrant sur deux modèles, dont l'émission au TeV est modérée et optimiste. Nous constatons qu'un angle de vue plus faible augmente le flux maximal de la rémanence à très haute énergie. Cet effet géométrique est le même pour la composante synchrotron de l'émission. Une augmentation intrinsèque de l'émissivité de la rémanence est également possible, si le milieu extérieur dans lequel le jet se propage est plus dense. Dans ce cas, l'effet est plus grand sur la composante SSC que synchrotron, mais est cependant limité à plus hautes densités par la production de paires. Les détections de rémanences à très haute énergie sont naturellement favorisées par les événements ayant lieu dans des milieux à forte densité qui, dans le cas des coalescences de binaires d'étoiles à neutrons, sont de potentiels marqueurs de systèmes produits avec des séparations très faibles.

Partie III : Population de binaires d'étoiles à neutrons

L'étude statistique de tels systèmes dans le contexte des observations gravitationnelles a motivé la seconde étude présentée dans cette thèse. Il existe deux canaux principaux de formation de systèmes binaires d'objets compacts (étoiles à neutrons, trous noirs) ayant des séparations suffisamment courtes initialement pour coalescer en un temps plus court que l'âge de l'Univers (Chap. 7). Le premier, le mode de formation par binaire isolée, suppose que les deux objets compacts sont formés par une binaire d'étoiles parentes massives. Leur co-évolution doit inclure un processus permettant une réduction spectaculaire de la séparation. Les étoiles les plus massives peuvent atteindre plusieurs centaines de rayons solaires lors des phases de géante, alors que la séparation requise entre les deux objets compacts ne doit pas excéder environ cinq rayons solaires. La réduction de la séparation est possible dans ce scénario par le processus d'enveloppe commune, lors de laquelle l'objet compact formé par l'étoile primaire (la plus massive, qui évolue le plus rapidement) orbite autour de l'étoile secondaire à l'intérieur de son enveloppe. Dans ce cas, la friction dynamique permet une migration dans l'enveloppe ainsi que l'éjection de cette dernière. Le second mode de formation est la formation dynamique dans des amas d'étoiles. Dans ce cas, la densité d'objets est grande et les interactions gravitationnelles peuvent permettre la formation de systèmes binaires. La formation dynamique a une contribution faible pour la population d'étoiles à neutrons, qui sont généralement éjectées des amas après leur formation, du fait de leur vitesse propre élevée après la supernova de leur progéniteurs. Le travail présenté ici se focalise donc sur la formation par binaire isolée.

J'ai utilisé un code de synthèse de population pour simuler l'évolution d'une population de systèmes binaires : COSMIC. Cette méthode suit l'évolution de systèmes binaires d'étoiles de manière simplifiée, de façon à pouvoir générer une population sur des échelles de temps courtes. Elle suppose donc un certain nombre d'approximations et se base sur une paramétrisation simplifiée de certains processus, que je présente dans le Chap. 8. Les propriétés initiales de la population d'étoiles parentes est échantillonnée : distribution de masses, de séparations, d'excentricités, fraction d'étoiles en systèmes binaires (typiquement estimée entre 30% et 70%). Ensuite, l'évolution des étoiles contient un certain nombre de phases importantes. Chaque étoile individuellement évolue à chaque pas de temps indépendamment de la présence d'un compagnon et suit donc sa voie dans le diagramme de Hertzsprung-Russel (voir Chap. 3). Les étoiles massives sont sujettes à des pertes de masse par vents stellaires de différents types, qui dépendent du type stellaire et des conditions de température et de luminosité. La métallicité a un impact fort sur ces vents, qui sont d'autant plus forts quand la métallicité est plus élevée. Lorsque la séparation entre les étoiles est faible, un transfert de masse est possible par débordement de lobe de Roche. En fonction de la réaction de l'étoile perdant une partie de sa masse, le transfert peut être stable et continu, ou instable, auquel cas une phase d'enveloppe commune débute. La transition d'un régime à l'autre est l'un des paramètres du modèle et dépend du type stellaire. La phase d'enveloppe commune, elle, est modélisée de manière simplifiée par deux paramètres, qui traduisent la structuration du profil de densité de l'enveloppe, et la fraction d'énergie orbitale transmise dans l'enveloppe. Cela permet de déterminer la masse d'enveloppe éjectée et la séparation après cette éjection. Enfin, une autre étape importante est l'explosion de chaque étoile en supernova. Du fait de l'asymétrie de l'explosion, l'objet compact qui se forme reçoit une vitesse initiale (un *kick*) qui peut l'éjecter de la binaire. Beaucoup de systèmes binaires sont détruits ainsi, et la description de ces *kicks* est également gérée par plusieurs paramètres du modèle. Après une phase d'enveloppe commune, il peut arriver qu'un cœur d'hélium soit mis à nu. Lorsqu'une telle étoile explose en supernova, l'intensité du *kick* peut être réduite, ce qui favorise la stabilité des systèmes pour lesquels cette phase a lieu. La question de la détermination de la masse des étoiles à neutrons au moment de leur formation est encore incertaine et nous avons choisi de ne pas l'étudier.

Dans l'étude présentée dans le Chap. 9, nous utilisons COSMIC avec un choix de paramètres correspondant aux modèles physiques les plus récents. Nous produisons une population synthétique de binaires d'étoiles à neutrons à différentes métallicités. En étudiant de manière systématique

l'évolution des étoiles parentes, nous avons pu mettre en évidence trois canaux de formation dominants. L'évolution standard contient deux étoiles de masses distinctes, ce qui permet à la primaire d'évoluer, exploser en supernova et former une étoile à neutrons alors que la secondaire est toujours sur la séquence principale. La secondaire évolue ensuite; une phase d'enveloppe commune se déclenche, puis le coeur d'hélium restant après l'éjection de l'enveloppe évolue à son tour, permettant un éventuel transfert de masse, avant d'exploser en supernova et ainsi former la seconde étoile à neutrons. Une deuxième voie d'évolution concerne des binaires de masses quasi-égales lors de la formation stellaire. Dans ce cas, l'échelle de temps d'évolution des deux étoiles est quasi-similaire et la phase d'enveloppe commune a lieu avant l'explosion de la primaire en supernova. Après l'éjection de l'enveloppe, le système contient donc deux étoiles d'hélium, qui vont évoluer tour à tour et exploser en supernovae. Enfin, une troisième voie d'évolution, très différente, concerne des étoiles de faible métallicité qui vont subir une première phase de transfert de masse intense de la primaire à la secondaire, si bien que la primaire devient trop peu massive pour former une étoile à neutrons, mais forme à la place une naine blanche à partir du coeur d'oxygène et de néon. La secondaire évolue ensuite, et du fait de sa masse élevée, permet une phase d'enveloppe commune, puis un transfert de masse sur la naine blanche. Lorsque la naine blanche dépasse la masse de Chandrasekhar du fait de l'accrétion, elle s'effondre et forme une étoile à neutrons, puis la secondaire s'effondre également en étoile à neutrons. Cette voie d'évolution est peu discutée dans la littérature mais est particulièrement intéressante car elle forme des systèmes à séparations extrêmement courtes qui permettent une coalescence très rapide. De plus, elle pourrait être la contribution dominante à faible métallicité. Nous avons enfin intégré les populations de binaires générées avec COSMIC dans un modèle incluant l'histoire du taux de formation stellaire, ainsi que la relation métallicité-redshift et sa dispersion, pour simuler une population astrophysique réaliste de telles binaires. Nous observons que la voie d'évolution comprenant l'effondrement par accrétion de naines blanches est dominante à haut redshift, ce qui permettrait d'expliquer la présence de systèmes à très faibles temps de coalescences dans des sites de formation stellaire et ainsi expliquer certaines observables discutées précédemment. Nous observons également que la voie standard est sous-dominante à tous redshifts, tandis que la voie comprenant des progéniteurs de masses équivalentes contribue pour la majorité des coalescences dans l'Univers local. Ainsi, les systèmes observés en ondes gravitationnelles et sondés par les sursauts gamma courts seraient différents de ceux présents en majorité à haut redshift. Les instruments futurs comme Einstein Telescope et Cosmic Explorer permettront de détecter la population de binaires d'étoiles à neutrons jusqu'à redshift ~ 2 et ainsi de comparer nos prédictions. Les systèmes simulés par synthèse de population ont également été utilisés pour simuler le fond diffus stochastique en ondes gravitationnelles pour les instruments actuels LIGO et Virgo. Cette étude a montré que leur contribution est sous-dominante par rapport à la population de binaires de trous noirs.

Partie IV : Conclusions et perspectives

Le travail de thèse présenté ici ouvre de nombreuses perspectives dans un contexte instrumental dynamique. Je détaille dans le Chap. 10 certaines pistes d'exploration à court et moyen terme. Concernant la modélisation des rémanences, le modèle que j'ai développé peut encore être amélioré en incluant la contribution du choc en retour, l'auto-absorption synchrotron ou un traitement plus précis de la dynamique aux temps longs. Il peut d'ores et déjà être appliqué aux sursauts gamma déjà détectés à très haute énergie, et devrait permettre l'étude des détections futures, notamment grâce au nouveau CTAO, et être un outil de choix pour l'étude des sursauts gamma détectés par SVOM, un satellite franco-chinois dédié dont le lancement est prévu en 2024, et auquel le groupe de l'IAP participe. Concernant la caractérisation de la population de binaires d'étoiles à neutrons, elle devrait être améliorée par les futurs interféromètres à ondes gravitationnelles, ce qui permettra d'affiner notre compréhension des voies d'évolution à l'aide de la méthode de synthèse de population.

La méthode présentée permet aussi une étude de la population galactique de binaires d'étoiles à neutrons, qui a des propriétés différentes de la population qui coalesce dans l'Univers local. De manière générale, les outils développés durant cette thèse s'inscrivent parfaitement dans le paysage de l'astronomie multi-messagers et permettront de nombreuses futures études associées.

Contents

Remerciements	i
Acknowledgments	iii
Résumé Court – Abstract	v
Résumé étendu	vii
Contents	1
Acronyms	5
Preface	7
I Introduction	9
1 Multi-Messenger Astronomy in Connection to Gamma-Ray Bursts	11
1.1 High-Energy and Multi-Messenger Electromagnetic Transients	12
1.1.1 The High-Energy Transient Sky	12
1.1.2 Other Messengers: Cosmic Rays, Neutrinos and Gravitational Waves	13
1.2 Gravitational Waves	14
1.2.1 Generalities	14
1.2.2 Gravitational Waves from Compact Binaries	15
1.2.3 Detecting Gravitational Waves	16
1.3 Gamma-Ray Bursts	19
1.3.1 Historical Overview and Main Observations	19
1.3.2 Theoretical Models of Gamma-Ray Bursts	22
1.3.3 Two Populations of Progenitors	24
2 Observable Signatures of Binary Neutron Star Mergers and the Case of GW 170817	27
2.1 Gravitational Waves Emission	28
2.2 Kilonova (and Kilonova Afterglow)	29
2.3 Gamma-Ray Burst	32
2.4 Gamma-Ray Burst Afterglow	33
2.5 Summary	36
3 Compact Object Binaries: Formation and Population	37
3.1 Single-Star Evolution and Formation of Compact Objects	38
3.2 Direct Observations: Galactic Populations of Compact Objects	41
3.3 A New Window: Gravitational-Wave Observations of Compact Object Binaries	42

3.4	Other Indirect Constraints	44
3.5	On the Doctoral Work Presented Next	46
II	The Very High Energy Afterglow of Structured Relativistic Jets	47
4	Recent Observational Advances: Towards a Better Understanding of the Physics of Gamma-Ray Burst Afterglows	49
4.1	Gamma-Ray Burst Afterglows from Jets with a Lateral Structure	50
4.2	The Very High Energy Emission of Gamma-Ray Burst Afterglows	53
5	Modelling the Synchrotron and Synchrotron Self-Compton Emission from a Decelerating Structured Relativistic Jet	57
5.1	Relativistic Outflow : Geometry and Structure	59
5.2	Dynamics of the Deceleration	64
5.3	Accelerated Electrons and Amplified Magnetic Field	68
5.4	Emissivity in the Comoving Frame	70
5.4.1	Synchrotron and Inverse Compton Radiation for a Single Electron	70
5.4.2	Radiative Regime of a Single Electron	74
5.4.3	Electron Distribution and Associated Emission	75
5.4.4	The Pure Synchrotron Case	79
5.4.5	The Synchrotron Self-Compton Case in Thomson regime	80
5.4.6	Self-consistent Calculation of the Electron Distribution and the Compton Parameter in the General Case	80
5.4.7	Pair Production	84
5.4.8	Extragalactic Background Light	85
5.4.9	Synchrotron Self-absorption	86
5.5	Observed Flux	86
5.6	Comparison with other Afterglow Models	88
5.7	Conclusion	90
6	Short Gamma-Ray Burst Afterglows at Very High Energies: the Case of GW 170817	93
6.1	Afterglow Observations of GW 170817	94
6.1.1	Detections from Radio to X-rays	94
6.1.2	Very High Energy Upper Limits	96
6.2	The Very High Energy Afterglow of GW 170817	97
6.2.1	Fitted Observational Data	97
6.2.2	Results from the Afterglow Fitting	98
6.2.3	Discussion: Inferred Parameters	105
6.2.4	Discussion: the Predicted Very High Energy Emission of GW 170817	107
6.3	Detectability of Post-Merger Afterglows at Very High Energy and Prospects for the CTAO	110
6.4	A Population of Short Merger Time Binaries?	114
6.5	Conclusion	116
III	Population of Binary Neutron Stars	119
7	Compact Object Binaries Formation Channels	121
7.1	Isolated Binary	122
7.2	Dynamical Formation	124

7.3	Population Synthesis Models	125
8	Evolving Binary Systems: Population Synthesis with COSMIC	127
8.1	Initial Properties of Binary Systems	128
8.2	Binary Stellar Evolution	132
8.2.1	Stellar Winds	133
8.2.2	Roche Lobe Overflow	138
8.2.3	Common Envelope	141
8.2.4	Supernova Kicks	144
8.2.5	Miscellaneous	148
8.3	Summary of COSMIC Parameters	151
9	The Evolutionary Tracks of Merging Binary Neutron Stars	155
9.1	Binary Stellar Evolution Modelling with COSMIC	156
9.1.1	Model Parameters	156
9.1.2	Sampling Protocol	157
9.2	Evolutionary Sequences Classification Method	158
9.3	Evolutionary Tracks	161
9.3.1	“Standard” Evolution	161
9.3.2	Equal-mass binaries	163
9.3.3	Accretion-Induced Collapse	165
9.4	Population Properties	167
9.4.1	Properties of the Evolutionary Tracks	167
9.4.2	Impact of Metallicity on the Evolutionary Tracks	172
9.4.3	Other Possible Model Choices	176
9.5	Evolution of the Merger Rate with Redshift	176
9.5.1	Computing the Merger Rate Density	176
9.5.2	The Stochastic Gravitational Wave Background from Binary Neutron Star Mergers	178
9.5.3	Results for the Binary Neutron Star Merger Rate	179
9.6	Astrophysical Consequences: a Population of Short Delay Times	180
IV	Conclusion and Perspectives	183
10	Conclusion and Perspectives	185
10.1	Main Results of this Doctoral Thesis	186
10.2	Perspectives for Future Studies	188
10.3	General Conclusion	194
	Bibliography	195
	Appendices	214
A	Radiative Regimes and Corresponding Electron Distributions	217
B	Comparison between our Afterglow Model and the Model of Gill & Granot (2018)	223
C	Derivation of the Observed Flux from a Distant Source with Relativistic Motion	227
D	Intersection Between a Component of the Lateral Structure and the Line of Sight	233

E Publications**237**

Acronyms

AGB	Asymptotic Giant Branch
AIC	Accretion-Induced Collapse
BBH	Binary Black Hole
BH	Black Hole
BNS	Binary Neutron Star
BSE	Binary Stellar Evolution
CCSN	Core-Collapse Supernova
CE	Common Envelope
CHeB	Core Helium Burning
EAGB	Early Asymptotic Giant Branch
EBL	Extragalactic Background Light
ECSN	Electron-Capture Supernova
FGB	First Giant Branch
GRB	Gamma-Ray Burst
GW	Gravitational Wave
He-GB	Naked Helium Star, Giant Branch
He-HG	Naked Helium Star, Hertzsprung Gap
He-MS	Naked Helium Star, Main Sequence
HG	Hertzsprung Gap
IC	Inverse Compton
IMF	Initial Mass Function
KN	Klein-Nishina
MCMC	Markov Chain Monte Carlo
MS	Main Sequence
NS	Neutron Star
NSBH	Neutron Star – Black Hole binary
PISN	Pair Instability Supernova

RLOF	Roche Lobe Overflow
SFH	Star Formation History
SFRD	Star Formation Rate Density
SN	Supernova
SSC	Synchrotron Self-Compton
TPAGB	Thermally Pulsating Asymptotic Giant Branch
USSN	Ultra-Stripped Supernova
VHE	Very High Energy
VLBI	Very Long Baseline Interferometry
WD	White Dwarf
WR	Wolf-Rayet
XRB	X-Ray Binary
ZAMS	Zero-Age Main Sequence

Preface

The doctoral thesis that I present hereafter has been conducted between October 1st, 2020 and September 30th, 2023 in the team *Astrophysique des Hautes Énergies et Univers Profond* at the Institut d’Astrophysique de Paris. My work was supervised by Prof. Frédéric Daigne and Dr. Irina Dvorkin, and has been motivated by recent developments in gravitational wave astronomy and in particular the breakthrough multi-messenger detection of the binary neutron star merger event GW 170817, which was associated with a short gamma-ray burst, a multi-wavelength afterglow and a kilonova. We are only entering the era of multi-messenger astronomy with gravitational waves and many theoretical improvements should be expected in the coming years. This work was conducted with the objective to take steps in this direction.

My doctoral work has focused on the study of binary neutron star mergers under two different – and complementary – angles. I developed a new realistic model to predict the gamma-ray burst afterglow emission in the scenario where it is radiated by electrons accelerated behind the forward shock produced by the deceleration of a structured jet in an external medium. In particular, I included the self-consistent calculation of very high energy emission from synchrotron self-Compton diffusions in both Thomson and Klein-Nishina regimes. Great attention was paid to implement this model in a computationally-efficient way such that it can be used in a Bayesian context to fit observational data. This model was used to derive afterglow flux predictions at very high energy for GW 170817 and discuss observability conditions of similar events by current and future instruments (**Publication I**, submitted, Appendix E.1, Pellouin & Daigne 2023). I also used this model to study the brightest gamma-ray burst ever observed, GRB 221009A as part of the GRANDMA observational follow-up campaign analysis (**Publication II**, published, Appendix E.2, Kann et al. 2023). This model aims to leverage as much information as possible from the available and future observations of *single* events.

To study the *population* of merging binary neutron stars, I used a population synthesis algorithm, COSMIC, which allows to simulate the evolution of stellar binaries and therefore study the properties of binary neutron star progenitors. I specifically studied the main evolutionary tracks and their relative contribution to the merging binaries, depending on the progenitor metallicities. I uncovered an evolution of the dominant track of binary neutron star formation with redshift (**Publication in preparation**, Pellouin et al. 2023). I focused more specifically on evolutionary tracks producing binary neutron stars with short merger times, which are also ideal candidates for enhanced very high energy afterglow emission due to the higher density of their environments at the location of the merger. This simulated population of binary neutron stars has also been used to study the stochastic gravitational-wave background induced by the non-detected population of binary neutron stars (**Publication III**, published, Appendix E.3, Lehoucq et al. 2023).

This document is split in four main parts. In Part I, I detail the observational and theoretical foundations of this work. Part II presents the gamma-ray burst afterglow model and predictions related to the very high energy emission of GW 170817. The discussion on the progenitors of binary neutron star mergers using population synthesis is covered in Part III, where I also provide details on the numerical treatment of stellar evolution in COSMIC. A summary of the main conclusions of my work and the perspectives they open for the future are gathered in Part IV. A series of Appendices

is included at the end, where I provide additional information on some technical aspects of my work; as well as my publications as co-author in the context of this doctoral thesis.

At the time of writing, only two binary neutron stars mergers have been observed by gravitational wave interferometers, and only one was a multi-messenger detection. As the detector sensitivities improve, the future of multi-messenger astronomy will be paved with more detections, where the models and tools developed during this thesis can be used. Multi-messenger astronomy is a vibrant and still emerging field of astrophysics and it certainly is exciting times to be part of this endeavour.

Part I

Introduction

Chapter 1

Multi-Messenger Astronomy in Connection to Gamma-Ray Bursts

Contents

1.1	High-Energy and Multi-Messenger Electromagnetic Transients	12
1.1.1	The High-Energy Transient Sky	12
1.1.2	Other Messengers: Cosmic Rays, Neutrinos and Gravitational Waves	13
1.2	Gravitational Waves	14
1.2.1	Generalities	14
1.2.2	Gravitational Waves from Compact Binaries	15
1.2.3	Detecting Gravitational Waves	16
1.3	Gamma-Ray Bursts	19
1.3.1	Historical Overview and Main Observations	19
1.3.2	Theoretical Models of Gamma-Ray Bursts	22
1.3.3	Two Populations of Progenitors	24

Astronomy historically consists in observing the light – and in some cases the absence of light – emitted by the objects and structures that make up the Universe. Since the first astronomical observations, this principle has remained true and today’s new discoveries still primarily originate from observations conducted across the electromagnetic spectrum. Nevertheless, photons are not the only messenger travelling through space and time to convey valuable information. Charged particles, cosmic rays, have been observed since the beginning of the twentieth century; and neutrinos more recently. In this thesis, I will mostly discuss a fourth messenger, Gravitational Waves (GWs) – propagating fluctuations of the structure of spacetime – which have been detected only since 2015. The observation of some astrophysical objects or events with these diverse messengers constitutes what we refer to as *multi-messenger* astronomy. In this chapter, I will discuss the essential aspects of multi-messenger astronomy to study transients: sources that exhibit varying properties on short timescales, ranging from milliseconds to years. In particular, I will focus on astrophysics related to Gamma-Ray Bursts (GRBs), which are extremely bright, short-lived flashes of gamma-ray emission and are associated to other multi-messenger and multi-wavelength emissions. In Sec. 1.1, I provide an overview of extreme electromagnetic transients and the multiple messengers that are used to detect them. I then discuss more specifically GWs in Sec. 1.2 and GRBs in Sec. 1.3, which are at the core of my work.

1.1 High-Energy and Multi-Messenger Electromagnetic Transients

1.1.1 The High-Energy Transient Sky

Multiple astrophysical transient phenomena exist in the Universe. Some of them are repeating, some others are not. Among them, the most energetic are often linked to extremely compact sources: Neutron Stars (NSs) or Black Holes (BHs) and their associated processes such as gravitational collapse, accretion or ejection. These sources usually radiate electromagnetically at high energies (X-rays and gamma-rays), and are also expected to be efficient multi-messenger sources (see *e.g.* Murase & Bartos 2019).

Some high-energy transients are associated to supermassive BHs ($M_{\text{BH}} \gtrsim 10^6 M_{\odot}$, Kormendy & Richstone 1995) located at the center of galaxies. Among them, we can quote blazar flares (Murase et al., 2018) and Tidal Disruption Events (TDEs), the destruction of stars by tidal effects in the vicinity of supermassive BHs (Rees, 1988; Gezari, 2021). Some X-ray sources located away from their host galaxy center and extremely bright, Hyper-Luminous X-ray sources (HLX, $L > 10^{41} \text{ erg} \cdot \text{s}^{-1}$, Colbert & Mushotzky 1999) are believed to be accreting intermediate-mass BH. Many high-energy transients are associated to stellar-mass compact objects: NSs or BHs with $M_{\text{BH}} \lesssim 100 M_{\odot}$. The most energetic transients include the cataclysmic events that produce these compact objects: Core-Collapse Supernovae (CCSNe), that I discuss in Secs. 3.1; long GRBs presented in Sec. 1.3; and compact object binary mergers (see Secs. 1.2 and 1.3 and Chapters 2 and 3). These are non-repeating transients. Less energetic (usually observable in X-rays) transients are flaring activity around accreting BHs or NS in X-ray binaries (see Sec. 3.2); magnetar flares; and Fast Radio Bursts (FRBs). These transients may be repeating.

Transient phenomena associated with stellar-mass compact objects can be extremely variable thanks to the small size of their progenitors. The causality argument also discussed in Sec. 1.3 leads to shortest variability timescales down to milliseconds, as observed for instance in GRB light curves.

The high-energy electromagnetic radiation in these transients is sometimes thermal, *e.g.* in the internal regions of accretion disks which radiate in X-rays; but is most of the time the result of distributions of accelerated particles out of thermal equilibrium, *e.g.* in shocks or in magnetic reconnection events. When these effects occur in a relativistic outflow (*e.g.* in blazars, GRBs, microquasars), they also benefit from Doppler boosting and relativistic beaming to reach the highest energies. In these cases, non-thermal particles can radiate by several processes, like synchrotron

radiation, Inverse Compton (IC) diffusions or pair production. These effects will be at the base of our radiative model for GRB afterglow emission discussed in Chapter 5.

High-energy ($h\nu \sim 1$ GeV) and Very High Energy (VHE) ($h\nu \sim 1$ TeV) observations of the transient sky are currently possible thanks to a very favourable instrumental context. In the GeV range, the atmospheric absorption prevents observations from the ground and the observatories are therefore space telescopes: Fermi-LAT (Atwood et al., 2009) and AGILE (Tavani et al., 2009). The detection of TeV photons is possible using the Čerenkov light emitted by the cascade of secondary particles generated by the interaction of VHE photons with the upper atmosphere. This technique is used with optical telescopes in particular by the High Energy Stereoscopic System (H.E.S.S., Hinton & HESS Collaboration 2004), located in Namibia; the Major Atmospheric Gamma Imaging Čerenkov (MAGIC, Lorenz & MAGIC Collaboration 2004; Aleksić et al. 2016a,b), located at La Palma (Canary Islands); the Very Energetic Radiation Imaging Telescope Array System (VERITAS, Holder et al. 2006), located in Arizona, U.S.A.; or in water for the High-Altitude Water Čerenkov Observatory (HAWC, Abeysekara et al. 2012); located in Mexico above 4000 m of altitude; and the Large High Altitude Air Shower Observatory (LHAASO, di Sciascio & Lhaaso Collaboration 2016; Cao et al. 2019), located in China.

The most extreme transient sources are also expected to be the most promising sources of multi-messenger emission, which I discuss now.

1.1.2 Other Messengers: Cosmic Rays, Neutrinos and Gravitational Waves

Three other messengers complete electromagnetic observations to make up multi-messenger astronomy. Cosmic Rays are mostly charged nuclei traveling through space. Most of them originate from within the Milky Way, where they are magnetically confined. The main source of these Galactic cosmic rays is thought to be acceleration in Supernova (SN) remnants. On the other hand, Ultra-High Energy Cosmic Rays (UHECRs, $h\nu > 10^{18}$ eV) have an extragalactic origin and their sources are still unknown. Most astrophysical candidates to accelerate nuclei to such high energy are extreme cosmic accelerators and therefore also sources of high-energy radiation. Most discussed candidates are Active Galactic Nuclei or GRBs. For more details on UHECRs, see the review by Kotera & Olinto (2011).

A third messenger to probe the high-energy transient universe are neutrinos: light and weakly interacting elementary particles. Because their extremely small cross-section makes them especially hard to detect, neutrino astronomy only started in the 1960s and was limited to Solar neutrinos at ~ 1 MeV. These neutrinos are emitted directly at the core of the Sun and are signatures of the weak interaction in the hydrogen fusion reaction (for a review on Solar neutrinos, see Haxton et al. 2013). Neutrinos are also expected to be produced in huge quantities during CCSNe, where they are thought to carry $\sim 99\%$ of the total kinetic energy after the collapse. On February 23rd, 1987, 11 neutrinos were detected by the Kamiokande detector (Hirata et al., 1987) and associated with SN 1987A, a Galactic SN. These neutrinos emerge from the thermal radiation of the extremely hot and compact region formed after the core collapse and are currently searched for with new generations of detectors like Super-Kamiokande, and soon Hyper-Kamiokande (see the review by Scholberg 2012).

Astrophysics with high-energy neutrinos has started more recently. Neutrinos can interact with the Earth and produce cascades of secondary particles. Their Čerenkov radiation can then be detected, either in ice for the IceCube detector, located at the South Pole (Aartsen et al., 2021) or in the sea for Antares (Ageron et al., 2011) and later KM3NeT (Adrián-Martínez et al., 2016) in the Mediterranean Sea. The first IceCube detection was reported in 2013 (IceCube Collaboration, 2013). A background is currently detected (Aartsen et al., 2014) and some individual detections have recently been associated to astrophysical sources. A neutrino event was associated with a blazar flare in TXS 0506+056 (IceCube Collaboration et al., 2018), and a neutrino excess with the nearby

active galaxy NGC 1068 (IceCube Collaboration et al., 2022).

These energetic neutrinos can be produced by proton-proton interactions, which could occur with cosmic rays escaping from their source and interacting with the surrounding interstellar medium. Energetic neutrinos could also be produced by the interaction between ultra-relativistic protons and gamma-ray photons. This second process can occur in most cosmic accelerators provided hadrons are accelerated. It is therefore specifically discussed for GRBs (Sec. 1.3), though no joint detection between a GRB and a neutrino event has been made yet. For a recent review, see Guépin et al. (2022).

Finally, the most extreme phenomena discussed briefly in Sec. 1.1.1 are associated with the accelerated motion of rapid distributions of compact masses during gravitational collapses. These include CCSNe or the merger of two compact objects. These two channels – which in particular are linked with the two classes of GRBs discussed in Sec. 1.3.3 – are also the most favourable sources for an intense signal of GWs. This is the fourth messenger of multi-messenger astronomy, that was first detected in 2015 (Abbott et al., 2016).

Among all the multi-messenger phenomena discussed in this section, this thesis will be focusing on GRBs, and in particular short GRBs associated with Binary Neutron Star (BNS) mergers, as I will discuss in Sec. 1.3. The two messengers that we explore in this work are therefore light – and in particular at VHE with Čerenkov telescopes – and GWs. I discuss them in more depth hereafter, in Sec. 1.2.

1.2 Gravitational Waves

1.2.1 Generalities

The theory of General Relativity (Einstein, 1915, 1916) that describes the structure of spacetime in the presence of distributions of mass and/or energy predicts the existence of GWs, which are propagating disturbances of the spacetime metric. GWs are the solutions to the wave equation formulated by Einstein (1916):

$$\square h_{\mu\nu} = -\frac{16\pi G}{c^4} T_{\mu\nu}, \quad (1.1)$$

where $h_{\mu\nu}$ is a small perturbation in the metric assumed to be almost Minkowskian far away from massive sources. In other words, the metric is expressed as $g_{\mu\nu} = \eta_{\mu\nu} + h_{\mu\nu}$ and $|h_{\mu\nu}| \ll 1$. $T_{\mu\nu}$ is the stress-energy tensor, and \square is the usual d'Alembert operator of the Minkowskian spacetime $\square \equiv \eta_{\mu\nu} \partial_\mu \partial_\nu$. In this context, GWs propagate at the speed of light in vacuum.

GWs are produced by the accelerated motion of masses. At leading order in source velocity and with no self-gravity, the GW luminosity of a source is given by the quadrupole formula:

$$L_{\text{GW}} = \frac{G}{5c^5} \langle \ddot{Q}_{ij} \ddot{Q}^{ij} \rangle, \quad (1.2)$$

where

$$Q_{ij}(t) = \int_{\text{source}} d^3x \rho(x; t) \left(x_i x_j - \frac{1}{2} \|x\|^2 \delta_{ij} \right) \quad (1.3)$$

is the Newtonian quadrupolar moment of the source. In this context, what are potentially luminous GW sources? If we consider a source with a radius R and a mass M , the quadrupolar moment can be approximated by $Q \sim sMR^2$. In this approximation, s is a dimensionless factor encompassing the source asymmetry. In the limit case where the source is spherically-symmetric, its quadrupolar moment $Q = 0$, *i.e.* $s = 0$. Non-zero quadrupolar moments are therefore generated by non-spherically-symmetric sources with $s > 0$. A source that produces GWs, which by definition are varying with time, must have a time-variable quadrupolar moment. This implies that masses within

the source are in accelerated motion. If we note v the characteristic velocity, the corresponding dynamical timescale scales as $t \sim R/v$. We therefore express Eq. 1.2 as

$$L_{\text{GW}} \sim \frac{G}{5c^5} \left(\frac{Q}{t^3} \right)^2 \quad (1.4)$$

$$\sim \frac{G}{5c^5} \frac{s^2 M^2 v^6}{R^2} \quad (1.5)$$

$$\sim \frac{c^5}{5G} s^2 \Xi^2 \beta^6 \quad (1.6)$$

where we have defined the compactness parameter

$$\Xi \equiv \frac{GM}{Rc^2} \quad (1.7)$$

and $\beta \equiv v/c$. From Eq. 1.6, we deduce the three conditions required for a source to emit GWs efficiently. Such a source must:

- Be as far as possible from spherical symmetry ($s > 0$);
- Be special-relativistic ($\beta \rightarrow 1$);
- Be general-relativistic ($\Xi \rightarrow 1$).

In this case, the GW luminosity is extremely intense: $c^5/5G \simeq 7 \times 10^{58} \text{ erg} \cdot \text{s}^{-1} \simeq 2 \times 10^{25} L_{\odot} \simeq 4 \times 10^4 M_{\odot} c^2 \cdot \text{s}^{-1}$.

1.2.2 Gravitational Waves from Compact Binaries

The best astrophysical candidates to fulfill these three requirements are compact object binaries, *i.e.* BNSs, Neutron Star – Black Hole binaries (NSBHs) or Binary Black Holes (BBHs)¹. These systems are formed of NSs and/or BHs, remnants of the final explosions of massive stars (see Sec. 3.1). After formation, these compact object binaries radiate their orbital momentum in the form of GWs, which leads to a gradual reduction of the orbital separation, until they eventually merge. The evolution of the binary separation a and of its eccentricity e over time due to the emission of GWs is given by (Peters, 1964):

$$\frac{da}{dt} = - \frac{64G^3 M_1 M_2 (M_1 + M_2)}{5c^5 a^3 (1 - e^2)^{7/2}} \left(1 + \frac{73}{24} e^2 + \frac{37}{96} e^4 \right), \quad (1.8)$$

$$\frac{de}{dt} = - \frac{304G^3 M_1 M_2 (M_1 + M_2)}{15c^5 a^4 (1 - e^2)^{5/2}} \left(1 + \frac{121}{304} e^2 \right) e, \quad (1.9)$$

where M_1 and M_2 are the masses of the two objects. Solving numerically the coupled system of differential equations Eqs. 1.8 and 1.9 is necessary to compute the exact merger time. In Iorio et al. (2023), the authors show an approximate analytical expression that is accurate to within 1% with the true solution for $e < 0.99$, which can be used to determine the merger time without solving Eqs. 1.8 and 1.9. In practice, the binary orbit quickly circularizes during the inspiral phase. If we consider for simplicity a binary system in a circular orbit, its merger time due to the emission of GWs, t_{merg} , is found by solving Eq. 1.8 with $e = 0$:

$$t_{\text{merg}} = \frac{5}{256} \frac{c^5}{G^3} \frac{a_1^4}{M_1 M_2 (M_1 + M_2)}, \quad (1.10)$$

¹CCSNe are less promising sources of GWs due to a higher level of spherical symmetry (see *e.g.* Fryer & New 2011).

where a_i is the initial orbital separation. For a symmetric system where $M_1 = M_2 = M$, the initial orbital separation therefore scales as

$$a_i \simeq 4.8R_\odot \left(\frac{M}{1.4 M_\odot} \right)^{3/4} \left(\frac{t_{\text{merg}}}{13.8 \text{ Gyr}} \right)^{1/4}. \quad (1.11)$$

As I discuss in more detail in Chapter 7, merging compact binaries must therefore initially form with extremely short separations, which puts strong constraints on the different phases of binary stellar evolution.

The GW signal $h(t)$ from the inspiral phase of a compact object binary system has two polarisation states, often noted with the $+$ and \times subscripts. The viewing angle between the angular momentum of the system and the line of sight from the observer to the source is noted ι . In this case,

$$\begin{cases} h_+(t) &= h(t) \frac{1+\cos^2\iota}{2} \cos[2\omega(t_{\text{ret.}})] \\ h_\times(t) &= h(t) \cos\iota \sin[2\omega(t_{\text{ret.}})] \end{cases}, \quad (1.12)$$

where $\omega(t_{\text{ret.}})$ is the system orbital frequency at the retarded time related to the observation time t and the distance D travelled by GWs: $t_{\text{ret.}} = t - D/c$. The frequency $\nu(t)$ of the GW signal is therefore twice the orbital frequency of the binary. The amplitude of the GW signal is

$$h(t) = \frac{64^{1/3} G^{5/3} \mathcal{M}_{\text{chirp}}^{5/3} \omega(t)^{2/3}}{c^4 D}, \quad (1.13)$$

where we defined the binary's chirp mass

$$\mathcal{M}_{\text{chirp}} \equiv \frac{(M_1 M_2)^{3/5}}{(M_1 + M_2)^{1/5}}. \quad (1.14)$$

If the binary orbit is circular in the last orbits before the merger, $\nu(t) = \frac{1}{\pi} \sqrt{G(M_1 + M_2)/a^3(t)}$ following Kepler's third law (Eq. 8.4). It can then be shown that $\mathcal{M}_{\text{chirp}}$ is simply given by

$$\mathcal{M}_{\text{chirp}} = \frac{c^3}{G} \left(\frac{5}{96\pi^{8/3}} \right)^{3/5} \dot{\nu}(t)^{3/5} \nu(t)^{-11/5}. \quad (1.15)$$

The chirp mass of the merging binary is thus given by the frequency of the signal $h(t)$ and its evolution with time. Analysis of GW observations often shows the evolution of $\nu(t)$ as a function of time in so-called *periodograms* (e.g. Fig. 2.1). Note that the signal amplitude scales as $h(t) \propto 1/D$, a significant difference with electromagnetic waves where the observed flux scales as $1/D^2$. Improvements of the instruments' sensitivity to GWs help improve the observable range much more rapidly than for electromagnetic observations.

1.2.3 Detecting Gravitational Waves

The passage of a GW in a region of space will affect the measured distances between free-falling test masses in an orientation-dependent way, such that

$$\frac{\Delta L}{L} = h_{ij} n^i n^j, \quad (1.16)$$

where n is a unit vector in the considered direction. From Eq. 1.13, we can deduce that the amplitude of the GW signal, and thus the typical variation of length induced by the passage of a GW scales as

$$h(t) \sim 3 \times 10^{-21} \left(\frac{\mathcal{M}_{\text{chirp}}}{1.3M_\odot} \right) \left(\frac{\nu(t)}{1 \text{ kHz}} \right)^{2/3} \left(\frac{D}{10 \text{ Mpc}} \right)^{-1}. \quad (1.17)$$

The signal is so faint that it implies to measure a variation of length of the size of an atom over a distance of $\sim 10^6$ km. Long thought impossible, this quest has been realised by the two Laser Interferometer Gravitational-Wave Observatory (LIGO) GW interferometers for the first time in 2015 (Abbott et al., 2016). The detectors essentially consist in extremely high-precision Michelson interferometers where all sources of noise are carefully removed. A simplified diagram of the LIGO interferometers is shown in Fig. 1.1.

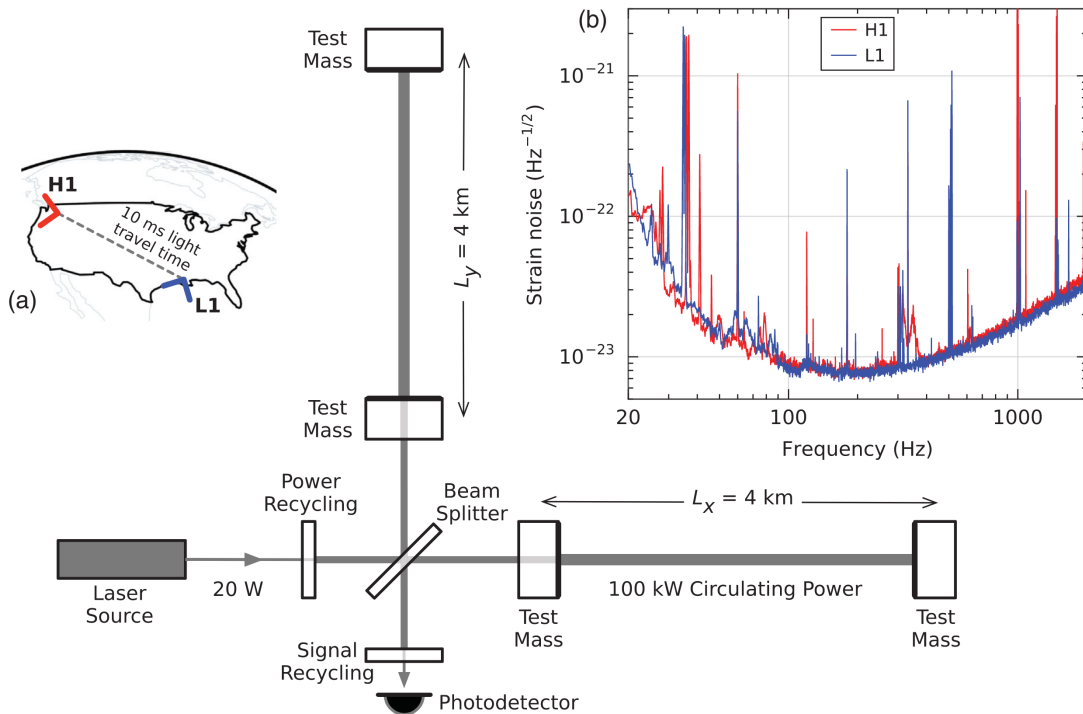


Fig. 1.1: Simplified diagram of the LIGO GW interferometers. A laser beam is split in two coherent beams propagating and recycled in two perpendicular cavities of length ~ 4 km. The signal is then recombined and the interference pattern informs on the loss of signal coherence from the passage of GWs. This figure is reproduced from Abbott et al. (2016).

On September 14th, 2015, the two LIGO interferometers detected the first compact object merger with GWs: GW 150914 (Abbott et al., 2016). The detectors' sensitivities at the time of detection are shown in Fig. 1.1. Fig. 1.2 also shows the modelled signal for this detection, as well as the evolution of the orbital frequency and separation. The signal's amplitude and frequency increase during the final cycles of the inspiral phase due to separation shrinkage, until the merger. Given the typical frequency of a stellar-mass compact object binary merger (~ 1 kHz, corresponding to the frequency range of audible sound waves, hence the frequent use of an analogy with sound for GWs), this signal is referred to as the *chirp* of the merger. GW 150914 was produced by a BBH at a distance of 410_{-180}^{+160} Mpc and contained two BHs whose masses were respectively $36_{-4}^{+5} M_{\odot}$ and $29_{-4}^{+4} M_{\odot}$ (Abbott et al., 2016).

In practice, the detection of the signal corresponding to the merger of a binary – its *waveform* – is done using the *matched filtering* technique (see *e.g.* Sathyaprakash & Schutz 2009). Real waveforms are more complex than the approximate signal shown in Eq. 1.12 and corrective effects such as the tidal forces acting on the compact objects must be accounted for. The computation of waveforms in the inspiral phase (*i.e.* before the merger) is usually performed using post-Newtonian expansions of the solutions to Eq. 1.1 (Blanchet & Damour 1989, for a review see *e.g.* Blanchet 2014). These expansions are only valid when the orbital separation is wide enough. The signal in the merger phase (*i.e.* upon contact of the two merging objects) and the ringdown (*i.e.* when the central remnant

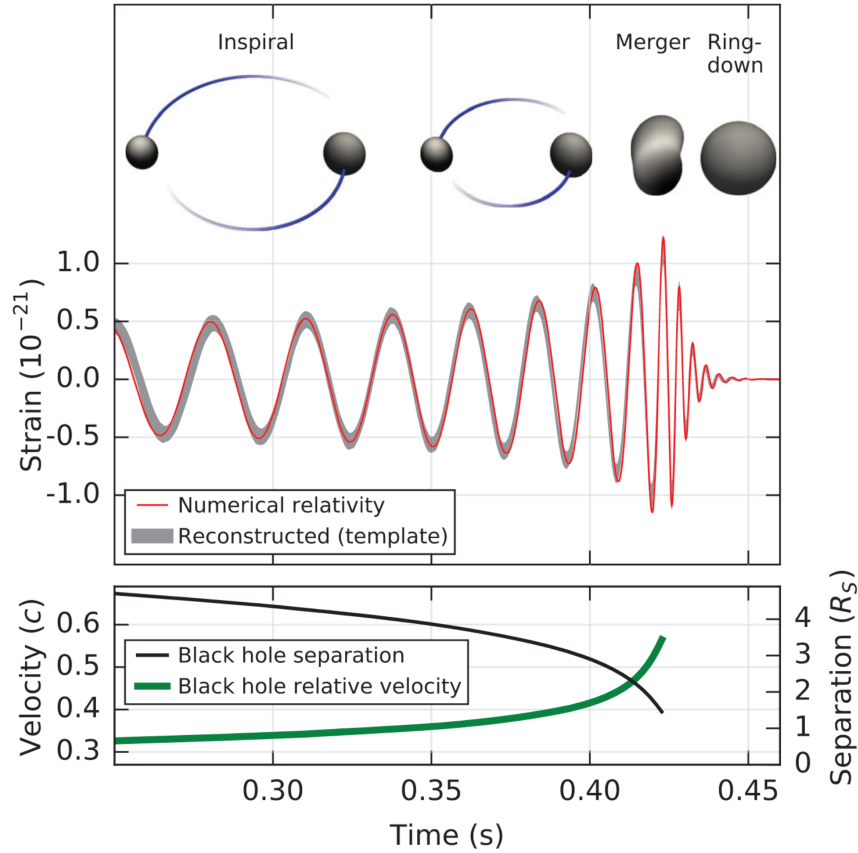


Fig. 1.2: Top: Modelled GW signal amplitude in the Hanford interferometer for GW 150914. The inset images show numerical relativity models of the BH horizons as the BHs coalesce. **Bottom:** The Keplerian effective black hole separation in units of Schwarzschild radii ($R_S = 2GM/c^2$) and the effective relative velocity given by the post-Newtonian parameter $v/c = (GM\pi\nu(t)/c^3)$, where $\nu(t)$ is the GW frequency calculated with numerical relativity and M is the total mass. This figure is reproduced from [Abbott et al. \(2016\)](#).

relaxes to a static object) are modelled using numerical relativity computations, where Eq. 1.1 is solved directly. Other techniques such as effective one-body simulations ([Buonanno & Damour, 1999](#)) and phenomenological approaches are used to compute complete waveforms. Because these techniques are computationally expensive, the automatic signal detection pipeline relies on real-time fitting of a bank of such waveforms: this is the matched filtering technique.

The amplitudes of the GW signal for the two polarisations are presented in Eq. 1.12. They depend on the source viewing angle, the distance and the chirp mass through Eq. 1.17. The chirp mass is well constrained by observations of the inspiral phase by following the evolution of $\nu(t)$ and $\dot{\nu}(t)$ as a function of t (see Eq. 1.15). However, the viewing angle and the distance are inherently correlated in the analysis of GW signals if the two polarisations are not individually measured. Another important aspect is that given the L-shape of the GW interferometers, they are more or less sensitive to each of the GW polarisations depending on the sky localisation of the source. To maximize the significance of sources detections, the two LIGO interferometers have the same orientation. The Virgo interferometer has a different orientation which covers the blind spots of the LIGO interferometers' antenna patterns, and allows to triangulate the sky localisation of an incoming GW. This has been especially useful for the follow-up observations of the BNS merger GW 170817 that I discuss in Chapter 2.

Since the detection of GW 150914, three observing runs have been conducted by the two LIGO interferometers ([LIGO Scientific Collaboration et al., 2015](#)) located in Hanford and Livingston (U.S.A.) and Virgo ([Acernese et al., 2015](#)) near Pisa (Italy), and have allowed to detect 90 compact object mergers. I discuss this population of detected sources in more detail in Sec. 3.3. At the time of writing, the fourth observing run O4 just started, also including a fourth interferometer with a yet more limited sensitivity, KAGRA (Japan, [Kagra Collaboration et al. 2019](#)), and new detections have already been reported. The sample of detected mergers is expected to be enriched with the successive future instrument upgrades.

1.3 Gamma-Ray Bursts

1.3.1 Historical Overview and Main Observations

GRBs were discovered serendipitously in the late 1960s by the Vela satellites. These were designed by the U.S. Army to monitor gamma-ray radiation from nuclear tests of the USSR. They were regularly triggered with short extra-terrestrial gamma-ray “bursts” of unknown origin. In 1973, six years after the first detection of a GRB, a first scientific publication reported 16 “short bursts of cosmic origin” ([Klebesadel et al., 1973](#)). More GRBs were detected with dedicated missions in the following years. However at the time, gamma-ray detectors did not have any localisation capability, and it was not possible to locate the GRB positions in the sky, except after a long delay by using triangulation between different satellites or spacecrafts (interplanetary network, [Hurley et al. 2011](#)). Therefore, the question of their progenitors led to the propositions of more than 100 different models, that can broadly be separated in two classes: either GRBs are produced by some ejection or accretion processes by sources within the Milky Way; or they are located at cosmological distances and emerge from cataclysmic events. A complete list of proposed GRB progenitors models was compiled by [Nemiroff \(1994\)](#). The class of galactic models was the most popular as cosmological models suffer severe energy budget constraints: given the observed gamma-ray luminosities from such distant objects, the intrinsic power of the sources has to be huge (see Sec. 1.3.2).

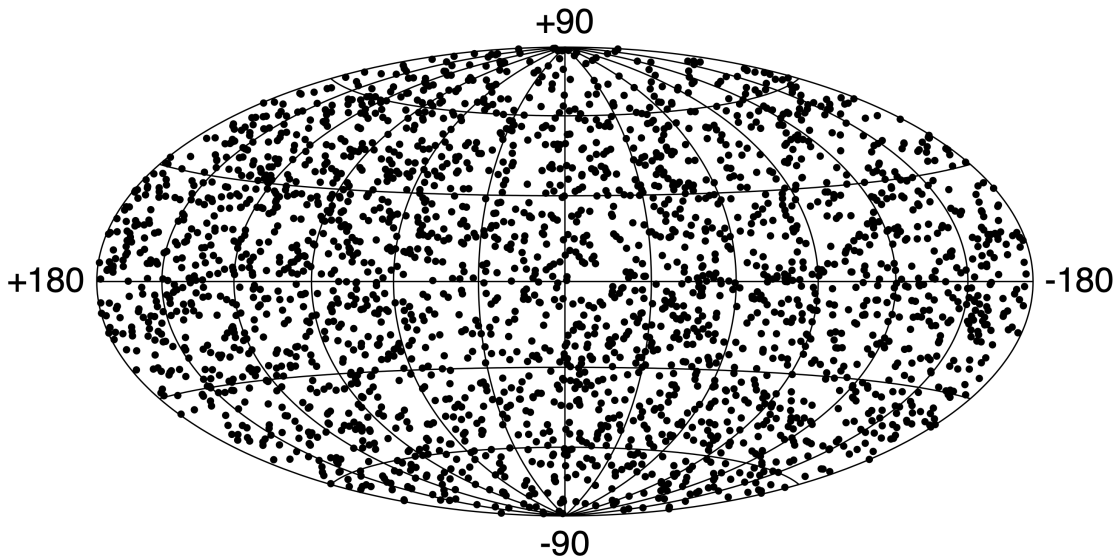


Fig. 1.3: Sky positions of 2408 GRBs detected with BATSE, in Galactic coordinates. The isotropic distribution indicates that GRB sources do not reside in the Galactic disk but are instead likely extragalactic. Figure credit: BATSE Team.

The general properties of GRBs have been discovered progressively with successive instruments. GRBs are usually extremely bright ($L_{\gamma,\text{iso}} > 10^{50} \text{ erg} \cdot \text{s}^{-1}$) and show short-time variability on timescales down to 1 – 100 ms. GRB light curves can differ a lot between different events: some consist in a peak of luminosity followed by a decline, while others have multiple pulses and sometimes precursor emission. Their spectra are non-thermal, thus indicating that they emerge from the radiation of accelerated particles. For a general introduction to GRB observations, see [Levan \(2018\)](#).

The launch of CGRO in 1991 set a new milestone for GRB physics. The Burst And Transient Source Experiment (BATSE) on its board was much more sensitive than previous experiments. During the time of the mission, BATSE revealed that the distribution of GRB localisations was isotropic in the sky, which is therefore a strong indirect indication for the cosmological origin of GRBs ([Paciesas et al., 1999](#); [Goldstein et al., 2013](#)). The distribution of sky positions of GRBs detected with BATSE is shown in [Fig. 1.3](#).

BATSE also uncovered that the distribution of GRBs durations is bimodal ([Kouveliotou et al., 1993](#); [Paciesas et al., 1999](#)), with a population of *short* GRBs, whose T_{90} (the duration of the time interval containing 90% of the total fluence) is such that $T_{90} < 2 \text{ s}$; and a population of *long* GRBs with $T_{90} > 2 \text{ s}$. We show the distribution of burst durations detected by BATSE in [Fig. 1.4](#). I also present these two populations in more detail in [Sec. 1.3.3](#). As can be observed in [Fig. 1.4](#), both classes overlap, and the T_{90} alone is not a strict criterion to classify GRBs in either of the categories. Additionally, the T_{90} measurement is affected by the distance to the source, which introduces a bias in the measured durations that favour observations of longer and brighter GRBs at larger distances; and reduces the fraction of accurate duration measurement to only $\lesssim 45\%$ of the entire sample of detections (in the context of the Swift mission, see [Moss et al. 2022](#)). Therefore, additional information such as the host galaxy type or the nature of potential detected electromagnetic counterparts must also be used to classify GRBs.

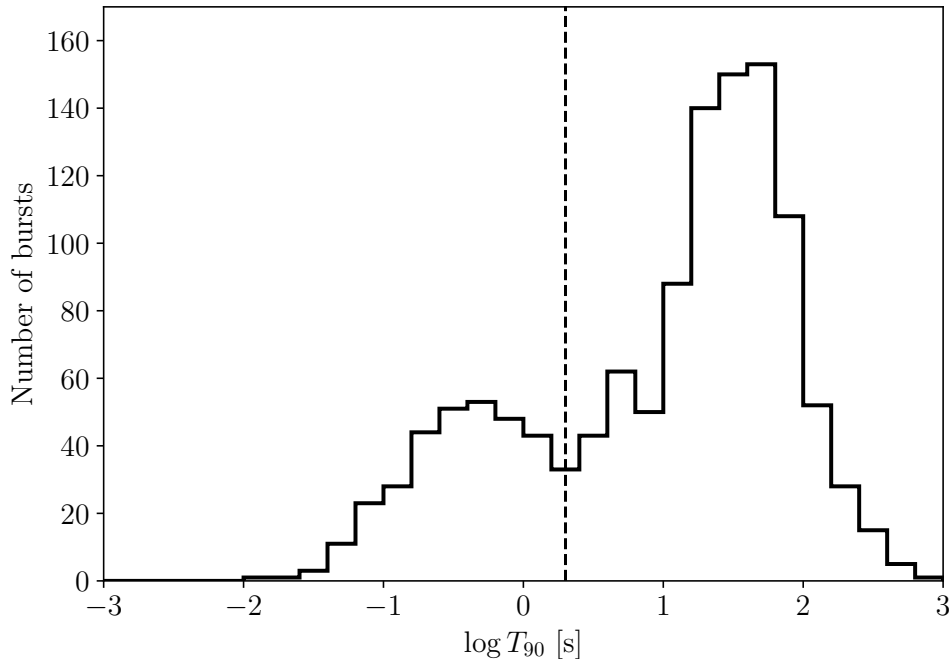


Fig. 1.4: Distribution of the T_{90} of the 2408 GRBs detected by BATSE. The population of GRBs can be divided between *short* and *long* GRBs, with a transition at $T_{90} \simeq 2 \text{ s}$, shown in dashed lines.

I anticipate on Sec. 1.3.2 to mention that such bright distant gamma-ray emission is associated to compact sources and ultra-relativistic jets. This was initially proposed by Paczynski (1986). These GRB jets were soon proposed to be the source of a longer-lasting transient powered by synchrotron radiation of a population of shock-accelerated electrons during the jet deceleration in the external medium: the GRB *afterglow* (Mészáros & Rees, 1997). The afterglow phase is now detected across the electromagnetic spectrum from radio to VHE as we discuss extensively in Chapter 2 in the case of GW 170817 and throughout Part II. It follows the *prompt* GRB emission, which constitutes the early gamma-ray signal.

The next breakthrough was made with the launch of BeppoSAX in 1996. This space telescope combined a gamma-ray detector to detect the GRB prompt emission, and an X-ray telescope allowing better localisation capabilities. BeppoSAX discovered X-ray afterglows and was able to distribute alerts with source localisations within a few hours. Following such a detection and localisation by BeppoSAX, the first GRB optical afterglow, GRB 970228, was detected in 1997 (van Paradijs et al., 1997). The same sequence led to the discovery of a new optical afterglow for GRB 970508 a few months later. In this case, absorption spectroscopy of the optical afterglow light curve, followed by the identification of the host galaxy and its spectral analysis, revealed that GRB 970508 was located at a redshift $z = 0.835$ (Metzger et al., 1997), thus providing the direct confirmation of the cosmological origin of GRBs. The number of afterglows detected with BeppoSAX was however still limited and all associated with long GRBs. Among them was the first long GRB associated with an optical SN: GRB 980425 and SN1998bw (Galama et al., 1998). This nearby GRB (~ 40 Mpc) was however intrinsically much weaker than most cosmic long GRBs.

The High Energy Transient Explorer 2 (HETE-2) space telescope launched in 2000 also combined gamma-ray and X-ray follow-up instruments. It increased the number of GRB detections with associated afterglows and uncovered the diversity of the GRB population, including soft events such as X-ray flashes or X-ray-rich GRBs. The second long GRB associated with a SN was observed by HETE-2: GRB 030329 (Stanek et al., 2003). This time, that long GRB had a standard luminosity. Such long GRB-SN associations provide strong evidence for the collapsar scenario (see Sec. 1.3.3). Finally, HETE-2 observed the first short GRB afterglow, GRB 050709 (Fox et al., 2005; Villasenor et al., 2005; Hjorth et al., 2005), indicating that the deceleration of an ultra-relativistic outflow occurs in both classes of GRBs.

In the following years, great effort was put to design a space telescope that could similarly detect GRBs in their prompt phase with a gamma-ray detector, and also point an X-ray telescope in the direction of the burst with more rapid slewing capabilities to detect the early-time afterglow, while having a better sky localisation. This is what the Neil Gehrels Swift observatory (Gehrels et al., 2004) was designed for. It was launched on November 20th, 2004 and allowed a detailed follow-up of the early X-ray afterglows of hundreds of GRBs. Swift has set a milestone by improving very significantly the fraction of GRBs detected with their X-ray afterglow ($> 90\%$). Thanks to the precise localisation of the afterglow, the redshift of approximately one third of Swift GRBs has been obtained, either with a photometric or spectroscopic determination based on the afterglow and host galaxy spectra. As of the end of June, 2023, Swift is still operating and has detected 1597 GRBs, of which 419 have associated redshifts. This allowed to study in more detail the statistical properties of GRBs (for a general review on Swift afterglow observations, see Gehrels et al. 2009), and in turn understand their progenitor populations. I discuss this in more detail in Sec. 3.4.

The 2000s and 2010s have marked the entry in an era with even more GRB detections, thanks to the Fermi Gamma-Ray Space Telescope (Fermi, Atwood et al. 2009), launched in 2008. Fermi unveiled an additional component in the spectra of the prompt emission at high energies > 100 MeV, thanks to its larger spectral coverage by its two on-board instruments: the Large Area Telescope (LAT, covering 20 MeV – 300 GeV) and the Gamma-ray Burst Monitor (GBM, covering 8 keV – 30 MeV). The LAT also discovered a long-lasting high-energy emission, probably associated to the afterglow (Ajello et al., 2019).

In 2017, a major breakthrough was the association of a short GRB with the merger of a BNS system, which marked the beginning of the era of multi-messenger astronomy with GWs and became the most significant association between a GRB and its progenitor. I discuss in detail this event, GW 170817 in Chapter 2. In recent years, the study of GRBs has also entered a new epoch with detections of their VHE emission (*i.e.* $h\nu \sim 1$ TeV) in the afterglow – and possibly also the prompt – phase, with Čerenkov telescopes. These new detections presented in Sec. 4.2, allow to probe another emission regime that requires a more detailed treatment of radiative processes during GRBs.

1.3.2 Theoretical Models of Gamma-Ray Bursts

GRBs are extragalactic sources detected at very bright luminosities. This implies that their intrinsic energy is colossal. The typical intrinsic isotropic-equivalent energy of a GRB is $E_{\gamma,\text{iso}} \sim 10^{52}$ erg. This quantity is defined as the total energy radiated by the source if its radiation is isotropic, *i.e.* not beamed. In practice, if the emission is beamed within a solid angle Ω , the true intrinsic energy is smaller, $E_{\gamma,\text{true}} = \frac{\Omega}{4\pi} E_{\gamma,\text{iso}}$. As GRBs also show short variability timescales $\delta t \sim 1 - 100$ ms, the typical size of the emitting region, if the source is assumed to be static, is given by the causality argument: $R \lesssim c\delta t \approx 3 \times 10^9$ cm $\approx 0.04R_{\odot}$.

At high energies, photons can produce electron-positron pairs (see also Sec. 5.4.6). This process has a minimum threshold $\epsilon_1\epsilon_2 \approx 2(m_e c^2)^2$. This corresponds to the typical observed spectral range of the observed GRB photon energy ($\epsilon \sim 1$ MeV). The optical depth to pair production is then approximately (see *e.g.* Lithwick & Sari 2001)

$$\tau_{\gamma\gamma} \sim 10^{12} \left(\frac{E_{\gamma,\text{iso}}}{10^{52} \text{ erg}} \right) \left(\frac{\delta t}{100 \text{ ms}} \right)^{-2} \left(\frac{E_p}{200 \text{ keV}} \right)^{\beta-2} \left(\frac{\epsilon_2}{1 \text{ MeV}} \right)^{\beta-1}, \quad (1.18)$$

where $\beta \approx 2.3$ is the photon index of the prompt gamma-ray spectrum, and E_p is the observed peak energy of the GRB. Therefore, $\tau_{\gamma\gamma} \gg 1$ given the typical observed properties of GRBs: these sources should be opaque to their own gamma-ray radiation due to pair production, and therefore not emit these gamma-ray photons. This puzzle has been known as the *compactness* puzzle.

The compactness problem is solved by introducing relativistic motion of the source. This was originally discussed by Rees (1966) in the context of radio sources. If the radiating source has an ultra-relativistic motion with $\Gamma \gg 1$ (see Eq. 5.1), relativistic beaming funnels all radiation in a cone in the direction of motion, with an opening angle $\theta \sim 1/\Gamma$. This has two implications: only a fraction of the emitting region, of size $R(1 - \cos\theta) \sim R/\Gamma^2$ is visible by a distant observer; and the interaction angle between photons is strongly reduced ($\sim 1/\Gamma$) compared to an isotropic photon field, which increases the threshold and reduces the interaction cross-section for pair production. The opacity in the case of a relativistic source is therefore

$$\tau_{\gamma\gamma,\text{rel}} = \tau_{\gamma\gamma} \times \Gamma^{-2(\beta+1)}. \quad (1.19)$$

For a source with a relativistic motion $\Gamma \gtrsim 100$, the compactness puzzle is solved. Other sources of opacity can in principle increase the total optical depth for gamma-ray photons and have been discussed in the context of GRBs, but pair production is the dominant source of opacity. As shown by Lithwick & Sari (2001); Hascoët et al. (2012b), $\Gamma \gtrsim 100$ remains the necessary condition for the successful gamma-ray emission of GRBs.

Given the extreme energy required to accelerate material at ultra-relativistic velocities, it is expected that the total mass ejected is relatively small. Additionally, material may only be accelerated in a narrow geometric region, in the form of a jet. This is confirmed by the subsequent observations of achromatic jet breaks in GRB afterglows (see Sec. 4.1 and Rhoads 1997), appearing when the relativistic beaming angle opens up to the jet opening angle during its deceleration (see Fig. 4.1).

GRBs are therefore emitted by jetted ultra-relativistic material from extragalactic sources, which naturally brings the following question: what are those sources? Given the typical variability

timescale, they are expected to be small regions of space, with radii $R \ll R_{\odot}$. The best sources for GRB emission are therefore naturally related to compact objects: NSs and BHs. Given the transient nature of GRBs and the huge energy they release, these sources are also expected to eject material and therefore be connected to explosive or destructive events involving the formation of such compact objects. The bimodal duration distribution shown in Fig. 1.4 hints towards two classes of progenitors: long GRBs associated with the core-collapse of some massive stars (*collapsars*); and short GRBs associated with BNS (and possibly NSBH) mergers. I discuss them in Sec. 1.3.3. In both cases, it is expected that the event produces a central remnant, typically a stellar-mass BH, and that an accretion disk immediately forms, either from the infalling of material from the outer envelope of the collapsing star in the collapsar scenario, or from the ejection of NS material by tidal forces upon merger in the BNS merger scenario.

The mechanisms responsible for the ejection and acceleration of the GRB jet are still poorly constrained. Several scenarios have been suggested in the literature:

- A thick accretion disk immediately forms around the central remnant. Its temperature is extremely high, such that the disk cools by radiating neutrinos. Subsequent neutrino-antineutrino annihilation can deposit energy along the rotation axis, where the baryonic content is typically lower due to the centrifugal force. This can lead to the relativistic ejection of a jet (Meszaros & Rees, 1992; Mochkovitch et al., 1993). However, this process is probably not efficient enough to be invoked for all observed GRBs. It also does not provide a natural collimation mechanism for the jet and is therefore usually not favoured.
- Most realistic models of jet ejection invoke a strong magnetic field at the base of the flow and are based on the *Blandford-Znajek* process (Blandford & Znajek, 1977). In this model, if the central object is a rotating Kerr BH, some of its energy can be extracted by magnetic currents in the ergosphere. Currently, most realistic GRB models introduce strong and large-scale magnetic fields at the base of the jet (see e.g. Tchekhovskoy et al. 2008). The efficiency of the conversion of magnetic energy to kinetic energy during the following propagation of the ejecta is another open issue, so that the magnetization of the ejecta at large distance is uncertain (Spruit et al., 2001; Granot et al., 2018).

During the early phases of its propagation, the jet can interact with the envelope of the collapsing star (in the collapsar scenario) or with material ejected before the jet launching (in the merger scenario). This gives rise to the development of a strong forward shock. At the head of the jet, a reverse shock also forms and separates the head from the rest of the jet. Material from the propagation medium is therefore pushed to the sides of the jet head, while ejected material is also deflected during the interaction with the reverse shock. These phenomena lead to the formation of a cocoon that surrounds the jet. As discussed in the review by Nakar (2020), the properties of the jet-cocoon interaction may in some cases lead to the further collimation of the jet, or if the cocoon feedback is weak, the jet remains conical. The propagation of the jet in the ejecta depends on the energy injection by the source of the jet, which is usually referred to as the *central engine*; and on the properties of the propagation medium. The energy from the central engine is used for the jet to pierce through the ejecta. If the rate of energy injection in the jet is too small or if the central engine is not active long enough, the jet may not escape its surrounding ejecta and is called a *choked* jet. On the contrary, jets that escape the surrounding material are *successful* jets. Due to this complex early-time interaction, the observed duration of GRBs is shorter than the ejection duration. It is therefore expected that short GRBs are contaminated by some long GRBs progenitors (Bromberg et al., 2013). Additionally, during this early propagation in a dense environment, the jet is expected to develop a lateral structure, which we discuss more extensively in Sec. 4.1.

The processes leading to the prompt emission of GRBs are still a matter of debate. It can be shown that reproducing the short-time variability observed in GRBs requires an *internal* dissipative process in the relativistic ejecta (Sari & Piran, 1997). Different dissipative and radiative processes

have been suggested in the literature for the origin of the GRBs prompt emission (see *e.g.* Piran 2004). The first emission zone is the photosphere, *i.e.* the region where the jet becomes transparent to its own radiation. If the emission occurs at the photosphere, the radiated spectrum should be quasi-thermal (Paczynski, 1986; Goodman, 1986; Daigne & Mochkovitch, 2002; Pe’er, 2008), but some authors have suggested that sub-photospheric dissipation may affect the spectrum to become non-thermal (Rees & Mészáros, 2005; Giannios & Spruit, 2007; Beloborodov, 2010). These models are known as *dissipative photospheric* models. Another possibility is that energy dissipation occurs in the optically thin regime above the photosphere. If the jet is weakly magnetized, colliding shells of ejecta with different Lorentz factors can produce the GRB emission (*internal shocks*, Rees & Meszaros 1994; Kobayashi et al. 1997; Daigne & Mochkovitch 1998). For highly magnetized jets, *magnetic reconnection* can dissipate significant quantities of energy (see *e.g.* Thompson 1994; Spruit et al. 2001; Zhang & Yan 2011). In these two scenarios, soft gamma-ray radiation is powered by the synchrotron radiation of accelerated electrons. The physics of the afterglow associated to the deceleration of the jet in the external medium is much better understood and will be discussed in detail in Part II.

1.3.3 Two Populations of Progenitors

I discussed the bimodal distribution of GRB durations in the BATSE sample previously (see in particular Fig. 1.4). Except for its duration, the prompt emission of long and short GRBs has similar properties, even if short GRB spectra are usually harder. Short GRB afterglows are however typically fainter, and the host galaxies of these two populations of GRBs also have different properties. This suggests that long and short GRBs share common physics – internal dissipation in a relativistic ejecta during the prompt phase, followed by the deceleration of a relativistic jet during the afterglow – but are associated with two distinct classes of progenitors.

Long Gamma-Ray Bursts and the Collapsar Scenario

Long GRBs are associated to a small fraction of the core-collapses of massive stars (Woosley, 1993), but the fraction of such massive stars leading to the emission of a long GRB is still uncertain (see *e.g.* Palmerio & Daigne 2021). The physics of CCSNe are described more extensively in Secs. 3.1 and 8.2.4, but I introduce some important elements here. The timescale of the core-collapse is a few milliseconds. After the collapse of the core, a central remnant is formed, a stellar-mass BH. Depending on the properties of the collapsing core (*e.g.* its angular momentum), the collapse may either be prompt or there may exist a transient hyper-massive NS that later collapses into a BH. These delayed and rapid collapse scenarios have been proposed by Fryer et al. (2012) and are described in Sec. 8.2.4. They affect the final mass of the central remnant and the amount of energy deposited back in the stellar envelope by infalling material being re-ejected after the collapse of the core.

GRB progenitors require particular conditions to successfully launch a relativistic jet in terms of mass, metallicity, rotation, or even the presence of a companion star, which make them rare among the total population of CCSNe (Levan et al., 2016). In the collapsar scenario, the central engine is a BH surrounded by an accretion torus and the envelope of the collapsing star. In this scenario, the GRB jet propagates through the stellar envelope, which is expected to have a gradual density decrease with radius (see Sec. 5.2, Eq. 5.16). Because massive stars evolve on short timescales (typically a few tens of Myrs, see Sec. 3.1), their explosions are expected to occur close to their formation sites, *i.e.* in star-forming regions.

Observationally, it has been found that most long GRBs occur in faint star-forming galaxies (*e.g.* Sokolov et al. 2001; Palmerio et al. 2019), and most of the time in the bright ultra-violet central regions of their hosts (Fruchter et al., 2006; Lyman et al., 2017). Both observations indicate that long GRBs are indeed located in star-forming regions.

Several long GRBs have been followed-up by optical telescopes which found associated SNe. The first such examples are the association between GRB 980425 and SN1998bw (Galama et al., 1998); and GRB 030329 (Stanek et al., 2003), as mentioned in Sec. 1.3.1. Note that puzzling GRBs are sometimes found. For instance, GRB 211211A was a recent long GRB, which was associated to a kilonova (Rastinejad et al., 2022; Yang et al., 2022; Troja et al., 2022a), a signature expected in the merger scenario discussed below. This stresses again the fact that GRB classification cannot be based on the duration only.

The core-collapse of a massive star can also generate GWs due to the anisotropies of the collapse. However, as discussed by *e.g.* Gottlieb et al. (2023), they are too faint to be detected by current GW interferometers. Nearby events could be detected with third-generation detectors, as I discuss in Chapter 10.

Short Gamma-Ray Bursts from Binary Neutron Star Mergers

The progenitors of short GRBs have long been uncertain. These bursts do not occur in specific galactic types, and therefore do not show signs of correlation with star formation. Most of the observational properties of short GRBs are detailed in Berger (2014). Contrary to long GRBs, the distribution of the galactic offsets in their hosts has a larger dispersion. Some of them are observed at large offsets (Fong & Berger, 2013). This supports the idea that short GRBs originate from the mergers of compact binaries, in particular BNSs or NSBH if the NS does not directly plunge into the BH during the merger (Eichler et al., 1989; Narayan et al., 1992; Mochkovitch et al., 1993). In this scenario, the BNS (or NSBH) is given a natal kick upon formation of the second compact object (see Sec. 8.2.4) and migrates in its host until the merger, induced by the radiation of GWs (see Eqs. 1.8 – 1.9). Because the merger time $t_{\text{merg}} \propto a^4$ (see Eq. 1.10), small variations in initial separations lead to much larger merger time differences.

BNS mergers are also expected to create an accretion disk made of a small fraction of material from the tidal disruption of both NSs at the merger. The external conditions at jet launching differ in BNS mergers. While GRB jets from collapsars initially propagate through the infalling envelope, GRB jets from BNS mergers are accelerated in the ejected material that will eventually produce the kilonova signal (see Sec. 2.2). This shows that due to the different profiles of the environments in which the jets propagate in both classes of progenitors, the observed GRB properties may differ.

The detection of GW 170817, presented in Chapter 2, set a milestone in the understanding of short GRB progenitors. This event was the first – and so far the only – association of a BNS merger detected with GWs, of a short GRB and the associated kilonova. This confirmed that BNS mergers are indeed at least a sub-class of short GRB progenitors. In this thesis, I specifically study such BNS mergers. I will describe in the next chapter the observations of GW 170817

Chapter 2

Observable Signatures of Binary Neutron Star Mergers and the Case of GW 170817

Contents

2.1	Gravitational Waves Emission	28
2.2	Kilonova (and Kilonova Afterglow)	29
2.3	Gamma-Ray Burst	32
2.4	Gamma-Ray Burst Afterglow	33
2.5	Summary	36

The mergers of Binary Neutron Star (BNS) systems have been long thought to be the most promising sources for multi-messenger observations with Gravitational Waves (GWs). On August, 17th, 2017, the first GW detection of a BNS merger was reported and was soon followed by electromagnetic counterparts. This event, known as GW 170817, became one of the most followed-up astrophysical transient source in the history of astronomy, and featured most of the detectable signatures predicted by the theory of BNS merger emission (*e.g.* Nakar 2020): the GW signal of the inspiral phase (Sec. 2.1), an optical/near-infrared kilonova (Sec. 2.2), a short Gamma-Ray Burst (GRB) (Sec. 2.3), and a GRB afterglow (Sec. 2.4). In this chapter, I present these observed signals associated to GW 170817 and relate them to corresponding emission processes and models.

2.1 Gravitational Waves Emission

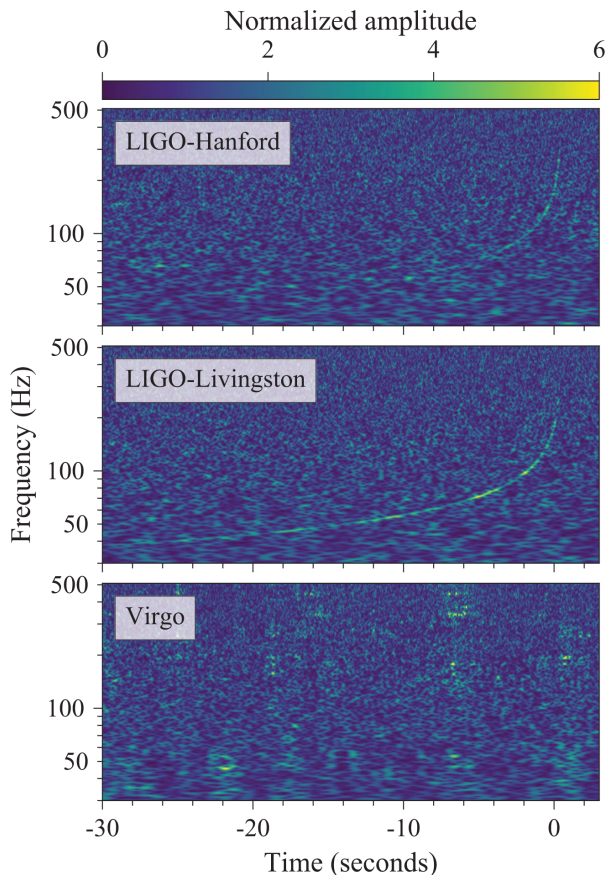


Fig. 2.1: Time-frequency map of the GW signal of GW 170817, as observed by the three GW interferometers LIGO-Hanford (top), LIGO-Livingston (middle) and Virgo (bottom). The inspiral is detected for ~ 100 s by the two LIGO interferometers, and no signal is detected by Virgo. In this figure, additional noise sources and a glitch in the signal of the LIGO-Livingston interferometer have been removed. This figure is reproduced from Abbott et al. (2017b).

As discussed in Sec. 1.2, the inspiral of a BNS up to its merger is expected to emit GW radiation. On August, 17th, 2017, the two LIGO interferometers (Ligo-Hanford and LIGO-Livingston) detected a transient GW signal lasting ~ 100 s. Binary Black Hole (BBH) mergers are only observable in the frequency band of these interferometers for at most a few seconds before the merger. This long-duration signal was therefore the signature of the merger of two lower-mass compact objects, later identified as two Neutron Stars (NSs). As reported in Abbott et al. (2017b) and shown in

Fig. 2.1, the signal was clearly detected by the two LIGO interferometers (though there was a glitch around the time of the merger in the LIGO-Livingston data that was corrected for the analysis of GW 170817); but not by Virgo. However, given the intensity of the signal in the two LIGO interferometers and the estimated source distance and sky localisation, the signal was within the sensitivity limits of Virgo and could have been detected. This was an indication that the merger was located in one of the blind spots of Virgo (see Sec. 1.2, Eq. 1.12). Thanks to the high significance of the signal in the LIGO interferometers and the non-detection by Virgo, the merger was localised within a 31 deg^2 (this was refined to 29 deg^2 a few hours later) area and the distance, though degenerate with the viewing angle was estimated to $D_L \sim 40_{-14}^{+8} \text{ Mpc}$ (Abbott et al., 2017c). I show the GW localisation in green in Fig. 2.2. After a systematic search for optical transients in galaxies located within this error region, which led to the historic detection of the kilonova (see Sec. 2.2), GW 170817 was later found to be hosted in NGC 4993, an old galaxy with a low star formation rate (Coulter et al., 2017; Pan et al., 2017), located at a distance $D_L = 40 \text{ Mpc}$. The distance to NGC 4993 was later refined to $D_L = 40.7 \pm 3.3 \text{ Mpc}$ (Cantiello et al., 2018). GW 170817 occurred at a projected distance of $\sim 1.9 \text{ kpc}$ to the galactic center. While this projected separation is smaller than typical short GRB offsets in their host galaxy, the surrounding stellar population is old and there is no evidence for the presence of a young stellar cluster in the vicinity of GW 170817 (Levan et al., 2017). This is consistent with a delay between the BNS formation and its merger, allowing a migration to regions of the galaxy with little star formation due to the natal Supernova (SN) kick imparted to the BNS upon formation, as introduced in Sec. 1.3.3. However, the small offset is a potential hint for a smaller natal kick than usual given to the binary. I also discuss this extensively throughout Part III.

The analysis of the GW inspiral signal allowed to constrain the chirp mass of the system with high accuracy (see Eq. 1.15): $\mathcal{M}_{\text{chirp}} = 1.188_{-0.002}^{+0.004} M_\odot$. The individual masses of the merging compact objects are however less constrained by the signal from the inspiral phase. In a scenario where the two NSs have low spins, the masses are $M_1 = 1.36 - 1.60 M_\odot$ and $M_2 = 1.17 - 1.36 M_\odot$ at 90% confidence (Abbott et al., 2017c, 2019b). Constraints were also put on the tidal deformability of the NSs, which in turn led to new constraints on the equation of state of ultra-dense matter in neutron stars interiors (Abbott et al., 2019b). The analysis of the GW signal (see Eq. 1.12) put constraints on the viewing angle $\iota \lesssim 55 \text{ deg}$. After an additional analysis including the accurate localisation and distance of NGC 4993, Finstad et al. (2018) refined this value to $\iota = 32_{-13}^{+10} \pm 1.7 \text{ deg}$.

Given the limited sensitivity of GW interferometers during the second observing run during which GW 170817 was detected, the ringdown signal after the merger could not be observed. This detection would inform on the newly-formed compact object and possibly on the presence – or not – of an unstable hypermassive NS for up to a few seconds, that is predicted in some BNS merger simulations (Bartos et al., 2013). The properties of the post-merger evolution and especially of the central collapsed object can modify the amount of ejected material, the outflow geometry, leading to potentially observable signatures in the electromagnetic counterparts (*e.g.* the possibility of a blue component in the kilonova, see Sec. 2.2 and Metzger 2017, 2019).

2.2 Kilonova (and Kilonova Afterglow)

As discussed in Metzger (2017, 2019), some material from the merging NSs may be ejected on a dynamical timescale (see also *e.g.* Rosswog et al. 1999) of a few milliseconds due to tidal forces or compression when the NS surfaces enter in contact. This dynamical ejecta typically has masses in the range $10^{-4} - 10^{-2} M_\odot$ (Hotokezaka et al., 2013) and an ejection velocity $v \sim 0.1 - 0.3c$.

Following the disruption of the progenitors, an accretion disk composed of some ejected material which is not immediately unbound or falling back onto the central remnant may also form around the central object (*e.g.* Metzger et al. 2009). This disk can seed a second outflow, mostly in the polar direction, over timescales of up to a few seconds. The disk wind ejecta is typically more massive

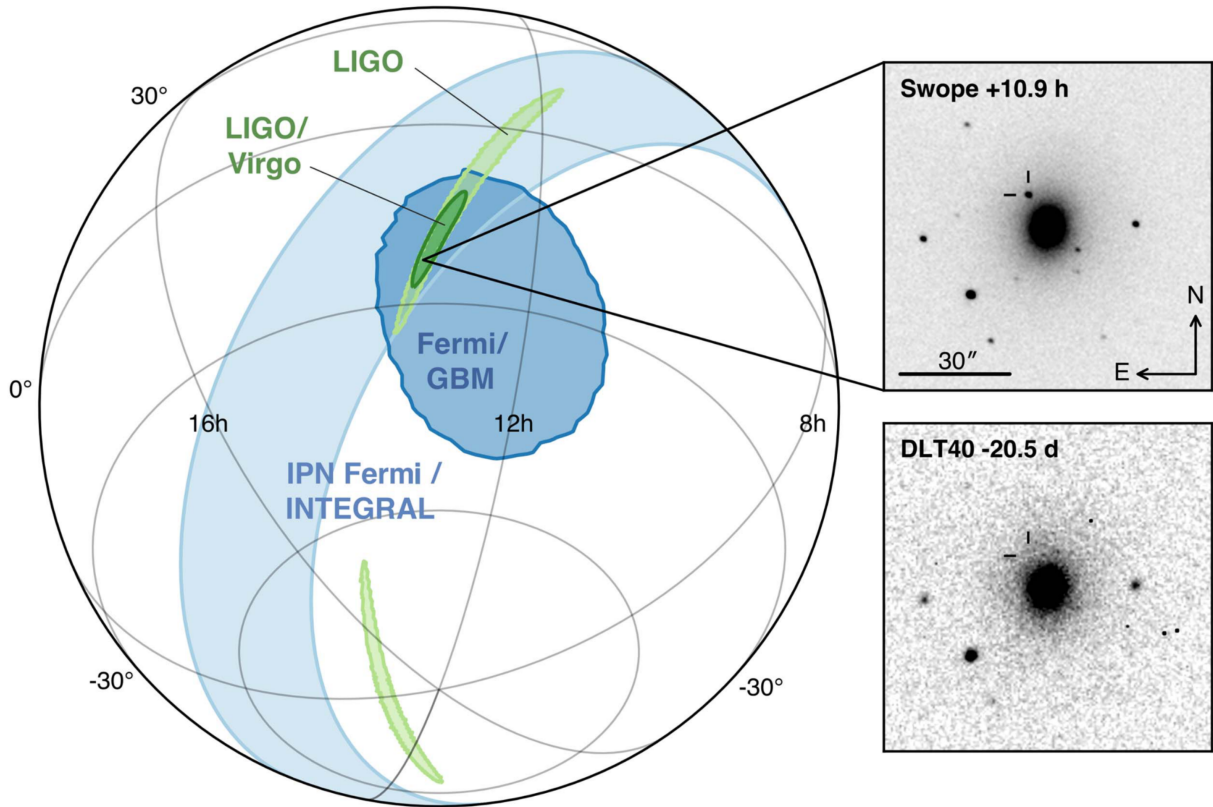


Fig. 2.2: Sky localisation of the GW, gamma-ray, and optical signals. The left panel shows an orthographic projection of the 90% credible regions from LIGO (190 deg^2 ; light green), the initial LIGO-Virgo localisation (31 deg^2 ; dark green), triangulation from the time delay between Fermi and INTEGRAL (light blue), and Fermi-GBM (dark blue). The inset shows the location of the apparent host galaxy NGC 4993 in the Swope optical discovery image at 10.9 h after the merger (top right) and the DLT40 pre-discovery image from 20.5 days prior to merger (bottom right). The reticle marks the position of the transient in both images. This figure and caption are reproduced from [Abbott et al. \(2017c\)](#).

($10^{-2} - 10^{-1} M_{\odot}$) and slower ($v \sim 0.01 - 0.1c$). Alternatively, such a neutrino-driven polar outflow could also be directly emitted by the central object if there is a transient hypermassive NS stage before the remnant collapses to a Black Hole (BH), as also presented in [Metzger \(2017, 2019\)](#).

Those different possible ejecta are neutron-rich and seeded with the iron from the crust of the NSs, but the neutron fraction differs: the equatorial dynamical ejecta from the disk has $Y_n \gtrsim 0.9$ while the polar ejecta has $Y_n \lesssim 0.7$. Due to the high neutron densities and the outflow velocities, the seed iron nuclei are enriched in neutrons by rapid neutron capture on timescales shorter than the radioactive β^- decay of the nuclei. This phenomenon is called the r -process and is responsible for the production of more than half of the elements heavier than iron ([Burbidge et al., 1957](#); [Cameron, 1957](#)). r -process is only efficient for a few seconds after the ejection of material. Simultaneously, β^- decay increases the atomic number of the newly synthesized elements by converting the neutrons in excess into protons: ${}^A_Z X_1 \rightarrow {}^A_{Z+1} X_2 + e^- + \bar{\nu}_e$. This occurs at a slower rate than the neutron capture, such that the elements are always in excess of neutrons. β^- decay then occurs on timescales of hours to days depending on the isotope considered, thus releasing radioactive energy in the outgoing material in that period. This energy heats up the ejecta, which radiates as it becomes optically thin. Given the different neutron fractions in the outflows, the r -process elements produced differ depending on the region. The equatorial outflow is more prone to be lanthanide-rich. Because lanthanides have higher opacities, this ejecta radiation peaks at later times and is redder. Conversely, the polar outflow does

not synthesize lanthanides and is bluer. This transient optical and near-infrared emission is known as the *kilonova*. It typically decays in timescales of a week. Note that if the polar ejecta is mainly powered by a neutrino-driven wind during a hypermassive NS stage, the blue kilonova could be a feature only present with low-mass BNSs. This is discussed for the second BNS merger detected in GWs, GW 190425 (Abbott et al., 2020a) with a high total mass (see Sec. 3.3). Unfortunately, no counterpart was detected, probably due to a large distance and a very large sky localisation error.

Modelling the kilonova emission requires to follow the seeding of energy in the ejecta from the radioactive decay of a population of unstable heavy elements, across multiple timescales. There are several underlying uncertainties that challenge kilonova models. The nuclear network (*i.e.* the transitions between elements and isotopes for all possible neutron-rich isotopes), including the details of all the interaction cross-sections and elements half-lives is currently limited by theoretical physics models. There are also uncertainties concerning the atomic physics of stable heavy nuclei in high ionization states, which challenges the interpretation of observed kilonova spectra. These current shortfalls in turn introduce uncertainties in the *r*-process yield of the kilonova ejecta, which impacts our understanding of the history of chemical enrichment of the Universe in heavy elements, which I discuss in Sec. 6.4.

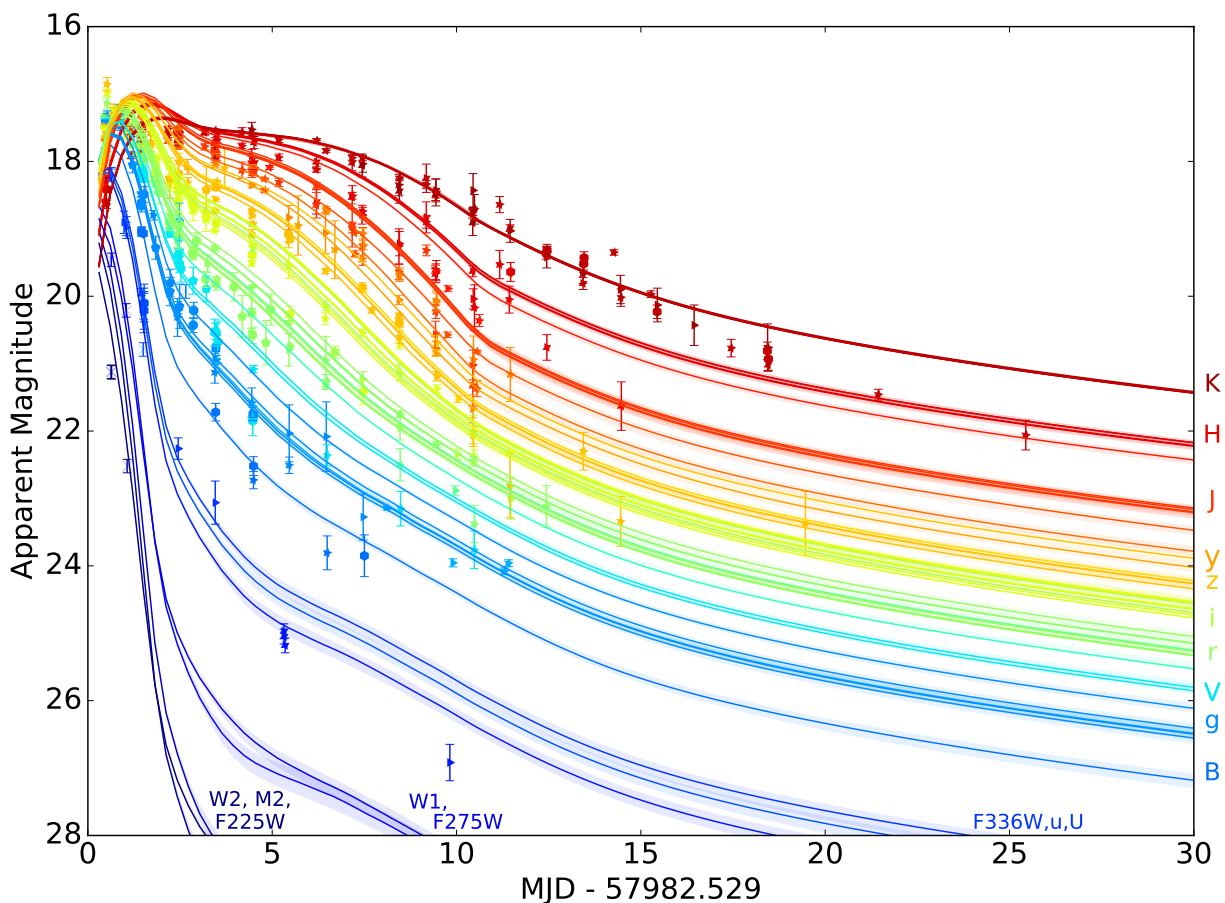


Fig. 2.3: Multi-wavelengths optical observations of the kilonova associated with GW 170817, AT2017gfo. The observing bands are shown on the right-hand side of the figure and span the ultraviolet, visible and infrared. References for the original data points can be found in Villar et al. (2017). The solid lines and contours show the best-fit kilonova models and their 1σ uncertainty for the respective observing bands. This figure is reproduced from Villar et al. (2017).

Following the reported localisation of the GW signal, GW 170817 (see Sec. 2.1) and the associated GRB, GRB 170817A (see Sec. 2.3), the optical transient discovered in NGC 4993 was the kilonova associated with the merger (Abbott et al., 2017c). An image of the host galaxy 20.5 days before the merger (observed with DLT40) and 10.9 h after the merger (observed with Swope) are shown in Fig. 2.2. The optical transient is clearly visible on the Swope image (Coulter et al., 2017).

Fig. 2.3 shows the light curve of the kilonova in several filters from the ultraviolet to the near-infrared. The optical transient decays between 0.45 and 29.4 days before becoming too faint to be distinguished from the host galaxy. As reported in Villar et al. (2017), the kilonova is well fitted by a model with three components as described above (the third component is a transition region between the blue and red ejecta). The total ejected mass is $\simeq 0.078 M_{\odot}$, leading to a high yield of r -process elements (Villar et al., 2017; Drout et al., 2017; Cowperthwaite et al., 2017). Additionally, Watson et al. (2019) have suggested the presence of strontium absorption lines in the kilonova spectra, which would constitute further direct evidence that the kilonova is indeed powered by the r -process and that BNS mergers are sites of r -process nucleosynthesis (see also Pian et al. 2017; Smartt et al. 2017).

As the kilonova ejecta propagates in the external medium, it sweeps up material and eventually decelerates. Similarly to the GRB afterglow described in Secs. 1.3 and 2.4, a kilonova afterglow is expected to be visible at late times (Nakar & Piran, 2011). In the case of GW 170817, some authors suggest its signatures have been detected in X-rays 3.5 years after the merger (Hajela et al., 2022), but this result is still debated, as I discuss in more detail in Sec. 6.1. From a theoretical point of view, the kilonova afterglow consists of synchrotron radiation which peaks at the ejecta deceleration time. Given the properties (Cowperthwaite et al., 2017) of the kilonova ejecta of GW 170817, Hajela et al. (2022) estimate that the kilonova afterglow is expected to peak a few years after the merger, though synchrotron radiation is already expected at earlier times (Nakar & Piran, 2011), as early as a few months after the merger. The detection of a kilonova afterglow several years after the merger of GW 170817 would be the last confirmation of the predicted electromagnetic counterparts to BNS mergers.

2.3 Gamma-Ray Burst

Approximately 1.7 s after the BNS merger time inferred from the GW signal (see Sec. 2.1), a weak GRB, GRB 170817A was detected by both Fermi-GBM (Goldstein et al., 2017) and INTEGRAL (Savchenko et al., 2017), as also described in Abbott et al. (2017c). Its sky localisation from both instruments is reported in the blue shaded areas of Fig. 2.2. They overlap the 90% credible region inferred with the GW detection, which very early was a hint that both events were indeed connected. Its duration was 2.0 ± 0.5 s, and GRB 170817A was classified as a short GRB. However, its extremely low peak isotropic-equivalent luminosity $L_{\gamma, \text{iso}} = 2 \times 10^{47}$ erg \cdot s $^{-1}$ and total isotropic equivalent energy $E_{\gamma, \text{iso}} = 6 \times 10^{47}$ erg make it approximately four orders of magnitudes less energetic than usual cosmological GRBs. Given its low luminosity, GRB 170817A was also significantly harder than its expected peak energy following the $E_{\gamma, \text{peak}} - L_{\gamma, \text{iso}}$ correlation (Ghirlanda et al., 2009; D’Avanzo et al., 2014). While the GRB low energy and luminosity can be explained by a high viewing angle, the peak energy cannot be reconciled with the correlation just described, no matter the viewing angle (Matsumoto et al., 2019). The delay between the merger and the GRB prompt emission emerges from the intrinsic delay of jet launching and early jet propagation in the kilonova ejecta (see Sec. 1.3.2).

This suggested that the prompt GRB emission of GRB 170817A may not be produced by the usual mechanism invoked for the observed cosmological population of short GRBs (see Sec. 1.3.2). The most convincing mechanism to explain the low luminosity of GRB 170817A given its large viewing angle is the *shock breakout* (see Sec. 1.3). This phenomenon occurs when ultra-relativistic material propagates in a slower ejecta (in the case of GW 170817 this is the kilonova ejecta), and

eventually reaches the edge of the ejecta. At this point, the ultra-relativistic shock breaks out of the ejecta and becomes visible to the distant observer. As discussed by [Gottlieb et al. \(2018\)](#), this phenomenon can explain the low luminosity of GRB 170817A, as well as the observed gradual softening of the GRB with time, that is explained by the progressive revealing of cooling material behind the shock. The shock breakout mechanism naturally produces hard emission peaks followed by softer tails, as discussed by [Nakar & Sari \(2012\)](#).

This description fits well with the observations of the various electromagnetic counterparts of GW 170817. As shown by the GRB afterglow observations described in Sec. 2.4, an ultra-relativistic jet was launched after the merger. This jet initially propagated in the dense and slower ejecta that later produced the kilonova emission. A shock front formed, and as it reached the outer layers of the kilonova ejecta, the shock breakout emission occurred ([Gottlieb et al., 2018](#)). The observed GRB therefore most probably originated from the shock breakout of material on the line of sight, and not directly from the ultra-relativistic off-axis GRB jet.

In this scenario, it cannot be deduced if the GRB jet of GW 170817 was successful or choked based only on the prompt observations. The afterglow observations described in Sec. 2.4 showed that the jet was indeed successful. As I discuss in Sec. 4.1, the early jet interaction in the kilonova is likely to shape it with a lateral structure. This has been confirmed by the afterglow light curve as I describe in the following Sec. 2.4.

2.4 Gamma-Ray Burst Afterglow

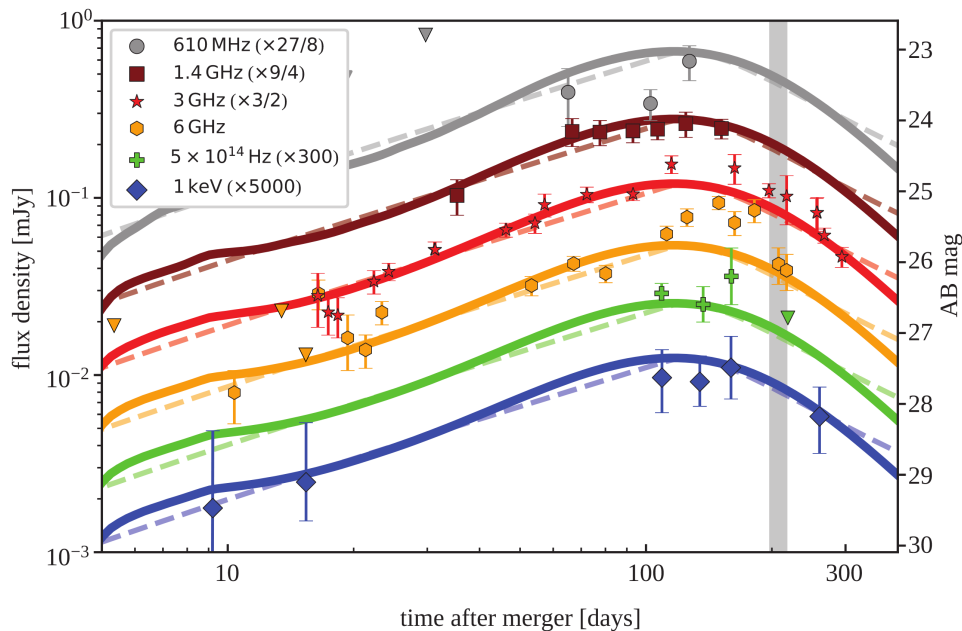


Fig. 2.4: Radio (grey circles, dark red squares, red stars and orange hexagons), optical (green crosses) and X-ray (blue diamonds) light curves of the afterglow of GW 170817 up to 300 days. Solid lines show a fit with a laterally-structured jet; while dashed lines show a fit with a radially-structured choked-jet-induced cocoon. This figure is reproduced from [Ghirlanda et al. \(2019\)](#).

Given that a GRB (Sec. 2.3) was observed jointly with GW 170817, it was clear that a relativistic jet was launched shortly after the merger. If this jet was successful to escape the kilonova ejecta (see Sec. 1.3.2), an associated GRB afterglow signal was expected to be detected. This non-thermal counterpart is powered by the synchrotron radiation of accelerated electrons at the forward shock

caused by the deceleration of the jet in the external medium (Mészáros & Rees, 1997). The afterglow signal is much longer-lived than the prompt radiation, as it is continuously radiating during the deceleration of the jet. If the GRB jet was instead initially choked, its energy injection could have alternatively led to a quasi-spherical, mildly-relativistic ejecta with a radial structure (Gottlieb et al., 2018). These two options are described in the context of GW 170817 in *e.g.* Kasliwal et al. (2017).

For the first 9.4 days that followed the merger of GW 170817, no afterglow emission could be detected. Then, a source with a slowly-increasing flux became detectable from radio to X-rays and eventually peaked ~ 130 days after the merger, before decaying for the following months and even years. This source was identified as the GRB afterglow of GW 170817. I present in extensive details its observational data in Sec. 6.1, and show in Fig. 2.4 the observed light curve at four different wavelengths (Ghirlanda et al., 2019). A full multi-wavelength light curve can be found in Fig. 6.1. The major difference between this GRB afterglow and the afterglows of GRBs at cosmological distances previously detected by Swift is the viewing angle. Because GRB jets are ultra-relativistic, relativistic beaming implies that they are observed on-axis at cosmological distances (*i.e.* $\theta_v < \theta_c$, where θ_v is the viewing angle and θ_c the jet opening angle). In this case, the afterglow of GW 170817 was observed at a much closer distance and significantly off-axis (see Sec. 2.1), which is why its emission first rose then peaked, as the jet decelerated in the external medium. This effect is described in more detail in Sec. 4.1. From the multi-wavelength light curve alone, the slow rise seen in Fig. 2.4 (Ghirlanda et al., 2019) can be explained either by the scenario with a successful jet, in which case it is due to the presence of a lateral structure around the jet observed off-axis; or by the scenario with a choked jet, in which case it emerges from the radiation of a radially-structured quasi-spherical ejecta.

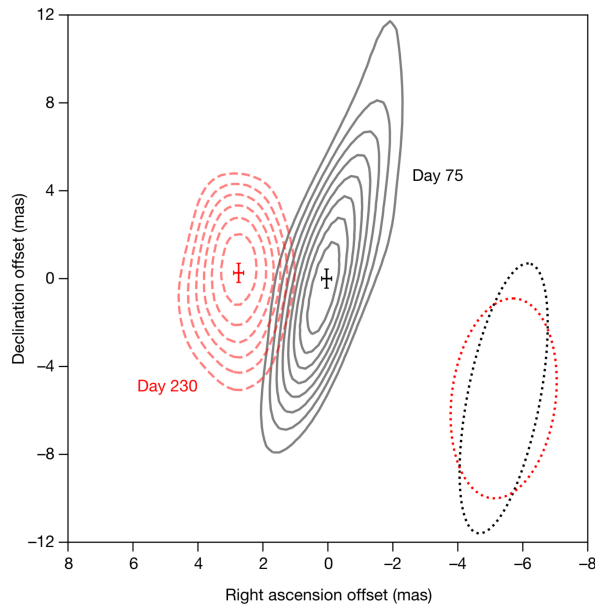


Fig. 2.5: Apparent displacement of the centroid of emission of the afterglow of GW 170817 observed with Very Long Baseline Interferometry (VLBI) at 4.5 GHz (radio). The red and black contours represent the position of the centroid of emission at 230 and 75 days, respectively, relative to its position at 75 days. The contours shown are the $3\sigma - 12\sigma$ credible intervals and the shapes of the synthesized beams for the images from each epoch are shown as dotted ellipses in the lower right corner. This figure is reproduced from Mooley et al. (2018a).

VLBI imaging was the most significant confirmation that the non-thermal transient observed at the location of GW 170817 was indeed the afterglow emission induced by the deceleration of a jet in the external medium. Mooley et al. (2018a, 2022) and Ghirlanda et al. (2019) showed that

the centroid of the emitting region had an apparent superluminal motion. This relativistic effect is produced by the motion of an ultra-relativistic source observed with a certain viewing angle θ_v . If the velocity of the source is $\beta = v/c$, then the apparent projected transverse motion of the source for the observer is

$$\beta_{\perp} = \frac{\beta \sin \theta_v}{1 - \beta \cos \theta_v}. \quad (2.1)$$

In this context, $\beta_{\perp} > 1$ for off-axis observations of ultra-relativistic material with $\beta \sim 1$.

In the case of GW 170817, and as represented in Fig. 2.5, the apparent proper motion of the source is $\beta_{\perp} \sim 4$. As discussed in Mooley et al. (2018a), the peak of the centroid of emission is located at $\theta_v - \theta_c \sim 1/\Gamma$, where θ_c is the core jet opening angle and Γ its Lorentz factor (see Chapter 5 for more details on these definitions). Using the point-source approximation, this leads to $\beta_{\perp} \approx \Gamma \approx 4$, thus confirming the presence of a relativistic outflow even 200 days after the merger. Another important element in these VLBI proper motion measurements is that the source is unresolved. An outflow with a radial structure would have been resolved at such distance, while a collimated off-axis jet is expected to be unresolved (Ghirlanda et al., 2019). It is often assumed that the jet is launched in the polar direction, *i.e.* perpendicular to the orbital plane prior to merger. Under this assumption, $\iota = \theta_v$ and joint constraints using the GW observations and the afterglow can be used to refine the value of the viewing angle. As I will discuss in Sec. 4.1, the off-axis observation of a laterally-structured jet reproduces well the observed data. Both elements thus indicate that the non-thermal emission detected is indeed the afterglow of a laterally-structured jet seen off-axis (see also Govreen-Segal & Nakar 2023).

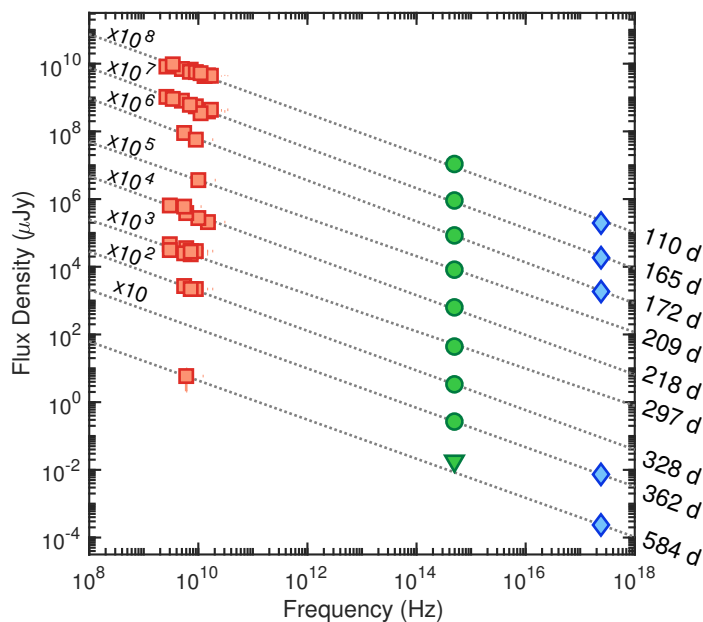


Fig. 2.6: Broadband spectral energy distribution of the afterglow of GW 170817 after the peak, at nine epochs between 110 and 524 days. Radio observations are shown in red, optical observations with the Hubble Space Telescope (HST) in green, and X-ray observations with Chandra in blue. This figure is reproduced from Fong et al. (2019).

In addition, as shown in Fig. 2.6 and discussed in Fong et al. (2019); Troja et al. (2019), the afterglow observations of GW 170817 show a similar temporal evolution at all frequencies, both before and after the peak of emission at ~ 130 days. This is a clear evidence that afterglow radiation is produced by a population of shock-accelerated electrons radiating by synchrotron and that these electrons remain in the same spectral regime during the whole evolution. These features are discussed extensively in the description of our afterglow model in Chapter 5.

2.5 Summary

I discussed in this chapter the expected signals associated to BNS mergers: first, the GW inspiral precursor, then the electromagnetic counterparts, a thermal kilonova, a prompt GRB emission followed by its non-thermal multi-wavelength afterglow emission. They were all discussed and predicted before the detection of GW 170817. Even though some of the observations of GW 170817 raise new questions, such as the origin of the GRB prompt emission or the origin and structure of the material surrounding the core jet, most theoretical predictions have been confirmed by this single event. GW 170817 was a major breakthrough event which has opened a new chapter for multi-messenger astronomy and put our models to the test. This exceptional event has also led to numerous advances in astrophysics, nuclear physics, fundamental physics and cosmology, among which we can quote constraints on NS radii and equations of state (Abbott et al., 2018); NS mass (Margalit & Metzger, 2017); GWs velocity and dark energy (Ezquiaga & Zumalacárregui, 2017); constraints on the Hubble constant H_0 (Abbott et al., 2017d; Hotokezaka et al., 2019); cosmological gravity (Baker et al., 2017); r -process nucleosynthesis (Drout et al., 2017); tests of General Relativity (Abbott et al., 2019c); among many others. Of specific interest for this thesis, the off-axis observation of the GRB afterglow from a structured jet has pushed the need for more detailed afterglow models. This important aspect is developed in Part II and in particular in Chapter 4.

Chapter 3

Compact Object Binaries: Formation and Population

Contents

3.1	Single-Star Evolution and Formation of Compact Objects	38
3.2	Direct Observations: Galactic Populations of Compact Objects	41
3.3	A New Window: Gravitational-Wave Observations of Compact Object Binaries	42
3.4	Other Indirect Constraints	44
3.5	On the Doctoral Work Presented Next	46

The detections of compact object mergers by the Gravitational Wave (GW) interferometers is opening a new avenue to study the population of compact objects. In particular, many questions are still open concerning their formation and their properties. In this chapter, I discuss the main ingredients of single-star evolution with a specific focus on Neutron Stars (NSs) and Black Holes (BHs) progenitors (Sec. 3.1). I then discuss the current observational constraints on the populations of compact object binaries, with again a focus on Binary Neutron Stars (BNSs). These can be broadly divided in three classes: compact objects in the Milky Way can be detected due to associated luminous emissions (Sec. 3.2), while extragalactic compact objects are now detected thanks to their GW emission at the merger (Sec. 3.3). Finally, I present some additional indirect constraints on the properties of the population of BNSs (Sec. 3.4).

3.1 Single-Star Evolution and Formation of Compact Objects

In this section, I will briefly describe the key quantities and evolutionary stages that are relevant to understand stellar evolution. Some of them are used by population synthesis models (see Sec. 7.3) to perform rapid stellar evolution calculations in the context of binary evolution. Here I focus on the simplest case where stars are isolated, so that their evolution depends only on their intrinsic properties. It is also assumed that their chemical composition is homogeneous at formation, that stars are spherically symmetric and therefore not highly rotating, and the effects of magnetic fields are neglected. These assumptions are also at the base of SSE (Hurley et al., 2000), which describes analytic prescriptions for rapid single-star evolution and is the building block of most population synthesis models available today (see Sec. 7.3), though some recent developments by Spera et al. (2019); Fragos et al. (2023) are now proposing updated prescriptions.

In the simplest approach used here, stars are entirely described by their mass M , radius R , luminosity L and metallicity Z . A star’s metallicity is the mass fraction of “metals” (*i.e.* all elements with atomic number $Z \geq 3$). As I discuss in Sec. 8.2.5, the Solar metallicity is now estimated to be $Z_{\odot} = 0.014$, with uncertainties depending on the determination method (see Asplund et al. 2009 for a review).

The population of stars in the Milky Way can broadly be divided into two distinct categories: young stars which are usually metal-rich and located in the disk and the spiral arms, and old stars which are usually more metal-poor and can be located not only in the disk but also in the bulge, the Galactic halo and globular clusters; though a great diversity is observed among the Galactic stellar population (see *e.g.* An & Beers 2020). As a whole, this diverse population of stars can be used to trace the history of chemical enrichment of the Milky Way.

Throughout stellar evolution until the formation of compact objects, two equilibria are always maintained: the hydrostatic equilibrium that equates the gravitational and the gas pressure forces; and thermal equilibrium which balances energy production by nuclear fusion at the stellar core and energy radiation in the form of neutrinos and light at the surface. In White Dwarfs (WDs) and NSs, the gravitational force is balanced by the pressure force due to the electron degeneracy pressure and the strong force, respectively. I will not discuss the specific case of these compact objects in what follows. From the aforementioned considerations, three timescales can be computed:

- The **dynamical timescale**, which is the typical time required for the star to adjust to a perturbation in the hydrostatic equilibrium:

$$\tau_{\text{dyn}} = \sqrt{\frac{R^3}{GM}} \approx 1600 \left(\frac{R}{R_{\odot}}\right)^{3/2} \left(\frac{M}{M_{\odot}}\right)^{-1/2} \text{ s.} \quad (3.1)$$

This is the shortest timescale, of order typically half an hour for a solar-mass star.

- The **Kelvin-Helmoltz timescale** or **thermal timescale**, which describes the typical timescale of the quasi-static contraction of the core at the end of a fusion cycle and the associated temperature increase:

$$\tau_{\text{KH}} = \frac{E_{\text{int}}}{L} \approx \frac{GM^2}{2RL} \approx 1.5 \times 10^7 \left(\frac{R}{R_{\odot}}\right)^{-1} \left(\frac{M}{M_{\odot}}\right)^2 \left(\frac{L}{L_{\odot}}\right)^{-1} \text{ yr}, \quad (3.2)$$

where E_{int} is the internal energy of stellar plasma. This timescale is much longer than the dynamical timescale. It also determines if the ignition of the next fusion cycle is possible.

- The **nuclear timescale**, is the time during which a stellar core can maintain nuclear fusion reactions and is therefore linked to the mass content of the star.

$$\tau_{\text{nuc}} = \frac{E_{\text{nuc}}}{L + L_{\nu}} = \phi f_{\text{nuc}} \frac{Mc^2}{L + L_{\nu}} \approx 10^{10} \left(\frac{M}{M_{\odot}}\right) \left(\frac{L + L_{\nu}}{L_{\odot}}\right)^{-1} \text{ yr}, \quad (3.3)$$

where L and L_{ν} are the light and neutrino luminosities, respectively ($L \ll L_{\nu}$ for hydrogen fusion during the main sequence), ϕ is the efficiency of rest-mass energy conversion by the nuclear reaction (0.7% for hydrogen fusion), and f_{nuc} is the fraction of mass above the temperature threshold (for the main sequence Sun, $f_{\text{nuc}} \simeq 10\%$).

From the above definitions, $\tau_{\text{dyn}} \ll \tau_{\text{KH}} \ll \tau_{\text{nuc}}$. Therefore, the timescale of stellar evolution is usually determined by the nuclear timescale of the main sequence and the stars can be assumed in thermodynamical equilibrium. From Eq. 3.3, we retrieve the lifetime of the Sun (~ 10 billion years); but also an important information: for Main Sequence (MS) stars, the luminosity increases strongly for higher masses ($L \propto M^{3.5}$ if $2 M_{\odot} \lesssim M \lesssim 50 M_{\odot}$), which combined with Eq. 3.3 implies that more massive stars have shorter lifetimes. A star with $3M_{\odot}$ has a lifetime of ~ 340 million years, with $10M_{\odot}$ this decreases to ~ 32 million years, down to ~ 3 million years for a $60M_{\odot}$ star. Conversely, low-mass stars that make up most of the stellar content of galaxies have lifetimes > 100 billion years, much longer than the current age of the Universe,

$$t_{\text{Hubble}} = 13.7 \text{ Gyr}, \quad (3.4)$$

using the Λ CDM model with cosmological parameters from [Planck Collaboration et al. \(2020\)](#).

Stellar evolution consists in a succession of phases.

1. The star forms from the collapse and fragmentation of a molecular cloud. Its initial properties are determined by the amount of mass that collapses under its own gravity, and on its metallicity. At the ignition of hydrogen fusion in the central region, the star is formed. This state is called the Zero-Age Main Sequence (ZAMS).
2. Main Sequence (MS) evolution, during which the star burns hydrogen in its core. This phase is the longest given the long nuclear timescale for hydrogen fusion. Stellar properties are very stable throughout this phase.
3. When the star exhausts its hydrogen nuclear fuel, thermal equilibrium is disrupted and the core starts to contract on a thermal timescale. Simultaneously, the envelope starts to expand. The subsequent stellar evolution is a series of fusion cycles which each halt when there is not enough material in the core for the reaction to occur. The transitions between fusion cycles occur on the thermal timescale, and lead to a gradual increase of mass and temperature in the core. The outer envelope is extremely affected by the evolution of the core and expands. During the phase of helium fusion, the star is a giant, and during the later cycles (for massive stars only), a supergiant. Each fusion cycle has a shorter nuclear timescale than the previous one, and the final production of iron has a typical nuclear timescale $\tau_{\text{nuc}} \sim 1$ day. In this post-main sequence phase, the stellar luminosity and radius can increase a lot compared to the initial stellar properties.

4. For the least massive stars, fusion stops well before the last possible nuclear fusion cycle (silicon to iron), when the contraction of the core is stopped by the degeneracy pressure of electrons, allowing a new hydrostatic equilibrium, the WD stage. The composition of the WD depends on the final fusion cycle before the collapse. WDs can be made of helium (HeWD) for the least massive progenitors ($M \lesssim 0.8M_{\odot}$), or of carbon and oxygen (COWD) for intermediate-mass progenitors ($0.8M_{\odot} \lesssim M \lesssim 8M_{\odot}$) or of oxygen, neon and silicon (ONeWD) for slightly more massive progenitors ($8M_{\odot} \lesssim M \lesssim 11M_{\odot}$). The most massive stars ($M \gtrsim 11M_{\odot}$) experience all fusion cycles in their core and produce iron. Because the reaction of iron fusion is endothermic, no more fusion occurs in a gradually growing central region of the star. When the iron core exceeds its *Chandrasekhar mass*, $\sim 1.26M_{\odot}$ (this value is lower than the Chandrasekhar mass of WDs due to the higher neutron fraction in the iron core), it collapses on the free-fall timescale (of the same order as the dynamical timescale τ_{dyn}) and produces either a NS if the progenitor is not too massive and the strong force induces enough pressure to counterbalance gravity; or a BH for the most massive cases. This *core collapse* typically lasts a few hundreds of milliseconds.

Depending on the star’s initial mass and metallicity, several different processes can occur after the MS and before the final collapse. For all stars, the phase of core helium burning is associated with a red giant phase: the star expands and its external layers therefore cool. The ignition of helium fusion is thought to produce helium flashes, which can repeat if the star finds itself in an oscillatory state, collapsing and expanding as it ignites and stops helium fusion. For the most massive stars, progenitors of NSs and BHs, mass losses by winds become important throughout their lifetime, and especially post-main sequence. I describe them in detail in Sec. 8.2.1. Because the successive cycles of nuclear fusion always occur in the most central regions with the highest temperature, massive stars have an onion-skin-like structure before collapsing.

Depending on their properties, stars are classified in different *stellar types*, e.g. MS, or Core Helium Burning (CHeB). The classification method used in most population synthesis algorithms is that described in [Tout et al. \(1997\)](#); [Hurley et al. \(2000\)](#). A useful way to track stellar evolution is to look at the evolution with time of the star’s luminosity and effective temperature, which are the quantities directly measured during observations. The effective temperature of a star, T_{eff} , is defined as the black-body temperature that would produce the same luminosity L as the star’s luminosity. If the star has a radius R , we therefore have

$$L = 4\pi R^2 \sigma T_{\text{eff}}^4, \quad (3.5)$$

where σ is the Stefan-Boltzmann constant. The $L - T_{\text{eff}}$ diagram is known as the Hertzsprung-Russel diagram. Examples of stellar evolution tracks at two different metallicities and for a range of stellar masses from [Riley et al. \(2022\)](#) are shown in Fig. 3.1. These stellar tracks were obtained with COMPAS ([Riley et al., 2022](#)), a population synthesis model that follows the prescriptions for single-star evolution described in [Hurley et al. \(2000\)](#), similarly to COSMIC ([Breivik et al., 2020](#)), that we use for our study described in Part III. In this diagram, each color corresponds to a different stellar type as defined by [Tout et al. \(1997\)](#), and summarized in Tab. 8.1. Note that the time spent by a star at each position of its stellar track shown in Fig. 3.1 is not directly deductible in such Hertzsprung-Russel diagrams. The time spent on the MS (in yellow) is indeed much longer than that in the later evolved stages.

Finally, it can happen that single stars lose their hydrogen envelopes due to stellar winds as they expand. This may happen during the phase of helium burning for the most massive stars, in which case the helium core is stripped of its envelope. These specific stars are called *stripped stars* or *naked helium stars*. While this occurs on rare occasions for isolated stars, the phases of mass transfer and Common Envelope (CE) make them much more common in binary systems. I do not discuss here the effects of the presence of the companion star in binary systems, which is done extensively in Chapters 8 and 9.

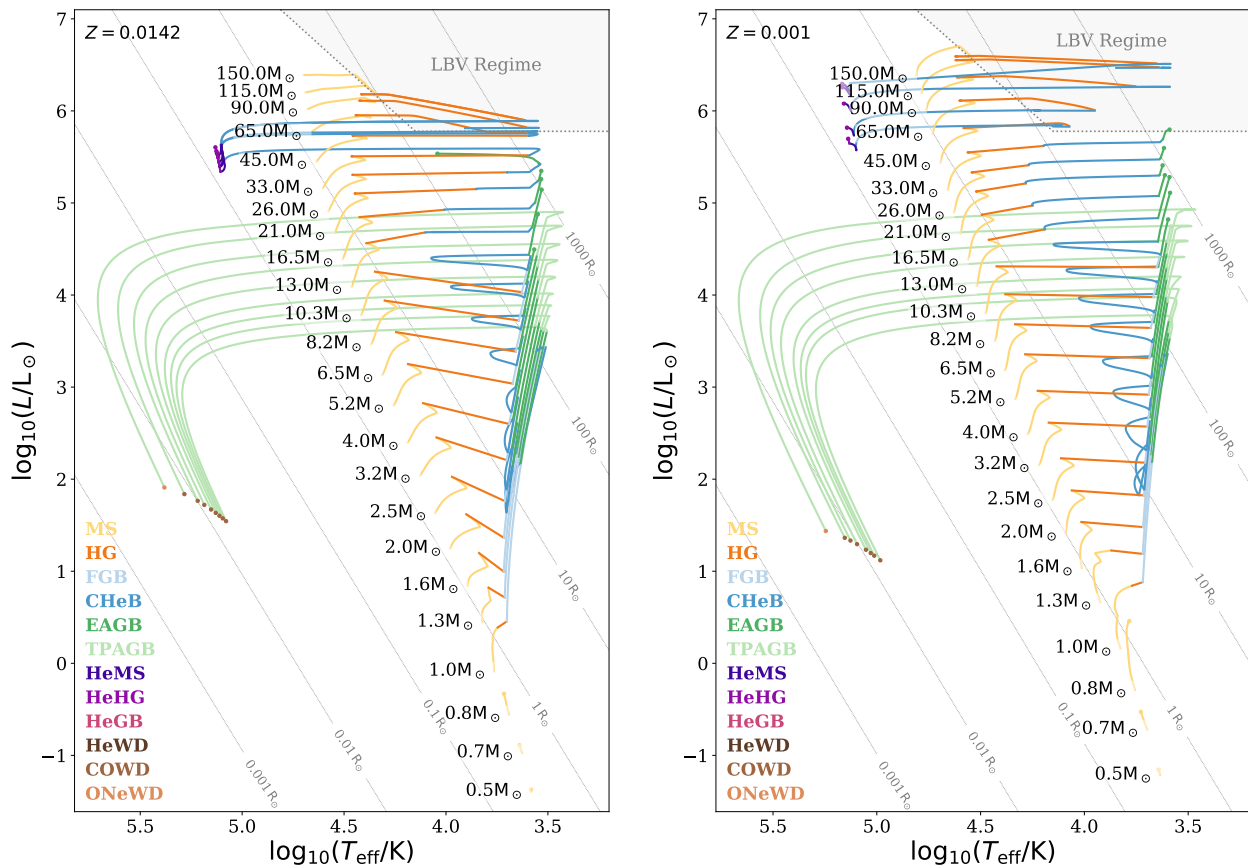


Fig. 3.1: Stellar tracks in the Hertzsprung–Russell diagram for two different ZAMS metallicities ($Z = 0.0142$, left; $Z = 0.001$, right) and stellar masses spanning $0.5–150M_{\odot}$. The gray diagonals represent lines of constant radii. The stellar evolution parameters used in this figure are described in Riley et al. (2022). This figure is reproduced from Riley et al. (2022).

In reality, most stars form in binaries. The exact fraction of stars in binary systems is uncertain but ranges between 30% and 70% (see Sec. 8.1 and *e.g.* Sana et al. 2012). The presence of a close companion can affect the stellar evolution processes and modelling stellar evolution in the presence of a companion is an active field of research. For example, the reader can refer to the Modules for Experiments in Stellar Astrophysics (MESA) numerical model for an open-source and regularly updated numerical model (Paxton et al., 2011, 2013, 2015, 2018; Jermyn et al., 2023).

Once formed, NSs emit only a very weak thermal radiation and are therefore observed in only three different situations: if they are pulsars (NSs in fast rotation emitting radio light at their magnetic poles); if they have a companion and accrete material by mass transfers (in this case they are X-Ray Binaries (XRBs)); if they are in a BNS or Neutron Star – Black Hole binary (NSBH) system and merge. I discuss the constraints on the population of NSs in binary systems in the following sections.

3.2 Direct Observations: Galactic Populations of Compact Objects

During the evolution of stellar binaries, phases of mass transfers are expected, in particular when one of the stars enters the giant or supergiant phase after the MS and the outer layers of stellar envelope can fill the star’s Roche lobe. In these cases, stable mass transfer can be initiated, as discussed in Sec. 8.2.2. If the companion of the giant is a NS, an accretion disk forms around it and is continuously fed by material from the giant. The temperature in the accretion disk gradually

increases towards the compact object, leading to soft X-ray emission. A polar corona is thought to also radiate hard X-rays, though this component is more debated. When in that state, the binary is called an X-Ray Binary (XRB). If the donor star has a mass $M \geq 8M_{\odot}$, the binary is referred to as a High-Mass X-Ray Binary (HMXRB). For a recent review on accreting compact objects in general, see [Chaty \(2022\)](#).

The observation of XRBs has allowed to detect multiple compact objects in association to massive stars. A recent catalog of HMXRB can be found in [Fortin et al. \(2023\)](#). To allow a significant mass flow from the stellar companion, the separation between both objects must be small (see Eq. 8.32 and Sec. 8.2.2). The loss of angular momentum is then thought to allow for further reduction of the separation. Still, the separation in observed XRBs is typically $\gtrsim 100 R_{\odot}$. Identifying the nature of the accreting compact object (NS or BH) is more challenging. The presence of variability and flashes in the light curves is a hint that the accreting compact object has a surface and is therefore a NS.

At their formation, NSs are in rapid rotation and in some cases can emit a beamed radio radiation along their magnetic poles ([Lorimer & Kramer, 2004](#)): these NSs are known as *pulsars*. Seen by a distant observer aligned with the beam of emission once every rotation period, pulsars appear as flashing radio sources with extremely precise periods. NSs can radiate as pulsars only for a limited time until they spin down and their magnetic field intensity decreases. Except in the case of *recycled* pulsars (millisecond pulsars) where accretion of mass from a companion spins up the pulsar again, they are usually young NSs (with ages $\lesssim 100$ Myr).

While XRBs with accreting NSs are detected after the formation of the first NS but before the Supernova (SN) of the secondary, it is therefore also possible to detect BNSs shortly after their formation, when the binary contains a pulsar, in which case it is known as a *binary pulsar* (only one of the NSs is a pulsar in this case). To date, only 15 binary pulsars have been detected in the Milky Way, sometimes with very short separations. These systems are compiled in [Dvorkin 2023](#). The most famous binary pulsar is probably the Hulse-Taylor pulsar ([Hulse & Taylor, 1975](#)). It is also in theory possible to detect BNS systems where the two NSs are pulsars: *double pulsars*. The only double pulsar observed so far is PSR J0737-3039 ([Burgay et al., 2003](#)), whose orbital separation is also the lowest of the observed sample: with an orbital period of ~ 2.4 h, the separation is $\sim 1 R_{\odot}$.

Galactic binary pulsars are used to constrain binary stellar evolution parameters of population synthesis models (see *e.g.* [Tauris et al. 2017](#); [Vigna-Gómez et al. 2018](#)). In these cases, the authors rely on their measured orbital period and eccentricity as features to reproduce statistically with the population of BNSs.

Binary pulsars therefore probe BNS shortly after the formation of the second NS of the system. This information is complementary to the GW population of BNS which is observed at its merger and that I discuss hereafter. Also, while the population of XRBs and binary pulsars is observed in the Milky Way, the population of merging BNSs detected in GWs is extragalactic.

3.3 A New Window: Gravitational-Wave Observations of Compact Object Binaries

The population of BNSs can also be observed thanks to the emission of GWs when they merge. This information is complementary to Galactic binary pulsars observations, which are typically observed when NSs are still young; while mergers occur with a delay time depending on the BNS's initial separation and eccentricity at formation (see Eq. 1.8 – 1.9) and typically consist in old NSs. However, we will see in Part III that there are scenarios for a population of fast mergers.

Since the first Binary Black Hole (BBH) merger detection in 2015 ([Abbott et al., 2016](#)), three GW observing campaigns (O1 - O2 - O3) have been run by the LIGO and Virgo interferometers, each time with increased sensitivity and therefore a higher rate of detections. The results have

been published successively (Abbott et al., 2019a, 2021b; The LIGO Scientific Collaboration et al., 2021a,b). Fig. 3.2 shows the increasing cumulative number of detections with time, where the effect of the instruments upgrade between the observing runs is clearly visible. At the time of writing, the fourth observing run O4 has just started with an extended observational range. The first detections are being reported and will help refine the understanding of the population properties inferred in the previous runs.

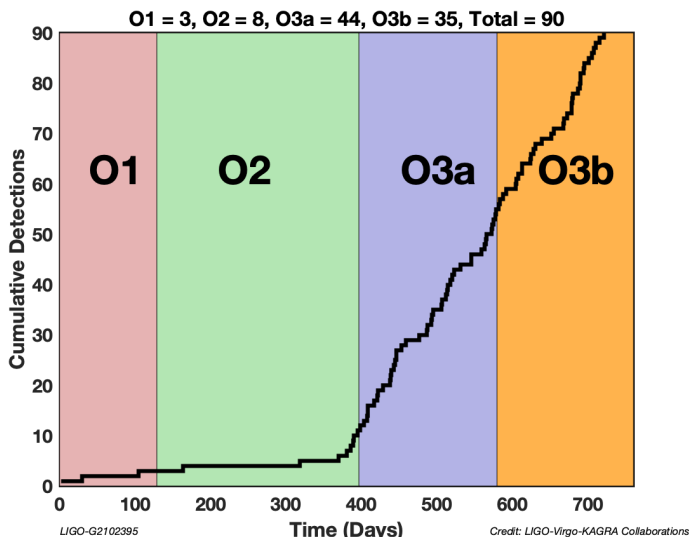


Fig. 3.2: Evolution of the number of confirmed detected GW signals from all compact object mergers in the three observing runs. The detection rate increases at each new observing run due to sensitivity upgrades of the interferometers. Credit: LVK Collaboration

After O3, the total number of GW detections was 90, including only 2 BNS mergers. So far, most statistical constraints concern only the population of BBHs. The masses of the merging compact objects and of their remnants are shown in Fig. 3.3. With this new data set, it has become possible to study the *population* of merging compact objects with a statistical approach. The interferometers have observational ranges of the order ~ 100 Mpc for BNS systems and up to ~ 1 Gpc for BBHs. They are therefore only sensitive to BNS mergers in the local universe ($z \sim 0$).

The main constraints on the population of compact object mergers concern BBH and are discussed in great detail in The LIGO Scientific Collaboration et al. (2021b). In particular, the mass distribution suggests that the higher mass gap caused by the total disruption of stars with carbon-oxygen core masses $\gtrsim 60M_{\odot}$ (Woosley & Heger, 2021) during Pair Instability Supernovae (PISNe) (see Sec. 8.2.5) is filled by some BHs. This may imply the need for the two formation channels for BBH: by isolated binary evolution (see Sec. 7.1) and by dynamical interactions in young, nuclear and globular clusters (see Sec. 7.2), as discussed by *e.g.* Mapelli et al. (2022). I provide more details on these formation channels in Chapter 7.

The inferred local merger rates for the three populations have been derived most recently in The LIGO Scientific Collaboration et al. (2021b). I show hereafter the most conservative estimates:

$$\begin{cases} \mathcal{R}_{\text{BNS}} &= 10 - 1700 \text{ Gpc}^{-3} \cdot \text{yr}^{-1} \\ \mathcal{R}_{\text{NSBH}} &= 7.8 - 140 \text{ Gpc}^{-3} \cdot \text{yr}^{-1} \\ \mathcal{R}_{\text{BBH}} &= 16 - 61 \text{ Gpc}^{-3} \cdot \text{yr}^{-1} \end{cases} . \quad (3.6)$$

So far, only two BNS mergers have been detected: GW 170817 that I discussed in detail in Chapter 2 and GW 190425 (Abbott et al., 2020a). This second BNS detected with GWs was located at a larger distance than GW 170817 ($D_L = 159_{-72}^{+69}$ Mpc) and its sky localisation was much less constrained (8284 deg^2). No electromagnetic counterpart to GW 190425 was therefore identified. A puzzling information in the detection of this merger is the masses of the two components: with a chirp mass of $1.44_{-0.02}^{+0.02} M_{\odot}$ and a total mass of $3.4_{-0.2}^{+0.4} M_{\odot}$, the two NSs of this system are more massive than all NSs detected electromagnetically, to the point where it cannot be totally excluded

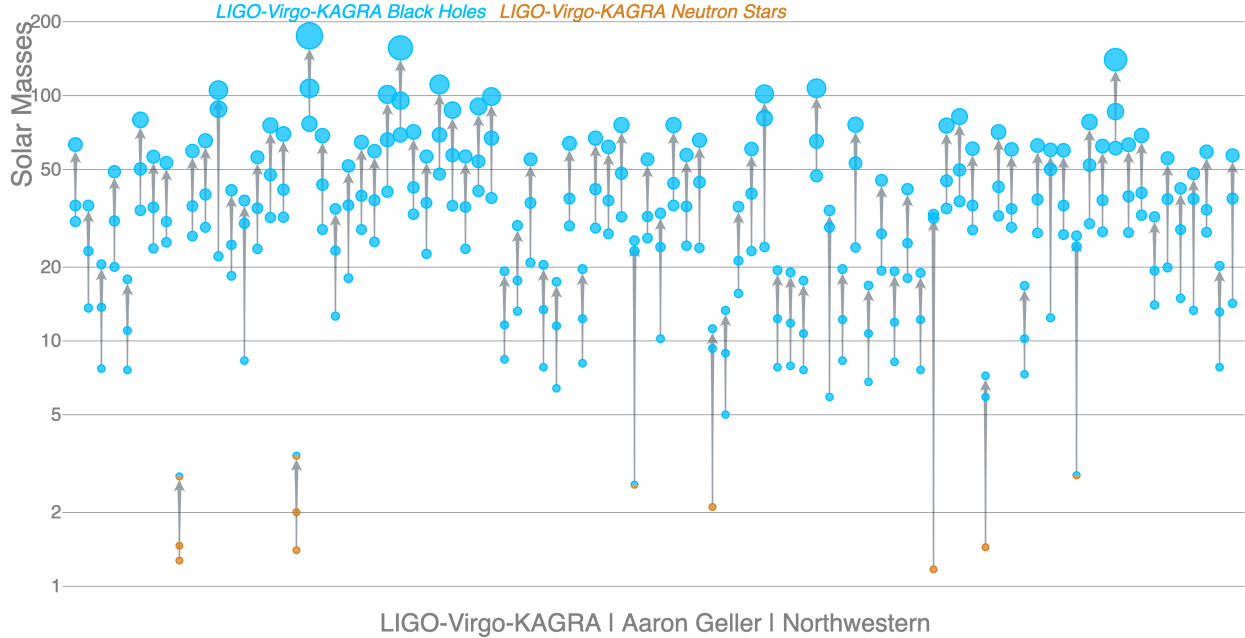


Fig. 3.3: Visualisation of the masses of merging compact objects and their remnants as detected in the three GW observing runs by LIGO/Virgo. Blue circles represent BHs, orange circles NSs, and circles with both colors denote objects of uncertain nature. Credit: LVK Collaboration

that one or both components may in fact be BHs. As highlighted in Sec. 2.2, the high mass of the NSs in this merger raised the question of the nature of the kilonova, were it detected: Would a blue component have emerged? In addition to these two BNS merger detections, the successive observing runs have unveiled a diversity of mergers with sometimes unexpected properties:

- GW 190412 (Abbott et al., 2020b), a BBH merger with an high mass ratio $M_1/M_2 \sim 3.75$;
- GW 190814 (Abbott et al., 2020c), a merger of a $\sim 23M_\odot$ BH and a $\sim 2.6M_\odot$ companion, which would be either the highest-mass NS ever detected, or the lowest-mass BH;
- GW 190521 (Abbott et al., 2020d), a BBH merger with a total mass of $\sim 150M_\odot$. The remnant is therefore an intermediate-mass BH, a class of BHs bridging the mass gap between stellar-mass BHs and supermassive BHs, but whose existence had not been that directly confirmed observationally.

With O4, we expect the number of BNS merger detections to increase and enter in the domain where more statistics can be drawn. Meanwhile, some other indirect constraints already provide additional insights into this population. I discuss them in the next section.

3.4 Other Indirect Constraints

I discussed in Sec. 1.3.3 the distribution of offsets of short Gamma-Ray Bursts (GRBs) in their host galaxies, with some short GRBs found in the central regions of their host galaxies, and others with large offsets. If we associate short GRBs to BNS mergers, this indirectly constrains the underlying distribution of delay times and shows it may have a large scatter. Additionally, some short GRB host galaxies are star-forming, while others are not, which also supports broad distributions of delay times. As I discuss in Sec. 6.4, these elements may also hint to a population of BNS formed with extremely short separations that merge on short timescales $\lesssim 100$ Myr.

The r -process powering the kilonova discussed in Sec. 2.2 requires extreme conditions to take place. Only two astrophysical sites meet the required conditions: BNS mergers and some rare energetic Core-Collapse Supernovae (CCSNe) (Symbalisty et al., 1985; Halevi & Mösta, 2018; Siegel et al., 2019). So far, the relative contribution of both sites is still debated. But with the direct observation of the kilonova of GW 170817 (Sec. 2.2), it became clear that BNS mergers do contribute to r -process nucleosynthesis and the subsequent chemical enrichment of galaxies.

In the Milky Way, the abundance of r -process elements is probed in stars by spectral identification of the absorption lines of europium (Eu). These lines are relatively easy to characterise, and europium is an element that can almost only be produced by the r -process and is therefore an unbiased tracer of these elements. In Fig. 3.4, I show a diagram showing the relative abundance of $[\text{Eu}/\text{Fe}]$ as a function of $[\text{Fe}/\text{H}]$ for 2214 Galactic stars, using the SAGA database (Suda et al., 2008). The quantities $[X/Y]$ are defined such that $[X/Y] = \log_{10}(X/Y) - \log_{10}(X_{\odot}/Y_{\odot})$. Stars with a higher $[\text{Fe}/\text{H}]$ are more metal-rich. They typically trace formation at later times in Galactic evolution, when the molecular clouds are already enriched by the products of stellar evolution from previous collapsed stars. Conversely, stars with low $[\text{Fe}/\text{H}]$ are representative of the Galactic environments at earlier times when the first stars formed.

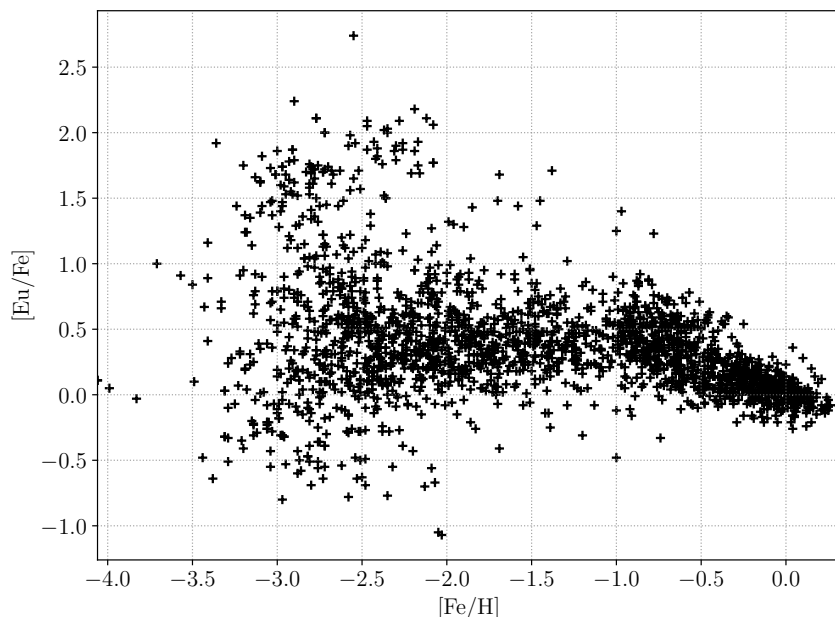


Fig. 3.4: Distribution of r -process abundances as a function of metallicity for a sample of Galactic stars. The enrichment in r -process elements is traced by the ratio $[\text{Eu}/\text{Fe}]$, while the stellar metallicity is probed by the ratio $[\text{Fe}/\text{H}]$. $[\text{Fe}/\text{H}] = [\text{Eu}/\text{Fe}] = 0$ corresponds to solar values. The sample of stars is taken from the SAGA database (Suda et al., 2008).

In Fig. 3.4, two important effects are visible. First, some stars have low metallicities ($[\text{Fe}/\text{H}] \lesssim -3$) but a significant excess of r -process elements ($[\text{Eu}/\text{Fe}] \gtrsim 1.5$). This means that a process must exist so that stars can form in environments enriched in r -process elements, while the products of massive star evolution have not yet been added. Second, the dispersion of r -process element abundances in low-metallicity stars is much higher. This indicates that the astrophysical events responsible for r -process nucleosynthesis must be rare and affect star-forming regions only locally. As discussed before, either rare cases of CCSNe or BNS mergers have been proposed as the main sites for r -process nucleosynthesis. In this thesis, I will only discuss the scenario with BNS-induced enrichment, motivated by the observation of the kilonova of GW 170817. In this context, the low-metallicity stars with high abundances of r -process elements and the observed scatter are indirect

evidence for the existence of tracks of fast BNS mergers (see *e.g.* the discussion in [Vangioni et al. 2016](#); [Dvorkin et al. 2021](#)). These are discussed in Sec. 6.4 and Chapter 9.

3.5 On the Doctoral Work Presented Next

The domain of multi-messenger astronomy with GWs has opened in 2017 with the detection of GW 170817 and its associated electromagnetic counterparts, in particular an afterglow produced by a structured jet observed off-axis. In the past years, the successive GW observing runs have opened new perspectives to study the populations of compact object binaries, in particular BNSs.

The doctoral thesis work presented hereafter aims to leverage these observations in two ways. In Part II, I summarize the main ingredients required to analyse recent observations of GRB afterglows with a consistent model which accounts for the jets' lateral structure and their potential Very High Energy (VHE) emission (Chapter 4). I then present the afterglow model developed during this thesis, that includes structured jets, with an extension to the VHE radiative processes for the population of shock-accelerated electrons (Chapter 5); and discuss results obtained on GW 170817 (Chapter 6). In particular, I highlight that BNS mergers in denser environments are more likely to be detected at VHE. In Part III, I introduce the main formation channels relevant for compact object binaries formation – the isolated binary and the dynamical channels – and provide an overview of population synthesis models (Chapter 7). I introduce one of them, COSMIC ([Breivik et al., 2020](#)), that I use to simulate populations of BNSs (Chapter 8). I then discuss the contributions of different binary evolutionary tracks with relative contributions that evolve with redshift. Some of these evolutionary tracks lead to short-delay time mergers, and are therefore more likely to be hosted in denser environments (Chapter 9).

Part II

The Very High Energy Afterglow of Structured Relativistic Jets

Chapter 4

Recent Observational Advances: Towards a Better Understanding of the Physics of Gamma-Ray Burst Afterglows

Contents

4.1	Gamma-Ray Burst Afterglows from Jets with a Lateral Structure . . .	50
4.2	The Very High Energy Emission of Gamma-Ray Burst Afterglows . .	53

Some recent detections of Gamma-Ray Burst (GRB) afterglows have lifted the curtain on some properties of the early jet propagation and the jet geometry, as well as on the properties of the associated radiation. These observations have motivated the development during this thesis of the model presented throughout Part II.

As I described in Sec. 1.3, most GRBs are detected at cosmological distances, with a few rare exceptions like GRB 980425 which was located at a distance ~ 36 Mpc (Galama et al., 1998). However, this GRB jet was probably observed on-axis. Recently GRB 170817A, associated to the Binary Neutron Star (BNS) merger GW 170817 was located only at a distance ~ 40 Mpc, *i.e.* $z \sim 0.01$ (see Chapter 2, Sec. 2.3). In this case the jet was observed off-axis. As I discuss in Sec. 4.1, this introduced new features in the observed light curve and helped us better constrain the jets' lateral structures.

In their journey from the source to the observer, Very High Energy (VHE) photons ($h\nu \sim 1$ TeV) are absorbed by infrared photons from distant galaxies, the Extragalactic Background Light (EBL) (see Sec. 5.4.8), to produce pairs. This dramatically depletes the VHE flux for distant sources, so that only local GRBs have chances to be detected at VHE. In this context, the VHE instruments listed in Sec. 1.1 have been used to detect VHE photons associated with GRBs. After many years of observations, the first detections have occurred since 2018. I discuss them in Sec. 4.2. These detections have pushed our need to update the GRB afterglow models by including radiative processes that can produce these VHE photons.

In the following sections, I discuss the detection of jet lateral structures (Sec. 4.1) thanks to GW 170817 and the first detections of GRB afterglows at VHE (Sec. 4.2).

4.1 Gamma-Ray Burst Afterglows from Jets with a Lateral Structure

GRB afterglows most of the time show a temporal decline in flux, up to a certain time where the decline steepens, though a diversity of early-time features like plateaus and flares are also found (see the review by Gehrels et al. 2009). In the scenario where an ultra-relativistic jet decelerates in the external medium, leading to a strong forward external shock, this steep temporal break has a natural explanation. As long as the jet is ultra-relativistic, relativistic beaming concentrates the emitted flux in a region of opening angle $\theta_{\text{coll}} \sim 1/\Gamma$, where Γ is the shocked medium Lorentz factor (see Secs. 5.1 and 5.2). If the jet has an opening angle θ_c and no lateral structure (a so-called *top-hat* jet), a first phase occurs where $\theta_{\text{coll}} \ll \theta_c$ (GRB jets are expected to have Lorentz factors $\Gamma \sim 100$). As the jet decelerates, its intrinsic emitted flux decreases, but this effect is partly compensated by the gradual opening of the collimation angle θ_{coll} , which reveals parts of the jets that were previously not visible. However, when the jet has decelerated enough so that $\theta_{\text{coll}} > \theta_c$, the jet becomes entirely visible. Thus, the intrinsic decrease of the radiated flux is no longer compensated by the larger visible region. The net effect is a steepening of the light curve. The transition where $\theta_{\text{coll}} \sim 1/\Gamma = \theta_c$ is called the *jet break*. These effects were first discussed by Rhoads (1997). I show in Fig. 4.1 a schematic view of this effect and the X-ray afterglow light curve of GRB 050318 (Perri et al., 2005).

Another impact of relativistic beaming is that off-axis observations of GRB afterglows at cosmological distances are unlikely. The line of sight indeed has to be within the beaming angle so that the flux is detected. Off-axis detections are therefore only possible once the jet Lorentz factor has decreased to $\Gamma \sim 1/\theta_v$, where θ_v is the viewing angle. The highest-fluence initial part of the afterglow emission is therefore missed. There are current efforts to detect *orphan afterglows*: these are the off-axis afterglows that are detected (typically in optical) without the associated GRB prompt emission (*e.g.* Metzger & Berger 2012; Ghirlanda et al. 2015; Lamb et al. 2018; Huang et al. 2020). The description of GRB jets with the top-hat model in the context of GRBs at cosmological distances is particularly appropriate since the viewing angle of detected GRB afterglows is $\theta_v < \theta_c$.

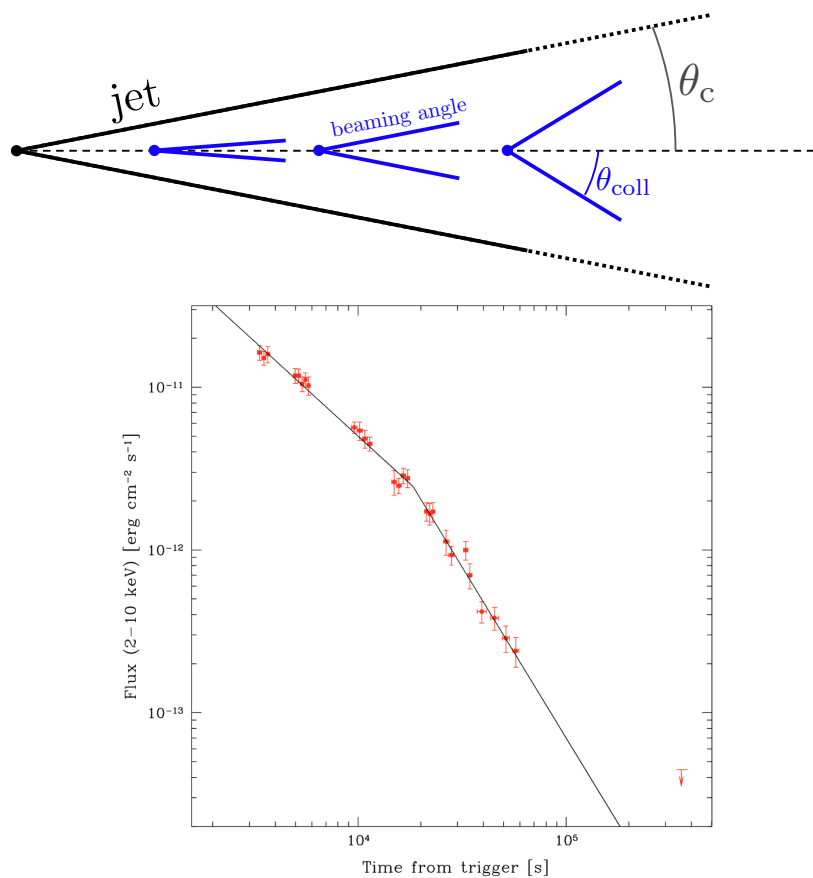


Fig. 4.1: Top: Schematic view of the relativistic beaming effect. The jet opening angle is shown in black, and the beaming angles at three epochs of the jet deceleration are shown in blue: $\theta_{\text{coll}} \ll \theta_c$; $\theta_{\text{coll}} = \theta_c$ and $\theta_{\text{coll}} > \theta_c$. When the beaming angle reaches the jet opening angle, a jet break appears in the on-axis afterglow light curve. **Bottom:** X-ray afterglow light curve of GRB 050318. The jet break is clearly visible at $\sim 2 \times 10^4$ s. This figure is reproduced from [Perri et al. \(2005\)](#).

The detected emission is therefore dominated by material radiating from the central parts of the jet on the line of sight. Any contribution from a putative lateral structure is subdominant. Off-axis afterglow light curves from top-hat jets are expected to be undetected first, then show a rapid rise until a peak, followed by a decline with the same slope as the post-jet break on-axis afterglows. With a lateral structure, this is altered, as I will discuss now.

In the early phases of the jet propagation, it interacts with the surrounding material. In the case of a long GRB associated with a Supernova (SN), the jet pierces through the outer envelopes of the collapsing star; while in the case of a short GRB associated with a BNS merger, the jet propagates in the kilonova ejecta (see Sec. 2.2). This interaction is expected to generate a lateral structure around the central part of the jet. Several 3D general-relativistic magneto-hydrodynamical simulations (GRMHD) have studied jets launching and their interaction with their environments, and exhibited a diversity of possible profiles for the lateral structure of the jet, when they are successful (see *e.g.* [Gottlieb et al. 2022](#)). These simulations also exhibit the diversity of outcomes after the jet propagation: choked and successful jets, shock breakouts (see Sec. 1.3). In our afterglow model presented in Chapter 5, we introduce several analytical descriptions of the lateral profiles (see Sec. 5.1). A structured jet viewed off-axis ($\theta_v > \theta_c$) will produce a light curve with a late-time peak. However, as discussed by [Granot et al. \(2002\)](#); [Nakar et al. \(2002\)](#), the time of the peak and its flux are independent of the lateral structure, and only depend on the properties of the central part of the jet (its core) and the viewing angle. The general properties of off-axis afterglows are discussed

in Beniamini et al. (2022). In particular, the properties of the lateral structure can only be probed during the initial phase before the peak of detected flux.

In the case of the afterglow of GW 170817, Very Long Baseline Interferometry (VLBI) imagery confirmed the presence of an ultra-relativistic and unresolved source (see Sec. 2.4, Mooley et al. 2018a, 2022; Ghirlanda et al. 2019). This is consistent with the detection of a jet viewed off-axis. The detected afterglow light curve (see Fig. 2.4) showed a slow rise and a peak at $t \sim 120 - 160$ days. This slow rise is directly due to the contribution of the lateral structure, as shown in *e.g.* D’Avanzo et al. (2018). As the jet decelerates, material at higher angles with respect to the line of sight becomes visible. In the case of the structured jet, material from the lateral structure with lower energy becomes visible at early times, but has a low flux. Gradually, more energetic material becomes visible until the peak, where the central part of the jet is finally uncovered. The slow rise is due to the progressive reveal of material between the line of sight and the core of the jet. As I show in Fig. 4.2, the contribution of the lateral structure at early times is necessary to reproduce the observations for GW 170817. However, as pointed out in *e.g.* Gill & Granot (2018), several structure profiles can reproduce the early rise, such as Gaussian or power-law jets (see the definitions in Sec. 5.1). In Fig. 4.2, we used our model described in Chapter 5 with best-fit parameters found in Chapter 6.

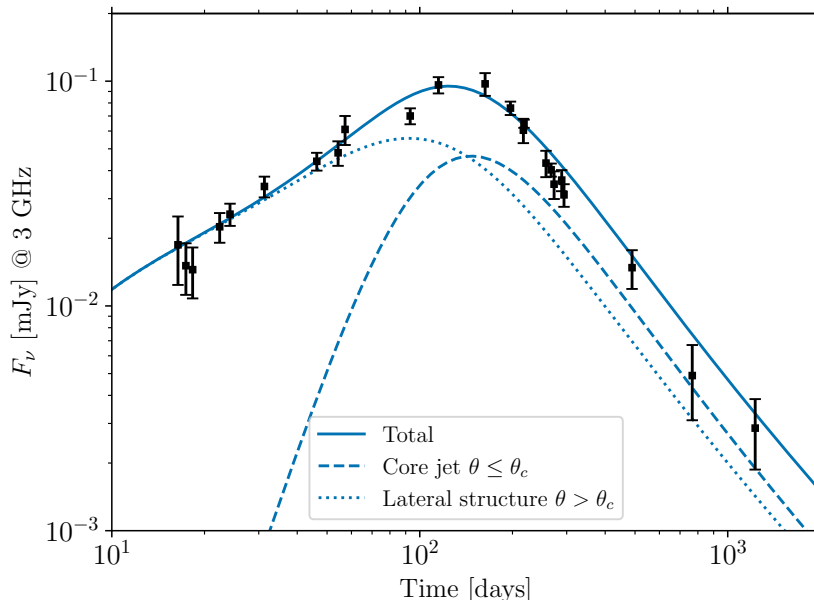


Fig. 4.2: Afterglow light curve of GW 170817 in the radio band (3 GHz). Observational data is shown in black and the resulting light curve using the model described in Chapter 5 with our best fit parameters (see Tab. 6.6) is shown in solid blue. In this model, the jet core angle is $\theta_c = 1.75$ deg and the viewing angle $\theta_v = 21.25$ deg. The contribution of the core of the jet is shown in dashed lines and the contribution of the lateral structure in dotted lines.

Such a lateral structure may be a common feature in GRBs due to the early propagation of the relativistic ejecta through the infalling envelope of the stellar progenitor (long GRBs) or the post-merger ejecta responsible for the kilonova emission (short GRBs) as highlighted in Bromberg et al. (2011). Possible signatures of such a lateral structure in GRBs at cosmological distance viewed slightly off-axis have been recently discussed, for instance to explain the complex phenomenology observed in the early afterglow (Beniamini et al., 2020a; Oganessian et al., 2020; Ascenzi et al., 2020; Duque et al., 2022) or the non-standard decay of the afterglow of the extremely bright GRB 221009A (O’Connor et al., 2023; Laskar et al., 2023; Gill & Granot, 2023). Accounting for the lateral structure of the jet in afterglow models has thus become necessary not only for GW 170817 but for other cosmic

GRBs as well.

4.2 The Very High Energy Emission of Gamma-Ray Burst Afterglows

Another important recent advance concerning GRB phenomenology has occurred since 2016: some long GRBs have been detected at VHE ($h\nu \sim 1$ TeV) with Čerenkov telescopes. So far, all detections at a high level of confidence concern the early afterglow of long GRBs: GRB 180720B (H.E.S.S., Abdalla et al. 2019); GRB 190114C (MAGIC Collaboration et al., 2019a,b); GRB 190829A (H. E. S. S. Collaboration et al., 2021); and GRB 201216C (MAGIC, Blanch et al. 2020). Two other bursts have been associated with VHE photons at $< 5\sigma$ confidence by MAGIC: GRB 160821B (Acciari et al., 2021), the only short GRB with candidate VHE photons observations; and GRB 201015A (Suda et al., 2022). A discussion on the recent observational status of GRBs at VHE can be found in Noda & Parsons (2022).

Among these bursts, the most exceptional given its multi-wavelength follow-up is GRB 190114C, located at a redshift $z \simeq 0.42$. Fig. 4.3 shows the light curves of its afterglow from radio to VHE (left panel), and the modelled spectra at two epochs (right panel) assuming Synchrotron Self-Compton (SSC) diffusions (see hereafter and in Chapter 5) power the VHE spectral component. The nature of the process powering the VHE component in this particular event is still debated, as SSC models struggle to reproduce simultaneously the late-time light curves and the early-time spectral properties with fixed microphysical parameters. This could be an element of future study (see Chapter 10).

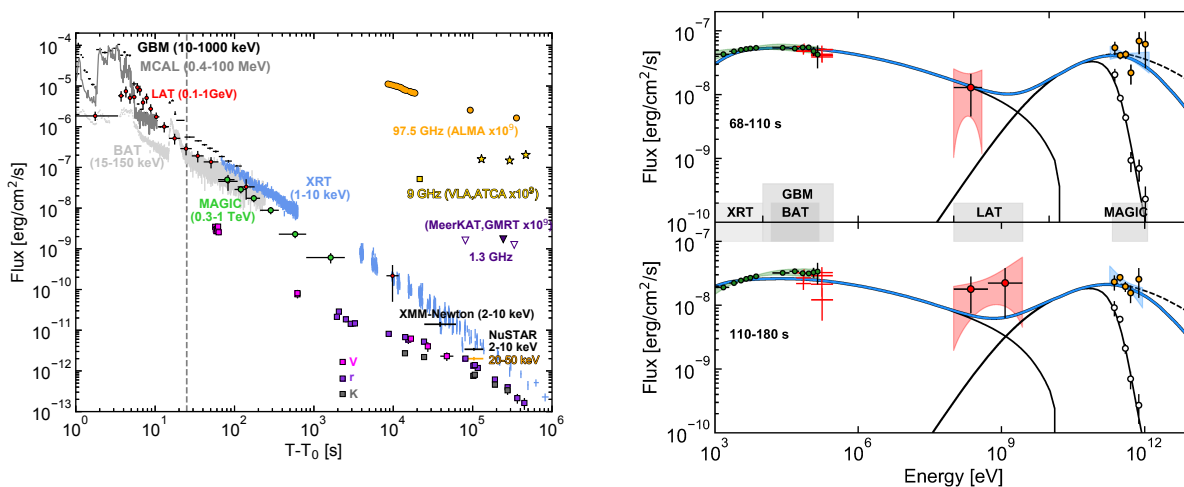


Fig. 4.3: **Left:** Multi-wavelength light curve of the afterglow of GRB 190114C, from radio to VHE. MAGIC observations between 0.3 and 1 TeV are shown in green. **Right:** Observed spectra between X-rays and VHE at two epochs. The blue curve shows the total modelled flux, dominated by synchrotron radiation at lower energy and SSC diffusions at higher energy. The white data points correspond to actual observations without correcting for EBL absorption (see Sec. 5.4.8). This figure is reproduced from MAGIC Collaboration et al. (2019b).

Even more recently, GRB 221009A, the brightest GRB ever observed, was detected by Fermi-GBM (Lesage et al., 2023), INTEGRAL (Rodi & Ubertini, 2023), Insight-HXMT (An et al., 2023) and even CubeSats such as GRBAlpha (Řípa et al., 2023). Its peak flux was so bright that it saturated the gamma-ray detectors onboard Fermi and INTEGRAL. Part of the explanation for GRB 221009A's extreme brightness is its nearby localisation at $z \simeq 0.15$, making it one of the

closest GRBs ever detected. However GRB 221009A was still intrinsically the most energetic GRB ever observed (see *e.g.* **Publication II**, Appendix E.2, Kann et al., 2023), with an isotropic-equivalent energy radiated in the prompt phase $E_{\gamma, \text{iso}} > 3 \times 10^{54}$ erg. GRB 221009A was also observed in X-rays with Swift (Vasilopoulos et al., 2023) and XMM-Newton (Tiengo et al., 2023). The X-ray images show series of concentric rings caused by the scattering of X-ray photons on dust clouds on the line of sight, a unique feature that allowed to determine the position of dust clouds in this direction in the Milky Way. What makes this burst even more fascinating is that it was soon reported in a GCN alert by the LHAASO collaboration to be associated with more than 5000 VHE photons (Huang et al., 2022). In fact, the results of the VHE signal were published in June 2023 and showed that more than 64000 VHE photons between 200 GeV and ~ 10 TeV constituted the VHE signal of GRB 221009A (LHAASO Collaboration et al., 2023). The VHE light curve between ~ 0.2 and 7 TeV is shown in Fig. 4.4. In the analysis of this data, LHAASO Collaboration et al. (2023) identify in the observations an emission peak after ~ 10 s, from which they estimate the jet initial Lorentz factor $\Gamma_0 \simeq 440$. At ~ 670 s a clear break is visible: after assuming that the observed TeV radiation is a signature of the afterglow of GRB 221009A, the authors interpret it as the signature of the jet break, hinting to an extremely narrow jet with an opening angle $\theta_c \simeq 0.6$ deg. A detailed multi-wavelength analysis of the whole observational data set of GRB 221009A could potentially yield original results given the outstanding characteristics of this burst.

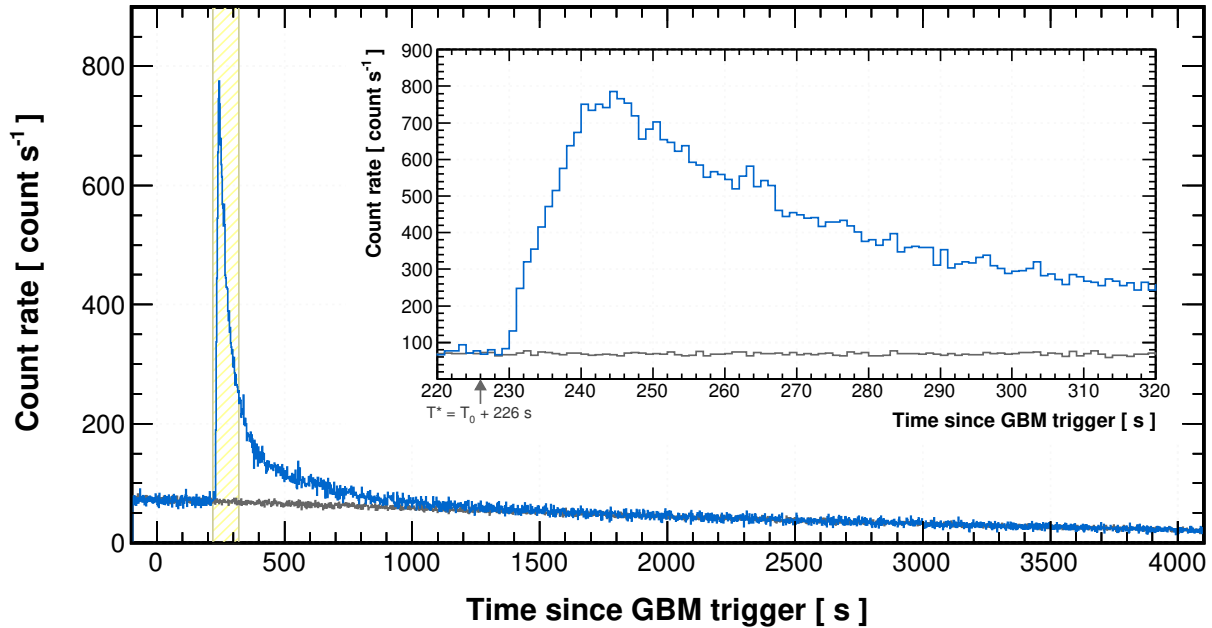


Fig. 4.4: Count-rate light curve of GRB 221009A observed by LHAASO. The energy range of photons observed is ~ 0.2 –7 TeV. The inset panel shows a zoomed-in view of the light curve from 220 to 320 s (yellow shaded zone) after the Fermi-GBM trigger (T_0), with the arrow indicating the reference time $T_* = T_0 + 226$ s, corresponding to the first saturation of the detector in the Fermi-GBM observations. Blue histograms are the data, and black histograms are the estimated background. This figure is reproduced from LHAASO Collaboration et al. (2023).

The GRANDMA Collaboration, including members of our group at IAP, is a network of telescopes dedicated to the optical follow-up campaigns of GRBs and Gravitational Wave (GW) alerts. GRB 221009A was followed-up by GRANDMA and I participated in the interpretation of the data using the model presented in Chapter 5. This work was conducted with data only partially available

at the time (optical observations from the GRANDMA collaboration, Swift-XRT and Insight-HXMT X-ray data) in a fast-response mode to provide first estimates of this GRB’s properties. This allowed to use for the first time the model presented in Chapter 5 in coupling with Bayesian analysis. Other co-authors performed the same study using `afterglowpy` (Ryan et al., 2020), another commonly used afterglow model. We found similar results with the synchrotron radiative model (Sec. 5.4.4), which provided a useful test of our model (for more details, see Sec. 5.6). These results were included in Kann et al. (2023, **Publication II**, Appendix E.2) where the observations of GRB 220109A by the GRANDMA network and Insight-HXMT are presented and discussed.

Our analysis in the context of the standard afterglow model shows puzzling results. The best-fit parameters indeed fail to reproduce either the temporal evolution of the afterglow light curve at late-time, or the spectral slope at early times. I show the best-fit light curves in Fig. 4.5. In orange, the model fails to reproduce the temporal evolution of the afterglow light curve, while in blue, the model misses the spectral slope at early times. Another puzzling observational feature is the absence of clear jet break in the observations. Assuming a top-hat jet, our model therefore predicts either a very narrow jet opening angle ($\theta_c \lesssim 0.5$ deg), or an extremely wide opening angle. Later observations at ~ 100 days did not exhibit a jet break, so this second option has since been ruled out. Several authors (*e.g.* Laskar et al. 2023; O’Connor et al. 2023; Gill & Granot 2023) have recently suggested that this behaviour may be the consequence of a laterally-structured jet. At the time at which our analysis was done, the radio observations reported in Laskar et al. (2023) were not available, but the radio fluxes are not reproduced by our models. All these analyses have been carried out using models only accounting for the synchrotron radiation and do not include processes for VHE emission, again as the LHAASO detection data was not available at the time. In this context, a re-analysis of the first study of Kann et al. (2023, **Publication II**, Appendix E.2) with a more complete data set and a full treatment of VHE emission will be carried out to leverage these unique observations.

The observations of these GRB afterglows at VHE challenge the simple radiative models where afterglow emission is pure synchrotron radiation from electrons accelerated at the forward shock. As I discuss in detail in Sec. 5.3 (see also the recent review Gill & Granot 2022), the synchrotron process is only efficient to radiate energy up to a maximum frequency ν_{\max} which, for an emitting region in relativistic motion with $\Gamma \sim 100$ is of about 10 GeV (see also Sec. 5.4.6). While synchrotron radiation by electrons may produce VHE photons with some specific magnetic field configurations, three main types of models have been proposed to explain VHE emission in GRB afterglows. (1) Synchrotron photons are upscattered by their seed electron populations at the shock, a process which is known as Synchrotron Self-Compton (SSC). This process has already been studied in the context of GRB afterglows and proposed as a candidate to explain the VHE emission of GRB 190114C (MAGIC Collaboration et al., 2019b). (2) Photons emitted by an external source (typically the thermal kilonova in the case of BNS mergers or the SN following a core-collapse) are upscattered by Inverse Compton (IC) diffusions on the shock-accelerated electrons. This process is called External Inverse Compton (EIC) and has been suggested to explain *e.g.* the GeV emission excess in GRB 211211A, a long GRB likely associated to a kilonova (Mei et al., 2022). (3) Synchrotron radiation is emitted by protons and ions accelerated at the shock, or more generally hadronic cascades occur at the shock front and produce VHE photons (for a review, see Kumar & Zhang 2015). The SSC process appears as the most promising to explain the diversity of VHE afterglows consistently, as it does not require the presence of a specific external source of radiation like EIC, or the more extreme energies required in hadronic scenarios.

However, while SSC emission can be efficiently computed analytically in the Thomson regime (*e.g.* Panaitescu & Kumar 2000; Sari & Esin 2001), several studies have pointed out the importance to also account for the Klein-Nishina (KN) attenuation at high energy (see *e.g.* Nakar et al., 2009; Murase et al., 2011; Beniamini et al., 2015; Jacovich et al., 2021; Yamasaki & Piran, 2022). In the KN regime, the IC power of an electron strongly depends on its Lorentz factor. This affects the

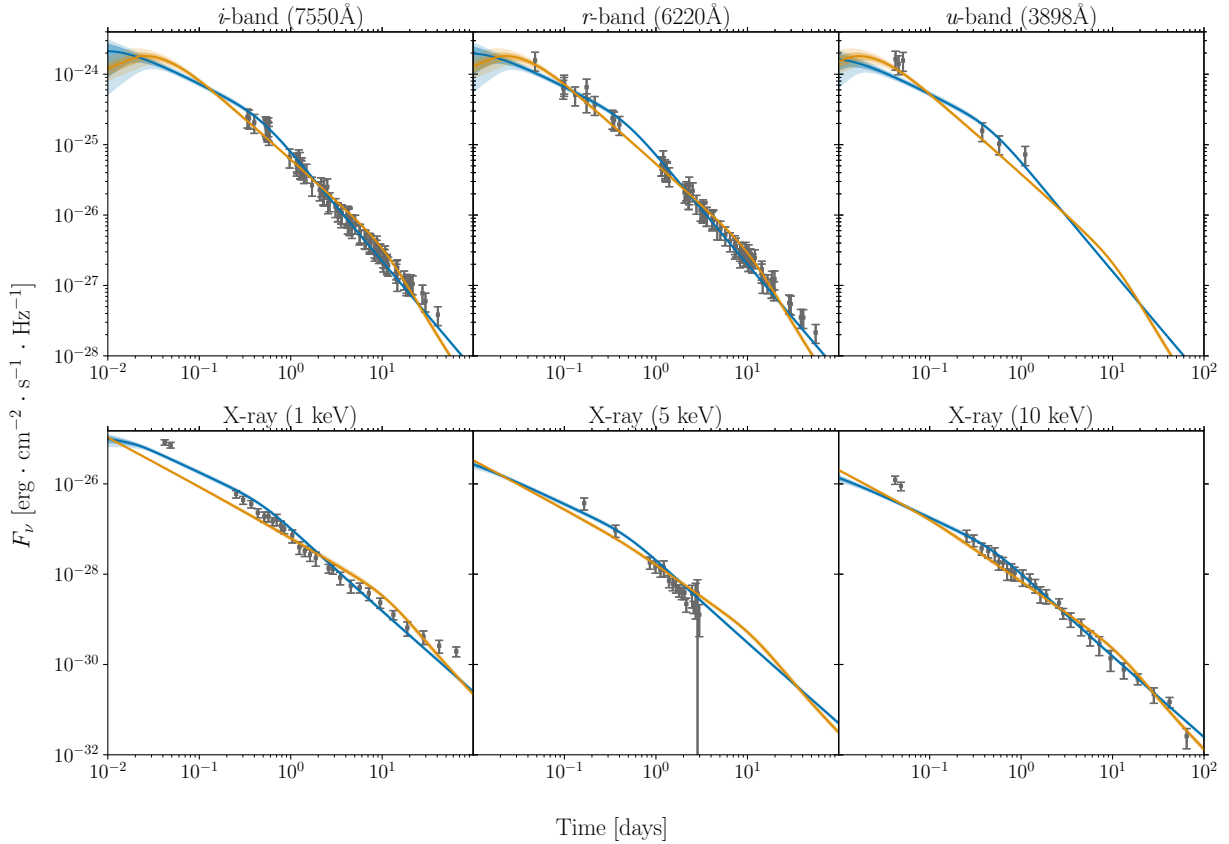


Fig. 4.5: Best-fit models of the multi-wavelength afterglow of GRB 221009A. Shown are the predicted light curves for the two classes of parameters discussed in Sec. 4.2 and found using a top-hat model with a fixed viewing angle $\theta_v = 0$ deg and assuming that only synchrotron radiation powers the emission at the forward shock. Observing frequencies or energies are shown on top of each panel, and the fitted observational data are displayed in gray. Blue curves show the model with a low θ_c and a spectral index $p \sim 2$ (see Sec. 5.3). Orange curves show the model with a high θ_c . More details can be found in Kann et al. (2023, **Publication II**, Appendix E.2).

cooling of the electron distribution and therefore also impacts the synchrotron spectrum (Derishev et al., 2001; Nakar et al., 2009; Bošnjak et al., 2009), which can significantly differ from the standard prediction given by Sari et al. (1998) for the pure synchrotron case.

Some recent works have already put to use afterglow models that include SSC diffusions and KN corrections, mostly to analyse the VHE observations of GRB 190114C (MAGIC Collaboration et al., 2019b; Wang et al., 2019; Derishev & Piran, 2021), GRB 190829A (Salafia et al., 2022b) or GRB 221009A (Sato et al., 2023). Along with these studies, several authors have proposed afterglow models with VHE emission (Nakar et al. 2009; Murase et al. 2010, 2011; Jacovich et al. 2021; Yamasaki & Piran 2022; Warren et al. 2022, see also the detailed review by Gill & Granot 2022), but none of them combine the effect of a lateral structure with SSC diffusions in both Thomson and KN regimes.

In this thesis, I developed such a model and implemented it numerically so that it can be coupled with Bayesian analysis. This model has been used to interpret the first afterglow detections of GRB 221009A shown in this chapter. In Chapter 5, I will describe this model in detail and show the results obtained with the analysis of GW 170817 in Chapter 6. In particular, I will discuss the VHE detectability conditions of similar events in the future. Multiple direct or indirect follow-up studies will be possible using this model. I discuss them in Chapter 10.

Chapter 5

Modelling the Synchrotron and Synchrotron Self-Compton Emission from a Decelerating Structured Relativistic Jet

Contents

5.1	Relativistic Outflow : Geometry and Structure	59
5.2	Dynamics of the Deceleration	64
5.3	Accelerated Electrons and Amplified Magnetic Field	68
5.4	Emissivity in the Comoving Frame	70
5.4.1	Synchrotron and Inverse Compton Radiation for a Single Electron	70
5.4.2	Radiative Regime of a Single Electron	74
5.4.3	Electron Distribution and Associated Emission	75
5.4.4	The Pure Synchrotron Case	79
5.4.5	The Synchrotron Self-Compton Case in Thomson regime	80
5.4.6	Self-consistent Calculation of the Electron Distribution and the Compton Parameter in the General Case	80
5.4.7	Pair Production	84
5.4.8	Extragalactic Background Light	85
5.4.9	Synchrotron Self-absorption	86
5.5	Observed Flux	86
5.6	Comparison with other Afterglow Models	88
5.7	Conclusion	90

The detection of the afterglow of GW 170817 with a clear jet lateral structure, as well as the recent observations of Gamma-Ray Burst (GRB) afterglows at Very High Energy (VHE) – discussed in Chapter 4 – have renewed the interest of disposing of semi-analytical models that include a laterally-structured jet and emission processes at VHE. In this work, the VHE emission from GRB afterglows is modelled with Synchrotron Self-Compton (SSC).

One major interest is to be able to use the afterglow observations of any GRB and infer the physical properties of the ejected material, the microphysics at the shock and to characterise the surrounding interstellar medium or stellar wind. The approach taken here is to build a semi-analytical model that can be implemented numerically and used to fit parameters to any GRB afterglow using Bayesian statistics (see Chapter 6). The key requirement is therefore that this semi-analytical model can be implemented numerically in a way that can generate synthetic data (typically light curves at a given observing frequencies/energies or spectra at given times) in a short computation time. This approach differs from detailed hydrodynamical simulations that follow the ejecta dynamics, which require longer integration times and do not include SSC in current implementations (*e.g.* van Eerten et al. 2012).

In this chapter, I discuss the ingredients included in this complete afterglow model, and show some details on their numerical implementation. Each section describes a distinct component to the model. Sec. 5.1 describes the geometry and the structure of the jet; Sec. 5.2 focuses on the treatment of the deceleration of the jet; Sec. 5.3 shows how the microphysics at the shock are accounted for. Sec. 5.4 describes the derivation of the comoving frame emission properties; and Sec. 5.5 is a description of the observer frame integration over surfaces of equal arrival time.

This chapter follows the description of the model presented in **Publication I**, of which I am the lead author (Appendix E.1, Pellouin & Daigne 2023, **submitted**), complemented by more details on the mathematical derivations and the numerical implementation.

A note on reference frames

In this chapter 5, I will refer to a variety of different reference frames that are useful to describe the different components of the model.

- The **observer frame** is attached to the observer, on Earth or in orbit. One of the frame axes is oriented in the direction of the observed source (line of sight), which can be observed from a certain viewing angle θ_v (see Fig. 5.8).
- The **source frame** is attached to the central engine of the ejected material, *i.e.* at the location of either the exploding star or the Binary Neutron Star (BNS) merger. Observer frame and source frame are simply connected by their luminosity distance D_L and the redshift z (time and wavelength dilation).
- The **comoving frame** of the emitting material is attached to the considered shocked region, either behind the forward shock or the reverse shock (see Fig. 5.1). Transformations from the comoving frame to the source frame are done *via* Lorentz transforms with the bulk Lorentz factor Γ of the considered region, which is evolving over time due to the jet deceleration in the external medium (see Sec. 5.2). Quantities in the comoving frame are expressed with a prime exponent, except when stated otherwise, *e.g.* t'_{dyn} . The Lorentz factor of the shock Γ_s differs from Γ . For the forward shock in the ultra-relativistic regime, $\Gamma_s = \sqrt{2}\Gamma$.
- I will sometimes refer to the frames attached to specific particles, for example the frame attached to an electron in motion. I will define the relevant **local frame** each time when it is necessary.

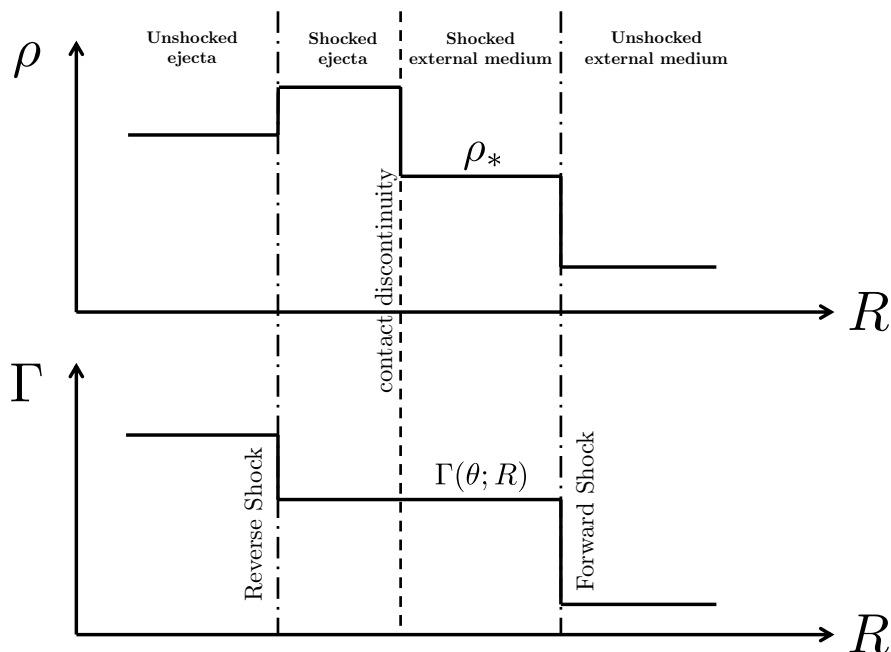


Fig. 5.1: Schematic of the forward and reverse shocks during the deceleration of the ejecta, in the frame where the unshocked external medium is at rest. The top graph shows the evolution of density across the different regions, while the bottom graph shows the evolution of the material Lorentz factor. The domain is divided in four regions: (1) unshocked external medium, upstream; (2) shocked external medium; (3) shocked ejecta; (4) unshocked ejecta, downstream. A long-lived forward shock forms between the shocked and unshocked external medium, and a short-lived reverse shock forms between the shocked and unshocked ejecta. A contact discontinuity separates the shocked ejecta and the shocked external medium. At this surface, the Lorentz factor and the pressure are continuous, but the magnetic field and density sharply change.

5.1 Relativistic Outflow : Geometry and Structure

Preliminary notes

The first ingredient needed to model the emission of GRB afterglows is the geometrical characterisation and the structure of the jet, where the radiation originates.

As described in Sec. 2.3 and Sec. 2.4, the phase of afterglow emission follows the prompt phase (see Sec. 1.3), that we do not aim to model here. Independently of the internal dissipation mechanism responsible for the prompt emission, a strong ultra-relativistic forward shock will form in the external medium during the deceleration of the jet¹. This leads to the structure shown in Fig. 5.1, with four distinct regions of shocked and unshocked ejecta and external medium, separated by the forward shock, a shorter-lived reverse shock and a contact discontinuity.

In this Part II, we model the afterglow emission by focusing on the contribution of electrons accelerated at the forward shock. The shocked external medium is assumed to be geometrically and optically thin.

We also do not model the contribution of the reverse shock, which can contribute to the early afterglow emission. It propagates in the unshocked ejecta from the contact discontinuity in the comoving frame (though due to the radial motion of the comoving frame, its motion is still in the radial direction away from the central engine, in the source frame). It is typically short-lived and only contributes at early times, as described in *e.g.* Kobayashi (2000). For now, we do not

¹Due to the short activity of the central engine, the ejecta is only a geometrically thin layer. A *jet* may therefore not be the most appropriate terminology to describe the geometry of the outflow. Some authors have thus suggested that we rather call it a *flying pancake*, which provides an image closer to reality. Given the assumption that the pancake is geometrically thin, I suggest here the *flying crêpe* terminology, but will still refer to the ejecta as a *jet*.

include its contribution in our model, but this can be added in the future. Conveniently, the numerical implementation of the afterglow model presented hereafter allows to easily include new models for the shock dynamics, as the treatment of the dynamics and all the radiative processes are decoupled. The reverse shock dynamics can be implemented in a later extension either in a semi-analytic way, similarly to the forward shock (Sari & Piran, 1999; Kobayashi, 2000), which has been validated by hydrodynamical simulations (Kobayashi & Sari, 2000). More complex approaches (Uhm & Beloborodov, 2007; Genet et al., 2007), which have also been validated by full hydrodynamical simulations (Lamberts & Daigne, 2018; Ayache et al., 2020), allow to take into account the possible radial structure of the ejecta, which is expected from the variability of the central engine (see Sec. 1.3). Including this complexity may be needed to explain the early afterglow, which shows some variability and diversity (*e.g.* plateaus, flares), as discussed *e.g.* in Uhm et al. (2012); Hascoët et al. (2017). Introducing the reverse shock may lead to future developments discussed of the model presented here, as discussed in Sec. 10.2.

Jet geometry description

We consider a laterally-structured jet. Its properties are defined by its kinetic energy and Lorentz factor $\Gamma(\theta; R)$, at all latitudes from the jet axis and throughout the propagation. We recall the definition of the Lorentz factor Γ of some material in motion with a velocity v , first introduced by Lorentz (1898, 1903) and named after him by Poincaré a few years later:

$$\Gamma \equiv \frac{1}{\sqrt{1 - \beta^2}}, \quad (5.1)$$

with

$$\beta \equiv \frac{v}{c}, \quad (5.2)$$

and c the speed of light in vacuum. We will follow the evolution of $\Gamma(\theta; R)$ with time at different latitudes as the jet decelerates in the external medium.

In a fully radial motion, the dynamics of the forward shock decelerating in the external medium is only constrained by the jet initial Lorentz factor Γ_0 and total energy E_0 (or equivalently total energy per solid angle ϵ_0), and by the external medium density profile. In our model, we therefore describe the jet with these two parameters. Specifically, in the lateral structure of the jet, the initial energy per solid angle $\epsilon_0(\theta)$ and the initial Lorentz factor $\Gamma_0(\theta)$ decrease with θ , the angle from the jet axis. We define θ_c as the opening angle of the core, *i.e.* the ultra-relativistic/ultra-energetic central part of the jet. We then express

$$\epsilon_0(\theta) = \epsilon_0^c \times f_a \left(\frac{\theta}{\theta_c} \right) \quad (5.3)$$

and

$$\Gamma_0(\theta) = 1 + (\Gamma_0^c - 1) \times g_b \left(\frac{\theta}{\theta_c} \right), \quad (5.4)$$

where ϵ_0^c is the initial kinetic energy per solid angle and Γ_0^c is the initial Lorentz factor, both on the jet axis ($\theta = 0$). Finally, f_a and g_b are the normalized profiles for the energy and Lorentz factor in the lateral structure, that I describe hereafter.

Lateral structure profiles

Until the detection of GW 170817, GRB afterglows were mostly modelled using the *top-hat* jet geometry, where the jet has no lateral structure and is simply described by a single initial Lorentz

factor Γ_0 , energy E_0 and jet half-opening angle θ_c . In other words

$$f_a(x) = g_b(x) = \begin{cases} 1 & \text{if } x < 1 \\ 0 & \text{if } x \geq 1 \end{cases}, \quad (5.5)$$

and there are no free parameters a and b to describe the jet structure. This was justified by the fact that GRBs were detected at cosmological distances, and thus special-relativistic collimation effects would not allow for detections at such high distances if the jets were not observed on-axis, as I discussed in Sec. 4.1. It was therefore not possible to probe the lateral structure because the observations were made on-axis or slightly off-axis (see *e.g.* Piran 2004).

The detection of GW 170817 was a turning point as it was observed at a very close distance (~ 40 Mpc, see Sec. 2.1 and *e.g.* Cantiello et al. 2018); significantly off-axis as confirmed by Very Long Baseline Interferometry (VLBI) observations (Mooley et al., 2018a, 2022; Ghirlanda et al., 2019); and shows evidence for a lateral structure due to the slow rise of the afterglow light curve (see Fig. 4.2 and Sec. 4.1). It has therefore become necessary to include lateral structures in the models. Different lateral structures have been suggested in the literature, following the photometric and VLBI observations of GW 170817's GRB afterglow and numerical hydrodynamical simulations (see Sec. 4.1).

Our fiducial model assumes a power-law structure with a core, as defined by Duque et al. (2019):

$$f_a(x) = \begin{cases} 1 & \text{if } x < 1 \\ x^{-a} & \text{if } x \geq 1 \end{cases}, \quad (5.6)$$

$$g_b(x) = \begin{cases} 1 & \text{if } x < 1 \\ x^{-b} & \text{if } x \geq 1 \end{cases}. \quad (5.7)$$

This prescription allows a direct comparison with a top-hat jet (see Eq. 5.5). For comparison with other studies, we also consider the following possible structures, that can be selected in the numerical simulations:

- A power-law jet as defined in Gill & Granot (2018): $f_a(x) = X^{-a}$ and $g_b(x) = X^{-b}$, with $X = \sqrt{1 + x^2}$.
- A power-law jet as defined in Ryan et al. (2020) and used in `afterglowpy`², a currently widely-used open-source GRB afterglow simulation Python package:

$$f_a(x) = \left(\sqrt{1 + x^2/a} \right)^{-a}. \quad (5.8)$$

Note that `afterglowpy` is limited to the self-similar evolution of the jet (see Sec. 5.2), which is independent of the initial value of the Lorentz factor. Therefore g_b is not defined in this case.

I compare our results with those obtained with `afterglowpy` in more details in Sec. 5.6.

- A Gaussian jet as defined in Gill & Granot (2018):

$$f_a(x) = g_b(x) = \max \left(e^{-\frac{x^2}{2}}; e^{-\frac{x_{\max}^2}{2}} \right), \quad (5.9)$$

where $x_{\max} = \theta_{\max}/\theta_c$ and θ_{\max} is defined as the angle where $\beta_{0,\min}(\theta_{\max}) = 0.01$ (their default assumption) or any other specific value. In this case, the free parameters a and b are therefore replaced by a new free parameter, $\beta_{0,\min}$. Ryan et al. (2020) also include Gaussian jets in their simulations and use a similar parametrization of the lateral structure for Gaussian jets in `afterglowpy`, but they impose $\theta_{\max} = 90$ deg, *i.e.* no cutoff to the lateral structure.

²<https://afterglowpy.readthedocs.io/en/stable/>

I show in Fig. 5.2 the different possible structures described above. Many other jet structures can be hypothesized and emerge from different models and simulations (see Sec. 4.1). However, from afterglow light curves and spectra characterisation only, it is impossible to distinguish between different lateral structure prescriptions, as they can usually reproduce the observations very well with realistic parameters. This is discussed in the case of GW 170817 by *e.g.* Takahashi & Ioka (2021).

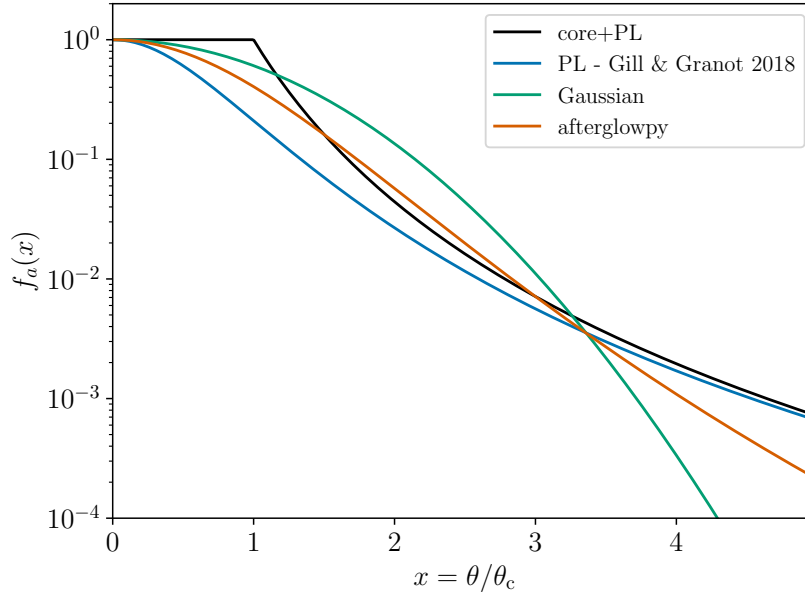


Fig. 5.2: Lateral energy structure profiles defined in Sec. 5.1, shown as a function of the ratio θ/θ_c .

Final considerations

The initial total kinetic energy of the jet and of its core are given respectively by integrating the energy per solid angle (Eq. 5.3) over all solid angles:

$$E_0 = 2 \int_0^{\pi/2} \epsilon_0(\theta) 2\pi \sin \theta d\theta, \quad (5.10)$$

$$E_0^c = 2 \int_0^{\theta_c} \epsilon_0(\theta) 2\pi \sin \theta d\theta. \quad (5.11)$$

The factor 2 accounts for the counter-jet, given that we only integrate over θ up to $\pi/2$. The factor 2π under the integrals is a consequence of the symmetry by revolution around the cone axis for such a geometry.

As is often the case in GRB prompt and afterglow emission modelling, we use the *isotropic-equivalent* energy of the core jet as a model parameter, rather than its true energy. The isotropic-equivalent energy of a top-hat jet is defined as the energy that would be contained if it were spherical, assuming the same average energy per unit solid angle. For an opening angle θ_c of the core jet, it leads to

$$E_{0,\text{iso}}^c = \frac{E_0^c}{1 - \cos \theta_c}. \quad (5.12)$$

From this definition, it is clear that $E_{0,\text{iso}}^c \geq E_0^c$. Given the typically narrow opening angles of GRB jets $\theta_c \lesssim 5$ deg, the true energy contained in the jets is typically 1 or 2 orders of magnitude smaller than the isotropic-equivalent energy.

For the power-law structure considered here (Eq. 5.6), we have

$$E_0^c = 4\pi\epsilon_0^c (1 - \cos \theta_c) \quad (5.13)$$

and

$$E_{0,\text{iso}}^c = 4\pi\epsilon_0^c. \quad (5.14)$$

With this description, $E_{0,\text{iso}}^c$, Γ_0^c , θ_c , a and b (or $\beta_{0,\text{min}}$ for the Gaussian jet) are the only four free parameters needed to fully describe the initial structure of the jet before the deceleration starts.

In the numerical implementation of the model, we suppress the lateral structure above a maximum angle θ_{max} . This angle is taken as the maximum between θ_ϵ , defined as the angle up to which a fraction $(1 - \epsilon)$ of the jet energy is contained, and the viewing angle θ_v . We therefore solve numerically for θ_ϵ the equation

$$(1 - \epsilon)E_0 = 2 \int_0^{\theta_\epsilon} \epsilon_0(\theta) 2\pi \sin \theta d\theta, \quad (5.15)$$

where E_0 is computed using Eq. 5.10.

In practice we use $\epsilon = 0.01$. Ryan et al. (2020) introduce a similar parameter, θ_W in `afterglowpy`, to minimize computation time. In our case, we checked on multiple numerical simulations that taking $\theta_{\text{max}} = \max(\theta_\epsilon; \theta_v)$ allows to keep a precise calculation at early times even at very large viewing angles.

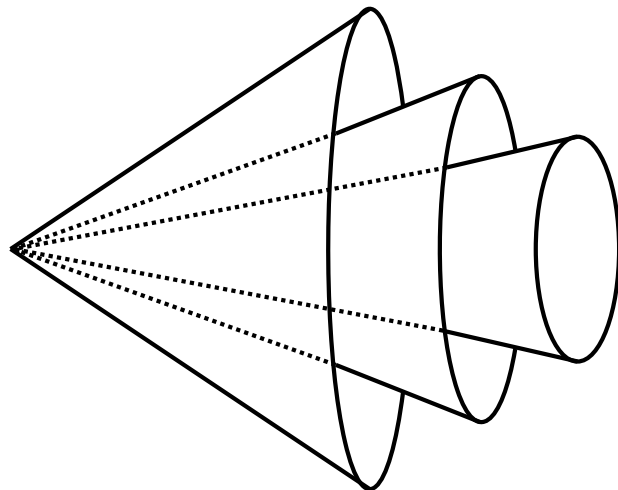


Fig. 5.3: Schematic of the lateral structure discretization used in the numerical implementation of the model.

Numerically, the lateral structure is discretized in $N + 1$ components, $i = 0$ being the core jet and $i \in \llbracket 1, N \rrbracket$ being rings at increasing angles in the lateral structure. Each component is defined by $\theta_{\min,i} \leq \theta \leq \theta_{\max,i}$ with $\theta_{\min,0} = 0$ and $\theta_{\max,0} = \theta_c$ for the core jet and $\theta_{\min,i} = \theta_{\max,i-1}$ for $i \in \llbracket 1, N \rrbracket$ and $\theta_{\max,N} = \theta_{\text{max}}$. Each component is treated independently with fixed limits in latitude (no lateral spreading). A representation of this treatment is shown in Fig. 5.3.

In reality, the jet material starts to have a lateral motion as it becomes mildly relativistic (Rhoads, 1999). Lateral spreading is limited in the ultra-relativistic phase (see Sec. 5.2), as the transverse velocity is expected to be of the order of $c_s/\Gamma \ll c$, where c_s is the sound speed. This effect is naturally resolved and observed in hydrodynamical simulations, but more complex to incorporate in a semi-analytic framework. Several prescriptions for a semi-analytic treatment of lateral spreading have been proposed and are discussed in *e.g.* Granot & Piran (2012); Duffell & Laskar (2018). Lateral expansion primarily attenuates the temporal slope of the post-jet break afterglow light curve. In our model, we do not include lateral spreading at the moment, but this feature can be added in a later version. For this reason, we will not include late-time observations of the afterglow of GW 170817 after 400 days in the fit presented in Chapter 6.

The dynamics is computed such that $R_i(t) = R(\theta_i; t)$ and $\Gamma_i(t) = \Gamma(\theta_i; t)$, where $R(\theta, t)$ and $\Gamma(\theta, t)$ are given by the solution for the dynamics of the deceleration discussed in Sec. 5.2, and where $\theta_i = (\theta_{\min,i} + \theta_{\max,i})/2$ for $i \geq 1$ and $\theta_0 = 0$. Another option could be to choose $\theta_i = \sqrt{\theta_{\min,i}\theta_{\max,i}}$ but with sufficient discretization in components, the effect of this choice is negligible. We define the successive $\theta_{\min,i}$ and $\theta_{\max,i}$ such that each component carries an equal amount of energy (except for the core, $i = 0$), though a linear increase can also be chosen. Finally, we typically choose a discretization comprised of $N = 15$ components, that we find to be a good compromise between model accuracy and computational efficiency.

5.2 Dynamics of the Deceleration

External medium

The next ingredient of our model is the description of the motion of the ejecta in the external medium. The structured outflow decelerates in an external medium, with an assumed density profile as a function of radius R :

$$\rho_{\text{ext}}(R) = \frac{A}{R^s}. \quad (5.16)$$

Two density profiles can be chosen: a **uniform** medium ($s = 0$) and a **wind** medium ($s = 2$). The former is the typical environment expected around BNS mergers, which occur in the interstellar medium where the density can be assumed to be constant. The value of the density itself is subject to variations, in particular depending on the delay time between the BNS formation and its merger. Short delay times favour mergers close to stellar formation sites, where the density is typically higher (see also Sec. 6.4). The latter is expected from the late-time ejection of material from the dying star due to stellar winds (see Sec. 8.2.1) before its explosion, and is more relevant for the discussion of long GRB afterglows.

A is defined such that

$$A = \begin{cases} n_{\text{ext}} m_p & \text{if } s = 0 \\ 5 \times 10^{-11} A_* & \text{if } s = 2 \end{cases}, \quad (5.17)$$

where n_{ext} is the external medium particle density (cm^{-3}), m_p is the proton mass, and A_* is a dimensionless scaling factor. For the wind medium,

$$A = \frac{\dot{M}_W}{4\pi v_W}, \quad (5.18)$$

and the factor $5 \times 10^{-11} \text{ g} \cdot \text{cm}^{-1}$ corresponds to a Wolf-Rayet (WR) wind with a mass-loss rate $\dot{M}_W = 10^{-5} M_\odot \cdot \text{yr}^{-1}$ and a velocity $v_W = 1000 \text{ km} \cdot \text{s}^{-1}$ (Chevalier & Li, 2000). Note that given the definition used in Eq. 5.16, A is a parameter whose dimension changes depending on the environment type. The values of n_{ext} or A_* are free parameters of the model.

Shock jump conditions

I presented in Fig. 5.1 the geometry of the shocked regions and in particular the different discontinuities in mass density ρ (top) and Lorentz factor Γ (bottom). For a fluid in non-relativistic motion, the shock jump conditions are the Rankine-Hugoniot relations (Rankine, 1870; Hugoniot, 1889), which correspond to the conservation of energy, momentum and mass. These were extended to ultra-relativistic strong shocks by Blandford & McKee (1976). A *strong* shock is such that the energy density in the shocked external medium is much greater than that of the external medium

at rest. Following [Blandford & McKee \(1976\)](#), the shocked external medium mass density ρ_* is therefore

$$\rho_*(\theta; R) = \frac{\gamma\Gamma(\theta; R) + 1}{\gamma - 1} \rho_{\text{ext}}(R), \quad (5.19)$$

where γ is the adiabatic index in the shocked region (here γ is not a Lorentz factor) and ρ_{ext} is defined in [Eq. 5.16](#); and the internal energy per unit mass in the shocked region is

$$\epsilon_*(\theta; R) = (\Gamma(\theta; R) - 1) c^2. \quad (5.20)$$

As long as the internal motion of particles is ultra-relativistic ($\epsilon_* \gg c^2$), which corresponds to the ultra-relativistic phase of the forward shock, the adiabatic index equals $\gamma = 4/3$ and [Eq. 5.19](#) can be expressed as

$$\rho_*(\theta; R) = (4\Gamma(\theta; R) + 3) \rho_{\text{ext}}(R), \quad (5.21)$$

which is the expression that we use in our model. The adiabatic index transfers towards $\gamma = 5/3$ for non-relativistic material. Some authors use transfer functions that compute the evolution of the adiabatic index during the jet deceleration, as described in [Mignone et al. \(2005\)](#). We keep this option for future additions to the model.

The question of the microphysical processes occurring at the forward shock is more challenging to account for. Particles are accelerated at the shock by turbulence, plasma instabilities and complex simulations are needed to track these effects. I describe in [Sec. 5.3](#) the parametrization used in our model.

Dynamics of the forward shock

We focus on the dynamics of the shocked external medium at the forward shock. It is computed assuming that (i) the dynamics of each ring of material at angle θ is independent of other angles; (ii) the lateral expansion of the outflow is negligible. As mentioned before, these two assumptions are questionable at late times, close to the transition to the Newtonian regime (see also [Rhoads 1997](#)).

We can compute the Lorentz factor $\Gamma(\theta; R)$ of the shocked material at angle θ and radius R in a simplified way, using energy conservation (see *e.g.* [Panaitescu & Kumar, 2000](#); [Gill & Granot, 2018](#)). We consider a system (assumed isolated) containing the ejected jetted material and all external medium material that is swept-up until the radius R ,

$$E_{\text{mass},0}^{\text{ej}} + E_{\text{kin},0}^{\text{ej}} + E_{\text{mass},0}^{\text{ext}} = E_{\text{mass},R}^{\text{ej}} + E_{\text{kin},R}^{\text{ej}} + E_{\text{mass},R}^{\text{ext}} + E_{\text{int},R}^{\text{ext}}, \quad (5.22)$$

where quantities at the end of the activity of the central engine after all material is ejected are described with the subscript 0, and quantities at a radius R during the deceleration are described with a subscript R . A subscript kin is used for kinetic energy, mass for rest-mass energy and int for internal energy. Finally, the superscript ej is used for the ejecta and ext for the external medium. Here we assume that the outer medium is initially at rest ($E_{\text{kin},0}^{\text{ext}} = 0$) and the swept-up material gains internal energy $E_{\text{int},R}^{\text{ext}}$ behind the shock front.

Let $\Gamma_0(\theta)$ be the initial Lorentz factor of material at angle θ ([Eq. 5.4](#)); $\epsilon_0(\theta)$ be the initial energy per solid angle ([Eq. 5.3](#)); $M_{\text{ej}}(\theta)$ be the ejected mass per unit solid angle at a given latitude θ from the jet core

$$M_{\text{ej}}(\theta) = \frac{\epsilon_0(\theta)}{\Gamma_0(\theta)}; \quad (5.23)$$

and $M_{\text{ext}}(R)$ be the total mass of the external medium per unit solid angle up to the radius R

$$M_{\text{ext}}(R) = \int_0^R r^2 \rho_{\text{ext}}(r) dr. \quad (5.24)$$

We can re-write Eq. 5.22 in the source frame as

$$\begin{aligned} & \Gamma_0(\theta)M_{\text{ej}}(\theta)c^2 + M_{\text{ext}}(R)c^2 \\ = & \Gamma(\theta; R)M_{\text{ej}}(\theta)c^2 + \Gamma(\theta; R)M_{\text{ext}}(R)c^2 + \Gamma(\theta; R)M_{\text{ext}}(R)\epsilon_*(\theta; R), \end{aligned} \quad (5.25)$$

where $\Gamma(\theta; R)$ is the shock Lorentz factor at latitude θ and radius R and $\epsilon_*(\theta; R)$ is the internal energy per unit mass of material at the shock front (Blandford & McKee, 1976), defined in Eq. 5.20. Developing and simplifying Eq. 5.25, we thus find

$$\Gamma_0(\theta)M_{\text{ej}}(\theta) + M_{\text{ext}}(R) = \Gamma(\theta; R)M_{\text{ej}}(\theta) + \Gamma^2(\theta; R)M_{\text{ext}}(R). \quad (5.26)$$

We finally define the normalized quantity

$$m(\theta; R) = \frac{M_{\text{ext}}(R)}{M_{\text{ej}}(\theta)/\Gamma_0(\theta)} = \left(\frac{R}{R_{\text{dec}}(\theta)} \right)^{3-s}, \quad (5.27)$$

where we have defined the deceleration radius of the material at angle θ :

$$R_{\text{dec}}(\theta) = \left(\frac{(3-s)\epsilon_0(\theta)}{4\Gamma_0^2(\theta)c^2} \right)^{1/(3-s)}. \quad (5.28)$$

Deceleration is negligible while $R \ll R_{\text{dec}}(\theta)$. In the end, we derive the expression of the Lorentz factor of the shocked external medium:

$$\Gamma(\theta; R) = \frac{\Gamma_0(\theta)}{2m(\theta; R)} \left[-1 + \sqrt{1 + 4m(\theta; R) + 4 \left(\frac{m(\theta; R)}{\Gamma_0(\theta)} \right)^2} \right]. \quad (5.29)$$

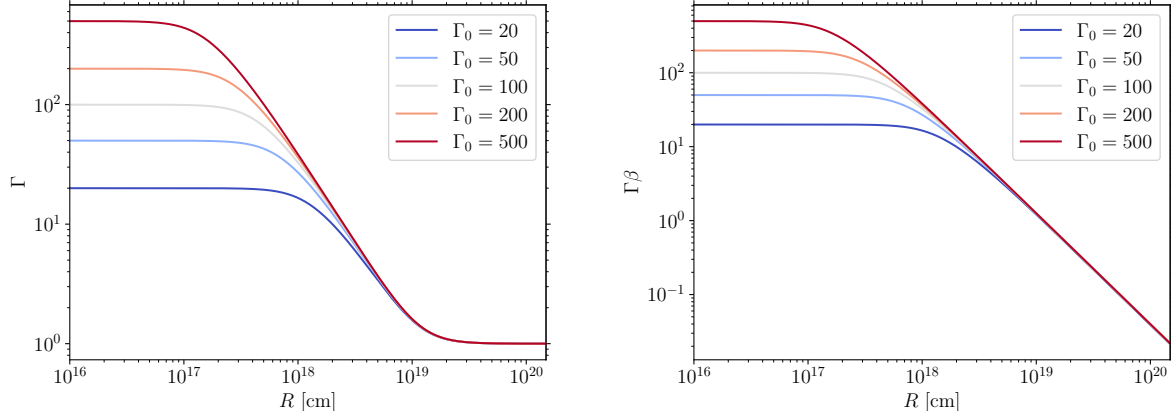


Fig. 5.4: $\Gamma(R)$ (left) and $\Gamma(R)\beta(R)$ (right) in the shocked external medium at $\theta = 0$ for different initial Lorentz factor values Γ_0 . The external medium is assumed uniform with $n_{\text{ext}} = 10^{-3} \text{ cm}^{-3}$, and the initial isotropic equivalent energy is $E_{0,\text{iso}} = 10^{52} \text{ erg}$. The deceleration radius (Eq. 5.28) decreases when Γ_0 increases, but the Newtonian radius (Eq. 5.30) is independent of Γ_0 . Once in the self-similar regime, the information on the initial Lorentz factor is therefore lost.

This description allows us to characterise the early-time dynamics in the coasting phase $R \ll R_{\text{dec}}(\theta)$ where the Lorentz factor remains constant. It branches continuously to the relativistic self-similar evolution (Blandford & McKee, 1976) for $R_{\text{dec}}(\theta) \ll R \ll R_{\text{N}}(\theta)$, where

$$R_{\text{N}}(\theta) = \Gamma_0^{\frac{2}{3-s}}(\theta)R_{\text{dec}}(\theta), \quad (5.30)$$

in which case $\Gamma(\theta; R) \propto (R/R_{\text{dec}}(\theta))^{-(3-s)/2}$. Finally, the dynamics enter the Sedov-Taylor phase (Sedov, 1946; Taylor, 1950) in the non-relativistic regime for $R \gg R_N(\theta)$. At that point, $\beta(\theta; R) \propto (R/R_N(\theta))^{-3/2}$. For $R \gg R_{\text{dec}}(\theta)$, the self-similar evolution becomes independent of the value of the initial Lorentz factor $\Gamma_0(\theta)$, as can be seen in Fig. 5.4. The continuous treatment of the coasting phase and the self-similar regime is not used in some models, which extend the self-similar solution to early times. The consequence is that the initial values of $\Gamma(\theta; R)$ diverge and subsequently the early phases of the afterglow light curve are not reproduced accurately. I show some examples in Sec. 5.6.

Once we know the Lorentz factor $\Gamma(\theta; R)$ and the velocity $\beta(\theta; R)$, which can be directly inferred by

$$\beta(\theta; R) = \frac{\sqrt{\Gamma^2(\theta; R) - 1}}{\Gamma(\theta; R)}, \quad (5.31)$$

the corresponding time t in the source frame is then given by

$$t(\theta; R) = \int_0^R \frac{dr}{\beta(\theta; r)c}. \quad (5.32)$$

This leads to the solution $R(\theta, t)$ and $\Gamma(\theta, t)$ used for the dynamics of each component of the structured jet (see Sec. 5.1).

Finally, we define the timescale of the adiabatic cooling of the shocked region due to its spherical expansion. In the source frame, the adiabatic expansion of the shocked region follows

$$\frac{dU}{dt} = -P \frac{dV}{dt}, \quad (5.33)$$

where U is the internal energy, P the pressure and V the volume of the region. Assuming $V \propto R^\alpha$, with $\alpha \leq 3$ and recalling $P = (\gamma - 1)u \approx (\gamma - 1)U/V$, where γ is the adiabatic index defined before, we therefore obtain

$$\frac{d \ln U}{dt} \approx -(\gamma - 1) \frac{d \ln V}{dt} \quad (5.34)$$

$$\approx -(\gamma - 1) \alpha \frac{d \ln R}{dt} \quad (5.35)$$

$$\approx -(\gamma - 1) \alpha \frac{\beta c}{R}, \quad (5.36)$$

using Eq. 5.32. Therefore, neglecting the first factor of order unity, the related *dynamical timescale* in the source frame is $t_{\text{dyn}} \approx R/\beta c$. In the comoving frame, it is expressed as

$$t'_{\text{dyn}}(\theta; R) = \frac{R}{\Gamma(\theta; R)\beta(\theta; R)c} = \frac{R}{c\sqrt{\Gamma^2(\theta; R) - 1}}. \quad (5.37)$$

Numerically, we compute the properties of the dynamics in an iterative manner. We initialize the jet at a radius $R \ll R_{\text{dec}}$, typically $R/R_{\text{dec}} = 10^{-6}$ to avoid numerical noise at too early times, and iterate over small values of dR . We then compute $\Gamma(\theta; R)$, $\beta(\theta; R)$, $M_{\text{ext}}(R)$, $dt = dR/(\beta(\theta; r)c)$ to deduce the new time t at $R + dR$. The iterative increment is given by

$$dR = R \times 10^{-2} \times \min \left[1; \min(1000; \beta(\theta; R)^{-2}) \times \min \left(1; \frac{\beta(\theta; R)}{1 - \beta(\theta; R)} (1 - \cos \theta_c) \right) \right]. \quad (5.38)$$

We stop the iteration at a given time t_{max} which corresponds to the latest observing time: later emission from the jet will only contribute at later times, regardless of the viewing angle. I show in Fig. 5.5 the variation of the parameter dR/R over the iterations, as well as the simultaneous value of $\Gamma(\theta; t)\beta(\theta; t)$. This method allows for a good sampling of the dynamics during all phases to produce

light curves that are smooth; while not over-discretizing which would slow down the computation. A first critical moment is at early times where a high enough discretization must allow to find a set $(t_{\text{obs}}^z; t)$ in the discretization of the dynamics such that the integral to compute the flux defined in Eq. 5.145 contains at least a few elements on which to integrate (otherwise the early-time light curves look jumpy). At late times, the discretization must be high enough for a similar reason: as the jet has a very slow radial motion, it behaves closer to a flashing surface. A fine enough discretization must be done in order to catch the emission time corresponding to the observer time. The impact of the discretization is maximal for on-axis observations.

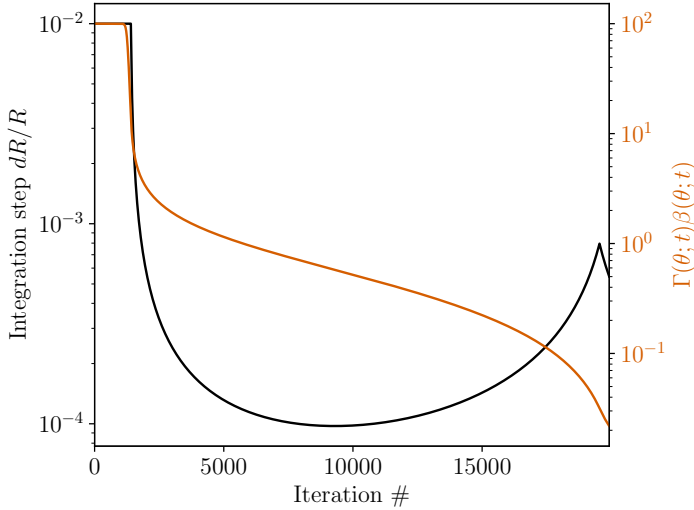


Fig. 5.5: Evolution of the discretization parameter dR/R defined in Eq. 5.38 during the iterations to generate the dynamical properties of the ejecta. The simultaneous velocity is shown for comparison with Fig. 5.4 which shows the same information as a function of a physical quantity: the radius R . This figure was created assuming $\Gamma_0 = 100$, $E_{0,\text{iso}}^c = 10^{52}$ erg, $\theta_c = 4$ deg and $t_{\text{max}} = 10^6$ days.

5.3 Accelerated Electrons and Amplified Magnetic Field

At the shock front, particles are accelerated by *Diffusive Shock Acceleration* (also known as first-order Fermi acceleration): they scatter off fluctuations in the local magnetic field and are recycled in the upstream and downstream material, gaining energy at every cycle (the mechanism was originally proposed by Axford et al. 1977; Bell 1978; Blandford & Ostriker 1978). Upstream (that is, in the unshocked region ahead of the jet), the magnetic field instabilities are caused by the turbulent motion of individual particles (plasma instabilities), while downstream (behind the shock) they directly originate from the shock (shock instabilities, Marcowith et al. 2016). Currently, many simulations are performed to understand the small-scale details of these instabilities and the conditions that lead to their development. Most of these simulations rely on the Particle In Cell (PIC) technique that follows directly individual particles and solves the equations of motion in a magnetized environment. Contrary to non-relativistic shocks, ultra-relativistic shocks are not always efficient accelerators. This depends strongly on the geometry of the initial magnetic field. As the external medium is very weakly magnetized, acceleration of electrons in the forward shock is expected to be efficient (see *e.g.* the review by Sironi et al. 2015).

In our model, we consider a shocked region where the physical conditions in the comoving frame are given by the mass density ρ_* , internal energy per unit mass ϵ_* , and dynamical timescale t'_{dyn} (*i.e.* characteristic timescale of the adiabatic cooling due to the spherical expansion), and we assume that the emission is produced by non-thermal shock-accelerated electrons, that radiate in a local turbulent magnetic field amplified at the shock. In practice, we consider only the forward external shock so that in this study, ρ_* , ϵ_* and t'_{dyn} are given by Eqs. 5.37, 5.21 and 5.20.

A detailed modelling of the microphysics at the shock throughout the jet propagation is still beyond the reach of current simulations given the great diversity of time and length scales involved.

In models of GRB afterglows, a standard parametrization of the microphysics at the shock is therefore usually assumed, that I describe now. We assume that a fraction ϵ_B of the internal energy is injected in the magnetic field, *i.e.*

$$u_B = \frac{B'^2}{8\pi} = \epsilon_B \rho_* \epsilon_*, \quad (5.39)$$

leading to

$$B' = \sqrt{8\pi\epsilon_B\rho_*\epsilon_*}; \quad (5.40)$$

and that a fraction ϵ_e of the internal energy is injected into the acceleration of non-thermal electrons, that represent a fraction ζ of all available electrons. Their number density (cm^{-3}) and energy density ($\text{erg} \cdot \text{cm}^{-3}$) in the comoving frame are therefore given respectively by

$$n_e^{\text{acc}} = \zeta \frac{\rho_*}{m_p} \quad (5.41)$$

and

$$u_e = \epsilon_e \rho_* \epsilon_*. \quad (5.42)$$

We also assume that the accelerated particles are injected instantaneously as a power-law at each dynamical time step, though in practice the exact timescale to reach this injection shape is not instantaneous. This leads to the following distribution of accelerated electrons (cm^{-3}) in the comoving frame:

$$n(\gamma) = (p-1) \frac{n_e^{\text{acc}}}{\gamma_m} \frac{1}{1 - \left(\frac{\gamma_{\text{max}}}{\gamma_m}\right)^{1-p}} \left(\frac{\gamma}{\gamma_m}\right)^{-p} \quad \text{for } \gamma_m \leq \gamma \leq \gamma_{\text{max}}, \quad (5.43)$$

where $\int_{\gamma_m}^{\gamma_{\text{max}}} n(\gamma) d\gamma = n_e^{\text{acc}}$. Assuming $\gamma_{\text{max}} \gg \gamma_m$,

$$n(\gamma) = (p-1) \frac{n_e^{\text{acc}}}{\gamma_m} \left(\frac{\gamma}{\gamma_m}\right)^{-p} \quad \text{for } \gamma_m \leq \gamma \leq \gamma_{\text{max}}. \quad (5.44)$$

We determine the minimum Lorentz factor γ_m using the energy injection condition in the population of electrons:

$$\int_{\gamma_m}^{\gamma_{\text{max}}} n(\gamma) \gamma m_e c^2 d\gamma = \epsilon_e \frac{n_e^{\text{acc}}}{\zeta} m_p \epsilon_*, \quad (5.45)$$

i.e. a fraction ϵ_e of the energy at the shock, contained in the population of protons (right) is used to accelerate the population of non-thermal electrons (left). Assuming $\gamma_{\text{max}} \gg \gamma_m$,

$$\gamma_m = \frac{p-2}{p-1} \frac{\epsilon_e m_p \epsilon_*}{\zeta m_e c^2}. \quad (5.46)$$

As discussed in Sec. 6.2, taking into account a realistic estimate of the maximum Lorentz factor γ_{max} up to which electrons can be accelerated at the shock is important to discuss the GeV-TeV afterglow emission. This was not included in the study by [Nakar et al. \(2009\)](#) on which our calculation of the emission (see Sec. 5.4) is based. Eqs. 5.44 and 5.46 above are obtained by assuming that the maximum Lorentz factor γ_{max} is much larger than γ_m . This is fully justified as we have typically $\gamma_{\text{max}}/\gamma_m > 10^6$ in the best fit models of GW 170817 at the peak (see Sec. 6.2).

The maximum electron Lorentz factor γ_{max} is evaluated by imposing that the acceleration timescale remains always shorter than the radiative and the dynamical timescales, which are the two relevant timescales for energy loss by the electrons either by radiation or adiabatic cooling, respectively, *i.e.*

$$t'_{\text{acc}}(\gamma) \leq \min(t'_{\text{rad}}(\gamma); t'_{\text{dyn}}). \quad (5.47)$$

The acceleration timescale is written as a function of the Larmor time R'_L/c (Bohm scaling),

$$t'_{\text{acc}}(\gamma) = K_{\text{acc}} \frac{R'_L(\gamma)}{c} = K_{\text{acc}} \frac{\gamma m_e c}{e B'}, \quad (5.48)$$

where $K_{\text{acc}} \geq 1$ is a dimensionless factor. In practice, electrons at γ_{max} are usually fast cooling and the maximum electron Lorentz factor is determined by the radiative timescale, $t'_{\text{rad}}(\gamma)$. Its evaluation is non-trivial when Inverse Compton (IC) scatterings are taken into account (see Sec. 5.4). The resulting detailed calculation of γ_{max} is explained at the end of Sec. 5.4.6. In our work, we assume $K_{\text{acc}} = 1$. Our value of γ_{max} should therefore be considered as an upper limit for the true value of the maximum electron Lorentz factor.

5.4 Emissivity in the Comoving Frame

Our calculation of the emission from non-thermal electrons is mostly taken from [Nakar et al. \(2009\)](#). The population of electrons cools down by adiabatic cooling, synchrotron radiation and via SSC scatterings. As we are interested in the VHE afterglow emission, we include in Sec. 5.4.7 the attenuation due to pair production, without including the emission of secondary leptons. So far, as we first focused on the afterglow of GW 170817 where the radio observations do not show any evidence for absorption, we have not included the effect of synchrotron self-absorption. This will be implemented later using a similar approach as for the pair production, that I already present in Sec. 5.4.9. In this Sec. 5.4, **all quantities are written in the comoving frame** attached to the jet. I therefore omit the prime to simplify the notations.

5.4.1 Synchrotron and Inverse Compton Radiation for a Single Electron

Synchrotron radiation

An electron in relativistic motion in a magnetic field is deflected by the Lorentz force and radiates energy in the process of synchrotron radiation, which is the relativistic extension of cyclotron radiation. The following derivations are valid assuming that (i) the magnetic field remains constant over the acceleration timescale (see Eq. 5.48) so that the electron dynamics can be averaged over the Larmor timescale; (ii) the energy lost by synchrotron is small compared to the initial energy of the electron; (iii) no quantum effects modify the emission properties, *i.e.* the magnetic field is not too strong. These conditions are satisfied throughout the propagation of the jet in the external medium during the afterglow phase. In this case, the synchrotron power of a single electron ($\text{erg} \cdot \text{s}^{-1}$) is given by

$$P^{\text{syn}}(\gamma) = 2\sigma_{\text{T}} c u_{\text{B}} \beta^2 \gamma^2 \sin^2 \alpha, \quad (5.49)$$

where α is the pitch angle between the incoming velocity direction of the electron and the orientation of the magnetic field. For simplicity, we approximate $\beta \simeq 1$ and use instead

$$P^{\text{syn}}(\gamma) = K_P \frac{4}{3} \sigma_{\text{T}} c u_{\text{B}} \gamma^2 = K_1 B^2 \gamma^2, \quad (5.50)$$

with $K_1 = K_P \frac{\sigma_{\text{T}} c}{6\pi}$ and K_P a dimensionless parameter. $K_P = 1$ corresponds to an isotropic probability distribution over the pitch angles α where $\langle \sin^2 \alpha \rangle = \frac{1}{4\pi} \int \sin^2 \alpha \, d\Omega = 2/3$, and Eq. 5.50 is derived in [Rybicki & Lightman \(1979\)](#). Note that here γ is the electron Lorentz factor in the comoving frame, while $\Gamma(\theta; R)$ defined previously (Eq. 5.29) is the shock front Lorentz factor. I will keep this distinction throughout Sec. 5.4, and lower case γ will always refer to particle Lorentz factors in the comoving frame.

The electron synchrotron frequency equals

$$\nu_{\text{syn}}(\gamma) = \frac{3}{2} \nu_{\text{L}} \gamma^2 \sin \alpha, \quad (5.51)$$

with the Larmor frequency

$$\nu_L = \frac{eB}{2\pi m_e c}. \quad (5.52)$$

We therefore express

$$\nu_{\text{syn}}(\gamma) = K_2 B \gamma^2, \quad (5.53)$$

with $K_2 = K_\nu \frac{e}{2\pi m_e c}$ and K_ν a dimensionless parameter. $K_\nu = 3\pi/8$ corresponds to the average over an isotropic distribution of pitch angles α where $\langle \sin \alpha \rangle = \frac{1}{4\pi} \int \sin \alpha \, d\Omega = \pi/4$. The dimensionless parameters K_P and K_ν depend on the assumptions made on the pitch angle of electron velocities relative to the magnetic field lines and different values are found in afterglow models, as listed in Tab. 5.1. By default, we use the same values as Gill & Granot (2018), taken from Granot et al. (1999) where they were obtained by fitting the broken-power law approximation of the synchrotron power of a power-law distribution of electrons to the exact calculation (see their Eq. 19 and Fig. 4). Note that $\nu_{\text{syn}}(\gamma)$ is often noted ν_c in many textbooks, not to be mistaken with $\nu_c = \nu_{\text{syn}}(\gamma_c)$ that we define in Eq. 5.75.

Reference	K_P	K_ν	$K_{P_{\text{max}}}$
Sari et al. (1998)	1	1	1
Panaitescu & Kumar (2000)	0.30	0.78	0.39
Sari & Esin (2001); Gill & Granot (2018)	$3.52 \frac{p-1}{3^{p-1}}$ $\simeq 0.745$ for $p = 2.16$	$3\pi/8$ $\simeq 1.178$	$0.88 \frac{32}{3\pi} \frac{p-1}{3^{p-1}}$ $\simeq 0.633$ for $p = 2.16$

Tab. 5.1: Values of the dimensionless parameters K_P ; K_ν and $K_{P_{\text{max}}}$ for different afterglow models used in each reference.

For cyclotron radiation, the emission power spectrum of a single electron is a Dirac distribution at a single frequency: the Larmor frequency. For a particle with relativistic motion, the beaming of the radiating antenna pattern leads to a more complex spectral shape because of relativistic beaming (the particle radiation is not visible when its motion is not aligned with the line of sight within $\theta \sim 1/\gamma$) and Doppler boosting (which increases the radiative power by frame transformation); that depends on the particle pitch angle, its velocity and the observing angle. Following Rybicki & Lightman (1979), the corresponding synchrotron power at frequency ν ($\text{erg} \cdot \text{s}^{-1} \cdot \text{Hz}^{-1}$) is given by

$$P_\nu^{\text{syn}}(\gamma) = P_{\text{max}} \Phi \left(\frac{\nu}{\nu_{\text{syn}}(\gamma)} \right), \quad (5.54)$$

with

$$P_{\text{max}} = \frac{P^{\text{syn}}(\gamma)}{\nu_{\text{syn}}(\gamma)} = \frac{K_1}{K_2} B = K_{P_{\text{max}}} \frac{\sigma_T m_e c^2}{3e} B, \quad (5.55)$$

$K_{P_{\text{max}}} = K_P/K_\nu$ and we impose $\int_0^\infty \Phi(x) dx = 1$. The exact spectral form of $\Phi(x)$ is found in Rybicki & Lightman (1979) (not averaged over a pitch angle distribution):

$$\Phi(x) = \frac{9\sqrt{3}}{8\pi} F(x), \quad (5.56)$$

where $F(x) = x \int_x^\infty K_{5/3}(u) du$ and $K_{5/3}$ is the modified Bessel function³ of order 5/3. In practice we adopt a simplified shape

$$\Phi(x) = \begin{cases} \frac{4}{3} x^{1/3} & \text{if } x \leq 1 \\ 0 & \text{if } x > 1 \end{cases}. \quad (5.58)$$

³Bessel functions of order k are the solutions to the differential equation

$$x^2 \frac{d^2 y}{dx^2} + x \frac{dy}{dx} + (x^2 - k^2) y = 0. \quad (5.57)$$

Modified Bessel functions are the extension of the solutions to the complex numbers.

The exact and approximate forms of $P_\nu^{\text{syn}}(\gamma)$ are shown in Fig. 5.6.

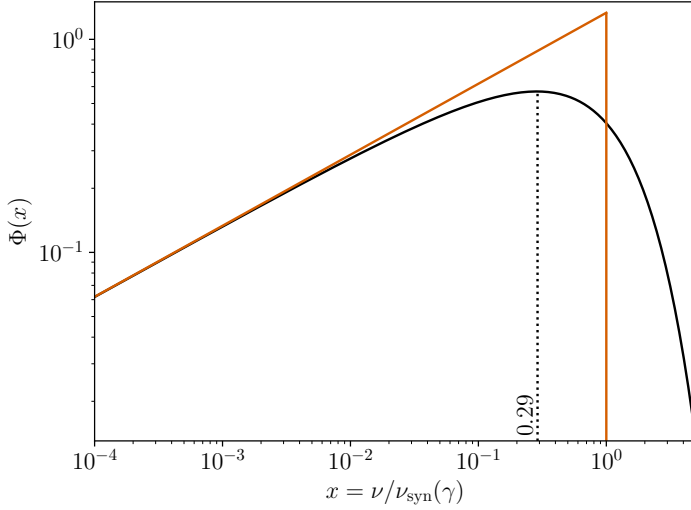


Fig. 5.6: Representation of the exact form of $\Phi(x)$ from Eq. 5.56 (black line) and its approximation from Eq. 5.58 (orange line). The power per unit frequency peaks at $\nu = 0.29\nu_{\text{syn}}(\gamma)$.

Inverse Compton scatterings

The synchrotron radiation of the electrons produces a photon field whose spectral number density is n_ν^{syn} ($\text{cm}^{-3} \cdot \text{Hz}^{-1}$). These photons can in turn scatter on the seed electrons *via* IC. This process is called Synchrotron Self-Compton (SSC). Depending on the total energy of the scattered photon and the electron, IC diffusions can occur in two regimes: Thomson and Klein-Nishina (KN). In the KN regime, when the energy of the scattered photon carries a very significant fraction of the initial energy of the electron, both the interaction cross-section and the outgoing photon energy are strongly depleted. These effects are found using quantum electrodynamics (Klein & Nishina, 1929). The IC power of an electron ($\text{erg} \cdot \text{s}^{-1}$) is then given by

$$P^{\text{SSC}}(\gamma) = \int_0^\infty d\nu n_\nu^{\text{syn}} \sigma_{\text{T}} f_{\text{KN}}(w) c \frac{4}{3} \gamma^2 g_{\text{KN}}(w) h\nu, \quad (5.59)$$

where

$$w = \frac{\gamma h\nu}{m_e c^2}; \quad (5.60)$$

and f_{KN} and g_{KN} are the KN corrections to the cross-section and to the mean energy of the scattered photon. The terms under the integral in Eq. 5.59 can be understood as the product between (i) the probability that a photon with frequency ν interacts with an electron of Lorentz factor γ [$n_\nu^{\text{syn}} \sigma_{\text{T}} f_{\text{KN}}(w) c$] and (ii) the mean energy of the scattered photons [$\frac{4}{3} \gamma^2 g_{\text{KN}}(w) h\nu$]. In the Thomson regime ($w \ll 1$), the cross section is σ_{T} and the mean energy of scattered photons is $\frac{4}{3} \gamma^2 h\nu$ for a seed synchrotron photon of frequency ν , so that $f_{\text{KN}}(w) = g_{\text{KN}}(w) = 1$ for $w \ll 1$. The expressions for f_{KN} (Klein & Nishina, 1929) and g_{KN} are

$$f_{\text{KN}}(w) = \frac{3}{4} \left[\frac{1+w}{w^3} \left(\frac{2w(1+w)}{1+2w} - \ln(1+2w) \right) + \frac{1}{2w} \ln(1+2w) - \frac{1+3w}{(1+2w)^2} \right], \quad (5.61)$$

$$g_{\text{KN}}(w) = \frac{1}{8w^4(1+2w)^3 f_{\text{KN}}(w)} \times \left[(18w + 102w^2 + 186w^3 + 102w^4 - 20w^5) - (9 + 60w + 141w^2 + 126w^3 + 12w^4 - 24w^5) \ln(1+2w) \right], \quad (5.62)$$

where Eq. 5.62 is obtained assuming that the upscattered photon energy distribution probability is a Dirac function such that after the IC scattering, $h\nu \rightarrow g_{\text{KN}}(w) \times \frac{4}{3} \gamma^2 h\nu$. I show the representations

of f_{KN} and g_{KN} on the left panel of Fig. 5.7. For simplicity, we do not write explicitly in Eq. 5.59 the dependency on the angle between the upscattered photon and the scattering electron which is discussed in Jones (1968); Nakar et al. (2009). We assume an isotropic seed radiation field. We also only account for single IC scatterings as the effects of multiple scatterings are expected to be negligible since the afterglow is produced in the optically thin regime.

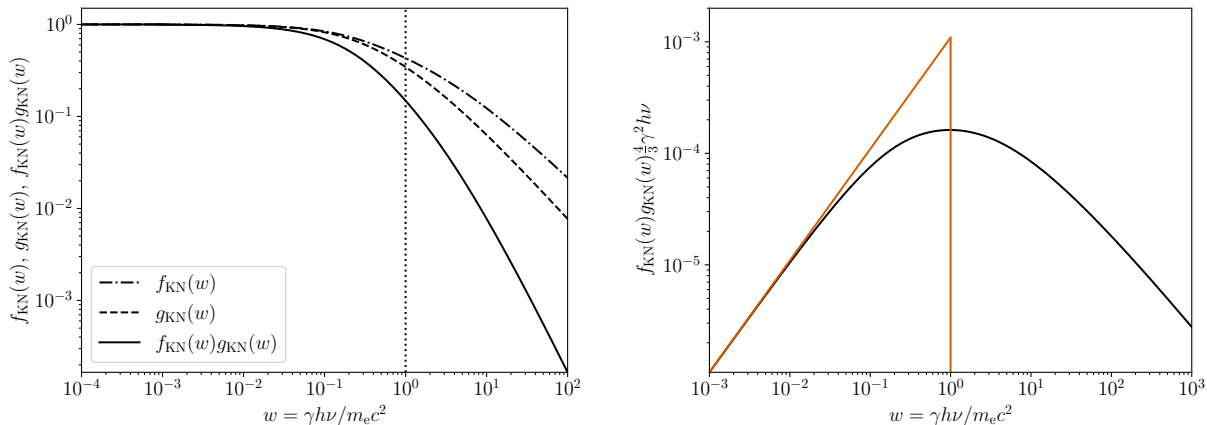


Fig. 5.7: **Left:** Cross-section correction for IC diffusions $f_{\text{KN}}(w) = \sigma(w)/\sigma_{\text{T}}$ (dash-dotted line); Correction for the mean scattered photon energy $g_{\text{KN}}(w)$ (dashed line); and product $f_{\text{KN}}(w)g_{\text{KN}}(w)$ as it appears in the expression in Eq. 5.59 (solid line) as a function of $w = \gamma h\nu/m_e c^2$. In the Thomson limit $w \ll 1$, $f_{\text{KN}}(w) \simeq g_{\text{KN}}(w) \simeq 1$. **Right:** Mean upscattered photon energy multiplied by the interaction cross-section correction as a function of w . The black line represents the case described by Eqs. 5.61 and 5.62, while the orange line is obtained with the approximation that we use in our model: $f_{\text{KN}}(w) = 1$ for $w \leq 1$ and 0 otherwise.

The Compton parameter is defined by

$$Y(\gamma) = \frac{P^{\text{SSC}}(\gamma)}{P^{\text{syn}}(\gamma)}. \quad (5.63)$$

When SSC scatterings all occur in the Thomson regime, the Compton parameter is constant, which allows to easily compute the synchrotron and SSC spectra self-consistently (see for example Panaitescu & Kumar 2000; Sari & Esin 2001; Beniamini et al. 2015). Here, we take into account KN corrections, which affect the IC component, but also the synchrotron component (Nakar et al., 2009) that can deviate significantly from the standard spectrum computed by Sari et al. (1998), as also discussed by Derishev et al. (2001); Bošnjak et al. (2009); Daigne et al. (2011) in the context of the prompt GRB emission.

Following Nakar et al. (2009) and using the same notations, we simplify the IC cross-section by assuming that scatterings are entirely suppressed in the KN regime: $f_{\text{KN}}(w) = 0$ for $w \geq 1$. We compare this assumption with the more precise definitions of f_{KN} and g_{KN} on the right panel of Fig. 5.7. Then, a synchrotron photon produced by an electron with Lorentz factor γ can only be upscattered by electrons with Lorentz factors below a certain limit $\hat{\gamma}$ to remain in the Thomson regime, *i.e.*

$$\hat{\gamma} = \frac{m_e c^2}{h\nu_{\text{syn}}(\gamma)} \propto \gamma^{-2}. \quad (5.64)$$

Note that $\hat{\gamma}$ is a decreasing function of γ : if the energy of the synchrotron photon is higher, the maximum energy of any electron on which it could be upscattered in the Thomson regime must be lower. Technically, we should always write $\hat{\gamma}(\gamma)$, but we will simplify the notations by only writing

$\hat{\gamma}$. For example, $\hat{\gamma}(\gamma_m)$ will be noted $\hat{\gamma}_m$. In an equivalent way, electrons with Lorentz factor γ will only scatter photons below the energy

$$h\tilde{\nu} = \frac{m_e c^2}{\gamma}. \quad (5.65)$$

Then it is also convenient to define $\tilde{\gamma}$ such that $\nu_{\text{syn}}(\tilde{\gamma}) = \tilde{\nu}$, *i.e.*

$$\tilde{\gamma} = \sqrt{\frac{\gamma m_e c^2}{h\nu_{\text{syn}}(\gamma)}} \propto \gamma^{-1/2}. \quad (5.66)$$

Electrons with a Lorentz factor γ can only scatter synchrotron photons produced by electrons with Lorentz factors below $\tilde{\gamma}$. The Lorentz factor γ_{self} is defined by the condition

$$\gamma_{\text{self}} = \hat{\gamma}_{\text{self}} = \tilde{\gamma}_{\text{self}} = \left(\frac{m_e c^2}{hK_2 B} \right)^{1/3}. \quad (5.67)$$

The term $m_e c^2 / hK_2 = 2\pi m_e^2 c^3 / K_\nu e h \approx 4.4 \times 10^{13}$ G is the quantum critical field B_{QED} above which quantum effects become non-negligible. In GRB jets, $B \ll B_{\text{QED}}$. Finally, from Eqs. 5.64, 5.66 and 5.67, we find these useful relations:

$$\hat{\gamma} = \frac{\gamma_{\text{self}}^3}{\gamma^2}, \quad (5.68)$$

$$\tilde{\gamma} = \frac{\gamma_{\text{self}}^{3/2}}{\gamma^{1/2}}. \quad (5.69)$$

The definition of $\tilde{\nu}$ allows to simplify the expression of the SSC power given by Eq. 5.59:

$$P^{\text{SSC}}(\gamma) = \frac{4}{3} \sigma_{\text{TC}} c \gamma^2 \int_0^{\tilde{\nu}} d\nu u_\nu^{\text{syn}}, \quad (5.70)$$

with the energy density of the seed synchrotron photons ($\text{erg} \cdot \text{cm}^{-3} \cdot \text{Hz}^{-1}$) defined as

$$u_\nu^{\text{syn}} = n_\nu^{\text{syn}} \times h\nu. \quad (5.71)$$

Then from Eqs. 5.50, 5.63 and 5.70 we get

$$Y(\gamma) = \frac{1}{K_P} \frac{\int_0^{\tilde{\nu}} d\nu u_\nu^{\text{syn}}}{u_B}. \quad (5.72)$$

Finally, the SSC power radiated at frequency ν ($\text{erg} \cdot \text{s}^{-1} \cdot \text{Hz}^{-1}$) for a single electron of Lorentz factor γ , $P_\nu^{\text{SSC}}(\gamma)$, is the result of IC scatterings by seed synchrotron photons of frequency $\nu_{\text{seed}} = \nu / (\frac{4}{3}\gamma^2)$ (see text above Eq. 5.61). Assuming a strict suppression in the KN regime leads to this simple expression:

$$P_\nu^{\text{SSC}}(\gamma) = \begin{cases} \sigma_{\text{TC}} c u_{\nu_{\text{seed}}=\nu/(\frac{4}{3}\gamma^2)}^{\text{syn}} & \text{if } h\nu \leq \frac{4}{3}\gamma m_e c^2 \\ 0 & \text{if } h\nu > \frac{4}{3}\gamma m_e c^2 \end{cases}. \quad (5.73)$$

5.4.2 Radiative Regime of a Single Electron

At the shock, the accelerated electrons can lose energy in two ways: by synchrotron and SSC radiation, or by the adiabatic cooling due to the expansion of the shock as it propagates through the

external medium. For the population of electrons at latitude θ and radius R , the radiative timescale (in the comoving frame) is given by

$$t_{\text{rad}}(\gamma) = \frac{\gamma m_e c^2}{P_{\text{syn}}(\gamma) + P_{\text{SSC}}(\gamma)} = \frac{m_e c^2}{[1 + Y(\gamma)] K_1 B^2 \gamma}. \quad (5.74)$$

In the case where no SSC diffusions are occurring, $t_{\text{rad}}(\gamma) \propto B^2 \gamma^{-1}$ is a decreasing function of γ , the electron Lorentz factor. More energetic electrons have a shorter radiation timescale and are therefore more efficiently radiating *via* synchrotron. Conversely, the characteristic timescale for adiabatic cooling is the dynamical timescale t_{dyn} , which is independent of γ (Eq. 5.37). For values of γ large enough, we always have $t_{\text{rad}}(\gamma) \ll t_{\text{dyn}}$. Note that these quantities vary throughout the shock propagation, but for simplicity here we do not note their dependency on θ and R .

To assess the cooling regime of a single electron, we thus define the cooling Lorentz factor γ_c such that $t_{\text{rad}}(\gamma_c) = t_{\text{dyn}}$, so that high-energy electrons with $\gamma \gg \gamma_c$ are radiatively efficient (**fast cooling**), and low-energy electrons with $\gamma \ll \gamma_c$ are mainly cooling *via* the adiabatic expansion and are radiatively inefficient (**slow cooling**). Then, computing self-consistently γ_c requires to solve the equation

$$\gamma_c [1 + Y(\gamma_c)] = \gamma_c^{\text{syn}}, \quad (5.75)$$

where

$$\gamma_c^{\text{syn}} = \frac{m_e c^2}{K_1 B^2 t_{\text{dyn}}} \quad (5.76)$$

is the value of the critical Lorentz factor obtained when only taking into account the synchrotron radiation. The procedure to compute γ_c and $Y(\gamma_c)$ in the most general case where the SSC cooling impacts the electron distribution will be discussed in Sec. 5.4.6.

5.4.3 Electron Distribution and Associated Emission

Electron distribution

I now look at the evolved electron distribution after injection at the shock, averaged over the dynamical timescale t_{dyn} . We note this time-averaged distribution of electrons $\bar{n}(\gamma)$. The instantaneous power of an electron is either dominated by the synchrotron and SSC radiation if $\gamma > \gamma_c$, or by the adiabatic cooling if $\gamma < \gamma_c$ (see Sec. 5.4.2). The power lost by adiabatic cooling over t_{dyn} is

$$P^{\text{ad}}(\gamma) = \frac{\gamma m_e c^2}{t_{\text{dyn}}}, \quad (5.77)$$

and the radiative power is $P^{\text{syn}}(\gamma) + P^{\text{SSC}}(\gamma) = [1 + Y(\gamma)] P^{\text{syn}}(\gamma)$ from Eq. 5.63. We follow Nakar et al. (2009) by keeping only the dominant term for the electron cooling, *i.e.*

$$P(\gamma) = \begin{cases} P^{\text{ad}}(\gamma) & \text{if } \gamma < \gamma_c \\ [1 + Y(\gamma)] P^{\text{syn}}(\gamma) & \text{if } \gamma \geq \gamma_c \end{cases}. \quad (5.78)$$

During the propagation of the shock front, the average number of electrons injected per unit time is $n(\gamma)/t_{\text{dyn}}$, for each dynamical time step. This is the source term of the evolution equation for $\bar{n}(\gamma)$:

$$\frac{\partial \bar{n}}{\partial t} - \frac{\partial}{\partial \gamma} \left(\bar{n}(\gamma) \frac{P(\gamma)}{m_e c^2} \right) = \frac{n(\gamma)}{t_{\text{dyn}}}, \quad (5.79)$$

where $n(\gamma)$ is the injection term defined in Eq. 5.44. We solve this equation for the steady state $\partial \bar{n} / \partial t = 0$, assuming that the dynamical timescale is much larger than the typical relaxation

timescale, and obtain

$$\bar{n}(\gamma) = \frac{m_e c^2}{P(\gamma) t_{\text{dyn}}} \int_{\gamma}^{\infty} d\gamma' n(\gamma') \quad (5.80)$$

$$= \frac{n_e^{\text{acc}} m_e c^2}{P(\gamma) t_{\text{dyn}}} \begin{cases} 1 & \text{if } \gamma \leq \gamma_m \\ \left(\frac{\gamma}{\gamma_m}\right)^{1-p} & \text{if } \gamma_m < \gamma < \gamma_{\text{max}} \\ 0 & \text{if } \gamma_{\text{max}} \leq \gamma \end{cases} . \quad (5.81)$$

To inject Eq. 5.78 in Eq. 5.81, we need to introduce γ_c . For the population of electrons, two cases are therefore possible:

- Either $\gamma_m > \gamma_c$, in which case all injected electrons have $\gamma > \gamma_c$ and radiate efficiently. This is the **fast cooling** regime for the *population* of electrons. In this case, over an integration step t_{dyn} , the electrons can cool radiatively down to a minimum value of γ_c .
- Otherwise, $\gamma_m < \gamma_c$, in which case only part of the electrons (again those with $\gamma > \gamma_c$) radiate efficiently. The others are individually slow cooling. This case is the **slow cooling** regime for the *population* of electrons. We assume that the adiabatic cooling of the electrons over the time step t_{dyn} is negligible, such that the minimal Lorentz factor of the distribution in this case remains the minimal injection Lorentz factor γ_m .

We therefore obtain the following evolved electron distributions:

- **Fast cooling** regime ($\gamma_m > \gamma_c$):

$$\begin{aligned} \bar{n}(\gamma) &= \frac{n_e^{\text{acc}} m_e c^2}{[1 + Y(\gamma)] P^{\text{syn}}(\gamma) t_{\text{dyn}}} \times \begin{cases} 0 & \text{if } \gamma < \gamma_c \\ 1 & \text{if } \gamma_c \leq \gamma \leq \gamma_m \\ \left(\frac{\gamma}{\gamma_m}\right)^{1-p} & \text{if } \gamma_m \leq \gamma \leq \gamma_{\text{max}} \\ 0 & \text{if } \gamma > \gamma_{\text{max}} \end{cases} \\ &= \frac{n_e^{\text{acc}}}{1 + Y(\gamma)} \frac{\gamma_c^{\text{syn}}}{\gamma_m^2} \times \begin{cases} \left(\frac{\gamma}{\gamma_m}\right)^{-2} & \text{if } \gamma_c \leq \gamma \leq \gamma_m \\ \left(\frac{\gamma}{\gamma_m}\right)^{-(p+1)} & \text{if } \gamma_m \leq \gamma \leq \gamma_{\text{max}} \end{cases} . \end{aligned} \quad (5.82)$$

- **Slow cooling** regime ($\gamma_m < \gamma_c$):

$$\begin{aligned} \bar{n}(\gamma) &= \frac{n_e^{\text{acc}} m_e c^2}{t_{\text{dyn}}} \times \begin{cases} 0 & \text{if } \gamma < \gamma_m \\ \frac{1}{P^{\text{ad}}(\gamma)} \left(\frac{\gamma}{\gamma_m}\right)^{1-p} & \text{if } \gamma_m \leq \gamma \leq \gamma_c \\ \frac{1}{[1+Y(\gamma)] P^{\text{syn}}(\gamma)} \left(\frac{\gamma}{\gamma_m}\right)^{1-p} & \text{if } \gamma_c \leq \gamma \leq \gamma_{\text{max}} \\ 0 & \text{if } \gamma > \gamma_{\text{max}} \end{cases} \\ &= n_e^{\text{acc}} \frac{\gamma_c^{\text{syn}}}{\gamma_m^2} \left(\frac{\gamma_c}{\gamma_m}\right)^{-(p+1)} \times \begin{cases} \frac{1}{1+Y(\gamma_c)} \left(\frac{\gamma}{\gamma_c}\right)^{-p} & \text{if } \gamma_m \leq \gamma \leq \gamma_c \\ \frac{1}{1+Y(\gamma)} \left(\frac{\gamma}{\gamma_c}\right)^{-(p+1)} & \text{if } \gamma_c \leq \gamma \leq \gamma_{\text{max}} \end{cases} . \end{aligned} \quad (5.83)$$

where we have used Eq. 5.75 (to introduce $1 + Y(\gamma_c)$ in the slow cooling regime) and the relation obtained from Eqs. 5.50 and 5.76:

$$\frac{m_e c^2}{P^{\text{syn}}(\gamma) t_{\text{dyn}}} = \frac{m_e c^2}{K_1 B^2 \gamma^2 t_{\text{dyn}}} = \frac{\gamma_c^{\text{syn}}}{\gamma^2} . \quad (5.84)$$

In practice, the evolved population expression derived in Eqs. 5.82 and 5.83 is only a good approximation asymptotically, when $\gamma_m \gg \gamma_c$ (fast cooling) or when $\gamma_c \gg \gamma_m$ (slow cooling). When

$\gamma_m \simeq \gamma_c$, a more careful solving of Eq. 5.79 should be conducted. To keep this work analytical, we omit this transition, and only verify that the transition between the fast and slow cooling regimes at $\gamma_m = \gamma_c$ is continuous with our definitions.

We now define $\gamma_{m,c} = \max(\gamma_m; \gamma_c)$ and $\gamma_{c,m} = \min(\gamma_m; \gamma_c)$ so that $\gamma_{m,c} = \gamma_m$ and $\gamma_{c,m} = \gamma_c$ in fast cooling and $\gamma_{m,c} = \gamma_c$ and $\gamma_{c,m} = \gamma_m$ in slow cooling. The minimum electron Lorentz factor is therefore $\gamma_{\min} = \gamma_{c,m}$. We also define the corresponding synchrotron frequencies $\nu_{m,c} = \nu_{\text{syn}}(\gamma_{m,c})$ and $\nu_{c,m} = \nu_{\text{syn}}(\gamma_{c,m})$. These quantities will be useful to simplify the notations in the next sections. We also always keep only the dominant term in the radiated power, *i.e.*

$$1 + Y(\gamma) = \begin{cases} 1 & \text{if } Y(\gamma) \leq 1 \\ Y(\gamma) & \text{if } Y(\gamma) > 1 \end{cases} . \quad (5.85)$$

As described in detail in Nakar et al. (2009), the resulting evolved electron distribution $\bar{n}(\gamma)$ shows several breaks in addition to γ_m and γ_c : another break is expected at γ_0 , defined such that

$$Y(\gamma_0) = 1 \quad (5.86)$$

and several additional breaks are possible and must be identified in an iterative way, as described in Sec. 5.4.6.

Following Sari et al. (1998) and Nakar et al. (2009), we approximate $\bar{n}(\gamma)$ and the associated synchrotron spectrum by broken power-laws to allow for a semi-analytical calculation. Electrons Lorentz factors are normalized by $\gamma_{m,c}$, *i.e.* $x = \gamma/\gamma_{m,c}$, and photon frequencies by $\nu_{m,c}$, *i.e.* $y = \nu/\nu_{m,c}$. Hence, from Eq. 5.53 the normalized synchrotron frequency of an electron with normalized Lorentz factor x is $y = x^2$. In the following, the notations introduced for characteristic electron Lorentz factors or photon frequencies are implicitly conserved for the normalized quantities. For instance $x_{\text{self}} = \gamma_{\text{self}}/\gamma_{m,c}$, $\hat{x} = \hat{\gamma}/\gamma_{m,c} = x_{\text{self}}^3/x^2$, $\tilde{\nu} = \tilde{\nu}/\nu_{m,c} = \tilde{x}^2$, etc.

Normalized electron distribution

Due to the introduction of SSC diffusions in both Thomson and KN regimes, we expect the electron distribution $\bar{n}(\gamma)$ to have several breaks. In the most general case, we therefore express it in the form

$$\bar{n}(\gamma) = \frac{1}{I_0} \frac{n_e^{\text{acc}}}{\gamma_{m,c}} f(x), \quad (5.87)$$

where $f(x)$ is the normalized broken power-law electron distribution with N breaks and power-law segments:

$$f(x) = \begin{cases} x^{-p_1} & \text{if } x_1 \leq x \leq x_2 \\ x_2^{p_2-p_1} x^{-p_2} & \text{if } x_2 \leq x \leq x_3 \\ x_2^{p_2-p_1} x_3^{p_3-p_2} x^{-p_3} & \text{if } x_2 \leq x \leq x_3 \\ \vdots & \vdots \\ x_2^{p_2-p_1} x_3^{p_3-p_2} \dots x_N^{p_N-p_{N-1}} x^{-p_N} & \text{if } x_N \leq x \leq x_{N+1} \end{cases} \quad (5.88)$$

with $x_1 = \gamma_{\min}/\gamma_{m,c}$ and $x_{N+1} = \gamma_{\max}/\gamma_{m,c}$. The dimensionless integral I_0 is given by

$$I_0 = \int_{x_1}^{x_{N+1}} f(x) dx, \quad (5.89)$$

to conserve the number density of electrons:

$$\int_{\gamma_{\min}}^{\gamma_{\max}} \bar{n}(\gamma) d\gamma = n_e^{\text{acc}}. \quad (5.90)$$

Other choices of normalization can be made. For example, we explored the possibility to have the correct radiative efficiency instead of the correct number density of electrons, but found this

other choice to be more challenging to implement. This essentially leads to other definitions of the normalization integrals but does not alter the method that I present here. I will not detail these other possibilities here.

Normalized synchrotron spectrum

The synchrotron power per electron and per unit frequency p_ν^{syn} ($\text{erg} \cdot \text{s}^{-1} \cdot \text{Hz}^{-1} \cdot \text{electron}^{-1}$) averaged over the timescale t_{dyn} is deduced from Eq. 5.54 using the simplified shape for Φ (Eq. 5.58). This leads to a broken power-law synchrotron spectrum:

$$p_\nu^{\text{syn}} = \frac{1}{n_e^{\text{acc}}} \int_{\gamma_{\text{min}}}^{\gamma_{\text{max}}} d\gamma \bar{n}(\gamma) P_\nu^{\text{syn}}(\gamma) \quad (5.91)$$

$$= \frac{\gamma_{\text{m,c}}^2 m_e c^2}{\gamma_c^{\text{syn}} \nu_{\text{m,c}} t_{\text{dyn}}} \times \frac{4}{3} y^{1/3} \int_{\max(x_1; y^{1/2})}^{x_{N+1}} dx \frac{f(x)}{x^{2/3}}, \quad (5.92)$$

where we used the definition of γ_c^{syn} from Eq. 5.76 and the relation $\nu_{\text{m,c}} = K_2 B \gamma_{\text{m,c}}^2$ from Eq. 5.53. Again following the approach of Sari et al. (1998) and Nakar et al. (2009), we define a spectral shape $g(y)$ for p_ν^{syn} in the form of power-law segments. In this definition, we want to ensure that the total synchrotron power per electron p^{syn} ($\text{erg} \cdot \text{s}^{-1} \cdot \text{electron}^{-1}$) is conserved:

$$p^{\text{syn}} = \int_0^\infty d\nu p_\nu^{\text{syn}} \quad (5.93)$$

$$= \frac{1}{n_e^{\text{acc}}} \int_{\gamma_{\text{min}}}^{\gamma_{\text{max}}} d\gamma \bar{n}(\gamma) P^{\text{syn}}(\gamma) \quad (5.94)$$

$$= \frac{I_2}{I_0} \frac{\gamma_{\text{m,c}}^2 m_e c^2}{\gamma_c^{\text{syn}} t_{\text{dyn}}}, \quad (5.95)$$

where we have used Eq. 5.50 and defined the dimensionless factor

$$I_2 = \int_{x_1}^{x_{N+1}} dx x^2 f(x). \quad (5.96)$$

Using Eqs. 5.92 and 5.93, we therefore express

$$p_\nu^{\text{syn}} \simeq \frac{1}{J_0} \frac{I_2}{I_0} \frac{\gamma_{\text{m,c}}^2 m_e c^2}{\gamma_c^{\text{syn}} \nu_{\text{m,c}} t_{\text{dyn}}} \times g(y), \quad (5.97)$$

where the dimensionless factor J_0 is

$$J_0 = \int_0^{x_{N+1}} dy g(y). \quad (5.98)$$

The spectral shape $g(y)$ is obtained from Eq. 5.92 and by keeping only the dominant term in the integral of $f(x)/x^{2/3}$. There are two main cases: either $y^{1/2} < x_1$, in which case the integral is a constant factor, and $p_\nu^{\text{syn}} \propto y^{1/3}$; or $y^{1/2} > x_1$, in which case, if the leading term corresponds to a segment of $f(x)$ of slope $-p_i$, $p_\nu^{\text{syn}} \propto y^{-\frac{p_i-1}{2}}$. In the general case, $g(y)$ therefore writes

$$g(y) = \begin{cases} x_1^{\frac{1}{3}-p_1} y^{\frac{1}{3}} & \text{if } y < x_1^2 \\ y^{-\frac{p_1-1}{2}} & \text{if } x_1^2 < y < x_2^2 \\ x_2^{p_2-p_1} y^{-\frac{p_2-1}{2}} & \text{if } x_2^2 < y < x_3^2 \\ x_2^{p_2-p_1} x_3^{p_3-p_2} y^{-\frac{p_3-1}{2}} & \text{if } x_3^2 < y < x_4^2 \\ \vdots & \vdots \\ x_2^{p_2-p_1} x_3^{p_3-p_2} \dots x_N^{p_N-p_{N-1}} y^{-\frac{p_N-1}{2}} & \text{if } x_N^2 < y < x_{N+1}^2 \end{cases}. \quad (5.99)$$

Finally we define ν_p as the peak frequency of the synchrotron spectrum, *i.e.* the frequency ν where $\nu^2 p_\nu^{\text{syn}}$ is maximum. This peak frequency corresponds to synchrotron photons emitted by electrons at Lorentz factor γ_p , *i.e.* $\nu_p = \nu_{\text{syn}}(\gamma_p)$. We note i_p the corresponding index of the break in the normalized distributions: $x_p = x_{i_p}$ and $y_p = y_{i_p} = x_p^2$.

Normalized SSC spectrum

The SSC power per electron and per unit frequency p_ν^{SSC} ($\text{erg} \cdot \text{s}^{-1} \cdot \text{Hz}^{-1} \cdot \text{electron}^{-1}$) emitted over the timescale t_{dyn} is deduced from Eq. 5.73 with u_ν^{syn} (Eq. 5.71) now expressed as

$$u_\nu^{\text{syn}} = n_e^{\text{acc}} p_\nu^{\text{syn}} t_{\text{dyn}}. \quad (5.100)$$

This leads to

$$p_\nu^{\text{SSC}} = \frac{1}{n_e^{\text{acc}}} \int_{\gamma_{\text{min}}}^{\gamma_{\text{max}}} d\gamma \bar{n}(\gamma) P_\nu^{\text{SSC}}(\gamma) \quad (5.101)$$

$$\simeq \frac{1}{J_0} \frac{I_2}{I_0} \frac{\tau_T}{I_0} \frac{\gamma_{\text{m,c}}^2 m_e c^2}{\gamma_c^{\text{syn}} \nu_{\text{m,c}} t_{\text{dyn}}} \times G(y), \quad (5.102)$$

where

$$\tau_T = n_e^{\text{acc}} \sigma_T c t_{\text{dyn}} \quad (5.103)$$

is the Thomson optical depth and where the normalized spectral shape is given by

$$G(y) = \int_{\max(x_1; \frac{3}{4} \frac{h\nu_{\text{m,c}}}{\gamma_{\text{m,c}} m_e c^2} y)}^{x_{N+1}} dx f(x) g\left(y_{\text{seed}} = \frac{3}{4} \frac{y}{\gamma_{\text{m,c}}^2 x^2}\right). \quad (5.104)$$

The cutoff at $x_{\text{KN}} = \gamma_{\text{KN}}/\gamma_{\text{m,c}}$ with

$$\gamma_{\text{KN}} = \frac{3}{4} \frac{h\nu}{m_e c^2} \quad (5.105)$$

is a direct consequence of the strict suppression assumed in the KN regime in Eq. 5.73: the VHE flux due to the scatterings occurring in the KN regime is neglected. Yamasaki & Piran (2022) introduce a factor f_{KN} in their calculations to compensate this approximation, which we do not include here. The KN regime affects the high energy part of the emitted spectrum: above a photon energy $h\nu = \frac{4}{3} \gamma_{\text{min}} m_e c^2$, we have $\gamma_{\text{KN}} > \gamma_{\text{min}}$ and the SSC emission is reduced. The SSC emission is even entirely suppressed ($G(y) = 0$) at very high photon energy $h\nu > \frac{4}{3} \gamma_{\text{max}} m_e c^2$ corresponding to $\gamma_{\text{KN}} > \gamma_{\text{max}}$.

In practice, $G(y)$ is computed exactly in our numerical implementation. Note also that $J_0 \simeq 2I_2$ when only the leading term is kept in the integrals. However all dimensionless factors I_0 , I_2 and J_0 are also computed exactly in our numerical implementation, which ensures the continuity of the electron distribution and emitted spectrum at the transition from the fast to the slow cooling regime, as well as between the different possible cases in both regimes (see Sec. 5.4.6). Because $G(y)$ is computed analytically in our numerical implementation, its shape appears smoother and the segments corresponding to the combinations of the segments of $f(x)$ and $g(y)$ add up at the transitions. This is clearly visible in *e.g.* Fig. 6.11.

5.4.4 The Pure Synchrotron Case

The standard pure synchrotron case where the SSC emission is neglected (*i.e.* $Y(\gamma) = 0$ for all electrons) is fully described in Sari et al. (1998). From Eq. 5.75, we have $\gamma_c = \gamma_c^{\text{syn}}$ in this case.

– In the **fast cooling** regime ($\gamma_m > \gamma_c$), the normalized distributions are given by

$$f(x) = \begin{cases} x^{-2} & \text{if } x_1 < x < x_2 \\ x_2^{p-1} x^{-(p+1)} & \text{if } x_2 < x < x_3 \end{cases}, \quad (5.106)$$

$$g(y) = \begin{cases} x_1^{-5/3} y^{1/3} & \text{if } y < x_1^2 \\ y^{-1/2} & \text{if } x_1^2 < y < x_2^2 \\ x_2^{p-1} y^{-p/2} & \text{if } x_2^2 < y < x_3^2 \end{cases}, \quad (5.107)$$

with $x_1 = \gamma_c/\gamma_m$, $x_2 = 1$ and $x_3 = \gamma_{\max}/\gamma_m$.

– In the **slow cooling** regime ($\gamma_m < \gamma_c$), they are given by

$$f(x) = \begin{cases} x^{-p} & \text{if } x_1 < x < x_2 \\ x_2 x^{-(p+1)} & \text{if } x_2 < x < x_3 \end{cases}, \quad (5.108)$$

$$g(y) = \begin{cases} x_1^{\frac{1}{3}-p} y^{\frac{1}{3}} & \text{if } y < x_1^2 \\ y^{-(p-1)/2} & \text{if } x_1^2 < y < x_2^2 \\ x_2 y^{-p/2} & \text{if } x_2^2 < y < x_3^2 \end{cases}, \quad (5.109)$$

with $x_1 = \gamma_m/\gamma_c$, $x_2 = 1$ and $x_3 = \gamma_{\max}/\gamma_c$.

Calculations using this prescription are labelled as "no SSC" in the following.

5.4.5 The Synchrotron Self-Compton Case in Thomson regime

If the KN regime is neglected, all IC scatterings occur in Thomson regime and the Compton parameter is the same for all electrons: $Y(\gamma) = Y^{\text{noKN}} = \text{cst}$. The corresponding solution is given by Sari & Esin (2001): the normalized distributions $f(x)$ and $g(y)$ are the same as in the pure synchrotron case above (Eqs. 5.106 – 5.109), but the value of the critical Lorentz factor γ_c is decreased due to the IC cooling:

$$\gamma_c = \gamma_c^{\text{syn}} / (1 + Y^{\text{noKN}}). \quad (5.110)$$

Using Eqs. 5.72, 5.97 and 5.100, we get

$$Y^{\text{noKN}} (1 + Y^{\text{noKN}}) = \frac{1}{K_P} \frac{p-2}{p-1} \frac{\epsilon_e}{\epsilon_B} \frac{\gamma_{m,c}}{\gamma_{c,m}} \frac{I_2}{I_0}. \quad (5.111)$$

As I_2/I_0 is a function of $\frac{\gamma_c}{\gamma_m} = \frac{1}{1+Y^{\text{noKN}}} \frac{\gamma_c^{\text{syn}}}{\gamma_m}$, this is an implicit equation to be solved numerically to obtain Y^{noKN} and γ_c . The limits are

$$(1 + Y^{\text{noKN}}) Y^{\text{noKN}} = \begin{cases} \frac{1}{K_P} \frac{\epsilon_e}{\epsilon_B} & \text{if } \gamma_m \gg \gamma_c \\ \frac{1}{K_P} \frac{\epsilon_e}{\epsilon_B} \frac{1}{3-p} \left(\frac{\gamma_m}{\gamma_c^{\text{syn}}} \right)^{p-2} & \text{if } \gamma_m \ll \gamma_c \end{cases}, \quad (5.112)$$

I give the details for this calculation in the general case in Sec. 5.4.6. Calculations using this prescription are labelled as "SSC (Thomson)" in the following.

5.4.6 Self-consistent Calculation of the Electron Distribution and the Compton Parameter in the General Case

Normalized Compton parameter

In the general case where the KN suppression at high energy is included, the Compton parameter $Y(\gamma)$ is a decreasing function of the electron Lorentz factor. From Eqs. 5.72, 5.97 and 5.100, we get

$$Y(\gamma) (1 + Y(\gamma_c)) = \frac{1}{K_P} \frac{p-2}{p-1} \frac{\epsilon_e}{\epsilon_B} \frac{\gamma_{m,c}}{\gamma_{c,m}} \frac{I_2}{I_0} \frac{1}{J_0} \int_0^{\tilde{y}} dy g(y). \quad (5.113)$$

Note that for low electron Lorentz factors γ , $\tilde{\nu}$ becomes very large so that, for $\tilde{\nu} > \nu_{\text{syn}}(\gamma_{\text{max}})$, we recover the Thomson regime, where the right-hand side of Eq. 5.113 is formally the same as in Eq. 5.111, even if the integrals I_0 and I_2 are different if the normalized electron distribution $f(x)$ is different.

As described in Nakar et al. (2009), when keeping only the leading term in the integral of $g(y)$, the corresponding scaling law for the Compton parameter is $Y(\gamma) = \text{cst}$ if $\tilde{\nu}$ is above the synchrotron peak frequency ν_p and $Y(\gamma) \propto \gamma^{-\frac{3-\tilde{p}}{2}}$ otherwise, where \tilde{p} is the slope of electron distribution in the power-law segment of the electron distribution including $\tilde{\gamma}$. The evolution of $Y(\gamma)$ can be understood as follows: for low values of γ , $\tilde{\nu}(\gamma) > \nu_p$. The population of scattered photons is dominated by the peak photons and the integral in Eq. 5.113 is roughly constant. As γ increases, $\tilde{\nu}$ decreases and when $\tilde{\nu}(\gamma) < \nu_p$, the majority of the population of upscattered photons is therefore at $\tilde{\nu}(\gamma) \propto \gamma^{-1}$ (Eq. 5.65). Therefore $Y(\gamma) \propto \gamma^{-1-\tilde{\alpha}}$ (from Eq. 5.113), where $\tilde{\alpha}$ is the slope of corresponding segment in $g(y)$, i.e. $\tilde{\alpha} = -\frac{\tilde{p}-1}{2}$. This leads us to introduce a normalized Compton parameter defined by

$$Y(\gamma) (1 + Y(\gamma_c)) = \frac{1}{K_P} \frac{p-2}{p-1} \frac{\epsilon_e}{\epsilon_B} \frac{\gamma_{m,c}}{\gamma_{c,m}} \frac{I_2}{I_0} h(x), \quad (5.114)$$

where $h(x)$ follows this scaling and is normalized so that Eq. 5.114 has the exact limit in the Thomson regime. This leads to

$$h(x) = \begin{cases} 1 & \text{if } x < \hat{x}_p \\ \frac{\hat{x}_p^{\frac{3-p_{i_p}-1}{2}}}{\hat{x}_p^{\frac{3-p_{i_p}-1}{2}}} x^{-\frac{3-p_{i_p}-1}{2}} & \text{if } \hat{x}_p < x < \hat{x}_{i_p-1} \\ \frac{\hat{x}_p^{\frac{3-p_{i_p}-1}{2}}}{\hat{x}_{i_p-1}^{\frac{p_{i_p}-1-p_{i_p}-2}{2}}} x^{-\frac{3-p_{i_p}-2}{2}} & \text{if } \hat{x}_{i_p-1} < x < \hat{x}_{i_p-2} \\ \vdots & \vdots \\ \frac{\hat{x}_p^{\frac{3-p_{i_p}-1}{2}}}{\hat{x}_{i_p-1}^{\frac{p_{i_p}-1-p_{i_p}-2}{2}}} \cdots & \vdots \\ \cdots \frac{\hat{x}_2^{\frac{p_2-p_1}{2}}}{\hat{x}_2^{\frac{p_2-p_1}{2}}} x^{-\frac{3-p_1}{2}} & \text{if } \hat{x}_2 < x < \hat{x}_1 \\ \frac{\hat{x}_p^{\frac{3-p_{i_p}-1}{2}}}{\hat{x}_{i_p-1}^{\frac{p_{i_p}-1-p_{i_p}-2}{2}}} \cdots & \vdots \\ \cdots \frac{\hat{x}_2^{\frac{p_2-p_1}{2}}}{\hat{x}_1^{\frac{p_1}{2}-\frac{1}{6}}} x^{-4/3} & \text{if } x > \hat{x}_1 \end{cases}. \quad (5.115)$$

We recall that i_p is the index of the break corresponding to the peak frequency of the synchrotron spectrum. In most cases (see Appendix A) we have $i_p = 2$, leading to

$$h(x) = \begin{cases} 1 & \text{if } x < \hat{x}_2 \\ \frac{\hat{x}_2^{\frac{3-p_1}{2}}}{\hat{x}_2^{\frac{3-p_1}{2}}} x^{-\frac{3-p_1}{2}} & \text{if } \hat{x}_2 < x < \hat{x}_1 \\ \frac{\hat{x}_2^{\frac{3-p_2}{2}}}{\hat{x}_1^{\frac{p_1}{2}-\frac{1}{6}}} x^{-4/3} & \text{if } x > \hat{x}_1 \end{cases}. \quad (5.116)$$

Self-consistent solution for the normalized electron distribution

Following Nakar et al. (2009), we define γ_0 by $Y(\gamma_0) = 1$ (Eq. 5.86) and assume $1 + Y(\gamma) = Y(\gamma)$ for $\gamma < \gamma_0$ and 1 otherwise. As $Y(\gamma)$ is a decreasing function with a constant first segment, if $Y(\gamma) < 1$ for $\gamma < \max(\gamma_c; \hat{\gamma}_p)$, then $Y(\gamma) < 1$ for all values of γ and γ_0 is therefore undefined. In these cases, we retrieve the "no SSC" solution. From Eqs. 5.82 and 5.83, this shows that the IC cooling will only affect the electron distribution in the interval

$$\max(\gamma_c; \hat{\gamma}_p) < \gamma < \gamma_0. \quad (5.117)$$

Therefore the solution is entirely determined by the orderings of γ_m , γ_c , γ_0 , $\hat{\gamma}_m$ and $\hat{\gamma}_c$, or equivalently by the ordering of γ_m , γ_c , γ_0 and γ_{self} . All possible cases and the corresponding solutions are listed

in Appendix A. In some cases, subcases are introduced as breaks can appear at $\widehat{\gamma}_0$, $\widehat{\gamma}_m$, $\widehat{\gamma}_c$, etc. All the most relevant cases for GRB afterglows are already described in Nakar et al. (2009) along with the detailed method to obtain the corresponding solution for the electron distribution. For completeness, I list in Appendix A the additional cases allowing to fully describe the parameter space, even in regions unlikely to be explored in GRBs.

Calculation of the critical Lorentz factor γ_c

From Eq. 5.114, we get the following equation for $Y(\gamma_c)$:

$$Y(\gamma_c) = \begin{cases} A \frac{\gamma_m}{\gamma_c^{\text{syn}}} \frac{I_2}{I_0} h(x_c) & \text{if } \gamma_m > \gamma_c \\ A \frac{\gamma_c}{\gamma_m} \frac{I_2}{I_0} h(x_c) & \text{if } \gamma_m < \gamma_c \text{ and } Y(\gamma_c) < 1 \\ \left(A \frac{\gamma_c^{\text{syn}}}{\gamma_m} \frac{I_2}{I_0} h(x_c) \right)^{1/3} & \text{if } \gamma_m < \gamma_c \text{ and } Y(\gamma_c) > 1 \end{cases} \quad (5.118)$$

where $A = \frac{1}{K_P} \frac{p-2}{p-1} \frac{\epsilon_e}{\epsilon_B}$ is a constant as the microphysics parameter ϵ_B , ϵ_e and p are assumed to be constant during the forward shock propagation. Note that $x_c = 1$ in the slow cooling regime $\gamma_m < \gamma_c$. A second useful relation is obtained from Eq. 5.114 and the definition of γ_0 :

$$Y(\gamma_c) = \frac{Y(\gamma_c)}{Y(\gamma_0)} = \frac{h(x_c)}{h(x_0)}. \quad (5.119)$$

This leads to an iterative procedure to compute $Y(\gamma_c)$, and deduce γ_c

$$\gamma_c = \begin{cases} \gamma_c^{\text{syn}} & \text{if } Y(\gamma_c) < 1 \\ \gamma_c^{\text{syn}}/Y(\gamma_c) & \text{if } Y(\gamma_c) > 1 \end{cases}. \quad (5.120)$$

We start by assuming $Y(\gamma_c) = Y^{\text{noKN}}$ as defined in Sec. 5.4.5 and then iterate as follows:

1. Compute γ_c from Eq. 5.120.
2. Knowing γ_m , γ_c , γ_{self} , scan the different possible cases for the ordering of γ_m , γ_c , γ_0 , $\widehat{\gamma}_m$ and $\widehat{\gamma}_c$ (and additional characteristic Lorentz factors for some cases) as listed in Appendix A and compute γ_0 from Eq. 5.119, which can be analytically inverted as provided for each case in Appendix A. Formally, this scan reduces to only a few cases on a vertical line of constant γ_{self} in the $(\gamma_{\text{self}}; \gamma_0)$ diagrams of Fig. A.1. We stop the scan of the possible cases when the ordering of all characteristic Lorentz factors including the obtained value of γ_0 is the correct one.
3. Having identified the correct case and therefore knowing the expression of $f(x)$, compute the integrals I_0 and I_2 .
4. Knowing also the expression of $h(x)$, compute an updated value of $Y(\gamma_c)$ from Eq. 5.118.
5. Start a new iteration at step 1 until convergence.

In practice we stop the procedure when the relative variation of γ_c in an iteration falls below ϵ_{tol} . We use $\epsilon_{\text{tol}} = 10^{-4}$, which is reached in most cases in less than 20 iterations. In the context of a full afterglow light curve calculation, as we expect Y to vary smoothly during the jet propagation, we use the value of $Y(\gamma_c)$ obtained at the previous step of the dynamics instead of Y^{noKN} to start the iterative procedure. Then we usually reach a convergence in only a few iterations.

Maximum electron Lorentz factor and synchrotron burnoff limit

The maximum Lorentz factor γ_{\max} of accelerated electrons is defined in Section 5.3 and is reached when the acceleration timescale becomes longer than the cooling timescale, *i.e.*

$$t_{\text{acc}}(\gamma_{\max}) = \min(t_{\text{rad}}(\gamma_{\max}); t_{\text{dyn}}), \quad (5.121)$$

where the dynamical timescale t_{dyn} and the acceleration timescale t_{acc} are defined by Eqs. 5.37 and 5.48. From Eqs. 5.74 – 5.75, the radiative timescale t_{rad} is given by

$$t_{\text{rad}}(\gamma) = \frac{t_{\text{dyn}}}{1 + Y(\gamma)} \frac{\gamma_c^{\text{syn}}}{\gamma}. \quad (5.122)$$

Eq. 5.121 can then be rewritten

$$\min \left[1; \frac{\gamma_c^{\text{syn}}}{\gamma_{\max}(1 + Y(\gamma_{\max}))} \right] = \tilde{K} \gamma_{\max}, \quad (5.123)$$

with

$$\tilde{K} = K_{\text{acc}} \frac{m_e c}{e B t_{\text{dyn}}}. \quad (5.124)$$

Then γ_{\max} is the solution of

$$\gamma_{\max}^2 [1 + Y(\gamma_{\max})] = \frac{\gamma_c^{\text{syn}}}{\tilde{K}} \quad (5.125)$$

except in unlikely cases where electrons at γ_{\max} are slow cooling ($\gamma_{\max} < \gamma_c$), that lead to $\gamma_{\max} = 1/\tilde{K}$.

In the present version of the model, we assume $\gamma_{\max} \gg \gamma_m$ so that the calculation of γ_c and the identification of the radiative regime and associated normalized electron distribution $f(x)$ and Compton parameter $h(x)$ is independent of γ_{\max} (see Sec. 5.4.6). Therefore the maximum Lorentz factor is determined once this radiative regime is identified. We follow an iterative procedure where the segments of $h(x)$ are explored successively starting from the last segment $x > \hat{x}_1$ (highest Lorentz factors):

1. We check if there is a solution of Eq. 5.125 in this segment, with the usual approximation for $1 + Y$, *i.e.*

$$\frac{\gamma_c^{\text{syn}}}{\tilde{K}} = \begin{cases} \gamma_{\max}^2 & \text{if } Y(\gamma_{\max}) < 1 \\ \gamma_{\max}^2 Y(\gamma_{\max}) & \text{if } Y(\gamma_{\max}) > 1 \end{cases}, \quad (5.126)$$

where $Y(\gamma_{\max})$ is computed from Eq. 5.114, which leads to

$$Y(\gamma_{\max}) = \begin{cases} A \frac{\gamma_m}{\gamma_{\text{syn}}} \frac{I_2}{I_0} h(x_{\max}) & \text{if } \gamma_m > \gamma_c \\ A \frac{\gamma_c}{\gamma_m} \frac{I_2}{I_0} h(x_{\max}) & \text{if } \gamma_m < \gamma_c \text{ and } Y(\gamma_{\max}) < 1 \\ \left(A \frac{\gamma_c}{\gamma_m} \frac{I_2}{I_0} h(x_{\max}) \right)^{1/3} & \text{if } \gamma_m < \gamma_c \text{ and } Y(\gamma_{\max}) > 1 \end{cases}. \quad (5.127)$$

The pre-factor A is the same as in Eq. 5.118.

2. If there is a solution in the considered segment, we stop the iterative procedure and keep the following value for the maximum electron Lorentz factor:

- the solution γ_{\max} found in the segment if $\gamma_{\max} > \gamma_c$ (fast cooling);
- the solution $\gamma_{\max} = 1/\tilde{K}$ otherwise (slow cooling).

3. If there is no solution in the considered segment:

- If the next segment is still at least partially in fast cooling regime (*i.e.* the upper bound is above γ_c), we start a new iteration at step 1. using this new segment;
- otherwise we stop the iterative procedure and keep for γ_{\max} the slow cooling solution $\gamma_{\max} = 1/\tilde{K}$.

In most cases, the maximum electron Lorentz factor is large enough to be in fast cooling regime ($\gamma_{\max} > \gamma_c$ so that $t_{\text{rad}}(\gamma_{\max}) < t_{\text{dyn}}$) with a negligible IC cooling ($Y(\gamma_{\max}) < 1$). In this case, the maximum Lorentz factor $\gamma_{\max} = \sqrt{\gamma_c^{\text{syn}}/\tilde{K}}$ leads to the usual synchrotron burnoff limit (see e.g. Piran & Nakar, 2010) for the high-frequency cutoff of the synchrotron spectrum in the comoving frame $h\nu_{\max} = h\nu_{\text{syn}}(\gamma_{\max}) = K_2 B \gamma_c^{\text{syn}}/\tilde{K}$:

$$h\nu_{\max} = \frac{1}{K_{P_{\max}} \frac{3he^2}{\sigma_T m_e c} K_{\text{acc}}} = \frac{160 \text{ MeV}}{K_{P_{\max}} K_{\text{acc}}}. \quad (5.128)$$

For the best-fit parameters of the afterglow of GW 170817 presented in Sec. 6.2, the Lorentz factor of the core jet at t_{peak} is $\Gamma \sim 10$. The limit is thus expected at ~ 1 GeV in the observer frame, as seen in Fig. 6.7.

Final calculation of the emission in the comoving frame

The procedure described in the previous paragraph allows not only to compute γ_c but also to identify the relevant case for the distribution of electrons and the Compton parameter (as listed in Appendix A). Therefore the functions $f(x)$, $g(x)$ and $h(x)$ are known, and the function $G(x)$ can be computed. Using Eqs. 5.97 and 5.102, this finally allows to compute at any frequency p_{ν}^{syn} and p_{ν}^{SSC} , the synchrotron and SSC powers per electron and per unit frequency averaged over the timescale t_{dyn} .

5.4.7 Pair Production

At VHE, another process can affect the emissivity: the production of electron-positron pairs from the interaction of two photons: $\gamma + \gamma \rightarrow e^+ + e^-$. This process called **pair production** depletes the SSC flux with more efficiency for the highest photons energies. In fact, pair production has an energy threshold to start occurring: if the two photons have energies $h\nu_{\text{seed}}$ and $h\nu$, the relation $h\nu_{\text{seed}}h\nu > 2(m_e c^2)^2/(1 - \cos \theta)$, where θ is the interaction angle, must be satisfied to enable potential pair production. The cross-section is then defined as

$$\frac{\sigma_{\gamma\gamma}(\nu; \nu_{\text{seed}})}{\sigma_T} = \frac{3}{16} (1 - y^2) \left[(3 - y^4) \ln \frac{1 + y}{1 - y} - 2y(2 - y^2) \right], \quad (5.129)$$

where

$$y^2 = 1 - 2 \frac{(m_e c^2)^2}{h\nu_{\text{seed}} h\nu (1 - \cos \theta)}, \quad (5.130)$$

and $y = 0$ corresponds to the threshold energy, while $y = 1$ is the limit case where the energy of one of the photons is infinite. We account for this mechanism by a simplified treatment, assuming an isotropic distribution of the low-energy seed photons, as for the SSC calculation, and approximating the cross section for pair production by a Dirac function at twice the threshold of the interaction, where the cross-section for pair production is maximum (indeed, the distribution is very peaked around this value, see Gould & Schröder 1967). In this context, VHE photons of frequency ν can produce pairs by interacting with low-energy photons at frequency

$$\nu_{\text{seed}} = 2 \frac{(m_e c^2)^2}{h^2 \nu}, \quad (5.131)$$

The characteristic timescale of this interaction is approximately given by

$$\frac{1}{t_{\gamma\gamma}(\nu)} = \int_0^\infty d\nu_{\text{seed}} n_{\nu_{\text{seed}}} c \sigma_{\gamma\gamma}(\nu; \nu_{\text{seed}}), \quad (5.132)$$

where we assume for simplicity⁴

$$\sigma_{\gamma\gamma}(\nu; \nu_{\text{seed}}) \simeq \sigma_{\text{T}} \nu_{\text{seed}} \delta \left(\nu_{\text{seed}} - 2 \frac{(m_e c^2)^2}{h^2 \nu} \right). \quad (5.133)$$

Using the definition $u_\nu = n_\nu h \nu$ (see Eq. 5.100) we therefore obtain

$$t_{\gamma\gamma}(\nu) = \frac{h}{\sigma_{\text{T}} c} \left[u_{\nu_{\text{seed}} = 2 \frac{(m_e c^2)^2}{h^2 \nu}} \right]^{-1}, \quad (5.134)$$

where $u_\nu = u_\nu^{\text{syn}} + u_\nu^{\text{SSC}} = n_e^{\text{acc}} (p_\nu^{\text{syn}} + p_\nu^{\text{SSC}}) t_{\text{dyn}}$. From the definition of τ_{T} (Eq. 5.103), this leads to

$$t_{\gamma\gamma}(\nu) = \frac{h}{\tau_{\text{T}}} \left[(p_{\nu_{\text{seed}}}^{\text{syn}} + p_{\nu_{\text{seed}}}^{\text{SSC}})_{\nu_{\text{seed}} = 2 \frac{(m_e c^2)^2}{h^2 \nu}} \right]^{-1}. \quad (5.135)$$

For very high frequencies ν , the seed photons for pair production have a low frequency and $p_{\nu_{\text{seed}}}^{\text{syn}} + p_{\nu_{\text{seed}}}^{\text{SSC}} \simeq p_{\nu_{\text{seed}}}^{\text{syn}}$.

The total emitted power per electron $p_\nu = p_\nu^{\text{syn}} + p_\nu^{\text{SSC}}$ is then corrected by a factor

$$\frac{t_{\gamma\gamma}(\nu)}{t_{\text{dyn}}} \left(1 - e^{-t_{\text{dyn}}/t_{\gamma\gamma}(\nu)} \right), \quad (5.136)$$

which in practice only attenuates the SSC component at high frequency where $t_{\gamma\gamma}(\nu) \ll t_{\text{dyn}}$. The effect of pair production on the SSC flux can be seen in Fig. 6.11.

5.4.8 Extragalactic Background Light

VHE photons also interact with infrared photons from distant galaxies to produce pairs on their path between the source and the observer. The diffuse extragalactic infrared radiation is part of the larger-band EBL spanning mostly frequencies from the infrared to the ultraviolet. The EBL is mostly due to star formation in distant galaxies. The interaction of VHE photons with the EBL leads to an exponential cutoff of the observed flux at the highest energies above ~ 1 TeV. Since these interactions occur during the photon propagation, this effect causes a stronger flux depletion for distant sources by increasing the optical depth. However, the details of the optical depth require to know with precision the spectral energy distribution of the EBL, in particular in infrared corresponding to the photons producing pairs after interacting with ~ 1 TeV VHE photons. This is currently challenging to measure and different works find slightly different values (see *e.g.* Franceschini et al. 2008; Finke et al. 2010; Domínguez et al. 2011; Gilmore et al. 2012). For a recent estimate, used to determine the intrinsic VHE emission of GRB 221009A in LHAASO Collaboration et al. (2023), see Saldana-Lopez et al. (2021) and references therein. The typical effect of the VHE flux attenuation due to EBL can be seen on the spectrum of GRB 190114C in Fig. 4.3 (right), where the white data points correspond to the observed flux, and the yellow points to the intrinsic emitted flux after removing the EBL absorption on the line of sight. This effect is only dependent on the

⁴Technically, the exact cross-section (Eq. 5.129) peaks for $y \simeq 0.7$. We express the cross-section with Eq. 5.133 rather than Eq. 5.129, which is normalised to match the exact cross-section for a power-law spectrum of the seed photons of slope $\beta = 2.3$. A more careful treatment can be implemented in the future where the optical depth is computed exactly using the exact shape of the synchrotron and SSC photon fields.

distance to the source and the energy of the photon considered, and can therefore be included as a post-processing step using tabulated values of the EBL flux from the literature. In Chapter 6, I discuss specifically the afterglow of GW 170817 which is located only at ~ 40 Mpc. Therefore, it is not necessary in this case to account for the effects of the EBL.

5.4.9 Synchrotron Self-absorption

At low photon energies (typically in the radio band), another process can lead to a depletion of the emitted synchrotron flux: **synchrotron self-absorption**. This process is exactly the opposite to synchrotron radiation: an electron with a relativistic motion in a magnetic field can absorb a seed photon during its gyration. The absorbed photon then gives away its energy to the electron, which in principle should affect the overall electron distribution $\bar{n}(\gamma)$ by adding higher-energy electrons and removing lower-energy electrons in the distribution. In good approximation, synchrotron self-absorption can be only assumed to affect the radio spectrum without modifying the electron distribution as it does not re-inject sufficient energy. The cross-section for synchrotron self-absorption of a photon with frequency ν by an electron with Lorentz factor γ is

$$\sigma_{\text{SSA}}(\gamma; \nu) = \frac{1}{8\pi m_e \nu^2} \frac{p_\nu}{\gamma} \left[2 - \frac{d \ln \bar{n}(\gamma)}{d\gamma} \right], \quad (5.137)$$

where $p_\nu = p_\nu^{\text{syn}} + p_\nu^{\text{SSC}}$. Synchrotron self-absorption is most efficient at low energies, such that $p_\nu \simeq p_\nu^{\text{syn}}$. The characteristic timescale for synchrotron self-absorption is approximately given by

$$\frac{1}{t_a(\nu)} = \frac{c}{8\pi m_e \nu^2} \times \int_{\gamma_1}^{\gamma_1^{N+1}} \frac{d\gamma}{\gamma} \bar{n}(\gamma) p_\nu \left[2 - \frac{d \ln \bar{n}(\gamma)}{d\gamma} \right]. \quad (5.138)$$

We can define the critical frequency for synchrotron self-absorption ν_a such that

$$t_a(\nu_a) = t_{\text{dyn}}. \quad (5.139)$$

For $\nu \gg \nu_a$, synchrotron self-absorption occurs on a timescale longer than the dynamical timescale and is therefore not efficient, while for $\nu \ll \nu_a$, it will affect the emission profile and the electron distribution.

In the context of our self-consistent model for synchrotron and SSC emission, we introduced in Sec. 5.4.6 the functions $f(x)$, $h(x)$ and $g(y)$ without accounting for ν_a which in principle will add a new break at low x in $f(x)$ and at low y in $g(y)$. However, at high x , $h(x) \ll 1$ in most cases. This effect should therefore not contribute to any modification of the VHE spectrum in most cases. Because this work is mainly motivated by modelling VHE emission, we have not included synchrotron self-absorption in the model yet, and leave it for future work. In a similar fashion as for our treatment of pair production, we can simply correct the total emitted power per electron by a factor

$$\frac{t_a(\nu)}{t_{\text{dyn}}} \left(1 - e^{-t_{\text{dyn}}/t_a(\nu)} \right). \quad (5.140)$$

5.5 Observed Flux

Once the emissivity in the comoving frame is known (Sec. 5.4), the flux measured by a distant observer with a viewing angle θ_v can then be computed by an integration over equal-arrival time surfaces, taking into account relativistic Doppler boosting and relativistic beaming, as well as the effect of cosmological redshift. This leads to the following expression of the flux density ($\text{erg} \cdot \text{s}^{-1} \cdot \text{cm}^{-2} \cdot \text{Hz}^{-1}$) in the observer frame measured at time t_{obs}^z and frequency ν_{obs}^z (Woods & Loeb, 1999):

$$F_{\nu_{\text{obs}}^z}(t_{\text{obs}}^z) = \frac{1+z}{4\pi D_L^2} \int_0^\infty dr \int_0^\pi d\psi \int_0^{2\pi} d\phi r^2 \sin \psi \times [\mathcal{D}^2(r, \psi, t) 4\pi j'_{\nu'}(r, \psi, \phi, t)]_{t = \frac{t_{\text{obs}}^z}{1+z} + \frac{r}{c} \cos \psi}, \quad (5.141)$$

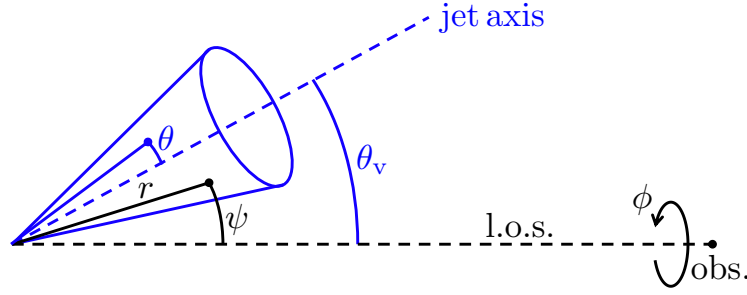


Fig. 5.8: Coordinates and notations used in the expression of the observed flux.

where we use spherical coordinates $(r; \psi; \phi)$ with the polar axis equal to the line-of-sight, ψ and ϕ the colatitude and longitude, and the jet axis in the direction $(\psi = \theta_v, \phi = 0)$ (see Fig. 5.8), and where z and D_L are the redshift and the luminosity distance of the source. Note that the angle ψ differs from θ used in Sec. 5.2 which is measured from the jet axis. The time t (source frame) and frequency ν' (comoving frame) are given by

$$t = \frac{t_{\text{obs}}^z}{1+z} + \frac{r}{c} \cos \psi \quad (5.142)$$

$$\nu' = (1+z) \frac{\nu_{\text{obs}}^z}{\mathcal{D}(r, \psi, t)}. \quad (5.143)$$

The Doppler factor is expressed as

$$\mathcal{D}(r, \psi, t) = \frac{1}{\Gamma(r, \psi, t) (1 - \beta(r, \psi, t) \cos \psi)} \quad (5.144)$$

and $j'_{\nu'}$ is the emissivity ($\text{erg} \cdot \text{cm}^{-3} \cdot \text{s}^{-1} \cdot \text{Hz}^{-1} \cdot \text{sr}^{-1}$) in the comoving frame. I provide the details of the derivation of Eq. 5.141 in Appendix C. Note that the condition on t for the computation of the emissivity under the integral implies that for a given observer time t_{obs}^z , the flux received comes from regions where those closer to the line of sight ($\psi \rightarrow 0$) radiated at later times than those further away. In the case of a decelerating afterglow jet, the bolometric emissivity decreases during the deceleration. The properties of the observed light curve arise therefore from a balance between the angle of the regions that contribute to the flux at a given time, their emissivity at the time of emission and the spectral properties of the emissivity.

In practice, following the discretization of the jet structure described in Sec. 5.1, the observer frame flux density $F_{\nu_{\text{obs}}^z}(t_{\text{obs}}^z)$ is computed as $F_{\nu_{\text{obs}}^z}(t_{\text{obs}}^z) = \sum_{i=0}^N F_{\nu_{\text{obs}}^z}^{(i)}(t_{\text{obs}}^z)$, where $F_{\nu_{\text{obs}}^z}^{(i)}(t_{\text{obs}}^z)$ are the contributions of the core jet ($i = 0$) and lateral rings ($i \in \llbracket 1, N \rrbracket$). To compute each contribution, the thin shell approximation allows to reduce the double integral over r and ψ in Eq. 5.141 to a simple integral over r , or equivalently over ψ or t , as I show in Appendix C. In addition, to improve the computation time, the remaining integral on ϕ is computed analytically. This leads to

$$F_{\nu_{\text{obs}}^z}^{(i)}(t_{\text{obs}}^z) = \frac{1+z}{4\pi D_L^2} \int_{t_{\text{min}}^{(i)}(t_{\text{obs}}^z)}^{t_{\text{max}}^{(i)}(t_{\text{obs}}^z)} dt \left[\frac{c}{2\Gamma(t)R(t)} \frac{\Delta\phi_i(\theta_v; \psi_i(t_{\text{obs}}^z; t))}{2\pi} \mathcal{D}^2(t_{\text{obs}}^z; t) 4\pi N_e(R(t)) p'_{\nu'}(t) \right]_{t=\frac{t_{\text{obs}}^z}{1+z} + \frac{r}{c} \cos \psi} \quad (5.145)$$

where

$$\cos(\psi_i(t_{\text{obs}}^z; t)) = \frac{c}{R_i(t)} \left(t - \frac{t_{\text{obs}}^z}{1+z} \right), \quad (5.146)$$

$$\mathcal{D}_i(t_{\text{obs}}^z; t) = \frac{1}{\Gamma_i(t) (1 - \beta_i(t) \cos \psi_i(t_{\text{obs}}^z; t))}, \quad (5.147)$$

$$N_e(r) = \zeta \frac{M_{\text{ext}}(r)}{m_p} \quad (5.148)$$

is the number of shock-accelerated electrons per unit solid angle ($M_{\text{ext}}(r)$ is defined in Eq. 5.24), and $p_{\nu'}^{(i)}(t)$ is the power per unit frequency and per electron in the comoving frame computed in Sec. 5.4 and evaluated here at time t and comoving frequency $\nu' = (1+z)\nu_{\text{obs}}^z/\mathcal{D}_i(t_{\text{obs}}^z; t)$. I provide the details of the derivation of Eq. 5.145 in Appendix C.

The limits of the integral $t_{\text{min}}^{(i)}(t_{\text{obs}}^z)$ and $t_{\text{max}}^{(i)}(t_{\text{obs}}^z)$ are defined by the condition $\psi_{\text{min},i} \leq \psi_i(t_{\text{obs}}^z; t) \leq \psi_{\text{max},i}$, (see Appendix C) where

$$\psi_{\text{min},i} = \begin{cases} \theta_{\text{min},i} - \theta_v & \text{if } \theta_v \leq \theta_{\text{min},i} \\ 0 & \text{if } \theta_{\text{min},i} \leq \theta_v \leq \theta_{\text{max},i} \\ \theta_v - \theta_{\text{max},i} & \text{if } \theta_{\text{max},i} \leq \theta_v \leq \pi/2 \end{cases}, \quad (5.149)$$

and $\psi_{\text{max},i} = \theta_v + \theta_{\text{max},i}$, *i.e.*

$$t - \frac{R_i(t)}{c} \cos(\psi_{\text{max},i}) \leq \frac{t_{\text{obs}}^z}{1+z} \leq t - \frac{R_i(t)}{c} \cos(\psi_{\text{min},i}). \quad (5.150)$$

Finally, we use the exact analytical calculation of the geometrical term $\Delta\phi_i$ defined by $\Delta\phi_i(\theta_v; \psi) = \int_0^{2\pi} d\phi f_i(\theta_v; \psi; \phi)$, where $f_i(\theta_v; \psi; \phi) = 1$ if the direction $(\psi; \phi)$ is contained in the component i (core jet or ring) and 0 otherwise. The analytical expression of $\Delta\phi_i(\theta_v; \psi)$ is presented in Appendix D.

The numerical implementation allows to select the level of approximation for the SSC emission (synchrotron only, Thomson or full calculation) and to include or not the attenuation due to the pair production (Sec. 5.4.7).

5.6 Comparison with other Afterglow Models

The most standard afterglow model assuming synchrotron radiation by a population of shock-accelerated electrons has been used in multiple works (*e.g.* Sari et al. 1998; Panaitescu & Kumar 2000; Sari & Esin 2001; Gill & Granot 2018; Ryan et al. 2020). However, some differences between the various models can be expected, in particular depending on the flux normalization method and the calculation of the jet dynamics. I now compare the results obtained with the model presented in this chapter to two other models of the afterglow of a structured jet: the model presented in Gill & Granot (2018) and `afterglowpy`, a public Python module to calculate GRB afterglow light curves and spectra, based on Ryan et al. (2020). Concerning the SSC component, we verified that we retrieve the subcases presented in Nakar et al. (2009), as discussed in Appendix A.

The first comparison is straightforward: with our default values of the normalization coefficients K_ν and K_p , the assumptions (dynamics, microphysics, radiation, calculation of observed quantities) of our model in the pure synchrotron case are exactly the same as in Gill & Granot (2018). We checked that we reproduce exactly the different cases in their Fig. 4. Some differences of notation are discussed and the reproduction of the figures are shown in Appendix B.

The case of `afterglowpy` requires a more detailed comparison as there are differences in some treatments of the afterglow physics:

1. **Early dynamics:** In `afterglowpy`, even the early-time dynamics is computed assuming the self-similar Blandford & McKee regime, *i.e.*

$$\Gamma(\theta; t) \propto \epsilon_0(\theta)^{1/2} n_{\text{ext}}^{1/2} t^{-3/2} \quad (5.151)$$

(see Sec. 2.1 in Ryan et al. 2020), whereas we include the coasting phase with $\Gamma \sim \text{cst}$ before a smooth transition towards the self-similar regime at the deceleration radius, as described in Sec. 5.2. Fig. 5.9 compares for a typical set of parameters the afterglow light curves from a top-hat jet viewed on-axis in radio, optical and X-rays obtained with our model (solid line),

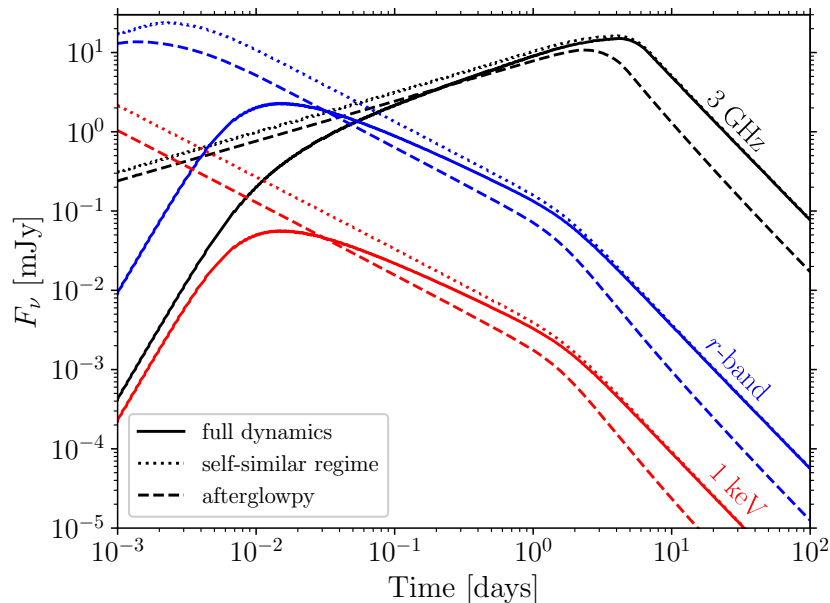


Fig. 5.9: Synthetic afterglow light curves of a top-hat jet viewed on-axis, in the synchrotron-only radiation regime. Solid lines show the results obtained using our model with full dynamics treatment (using Eq. 5.29), while dotted lines follow the self-similar solution at all times (Eq. 5.151). Dashed lines are obtained with `afterglowpy` without lateral expansion. The fluxes are computed in radio at 3 GHz (black), in optical in r -band at 5.06×10^{14} Hz (blue) and in X-rays at 1 keV (red). The parameters used for this figure are $E_{0,\text{iso}}^c = 10^{52}$ erg, $\theta_c = 4$ deg, $n_{\text{ext}} = 10^{-3}$ cm $^{-3}$, $\epsilon_e = 10^{-1}$, $\epsilon_B = 10^{-1}$, $p = 2.2$, $D_L = 100$ Mpc.

`afterglowpy` (dashed line) and our model where the dynamics has been forced to be in the self-similar regime at all times (dotted line). This allows to check that both models with the same self-similar dynamics agree well, except for the flux normalization as discussed below, and that the model with the full dynamics converges progressively towards the same solution: following the peak at the deceleration radius (at $\sim 10^{-2}$ days in this example), the light curve obtained with the full dynamics smoothly converges towards the self-similar solution, and both light curves are identical at late times (typically after the jet break at ~ 2 days in this example). On the other hand, the self-similar approximation strongly over-estimates the fluxes until the deceleration radius and the full dynamics should always be included when considering early observations. In the case of GW 170817 discussed in Chapter 6, the earliest detection by *Chandra* was obtained 9 days after the merger, by which time the core jet dynamics has reached the self-similar regime.

2. **Late dynamics:** contrary to `afterglowpy`, the present version of our model does not include lateral expansion of the ejecta. When comparing with `afterglowpy`, we therefore deactivate this option in the latter, which leads to the excellent late-time agreement seen in Fig. 5.9. As discussed in Sec. 5.2, the impact of the lateral spreading is expected to be very limited as long as the core jet is relativistic (see e.g. Woods & Loeb, 1999; Granot & Piran, 2012; van Eerten & MacFadyen, 2012; Duffell & Laskar, 2018), so that we stop the jet propagation when the core Lorentz factor reaches $\Gamma = 2$ in the simulations of GW 170817’s afterglow discussed in Chapter 6. In addition, we exclude observations after 400 days from the data set used for the afterglow fitting, which corresponds to $\Gamma \gtrsim 3 - 4$ for the core jet in our best fit models.
3. **Flux normalization:** `afterglowpy` relies on a scaling to `boxfit` (van Eerten et al., 2012), while in our model, this normalization is derived from analytical approximations detailed

throughout this chapter. This leads to the difference of normalization seen in Fig. 5.9 when comparing `afterglowpy` with our model where the same self-similar dynamics is forced. The flux ratio varies between 1 and 5 at all wavelengths. When exploring a broad parameter space, varying the angle, energy injection, microphysical parameters, we checked that the flux ratio never exceeds 5.

To conclude this comparison, we note that `afterglowpy` and our model (in pure synchrotron mode) have been used in Kann et al. (2023, **Publication II**, Appendix E.2, see also Sec. 4.2) for two independent Bayesian inferences of the parameters of the afterglow of GRB 221009A using the same set of early observational data and converged towards very similar solutions.

5.7 Conclusion

In this chapter, I described a detailed model of the afterglow of a laterally-structured jet from radio to VHE, where emission is produced in the shocked external medium behind the forward external shock. This model builds on previous models proposed in the literature and combines for the first time a semi-analytical treatment of both the jet structure and the SSC diffusions producing VHE radiation in both Thomson and KN regimes. The dynamics does not include the late lateral expansion of the ejecta. Such effects, as well as the contribution of the reverse shock, will be implemented in the future.

The main challenge addressed in this chapter is the self-consistent calculation of the synchrotron and SSC emission while accounting for the two different IC regimes: Thomson and KN. We based our approach on the method proposed by Nakar et al. (2009), extended to include additional effects: the maximum electron Lorentz factor γ_{\max} is also computed self-consistently, leading to a realistic estimate of the high-energy cutoff of the synchrotron component, and the attenuation at high-energy due to pair production is also included. The values of γ_c and $Y(\gamma_c)$, as well as the spectral regimes are determined numerically. Synchrotron self-absorption, that is relevant at low radio frequencies has not been included yet. The model described allows to compute afterglow light curves and spectra.

I list in this section all the parameters required to perform a simulation as well as their numerical labels in Tab. 5.2. In Tab. 5.3, I show the different other additional parameters that are useful to select the calculation assumptions. The implementation of the model is computationally-efficient, allowing for afterglow fitting. I present results concerning the afterglow of GW 170817 in the next chapter.

Parameter	Name	Description
$E_{0,\text{iso}}^c$	E0iso	Isotropic-equivalent energy (erg) in the core of the jet (Eq. 5.12)
Γ_0^c	gamma0	Initial Lorentz factor of the core of the jet (Eq. 5.4)
s	s	External medium density profile ($s = 0$: uniform; $s = 2$: wind, Eq. 5.17)
n_{ext}	n_ext	Particle density (cm^{-3}), for $s = 0$, None for $s = 2$ (Eq. 5.17)
A_*	a_star	Normalization factor, for $s = 2$, None for $s = 0$ (Eq. 5.17)
ϵ_B	eps_B	Fraction of energy to amplify the magnetic field (Eq. 5.39)
ϵ_e	eps_e	Fraction of energy to accelerate the electrons (Eq. 5.42)
ζ	zeta	Fraction of electrons accelerated at the shock (Eq. 5.41)
p	p	Slope of electron Lorentz factor profile at injection (Eq. 5.44)
θ_c	theta_jet_deg	Core jet opening angle in deg (Appears in multiple places)
θ_v	theta_obs_deg	Viewing angle in deg (Sec. 5.5)
D_L	dist_Mpc	Luminosity distance (Mpc) to the source (Sec. 5.5)
structure	lateral_profile	What lateral profile to choose (default: Eq. 5.7)
a	a	Power-law slope for initial lateral energy profile (Eq. 5.3)
b	b	Power-law slope for initial lateral Lorentz factor profile (Eq. 5.4)
$\beta_{0,\text{min}}$	beta_min	For Gaussian jets: limits the extent of the lateral structure (Sec. 5.1)

Tab. 5.2: Afterglow model parameters.

Parameter	Name	Description
γ	adiabatic	Adiabatic index at the shock. Default: $\gamma = 4/3$
K_{acc}	coef_t_acc	Scaling coefficient for the acceleration timescale (Eq. 5.48). Default: $K_{\text{acc}} = 1$
K_ν	coef_nu	Scaling coefficient for the synchrotron frequency (Eq. 5.53; Tab. 5.1). Default: $K_\nu = 3\pi/8$
$K_{P_{\text{max}}}$	coef_p_max	Scaling coefficient for the synchrotron power (Eq. 5.50; Tab. 5.1). Default: $K_{P_{\text{max}}} = 0.633$
N	N_rings	Total number of rings in the lateral structure. Default: $N = 15$
discretization	discretization	Under which criterion to sample the lateral structure. Default: constant energy per ring
F_ν or L_ν ?	flux_lum	Compute the observed flux or luminosity. Default: compute the flux
include γ_{max} ?	gmax_flag	To include the synchrotron burnoff. Default: True
include $\gamma\gamma \rightarrow e^+e^-$?	pair_prod_flag	To include pair production. Default: True
radiative model	inv_compton_flag	Select which radiative model to use. Default: our complete model
afterglowpy ?	afterglowpy_dynamics	Extend the self-similar solution to early times Default: False

Tab. 5.3: Additional afterglow model parameters. These are typically set to a default value but can be modified for an exploration of other physics or comparison with other works.

Chapter 6

Short Gamma-Ray Burst Afterglows at Very High Energies: the Case of GW 170817

Contents

6.1	Afterglow Observations of GW 170817	94
6.1.1	Detections from Radio to X-rays	94
6.1.2	Very High Energy Upper Limits	96
6.2	The Very High Energy Afterglow of GW 170817	97
6.2.1	Fitted Observational Data	97
6.2.2	Results from the Afterglow Fitting	98
6.2.3	Discussion: Inferred Parameters	105
6.2.4	Discussion: the Predicted Very High Energy Emission of GW 170817	107
6.3	Detectability of Post-Merger Afterglows at Very High Energy and Prospects for the CTAO	110
6.4	A Population of Short Merger Time Binaries?	114
6.5	Conclusion	116

The Binary Neutron Star (BNS) merger event GW 170817 is probably the most remarkably followed-up transient in modern astronomy. As described in Chapter 2, following the Gravitational Wave (GW) trigger, a Gamma-Ray Burst (GRB) was detected, followed in the next days and months by a detailed follow-up of its kilonova and GRB afterglow emission. In this chapter, I present our study of the GRB afterglow of GW 170817, obtained with the model presented in Chapter 5. These results are also presented in **Publication I** (Appendix E.1, Pellouin & Daigne 2023, **submitted**).

6.1 Afterglow Observations of GW 170817

6.1.1 Detections from Radio to X-rays

I described in Sec. 2.4 the properties of the afterglow of GW 170817. Its monitoring initially started by a week where no non-thermal emission could be detected at the location of the source. Only the thermal kilonova was detected (see Sec. 2.2). Its emission was observed in optical bands for up to 30 days (see *e.g.* Villar et al. 2017) as a fainting source. 9.2 days after the merger, the non-thermal component emerged from radio to X-rays and was observed up to its peak, ~ 120 days after the merger. When the first optical detection of the afterglow was made (at 109 days, Lyman et al. 2018), the kilonova was therefore not detectable since a few weeks and subsequently does not contaminate the optical afterglow observations. The afterglow peak was followed by a decay, also monitored in the next months. At the time of writing, almost 5 years after the merger, radio and X-ray observing proposals are still undertaken. I report in Tab. 6.1 the publications where all the observations and upper limits on the afterglow of GW 170817 can be found, sorted by instrument.

Radio	
VLA	Alexander et al. (2017); Hallinan et al. (2017); Mooley et al. (2018a,b,c) Dobie et al. (2018); Margutti et al. (2018); Alexander et al. (2018) Hajela et al. (2019); Makhathini et al. (2021) Balasubramanian et al. (2021, 2022)
ATCA	Hallinan et al. (2017); Mooley et al. (2018b,c); Dobie et al. (2018) Troja et al. (2019, 2020); Makhathini et al. (2021)
uGMRT	Hallinan et al. (2017); Kim et al. (2017) Mooley et al. (2018c); Resmi et al. (2018)
MeerKAT	Mooley et al. (2018b); Makhathini et al. (2021)
eMERLIN	Ghirlanda et al. (2019); Makhathini et al. (2021)
Optical	
HST	Lyman et al. (2018); Fong et al. (2019); Piro et al. (2019) Lamb et al. (2019); Makhathini et al. (2021)
X-rays	
Swift-XRT	Evans et al. (2017)
NuSTAR	Evans et al. (2017); Troja et al. (2018)
Chandra	Margutti et al. (2017); Troja et al. (2017); Haggard et al. (2017) Nynka et al. (2018); Ruan et al. (2018a,b); Piro et al. (2019) Hajela et al. (2019); Troja et al. (2019, 2020, 2022b) Hajela et al. (2022); O'Connor & Troja (2022)
XMM-Newton	D'Avanzo et al. (2018); Piro et al. (2019)

Tab. 6.1: Published references where observational data of the afterglow of GW 170817 is reported. Data up to 940 days have been compiled by Makhathini et al. (2021). Radio and X-ray observations after 3 years are found in the more recent references and discussed in Sec. 6.1.1.

Because of the variety of instruments and methods used for the detections, the reported flux density values or upper limits in the different references may not all rely on the same assumptions for data analysis. For this reason, [Makhathini et al. \(2021\)](#) reprocessed all available observational data up to 940 days with unified assumptions and data processing techniques. We use the values they report as the observational data to which we will fit our model. As discussed below, we will only fit data up to 400 days, but even more recent observations have been conducted ~ 3.5 years post-merger in radio with the VLA ([Balasubramanian et al., 2021](#)) and in X-rays with Chandra ([Troja et al., 2022b](#); [Hajela et al., 2022](#)); and again ~ 4.5 years post-merger with the VLA ([Balasubramanian et al., 2022](#)) and Chandra ([O'Connor & Troja, 2022](#)). The radio and X-ray observations at 3.5 year post-merger as reported in [Balasubramanian et al. \(2021\)](#) are included in the observational data set that we use, and can be accessed online¹. I show the afterglow observations of GW 170817 in Fig. 6.1. All observations from radio to X-rays are compatible with a unique power-law spectrum with a fixed spectral slope (see also Fig. 2.6). In the context of the synchrotron radiation model, and with reasonable assumptions, the long-lasting afterglow is in the slow cooling regime (see Sec. 6.2). Assuming a simple spectral profile as proposed by [Sari et al. \(1998\)](#) and described in Sec. 5.4.4, it is clear that $\nu_m < 10^9$ Hz and $h\nu_c > 1$ keV in the observer frame. This constrains the parameter space but is not as strong as the direct observation of the passage of a spectral break in a band at a given time, which would put much tighter constraints. Another interesting constraint could be put by the detection of the spectral transition at ~ 1 GeV (corresponding to ν_{\max}), between the synchrotron and Synchrotron Self-Compton (SSC) component. This would require more sensitive instruments in this band, which is currently observed by Fermi-LAT ([Atwood et al., 2009](#)) and AGILE ([Tavani et al., 2009](#)).

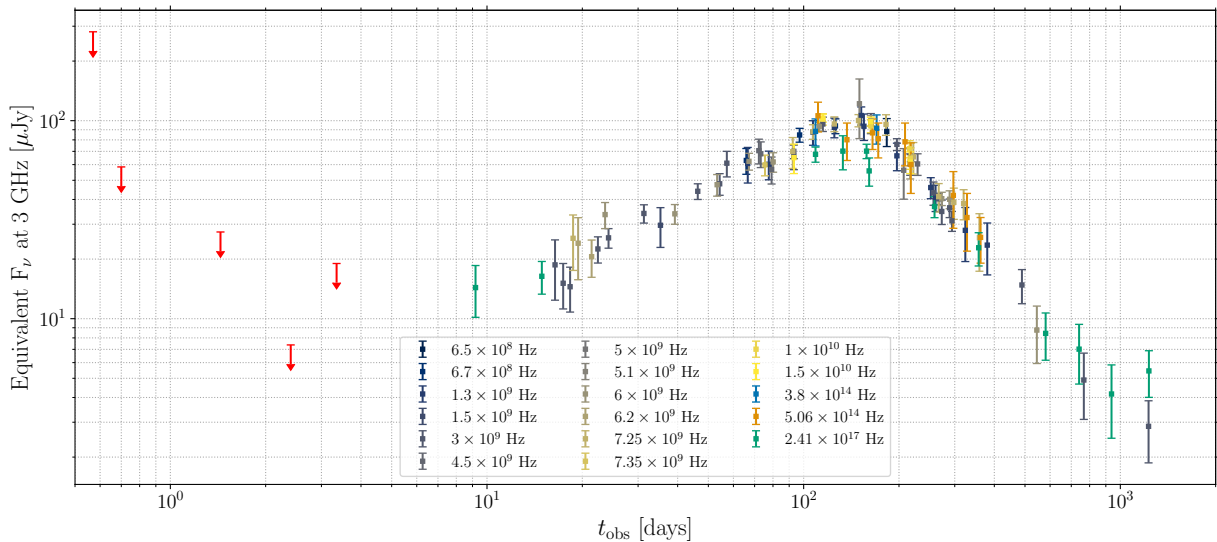


Fig. 6.1: GW 170817 GRB afterglow observations. Data has been rescaled to an equivalent flux density at 3 GHz such that $F_{\nu}^{\text{eq}} = F_{\nu}(\nu/3 \text{ GHz})^{(p-1)/2}$, here with $p = 2.14$, corresponding to the slow cooling spectral regime with $\nu_m < \nu < \nu_c$ (see [Sari et al. 1998](#) and Sec. 5.4.4). Red arrows are the most constraining upper limits reported in Tab. 6.2.

The decreasing flux of the afterglow of GW 170817 make the extraction of late-time data particularly complex, especially in X-rays. The observed source flux is down to a few photons over long exposure times. This is enough to still statistically detect the source at more than 3σ confidence (see for example the analysis by [Troja et al. 2022b](#)), but very limited for a precise spectral analysis in

¹<https://github.com/kmooley/GW170817/>, corresponding version: commit from May 19, 2021.

the observing band. As a consequence, the reported flux densities at 1 keV are much more sensitive to the spectral model used in the data post-processing.

There is currently an ongoing discussion about the late-time X-ray light curve of the GRB afterglow of GW 170817. [Hajela et al. \(2022\)](#) possibly detect a deviation to the theoretical afterglow light curve at late times, a rebrightening that they suggest could be the late-time contribution of the kilonova afterglow, produced by the external shock due to the deceleration of the quasi-spherical ejecta responsible for the kilonova emission (see Sec. 2.2, [Nakar & Piran 2011](#)). The kilonova afterglow is only expected to occur at late times, as the ejecta deceleration starts much later than the afterglow, typically years after the merger. At such late times, the GRB afterglow may be faint enough to allow the detection of the kilonova afterglow, observed as an excess of X-ray radiation: a rebrightening. [Troja et al. \(2022b\)](#) analysed the same Chandra X-ray data with a different data analysis method and found that there is no statistically significant deviation to the GRB afterglow predictions in the observations at 3.5 years. Future X-ray observations should solve this tension: if the X-ray excess is due to the kilonova afterglow emission, it is expected to rise in the coming years.

As discussed in Chapter 5, our model currently does not include a treatment of the lateral expansion of the jet in the mildly- and non-relativistic regimes. In particular, this implies that, by construction, this model cannot introduce changes in the temporal slope of the light curve at a given frequency, except in the case of a change of spectral regime, which would be abrupt and easily recognizable. For this reason and the data analysis arguments presented above, we choose not to include observations after 400 days (where we expect $\Gamma \lesssim 4$ for the core of the jet) in the data set used for the model fitting. We therefore use the 94 data points reported in observations and as reprocessed by [Makhathini et al. \(2021\)](#), from radio to X-rays, and between 9.2 days and 380 days.

6.1.2 Very High Energy Upper Limits

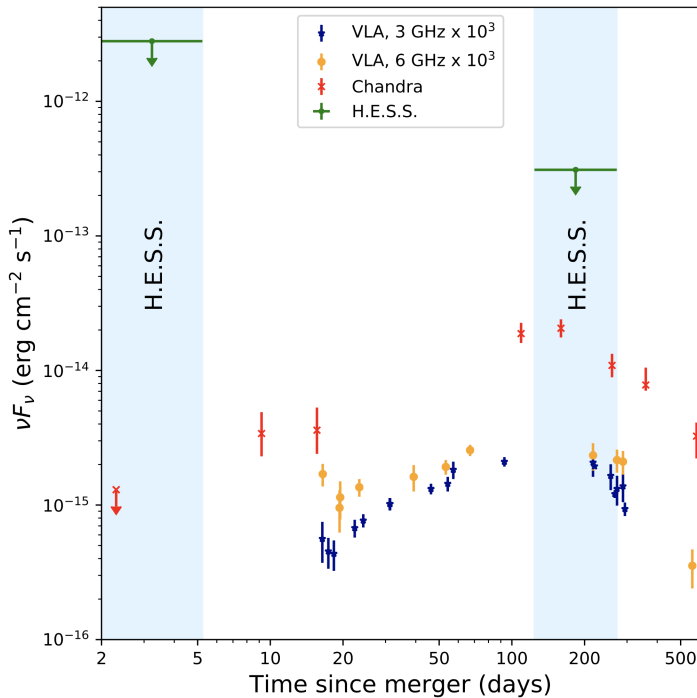


Fig. 6.2: Reproduction of Fig. 1 ([Abdalla et al., 2020](#)). Shown are the H.E.S.S. observation windows (blue areas), VLA radio data at 3 GHz (blue stars) and 6 GHz (orange circles), as well as X-ray data (red crosses). The H.E.S.S. 1 – 10 TeV energy flux upper limits (green arrows) are derived for the prompt and the long-term follow-up. The peak upper limit is $3.2 \times 10^{-13} \text{ erg} \cdot \text{s}^{-1} \cdot \text{cm}^{-2}$ in the 1 – 10 TeV band, over 53.9 h of observations between 124 and 272 days.

In addition to the observations from radio to X-rays, Very High Energy (VHE) follow-ups have been conducted by H.E.S.S., a few days after the merger ([Abdalla et al., 2017](#)) and around its peak ([Abdalla et al., 2020](#)). Both observations did not lead to a source detection between ~ 0.1 and ~ 20 TeV. The upper limits are shown in [Abdalla et al. \(2020\)](#) and reproduced in Fig. 6.2. The

first upper limit was obtained when the source flux was intrinsically very weak, before its detection by other instruments, and over only a few nights. It will not be the focus of our study. The second upper limit is ~ 10 times deeper and at the observation peak. I study in Sec. 6.2 the flux predicted by our model at VHE at that time and discuss observability conditions in Sec. 6.3.

MAGIC also conducted observations around the afterglow peak, but found a less constraining upper limit (see Salafia et al. 2022a), while the HAWC collaboration searched for coincident VHE photons in the first hours following the event (Galván et al., 2019), but found no significant source. We decide not to use this less constraining information in our study.

6.2 The Very High Energy Afterglow of GW 170817

6.2.1 Fitted Observational Data

In its numerical implementation, our model allows for simultaneous, multi-wavelength modelling, which optimises the computation time for data fitting (we only compute fluxes at the corresponding times and frequencies). We use 94 data points, from radio to X-rays between 9.2 and 380 days, as compiled and reprocessed homogeneously by Makhathini et al. (2021) and discussed in Sec. 6.1.1. We also include 5 constraining early-time upper limits also reported in Makhathini et al. (2021), as shown in Tab. 6.2. Early-time constraints are useful to restrict the posterior models to those with a single peak in flux density, as I discuss next. All these flux measurements and upper limits are fitted simultaneously.

Time	Frequency	Instrument	Upper limit
0.57	9.7×10^9	VLA	144
0.70	1.2×10^{18}	NuSTAR	7.3×10^{-4}
1.44	1.0×10^{10}	VLA	13.8
2.40	2.41×10^{17}	Chandra	2.3×10^{-4}
3.35	3×10^9	VLA	19

Tab. 6.2: Early-time upper limits used in the afterglow fitting. Times are given in days, frequencies in Hz, and upper limits in μJy . These flux upper limits are selected as the most constraining among all the early observations listed in the compilation by Makhathini et al. (2021) (see Fig. 6.1).

As discussed previously, in this study, we choose not to include late-time observations after 400 days in the fits. Indeed, we expect jet lateral spreading to play a role at late times, when the shock front reaches Lorentz factors $\Gamma \lesssim 3$, by which point our model cannot accurately describe the jet dynamics (see Sec. 5.2). In addition, other emission sites (*e.g.* the kilonova afterglow, Nakar & Piran 2011) could also contribute to the observed flux at late times (see Sec. 6.1.1). Including the latest observations (Hajela et al., 2022) which were not included in the compilation by Makhathini et al. (2021) is also difficult: a correct modelling in this case should be expressed in photon counts and account for the instrumental response and low-statistics effects. The result of such an analysis is currently unclear, with an uncertain late rebrightening discussed in Sec. 6.1.1. Interpreting the late evolution of GW 170817’s afterglow seems to require a dedicated study, and we therefore exclude this phase from the analysis presented here.

Finally, we do not include the H.E.S.S. upper limit at the peak (Abdalla et al., 2020) as it does not constrain the fit (see Sec. 6.2.3).

About Double-Peaked Afterglow Light Curves

For a power-law structure as defined by Eqs. 5.6 and 5.7, the deceleration radius scales as $R_{\text{dec}}(\theta) \propto \theta^{\frac{2b-a}{3-s}}$. It therefore follows that the deceleration radius decreases with θ if $2b > a$. In

this case, we expect the light curves to have the properties already discussed in Sec. 4.1. However, light curve shapes can deviate from the single-peak scenario and have two peaks. Beniamini et al. (2020b) derived the conditions for the observed afterglow light curve to have a single peak, as in the case of GW 170817. For an off-axis observation with a large viewing angle, these conditions are

- $\Gamma_0^c \theta_c > 1$;
- $2b > a/(4-s)$ (*i.e.* $8b > a$ for a uniform external medium);
- $b > -\ln \Gamma_0^c / \ln \theta_c$;
- $\theta_v > \theta_c (\Gamma_0^c \theta_c)^{\frac{1}{b-1}}$.

In the case of the afterglow of GW 170817, the observed light curve is single-peaked. However, a first parameter exploration using only the 94 observations contained a significant fraction of double-peaked light curves, with a first peak occurring at very early times before 1 day, and the second at $t \sim 120$ days. This is compatible with the detections starting after 9 days, but not with the constraining earlier-time upper limits in radio and X-rays. For this reason, we decided to add 5 constraining early-time upper limits in the fitted data, represented by the red arrows in Fig. 6.1 and reported in Tab. 6.2. These constraints eliminate most of the double-peaked light curves (see Fig. 6.6), and we always have $8b > a$ so that the deceleration radius is larger at high latitude (see Sec. 6.2). We verify that our posterior sample satisfies the single-peak conditions from Beniamini et al. (2020b) in Fig. 6.3 in most cases, except for the last constraint. This is discussed in Sec. 6.2.3.

6.2.2 Results from the Afterglow Fitting

Bayesian Analysis

Parameter	Bounds	Type
$E_{0,\text{iso}}^c$ (erg)	$10^{50} - 10^{56}$	log-uniform
θ_c (deg)	0.5 – 10	uniform
θ_v (deg)	0 – 50	uniform
n_{ext} (cm^{-3})	$10^{-6} - 10^0$	log-uniform
ϵ_B	$10^{-6} - 1$	log-uniform
ϵ_e	$10^{-4} - 1$	log-uniform
ζ	$10^{-4} - 1$	log-uniform
p	2.1 – 2.4	uniform
a	0.1 – 7	uniform
Γ_0^c	$10^1 - 10^3$	log-uniform
b	0 – 6	uniform

Tab. 6.3: Free parameters of the Markov Chain Monte Carlo (MCMC) exploration, with their prior bounds and shape.

We perform a Bayesian analysis on the GW 170817 afterglow data using the MCMC algorithm of the Python suite `emcee` (Foreman-Mackey et al., 2013, 2019). We run three separate fits where the assumptions for the radiative processes in the shocked region differ:

1. "no SSC": radiative emission is only produced by synchrotron radiation, as described in Sari et al. (1998) and Sec. 5.4.4;
2. "SSC (Thomson)": SSC is taken into account assuming that all scatterings occur in Thomson regime, as described in Sari & Esin (2001) and Sec. 5.4.5;
3. "SSC (with KN)": SSC is taken into account including the Klein-Nishina (KN) regime, as described in Sec. 5.4.6.

We use (log-)uniform priors over large intervals in order to remain as agnostic as possible. The priors used for these three fits are identical and presented in Tab. 6.3. Additional constraints on the viewing angle can be obtained by combining the GW signal and the accurate distance and localisation of the host galaxy (Finstad et al., 2018), or by combining the afterglow photometry and VLBI imagery (Govreen-Segal & Nakar, 2023), and the density of the external medium can be constrained from direct observation of the host galaxy (Hallinan et al., 2017; Hajela et al., 2019). We do not include them to focus on constraints obtained from the afterglow modelling only. We also restrict ourselves to the structure presented in Eqs. 5.6 and 5.7, as the observations cannot help distinguish between the different lateral structure prescriptions, as discussed in Sec. 5.1.

For each of the three fits, we initialize 50 independent chains and run 10000 iterations per chain. After studying the convergence speed, we remove the first 2000 iterations for each chain and show the posterior distributions for the remaining 400000 samples of parameters.

The likelihood that we use for our study is based on a modified χ^2 calculation to account for the upper limits:

$$\ln \mathcal{L} = -\frac{1}{2} \times \left[\sum_i \frac{(m_i - d_i)^2}{\sigma_i^2} + \sum_j \frac{(\max\{u_j; m_j\} - u_j)^2}{\sigma_j^2} \right], \quad (6.1)$$

where the first sum concerns observational data (subscripts i) while the second sum concerns upper limits (subscripts j). The quantities m_i and m_j are the model flux densities at each observing time and frequency of the observational data set; d_i is the flux density value of a detection; σ_i its associated uncertainty; u_j is a flux upper limit presented in Tab. 6.2; and σ_j is an equivalent uncertainty that we arbitrarily define as $\sigma_j = 0.2u_j$, which roughly corresponds to the typical uncertainties for the detections. Adding this element accommodates for some models whose predictions are slightly above the reported upper limit. Note that the quantity $\max\{u_j; m_j\}$ in the second term implies that it behaves as a penalty added only for predicted fluxes m_j above the observed upper limits. Another option would be to force the likelihood to diverge as soon as one of the modelled fluxes is above the corresponding upper limit.

Posterior Distributions

Parameter	Model		
	no SSC	SSC (Thomson)	SSC (with KN)
$\log E_{0,\text{iso}}^c$ [erg]	53.70 ^{+1.21} _{-1.15}	54.11 ^{+1.14} _{-1.30}	53.70 ^{+1.12} _{-1.32}
θ_c [deg]	1.77 ^{+1.12} _{-0.89}	1.85 ^{+1.28} _{-0.82}	2.07 ^{+0.83} _{-0.82}
θ_v [deg]	21.81 ^{+7.69} _{-7.02}	17.16 ^{+2.50} _{-2.35}	22.67 ^{+5.94} _{-5.58}
$\log n_{\text{ext}}$ [cm ⁻³]	-1.09 ^{+1.09} _{-1.28}	-1.61 ^{+1.08} _{-1.23}	-1.03 ^{+1.03} _{-1.14}
$\log \epsilon_B$	-4.09 ^{+1.36} _{-1.01}	-4.43 ^{+1.39} _{-1.54}	-4.08 ^{+1.19} _{-0.97}
$\log \epsilon_e$	-2.73 ^{+0.99} _{-1.27}	-2.97 ^{+1.13} _{-1.03}	-2.81 ^{+1.15} _{-1.13}
$\log \zeta$	-0.68 ^{+0.68} _{-1.05}	-0.96 ^{+0.96} _{-0.96}	-0.81 ^{+0.81} _{-1.07}
p	2.14 ^{+0.02} _{-0.02}	2.14 ^{+0.01} _{-0.01}	2.14 ^{+0.01} _{-0.02}
a	3.14 ^{+0.30} _{-0.29}	3.34 ^{+0.66} _{-0.50}	3.19 ^{+0.30} _{-0.27}
$\log \Gamma_0^c$	2.68 ^{+0.32} _{-0.53}	2.62 ^{+0.38} _{-0.49}	2.64 ^{+0.36} _{-0.51}
b	2.13 ^{+0.84} _{-0.78}	2.20 ^{+1.07} _{-0.97}	2.24 ^{+0.79} _{-0.80}

Tab. 6.4: Median posterior values for the free parameters of the three fits of the afterglow of GW 170817 presented in Sec. 6.2. Uncertainties reported are the 90 % credible intervals of each parameter’s posterior distribution.

I present the marginalized posterior distribution of the free parameters for the three fits in Fig. 6.3, complemented by Fig. 6.4, which shows the corresponding joint and marginalized posterior

distributions at 3σ credibility ("corner plot"). I also show in Fig. 6.3 the distribution of some derived quantities, the true initial kinetic energy of the ejecta E_0 as deduced from Eq. 5.10, the ratio of the viewing angle over the opening angle of the core jet θ_v/θ_c and the four conditions for single-peaked light curves described by Beniamini et al. (2020b) and in Sec. 6.2.1. The three fits lead to similar distributions across the parameter space, with a few exceptions discussed in Sec. 6.2.3. The median parameter values as well as their 90% credible intervals are reported in Tab. 6.4. I finally show in Tab. 6.5 the median values of the derived quantities shown in Fig. 6.3.

Derived quantity	Model		
	no SSC	SSC (Thomson)	SSC (with KN)
$\log E_0$ [erg]	$51.95^{+1.05}_{-1.13}$	$52.41^{+1.04}_{-1.22}$	$52.07^{+1.01}_{-1.19}$
θ_v/θ_c	$11.95^{+5.29}_{-4.54}$	$9.84^{+2.80}_{-2.59}$	$11.19^{+3.58}_{-3.45}$
$\log(E_{0,\text{iso}}^c/n_{\text{ext}})$ [erg · cm ³]	$54.90^{+1.08}_{-1.18}$	$55.77^{+0.42}_{-0.43}$	$54.79^{+0.86}_{-0.85}$
$\log \theta_c \Gamma_0^c$	$1.15^{+0.48}_{-0.58}$	$1.12^{+0.43}_{-0.54}$	$1.17^{+0.44}_{-0.61}$
$8b/a$	$5.40^{+1.81}_{-2.05}$	$5.36^{+1.95}_{-1.94}$	$5.54^{+1.91}_{-1.96}$
$-b \log \theta_c / \log \Gamma_0^c$	$1.21^{+0.23}_{-0.25}$	$1.29^{+0.27}_{-0.28}$	$1.22^{+0.25}_{-0.22}$
$(b-1) \log(\theta_v/\theta_c) / \log(\Gamma_0^c \theta_c)$	$1.09^{+0.38}_{-0.38}$	$1.10^{+0.39}_{-0.39}$	$1.10^{+0.40}_{-0.34}$

Tab. 6.5: Median posterior values for several derived quantities for the three fits of the afterglow of GW 170817 presented in Sec. 6.2. Uncertainties reported are the 90 % credible intervals of each quantity's posterior distribution. The four last rows correspond to the quantities appearing in the conditions for single-peak light curves (Sec. 6.2.1).

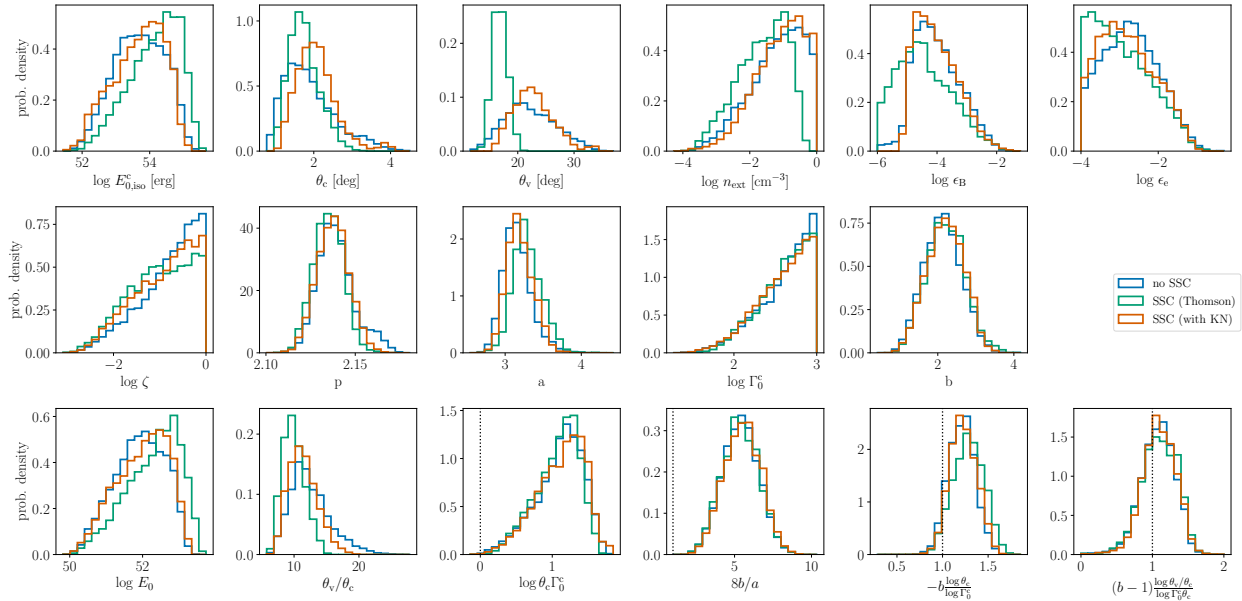


Fig. 6.3: Comparison of the marginalized posterior distributions for the three fits of the afterglow of GW 170817 presented in Sec. 6.2, which differ only by the treatment of the radiative processes: "no SSC" in blue; "SSC (Thomson)" in green; "SSC (with KN)" in orange. The first two rows show the inferred direct distributions of model's free parameters. The last row shows the distributions of several quantities derived from these parameters: E_0 (true energy of the jet, see Eq. 5.10), ratio θ_v/θ_c , and four quantities used in the conditions for single-peaked light curves from Beniamini et al. (2020b) and described in Sec. 6.2.1, $\log \theta_c \Gamma_0^c$, $8b/a$; $-b \frac{\log \theta_c}{\log \Gamma_0^c}$ and $(b-1) \frac{\log \theta_v/\theta_c}{\log \Gamma_0^c \theta_c}$.

The detailed joint posterior distributions for the "SSC (with KN)" model where emission is produced by synchrotron radiation and SSC diffusions in both Thomson and KN regimes are shown in Fig. 6.5. In this figure, which is representative of the results obtained with the three fits, we observe typical correlations between some of the afterglow parameters, like θ_c and θ_v , $E_{0,\text{iso}}^c$ and n_{ext} , or ϵ_e and ϵ_B . Some other parameters are anti-correlated, like $E_{0,\text{iso}}^c$ and ϵ_B , or n_{ext} and ϵ_B . Such degeneracies in the model parameters are expected when only the synchrotron component is observed (see *e.g.* Aksulu et al., 2022). In the case of GW 170817, the afterglow light curves can in first approximation be described by five quantities – peak time, peak flux, temporal slopes of the rising and decreasing phase, and spectral slope – which does not allow to constrain all the free parameters listed in Tab. 6.3.

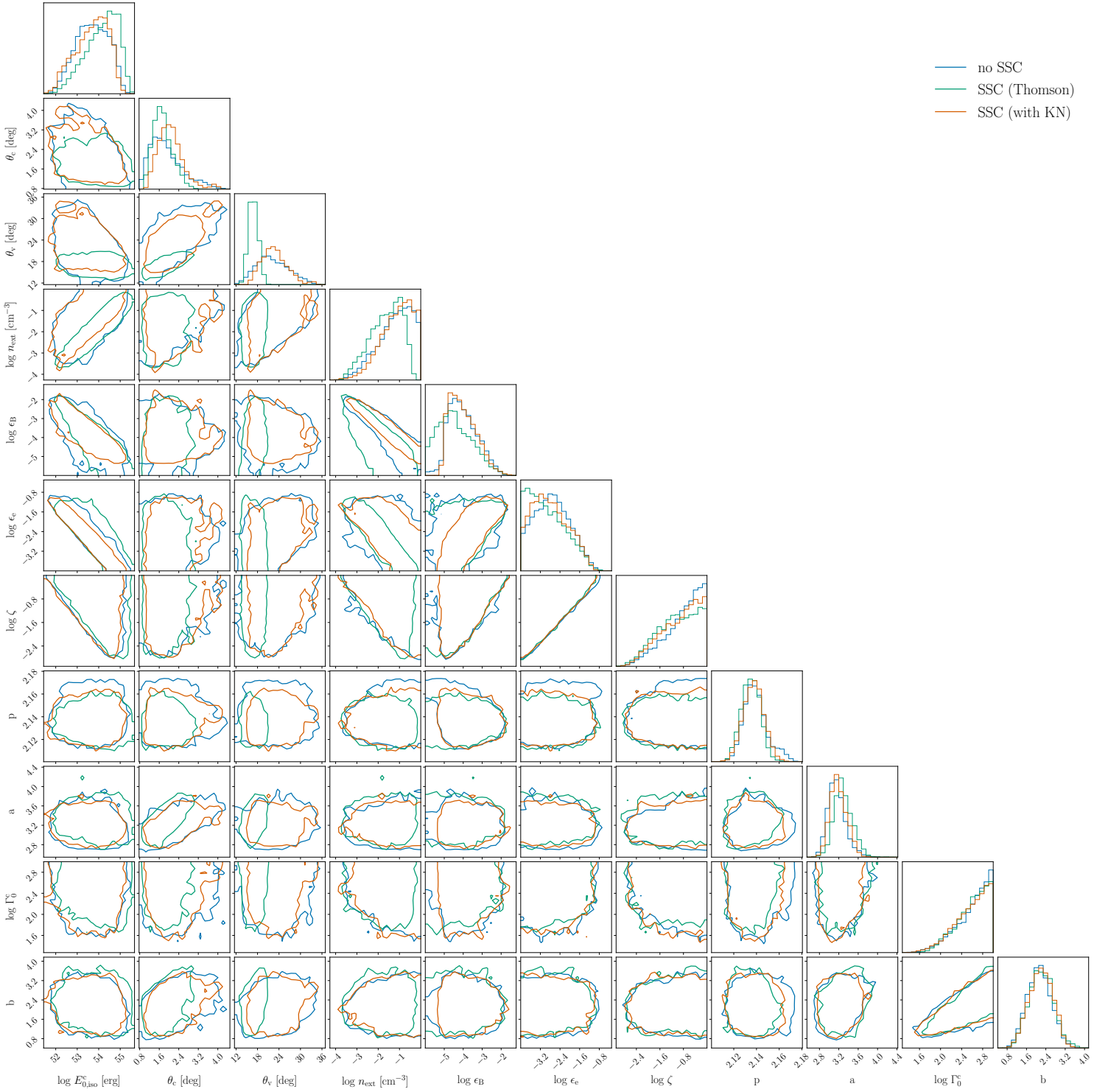


Fig. 6.4: Posterior joint and marginalized distributions of the model's free parameters, $E_{0,\text{iso}}^c$, θ_c , θ_v , n_{ext} , ϵ_B , ϵ_e , ζ , p , a , Γ_0^c , b for the three fits of the afterglow of GW 170817 presented in section 6.2, which differ only by the treatment of the radiative processes: in blue, no SSC diffusions are taken into account ("no SSC"); in green, SSC diffusions are assumed to be only in the Thomson regime ("SSC (Thomson)"); in orange, the SSC diffusion is depleted at high energy in the KN regime ("SSC (with KN)"). The priors are all uniform or log-uniform and are shown in Tab. 6.3. Fitted data includes all points until $t_{\text{max}} = 400$ days, as well as 5 early-time upper limits (see Sec. 6.1). The colored contours correspond to the 3σ confidence intervals for each model and each parameter.

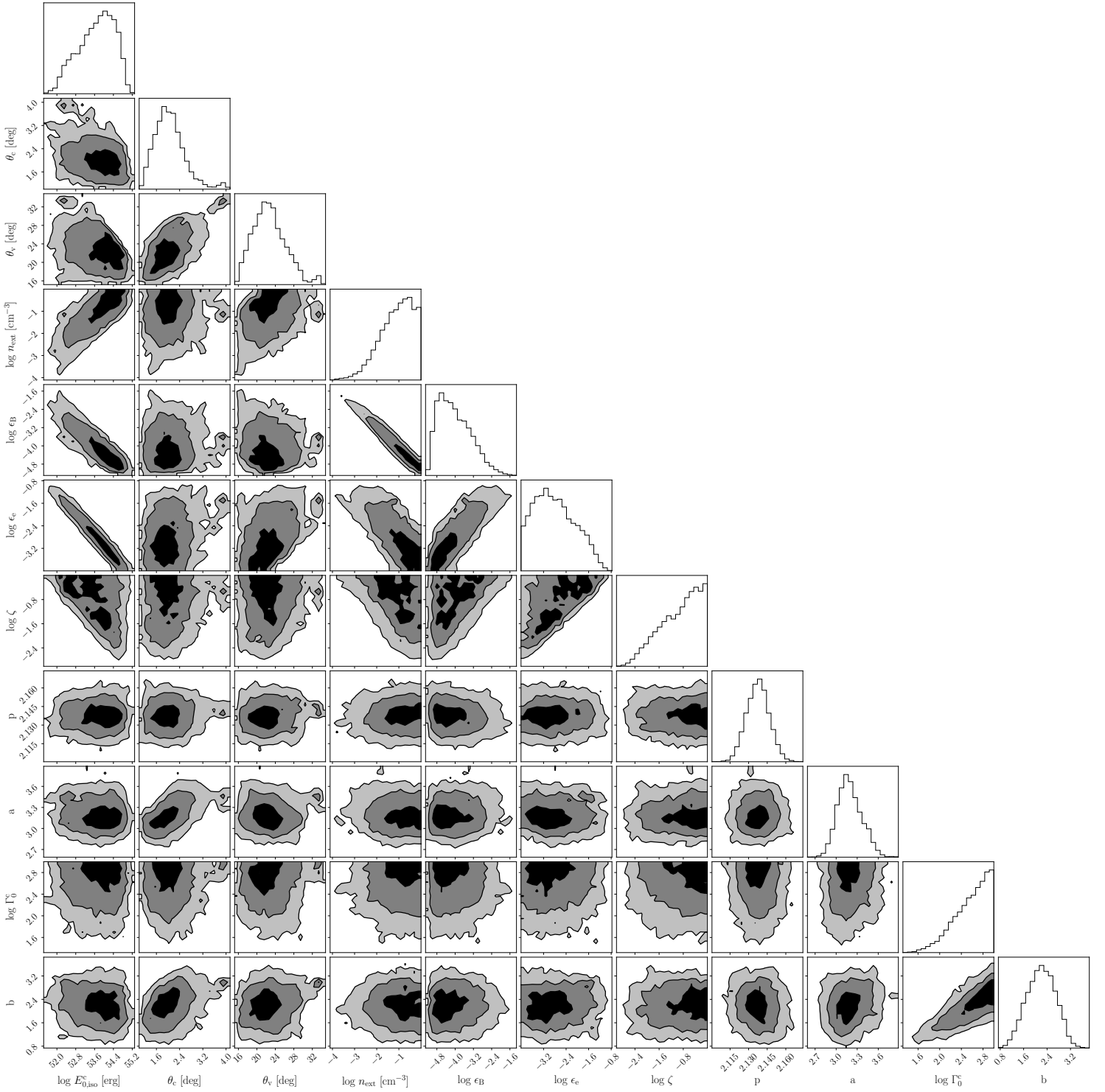


Fig. 6.5: Posterior joint and marginalized distributions of the model's free parameters, $E_{0,iso}^c$, θ_c , θ_v , n_{ext} , ϵ_B , ϵ_e , ζ , p , a , Γ_0^c , b , for the "SSC (with KN)" fit of the afterglow of GW 170817 presented in Sec. 5.4.6 which includes SSC diffusions in both Thomson and KN regimes. The priors are all uniform or log-uniform and are shown in Tab. 6.3. Fitted data includes all points until $t_{max} = 400$ days, as well as 5 early-time upper limits (see Sec. 6.1). The colored contours correspond to the 1σ , 2σ and 3σ confidence intervals for each parameter.

Post-processing: Light Curves and Spectra

Our numerical algorithm is optimised to compute the flux only at the time and frequencies required to fit the observational data. To draw light curves and spectra, a post-processing step is therefore required. In this post-processing step, we re-sample 20000 light curves at several observing frequencies (3 GHz, 1 keV and 1 TeV) and spectra at several observing times (20 days, 110 days, 400 days), where the set of parameters is directly drawn from the posterior sample, for each of the three fits. At each observing time (for the light curves) or at each frequency (for the spectra), we then determine the 68% and 97.5% credible intervals for the distribution of predicted flux densities, that we use to draw confidence contours around the median value of the light curves and spectra. Because the posterior samples are similar between the three models, I show only the results for the most realistic case ("SSC (with KN)" model) in Figs. 6.6 (light curves) and 6.7 (spectra). However, as the treatment of SSC is different in the three fits, even similar posterior distributions of the parameters lead to different VHE emission.

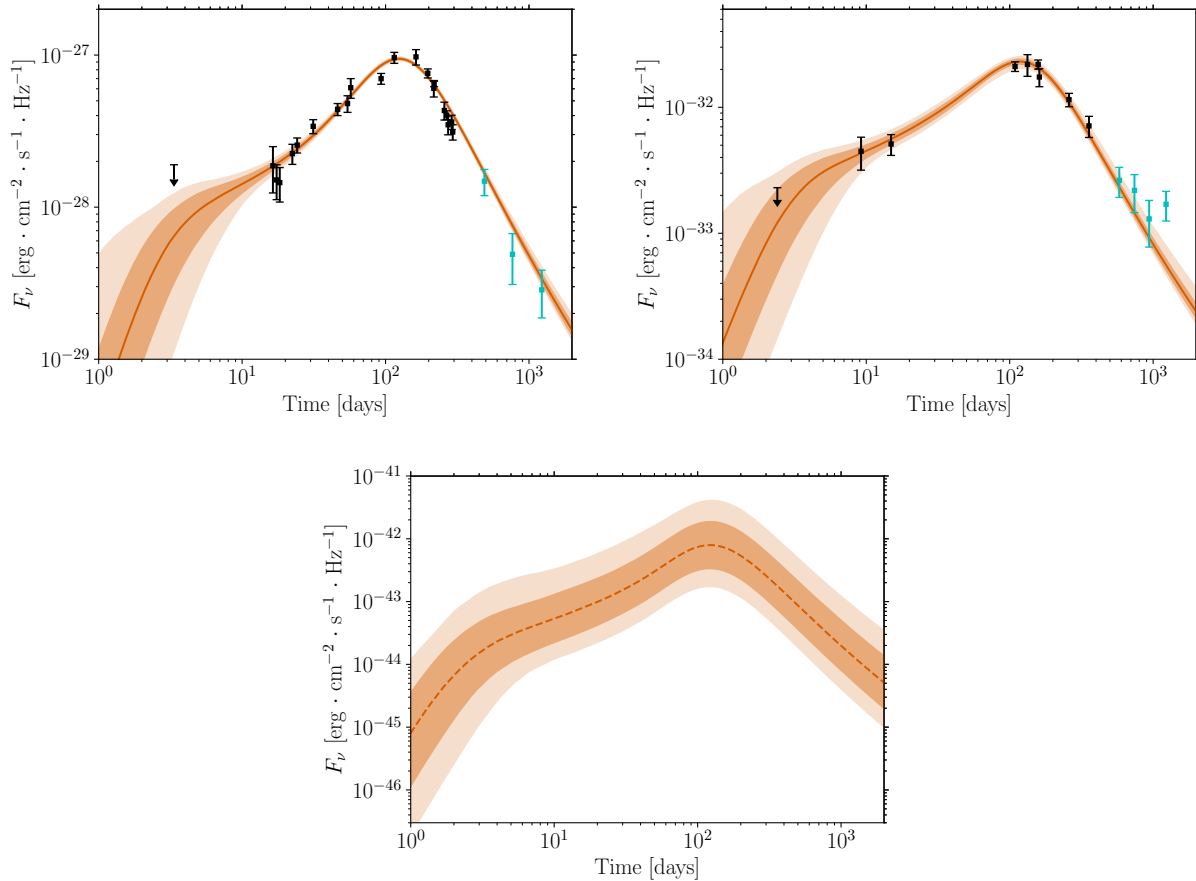


Fig. 6.6: Posterior distributions of the light curves for the "SSC (with KN)" fit of the afterglow of GW 170817. The observing bands are radio at $\nu_{\text{obs}} = 3$ GHz (top left); X-rays at $h\nu = 1$ keV (top right); and VHE at $h\nu = 1$ TeV (bottom). Solid lines represent the median value at each observing time, dark contours the 68% confidence interval and light contours the 97.5% confidence interval. Late-time observations not used in the fit are shown in blue. The H.E.S.S. upper limit (Sec. 6.1.2) is not shown on the 1 TeV light curve as it is ~ 2 orders of magnitude above the peak.

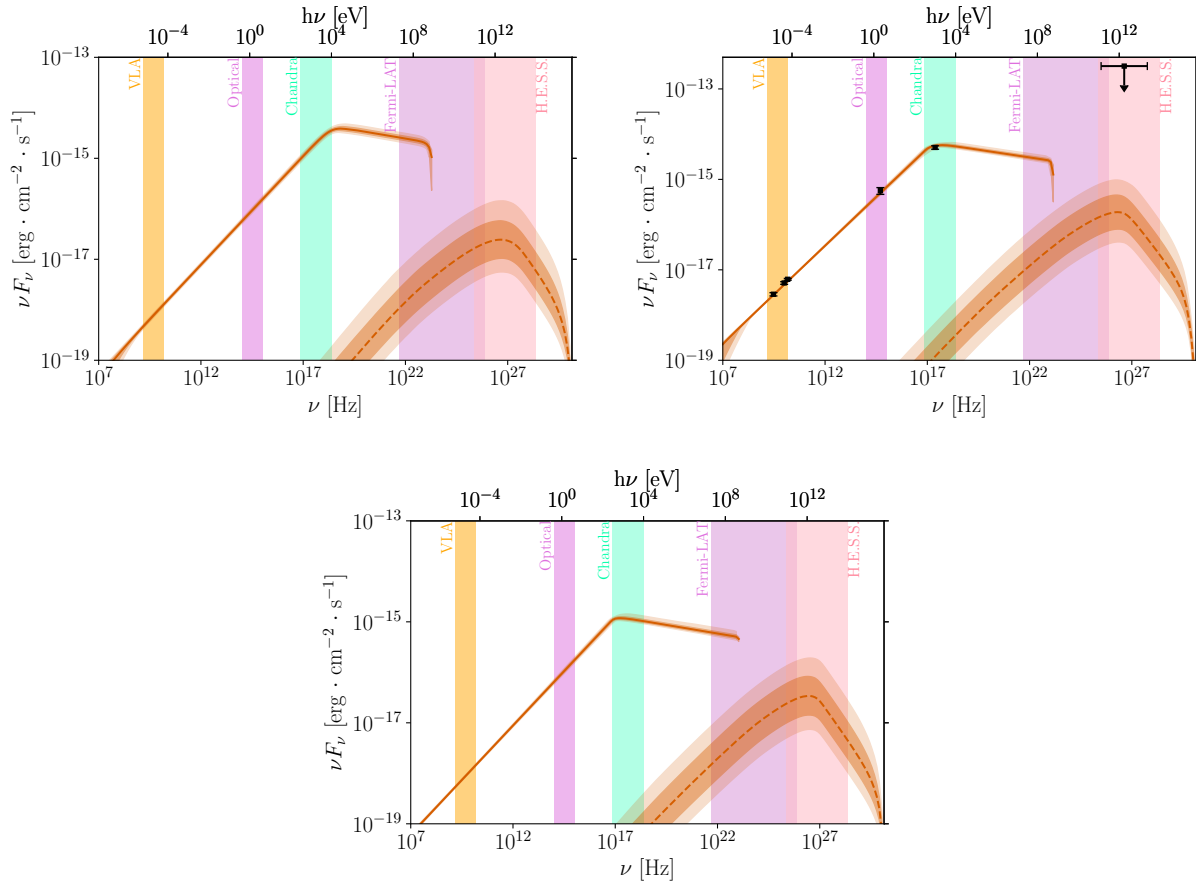


Fig. 6.7: Posterior distributions of the afterglow spectrum for the "SSC (with KN)" fit of the afterglow of GW 170817. The observing times are $t = 20$ days (top left); $t = 110$ days (top right); and $t = 400$ days (bottom). Data points in the central panel show the multi-wavelength observations around the afterglow peak at $t_{\text{obs}} = 110 \pm 4$ days. The upper limit from H.E.S.S. is also indicated (Abdalla et al., 2020). The low-energy component (solid line) is produced by synchrotron radiation, while the high-energy emission (dashed line) is powered by SSC diffusions. Thick lines represent the median value at each observing frequency, dark contours the 68% confidence interval and light contours the 97.5% confidence interval. Some instrument observing spectral ranges are shown in colors.

6.2.3 Discussion: Inferred Parameters

As seen in Fig. 6.6, the afterglow of GW 170817 is very well fitted by the model. The model predicts accurately the flux at all times, with a very small dispersion. The dispersion of the predicted flux is of course larger at very early or very late times where we do not include any data point in the fit. The same quality of the model prediction is observed in the spectrum on Fig. 6.7. The frequency $\nu_{\text{m,obs}}$ is below the data points at the lowest frequency, with some dispersion in absence of observational constraints. The critical frequency $\nu_{\text{c,obs}}$ is found to be in X-rays, at the frequency of the highest frequency data points.

The inferred values of most model parameters (Fig. 6.3 and Tab. 6.4) are very similar to the results obtained in previous studies modelling the same afterglow with the synchrotron radiation from a decelerating structured jet (Troja et al., 2019; Lamb et al., 2019; Ghirlanda et al., 2019; Ryan et al., 2020), with some exceptions, due to different priors. A first difference concerns the viewing and core jet opening angles θ_v and θ_c . Even if the values inferred by the "SSC (with KN)" fit are comparable with values found in previous studies, the corresponding ratio $\theta_v/\theta_c \sim 11$ is on the higher

end of the other predictions. [Nakar & Piran \(2021\)](#) give a compilation of these predictions and show that afterglow light curves can only constrain this ratio and not the two parameters independently, which is confirmed by the strong correlation observed in [Fig. 6.5](#). This difference is probably due to the flat and broad priors we use for these two parameters, whereas most previous studies use much stricter priors based on an external constraint, either on the viewing angle derived from GW data using the value of the Hubble constant from Planck (as in [Troja et al., 2019](#); [Ryan et al., 2020](#)) or a constraint on the viewing angle and the core jet using Very Long Baseline Interferometry (VLBI) imagery (as in [Ghirlanda et al., 2019](#); [Lamb et al., 2019](#)). The marginalized distributions of θ_v and θ_c show that a restricted region of the parameter space has been explored by the MCMC chains for these parameters, as is also visible on [Fig. 6.4](#).

When comparing with the results of [Ryan et al. \(2020\)](#), where the assumptions are the closest to those of our "no SSC" fit and where the light curves are computed using `afterglowpy` with which we compared our model in [Sec. 5.6](#), we also find that our predicted values for $E_{0,\text{iso}}^c$ and n_{ext} are about one order of magnitude higher. From [Fig. 6.5](#), it appears that it is also an effect of our different priors for the angles. However we observe the expected strong correlation between these two parameters and the inferred ratio $E_{0,\text{iso}}^c/n_{\text{ext}} \sim 10^{55} \text{ erg} \cdot \text{cm}^{-3}$ is close to the value obtained by [Ryan et al. \(2020\)](#). Using similar priors for the angles, or including a constraint on the external density from the observation of the host galaxy ([Hallinan et al., 2017](#); [Hajela et al., 2019](#)) would then reduce the inferred values for these two parameters. I discuss below the fact that detections in the VHE range would help to break this degeneracy and allow for a more precise determination of the energy and external density independently of such external constraints.

The inferred values for the microphysics parameters ϵ_B and p are very close to those obtained in previous studies. The value of ϵ_e is slightly lower, but we also find that the median value for the fraction of accelerated electrons is ~ 0.15 , whereas this parameter is not included in past studies. Both parameters are strongly correlated, as seen in [Fig. 6.5](#). Overall, the values of these microphysical parameters, including ζ , are in a good agreement with the current understanding of the plasma physics at work in relativistic collisionless shocks (see e.g. [Sironi et al., 2015](#)) and comparable to values obtained for cosmological short GRBs by [Fong et al. \(2015\)](#). The inferred value $\zeta < 1$ leads to the question of a possible contribution to the radiation of the remaining thermal electrons (see e.g. [Warren et al., 2022](#)). Assuming $\zeta = 1$ as in previous studies is relevant in the case of GW 170817 as the observed emission is dominated by the synchrotron radiation, and the cooling break $\nu_{c,\text{obs}}$ is not detected. However these microphysics parameters impact the synchrotron and SSC components in different manners, as discussed below, and must therefore be considered to predict the VHE emission and for any afterglow observation where the passage of the cooling break ν_c is detected.

As shown in the second row of [Fig. 6.3](#) and in [Tab. 6.5](#), the inferred values of the parameters describing the initial lateral structure of the ejecta are in good agreement with the conditions established in [Beniamini et al. \(2020b\)](#) and listed in [Sec. 6.2.1](#) to get a single-peak light curve: note that in practice, double-peak light curves are not excluded *a priori* in our MCMC, but are disfavoured thanks to the inclusion of early upper limits ([Tab. 6.2](#)). Finally, we note that the initial distribution of the Lorentz factor (Γ_0^c and b) is not well constrained, which was expected as most of the observed emission is produced in the self-similar stage of the deceleration. A correlation is observed between Γ_0^c and b . This can be explained by the fact that the lateral structure is required to reproduce the early-time slow rise of the light curve ([Nakar & Piran, 2018](#)). Specifically, some material needs to have lower initial Lorentz factors to overcome effects of Doppler boosting out of the line of sight. With a higher core Γ_0^c , a steeper decrease in $\Gamma_0(\theta)$ is required for material at a given latitude θ to have a sufficiently low initial Lorentz factor that the observed slow rise can be reproduced, leading to higher values of b .

6.2.4 Discussion: the Predicted Very High Energy Emission of GW 170817

I now discuss the predicted VHE emission of the afterglow of GW 170817. The predicted light curve at 1 TeV is plotted in Fig. 6.6 and the VHE component of the spectrum at the peak of the light curve is shown in Fig. 6.7, where the upper limit obtained by H.E.S.S. (Abdalla et al., 2020) is also indicated. It appears that (i) the synchrotron emission extends at most up to the GeV range (due to the synchrotron burnoff limit discussed in Sec. 5.3) and the VHE emission is then entirely due to the SSC process; (ii) even taking into account the dispersion, the predicted flux at 1 TeV is at least two orders of magnitude below the upper limit of $3.2 \times 10^{-13} \text{ erg} \cdot \text{s}^{-1} \cdot \text{cm}^{-2}$ obtained around the peak by H.E.S.S. (Abdalla et al., 2020), which is therefore not constraining. It is also clear when comparing the top and bottom panels in Fig. 6.6 that the dispersion of the predicted VHE flux is much larger than for the synchrotron component which is well constrained by the observations from radio to X-rays. This is also shown in the distribution of the predicted peak flux and peak time in radio and at 1 TeV in Fig. 6.8. Note that the VHE light curve peaks a few days before the light curves from radio to X-rays, due to a different evolution of the synchrotron and SSC components. This result is due to the fact that the dependency of the SSC component on the model parameters is complex and very different from the dependencies of the synchrotron component identified by Sari et al. (1998). This also highlights the interest of detecting the VHE emission for the inference of model parameters, as some of the degeneracies visible in Fig. 6.5 would be broken.

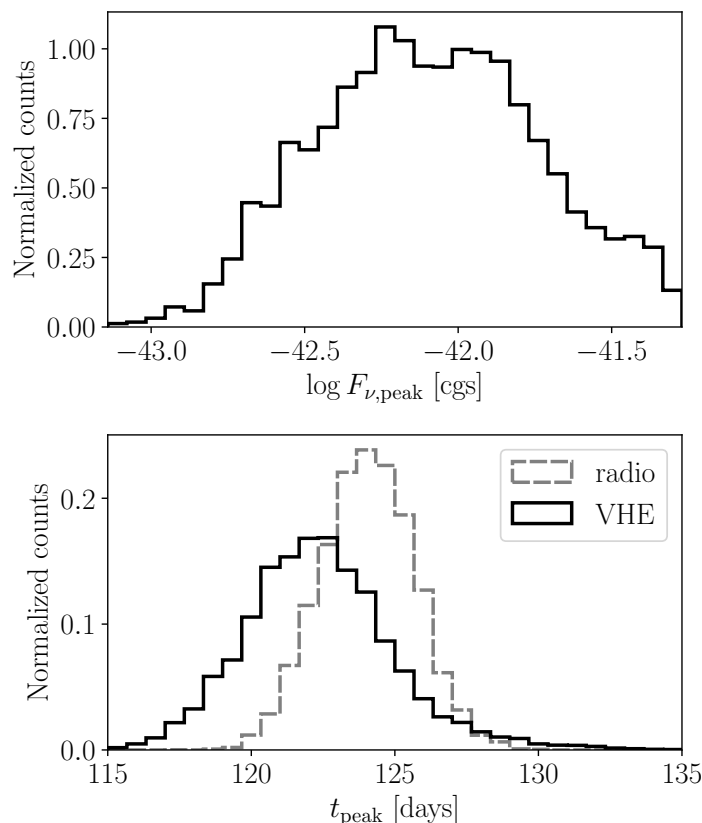


Fig. 6.8: Posterior distributions of the VHE peak flux density (top) and the radio (solid black line) and VHE (dashed grey line) peak times (bottom) for the "SSC (with KN)" fit of the afterglow of GW 170817.

In the afterglow of GW 170817, the synchrotron spectrum is in slow cooling, with a spectral peak determined by the critical Lorentz factor γ_c . If Inverse Compton (IC) scatterings occurred in Thomson regime, the peak of the SSC component would be due to the diffusion of photons at ν_c by

the electrons at γ_c (Sari & Esin, 2001), and this peak should be intense as $\epsilon_e \gg \epsilon_B$ (see Eq. 5.111). However, the predicted VHE emission is actually very weak because of a strong KN attenuation. To illustrate this effect, we select in Tab. 6.6 two reference sets of parameters, taken from the posterior sample. They are respectively in the 68% and 97.5% confidence intervals for the "SSC (with KN)" fit and fit perfectly well the observed light curves, as can be seen in Fig. 6.9. The first set of parameters ("Moderate") corresponds to a predicted VHE flux which is close to the mean, whereas the second set of parameters ("Optimistic") corresponds to a predicted VHE flux on the highest end of the confidence interval: see the two predicted light curves at 1 TeV and peak spectra in Fig. 6.9. In both cases, we selected sets of parameters having a low density, and therefore a low energy (see discussion in Sec. 6.2.3).

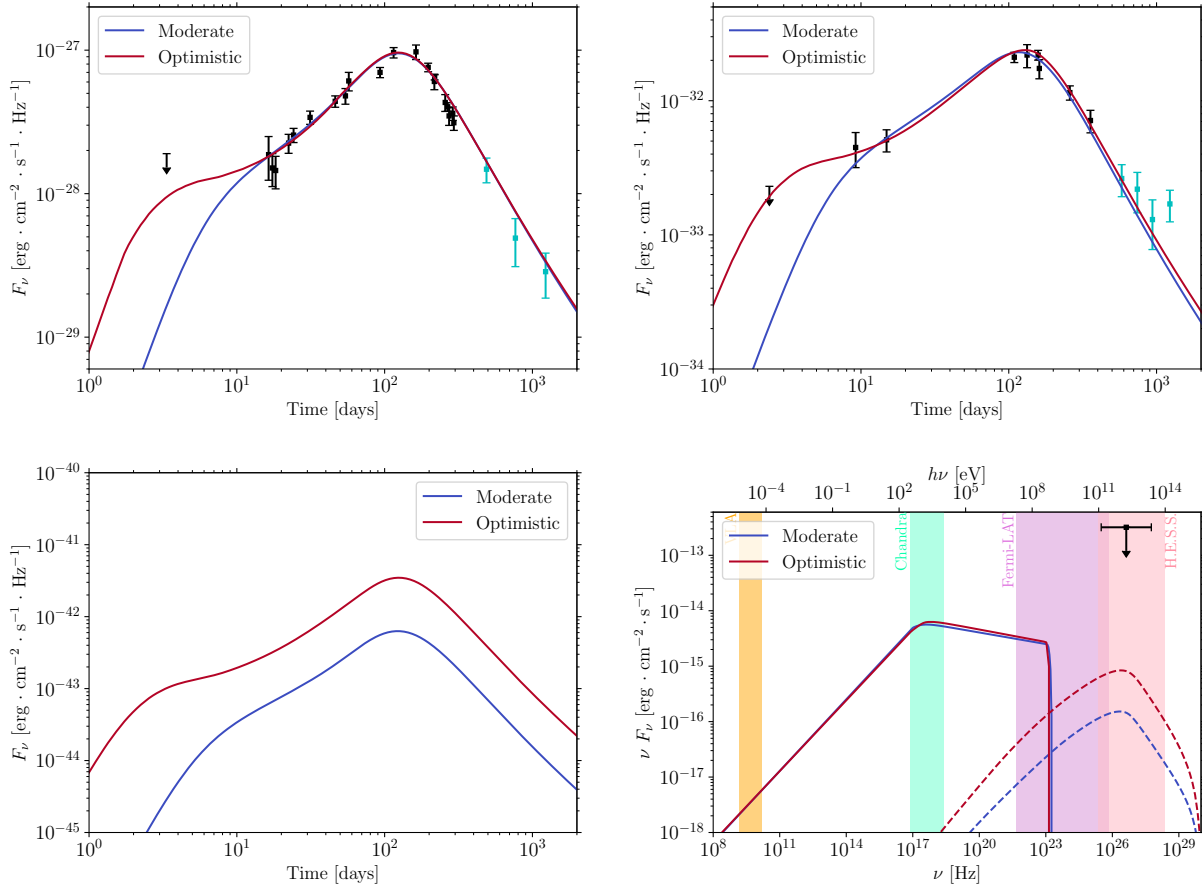


Fig. 6.9: From top to bottom, left to right: radio (3 GHz), X-ray (1 keV) and VHE (1 TeV) light curves; and afterglow spectrum around the peak $t_{\text{obs}} = 110$ days, for the "Moderate" (in blue) and "Optimistic" (in red) references cases (see Tab. 6.6). The upper limit from H.E.S.S. is indicated for comparison (Abdalla et al., 2020). The peak times are $t_{\text{peak}} = 123$ and 125 days, respectively. While the synchrotron component is constrained by observations and similar in both models, the VHE peak differs by a factor ~ 7 .

Fig. 6.10 shows for these two reference cases the evolution of $Y(\gamma_c)$ and $\gamma_c/\hat{\gamma}_c$ for the core jet, computing the SSC emission either by assuming that all scatterings are in Thomson regime like in the "SSC (Thomson)" fit, or by including the KN attenuation like in the "SSC (with KN)" fit. The figure shows that, in the full calculation, $\gamma_c/\hat{\gamma}_c \gg 1$ during the whole evolution, so that the scatterings of photons at ν_c by electrons at γ_c are strongly reduced by the KN regime. The Compton parameter $Y(\gamma_c)$ then remains very low. This confirms the origin of the weak VHE emission in the afterglow of GW 170817. In this regime of weak SSC emission, the synchrotron component is unaffected by the

Parameter	"Moderate"	"Optimistic"
$E_{0,\text{iso}}^c$ (erg)	4.12×10^{52}	5.07×10^{52}
θ_c (deg)	1.75	1.31
θ_v (deg)	21.25	24.40
n_{ext} (cm^{-3})	4.25×10^{-3}	1.52×10^{-2}
ϵ_B	1.61×10^{-3}	4.79×10^{-4}
ϵ_e	1.87×10^{-2}	3.54×10^{-2}
ζ	1	3.57×10^{-1}
p	2.139	2.149
a	2.98	2.95
Γ_0^c	184	164
b	2.01	1.34

Tab. 6.6: Reference cases: both sets of parameters are in the 97.5% confidence interval of the distributions inferred by the "SSC (with KN)" fit of the afterglow of GW 170817. They differ by the predicted VHE flux, which is either close to the median ("Moderate" case) or at the higher end of the confidence interval ("Optimistic" case).

IC cooling, $\gamma_c \simeq \gamma_c^{\text{syn}}$, and this explains why the results of the "no SSC" and "SSC (with KN)" fits are so close (Tab. 6.4). On the other hand, Fig. 6.10 also shows that Y^{noKN} overestimates $Y(\gamma_c)$ in this case, leading to $Y(\gamma_c) > 1$. The critical Lorentz factor is therefore given by $\gamma_c \simeq \gamma_c^{\text{syn}}/Y(\gamma_c)$, which leads to an overestimation of γ_c^{syn} in the MCMC to maintain the cooling break above the X-ray measurements (increased $E_{0,\text{iso}}$ and lower ϵ_B). This explains the observed difference between the values of the model parameters inferred in the "SSC (Thomson)" and "SSC (with KN)" fits in Tab. 6.4. The value of $\gamma_c/\widehat{\gamma}_c \gg 1$ in this case (green curves in the top panel of Fig. 6.10) proves that the Thomson regime is not justified.

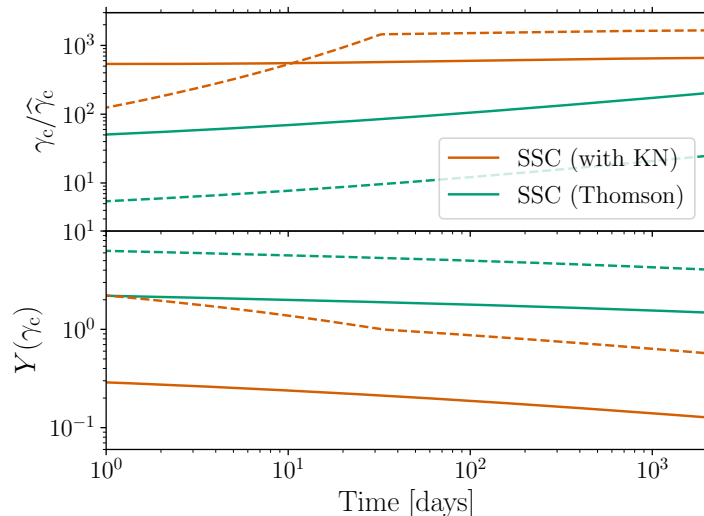


Fig. 6.10: Evolution of $\gamma_c/\widehat{\gamma}_c$ (top) and of the Compton parameter at γ_c in the core jet, $Y(\gamma_c)$ (bottom). These quantities are shown as a function of the observer time for the "Moderate" (solid lines) and "Optimistic" (dashed lines) references cases (see Tab. 6.6), in the "SSC (Thomson)" case (green lines) and in the "SSC (with KN)" case (orange lines).

As the upper limit of H.E.S.S. was obtained close to the predicted peak with an already long exposure time of 53.9 hours (see Fig. 6.2, Abdalla et al. 2020), our prediction shows that it was unfortunately impossible to detect the VHE afterglow of GW 170817 with instruments currently available. I discuss in the next section the conditions that would make a post-merger afterglow detectable at VHE in the future, especially in the context of the increased sensitivity expected with the Čerenkov Telescope Array Observatory (CTAO, Cherenkov Telescope Array Consortium et al. 2019).

6.3 Detectability of Post-Merger Afterglows at Very High Energy and Prospects for the CTAO

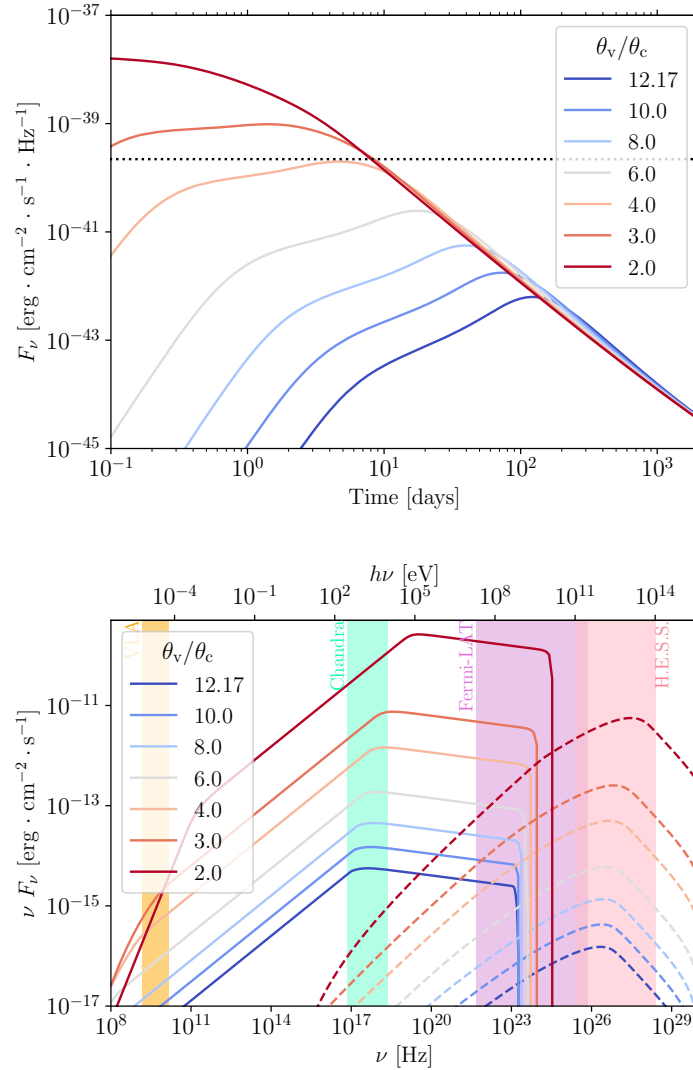


Fig. 6.11: Light curves at 1 TeV (top panel) and spectra at light curve peak (bottom panel) of the "Moderate" reference case (see Tab. 6.6) for varying viewing angles. The case fitting the afterglow of GW 170817 corresponds to $\theta_v/\theta_c = 12.17$. The dotted line on the light curve is the assumed CTAO sensitivity for a 50 hrs observation described in Sec. 6.3: 5×10^{-14} erg · s⁻¹ · cm⁻². The peak times at which spectra are calculated and the peak fluxes are reported in Tab. 6.7.

Even if the VHE afterglow of GW 170817 was not detectable, deeper observations of similar

events can be expected in the future, in particular with the CTAO. The off-axis afterglow phase is of particular interest because after a few days, full-night observations can be conducted without a significant intrinsic source flux variability over the observation time. I investigate in this section the conditions that would make such an event detectable by current instruments and the upcoming CTAO. For this study, we assume a CTAO detection sensitivity at 1 TeV about 6 times better than that of H.E.S.S., as expected from [Cherenkov Telescope Array Consortium et al. \(2019\)](#). For an exposure time of ~ 50 hours as for the H.E.S.S. deep observations of GW 170817 ([Abdalla et al., 2020](#)), this leads to a detection sensitivity at 1 TeV of $5 \times 10^{-14} \text{ erg} \cdot \text{s}^{-1} \cdot \text{cm}^{-2}$.

A geometrical effect such as a lower viewing angle naturally increases the peak of the observed flux, and has a similar effect on the synchrotron and SSC components. In Fig. 6.11, I show for the "Moderate" reference case the light curves (top) and spectra at the time of the 1 TeV emission peak (bottom), for gradually decreasing viewing angles. The 1 TeV light curves peak at earlier times when the viewing angle decreases, and the peak flux reaches higher values. I report these values in Tab. 6.7. As expected, the relative flux increase at the time of peak is similar for the synchrotron and the SSC components (Fig. 6.11, bottom) and all light curves follow a similar long-term evolution, when the entire jet emission becomes visible to the off-axis observer. For the "Moderate" (resp. "Optimistic") reference case (Tab. 6.6), we find that a ratio $\theta_v/\theta_c \lesssim 3$ (resp. $\theta_v/\theta_c \lesssim 6$) would have made the afterglow of GW 170817 detectable by H.E.S.S., provided the conditions had allowed for a very early deep observation. With the CTAO, the VHE emission could have been detected up to $\theta_v/\theta_c \simeq 4$ (resp. $\theta_v/\theta_c \simeq 8$). In such a scenario, the emission peaks at ~ 5 days (resp. 13 days). This opens up interesting perspectives, even if the expected detection rate of nearby events at small viewing angles is low (see *e.g.* [Duque et al., 2019](#); [Mochkovitch et al., 2021](#)).

"Moderate" model			"Optimistic" model		
θ_v/θ_c	t_{peak} (days)	$\nu F_{\nu, \text{peak}}$ ($\text{erg} \cdot \text{s}^{-1} \cdot \text{cm}^{-2}$)	θ_v/θ_c	t_{peak} (days)	$\nu F_{\nu, \text{peak}}$ ($\text{erg} \cdot \text{s}^{-1} \cdot \text{cm}^{-2}$)
12.17	122	1.5×10^{-16}	18.6	125	8.4×10^{-16}
10	72.5	4.3×10^{-16}	10	24.2	2.1×10^{-14}
8	39.5	1.4×10^{-15}	8	13.1	6.5×10^{-14}
6	17.4	5.9×10^{-15}	6	5.79	2.7×10^{-13}
4	4.66	4.8×10^{-14}	4	1.53	2.1×10^{-12}
3	1.43	2.4×10^{-13}	3	0.42	1.0×10^{-11}
2	0.06	4.9×10^{-12}	2	0.02	1.6×10^{-10}

Tab. 6.7: Times and flux densities of the peak of VHE emission at 1 TeV for the different viewing angles presented in Fig. 6.11, and for the "Moderate" and "Optimistic" VHE reference cases. For comparison, the H.E.S.S. upper limit is $3.2 \times 10^{-13} \text{ erg} \cdot \text{s}^{-1} \cdot \text{cm}^{-2}$ and the projected CTAO sensitivity is $5 \times 10^{-14} \text{ erg} \cdot \text{s}^{-1} \cdot \text{cm}^{-2}$.

Under some conditions, the predicted VHE emission could also be intrinsically brighter. As discussed in Sec. 6.2.4, the VHE afterglow of GW 170817 is weak because of a strong KN attenuation ($\gamma_c/\widehat{\gamma}_c \gg 1$). The regime for the diffusions of photons at ν_c by electrons at γ_c is affected by several parameters ([Nakar, 2007](#)). When the diffusions occur in the Thomson regime, the predicted scaling in the core jet is

$$\frac{\gamma_c}{\widehat{\gamma}_c} \propto \frac{1}{(1 + Y_c)^3} \frac{1}{\epsilon_B^{5/2} n_{\text{ext}}^{3/2} \epsilon_0^c}. \quad (6.2)$$

Therefore, the Thomson regime is favoured by a high magnetic field, a high density or a high kinetic energy. As ϵ_B is determined by plasma instabilities at the ultra-relativistic shock ([Sironi et al., 2015](#)), it should not vary much from an afterglow to another. On the other hand, the external density and the kinetic energy may differ between mergers. We focus here on the effect of the external density, which is slightly stronger. Fig. 6.12 shows the evolution of the afterglow emission for the "Moderate" reference case when n_{ext} increases up to $\sim 10 \text{ cm}^{-3}$, all other parameters being kept constant. A

higher external density leads to an earlier peak time at higher luminosities (their values are reported in Tab. 6.8) but affects differently the synchrotron and the SSC flux: as expected, the SSC process becomes more efficient and the relative SSC-to-synchrotron ratio increases. The transition from the weak SSC emission due to a strong KN attenuation described in Sec. 6.2.4 to a more efficient case in Thomson regime occurs in this reference case above $n_{\text{ext}} \sim 1 \text{ cm}^{-3}$. This corresponds to the radiative regime S15 in Appendix A, with spectral breaks at $\nu_m < \nu_c < \hat{\nu}_c < \nu_0$. This effect can clearly be observed on the bottom panel of Fig. 6.12, showing the observed spectrum at the peak emission. At the largest external densities ($n_{\text{ext}} > 1 \text{ cm}^{-3}$), the increase of the VHE flux stalls for two reasons. Firstly, the strong SSC emission starts to affect significantly the synchrotron spectrum, which features two peaks (visible on the bottom panel of Fig. 6.12). The cooling frequency ν_c at the peak also decreases, shifting the SSC peak to lower frequencies so that the flux at 1 TeV does not increase as significantly as the SSC peak flux.

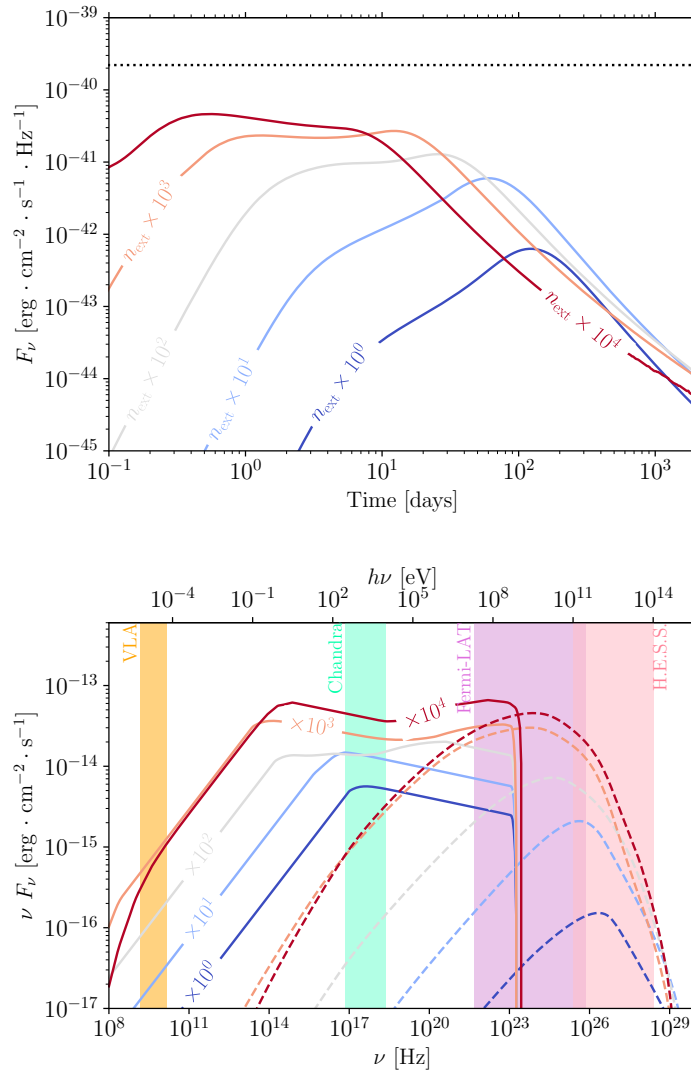


Fig. 6.12: Light curves at 1 TeV (top panel) and spectra at light curve peak (bottom panel) of the "Moderate" reference case (see Tab. 6.6) for varying viewing angles. The case fitting the afterglow of GW 170817 corresponds to $n_{\text{ext}} = 4.25 \times 10^{-3} \text{ cm}^{-3}$. The dotted line on the light curve is the assumed CTAO sensitivity for a 50 hrs observation described in Sec. 6.3: $5 \times 10^{-14} \text{ erg} \cdot \text{s}^{-1} \cdot \text{cm}^{-2}$. The peak times at which spectra are calculated and the peak fluxes are reported in Tab. 6.8.

"Moderate" model			"Optimistic" model		
n_{ext} (cm ⁻³)	t_{peak} (days)	$\nu F_{\nu, \text{peak}}$ (erg · s ⁻¹ · cm ⁻²)	n_{ext} (cm ⁻³)	t_{peak} (days)	$\nu F_{\nu, \text{peak}}$ (erg · s ⁻¹ · cm ⁻²)
4.25×10^{-3}	122	1.5×10^{-16}	1.52×10^{-2}	125	8.4×10^{-16}
4.25×10^{-2}	60.0	1.4×10^{-15}	1.52×10^{-1}	15.3	1.5×10^{-15}
4.25×10^{-1}	25.6	3.1×10^{-15}	1.52×10^0	0.76	8.1×10^{-15}
4.25×10^0	12.2	6.5×10^{-15}	1.52×10^1	0.11	3.1×10^{-14}
4.25×10^1	0.55	1.1×10^{-14}	1.52×10^2	0.08	2.9×10^{-14}

Tab. 6.8: Times and flux densities of the peak of VHE emission at 1 TeV for the different external medium densities presented in Fig. 6.12, and for the "Moderate" and "Optimistic" VHE reference cases. For comparison, the H.E.S.S. upper limit is 3.2×10^{-13} erg · s⁻¹ · cm⁻² and the projected CTAO sensitivity is 5×10^{-14} erg · s⁻¹ · cm⁻².

A second limitation, dominant at the highest densities, comes from the pair production. This phenomenon becomes all the more dominant as n_{ext} increases, as I show on the peak spectra in Fig. 6.13. In fact, we see on Fig. 6.14 that the light curve at 1 TeV is affected by pair production with different intensities through time. In this case, the peak time is even displaced when pair production is accounted for, and the flux attenuation at 1 TeV is as high as a factor 5. Pair production may be the most impacting process limiting the potential observations of short GRB afterglows at VHE.

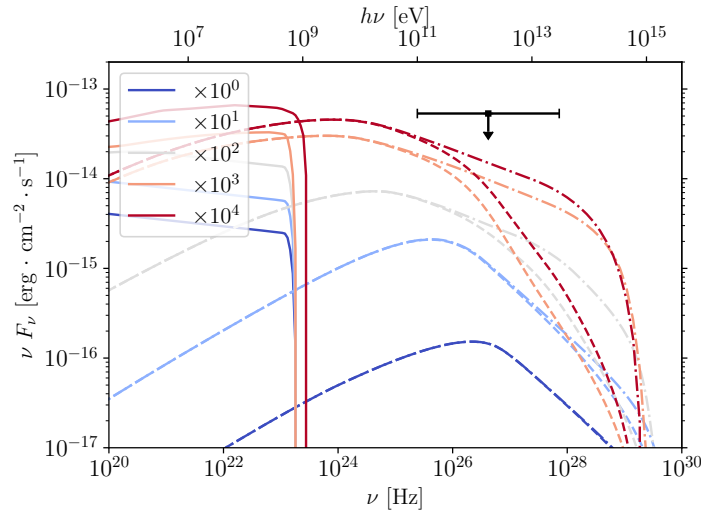


Fig. 6.13: High-energy spectra at light curve peak of the "Moderate" reference case (see Tab. 6.6) for varying external medium densities n_{ext} . The peak times at which spectra are calculated are given in Tab. 6.8 and correspond to the 1 TeV light curve peak when pair production is accounted for. Solid lines show the synchrotron component, dashed lines the SSC component with the attenuation due to pair production (Eq. 5.136), and dash-dotted lines the SSC component without accounting for pair production. The difference due to pair production becomes significant at the highest energies. The parameters used are presented in Tab. 6.6.

Even taking into account these limitations, a higher external density clearly favours a brighter VHE emission, even if both the "Moderate" and "Optimistic" reference cases remain undetectable by H.E.S.S. or the CTAO at the reference viewing angle. We conclude that post-merger VHE afterglows should become detectable in the future only under several favourable conditions, *e.g.* a higher external density and a slightly lower viewing angle. For instance, the "Moderate" (resp. "Optimistic") reference case with an external density $n_{\text{ext}} = 1$ cm⁻³ and a viewing angle $\theta_v/\theta_c = 6$ should be detectable by the CTAO up to a distance of ~ 90 Mpc (resp. ~ 400 Mpc). Note

however that two additional effects should be included in the "Optimistic" case and may reduce this maximum distance: (i) at 400 Mpc, the attenuation by the Extragalactic Background Light (EBL) is not negligible anymore at 1 TeV, (see Sec. 5.4.8 and Domínguez et al. 2011); (ii) in this case, the VHE afterglow peaks very early (~ 1 day). This would require an early follow-up which will necessarily be less deep due to a limited exposure time. It remains that detections with the CTAO above 100 Mpc are possible in the "Optimistic" case. As some parameters that are naturally degenerate in an afterglow fit including only synchrotron radiation, such as n_{ext} and ϵ_B , have different effects on the SSC emission, such VHE detections would therefore better constrain the parameter space and allow for a better understanding of the physical conditions in the post-merger relativistic ejecta.

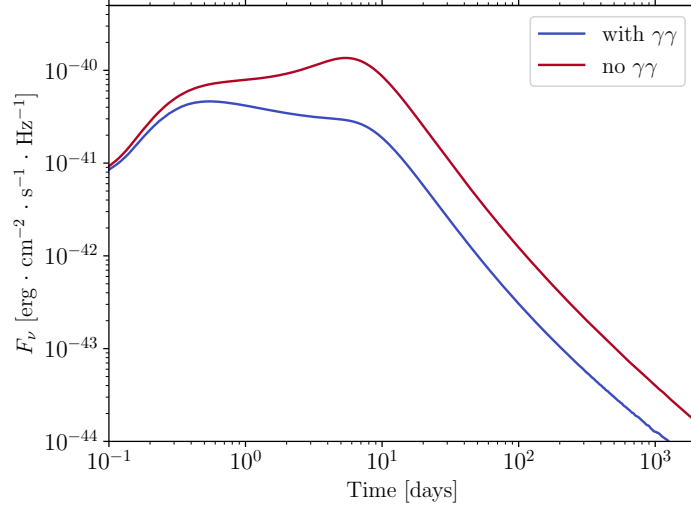


Fig. 6.14: VHE light curves at 1 TeV, for the "Moderate" reference case (see Tab. 6.6), with $n_{\text{ext}} = 4.25 \times 10^1 \text{ cm}^{-3}$ (where pair production is significant). In blue, the calculation includes pair production (Eq. 5.136), in red pair production is not accounted for. With such a strong $\gamma\gamma$ attenuation, the contribution to the emission of secondary leptons, which is not taken into account in our model, should be discussed.

6.4 A Population of Short Merger Time Binaries?

Another direct consequence of the impact of n_{ext} on SSC emission is that short GRB afterglows detected at VHE are more likely to originate from mergers occurring in a denser environment. Such VHE detections could therefore be unique probes to high-density media at the location of BNS mergers, which are sought clues for short merger time binaries. Fast mergers are indeed expected to occur close to their formation sites, where the external medium density is expected to be higher (see *e.g.* the discussion in Duque et al., 2020). Direct observations to constrain this population of short merger times BNSs are still sparse: only a dozen Galactic binary pulsars (Sec. 3.2), and two GW events associated to BNS mergers (Sec. 3.3). So far, they do not constrain the distribution of BNS merger times. However there are several indices, both observational and theoretical, that indicate that such a population may exist, as I discuss below.

From Short Gamma-Ray Bursts

It is still unclear what fraction of GRBs can be confidently associated with merging BNSs. The bimodal distribution of GRB duration is often associated with the two classes of progenitors: short GRBs arising from BNS mergers and long GRBs resulting from the collapse of massive stars (see Sec. 1.3). It has been clear however that some long GRBs are associated with counterparts related

to mergers (like a kilonova *e.g.* for GRB 211211A , [Rastinejad et al. 2022](#)), while some short GRBs could be associated with collapsars due to relativistic ejection close to the threshold between choked and successful jet (see Sec. 1.3). The GRB duration alone is not enough to determine the progenitor type (see Sec. 1.3.3). The short GRB associated with GW 170817 is the only one with a clear association to a merger event, thanks to its detection by GWs (see Chapter 2). In short, these observations suffer from several observational biases like afterglow detection, host galaxy association and projection effects, probably leading to sample incompleteness that is challenging to quantify in order to study the underlying merger population, but several studies have put forward elements of evidence for short merger time binaries among the GRBs associated with BNS mergers.

In Sec. 3.4, I introduced the high dispersion of the projected offsets of short GRBs in their host galaxies. Only a small fraction of GRBs has a high-confidence host galaxy association, but when studying the offsets in these hosts for the most complete sample up to date, [Fong et al. \(2022\)](#) found that the population of short GRBs has a component at low offsets, consistent with a tail below 1 half-light radius for $\sim 20\%$ of systems found in [Fong & Berger \(2013\)](#) and [Berger \(2014\)](#). Mergers occurring closer to the galactic centers are more likely to result from short merger time binaries which do not have sufficient time to migrate to the outskirts of their host galaxy due to their natal kicks. Projection effects are a source of uncertainty in the studies of offset distributions.

The joint study of the sample of short GRBs described in [Fong et al. \(2022\)](#) by [Nugent et al. \(2022\)](#) indicates that $\sim 84\%$ of short GRB host galaxies are star-forming. This is surprising in the scenario where BNS mergers are the progenitors of short GRBs, as we expect a broad dispersion of merger times, *i.e.* a population of mergers occurring in evolved galaxies with little star formation. Additionally, at higher redshifts, $z > 1$, the population of merging BNS is also a younger stellar population with ages $\lesssim 1$ Gyr. Both findings are indicators of the existence of a short merger time channel.

From r -process enrichment

Additionally, if BNS mergers are the dominant site for r -process nucleosynthesis as discussed in Sec. 3.4 and suggested in *e.g.* [Lattimer & Schramm \(1974\)](#); [Goriely et al. \(2011\)](#); [Just et al. \(2015\)](#); [Côté et al. \(2017\)](#), another more indirect evidence is provided by the observed large scatter of [Eu/Fe] abundances in extremely metal-poor stars shown in Fig. 3.4 (see the compilation by [Suda et al., 2008](#)). In particular, the existence of low-metallicity stars with high abundances in r -process elements requires fast mergers allowing their production when the environment is still extremely metal-poor (see *e.g.* [Vangioni et al., 2016](#); [Côté et al., 2019](#); [Dvorkin et al., 2021](#)). Some ultra-faint dwarf galaxies have also been observed with high concentrations in r -process elements, while their stellar population is old, which therefore hints towards early-time enrichment ([Beniamini et al., 2016](#)).

Another observation is that stars with higher metallicities ($[\text{Fe}/\text{H}] > -1$) typically have lower ratios [Eu/Fe]. This also supports early-time enrichment in r -process elements: the recent history of chemical enrichment is more efficient for products of Core-Collapse Supernovae (CCSNe) than for r -process nucleosynthesis from BNS mergers. This again implies the need for a population of short delay times BNS mergers.

The relative contribution to the enrichment between merging BNSs and rare hypermassive collapsars is an underlying source of uncertainty to these conclusions. All arguments related to r -process enrichment also suffer from uncertainties on the exact yields for each BNS merger, which is still poorly understood as I discussed in Sec. 2.2. Finally, the detailed modelling of the BNS merger rate through cosmic time is highly uncertain and poorly constrained yet.

From BNS population studies

Another indicator of a possible population of short merger time BNSs is the direct study of Galactic binary pulsars (see Sec. 3.2). Some of them have been found to have total merger times $\Delta t_{\text{GW}} \lesssim 100$ Myr. Inferring the exact relative contribution of short merger time binaries among the total population of BNSs is challenged by observational biases: BNS systems with shorter separations are easier to detect; and younger systems are also more likely to be seen. Still, these observations indicate the presence of short merger time BNSs.

Theoretically, BNSs can easily form in Active Galactic Nuclei disks, due to the higher density of material and the disk dynamics. In this case, the separation is expected to decrease on short timescales from dynamical friction rather than from the emission of GWs, leading to short merger times.

From the point of view of Binary Stellar Evolution (BSE), there are two main ways short separation BNSs can form: either from lucky natal kicks during the second Supernova (SN) (Kalogera, 1996), or from multiple phases of mass transfer and an efficient Common Envelope (CE) (Dominik et al., 2012). Some Neutron Star (NS) in the Milky Way have been observed with low proper velocities, indicating low natal kicks at birth, which may favour short merging times. The phase of CE has never been observed yet, but its impact has been studied using *population synthesis*: models allowing to simulate the evolution of billions of stellar binaries (see Sec. 7.3). Some results obtained with population synthesis show the presence of a population of short merger time BNSs in the case of an efficient CE phase where most of the binary’s angular momentum is evacuated. As I also discuss in Chapter 9, different evolutionary tracks can produce BNSs. Some of them feature an additional phase of mass transfer, more prone to shrink the orbital separation by carrying away angular momentum during ejection phases. Population synthesis relies on several approximations on the key evolutionary stages of stellar binaries, as discussed in Chapter 8, but they also indicate the presence of a fraction of BNS systems with short merger times.

6.5 Conclusion

In this Part II, I have first presented the motivations to build a model accounting for the VHE emission of laterally-structured jets in the context of the off-axis observations of GW 170817 and the recent VHE detections of some GRBs (Chapter 4). In Chapter 5, I presented this model in detail, and in this Chapter 6, I presented the results of our study of the VHE afterglow of GW 170817.

We used this model to fit the multi-wavelength afterglow of GW 170817, including radio to X-ray observations up to 400 days and five early-time upper limits. We inferred the model parameters using three different assumptions for the emission: pure synchrotron, synchrotron and SSC assuming that all scatterings occur in Thomson regime, and full synchrotron and SSC calculation taking into account the KN regime. We obtain excellent fits in the three cases, with similar constraints on the parameters for the pure synchrotron case and the full calculation with SSC in Thomson and KN regimes, whereas the case where all scatterings are assumed to be in the Thomson regime deviates significantly. The SSC emission in the afterglow of GW 170817 is indeed weak due to a strong KN attenuation, which confirms the need to include the self-consistent calculation of the SSC emission in the KN regime in afterglow models. The predicted VHE flux at the peak has a large dispersion but remains about two orders of magnitude below the upper limit obtained around the peak by H.E.S.S. This shows that the VHE afterglow of GW 170817 was undetectable by current instruments, but that future detections of similar events would break some degeneracies among the model parameters and allow better constraints on the physics of the relativistic ejecta.

We then studied how such post-merger VHE afterglows may become detectable in the future, in the context of the improved sensitivity of the CTAO. Beyond the evident effect of a less off-axis viewing angle, we show that the efficiency of the SSC emission becomes larger in external media

with higher densities than GW 170817. For instance, a similar ultra-relativistic jet in a medium of density $\sim 1 \text{ cm}^{-3}$ and seen slightly less off-axis than GW 170817 may become detectable by the CTAO at 100-400 Mpc.

This bias of VHE afterglow detections in favour of high-density environments offers a new probe of a possible population of fast mergers. With a short merger time, a merger should indeed occur in more central, and denser, regions of its host galaxy. Thus, future detections of such VHE afterglows would not only advance our physical understanding of relativistic jets produced after a BNS merger, but also constrain the physics of the evolution of massive binary systems. This last aspect is the core of the research presented in Part [III](#).

Part III

Population of Binary Neutron Stars

Chapter 7

Compact Object Binaries Formation Channels

Contents

7.1	Isolated Binary	122
7.2	Dynamical Formation	124
7.3	Population Synthesis Models	125

Understanding the formation of Binary Neutron Stars (BNSs) is an important challenge to interpret not only their detection rate by Gravitational Wave (GW) interferometers, but also other multi-messenger information like the properties of their host galaxies, their offset distributions or the density of the environment in which the merger ejecta propagates. This last aspect has direct consequences on the detectability of the afterglows – in particular at Very High Energy (VHE) – as I discussed in Part II. A crucial information is the delay time between stellar formation and BNS merger, which is directly linked to the orbital separation when the secondary Neutron Star (NS) forms.

In recent years, the observation of the mergers of BNSs (Abbott et al., 2017a,b,c), Neutron Star – Black Hole binaries (NSBHs) (Abbott et al., 2021a) and Binary Black Holes (BBHs) (Abbott et al., 2019a, 2021b; The LIGO Scientific Collaboration et al., 2021a,b) with GWs has confirmed that a population of merging compact objects indeed exists.

Yet, as introduced in Sec. 1.2, the merger time of a binary from the emission of GWs $t_{\text{merg}} \propto a^4$ for circular orbits (Eqs. 1.8 – 1.11). A BNS system with symmetric masses $M = 1.4M_{\odot}$ therefore needs to have an initial orbital separation $a_i \lesssim 4.8R_{\odot}$ to merge within the age of the Universe t_{Hubble} (Eq. 3.4, see also Mandel & Broekgaarden 2022). However, stellar progenitors of NSs and Black Holes (BHs) are massive stars, whose radii during late stages of stellar evolution can reach $\sim 100 - 1000 R_{\odot}$. A process must therefore take place to allow for a significant separation shrinkage during or after the compact objects formation. Following this observation, two main formation channels have been proposed and can provide such processes:

- An isolated system of massive progenitor stars co-evolves and the separation is reduced during one of the phases of binary stellar evolution. This typically requires a phase of Common Envelope (CE) that allows for the migration of the first-formed compact object in the envelope of the secondary. I discuss this **isolated binary** formation channel in Sec. 7.1.
- Compact objects form in a dense environment like a globular cluster, so that close compact object binaries form through dynamical capture or hardening from three-body encounters within the cluster. This is the **dynamical formation** channel, that I introduce in Sec. 7.2.

For a detailed review on both formation channels, the reader can refer to Mapelli (2021).

7.1 Isolated Binary

The most promising formation channel to produce BNS systems is the isolated binary channel. Galactic observations have shown that a significant fraction of stars are formed in binary systems (sometimes even triple or quadruple systems). The exact binary fraction is quite uncertain and varies depending on the work, but typically ranges between 30 – 70% (see *e.g.* Sana et al. 2012). This is expected as stellar formation theory favours the production of multiple systems, as stars form in the collapse and fragmentation of dust clouds that are massive enough to produce hundreds of stars (*e.g.* McKee & Ostriker 2007). Once formed, massive stellar binaries evolve jointly on relatively short timescales (depending on the initial mass, between ~ 10 Myr and ~ 100 Myr, see Sec. 3.1). With specific initial conditions, they can form NSs. The details of the model assumptions for the evolutionary phases of such massive binaries are given in Chapter 8, but I show here a synthetic view on the key elements of Binary Stellar Evolution (BSE) that are relevant to understand the isolated binary scenario.

The isolated binary scenario follows the joint evolution of two stars in a close orbit. If the separation is initially too wide for binarity to play a significant role in stellar evolution, the binary is called *detached* and it is expected that the final products of stellar evolution as well as the properties of the compact objects binary can be estimated by only studying single star evolution, as described in Sec. 3.1. In such cases, it is unlikely that the post-evolution binary can merge within t_{Hubble} ,

because the initial orbital separation is too high for efficient shrinkage by emission of GWs (see Eq. 1.11). Some of these BNSs with wide separations can be observed, in particular when one of the NSs is a pulsar, as I discussed in Sec. 3.2. These may be the product of the evolution of detached binaries, but are not the core of our work.

When binaries are in closer orbit, the presence of a companion affects the evolution of both stars in several ways. I present here a typical evolutionary track that is thought to produce BNS systems which can merge within t_{Hubble} : more details on this scenario, as well as other evolutionary tracks can be found in Chapter 9 (Sec. 9.3).

A binary made of two stars with initial masses ranging between ~ 8 and $\sim 20 M_{\odot}$ forms from the collapse and fragmentation of a dust cloud (McKee & Ostriker, 2007). The initial conditions when hydrogen fusion is triggered are called the Zero-Age Main Sequence (ZAMS) (see Secs. 3.1 and 8.1) conditions. Stars that are massive typically exhaust their nuclear fuel through fusion cycles in $\lesssim 100$ Myr and thus evolve rapidly on the main sequence (Sec. 3.1). The primary star – the most massive – is the first to complete hydrogen fusion into helium. When the fusion of helium in the core starts (Core Helium Burning (CHeB)), the radius of the primary increases and the star reaches the Asymptotic Giant Branch (AGB). At that stage, depending on the separation and on the metallicity of the stars (stellar winds influence the amount of mass lost in giant phases and the radius that massive stars reach during these phases), as well as on the evolutionary stage of the secondary star, a first phase of mass transfer from the primary to the secondary can occur. This episode of mass transfer is typically stable (for a definition, see Sec. 8.2.2). Some of the mass is accreted by the companion star and the rest of the hydrogen envelope is lost through stellar winds. The helium core of the primary is massive enough that the now-stripped star can ignite a new fusion cycle. Eventually, the primary forms an iron core and collapses into a NS. During the Supernova (SN), a natal kick is given to the NS due to the asymmetry in the explosion, and is likely to disrupt the binary. Natal kicks from SNe are a major source of uncertainty in BSE and it is expected that a very small fraction of binary systems survives both SN explosions (see Sec. 8.2.4). If it is the case, after the SN of the primary, the binary now contains a NS and a massive secondary companion.

The secondary in turn evolves and reaches the AGB. At that stage, a new phase of mass transfer starts, this time from the secondary onto the NS. Given the low mass ratio between the donor star and its companion $M_{\text{don}}/M_{\text{comp}}$, mass transfer is typically unstable: the NS cannot accrete material at the same rate as it falls onto it, and the outer envelope of the secondary starts to engulf the NS. This is the CE (see Sec. 8.2.2 and 8.2.3). This phase shrinks the orbital separation and produces BNS systems with separations $\lesssim 5 R_{\odot}$. Dynamical friction while the NS orbits in the envelope of the secondary during the CE leads to a significant loss of orbital angular momentum, that is transferred to the envelope, that may thus be ejected. In a fraction of cases, the NS may even merge with the stellar core during the CE phase (Thorne-Zytkow object, Thorne & Zytkow 1975). The precise understanding of CE is not yet achieved and detailed simulations are computationally expensive and incompatible with a use in the context of population synthesis. CE is therefore a major source of uncertainty in the models of BSE in the isolated binary scenario. After the envelope is ejected because of angular momentum transfer, the binary separation has now shrunk, and the secondary only retains its helium core. This core then expands again due to the different fusion cycles taking place: another phase of mass transfer can start at that stage, until the explosion of the secondary in a SN. If the binary survives this second explosion, it is now made of two NSs with a short orbital separation. Orbital decay by the emission of GWs is efficient and the binary can merge within t_{Hubble} .

Many variations of this scenario can lead to the production of BNSs, but they all feature the key evolutionary steps mentioned here (be they occurring at different epochs of stellar evolution or with different properties). In the steps described here, the major uncertainties that play a role in BSE are:

- Mass losses *via* stellar winds;
- Mass transfers between the two stars;
- The phases of Common Envelope (CE);
- Supernova (SN) kicks.

The variation of metallicity also plays a role in these different phases. As we found in the work presented in this Part III, this also affects the properties of the merging population through cosmic times (see Sec. 9.5).

It is extremely challenging to model BSE with precision, given the different timescales relevant during a star’s lifetime (see Sec. 3.1). To simulate the evolution of binary stars, one approach consists in modelling a few binaries in great detail with computationally-expensive simulations (see *e.g.* MESA, Paxton et al. 2011, 2013, 2015, 2018; Jermyn et al. 2023). Another option is to rely on (semi-)analytic approximate prescriptions for these different phases and compute the evolutionary phases of billions of stellar binaries; for comparisons with the observed population as a whole. This last option is what is done by *population synthesis* models, which are calibrated using the more detailed simulations, and that I introduce in Sec. 7.3 and in Chapter 8.

7.2 Dynamical Formation

I mentioned that stars are likely to form in binary systems. In fact, most stars even form in clusters resulting from the collapse and fragmentation of much bigger interstellar clouds. They are observed in so-called young star clusters. Much older and massive clusters, globular clusters, are made of a population of old stars. Though the details of their formation is poorly understood, studies of the stellar dynamics show that they also contain a population of compact objects (Askar et al., 2017). This population is thought to be produced much earlier in the clusters’ history, when the shorter-lived massive stars exploded in SNe. Finally, compact objects are also found in nuclear clusters – massive stellar clusters located near the center of galaxies. They are more massive than young and globular clusters and therefore have a higher escape velocity, which makes them more likely to retain the compact objects (see *e.g.* Fragione & Kocsis 2018).

Young star clusters, globular clusters and nuclear clusters have been studied as good hosts for the *dynamical channel* of compact objects binary formation. The contribution of young star clusters is expected to be sub-dominant due to their lower mass. As an example, I briefly describe the principle of the dynamical channel in globular clusters.

A population of millions of stars is initially born simultaneously and is gravitationally bound together. The most massive stars evolve faster and quickly form BHs and NSs. These compact objects receive a natal kick during the SN, and may therefore be ejected from the cluster at that stage. In fact, given the lower mass of NSs, they typically receive higher-velocity kicks and it is expected that most of them are directly ejected from the clusters upon formation. Similarly, they are more likely to be ejected from the cluster during gravitational encounters with other stars due to their lower mass. Globular clusters are therefore not good candidates for the efficient formation of BNS and NSBH systems (see *e.g.* Ye et al. 2020). This finding is another motivation for the focus given to the isolated binary scenario in the study of BNSs.

Conversely, the dynamical channel is believed to contribute significantly to the observed population of merging BBHs. Because BHs are more massive at birth, they receive lower natal kicks and are therefore retained in the gravitational potential of the cluster. Through multiple-body interactions, a progressive mass segregation occurs in the clusters, and the most massive objects progressively sink towards their center.

In such environments, there are several dynamical processes – driven by gravitational energy transfer during approaches in this dynamically active environment – that can lead to the formation of BBHs with close separations. They all are different manifestations of the same scenario: a three-

body encounter, when a massive object such as a star or another compact object comes close enough to a binary system that it modifies its orbital properties. For this to happen, the third body must come within a distance shorter than a few times the binary orbital separation. In the event of such an encounter, several processes can occur:

- If a compact object encounters a binary where the first compact object is not yet formed, it can modify the separation and eccentricity of the stellar binary, and trigger phases of mass transfers, leading to a complete modification of the evolution of the system;
- If the compact object binary has formed (typically a BBH), the multiple three-body encounters it will experience within the cluster are expected to – on average – reduce the binary separation. This process is called *hardening*.
- In some extreme cases, it is even possible that a wandering BH removes one of the components of the binary and pairs with the remaining object. This is a dynamical exchange.

Interestingly, because of the multiplicity of these interactions in globular clusters, it has even been suggested that hierarchical mergers can occur, leading to a progressive BH mass growth in and beyond the pair instability mass gap discussed in Secs. 3.3 and 8.2.5 (see *e.g.* Mapelli et al. 2022). The excess of observed mergers with a component within this mass gap could also imply that more massive BBHs are more likely to be the products of hierarchical growth in a cluster rather than a direct formation from an isolated binary. This channel can also naturally explain mergers with unequal mass ratios like GW 190412 (see Sec. 3.3), as suggested in Rodriguez et al. (2020).

In the work presented in this thesis, I specifically study BNS systems. Because it is expected that most NSs are ejected from clusters when they form, I make the assumption that BNSs are only produced by the isolated binary scenario.

7.3 Population Synthesis Models

A common way to study the population of compact objects numerically in the isolated binary scenario is to use simplified models that simulate the evolution of massive binaries in short computation times. These models are known as *population synthesis* models. In fact, it is key to be able to simulate the fate of binary systems efficiently, as it is impossible to directly infer the properties of the formed compact objects directly from the initial binary properties. First, some processes in BSE involve stochasticity, like the SN kicks (intensity, orientation) that depend on the details of the explosion. Second, the stellar tracks (see Sec. 3.1) followed by single stars, especially the most massive stars, are extremely sensitive to very small changes (*e.g.* in initial mass) which can lead to the formation of one type of remnant or another (see the stellar tracks presented in Fig. 3.1 and *e.g.* Sukhbold et al. 2016). In this context, the presence of a close companion can therefore widely disturb the stellar evolution. There is thus no other choice than to follow individually all binaries throughout their evolution.

To be computationally efficient, population synthesis models rely on pre-computed stellar tracks for *single* stars. Initially, these stellar tracks are computed using much more detailed single-star evolution models such as MESA as discussed in Sec. 3.1. At each time step, the population synthesis algorithm evaluates the properties of each star of the binary using fitting formulae to pre-computed evolutionary tracks. These are then used to deduce stellar properties to the next time step. This is done assuming that on this timescale, the impact of the companion does not affect single-star evolution. In practice, this requires a fine sampling of the time-integration of binary stellar evolution, especially at low metallicities for massive progenitors (see Sec. 8.2.5 and Banerjee et al. 2020). The properties related to binarity (*e.g.* mass exchanges, orbital parameters) are treated independently at each time step. Two important approximations are therefore used by nature in population synthesis codes: (i) the evolutionary tracks they rely on are based on single star evolution; (ii) the interpolation at each time step treats binary properties independently.

As of today, no simulations have yet incorporated more complex effects such as stellar magnetic fields and rotation in population synthesis codes. For massive stars, they can however play an important role to shape their fate, especially at late evolutionary stages in the giant phase (Limongi & Chieffi, 2018).

Population synthesis is not only useful to study the population of merging compact objects. It can also be used to statistically study the properties of X-Ray Binaries (XRBs) and the recycling of pulsars into millisecond pulsars; to look at the population of galactic BNSs; more generally to study their host galaxies; among others. In short, they can trace all the populations I discussed in Chapter 3. Several groups have therefore developed their own numerical tools with different ingredients depending on their focus of study, so that there are now multiple population synthesis codes currently used worldwide. I list them in Tab. 7.1. Many of these models (StarTrack, COSMIC, COMPAS, binary_c, ...) however derive from the same base: BSE (Hurley et al., 2002). Though they have several differences, it is worth noting that the stellar tracks on which they are based are thus the same, taken from Pols et al. (1998). Recently, some population synthesis codes have been published, that feature their own evolutionary tracks, most notably POSYDON (Fragos et al., 2023) and SEVN (Spera et al., 2019), which are based on more recent results using MESA. They also rely on interpolations between the tracks rather than on fitting formulae. Recent studies suggest that more recent prescriptions for the stellar tracks have a significant impact on the properties of the remnants (Iorio et al., 2023).

Code Name	Reference
SeBa	Toonen et al. (2012), based on Portegies Zwart & Verbunt (1996) with ingredients from Hurley et al. (2002)
BSE	Hurley et al. (2002), using single-star evolution from Hurley et al. (2000)
–	Podsiadlowski et al. (2003)
StarTrack	Belczynski et al. (2002, 2008, 2020)
–	Mapelli et al. (2013), a modified version of SeBa
The Brussels code	Vanbeveren et al. (1998); De Donder & Vanbeveren (2004)
BPASS	Mennekens & Vanbeveren (2014)
MOBSE	Eldridge et al. (2008); Eldridge & Stanway (2016); Eldridge et al. (2017)
COMPAS	Stevenson et al. (2017); Riley et al. (2022)
ComBinE	Stanway & Eldridge (2018)
SEVN	Mapelli et al. (2017); Giacobbo et al. (2018)
–	Giacobbo & Mapelli (2018, 2019, 2020)
COSMIC	Stevenson et al. (2017); Riley et al. (2022)
binary_c	Kruckow et al. (2018)
The Scenario Machine	Spera et al. (2015); Spera & Mapelli (2017); Spera et al. (2019)
POSDON	Tanikawa et al. (2021), extending BSE to high-mass and metal-poor stars
TRES	Breivik et al. (2020)
	Izzard et al. (2004, 2006, 2009)
	Lipunov et al. (1996, 2009)
	Fragos et al. (2023)
	Toonen et al. (2016)

Tab. 7.1: A list of population synthesis codes used in the literature. For a list of detailed binary evolution codes or hydrodynamical codes, see the review by De Marco & Izzard (2017).

Because they rely on many simplifying assumptions, population synthesis codes are roughly 10^7 times quicker than detailed binary evolution simulations. They are therefore perfectly designed to study the population of compact object binaries. In the next Chapter 8, I present COSMIC (Breivik et al., 2020), the population synthesis model that I used to study the evolution of BNS progenitors with redshift in the study presented in the next Chapter 9.

Chapter 8

Evolving Binary Systems: Population Synthesis with COSMIC

Contents

8.1	Initial Properties of Binary Systems	128
8.2	Binary Stellar Evolution	132
8.2.1	Stellar Winds	133
8.2.2	Roche Lobe Overflow	138
8.2.3	Common Envelope	141
8.2.4	Supernova Kicks	144
8.2.5	Miscellaneous	148
8.3	Summary of COSMIC Parameters	151

In the work presented in the next Chapter 9, we aim to study the population of Binary Neutron Stars (BNSs) using population synthesis. Among the codes presented in Tab. 7.1, we chose to use COSMIC (Breivik et al., 2020) for this study, as it includes recent developments of binary evolution models, and it is regularly updated and open-source. All the work presented in this thesis has been conducted with the version 3.4.0 of COSMIC¹. In this chapter, I provide more details on the physical assumptions for binary stellar evolution used in COSMIC and focus on the most relevant aspects to BNS formation. Some of the physics found in COSMIC but not directly relevant to this work will be overlooked, like the treatment of the compact object magnetic fields, pulsar properties, among others. Sec. 8.1 is dedicated to the initial properties of the population of binaries, which is later evolved using the analytic prescriptions described throughout Sec. 8.2. In Sec. 8.3, all the parameters and flags used in our work are compiled, including those not discussed in the core of this chapter.

8.1 Initial Properties of Binary Systems

Overview

Studying binary stellar evolution for a given stellar population using COSMIC requires to draw from an initial population of binaries, which are individually determined by their metallicity (Z), the mass of the primary (M_1), the mass ratio between the secondary and the primary ($q = M_2/M_1$ – Note that $0 < q < 1$ by definition), their orbital separation (a), their eccentricity (e), and their birth time (T_0). Seed binaries are often referred to as Zero-Age Main Sequence (ZAMS) stars.

In practice, as the main role of population synthesis codes such as COSMIC is to study binary stellar evolution and generate a population of compact object binaries, we choose to disregard the birth time parameter T_0 , and only simulate the evolution of a “virtual” population comprised of binaries with the same birth time. Only at a later stage, to simulate an astrophysical population, will we convolve the information on the binary population with a distribution of birth times (see Sec. 9.5). Similarly, we choose to create a grid of N_{met} metallicities at which the population of binaries will be initialized, and generate N_{met} populations independently where all stars have the same initial metallicity (see Sec. 9.1). The metallicity distribution of individual binaries will also be taken into account at a later stage when generating an astrophysical population. To initialize a population of binaries with COSMIC, we therefore need information on the following initial distributions:

- primary mass (M_1);
- mass ratio ($q = M_2/M_1$);
- orbital separation (a);
- eccentricity (e).

In the simplest approach, these distributions are assumed to be independent. However, a study of several surveys probing a wide range of binary types and separations by Moe & Di Stefano (2017) has shown that this assumption may not be realistic. They find statistical evidence for five distinct groups that depend on the primary mass, and whose distributions of mass ratios, separations and eccentricity follow separate distributions. COSMIC allows to initialize a population following this prescription, but for an easier analysis and given the unknowns regarding the dependency of these relations with metallicity, we choose to sample the initial binary parameters independently.

In the following, I will refer to the probability density functions from which each independent initial parameter will be sampled as the *distributions*. Formally, we could note them f , defined such that $dN/dx = f(x)$ where x is the parameter sampled, and $\int_{x_{\text{min}}}^{x_{\text{max}}} f(x)dx = 1$.

¹<https://cosmic-popsynth.github.io/>

Primary mass distribution

The stellar mass distribution has first been studied by [Salpeter \(1955\)](#) using catalogs of stellar luminosities available at the time to deduce a mass distribution function of the form

$$\xi(M) \propto M^{-2.35}, \quad (8.1)$$

where $\xi(M)$ is the probability for a given star to have a mass between M and $M+dM$, *i.e.* if we note N the total number of stars, $dN = \xi(M)dM$. ξ is normalized such that $\int_{M_{\min}}^{M_{\max}} \xi(M)dM = 1$. Note that in [Salpeter \(1955\)](#), this relation is defined as $dN = \xi^{\text{Sal.}}(M)d \log M$, leading to the exponent -1.35 instead of -2.35 .

A follow-up study by [Kroupa et al. \(1993\)](#) using new galactic observations up to 5.2 pc and results on massive stars by [Scalo \(1986\)](#) found a 3-component Initial Mass Function (IMF) of the form

$$\xi(M) \propto \begin{cases} M^{-1.3} & \text{if } 0.08 \leq M/M_{\odot} \leq 0.5 \\ M^{-2.2} & \text{if } 0.5 \leq M/M_{\odot} \leq 1 \\ M^{-2.7} & \text{if } 1 \leq M/M_{\odot} \end{cases}. \quad (8.2)$$

Subsequently, [Kroupa \(2001\)](#) proposed a revised IMF function of the form

$$\xi(M) \propto \begin{cases} M^{-0.3} & \text{if } 0.01 \leq M/M_{\odot} \leq 0.08 \\ M^{-1.3} & \text{if } 0.08 \leq M/M_{\odot} \leq 0.5 \\ M^{-2.3} & \text{if } 0.5 \leq M/M_{\odot} \end{cases}. \quad (8.3)$$

Changes in the IMF form are mostly due to a more careful representation of low-mass stars between 0.01 and 0.08 solar masses, not accounted for in the previous study by [Kroupa et al. \(1993\)](#). These primary mass distributions are shown on the top left panel of [Fig. 8.1](#).

With COSMIC, it is possible to sample the primary mass from these three IMFs, from $0.08M_{\odot}$ up to $150M_{\odot}$. Note that this truncates the low-mass tail of the IMF from [Kroupa \(2001\)](#). This has no consequence on the study of binaries with Neutron Stars (NSs) and Black Holes (BHs) since their progenitors have masses well above this cut. A user-specified IMF can also be provided, with arbitrary slopes and cutoff masses. Finally, it is worth noting that these IMFs rely on a characterisation of the fraction of stars in binary systems that is inferred directly by using the observations. This parameter is quite uncertain (see the discussion below), and variations can lead to corrections to these distributions. Studies based on population synthesis assume that the IMF is universal, no matter the galactic type or the stellar content, and regardless of the metallicity or redshift of the initial population. This universality can be questioned. New studies using more recent data such as *Gaia* observations ([Gaia Collaboration et al., 2021](#)) would be useful to update the IMF shape and the binary fraction in the Milky Way.

Mass ratio distribution

The determination of the mass of the secondary in COSMIC is done assuming a flat distribution in $q = M_2/M_1$. This is motivated by studies of galactic binaries by [Mazeh et al. \(1992\)](#) and [Goldberg & Mazeh \(1994\)](#) which compile mass information for 23 galactic binaries with orbital periods shorter than 2000 days, and suggest a flat distribution in mass ratios. More recently, [Sana et al. \(2012\)](#) studied a sample of 40 Galactic binaries located in five young stellar clusters. This sample specifically contains O-type stars, blue supergiants which are young massive stars on the Main Sequence (MS) and therefore good tracers of the properties of binary systems with massive stars at their formation (see [Sec. 3.1](#) for the evolutionary timescales). They also observed a flat distribution of mass ratios.

However, some other works instead indicate that the distribution of mass ratios could be favouring lower mass ratios. [Goldberg et al. \(2003\)](#) stress that in the previous studies, a correcting factor was introduced to account for non-detected binaries. This correction was introducing a bias in the

intrinsic mass ratio distribution that was inferred. In this study, [Goldberg et al. \(2003\)](#) analyse this time 129 binaries, lowering low-statistics effects, and find this mass ratio distribution with more systems at lower mass ratio. In fact, that idea was first discussed in [Duquennoy & Mayor \(1991\)](#), which is often quoted as a pioneering study but relied on a biased sample of binaries with unreliable parallax estimates ([Geller et al., 2019](#)). More discussion on that issue can be found in [Kroupa et al. 1993](#) (Sec. 4.3.2). [Kobulnicky & Fryer \(2007\)](#) discuss the possibility for a two-component population, made of symmetric binaries and binaries whose initial mass ratios are uniformly distributed between $0 < q < 1$. More recently, [Moe & Di Stefano \(2017\)](#) have argued that the mass ratio is directly correlated to the primary mass in a power law.

Because there is yet no strong evidence for a statistically relevant non-uniform mass ratio distribution, a flat distribution is assumed in COSMIC. Again, new works with more statistics and a careful study of the observational biases could help solving this tension and refining the prescription. I show the distribution of initial mass ratios in the bottom right panel of Fig. 8.1.

We note that in COSMIC, the mass ratio is sampled uniformly between q_{\min} and 1, where $q_{\min} \simeq 0.1$ decreases with the primary mass for $M_1 > 5M_{\odot}$, ranging between 0.13 ($M_1 = 5M_{\odot}$) and 0.02 ($M_1 = 150M_{\odot}$); and is fixed to $q_{\min} = 0.1$ for systems where $M_1 < 5M_{\odot}$. User-specified values for q_{\min} or $M_{2,\min}$ (minimum mass of the secondary) can also be used.

Initial separation distribution

We stress again that in all the studies shown in this Sec. 8.1, inferring the properties of the intrinsic population from the observed one is a major difficulty given the biases in the mass and separation ranges covered in the observed sample. For example, wide binaries or more extreme mass ratios are the most affected by selection effects and as a result, constraints on the intrinsic distributions for these values is the most uncertain.

The distribution of initial separations has first been investigated by [Öpik \(1924\)](#) and later by [Abt \(1983\)](#) on a population of various stellar types. Both analyses found a distribution $f(a)$ uniform in $\log a$, *i.e.* $f(a) \propto 1/a$, sometimes referred to as Öpik’s law, as also assumed in StarTrack (see [Dominik et al. 2012](#)). However, the more recent study by [Sana et al. \(2012\)](#) has found a steeper orbital period distribution $f(\log P) \propto (\log P)^{-0.55}$, where separation and orbital period are related by Kepler’s third law ([Kepler, 1619](#)):

$$\frac{P^2}{a^3} = \frac{4\pi^2}{G(M_1 + M_2)}. \quad (8.4)$$

Given the range of masses probed in [Sana et al. \(2012\)](#) which favours high masses binaries, [Renzo et al. \(2019\)](#) instead introduce a mass-dependent period distribution, flat in $\log P$ up to $15M_{\odot}$ and following [Sana et al. \(2012\)](#) for $M_1 > 15M_{\odot}$. These three distributions of initial separations can be chosen for the independent initial parameter sampling with COSMIC and are shown on the bottom left panel of Fig. 8.1. We note that a minimal separation is required, such that it is greater than the initial Roche radius (see Eq. 8.32) of the primary, to prevent the initialization of binary systems with ongoing mass transfer (Sec. 8.2.2). A maximum separation is also set to $10^5 R_{\odot}$ for the log-uniform distribution, whereas a maximum orbital period is set to $10^{5.5}$ days for the other distributions. Once again, the initial parameters can instead be chosen from correlated distributions, following [Moe & Di Stefano \(2017\)](#).

Eccentricity distribution

The last initial parameter distribution to characterise is the eccentricity distribution. Assuming that the population of binaries follows a Boltzmann distribution in binding energy, [Jeans \(1919\)](#) showed that the expected distribution of eccentricities should take the form $f(e) \propto 2e$. This was later

verified by [Heggie \(1975\)](#) using N-body simulations. This eccentricity distribution is often named *thermal*, as a reference to the *thermalized* energy distribution across the binaries which is possible if several dynamical encounters are experienced by the population of binaries. However, in a realistic astrophysical context, *e.g.* in a young stellar cluster, it is unlikely that this equilibrium is reached at the formation time of the binaries. [Geller et al. \(2019\)](#) instead argue that the intrinsic eccentricity distribution should be uniform, and that it is impossible to convert a uniform distribution to a thermal distribution even within the cluster lifetime. An interesting consequence is that observing one or the other would put strong constraints on the models. Finally, [Sana et al. \(2012\)](#) use Monte Carlo simulations to infer the initial distributions shape (assumed to be power laws and mutually independent) from the stellar observations. They find an eccentricity distribution $f(e) \propto e^{-0.45}$ up to $e_{\max} = 0.9$. The three distributions shown here have opposite trends and can therefore impact the predicted compact object populations. I show them in the central bottom panel of Fig. 8.1. For exploration, a population of binaries with circularized orbits can also be generated with COSMIC, *i.e.* $e = 0$.

Binary fraction

A final, but highly uncertain parameter is the fraction of stars in binary systems, as already introduced in Sec. 3.1. Most of the studies mentioned earlier derive their distribution functions under the assumption – derived from the observational data used – of a specific binary fraction. Typically, this fraction ranges between ~ 0.3 and ~ 0.7 (see Sec. 8.1 and *e.g.* [Sana et al. 2012](#)). Motivated by the observations of [Kouwenhoven et al. 2009](#), [Kraus & Hillenbrand 2009](#) and [Sana et al. 2012](#), [van Haften et al. \(2013\)](#) derive a binary fraction function \mathcal{B} that increases with the primary mass M_1 , of the form:

$$\mathcal{B}(M) = \frac{1}{2} + \frac{1}{4} \log_{10} \left(\frac{M}{M_{\odot}} \right), \quad (8.5)$$

where \mathcal{B} is defined as

$$\mathcal{B}(M) = \frac{N_{\text{binary}}(M_1 = M)}{N_{\text{single}}(M) + N_{\text{binary}}(M_1 = M)} \quad (8.6)$$

and $0.08 \leq M/M_{\odot} \leq 100$. $\mathcal{B}(M)$ therefore varies between 0.22 and 1. This varying binary fraction can also be used in COSMIC.

Summary of the binary initial properties

The different distributions described in this section are illustrated in Fig. 8.1. The different slopes for the mass distributions are clearly visible on the top left panel, where we can in particular observe the high mass variation between the prescriptions of [Kroupa et al. \(1993\)](#) and [Kroupa \(2001\)](#). Because primary masses are not sampled below $0.08M_{\odot}$, the first segment of the distribution of [Kroupa \(2001\)](#) is not visible. The distributions of orbital periods and eccentricities are significantly different between the models, as shown on the bottom left and central panels. It can be noted that the power-law separation distribution for massive stars with $M > 15M_{\odot}$ of [Renzo et al. \(2019\)](#) is not clearly visible in this figure, mostly because the overall contribution of such high-mass stars to the total population is small. We however expect these differences to play a significant role in the study of the populations of NSs and BHs. The thermal distribution of eccentricities drops for $e \gtrsim 0.9$ because highly eccentric orbits are more likely to have a periastron below the Roche radius of the primary, even for increasing separations, and to thus be discarded. Finally, it can be noted that the distribution of mass ratios q does not seem to follow a uniform distribution. This effect is caused by the lower limit on the mass of the secondary star. Because most stars are also the least massive, especially with the [Salpeter \(1955\)](#) primary mass function, the cut at low secondary masses

favours more symmetric mass ratios at low primary masses. For example, if the primary has a mass $M_1 = 0.2M_\odot$ and the minimum mass for the secondary is set to $M_{2,\min} = 0.08M_\odot$, the possible mass ratio only ranges between $0.4 < q < 1$.

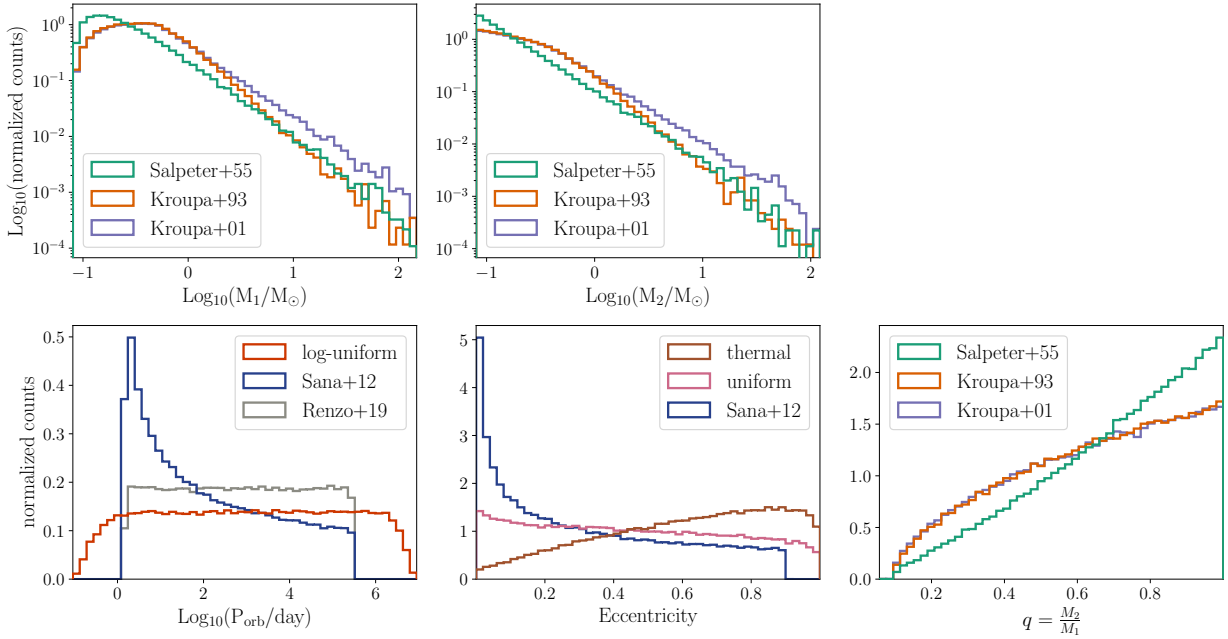


Fig. 8.1: Initial binary distributions for the different models presented in Sec. 8.1. The distributions of M_1 , M_2 and q are shown assuming a log-uniform period distribution and a thermal eccentricity distribution. The distributions of P_{orb} are shown with the primary mass distribution from Kroupa (2001) and a thermal eccentricity distribution. The distributions of eccentricities are shown assuming the primary mass distribution from Kroupa (2001) and a log-uniform period distribution.

8.2 Binary Stellar Evolution

The joint evolution of binary systems is challenging to model accurately, as described in Chapter 7. Population synthesis models aim at rapidly evaluating the key processes occurring during the binary’s lifetime. To do so, they rely on a simplified treatment of complex processes that are, each individually, entire research domains. Most of the prescriptions used and presented below are often valid on a restricted domain of the parameter space (*e.g.* certain ranges of primary mass), but are extrapolated to accommodate for the variety of values that can be found in the entire population. It is key to keep that in mind when evaluating the uncertainties relative to each process modelled in COSMIC. COSMIC in particular is based on the evolution algorithms proposed by Tout et al. (1997); Hurley et al. (2000, 2002). They rely on analytic fitting formulae to models of single star evolution defined in Pols et al. (1998) (see also Sec. 3.1). In particular, the description of stellar evolution relies on the definition of separate stellar types (Hurley et al., 2000). I summarize them in Tab. 8.1, to which I encourage the reader to refer to as often as needed. Note that several physical processes such as stellar winds are only active for certain stellar types. How they are defined and when a star changes of stellar type is therefore crucial to accurately follow stellar tracks. In a recent study, Iorio et al. (2023) have proposed slightly different definitions of stellar types and found differences in the modelled stellar tracks.

Indicator	Stellar Type
0	Low-Mass Main Sequence (MS) star ($M < 0.7M_{\odot}$)
1	Main Sequence (MS) star ($M > 0.7M_{\odot}$)
2	Hertzsprung Gap (HG)
3	First Giant Branch (FGB)
4	Core Helium Burning (CHeB)
5	Early Asymptotic Giant Branch (EAGB)
6	Thermally Pulsating Asymptotic Giant Branch (TPAGB)
7	Naked Helium Star, Main Sequence (He-MS)
8	Naked Helium Star, Hertzsprung Gap (He-HG)
9	Naked Helium Star, Giant Branch (He-GB)
10	Helium White Dwarf (WD)
11	Carbon/Oxygen White Dwarf (WD)
12	Oxygen/Neon White Dwarf (WD)
13	Neutron Star (NS)
14	Black Hole (BH)
15	Massless Remnant

Tab. 8.1: Stellar types indicators used in COSMIC. They correspond to the definitions of [Pols et al. \(1998\)](#).

In the following sections, I highlight the key evolutionary elements that can occur during the evolution of binary systems: stellar winds (Sec. 8.2.1), Roche Lobe Overflow (RLOF) (Sec. 8.2.2), Common Envelope (CE) (Sec. 8.2.3), Supernova (SN) kicks (Sec. 8.2.4) and some miscellaneous elements (Sec. 8.2.5). I mostly focus on those relevant to the formation of BNSs, Neutron Star – Black Hole binaries (NSBHs) and Binary Black Holes (BBHs).

8.2.1 Stellar Winds

During their life, stars are prone to losses of mass due to stellar winds. The mass loss rate for a single star depends on various factors such as the stellar type, the metallicity, and on the types of winds. The rates can also be affected by binarity. Constraints on stellar winds used in population synthesis come sometimes from numerical simulations, sometimes directly from observations. Here I present the typical types of winds that can affect stellar masses in COSMIC.

We first note that using the flag `windflag`, it is possible to select several prescriptions, for example to reproduce exactly the implementation by [Hurley et al. \(2000\)](#) or by [Belczynski et al. \(2008\)](#). Because more recent studies have led to newer models, as will be shown hereafter, I only discuss here the most up-to-date description of stellar winds, using `windflag = 3`.

Wind calculation in COSMIC

The different winds (\dot{M}_{LBV} , \dot{M}_{VK} , \dot{M}_{NJ} , \dot{M}_{VW} , $\dot{M}_{\text{KR,corr}}$, \dot{M}_{WR} , that I will define individually in this section) that can affect the stellar mass depend on the stellar type, and are summarized as follows:

- For all MS stars and stars on the FGB or at CHeB:

$$\dot{M}_{\text{wind}} = \begin{cases} \dot{M}_{\text{LBV}} & , \text{if } L/L_{\odot} > 6 \times 10^5 \text{ and } R/R_{\odot} (L/L_{\odot})^{1/2} > 10^5 \\ \dot{M}_{\text{VK}} & , \text{if } 12500 \text{ K} < T_{\text{eff}} < 50000 \text{ K} \\ \max[\dot{M}_{\text{NJ}}; \dot{M}_{\text{KR,corr}}] & , \text{otherwise} \end{cases} \quad (8.7)$$

- For stars on the Asymptotic Giant Branch (AGB), *i.e.* EAGB, TPAGB:

$$\dot{M}_{\text{wind}} = \begin{cases} \dot{M}_{\text{LBV}} & , \text{if } L/L_{\odot} > 6 \times 10^5 \text{ and } R/R_{\odot} (L/L_{\odot})^{1/2} > 10^5 \\ \dot{M}_{\text{VK}} & , \text{if } 12500 \text{ K} < T_{\text{eff}} < 50000 \text{ K} \\ \max [\dot{M}_{\text{NJ}}; \dot{M}_{\text{KR,corr}}; \dot{M}_{\text{VW}}] & , \text{otherwise} \end{cases} \quad (8.8)$$

- For naked Helium stars, *i.e.* He-MS, He-HG, He-GB:

$$\dot{M}_{\text{wind}} = \dot{M}_{\text{WR}} \quad (8.9)$$

- For WDs, NSs, BHs:

$$\dot{M}_{\text{wind}} = 0. \quad (8.10)$$

I now review these different wind expressions.

The different types of stellar winds

Nieuwenhuijzen & de Jager (1990) have studied empirically 247 massive stars with a luminosity $L > 4000 L_{\odot}$ and fitted the observed mass loss rates with a simple formula including the stellar luminosity L , the stellar mass M and the stellar radius R . Hurley et al. (2000) add a modification to this formula depending on the stellar metallicity Z , as suggested in Kudritzki et al. (1989). The mass-loss rate applied to all massive luminous stars ($L > 4000 L_{\odot}$) is therefore

$$\dot{M}_{\text{NJ}} = 9.6 \cdot 10^{-15} \times \min \left[1, \frac{L - 4000}{500} \right] \times \left(\frac{Z}{Z_{\odot}} \right)^{1/2} \left(\frac{R}{R_{\odot}} \right)^{0.81} \left(\frac{L}{L_{\odot}} \right)^{1.24} \left(\frac{M}{M_{\odot}} \right)^{0.16} M_{\odot} \cdot \text{yr}^{-1}. \quad (8.11)$$

In evolved stars, *i.e.* stars on the HG, the FGB, CHeB, Early Asymptotic Giant Branch (EAGB) and Thermally Pulsating Asymptotic Giant Branch (TPAGB), the envelope is also subject to mass loss due to photon line absorption. The expression derived by Kudritzki & Reimers (1978) (initially for red giants) is used to describe these absorption lines-driven mass loss rates:

$$\dot{M}_{\text{KR}} = \eta \times 4 \cdot 10^{-13} \frac{L}{L_{\odot}} \frac{R}{R_{\odot}} \left(\frac{M}{M_{\odot}} \right)^{-1} M_{\odot} \cdot \text{yr}^{-1}, \quad (8.12)$$

where η is a free scaling parameter of order unity, that can be provided in COSMIC using `neta`. Typically, $\eta = 0.5$, as proposed² by Hurley et al. (2000).

Tout & Eggleton (1988) have measured stellar masses in close binaries where mass transfers have exchanged the mass ratio (the secondary becoming the most massive star). They argue that some enhancement of the mass loss rates must occur in order to reproduce their observations, and propose an expression of the enhancement of \dot{M}_{KR} that depends on the torque induced by tidal friction between the two stars and which scales as $(R/R_L)^6$, where R is the stellar radius and R_L the Roche radius (see Sec. 8.2.2). They propose

$$\dot{M}_{\text{KR,corr}} = \dot{M}_{\text{KR}} \times \left[1 + B_{\text{W}} \cdot \left(\min \left(\frac{1}{2}, \frac{R}{R_L} \right) \right)^6 \right], \quad (8.13)$$

where $B_{\text{W}} \simeq 10^4$ and the saturation at $R = 1/2R_L$ is imposed by the corotation of the giant at large radii. B_{W} is a parameter that can be supplied in COSMIC using `bwind`. We typically set $B_{\text{W}} = 0$, as this effect still remains very uncertain, as suggested³ by Hurley et al. (2002).

²Eq. 106 in Hurley et al. (2000) has a typo with an extra η . The correct rate is directly proportional to η , as in Eq. 8.12.

³There is a typo in Eq. 12 in Hurley et al. (2002), where min of Eq. 8.13 has been replaced by max.

For stars on the AGB (EAGB and TPAGB), [Vassiliadis & Wood \(1993\)](#) have introduced another mass loss process leading to an exponential increase in mass-loss rate at the very end of the AGB phase, until a saturation rate during a *superwind* phase. This phase is triggered by the stellar thermal pulsations. Indeed, stars on the AGB experience thermal pulses (also known as helium shell flashes, see Sec. 3.1), which modify the rotation period on rapid timescales. COSMIC uses the formula proposed by [Vassiliadis & Wood \(1993\)](#) to describe these winds:

$$\log \dot{M}_{\text{VW}} = \min \left(-8.87 + \log \frac{L}{L_{\odot}}; -11.4 + 0.0125 \left[P_0 - 100 \cdot \max \left(\frac{M}{M_{\odot}} - 2.5; 0 \right) \right] \right) M_{\odot} \cdot \text{yr}^{-1}, \quad (8.14)$$

where P_0 is the Mira period pulsation (in days), empirically determined by [Wood \(1990\)](#) as

$$\log P_0 = \min \left(3.3; -2.07 - 0.9 \log \frac{M}{M_{\odot}} + 1.94 \log \frac{R}{R_{\odot}} \right) \text{ days}, \quad (8.15)$$

and which saturates at $P_{0,\text{max}} = 2000$ days. The correction to P_0 in Eq. 8.14 for massive stars with $M > 2.5M_{\odot}$ allows a delayed onset of the superwind phase. \dot{M}_{VW} saturates to a maximum value in the superwind phase, as proposed originally in [Hurley et al. \(2000\)](#).

One update in COSMIC compared to BSE is the inclusion of metallicity-dependent winds for the most massive O and B stars on the main sequence following the prescription of [Vink et al. \(2001\)](#). In this description, the mass loss rate for massive stars is line-driven and depends on their metallicity Z , luminosity L , mass M and effective temperature T_{eff} . [Vink et al. \(2001\)](#) define two separate regimes: $12500 \text{ K} < T_{\text{eff}} < 22500 \text{ K}$ and $27500 \text{ K} < T_{\text{eff}} < 50000 \text{ K}$. In the temperature ranges $T_{\text{eff}} \sim 25000 \text{ K}$, there is a jump in wind efficiency due to the recombination of Fe^{IV} ions into Fe^{III} , which is more efficient to amplify line-driven winds. To bridge this intermediate T_{eff} gap, [Belczynski et al. \(2010\)](#) propose a modification to the equations from [Vink et al. \(2001\)](#), that is also used by [Rodriguez et al. \(2016\)](#) and implemented in COSMIC. They are expressed as follows:

– If $12500 \text{ K} < T_{\text{eff}} < 25000 \text{ K}$:

$$\begin{aligned} \log \dot{M}_{\text{VK}} = & \alpha_{\text{VK}} \cdot \log \frac{Z}{Z_{\odot}} - 6.68 + 2.21 \log \frac{L/L_{\odot}}{10^5} - 1.339 \log \frac{M/M_{\odot}}{30} \\ & - 1.601 \log \frac{v_{\infty}/v_{\text{esc}}}{2} + 1.07 \log \frac{T_{\text{eff}}}{2 \cdot 10^4} M_{\odot} \cdot \text{yr}^{-1}, \end{aligned} \quad (8.16)$$

where the ratio between the wind velocity at infinity and the wind escape velocity is $v_{\infty}/v_{\text{esc}} = 1.3$.

– If $25000 \text{ K} < T_{\text{eff}} < 50000 \text{ K}$:

$$\begin{aligned} \log \dot{M}_{\text{VK}} = & \alpha_{\text{VK}} \cdot \log \frac{Z}{Z_{\odot}} - 6.697 + 2.194 \log \frac{L/L_{\odot}}{10^5} - 1.313 \log \frac{M/M_{\odot}}{30} \\ & - 1.226 \log \frac{v_{\infty}/v_{\text{esc}}}{2} + 0.933 \log \frac{T_{\text{eff}}}{4 \cdot 10^4} - 10.92 \left(\log \frac{T_{\text{eff}}}{4 \cdot 10^4} \right)^2 M_{\odot} \cdot \text{yr}^{-1}, \end{aligned} \quad (8.17)$$

where $v_{\infty}/v_{\text{esc}} = 2.6$.

The effective temperature T_{eff} (see Eq. 3.5) is defined in this case as

$$T_{\text{eff}} = 1000 \times \left(1130 \times \frac{L/L_{\odot}}{(R/R_{\odot})^2} \right)^{1/4} \text{ K}. \quad (8.18)$$

The value of α_{VK} is described in Eqs. 8.21 and 8.24, and depends on the chosen model for the metallicity-dependence of stellar winds.

These winds are efficient for stars with ZAMS masses $M_{\text{ZAMS}} \gtrsim 3 M_{\odot}$ which are initially in the correct range of effective temperature.

The most luminous stars, called Luminous Blue Variables (LBVs) experience eruptive mass ejection events that can eject up to a solar mass of material per event (Humphreys & Davidson, 1994). Additional mass loss is therefore assumed in COSMIC for these stars, under the condition that $\frac{L}{L_{\odot}} > 6 \times 10^5$ and $\frac{R}{R_{\odot}} \left(\frac{L}{L_{\odot}}\right)^{1/2} > 10^5$ (Humphreys & Davidson, 1994). The mass loss rate is then defined as

$$\dot{M}_{\text{LBV}} = 1.5 \cdot 10^{-4} \left(\frac{Z}{Z_{\odot}}\right)^{\alpha_{\text{LBV}}} M_{\odot} \cdot \text{yr}^{-1}. \quad (8.19)$$

We note that this expression is an adaptation of that proposed by Humphreys & Davidson (1994) and originally used by Hurley et al. (2000). I discuss the value of α_{LBV} in Eqs. 8.21 and 8.24

For naked Helium stars, *i.e.* Naked Helium Star, Main Sequence (He-MS), Naked Helium Star, Hertzsprung Gap (He-HG), Naked Helium Star, Giant Branch (He-GB); Wolf-Rayet (WR)-like stellar winds are applied. The model uses the mass-loss rate originally proposed by Hamann et al. (1995) based on a fit to the observed mass-loss rates for WR stars. However, the exact rates are very uncertain, and other subsequent studies including the effect of wind clumpiness have concluded that the estimation by Hamann et al. (1995) may be overestimated by a factor of ~ 10 . Following results obtained from numerical simulations in Vink & de Koter (2005), WR winds are computed depending on metallicity and luminosity. The scaling parameter and the shape of the formula are provided by Yoon & Langer (2005), and COSMIC uses the expression proposed by Belczynski et al. (2010):

$$\dot{M}_{\text{WR}} = 10^{-13} \left(\frac{L}{L_{\odot}}\right)^{1.5} \left(\frac{Z}{Z_{\odot}}\right)^{\alpha_{\text{WR}}} M_{\odot} \cdot \text{yr}^{-1}. \quad (8.20)$$

Note that this expression is different from that of BSE, proposed by Hurley et al. (2000), where $\dot{M}_{\text{WR}} = (1 - \mu) \times 10^{-13} (L/L_{\odot})^{3/2} M_{\odot} \cdot \text{yr}^{-1}$. It is possible to use this expression in COSMIC by applying `windflag` = 0 and specifying the parameter `hewind` = $1 - \mu$. This parameter is inactive for the standard model `windflag` = 3. α_{WR} is presented in Eqs. 8.21 and 8.24.

Dependence on Metallicity

In some of the cases listed before, the impact of metallicity is taken into account in the expression of stellar winds, using a scaling index α . The values obtained in the original studies are:

$$\begin{cases} \alpha_{\text{VK}} = 0.85 & \text{for } \dot{M}_{\text{VK}} & \text{in Eqs. 8.16 and 8.17} \\ \alpha_{\text{LBV}} = 0 & \text{for } \dot{M}_{\text{LBV}} & \text{in Eq. 8.19} \\ \alpha_{\text{WR}} = 0.86 & \text{for } \dot{M}_{\text{WR}} & \text{in Eq. 8.20} \end{cases} \quad (8.21)$$

With these values, LBV winds do not depend on metallicity and have a constant rate, as discussed by Belczynski et al. (2010); though this assumption is quite uncertain. In fact, more recent studies have shown that the metallicity-dependency of stellar winds can be affected by the Eddington factor Γ_e , which is defined, for a fully ionized plasma as (see *e.g.* Gräfener et al. 2011)

$$\Gamma_e = \frac{L}{L_{\text{Edd}}} = \frac{\chi_e}{4\pi Gc} \frac{L}{M}, \quad (8.22)$$

where L_{Edd} is the Eddington luminosity (Eddington, 1921), χ_e is the electron Thomson scattering opacity. Gräfener et al. (2011) provide an equivalent expression of Γ_e that is used in COSMIC:

$$\log \Gamma_e = \min \left(0; -4.813 + \log(1 + X_{\text{H}}) + \log \frac{L}{L_{\odot}} - \log \frac{M}{M_{\odot}} \right), \quad (8.23)$$

where X_{H} is the hydrogen mass fraction at the surface, appearing through χ_e . The values of X_{H} for the different stellar types are given in Tab. 8.2.

Stellar Type	X_{H}
MS	0.7
HG	0.6
FGB	0.5
CHeB	0.4
EAGB, TPAGB	0.2
He-MS, He-HG, He-GB	0.0

Tab. 8.2: Value of X_{H} for the different stellar types. For more evolved stars, the hydrogen mass fraction at the surface decreases. Note that these values are assumed here to be independent of metallicity.

Gräfener & Hamann (2008) showed that mass loss rates increase with the Eddington factor Γ_e , thanks to detailed WR winds numerical simulations. Vink et al. (2011) also exhibited this behaviour in an independent study. This prompted Tang et al. (2014) to propose a fit to the evolution of α with Γ_e that was found by Gräfener & Hamann (2008):

$$\alpha_{\text{VK}} = \alpha_{\text{LBV}} = \alpha_{\text{WR}} = \alpha = \begin{cases} 0.85 & \text{if } \Gamma_e < 2/3 \\ 2.45 - 2.4\Gamma_e & \text{if } 2/3 \leq \Gamma_e \leq 1 \end{cases} \quad (8.24)$$

In this expression, the mass-loss rate dependence on metallicity decreases with Γ_e : for more intense winds, the influence of metallicity becomes weaker (see also Giacobbo et al. 2018).

With the parameter `eddlimflag`, it is possible either to activate an Eddington-limited metallicity dependence of stellar winds, as in Eq. 8.24 (`eddlimflag` = 1); or to fix constant scaling indices as in Eq. 8.21 (`eddlimflag` = 0).

Mass accretion onto the companion

In the binary system, part of the mass lost through winds by one of the stars may be accreted by the companion, which will gain mass. The average accretion rate over an orbit is assumed to follow the Bondi & Hoyle (1944) mechanism. The derivation of this value follows the method described in Boffin & Jorissen (1988), and assumes that the timescale of mass transfer is longer than the orbital period and that the winds are spherically symmetric and supersonic. The average accretion rate on the companion star over one orbital period $\langle \dot{M}_{\text{c,acc}} \rangle$ is then given by

$$\langle \dot{M}_{\text{c,acc}} \rangle = \frac{-1}{\sqrt{1-e^2}} \left(\frac{GM_{\text{c}}}{v_{\text{wind}}} \right)^2 \frac{\alpha_{\text{wind}}}{a^2} \frac{1}{[1 + (v_{\text{orb}}/v_{\text{wind}})^2]^{3/2}} \dot{M}_{\text{d,wind}}, \quad (8.25)$$

where a is the orbital separation of the binary, e its eccentricity, $\dot{M}_{\text{d,wind}}$ the mass loss rate of the donor star (assumed to be constant over one orbital period), M_{c} the mass of the companion star and v_{orb} the orbital velocity of a binary system whose circular orbit has the same orbital period as the binary's. v_{wind} is the wind velocity, presented in Eq. 8.27, and α_{wind} is a scaling factor of order unity (see below).

For highly eccentric orbits, Eq. 8.25 diverges, so to prevent the secondary from accreting more mass than what is ejected by the primary, it is imposed that

$$\left| \dot{M}_{\text{c,acc}} \right| \leq 0.8 \times \left| \dot{M}_{\text{d,wind}} \right|. \quad (8.26)$$

The parameter α_{wind} allows for a scaling of the accretion rate, and is typically set to $\alpha_{\text{wind}} = 3/2$ using the parameter `acc2` in COSMIC. This matches exactly the derivation of Bondi & Hoyle (1944) and is compatible with the lower limits found by Boffin & Jorissen (1988).

Finally, the wind velocity v_{wind} is assumed to be proportional to the escape velocity at the stellar surface by Hurley et al. (2002):

$$v_{\text{wind}}^2 = 2\beta_{\text{wind}}G\frac{M_{\text{d}}}{R_{\text{d}}}, \quad (8.27)$$

where M_{d} is the mass of the donor star and R_{d} its radius. A new scaling parameter is used in Eq. 8.27: β_{wind} . Following Belczynski et al. (2008), the value of β_{wind} depends on the stellar type and the stellar mass. It is defined as follows:

- For stars on the MS,

$$\beta_{\text{wind}} = \begin{cases} 0.5 & \text{if } M_{\text{d}} \leq 1.4M_{\odot} \\ 0.5 + 7 \times \frac{M_{\text{d}} - 1.4}{120 - 1.4} & \text{if } 1.4M_{\odot} \leq M_{\text{d}} \leq 120M_{\odot} \\ 7 & \text{if } M_{\text{d}} \geq 120M_{\odot} \end{cases} \quad (8.28)$$

- For evolved stars (HG, FGB, CHeB, EAGB, TPAGB),

$$\beta_{\text{wind}} = 0.125 \quad (8.29)$$

- For naked Helium stars (He-MS, He-HG, He-GB),

$$\beta_{\text{wind}} = \begin{cases} 0.125 & \text{if } M_{\text{d}} \leq 10M_{\odot} \\ 0.125 + 7 \times \frac{M_{\text{d}} - 10}{120 - 10} & \text{if } 10M_{\odot} \leq M_{\text{d}} \leq 120M_{\odot} \\ 7 & \text{if } M_{\text{d}} \geq 120M_{\odot} \end{cases} \quad (8.30)$$

More massive stars therefore have higher-speed winds than their low-mass counterparts, and the wind velocity is interpolated in-between. All evolved stars are assumed to have low-velocity winds. The standard approach in COSMIC is to use this description using $\beta_{\text{wind}} = -1$, but it is also possible to mimic the behaviour of BSE by supplying a value of β_{wind} that will be the same for all stellar types, typically 0.125 as suggested by Hurley et al. (2002).

Finally, mass losses by winds in binary systems carry some specific angular momentum from the donor. Upon accretion, it is not obvious that all the angular momentum carried by the wind is transferred to the secondary. In fact, 3-dimensional hydrodynamical simulations as conducted by Ruffert (1999) already hinted that the fraction of angular momentum transferred is between 0 and 0.7. To account for this uncertainty, a new parameter μ_{wind} is introduced in the equation of angular momentum transfer, which is defined as

$$\dot{J}_{\text{d}} = \frac{2}{3}\dot{M}_{\text{d,wind}}h_{\text{d}} + \frac{2}{3}\mu_{\text{wind}}\dot{M}_{\text{c,acc}}h_{\text{c}}, \quad (8.31)$$

where \dot{J}_{d} is the variation of spin of the donor star, h_{d} and h_{c} are the specific angular momenta of the donor and companion star, respectively. μ_{wind} is provided in COSMIC using the parameter `xi` and is typically set to $\mu_{\text{wind}} = 0.5$.

8.2.2 Roche Lobe Overflow

When the orbit of the binary shrinks, or when stellar evolution causes one or the other of the stars to expand, they may fill their Roche Lobe and transfer material from their outer envelope to the companion *via* the Lagrange point L_1 . When mass transfer is stable, that is when the mass accretion rate is higher than the mass loss rate, this process is called Roche Lobe Overflow (RLOF). Otherwise, it leads to a runaway envelope expansion of the donor until it fully engulfs the companion, in a so-called Common Envelope (CE). Through this section, I refer to the star that fills its Roche lobe and loses mass as the **donor**, and to that which receives material as the **companion**. Note

that the donor is not necessarily the primary star, defined as the initially more massive of the two at ZAMS, because of potential previous phases of mass transfers during the binary evolution.

The Roche radius of a star, shown below, has been determined by Eggleton (1983), who refined within errors $\lesssim 1\%$ a first approximate by Paczyński (1971). It corresponds to the radius of a sphere of the same volume as that enclosed by the last stable equipotential passing through L_1 (see also Tout et al. 1997):

$$\frac{R_L}{a} = \frac{0.49q^{2/3}}{0.6q^{2/3} + \ln(1 + q^{1/3})}, \quad (8.32)$$

where $q = M_2/M_1$ and a is the orbit semi-major axis. I show a graphical representation of Eq. 8.32 on the left side of Fig. 8.2. The equipotentials in the frame in co-rotation with the orbital motion are shown on the right side of Fig. 8.2. To find the Roche radius of the companion, replace q in Eq. 8.32 by $q' = M_1/M_2$. As stressed in Hurley et al. (2002), this formula is only valid for a system whose orbit has circularized, *i.e.* $e = 0$. In most cases, because of tidal effects affecting the stellar envelope, this hypothesis is verified. When it is not, total circularization is assumed at the onset of RLOF.

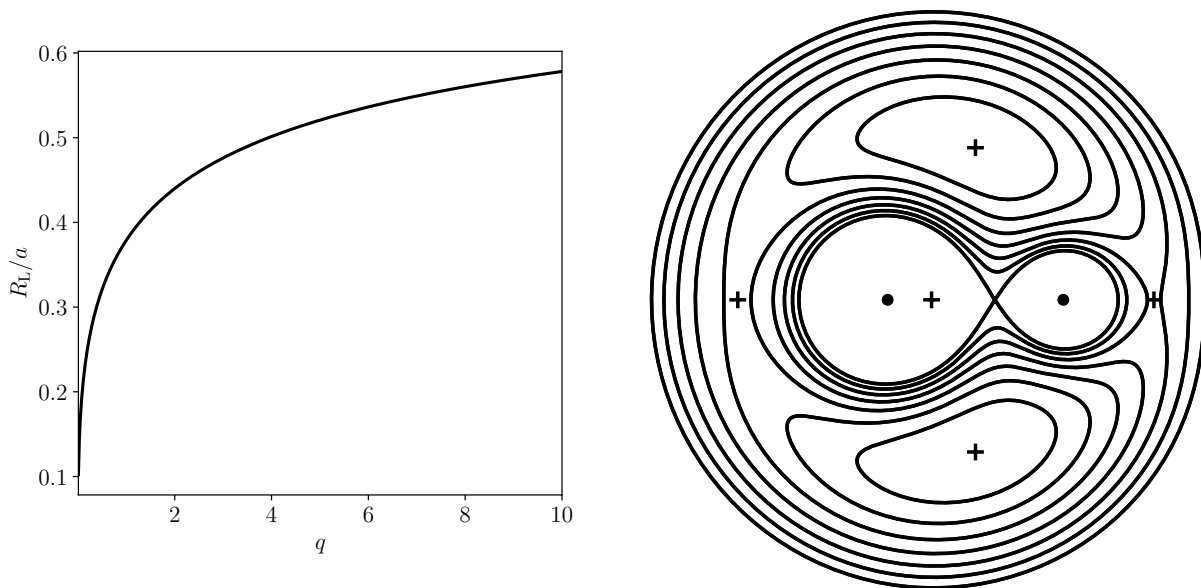


Fig. 8.2: **Left:** Roche radius as a function of the mass ratio (Eq. 8.32). **Right:** Roche equipotentials in the frame in co-rotation with the orbital motion, for a system with $q = 3$. The two black dots represent the positions of the center of masses, and the cross between these points is the center of mass of the system. The other crosses represent the Lagrange points, except L_1 , which is located at the intersection of the innermost equipotential.

Once RLOF starts, the stability of the process is governed by two quantities: (1) the reaction of the donor radius to mass loss; (2) the reaction of the Roche radius of the donor to mass loss. In fact, the accreting companion also reacts upon accreting mass, but this response is not accounted for in the simple method described hereafter. Following Webbink (1985), we therefore define

$$\zeta_* \equiv \frac{\partial \log R}{\partial \log M}, \quad (8.33)$$

the derivative of the donor radius with respect to its mass and

$$\zeta_L \equiv \frac{\partial \log R_L}{\partial \log M}, \quad (8.34)$$

the derivative of the Roche radius of the donor with respect to its mass (see also Paczyński & Sienkiewicz 1972). When $\zeta_* \geq \zeta_L$, mass transfer is stable: the Roche radius increases faster than the stellar radius as the donor loses mass. When $\zeta_* < \zeta_L$, mass transfer is unstable: the stellar radius increases faster than the Roche radius, allowing for more mass being transferred in a runaway process. Note that these quantities are negative.

In fact, upon mass loss, two equilibria are disturbed in the donor star: hydrostatic equilibrium and thermal equilibrium (see Sec. 3.1). The two timescales on which the star will react are however very different. A new hydrostatic equilibrium can be reached on the dynamical timescale (Eq. 3.1), which is typically much shorter than the Kelvin-Helmholtz timescale for thermal readjustment (Eq. 3.2). Therefore, the first quantity to consider is the adiabatic response of the star to mass loss, that is encompassed in the derivative of its radius with respect to the mass, only accounting for adiabatic variations:

$$\zeta_{\text{ad}} \equiv \left(\frac{\partial \log R}{\partial \log M} \right)_{\text{ad}}. \quad (8.35)$$

The criterion for mass transfer stability can therefore be rewritten as $\zeta_{\text{ad}} \geq \zeta_L$. If this criterion is met, the star shrinks below its Roche radius on the dynamical timescale. It then tries to reach the new thermal equilibrium imposed by its new mass, on the Kelvin-Helmholtz timescale, after which it has reached its equilibrium radius. We therefore define the radius derivative with respect to the mass, only accounting for thermal transfers,

$$\zeta_{\text{eq}} \equiv \left(\frac{\partial \log R}{\partial \log M} \right)_{\text{eq}}. \quad (8.36)$$

Because $\zeta_{\text{ad}} \gg \zeta_{\text{eq}}$, depending on the ordering between ζ_L , ζ_{ad} and ζ_{eq} , three types of mass transfers can take place⁴:

- **If $\zeta_L \leq \zeta_{\text{eq}}$: Stable mass transfer.** The stellar radius increases more slowly than the Roche radius upon mass loss. The process is self-regulating, until the star fills its Roche lobe again later during its evolution, either on a nuclear timescale, or on the timescale of angular momentum loss leading to the orbit shrinkage. Hurley et al. (2002) refer to this type of mass transfer as **nuclear mass transfer**.
- **If $\zeta_{\text{eq}} < \zeta_L < \zeta_{\text{ad}}$: Thermal mass transfer.** As the star fills its Roche lobe, its radius shrinks compared to the Roche radius on a dynamical timescale, allowing to reach hydrostatic equilibrium. However, on the thermal timescale, the star reaches its new thermal equilibrium and fills its Roche lobe again. Mass is therefore transferred on the thermal timescale, but the process is still dynamically stable. This is an intermediate state with a self-regulated mass flow from the donor which is never at thermal equilibrium, and can occur only in evolutionary phases of expanding envelopes.
- **If $\zeta_{\text{ad}} \leq \zeta_L$: Dynamically unstable mass transfer.** In this scenario, as soon as the star fills its Roche lobe, its radius expansion rate is higher than that of the Roche radius. This leads to a phase of **Common Envelope (CE)**.

In the literature, *radiative* and *convective* envelopes are often distinguished in the discussions about mass transfer stability. Typically, stars with hotter photospheres of $T_{\text{ph}} \gtrsim 9000$ K have radiative envelopes. Upon mass loss, these stellar envelopes shrink rapidly and the conditions for mass transfer stability are more easily attained. Conversely, stars with cooler photospheres of $T_{\text{ph}} \lesssim 9000$ K have convective envelopes. They either expand or keep a constant radius when losing mass. They are thus more prone to be donors for unstable mass transfer events. Typically, stars with deep convective envelopes are the red giants and supergiants. We stress here that these

⁴This discussion is based on the course on binary evolution by O. Pols, available at https://www.astro.ru.nl/~onnop/education/binaries_utrecht_notes/

descriptions are much more simplistic than what real stellar structures can be, in particular when accounting for effects like rotation and magnetic fields. They must therefore be taken with caution but provide a good estimate of the behaviour of envelopes with mass loss.

In practice, the stability of mass transfer is determined simply using a critical mass ratio q_{crit} . **If $q = M_{\text{don}}/M_{\text{comp}} > q_{\text{crit}}$, mass transfer is dynamically unstable and a CE follows.** q_{crit} is defined such that $\zeta_{\text{ad}} = \zeta_{\text{L}}$ (Hurley et al., 2002), where ζ_{L} is a function of q using Eq. 8.32. If mass transfer is conservative (*i.e.* total mass and angular momentum are conserved), Tout et al. (1997) found that

$$\zeta_{\text{L}} \simeq 2.13q - 1.67. \quad (8.37)$$

Then, using mass-radius models for the different stellar types, it is possible to estimate ζ_{ad} , which leads to an explicit expression for q_{crit} . One estimate using fits to detailed stellar models of red giants is provided in Hurley et al. (2002):

$$q_{\text{crit}} = \frac{1}{2.13} \left[1.67 - x + 2 \left(\frac{M_{\text{c,don}}}{M_{\text{don}}} \right)^5 \right], \quad (8.38)$$

where $x \simeq 0.3$ is typically defined such that $R \propto M^{-x}$ but varies as a function of stellar composition. Another estimation using condensed polytropes (Hjellming & Webbink, 1987) was provided by Webbink (1988):

$$q_{\text{crit}} = 0.362 + \left[3 \left(1 - \frac{M_{\text{c,don}}}{M_{\text{don}}} \right) \right]^{-1}. \quad (8.39)$$

This parameter is of prime importance as it characterises the limit between stable and unstable mass transfers. Several different values of q_{crit} depending on stellar type can be found in the literature and are used in the different population synthesis codes. In StarTrack, Belczynski et al. (2008) employ a similar approach as Hurley et al. (2002) but fix different values for q_{crit} . In binary_c, Claeys et al. (2014) also account for the companion’s response to mass increase. Indeed, companion stars with a radiative envelope will also expand upon accretion, and may also fill their Roche lobe in turn. The value of q_{crit} thus depends also on the companion type (see their Tab. 2). More recently, Neijssel et al. (2019) have used in COMPAS a different set of values for q_{crit} , in particular assuming that mass transfers from *stripped* stars (*i.e.* Helium stellar cores which lost their Hydrogen envelope) is always stable. This has been pointed out by several recent works like Tauris et al. (2015). In this work, the authors also derive analytical expressions for the final separation and the remaining core mass after the phase of stable mass transfer, in the case where the accreting companion is a NS or a BH, that I describe in more detail at the end of Sec. 8.2.3. This specific mass transfer mode is known as *case BB* mass transfer, the “BB” indicating that both stars have evolved off the main sequence. The quest to characterise the stability of mass transfer is still ongoing, as updated values for q_{crit} have recently been proposed by Temmink et al. (2023), using detailed binary evolution with MESA.

In Tab. 8.3, I report the different values of q_{crit} assumed in these different approaches, and that can be selected in COSMIC using the flag `qcflag`. The definitions of stellar types can be found in Tab. 8.1.

8.2.3 Common Envelope

Common Envelope (CE) during binary evolution was first proposed by Paczynski (1976), to explain the observation of very short-period binaries, like cataclysmic variables, low-mass X-Ray Binaries (XRBs) and WD binaries. The formation of these systems, which all contain at least one WD, requires progenitors that expand in red giants during stellar evolution. The initial orbits must therefore be wide enough to avoid the binary disruption during the giant phase, and a process must be invoked to reduce the separation drastically: the CE. Nowadays, the detection of BNS and BBH

Stellar Type	qcflag					
	0	1	2	3	4	5
MS, $M < 0.7M_{\odot}$	0.695	0.695	0.695/1	0.695/1	3	1.717
MS, $M > 0.7M_{\odot}$	3	3	1.6/1	1.6/1	3	1.717
HG	4	4	4/4.7619	4/4.7619	3	3.825
FGB	Eq. 8.38	Eq. 8.39	Eq. 8.38 /1.15	Eq. 8.39 /1.15	3	Eq. 8.39
CHeB	3	3	3/3	3/3	3	3
EAGB, TPAGB	Eq. 8.38	Eq. 8.39	Eq. 8.38 /1.15	Eq. 8.39 /1.15	3	Eq. 8.39
He-MS	3	3	3/3	3/3	1.7	∞
He-HG	0.784	0.784	4/4.7619	4/4.7619	3.5	∞
He-GB	0.784	0.784	0.784/1.15	0.784/1.15	3.5	∞
WD, NS, BH	0.628	0.628	3/0.625	3/0.625	0.628	0.628

Tab. 8.3: Values of q_{crit} depending on the donor star type. Five different sets of values can be used using `qcflag`. If `qcflag` = 0, the default values of BSE (Hurley et al., 2002) are used. If `qcflag` = 1, the default values of BSE (Hurley et al., 2002) are used, using the estimation for q_{crit} from Webbink 1988 (Eq. 8.39) for donors on the giant branch. If `qcflag` = 2, the values from `binary_c` (Claeys et al., 2014) are used, and q_{crit} depends on the companion type. For donors on the giant branch, Eq. 8.38 is used. If `qcflag` = 3, the values from `binary_c` are used, using this time Eq. 8.39 for donors on the giant branch. If `qcflag` = 4, the values from StarTrack (Belczynski et al., 2008) are used, except for WDs, NSs and BHs, where the values of BSE are assumed. If `qcflag` = 5, values similar to those used in COMPAS (Neijssel et al., 2019) are used. The mass transfers from stripped stars are always assumed to be dynamically stable. For WDs, NSs and BHs, the values of BSE are assumed.

mergers is another indicator for this phase of CE: these binaries would not have time to merge within the Hubble time due to the radiation of Gravitational Waves (GWs) if their initial separation was that of their progenitors' radii (see Eq. 1.10).

The phase of CE is probably the most uncertain of all, as a detailed treatment requires complex hydrodynamical simulations including physical processes with timescales orders of magnitude apart (see *e.g.* the review Ivanova et al. 2013). CE is triggered at the onset of unstable mass transfer, as described in Sec. 8.2.2. At that stage, the evolution of the binary occurs on a very short timescale. Both stars share their envelopes and their cores spiral in this environment because of dynamical friction, thus shrinking the orbit. In the mean time, the lost orbital energy of the binary is gradually transferred to the envelope, which expands in response, and can be partially or totally ejected. When it is the case, the effects of friction become less intense and the binary is left with the two cores of the progenitors, brought closer by the process. Note that the objects which are considered to have a *core* among the list in Tab. 8.1 are stars on the FGB, CHeB or on the AGB, He-GB, NSs and BHs, *i.e.* evolved stars or remnants (except WDs). As I discuss later, when one of the objects does not have a clear core, it can be destroyed instantaneously during the CE phase. In this scenario, CE therefore only occurs between an evolved, giant star and either another evolved star, or a stellar remnant.

A simplified treatment to determine the outcome of CE evolution is used in COSMIC, following the $\alpha\lambda$ formalism, which relies on a simple energy budget argument, as discussed below and originally proposed by Webbink (1984). Another formalism can be used, and was introduced by Nelemans et al. (2000), this time using a similar approach based on the loss of angular momentum during the spiral-in phase of the CE. It is referred to as the γ formalism, but I will not discuss it more here, as it is not included in COSMIC.

A fraction α_{CE} of the orbital energy is assumed to be lost when the donor core and the companion spiral in the CE. This energy is injected in the envelope and will affect its binding energy to the

core, by expanding it and possibly ejecting its outer parts:

$$\Delta E_{\text{bind}} = \alpha_{\text{CE}} \Delta E_{\text{orb}}. \quad (8.40)$$

Higher values of α_{CE} increase the likelihood of envelope ejection, while lower values favour core mergers during the CE phase, because the spiral-in phase can last longer. By definition, $0 \leq \alpha_{\text{CE}} \leq 1$, but values of $\alpha_{\text{CE}} > 1$ are also discussed in the literature (Fragos et al., 2019; Santoliquido et al., 2021). In particular, α_{CE} can be greater than 1 if some other energy source can contribute to the envelope expansion. The exact value of α_{CE} is, as of now, extremely uncertain. There is also *a priori* no reason for it to be universal, regardless of stellar types and structures, or even during the entire CE phase.

The other ingredient required to compute analytically the outcome of CE evolution is the binding energy of the envelope to the donor core E_{bind} . It is parametrized as follows:

$$E_{\text{bind}} = -\frac{GM_{\text{don}}M_{\text{env,don}}}{\lambda R_{\text{don}}}, \quad (8.41)$$

where M_{don} is the total mass of the donor star, R_{don} its radius and $M_{\text{env,don}}$ the mass of its envelope. The parameter λ can be understood as the ratio between the approximate value given by $-GMM_{\text{env}}/R$ and the true binding energy that should be computed as

$$E_{\text{bind}}^{\text{true}} = -\int_{M_c}^M \frac{Gm}{R(m)} dm, \quad (8.42)$$

where M_c is the mass of the core of the donor star. λ is also a measure of the stiffness of the mass-radius relation: lower values of λ correspond to stellar structures with a higher concentration of mass towards the center. Typically, λ is of order unity. Note that in the literature, several variations of this formulation are proposed, *e.g.* using M_{don} instead of $M_{\text{env,don}}$, and that caution must be taken in the exact interpretation of α_{CE} and λ when comparing the results of different studies. In COSMIC, λ can be set to a fixed value for all stellar types. Another possibility is to use tabulated values from fitting formulae depending on stellar types and the envelope mass, as described in the PhD thesis of Izzard (2004), which are based on simplified numerical simulations of stellar evolution and structure (Eggleton 1971, Pols et al. 1995). α_{CE} and λ are two model ingredients used by COSMIC, that are given by the parameters `alpha1` and `lambdaf`, respectively. Setting `lambdaf = 0` activates the stellar type-dependent expression of λ . The expressions used in COSMIC are detailed in the Appendix A of Claeys et al. (2014), and range between 0.25 and 0.75 for stars on the HG, between 1 and 2 for stars in the CHeB phase or on the FGB or the AGB, and $\lambda = 0.5$ for Helium stars. In our simulations, we use the variable definition of λ depending on stellar types, *i.e.* `lambdaf = 0`. In this case again, the parameters α_{CE} and λ are assumed to be universal, but some studies have pointed out that they may themselves be related to the orbital properties and the component masses at the beginning of the CE phase (see for example Davis et al. 2012).

In the literature, different prescriptions are taken for the calculation of the orbital energy E_{orb} . Two can be selected with COSMIC, using the parameter `ceflag`:

$$E_{\text{orb}} = -\frac{1}{2} \frac{GM_{\text{don}}M_{\text{comp}}}{a}, \quad (8.43)$$

using the total masses of the donor M_{don} and of the companion M_{comp} including the stellar envelopes as in de Kool (1990); or

$$E_{\text{orb}} = -\frac{1}{2} \frac{GM_{c,\text{don}}M_{c,\text{comp}}}{a}, \quad (8.44)$$

using the core masses noted with the subscript c, like in Hurley et al. (2002). In this second case, $M_{c,\text{comp}} = M_{\text{comp}}$ if the companion star has no core-envelope separation (*e.g.* a main sequence star).

Note that in this case, it is important to add the binding energy of the envelope of the companion (if a core-envelope boundary exists) to the total binding energy in Eq. 8.41, as in Eq. 69 in Hurley et al. (2002). We typically use `ceflag` = 1 in our simulations, therefore computing the orbital energy with the total masses.

Assuming that the envelope is entirely ejected at the end of the CE phase, $E_{\text{bind},f} = 0$ and that the mass of the companion (or its core when following Hurley et al. 2002) is unaffected by CE, it is therefore possible to solve for the final separation a_f using Eqs. 8.40, 8.41 and 8.43 or 8.44:

$$E_{\text{orb},f} = E_{\text{orb},i} + \frac{E_{\text{bind},i}}{\alpha_{\text{CE}}}. \quad (8.45)$$

In this expression, because of the envelope ejection, the final orbital energy $E_{\text{orb},f}$ is now computed using the two naked cores of the progenitor stars. Given the very short timescale of the CE phase, it is assumed that no accretion on either of the cores occurs in the process. Also, this step is numerically treated as instantaneous. When a binary enters a CE phase, its final properties are immediately inferred, in particular the naked core masses, and the final separation, using Eqs. 8.43 and 8.45.

The final separation a_f and the masses of the two remnants can then be used to compute their Roche radii R_L , using Eq. 8.32. If one of the remnants fills its Roche lobe, then it is assumed that there has been coalescence of the cores during the CE phase. It is also possible to enforce automatic mergers if CE occurs with a companion without clear core-envelope boundary (a MS star, a star on the HG, a He-MS or He-HG, or a WD), using the parameter `cemergeflag`. In this case, the entire companion is incorporated in the envelope of the donor and is simply destroyed. It cannot leave a remnant. Belczynski et al. (2008) argue that this is the most physically-motivated choice. In our work, we have explored both of these options and found that they play a significant role in the existence of some evolutionary channels (see Chapter 9). For the study presented in Chapter 9, we assume that companions are destroyed during CE when they do not have a core.

As introduced at the end of Sec. 8.2.2, in the case where the donor star is a stripped star and the accretor a NS or a BH, Tauris et al. (2015) have studied the phase of mass transfer in detail. In practice, it is possible to use the fitting formulae proposed in Tauris et al. (2015) to infer the final separation and the core mass in this case, using the flag `cehstarflag`. In this case, instead of using the expressions derived in the CE phase above, the final core mass of the donor $M_{\text{c,don},f}$ depends only on the initial donor mass $M_{\text{don},i}$ and the initial orbital separation $P_{\text{orb},i}$:

$$M_{\text{c,don},f} = M_{\text{don},i} \left(\frac{1}{400P_{\text{orb},i}} + 0.49 \right) - \left(\frac{0.016}{P_{\text{orb},i}} - 0.106 \right); \quad (8.46)$$

and the mass of Helium left in the envelope is before the SN of the stripped star is

$$M_{\text{env},f} = \begin{cases} 0.18P_{\text{orb},i}^{0.45} \left(\ln M_{\text{c,don},f}^4 - 1.05 \right) & \text{if } 0.06 \leq P_{\text{orb},i} \leq 2 \text{ days} \\ M_{\text{c,don},f} \left(\ln P_{\text{orb},i}^{-0.2} + 1 \right) + \ln P_{\text{orb},i}^{0.5} - 1.5 & \text{if } P_{\text{orb},i} > 2 \text{ days} \end{cases}. \quad (8.47)$$

Combining these equations, it is straightforward to deduce $M_{\text{env},f}$ and thus a_f using the expressions above. As *case BB* mass transfer is a robust feature of binary stellar evolution in the context of BNS formation, choosing to activate this option with `cehstarflag` impacts the properties of the compact object binaries.

8.2.4 Supernova Kicks

At the end of their evolution, stars explode and produce SNe, which play a major role in the evolution of binary systems, as their asymmetries give rise to natal kicks which are likely to unbind the binary. Depending on the progenitor masses, these SNe can involve different physical processes

that differ from the core-collapse introduced in Sec. 3.1, such as electron capture or pair instability. These SNe therefore have different properties, as we will see in this section.

During the SN, the stellar core collapses and produces a compact remnant: WD, NS or BH. Most of the progenitor mass in the outer layers is ejected in the process. This has a key consequence on the binary orbit. The instantaneous loss of mass by the system modifies the orbital properties of the binary and shifts its center of mass, in many cases unbinding the binary. For more details on how the binary is affected by the loss of mass, refer to the Appendix A1 in Hurley et al. (2002) which details these calculations.

In addition, because SNe ejecta are not perfectly spherically symmetric (see *e.g.* Janka & Mueller 1994; Burrows & Hayes 1996; Wongwathanarat et al. 2015), it is expected that the remnant of the exploding star should be given a natal kick from the conservation of angular momentum, which may also contribute to the disruption of the binary. Anisotropies in the neutrino emission may also contribute to the natal kicks of NSs and BHs (see *e.g.* Woosley 1987; Tamborra et al. 2014).

Natal kicks: Observations

Observational constraints on the typical values of the natal kicks of NSs are mostly based on the proper motion of young pulsars, which are believed to represent well the kick received at formation because their dynamics has not yet been too affected by their environment and the Galactic potential. By studying the proper motions of 233 Galactic pulsars using either pulsar timing methods or interferometry, and restricting the focus on the 73 youngest which were formed less than 3 Myr ago, Hobbs et al. (2005) found that their natal kicks are well reproduced by a Maxwellian distribution:

$$P(v_k) = \sqrt{\frac{2}{\pi}} \frac{v_k^2}{\sigma_k^3} \exp\left(-\frac{v_k^2}{2\sigma_k^2}\right), \quad (8.48)$$

with a dispersion $\sigma_k = 265 \text{ km} \cdot \text{s}^{-1}$. In COSMIC, this natal kick distribution is assumed for all Core-Collapse Supernova (CCSN) remnants, and σ_k can be provided by the user under the label `sigma`, and is typically set to the value found by Hobbs et al. (2005).

However, some other studies have suggested that a single Maxwellian may not be the most accurate representation of pulsar natal kicks. In a more recent study, Verbunt et al. (2017) used Very Long Baseline Interferometry (VLBI) observations of 19 pulsars younger than 10 Myr to constrain their proper motions. They find that a distribution with two Maxwellians at lower and higher velocities ($\sigma_{k,\text{low}} = 130 \text{ km} \cdot \text{s}^{-1}$ and $\sigma_{k,\text{high}} = 520 \text{ km} \cdot \text{s}^{-1}$) better fits the observed proper motions, which could hint to two different formation mechanisms (see the paragraph on reduced kicks). Other works also indicate the presence of two populations of pulsar velocities, and can be found in *e.g.* Giacobbo & Mapelli (2020).

These studies focus on observations of single pulsars. One additional source of uncertainty comes for SNe occurring in binary systems. It is indeed possible that due to tidal interactions with the companion, the successive SNe have different properties than those of single stars, in particular due to modified ejecta spatial distributions. This could affect the natal kicks of NSs and BHs in binary systems.

Eq. 8.48 also assumes that kick intensities are independent of their orientation. In fact, because of stellar rotation and of binarity, their orientation may be preferentially oriented in some directions. To study these effects in a systematic way, it is possible to manually specify the values for kick intensity and orientations with the parameter `natal_kick_array`, or to restrain the kick orientation to a certain polar angle with `polar_kick_angle`. We do not explore these possibilities in this work.

Natal kicks: Analytical models

Given all these uncertainties, a variety of models have been proposed to describe analytically the properties of NS and BH natal kicks, and many studies in the literature have discussed their impact

on the observed population of merging BNSs, NSBHs and BBHs.

[Giacobbo & Mapelli \(2020\)](#) propose a correction to the Maxwellian distribution found by [Hobbs et al. \(2005\)](#), by modulating the intensity of the natal kick depending on the mass m_{ej} ejected during the SN and on the remnant mass m_{rem} . Therefore, if $v_{\text{k,H05}}$ is a kick velocity randomly chosen in the Maxwellian distribution (Eq. 8.48) with $\sigma_{\text{k}} = 265 \text{ km} \cdot \text{s}^{-1}$, it will be modified following

$$v_{\text{k}} = v_{\text{k,H05}} \frac{m_{\text{ej}}}{\langle m_{\text{ej}} \rangle} \frac{\langle m_{\text{NS}} \rangle}{m_{\text{rem}}}, \quad (8.49)$$

where $\langle m_{\text{ej}} \rangle = 9M_{\odot}$ is the average ejecta mass and $\langle m_{\text{NS}} \rangle = 1.2M_{\odot}$ is the average NS mass. The kicks are therefore reduced for more massive remnants and lower ejected masses, and the binary is more likely to survive the SN.

Another prescription explored by [Giacobbo & Mapelli \(2020\)](#) is to only account for the ejected mass, so that

$$v_{\text{k}} = v_{\text{k,H05}} \frac{m_{\text{ej}}}{\langle m_{\text{ej}} \rangle}. \quad (8.50)$$

Alternatively, by using detailed single star and binary evolution using BPASS ([Eldridge et al., 2017](#); [Stanway & Eldridge, 2018](#)), [Bray & Eldridge \(2016\)](#) derive another expression for NSs' natal kicks that reproduces the observed proper motions studied by [Hobbs et al. \(2005\)](#):

$$v_{\text{k}} = \alpha \left(\frac{m_{\text{ej}}}{m_{\text{rem}}} \right) + \beta, \quad (8.51)$$

where $\alpha = 70 \text{ km} \cdot \text{s}^{-1}$ and $\beta = 120 \text{ km} \cdot \text{s}^{-1}$.

Those four options (proposed by [Hobbs et al. 2005](#), [Giacobbo & Mapelli 2020](#) and [Bray & Eldridge 2016](#)) can be explored in COSMIC using the flag `kickflag`.

Reduced natal kicks

In some cases, it has been hypothesized that SNe may generate lower natal kicks due to weaker explosion energies, which could explain the bimodal proper motion distributions found by *e.g.* [Bray & Eldridge \(2016\)](#). The most standard way that a single star may produce a NS or a BH is through CCSN (introduced in Sec. 3.1), where the most massive stars form a growing core of iron at the end of all nuclear fusions cycles, that ultimately exceeds the Chandrasekhar mass and collapses. The energy output of CCSNe and multi-scale turbulence allow for high ejecta velocities, large asymmetries and therefore, high kick velocities (see *e.g.* results using hydrodynamical simulations of CCSNe by [Wongwathanarat et al. 2013](#) or neutrino-driven CCSNe by [Janka 2017](#)).

In parallel, another type of SN has been proposed as early as 1980 ([Miyaji et al., 1980](#)): Electron-Capture Supernova (ECSN). [Ivanova et al. \(2008\)](#) studied the population of NSs formed via ECSN in globular clusters and provide a review of this process (see their Sec. 2.1.2), that can be summarized as follows. If a degenerate Oxygen-Neon-Magnesium (ONeMg) core reaches a critical mass $M_{\text{ECSN}} = 1.38M_{\odot}$ ([Nomoto 1984, 1987](#)), the electrons in this core are captured by ^{24}Mg and ^{20}Ne before the next fusion cycle producing iron. Therefore, the degeneracy pressure of the electrons drops and the support of the core against gravity cannot be maintained, leading to a collapse. The difference with a CCSN is that the explosion energy is much lower for an ECSN, as shown in numerical simulations (*e.g.* [Kitaura et al. 2006](#); [Dessart et al. 2006](#)). Consequently, the Standing Accretion Shock Instability (SASI, [Foglizzo 2002](#)) – which is at the origin of the asymmetries in CCSNe and leads to high natal kicks (*e.g.* [Blondin & Mezzacappa 2007](#)) – fails to develop, and the resulting kicks are much smaller (typically more than 10 times smaller, according to [Ivanova et al. 2008](#)).

In theory, there are 3 ways ECSNe can occur:

- Single stars with initial masses of $7 - 10M_{\odot}$ can develop degenerate ONeMg cores. For more massive stars with $M \gtrsim 10M_{\odot}$, oxygen, neon and magnesium can undergo nuclear fusion in non-degenerate conditions to produce an iron core, and for less massive stars, the ONeMg core cannot form in the first place. For stars in binary systems, with mass transfer episodes, this mass range can be significantly increased. It has been found that the key condition for a degenerate ONeMg core to develop is the He core mass at the start of the AGB. However, the range of He core masses that lead to ECSNe events is still uncertain. Typical values that can be found in the literature are $1.6 - 2.25M_{\odot}$ (Hurley et al., 2002); $1.4 - 2.5M_{\odot}$ (Podsiadlowski et al., 2004); $1.85 - 2.25M_{\odot}$ (Belczynski et al., 2008); $2 - 2.5M_{\odot}$ (Andrews et al., 2015). COSMIC allows to manually indicate this mass range with the parameters `ecsn` and `ecsn_mlow`.
- A degenerate ONeMg WD in a binary system can accrete CO or ONe material from its companion until it reaches M_{ECSN} (e.g. Nomoto & Kondo 1991, Saio & Nomoto 2004, Dessart et al. 2006). This type of event is called Accretion-Induced Collapse (AIC). Low kicks in case of AIC events can be enabled in COSMIC using the flag `aic`. I will discuss in Sec. 9.3.3 binary systems that include an AIC. As I also highlight in Sec. 9.5, an evolutionary track for the formation of BNSs which includes an AIC may be dominant at high redshifts.
- Finally, the merger of two WDs can theoretically also generate an ECSN.

In the formation pathways of BNS and NSBH in the isolated binary scenario, ECSN can occur in the first two cases (the merger of two WDs does not produce a new compact object binary). These cases in majority lead to the production of NSs, hence ECSNe are not expected to occur during the evolution of BBHs progenitors. AIC also appears in some formation channels of BNSs as will be discussed in Chapter 7. As most population synthesis models tend to overestimate the predicted BBH merger rate compared to the BNS rate that is observed, the existence of reduced kicks for some of the NS progenitors may be the condition to reconcile these quantities, by allowing more BNS systems to form.

During binary evolution, episodes of mass transfers can occur, in particular as one of the stars reaches the AGB. In such cases, it can happen that the star is stripped of its hydrogen envelope, either through RLOF or CE, as also introduced in Sec. 3.1. When that happens, the helium stellar core is left *naked*, and these stars are often referred to as *stripped stars/cores*, or *naked helium stars/cores*. Typically, their masses are roughly $\sim 1.5M_{\odot}$ (Tauris et al. 2013, 2015). All fusion cycles can occur in the core of stripped stars, depending on their mass. They can therefore explode in SNe. Because the mass of material ejected in such events is much lower than in classical CCSNe, it is also expected that the natal kicks resulting from such SNe are also reduced. Stripped stars exploding in SNe are usually referred to as Ultra-Stripped Supernovae (USSNe). Using the flag `ussn` in COSMIC, it is also possible to sample reduced kicks in the case of such events.

For all the scenarios mentioned here, the parameter `sigmadiv` in COSMIC allows to sample kicks on a Maxwellian distribution with a (common and unique) reduced dispersion, that is typically set to $\sigma_{k,\text{low}} = 20 \text{ km} \cdot \text{s}^{-1}$. This is the value that is used in our simulations.

Natal kick modulation for BHs

Natal kicks received by BHs are much less constrained observationally than those of NSs (see e.g. Wong et al. 2014; Giacobbo & Mapelli 2020 and references therein). Different theoretical studies have indicated that BH natal kicks may follow different distributions than NS natal kicks. In particular, Fryer et al. (2012) studied the mass and velocity distributions of BHs using semi-analytical descriptions of the SNe. They specifically highlight two extreme regimes: the *rapid* and *delayed* regimes, characterised by the delay of shock revival. At the onset of the CCSN, the iron core collapses, leading to electron capture onto the iron nuclei, thus removing the force induced by the electron degeneracy pressure that counteracted the gravitational force. The collapse of the iron core thus occurs in a few hundreds of milliseconds. It halts when the compression is high

enough that nuclear forces provide a new pressure-induced force to balance gravity. At that stage, neutron degeneracy pressure also has a similar effect and a so-called proto-NS is formed. Because the collapse of the core stops abruptly, infalling material bounces on the proto-NS and a shock propagates outwards. It then stalls when most of its energy is lost. Between the proto-NS and the region where the shock stalls, several instabilities appear (*e.g.* Rayleigh-Taylor instability, SASI) and can be used to convert the neutrino flux coming from the proto-NS into kinetic energy, that is in turn used to revive the shock. If this energy overcomes that of infalling stellar material, the envelope is entirely ejected and the SN is successful. In the *rapid* scenario, shock revival occurs in less than 250 ms after the bounce, whereas in the *delayed* scenario, it can take much longer.

During the phase of shock stalling and revival, some material may fall back onto the proto-NS, thus increasing the mass of the remnant (no matter if it is a NS or a BH). Fryer et al. (2012) provide fitting formulae for the mass fraction of stellar envelope that falls back onto the compact remnant, f_{fb} in the *rapid* and *delayed* scenarios. Because this fraction of mass is not ejected during the SN, it is expected that the kicks are more damped as f_{fb} increases. Fryer et al. (2012) modulate the BH natal kicks using the simple approximation

$$v_{\text{k}} = (1 - f_{\text{fb}}) \times v_{\text{k,H05}}. \quad (8.52)$$

Another suggested option is that the kick intensities simply scale down proportionally to the BH mass:

$$v_{\text{k}} = \frac{m_{\text{max,NS}}}{m_{\text{BH}}} \times v_{\text{k,H05}}, \quad (8.53)$$

where $m_{\text{max,NS}}$ is the maximal NS mass, that I discuss in Sec. 8.2.5. In theory, f_{fb} can also vary with mass. In particular, the most massive stars are expected to collapse directly into BHs without a transient proto-NS phase. In this case, the entire envelope is expected to fall back into the BH, $f_{\text{fb}} = 1$ and the BH is given no kick upon formation. Fallback also modifies the mass of the remnant, as discussed in Sec. 8.2.5.

In COSMIC, if `kickflag` is set such that the kicks are sampled following Hobbs et al. (2005), it is possible to scale them down using Eq. 8.52 or Eq. 8.53; with the flag `bhflag`. It is also possible to assume that BHs are given no natal kicks at formation, or that they simply follow Hobbs et al. (2005), again using `bhflag`. Additionally, it is possible to manually correct the Maxwellian dispersion σ_{k} by a constant fraction for BH remnants, using the parameter `bhsigmafrac`.

8.2.5 Miscellaneous

Remnant masses

At the end of stellar evolution, the mass of the remnant formed after a SN is calculated. In the original version of BSE, the mass of the NS or BH remnant is given by Eq. 92 in Hurley et al. (2000):

$$\frac{M_{\text{rem}}}{M_{\odot}} = 1.17 + 0.09 \frac{M_{\text{c}}}{M_{\odot}}, \quad (8.54)$$

where M_{c} is the carbon-oxygen core mass of the progenitor right before SN. As identified by Belczynski et al. (2002), this prescription leads to very small remnant masses, especially for BHs, even when the ZAMS mass of the progenitor is very high. They instead proposed another expression of the remnant mass that depends on both the mass of carbon-oxygen M_{CO} and the mass of iron-nickel M_{FeNi} in the core:

$$M_{\text{rem}} = \begin{cases} M_{\text{FeNi}} & \text{if } M_{\text{CO}} \leq 5 M_{\odot} \\ M_{\text{FeNi}} + f_{\text{fb}}(M - M_{\text{FeNi}}) & \text{if } 5 M_{\odot} \leq M_{\text{CO}} \leq 7.6 M_{\odot} \\ M & \text{if } M_{\text{CO}} \geq 7.6 M_{\odot} \end{cases}. \quad (8.55)$$

In this expression, the amount of fallback material from the envelope increases with the core mass, and for the most massive stars, the remnant BH contains all the pre-SN material. In a revision in [Belczynski et al. \(2008\)](#), the authors update the expression of M_{FeNi} as a function of M_{CO} , included in Eq. 8.55. Note that these three prescriptions were initially suggested only for progenitors with solar metallicity, and that their usage for sub-solar metallicity SNe is highly uncertain. As introduced in Sec. 8.2.4, [Fryer et al. \(2012\)](#) described the *rapid* and *delayed* mechanisms for SN explosions which impact the amount of material falling back onto the remnant and therefore, its final mass. At solar metallicity, this difference is minor.

These different models for the determination of the remnant mass can be used in COSMIC, using the flag `remnantflag`. They are crucial in the determination of the mass spectrum of the population of BBH. In this thesis, I focus on BNSs where the mass of the NSs is still poorly understood today. However, given constraints on the NS stability, the mass range covered by NSs is reduced to $1 M_{\odot} \lesssim M_{\text{NS}} \lesssim 3 M_{\odot}$ (depending on the equation of state), with most simulations producing NSs with masses $\sim 2.2 M_{\odot}$. Given the uncertainties in NS masses in link with the progenitor properties, we choose not to study in depth the statistics of NS masses when analysing our results and typically use the *delayed* prescription of remnant masses.

In addition, it has been proposed that there exist two *mass gaps* where compact objects cannot form:

- The lower mass gap, $2 \lesssim M/M_{\odot} \lesssim 5$ at the limit between the maximum NS mass possible for a given equation of state, and a potential lower limit for BH masses (see *e.g.* [Bailyn et al. 1998](#); [Özel et al. 2010](#); [Fryer et al. 2012](#)). Already, the detection of some NSs with masses within this mass gap hinted that it may not exist in reality ([de Sá et al. 2022](#), see also the review [de Sá et al. 2023](#)). The recent GW observation of GW 190814 ([Abbott et al., 2020c](#)) and other GW events during O3 with a component in the lower mass gap further challenged this model ([Farah et al., 2022](#); [Ye & Fishbach, 2022](#)). Concerning the range of remnant mass $2 \lesssim M/M_{\odot} \lesssim 5$, the question is now more to understand *what* is the remnant, rather than *if* a remnant forms. Indeed, some numerical simulations have suggested that in this range of remnant mass, there is no clear transition from NSs to BHs but rather a discontinuous alternation between both types. In population synthesis models, this effect is not accounted for yet, which is an important approximation. In COSMIC, the parameter `mxns` sets the maximum mass for NSs $M_{\text{max,NS}}$, above which all remnants are assumed to be BHs. Typically, $M_{\text{max,NS}} = 3 M_{\odot}$.
- The upper mass gap, $60 \lesssim M_{\text{BH}}/M_{\odot} \lesssim 120$ is the range where Pair Instability Supernova (PISN) and pulsational PISN SNe can occur. The higher and lower limits of this mass gap are still poorly constrained (see [Woosley & Heger 2021](#) and references therein). This mass gap has been explored with numerical simulations of SNe and is more robust than the lower mass gap. In this mass range, during the collapse of the progenitor, gamma-ray photon interaction produces electron-positron pairs (see also Sec. 5.4.7). This immediately increases the temperature and the pressure in the collapsing star, allowing for more material to undergo nuclear fusion, in a runaway process that leads to a thermonuclear explosion, totally destroying the progenitor: this is the PISN. For slightly lower-mass progenitors, a new equilibrium can be reached at the ignition of additional nuclear fusion and the star simply expels parts of its envelope. When it collapses again, the process repeats, and the star gradually loses its mass in pulses, until it finally collapses when its mass is lower than the upper mass gap: this is the *pulsational* PISN ([Woosley, 2017](#)). At lower masses, progenitors undergo usual CCSN, while above the upper mass gap, photo-disintegration prevents the surge of pressure and the progenitor promptly collapses as a BH. As a result, it is expected that no BHs can form directly in the range of mass of the upper mass gap. As discussed in Chapter 7, the observation of GWs from some systems with one component in the upper mass gap suggests that at least part of

the population of merging BBHs is formed in dynamically active regions where they can grow in mass after their formation. In COSMIC, several prescriptions can be used to determine whether a star is in the upper mass gap, and if it will undergo a pulsational PISN, in which case the remnant mass is also affected. These prescriptions are activated with the flag `pisn` and described in detail in Breivik et al. (2020), but obviously do not affect the properties of the BNS systems that we study.

A note on metallicity

Stellar metallicity is defined as the mass fraction of metals in the star composition, where we name *metals* all elements besides hydrogen and helium.

As discussed multiple times throughout this chapter, metallicity plays a significant role in shaping the products of stellar evolution in binaries. The impact of metallicity on the evolutionary tracks of BNS progenitors will be discussed in Chapter 9. As of now, COSMIC can only evolve systems whose metallicity is above $Z_{\min} = 10^{-4}$. Below this value, some assumptions fail and it is thought that the description of stellar evolution differs.

In this context, an important parameter is the exact value of solar metallicity Z_{\odot} , as most relations introducing a metallicity-dependence are scaled with respect to solar metallicity. However the exact determination of this value requires to understand in detail the composition of the Sun. Anders & Grevesse (1989) have originally inferred that $Z_{\odot} = 0.02$ using models of solar compositions calibrated to abundance observations (they therefore inferred the bulk metallicity). In a more recent work, Asplund et al. (2009) have revised this value to $Z_{\odot} = 0.014$, this time calibrating their results on observations from the outer convective region. In all studies prior to these updates, the default value for solar metallicity was $Z_{\odot} = 0.02$. In COSMIC and most recent works, $Z_{\odot} = 0.014$. Z_{\odot} is a parameter of COSMIC parsed via `zsun`.

Evolution sampling

Depending on the stellar type, three parameters in COSMIC define which time step to use for each iteration of the binary evolution (and thus also single star evolution). They are defined as the ratio between the desired time step and the estimated time spent by the star in that evolutionary stage. The parameter `pts1` sets the sampling for evolution on the MS; `pts2` the sampling for stars on the giant branch (FGB, CHeB, EAGB, TPAGB, He-GB); and `pts3` the sampling for stars on the HG, He-MSs and He-HG. As highlighted in Banerjee et al. (2020), care must be taken when setting these parameters. Too large time steps will indeed introduce unphysical deviations to the actual stellar tracks computed for single star evolution, while too small time steps will lead to needlessly long computation times. As can be seen in their Fig. 5, some spikes in the remnant masses appear at low metallicities and high ZAMS masses, when using the default values suggested in Hurley et al. (2000). They suggest to use `pts1 = 0.001`, `pts2 = 0.01` and `pts3 = 0.02` to optimise accuracy and computation time, which is a factor 50 increase in time sampling for MS stars compared to Hurley et al. (2000). These values are used by default in COSMIC. For BNS progenitors, it is possible to reduce the sampling, as the accuracy remains good even at the lowest metallicities. This allows for a quicker computing speed.

8.3 Summary of COSMIC Parameters

In this section, I summarize the different flags and parameters used in COSMIC and reference where they are first described and introduced. I provide the reference values we use in our standard model which will be used in Chapter 9. The version of COSMIC used throughout this work is v3.4.0⁵. In the following tables, I use the convention that the reference values for flags are noted as integers, and the values for physical parameters (usually directly used in an equation) are specified as decimal numbers. When a parameter is not defined in an equation, I provide the link to its first occurrence in the chapter.

Zero-Age Main Sequence (ZAMS) properties (Sec. 8.1)

Parameter	Value	Defined in	Description
sampling_method	independent	Sec. 8.1	Select if the initial parameters at ZAMS are drawn independently or following Moe & Di Stefano (2017)
primary_model	kroupa01	Eqs. 8.1 – 8.3	Model of primary mass distribution
porb_model	sana12	Sec. 8.1	Model of initial separations
ecc_model	sana12	Sec. 8.1	Model of eccentricity distribution
qmin	−1	Sec. 8.1	Minimum mass ratio ^a
m2_min	–	Sec. 8.1	Minimum secondary mass ^b
binfrac_model	0.5	Sec. 8.1	Fraction of stars in binary systems

Tab. 8.4: Parameters for the initial sampling of the population of stellar progenitors at ZAMS. ^aqmin= −1 sets the variable minimal mass ratio depending on the mass of the primary discussed in Sec. 8.1. ^bqmin and m2_min cannot be used simultaneously.

Wind flags (Sec. 8.2.1)

Parameter	Value	Defined in	Description
windflag	3	Sec. 8.2.1	Select the model for wind mass loss for each star
neta	0.5	Eq. 8.12	η : Kudritzki & Reimers (1978) mass-loss coefficient
bwind	0.0	Eq. 8.13	B_W : Binary-enhanced mass loss parameter.
hewind	0.5	Sec. 8.2.1	$(1 - \mu)$: Naked helium star mass loss parameter
eddlimflag	0	Eqs. 8.21 – 8.24	Adjust or not metallicity dependence for stars near the Eddington limit
acc2	1.5	Eq. 8.25	α_{wind} : Bondi & Hoyle (1944) wind accretion factor
beta	−1	Eqs. 8.27 – 8.30	β_{wind} : Wind velocity factor
xi	0.5	Eq. 8.31	μ_{wind} : Angular momentum transfer

Tab. 8.5: Parameters and flags related to the treatment of stellar winds. The first 5 parameters are used in single-star wind description, whereas the 3 last parameters are used in the description of the wind interaction with the secondary. hewind is active only if windflag = 0 (BSE wind description). With beta = −1, Eq. 8.30 is used.

⁵Available on <https://github.com/COSMIC-POPSYNTH/COSMIC/tree/v3.4.0>. See the documentation on <https://cosmic-popsynth.github.io/>.

Roche Lobe Overflow (RLOF) and Common Envelope (CE) (Sec. 8.2.2 and 8.2.3)

Parameter	Value	Defined in	Description
qcflag	5	Tab. 8.3	Select the model to determine the critical mass ratios between stable and unstable mass transfers
qcrit_array	^a	–	User-input critical mass ratios
alpha1	1.0	Eq. 8.40	α_{CE} : CE efficiency parameter
lambdaf	0	Eq. 8.41	λ : Binding energy factor for CE evolution ^b
ceflag	1	Eqs. 8.43 – 8.44	Compute the orbital energy with total or core masses
cekickflag	2	–	Use post- or pre-CE values of mass and separation if a SN occurs during CE
cemergeflag	1	Sec. 8.2.3	Determine whether stars that begin a CE without a distinct core-envelope boundary automatically lead to merger in a CE
cestarflag	0	Eqs. 8.46 – 8.47	Use or not the fitting formulae from Tauris et al. (2015) during RLOF from a stripped star

Tab. 8.6: Parameters and flags related to the treatment of mass transfers and CE. ^aqcrit_array can be used to enter user-specified critical mass ratios for each stellar type. It is a table with 16 elements corresponding to the stellar types described in Tab. 8.1. ^blambdaf = 0 sets the stellar-type dependent values of Claeys et al. (2014).

Supernova (SN) kicks (Sec. 8.2.4)

Parameter	Value	Defined in	Description
kickflag	0	Eqs. 8.48 – 8.51	Set the particular natal kick prescription to use
sigma	265.0	Eq. 8.48	σ_{k} : Dispersion for the Maxwellian distribution of natal kicks
bhflag	1	Eqs. 8.52 – 8.53	Sets the model of SN kicks for BHs
bhsigmafrac	1.0	Sec. 8.2.4	Scale down σ for BHs by this factor
polar_kick_angle	90	Sec. 8.2.4	Opening angle of the SN kick relative to the pole of the exploding star
natal_kick_array	^a	Sec. 8.2.4	User-input values for the SN natal kick
sigmadiv	–20.0	Sec. 8.2.4	Set the modified ECSN kick strength
ecsn	2.25	Sec. 8.2.4	Maximum helium star mass for ECSN
ecsn_mlow	1.6	Sec. 8.2.4	Minimum helium star mass for ECSN
aic	1	Sec. 8.2.4	Reduce kicks for AIC
ussn	1	Sec. 8.2.4	Reduce kicks for USSNe

Tab. 8.7: Parameters and flags related to the treatment of SN kicks. The first 6 parameters are used for standard CCSN kicks, while the last 5 parameters are related to the use of reduced kicks. sigmadiv, bhflag, bhsigmafrac, aic and ussn are only active when kickflag = 0. ^anatal_kick_array is a 2×5 array containing user-specified values for the kick parameters (v_{k} , co-lateral polar angle, azimuthal angle, mean anomaly, random seed) for the primary and the secondary star.

Remnant masses

Parameter	Value	Defined in	Description
<code>pisn</code>	-2	Sec. 8.2.5	Model for the PISN progenitor core mass range
<code>remnantflag</code>	3	Eqs. 8.54 – 8.55	Remnant mass prescription used for NSs and BHs
<code>mxns</code>	3.0	Sec. 8.2.5 – 8.53	Maximum mass for NSs / Minimum mass for BHs
<code>rembar_massloss</code>	0.5	–	Correction factor to the baryonic mass of the remnant due to the energy loss in neutrinos

Tab. 8.8: Parameters and flags related to the treatment of remnant masses.

Solar metallicity

Parameter	Value	Defined in	Description
<code>zsun</code>	0.014	Sec. 8.2.5	Value of solar metallicity

Tab. 8.9: Parameter for solar metallicity.

Sampling

Parameter	Value	Defined in	Description
<code>pts1</code>	0.001	Sec. 8.2.5	Relative time step for MS stars,
<code>pts2</code>	0.01	Sec. 8.2.5	for FGB, CHeB, EAGB, TPAGB, He-GB stars,
<code>pts3</code>	0.02	Sec. 8.2.5	for HG, He-MSs and He-HG stars

Tab. 8.10: Parameters defining the sampling discretization. They represent the time step for each iteration, relative to the estimated lifetime of the star in its given evolutionary stage.

Other parameters not discussed here

Parameter	Value	Description
bhspinflag	0	Prescription for BH spin at formation
bhspinmag	0.0	BH spin value or upper limit of the uniform distrib. of BH spins
grflag	1	Activate orbit evolution from the emission of GWs
eddfac	1.0	Eddington limit factor for mass transfer
gamma	-2	Angular momentum prescriptions for mass lost during RLOF at super-Eddington rates
don_lim	-1	Model for the rate of mass loss through RLOF
acc_lim	-1	Limit the amount of mass accreted during RLOF
tflag	1	Activate tidal circularization
ST_tide	1	Use Belczynski et al. (2008) for tides prescription
fprimc_array	^a	Control the scaling factor for convective tides
ifflag	0	Activate initial-final WD mass relation
wdflag	1	Model for the WD cooling law
epsnov	0.001	Fraction of accreted matter retained in a nova eruption
bdecayfac	1	Model for accretion-induced field decay of pulsars
bconst	3000	Parameter for magnetic field decay timescale for pulsars
ck	1000	Other parameter for magnetic field decay timescale for pulsars
rejuv_fac	1.0	Mixing factor in MS star collision
rejuvflag	0	Model to use for the mixing in MS star collision
bhms_coll_flag	0	Allow stars colliding with BH to not be destroyed if $M_{\text{star}} > M_{\text{BH}}$
htpmb	1	Model for magnetic breaking
ST_cr	1	Model for convective vs. radiative boundaries

Tab. 8.11: bhspinflag and bhspinmag tackle the remnant spins; grflag the orbital decay by emission of GWs; eddfac, gamma, don_lim and acc_lim the properties of stable mass transfer; tflag, ST_tide and fprimc_array the effects of tides on the components of the binary; ifflag, wdflag and epsnov are related to WDs; bdecayfac, bconst and ck treat the physics of pulsars; rejuv_fac, rejuvflag and bhms_coll_flag are mixing variables; htpmb a model selection for magnetic breaking; and ST_cr selects the model for the limit between convective and radiative envelopes. ^afprimc_array is an array with 16 elements corresponding to the scale factors for each stellar type.

Chapter 9

The Evolutionary Tracks of Merging Binary Neutron Stars

Contents

9.1	Binary Stellar Evolution Modelling with COSMIC	156
9.1.1	Model Parameters	156
9.1.2	Sampling Protocol	157
9.2	Evolutionary Sequences Classification Method	158
9.3	Evolutionary Tracks	161
9.3.1	“Standard” Evolution	161
9.3.2	Equal-mass binaries	163
9.3.3	Accretion-Induced Collapse	165
9.4	Population Properties	167
9.4.1	Properties of the Evolutionary Tracks	167
9.4.2	Impact of Metallicity on the Evolutionary Tracks	172
9.4.3	Other Possible Model Choices	176
9.5	Evolution of the Merger Rate with Redshift	176
9.5.1	Computing the Merger Rate Density	176
9.5.2	The Stochastic Gravitational Wave Background from Binary Neutron Star Mergers	178
9.5.3	Results for the Binary Neutron Star Merger Rate	179
9.6	Astrophysical Consequences: a Population of Short Delay Times	180

We use COSMIC (Breivik et al. 2020, see Chapter 8) to study the properties of Binary Neutron Star (BNS) mergers across cosmic times. In this chapter, I briefly summarize our choices of model parameters in Sec. 9.1, before presenting our method to separate the population in several evolutionary tracks (Sec. 9.2), that I describe in more detail in Sec. 9.3. In Sec. 9.4, I discuss the physical properties of the BNS progenitors at Zero-Age Main Sequence (ZAMS) and of the BNS systems upon formation. Sec. 9.5 describes our analysis of the merger rate variation with redshift. Finally, I discuss the astrophysical consequences of this work in Sec. 9.6. We specifically study the sub-population of short delay times binaries (see also Sec. 6.4) and the corresponding evolutionary tracks, and show how this population may exist at high redshift. The results presented hereafter will soon be submitted in Pellouin et al. (2023), **in prep.** In Sec. 9.5.2, I also present the results from **Publication III** (Appendix E.3, Lehoucq et al. 2023) where the simulated population of BNSs is used to compute the stochastic Gravitational Wave (GW) background.

It is *a priori* impossible to determine which is the evolutionary track that will be followed by the binary solely based on the initial masses, separation, eccentricity and metallicity, which also motivates our choice to rely on population synthesis for this study.

Throughout this section, I will sometimes refer to the indicators used in COSMIC for the stellar types and the evolutionary stages that mark the binary history. The stellar types were defined in Tab. 8.1, and the evolutionary stages are defined in Tab. 9.1.

Indicator	Evolutionary State
1	Initial state
2	Change of stellar type
3	Beginning of a phase of Roche Lobe Overflow (RLOF)
4	End of a phase of RLOF
5	Contact between the 2 stars
6	Coalescence
7	Beginning of a phase of Common Envelope (CE)
8	End of a phase of CE
9	No remnant leftover
10	Maximum evolution time reached
11	Binary disruption
12	Beginning of a symbiotic phase
13	End of a symbiotic phase
14	Blue straggler
15	Supernova (SN) of the primary
16	SN of the secondary

Tab. 9.1: `evol_type` indicators used in COSMIC. They mark the key evolutionary stages of the binary evolution at which data is saved.

9.1 Binary Stellar Evolution Modelling with COSMIC

9.1.1 Model Parameters

For this study, we rely on the physical models included in COSMIC. We choose to set the values of the parameters and flags to those reported in Tabs. 8.4 – 8.11. Note that for some of them, this does not correspond to the default values for the version of COSMIC used for this study, v.3.4.0. I describe our most important choices in the following paragraphs.

We initialize the population of binaries assuming a primary mass distribution following Kroupa (2001), and sample the initial separations and eccentricities following the distributions of Sana et al.

(2012), as defined in Sec. 8.1. We therefore assume that these three quantities are independent. We also assume a binary fraction of 50%, though this quantity does not affect the results of population synthesis directly and can be modified later (see Eq. 9.6 and Sec. 9.5).

We use the default parameters for the treatment of winds, following the mass-loss rate formulae summarized in Eqs. 8.7 – 8.10 and in Sec. 8.2.1. In particular, we do not include Eddington-limited winds from 8.24 as discussed in [Giacobbo et al. \(2018\)](#). This can be added in a later comparative study.

During the phase of CE, we fix $\alpha_{\text{CE}} = 1$ and use the stellar type-dependent values of λ as discussed in Sec. 8.2.3 and [Claeys et al. \(2014\)](#). For this study, we assume that mass transfer from stripped stars is always dynamically stable, *i.e.* a critical mass ratio between stable and unstable mass transfer $q_{\text{crit}} = +\infty$ in these cases, as also assumed in COMPAS ([Neijssel et al., 2019](#)). We explored other options for the value of `qcflag` which selects the choice of values for q_{crit} depending on the stellar types. Some of the results are presented in Sec. 9.4.3. Finally, we assume that companions without a clear core-envelope boundary entering a phase of CE are instantly destroyed ([Belczynski et al., 2008](#)). As discussed in Sec. 9.4.3, this removes some evolutionary tracks in the total population of BNSs.

We sample SN kicks following the Maxwellian distribution (Eq. 8.48) with $\sigma_{\text{k}} = 265 \text{ km} \cdot \text{s}^{-1}$ ([Hobbs et al., 2005](#)); and with an isotropic distribution of orientations. However, for Ultra-Stripped Supernovae (USSNe), Electron-Capture Supernovae (ECSNe) and the Accretion-Induced Collapse (AIC) of a White Dwarf (WD) into a Neutron Star (NS), we assume that the kick velocities are much reduced and instead use $\sigma_{\text{k, low}} = 20 \text{ km} \cdot \text{s}^{-1}$ (see Sec. 8.2.4 for more details).

We model the remnant mass assuming the *rapid* scenario ([Fryer et al., 2012](#)), which naturally introduces a mass gap between NSs and Black Holes (BHs). For comparison, we also explored the *delayed* scenario, as shown in Sec. 9.4.3.

Finally, the solar metallicity is assumed to be $Z_{\odot} = 0.014$ ([Asplund et al., 2009](#)), and all other quantities that do not impact the properties of the BNS systems that we follow are set to their standard values (see Tab. 8.11).

The goal of this study is not to perform a systematic sampling of the possible parameter values; but rather to focus on one physically-motivated model with standard values and focus – for this model – on the evolutionary tracks that lead to the formation of BNSs.

9.1.2 Sampling Protocol

We create a grid of metallicities ranging from $Z = 9.5 \times 10^{-5}$ ($6.8 \times 10^{-3} Z_{\odot}$, the minimum metallicity allowed in BSE ([Hurley et al., 2002](#)) and thus in COSMIC) to 0.028 ($2Z_{\odot}$). In practice, this last metallicity bin is not used in our calculation of the merger rate (see Sec. 9.5), and the details of stellar evolution at super-solar metallicities are more uncertain; but we keep this bin for our study of Binary Stellar Evolution (BSE). The metallicity grid we use is thus 0.000095; 0.00014; 0.00021; 0.0003; 0.00044; 0.00065; 0.00095; 0.0014; 0.0021; 0.003; 0.0044; 0.0065; 0.0095; 0.014(; 0.028), *i.e.* 14 (15) metallicity values.

For each of these metallicities, we sample and evolve 9.55×10^9 binaries using the model parameters described in Sec. 9.1. We do not use the `match` feature of COSMIC that automatically stops the sampling once the properties of the BNS masses and/or separations and/or eccentricities have converged to a stable distribution (for a more complete description, see [Breivik et al. 2020](#)). While this feature is useful to ensure the properties of the final sample of BNSs are statistically robust, it makes the direct comparison between populations at several metallicities more complex. In our case, we decide to use a single random seed across all metallicities, meaning that the initial population is the same for all metallicities. For a given binary, the stochastic processes such as SN kick intensity and orientations are also seeded, which means that a direct comparison between individual binary systems across the metallicity bins is possible. A potential downside of our approach is that in some

metallicity bins, the total number of BNS systems may be quite low ($\sim 10^4$) and thus the studied distributions slightly biased by the random seed. For a more accurate simulation, the random seed should also be varied across metallicities, but this is not expected to impact the results provided the BNS sample is large enough.

We store the information of all binaries that produce BNS systems that remain gravitationally bound (*i.e.* successful BNS formation). Some of them have initial orbital properties (separation and eccentricity) that prevent them from merging within the Hubble time (see Chapter 7). We mark them as non-merging systems and remove them from our study. Note however that this population of non-merging binaries is expected to contribute to the population of BNSs observed in the Milky Way for example (see Sec. 3.2). It could therefore be possible to use the complete sample in a future joint study between the merging BNS population and the Galactic population, as discussed in Chapter 10. Additionally, when studying these long-delay time systems, we find that the evolutionary tracks that lead to their formation can be different than those producing shorter-separation binaries. This is thus of interest in the context of the study of binary stellar evolution, as I also discuss below.

9.2 Evolutionary Sequences Classification Method

tphys	mass_1	mass_2	kstar_1	kstar_2	sep	ecc	evol_type
0.00	8.49	7.69	1	1	223.59	0.38	1
33.48	8.48	7.69	2	1	223.65	0.38	2
33.56	8.48	7.69	2	1	137.87	0.00	3
33.60	6.94	9.23	3	1	138.62	0.00	2
33.60	5.76	10.41	4	1	156.87	0.00	2
33.81	1.90	14.27	4	1	725.27	0.00	4
33.99	1.87	14.29	7	1	723.45	0.00	2
38.71	1.87	14.29	8	1	723.81	0.00	2
39.19	1.87	14.29	9	1	723.89	0.00	2
39.20	1.87	14.29	9	1	721.10	0.00	3
39.27	1.83	14.32	9	1	741.81	0.00	15
39.27	1.19	14.32	13	1	2658.22	0.72	2
39.27	1.19	14.32	13	1	2658.22	0.72	4
41.82	1.19	14.32	13	2	2657.28	0.72	2
41.86	1.19	14.32	13	4	2657.36	0.72	2
43.32	1.19	14.20	13	4	737.33	0.00	3
43.32	1.19	14.20	13	4	737.33	0.00	7
43.32	1.19	5.20	13	7	2.49	0.00	8
43.32	1.19	5.20	13	7	2.49	0.00	4
44.36	1.19	5.15	13	8	2.43	0.00	2
44.42	1.19	5.14	13	8	2.41	0.00	3
44.43	1.19	5.13	13	8	2.40	0.00	16
44.43	1.19	1.46	13	13	4.16	0.43	2
44.43	1.19	1.46	13	13	4.16	0.43	4
5018.03	1.19	1.46	13	13	0.00	0.00	3
5018.03	1.87	2.66	15	14	0.00	-1.00	6
13700.00	0.00	2.66	15	14	0.00	-1.00	10

Tab. 9.2: Stored data for a given binary, in the `bpp` table. I show here all rows (*i.e.* all events in the binary evolution where data is saved) but restrict to only a few columns. `tphys` is the time of evolution of the binary (in Myrs); `mass_1` and `mass_2` are respectively the primary and secondary masses (in solar masses); `kstar_1` and `kstar_2` are their stellar types across the binary evolution (see Tab. 8.1). `sep` is the binary orbital separation (in solar radii), `ecc` the orbital eccentricity, and `evol_type` is a flag indicating the event occurring at that time (see Tab. 9.1).

How to define an evolutionary track is a quite tricky question. To classify the evolution history of binaries, we need to rely on human analysis and on an understanding of the processes involved at the different stages of each binary’s evolution: stellar types, mass transfer events, SN types, ... This has been done by several authors in the context of Binary Black Hole (BBH) and Neutron Star – Black Hole binary (NSBH) systems (see *e.g.* Vigna-Gómez et al. 2018; Neijssel et al. 2019; Bavera et al. 2021; Broekgaarden et al. 2021, 2022; Iorio et al. 2023). How to convert this method into an automatic, numerical analysis of the systems that make a population? For each simulation at a given metallicity, we store the information on only the binaries that produce gravitationally-bound BNS systems (at that stage they can have delay times greater than the Hubble time, see Sec. 9.1). The information stored contains all the stellar properties and binary properties at key stages of stellar evolution: whenever one of the stars evolves to a new stellar type; when a phase of mass transfer starts or stops; at the onset of CE; before and after a SN event, and more generally any of the events listed in Tab. 9.1. This is stored in a single table for all systems, that COSMIC names `bpp`. I give an example of some properties stored for a given system in Tab. 9.2.

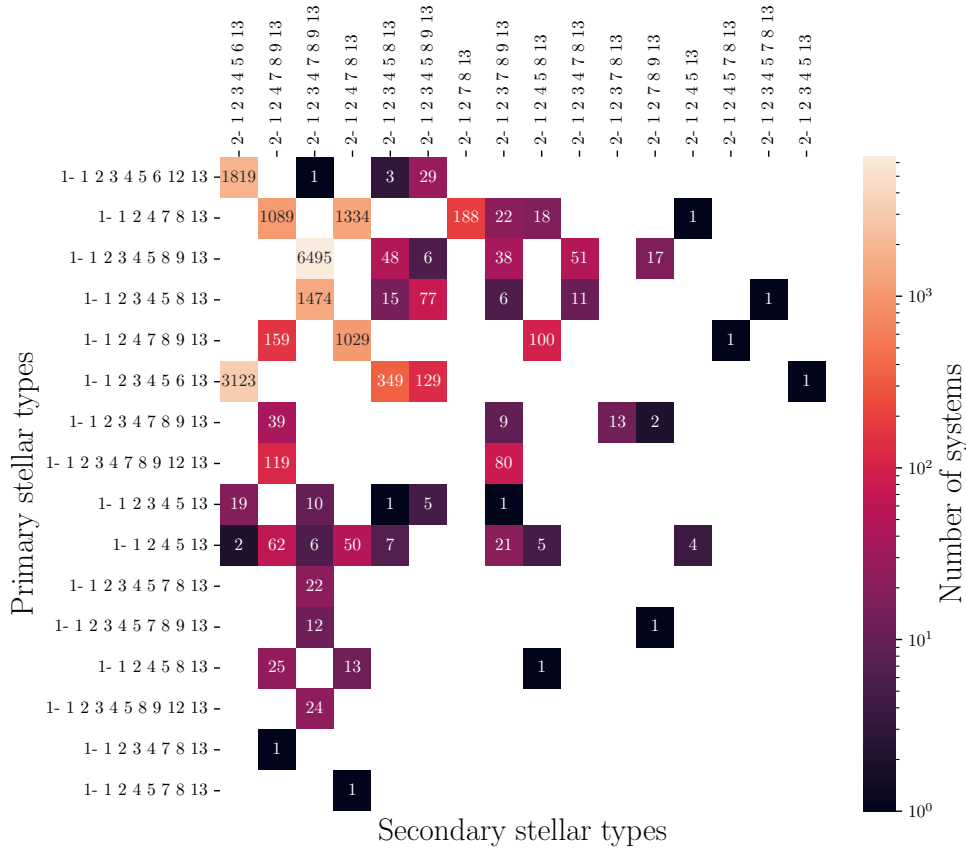


Fig. 9.1: Example of the number of BNS systems for each sequence of stellar types of the primary (rows) and of the secondary (columns), at $Z = 0.014$. The combination of primary and secondary evolutionary sequences creates 58 evolutionary tracks, but 95% systems are found in 11 of them. The sequences of numbers on the y axis and on the x axis are the series of stellar types (see Tab. 8.1) for the primary and the secondary, respectively.

Numerically, we first need to identify evolutionary *sequences*, *i.e.* to group systems which have similar sequences of events using the information from Tab. 9.2. One way to define evolutionary sequences is to group binaries based on their sequence of `evol_type` (see Tab. 9.1). That way, the same categories will group systems with exactly the same sequence of events in the binary life. However, such a method leads to a relatively large number of evolutionary sequences that are in fact

extremely close. For example, with this classification if the beginning of a phase of mass transfer and a change of stellar type are reversed, we define another evolutionary track, while both physical situations may be extremely similar.

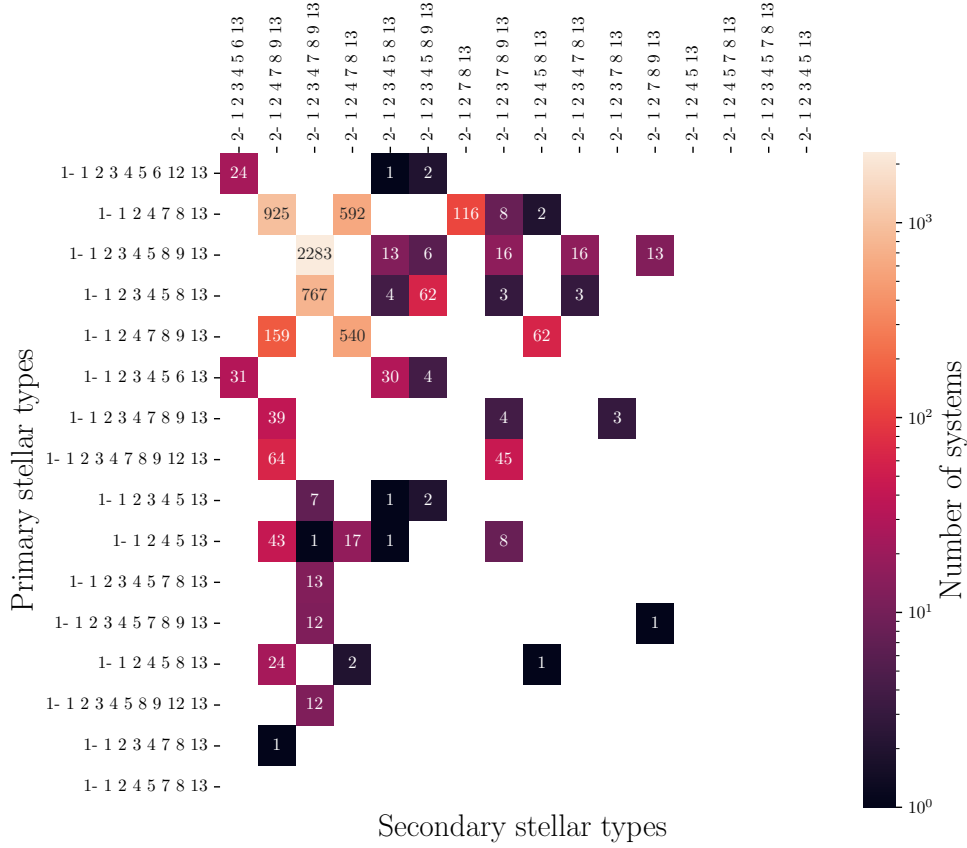


Fig. 9.2: Same as Fig. 9.1, but only showing systems with $\Delta t_{\text{delay}} < t_{\text{Hubble}}$.

We instead use another method to define evolutionary sequences: the sequence of different stellar types for both the primary and the secondary. This reduces a lot the amount of evolutionary sequences, as can be seen in Fig. 9.1. This method however does not guarantee *a priori* that systems with the same evolutionary sequence have similar binary evolution history. A single evolutionary sequence could in principle contain binaries with a single phase of CE, and some others with two CE events; or some systems where the SN of the primary happens while the secondary is on the Main Sequence (MS) and others where the secondary has already evolved. In short, the combination of the two individual sequences of stellar types does not inform us of the details of the binary evolution. However, as I discuss in Sec. 9.3, we verified that for all the evolutionary sequences defined with this method, the details of binary stellar evolution are indeed very similar. We therefore decide to use that classification method as a first step. In Fig. 9.1, I show the number of systems for each combination of primary and secondary stellar type sequences found at solar metallicity, before filtering out the systems with large delay times greater than t_{Hubble} . We find that in this case the 11 most represented evolutionary sequences make up to 95% of the population of BNSs. The same population is shown in Fig. 9.2, this time only showing the systems that merge within t_{Hubble} . It can clearly be seen that some evolutionary sequences are almost entirely filtered out (*e.g.* in the top left corner), because they produce high-separation BNSs. We do not analyse in particular these evolutionary sequences but leave that to a future study of the Galactic population. Note finally that the dominant evolutionary sequences are not necessarily the same at all metallicities (see Sec. 9.4.2).

We therefore repeat the same process over the populations at different metallicities to exhibit all dominant sequences. In the next section, I discuss how we merge the evolutionary sequences in evolutionary *tracks*.

9.3 Evolutionary Tracks

We extracted the 13 evolutionary sequences (as defined in Sec. 9.2) that make up most of the population of BNSs across metallicities, and analysed each of them individually. We confirmed that for each sequence, all systems indeed have a similar evolution history, even if in most cases the sequences of `evol_types` can be diverse (mostly due to some exchanges of the orders of events in the binary history). More interestingly, we confirmed that these 13 evolutionary tracks can in fact be grouped in only three categories with different binary histories, that I describe in more detail in the next sections.

9.3.1 “Standard” Evolution

The first evolutionary track is the most standard one, and is similar to that described in Sec. 7.1. It also corresponds to Channel I in Vigna-Gómez et al. (2018); Neijssel et al. (2019); Broekgaarden et al. (2021); Iorio et al. (2023), and was already discussed in multiple articles in the past (*e.g.* van den Heuvel & De Loore, 1973; Tauris & van den Heuvel, 2006; Belczynski et al., 2018) as the dominant evolutionary track to produce BBHs. It contains systems with the following two evolutionary sequences: 1- 1_2_3_4_7_8_9_13 / 2- 1_2_4_7_8_13 and 1- 1_2_4_5_6_13 / 2- 1_2_4_7_8_9_13 (see Tab. 8.1). The former concerns higher metallicity systems, while the latter concerns lower metallicities.

I describe here a representative example of this evolutionary track. Figures in the text correspond to this example, for which I also show the evolution of the properties in Fig. 9.3. Initially, the binary has an unequal mass ratio (in this example, $q \simeq 0.9$ is quite on the high end of the distribution shown in Fig. 9.19), such that the evolution timescale of the primary is shorter than that of the secondary.

When the primary leaves the MS (after ~ 33 Myr), it grows in radius and loses a significant amount of its mass ($\sim 6.5 M_{\odot}$) during a phase of stable mass transfer. This mass is transferred to the secondary. This phase lasts for $\lesssim 1$ Myr. The primary is left without envelope as a Naked Helium Star, Main Sequence (He-MS), until it again evolves into a Naked Helium Star, Hertzsprung Gap (He-HG) after ~ 5 Myr. At that stage, a brief episode of mass transfer is triggered and the primary explodes in a SN. Given the progenitor mass at the moment of the explosion, the remnant formed is a NS. In this example, after the SN the separation of both stars increases (to $\sim 2500 R_{\odot}$), as well as the orbital eccentricity ($e \sim 0.7$). The secondary in turn evolves after a short time (2 Myr) given the mass gained during the first episode of mass transfer. When helium fusion in the core ignites, the secondary enters the giant phase and CE starts ~ 2 Myr later, due to the prior eccentricity of the orbit. At the end of the CE phase, the secondary is stripped of its envelope and the orbital separation is reduced to $\sim 2.5R_{\odot}$, while friction during the CE circularizes the orbit. Because of the short orbital separation, a continuous mass transfer from the stripped star onto the NS occurs (*case BB* mass transfer, see Sec. 8.2.2 and Tauris et al. 2015). Shortly after, the secondary explodes in a USSN and forms the second NS of the system. Because of the reduced NS kick, the system is given a new initial orbital separation ($\sim 4R_{\odot}$) and eccentricity ($e \simeq 0.4$) but has increased chances of survival. This system eventually merges due to the radiation of GWs after ~ 5 Gyr. A schematic representation of the key phases presented here is shown in Fig. 9.4.

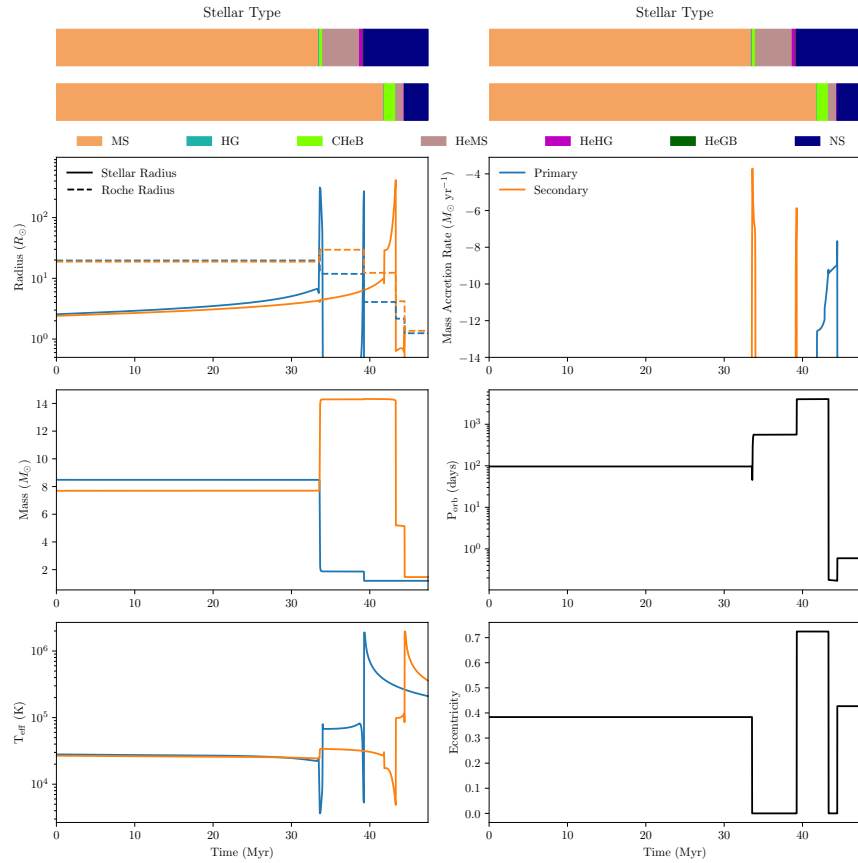


Fig. 9.3: Evolution of a binary system of the “standard” evolutionary track forming a BNS at $Z = 0.00044$. The top color bars show the evolution of stellar types of the primary and the secondary during the binary evolution. On the left-hand side column, from top to bottom, I show the evolution of stellar radii, masses and effective temperatures of the 2 stars. On the right-hand side I show the evolution of mass accretion rates of the stars, and of the orbital period and orbital separation of the system. Quantities are shown in blue for the primary and in orange for the secondary. Black lines are the orbital properties of the system.

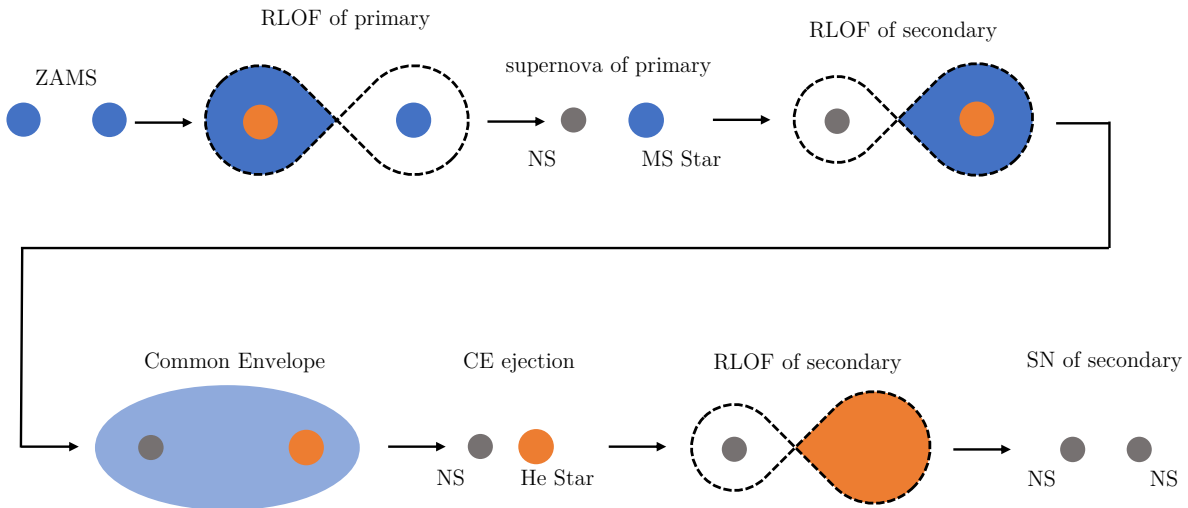


Fig. 9.4: Schematic representation of the key phases of the “standard” evolutionary track. Main sequence stars and hydrogen envelopes are shown in blue, helium cores and naked helium stars are shown in orange, while NSs are shown in black.

This standard process therefore features a phase of CE between a giant and a NS, and a later phase of mass transfer between the stripped star and the NS (*case BB* mass transfer, [Tauris et al. 2015](#)). As will be discussed in Sec. 9.4.2, it however does not produce as many systems as the other evolutionary tracks with our choice of model parameters, in particular at high metallicities, though it is believed to be the major evolutionary track for BBH formation as mentioned in the first paragraph.

In fact, with our model, two other evolutionary tracks instead dominate the contributions to the merger rate history.

9.3.2 Equal-mass binaries

At all metallicities, many BNS systems are produced from the evolution of binary systems whose ZAMS stellar masses were almost equal ($q \simeq 1$). In the example shown in Fig. 9.5, $M_1 = 13.44M_\odot$ and $M_2 = 13.21M_\odot$, *i.e.* $q = 0.98$. The separation is initially of $\sim 2900R_\odot$ and the eccentricity $e \simeq 0.69$. Both stars evolve on similar timescales and both are in their Core Helium Burning (CHeB) phase after 16.44 Myr. Due to the expansion of both stellar envelopes, and to the primary’s slightly higher mass and thus radius, a phase of stable mass transfer is initiated, leading to the circularization of the orbit and therefore to the reduction of the separation. Both stars enter in contact and a joint phase of CE occurs, where the two helium cores orbit within the common envelope. After the envelope ejection, the helium cores have a separation of $\sim 8.7R_\odot$, and most of the mass has been lost by the binary. The primary is slightly more massive than the secondary, and therefore evolves first and explodes in an USSN. Then the secondary evolves, stable mass transfer onto the NS follows (*case BB* mass transfer), until the secondary explodes in an USSN. A schematic representation of the key phases presented here is shown in Fig. 9.6.

Several variations of the example described above and shown in Fig. 9.5 can be found within this evolutionary track, and correspond to 9 evolutionary sequences, but they all share the same distinctive feature of this evolutionary track: a quasi-equal initial mass ratio, leading to a synchronized evolution of both stars and a phase of CE with the 2 stars on their giant phase. Variations depend on the exact stellar types at the moment of the CE (CHeB or Early Asymptotic Giant Branch (EAGB)) and the stellar types of the remaining helium cores at the end of CE. In the cases where the primary is on the EAGB at the onset of CE, the remaining helium cores after CE are already on the Hertzsprung Gap (HG). A second source of variation is the nature of the stellar type of the naked helium stars at the moments of the SNe. Final variations are found depending on the metallicities, but again, share the same distinct features of this evolutionary track. Note that binary systems in this track typically evolve on a faster timescale than the others, due to the joint evolution of the primary and the secondary. The time between binary formation at ZAMS and BNS formation is typically $\Delta t_{\text{evol}} \sim 20$ Myr.

This evolutionary track is also discussed in the literature, for example in [Vigna-Gómez et al. \(2018\)](#) where it is labelled Channel II; [Neijssel et al. \(2019\)](#) where it is labelled Channel III and [Broekgaarden et al. \(2021\)](#); [Iorio et al. \(2023\)](#) where it is labelled Channel IV. This evolutionary track was also discussed in various contexts by *e.g.* [Brown \(1995\)](#); [Bethe & Brown \(1998\)](#); [Dewi et al. \(2006\)](#); [Justham et al. \(2011\)](#); [Hwang et al. \(2015\)](#). Note that the existence of this evolutionary track is more subject to our choice of model parameters than the others. Indeed, because we impose $q_{\text{crit}} = +\infty$ for mass transfers from stripped stars, this evolutionary track only features one phase of CE. With other choices of parameters, there would be additional variations with 1 or 2 additional phases of CE with the helium cores, increasing the amount of systems with mergers before the BNS formation. I discuss this in Sec. 9.4.3.

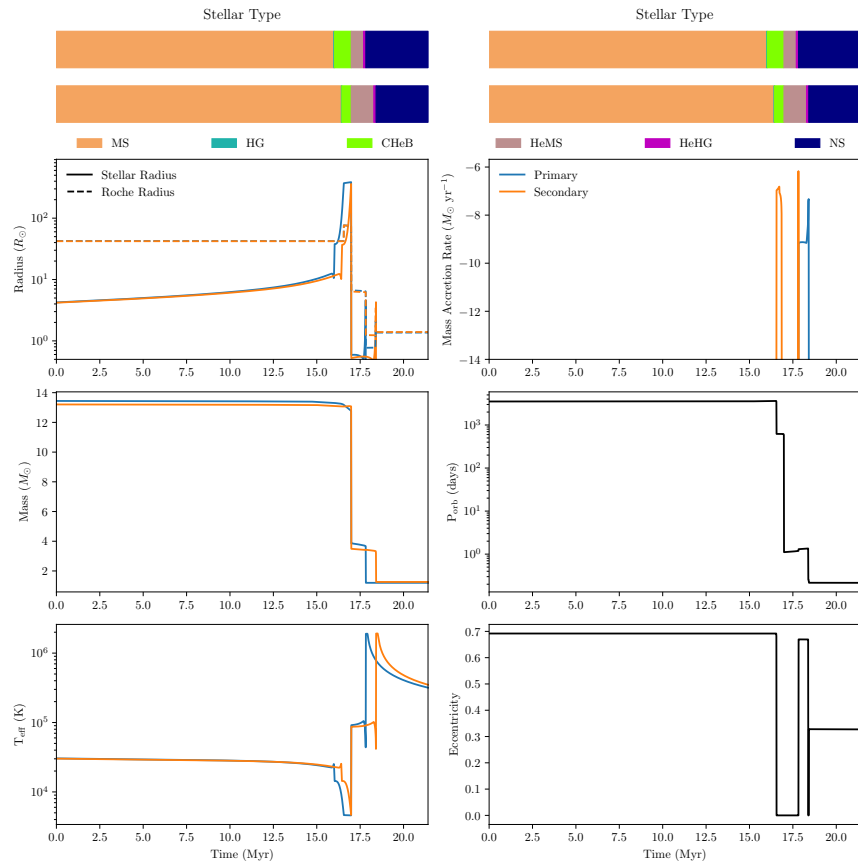


Fig. 9.5: Evolution of a binary system on the “equal-mass” evolutionary track forming a BNS at $Z = 0.0065$. The top color bars show the evolution of stellar types of the primary and the secondary during the binary evolution. On the left-hand side column, from top to bottom, I show the evolution of stellar radii, masses and effective temperatures of the 2 stars. On the right-hand side I show the evolution of mass accretion rates of the stars, and of the orbital period and orbital separation of the system. Quantities are shown in blue for the primary and in orange for the secondary. Black lines are the orbital properties of the system.

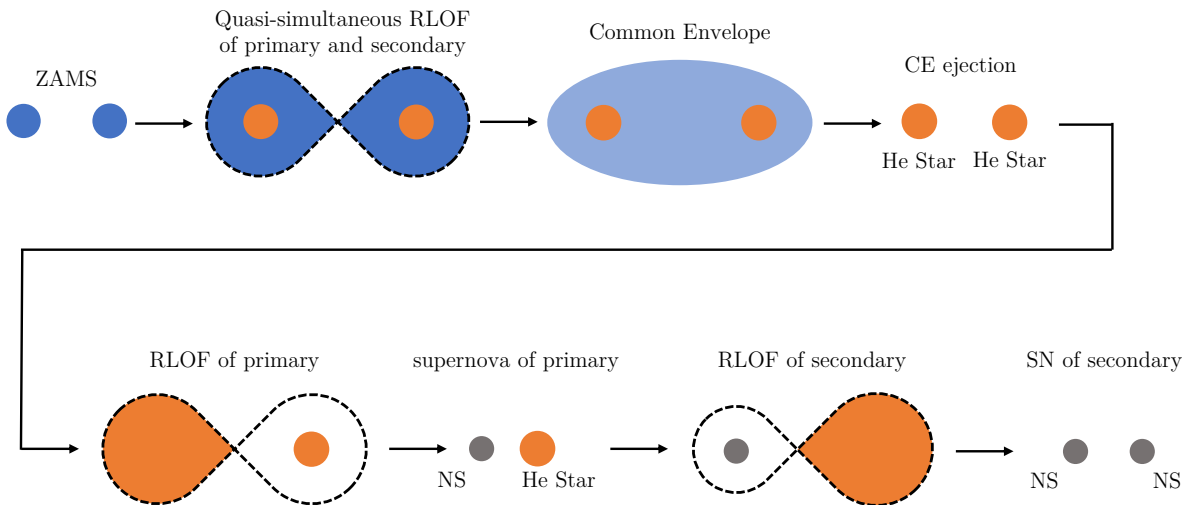


Fig. 9.6: Schematic representation of the key phases of the “equal-mass” evolutionary track. Main sequence stars and hydrogen envelopes are shown in blue, helium cores and naked helium stars are shown in orange, while NSs are shown in black.

We note that the works by Neijssel et al. (2019); Broekgaarden et al. (2021); Iorio et al. (2023) discuss an evolutionary track with only stable mass transfers, which we do not find in our work. In these articles, the authors focus on the populations of BBHs and NSBHs where, due to the higher progenitor masses, transfers of mass can last longer and therefore shrink the orbit significantly. Additionally, because of the higher remnant masses, systems with higher initial separations have a lower probability to be disrupted by either of the SNe: this enables the possibility of detached binaries with only stable mass transfers that still produce compact object remnants that remain gravitationally bound.

9.3.3 Accretion-Induced Collapse

The final evolutionary track found with this model features the AIC of a WD into a NS. It corresponds to two different evolutionary sequences: 1- 1_2_3_4_7_8_9_12_13 / 2- 1_2_4_7_8_9_13 and 1- 1_2_4_7_8_9_12_13 / 2- 1_2_4_7_8_9_13. The latter is dominant at the lowest redshifts and differs from the former only by one element: the primary does not enter the First Giant Branch (FGB). The physical properties of both sequences are however similar. I show an example of such a system in Fig. 9.7. In this evolutionary track, the initial mass ratio can reach much lower values $0.5 \lesssim q < 1$. In this example, $q \simeq 0.48$. The initial mass of the secondary can be lower than the typical mass of NS progenitors (here $M_2 = 4.06 M_\odot$), due to the first phase of mass transfer.

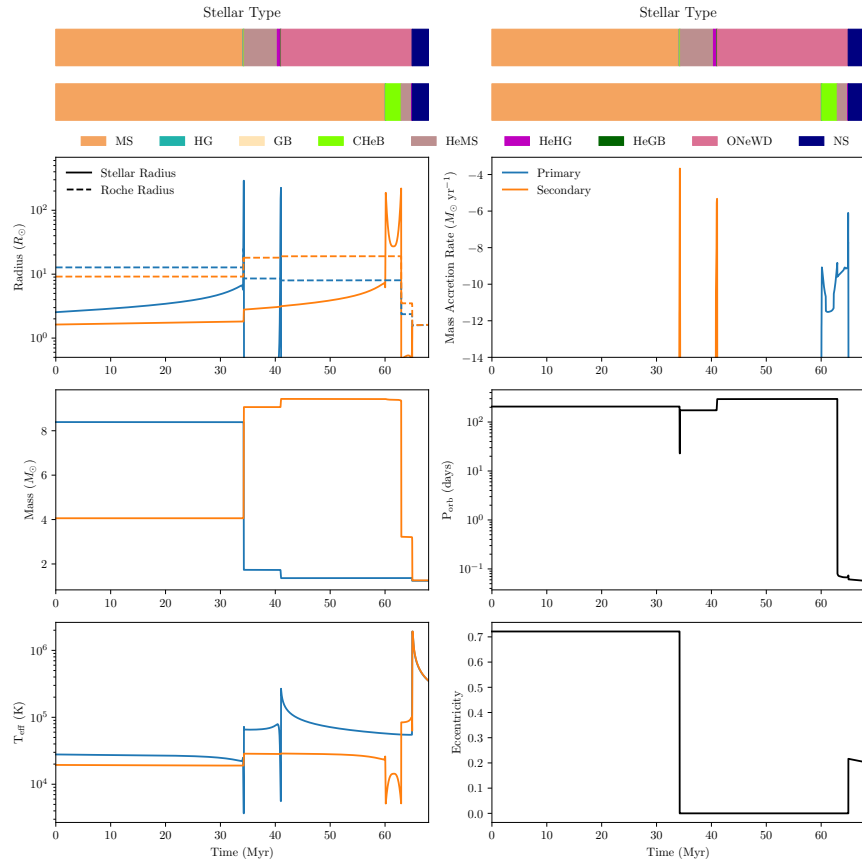


Fig. 9.7: Evolution of a binary system on the “AIC” evolutionary track forming a BNS at $Z = 0.00044$. The top color bars show the evolution of stellar types of the primary and the secondary during the binary evolution. On the left-hand side column, from top to bottom, I show the evolution of stellar radii, masses and effective temperatures of the 2 stars. On the right-hand side I show the evolution of mass accretion rates of the stars, and of the orbital period and orbital separation of the system. Quantities are shown in blue for the primary and in orange for the secondary. Black lines are the orbital properties of the system.

In this evolutionary track, the primary evolves first from the MS after 34 Myr. When it reaches the HG, a phase of stable mass transfer starts, reducing the orbital separation and circularizing the orbit. During this event of mass transfer, the primary evolves and loses more mass to the companion. Because the mass transfer is not entirely conservative (some mass is lost by the binary), the separation increases again, until the primary has lost its entire hydrogen envelope and becomes a helium star. All these events occur on timescales $\lesssim 0.1$ Myr. At that point, the secondary has a mass that can be higher than the initial primary mass. The primary helium star evolves (here in ~ 6 Myr), and a new phase of mass loss can occur. When the primary enters the Naked Helium Star, Giant Branch (He-GB), the remaining core mass is therefore much lower than in the other scenarios (here $1.36 M_{\odot}$). At the moment of the SN, the primary collapses into an oxygen-neon WD. As all the mass of the helium core forms the WD, no natal kick is imparted to the WD. The orbit thus remains circular. In turn, the (now massive) secondary leaves the MS and evolves, roughly 20 Myr later. When it reaches the HG, a phase of CE is triggered, with the WD. After the envelope ejection, the orbital separation is reduced to an extremely low value (here $1.3 R_{\odot}$). Throughout the evolution of the helium star, stable mass transfer occurs and gradually increases the mass of the WD. When it reaches the Chandrasekhar mass (Chandrasekhar, 1931) by accretion, the WD collapses and forms a NS of $1.24 M_{\odot}$ (this value is unique for all systems by construction in COSMIC but would nevertheless be expected to have a low dispersion). Just after, the secondary in turn collapses into a NS thanks to the mass gained during the first phase of mass transfer. The BNS system formed that way has an extremely short initial separation and merges in typically a few tens of Myr (see Sec. 9.4). A schematic representation of the key phases presented here is shown in Fig. 9.8.

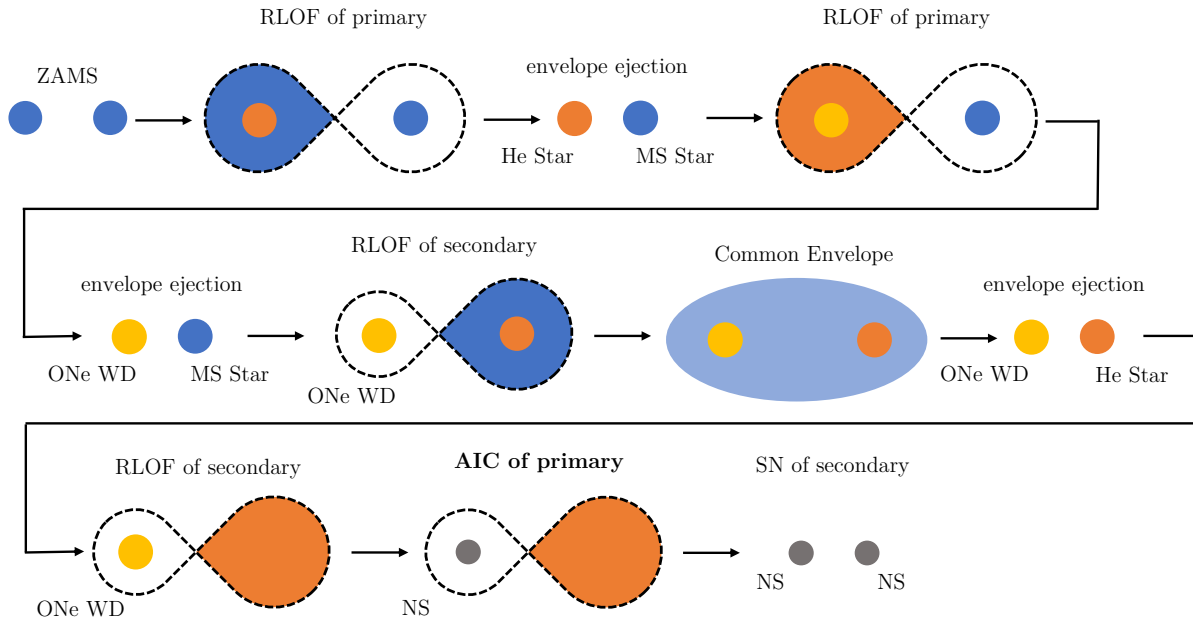


Fig. 9.8: Schematic representation of the key phases of the “AIC” evolutionary track. Main sequence stars and hydrogen envelopes are shown in blue, helium cores and naked helium stars are shown in orange, oxygen-neon cores and oxygen-neon WDs are shown in yellow, while NSs are shown in black.

This evolutionary track has not been discussed much in the literature in the context of the population of merging BNSs, except in Wang & Liu (2020), where the authors show in particular the limited parameter space (P_{orb}, M_1, M_2) within which this process can occur. The AIC of a WD by accretion from a companion is discussed in a more general context in *e.g.* Meng et al. (2009); Wang & Han (2010). As I show in Sec. 9.5 – with our choice of model – it dominates to the merging

population at low metallicity.

9.4 Population Properties

We now study the properties of the evolutionary tracks defined in Sec. 9.3 in more detail, from a statistical perspective. In Sec. 9.4.1, I show results at given metallicity values and across the evolutionary tracks, while in Sec. 9.4.2, I evaluate the impact of metallicity on each evolutionary track. In the following discussion, we will use 3 different important durations of the binary evolution:

- The **evolution time**, Δt_{evol} , is the time interval between the ZAMS and the BNS formation. In other words, Δt_{evol} represents the time of evolution of the stellar progenitors, up until the formation of the BNS.
- The **merger time**, Δt_{GW} , is the time delay between the formation of the BNS and its merger due to the emission of GWs discussed in Sec. 1.2, and computed from Eqs. 1.8 – 1.9.
- The **delay time**, Δt_{delay} is the total time between the ZAMS and the merger of the BNS system:

$$\Delta t_{\text{delay}} \equiv \Delta t_{\text{evol}} + \Delta t_{\text{GW}}. \quad (9.1)$$

9.4.1 Properties of the Evolutionary Tracks

In this section, I discuss the relative contributions of each of the evolutionary tracks presented in Sec. 9.3 to the population of BNSs at given metallicities. First, we look at the properties of the stellar progenitors to those systems at different metallicities. In Figs. 9.9 – 9.11, I show the distributions of initial binary properties at ZAMS, for the population of binaries forming BNSs which merge within the Hubble time.

Note that the systems of higher metallicities are more likely to form at lower redshift (see Eq. 9.6 and Sec. 9.5), in which case the tail of the population with the longest merger times does not contribute to the total population of BNSs which merged through cosmic time until today, even if their merger time is lower than the Hubble time. We decide to filter the entire population based on $\Delta t_{\text{delay}} < t_{\text{Hubble}}$ to simplify our comparative studies, but the exact shapes of the distributions of delay times are accounted for in our calculation of the merger rate (see Sec. 9.5), and do not include systems where $t(z_{\text{ZAMS}}) + \Delta t_{\text{delay}} > t_{\text{Hubble}}$, where $t(z_{\text{ZAMS}})$ is the time at which the progenitor binary is formed.

When looking at the relative contributions of each evolutionary track at given metallicities, we see that they divide the progenitor properties in different sections: AIC usually occurs for shorter-separation binaries, while the track with equal mass ratios is usually found for more massive progenitors with larger separations. The initial eccentricity is not a relevant parameter to identify these tracks.

We also notice that the relative contributions of each of the evolutionary tracks to the total population varies with metallicity, as we will also see in Sec. 9.5. AIC is dominant at lower metallicities (see Fig. 9.9), while the equal-mass ratio evolutionary track dominates at higher metallicities (see Fig. 9.11). This in turn affects the merger rate density evolution with redshift (see Sec. 9.5). Note also that the initial eccentricity of the system does not impact in specific ways the chances of BNS formation, and also not the evolutionary tracks. We retrieve the sampled eccentricity distribution of Sana et al. (2012) shown in Fig. 8.1. The equal mass ratio evolutionary track contributes to a significant peak in the distributions of q at $q \simeq 1$ (by definition).

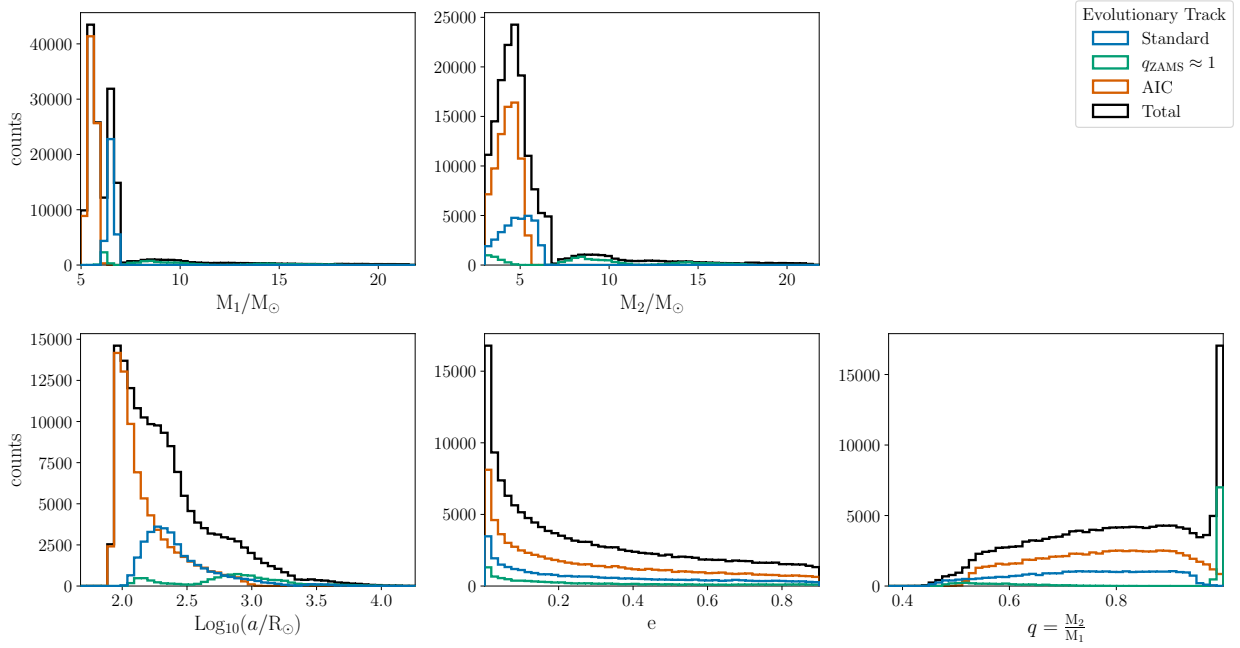


Fig. 9.9: Distribution of the properties of the population of BNS progenitors, at their formation (ZAMS) and at metallicity $Z = 9.5 \times 10^{-5}$. We only show the progenitors of BNS systems whose delay time $\Delta t_{\text{delay}} < t_{\text{Hubble}}$. In blue, we show the standard evolutionary track (Sec. 9.3.1); in green the evolutionary track with equal-mass progenitors (Sec. 9.3.2); and in orange the AIC evolutionary track (Sec. 9.3.3). In black, we show the total population. From left to right, top to bottom, the five panels show the distributions of (1) primary masses; (2) secondary masses; (3) initial orbital separations; (4) initial orbital eccentricities; (5) initial mass ratios.

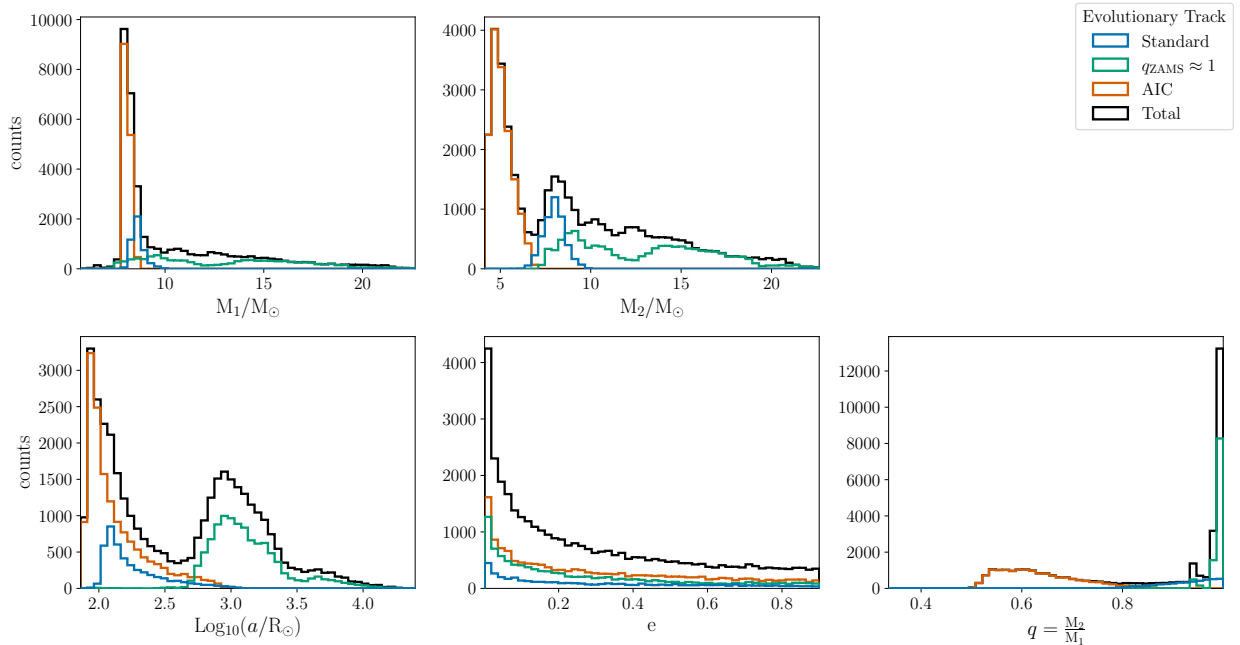


Fig. 9.10: Same as Fig. 9.9 at $Z = 9.5 \times 10^{-4}$.

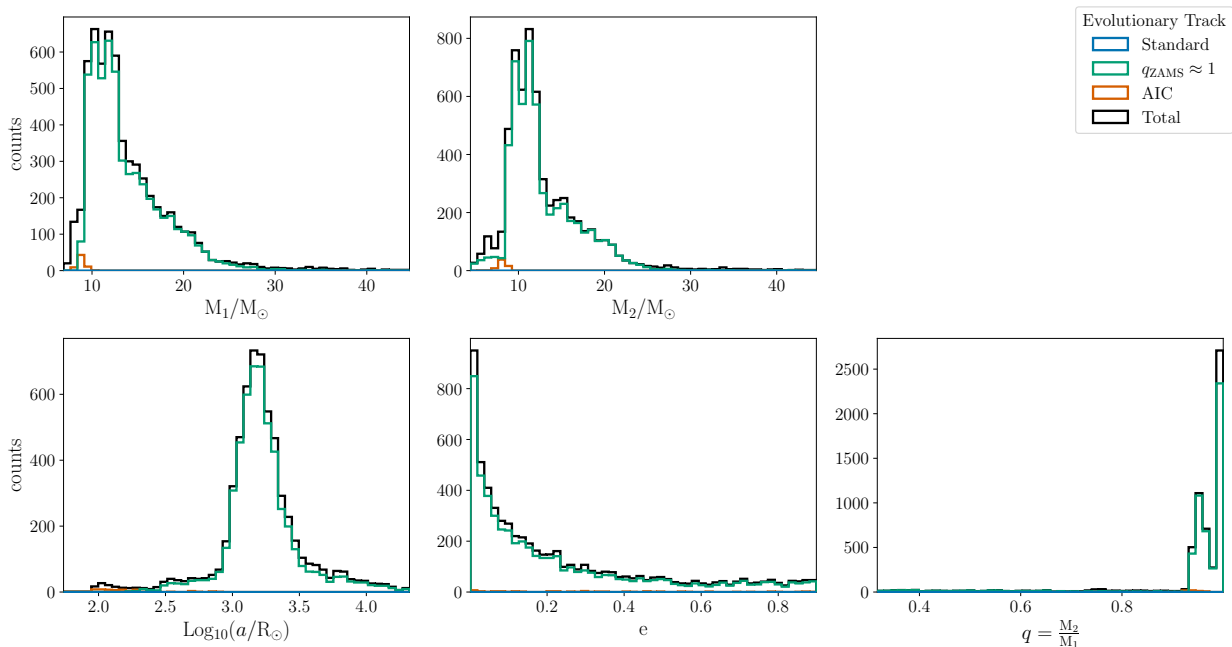


Fig. 9.11: Same as Fig. 9.9 at $Z = 1.4 \times 10^{-2}$. Note here the change of scale for M_1 and M_2 which span higher masses than at lower metallicities due to stellar winds.

We now look at the properties of the BNS systems at their formation, *i.e.* right after the secondary SN. I show some of the distributions of properties for four parameters at the instant of BNS formation (separation, Δt_{evol} , Δt_{GW} and Δt_{delay}) in Figs. 9.12 – 9.14. In this work, we do not discuss the distributions of NS masses given the uncertainties on their determination in COSMIC, as discussed in Sec. 8.2.5.

One clear property observable on the distribution of delay times is that, for individual metallicities, it does not follow the distribution which scales as $1/t$ as often assumed in the literature (*e.g.* Chruslinska et al. 2018). In fact, depending on the metallicity and on which evolutionary track is dominant, the distribution of delay times can be flat (see Fig. 9.14) or extremely peaked (see Fig. 9.12). We study more in depth the evolution of the binary properties with metallicity in Sec. 9.4.2, but already highlight here that a significant fraction of binaries has a delay time dominated by the stellar evolution timescale, with extremely short merger times.

Another observation is that the different evolutionary tracks are well distinguished by the progenitor binary evolution time Δt_{evol} . Progenitors with equal mass ratios evolve more rapidly due to their initially higher masses (see *e.g.* Figs. 9.9 and 9.12), BNSs formed *via* the standard evolutionary track have slightly longer formation times, while the longest formation times are required for the AIC evolutionary track, mostly due to the smaller total mass in the system.

In Fig. 9.15, I show the joint distributions of the formation and merger times for the three evolutionary tracks. This joint representation allows to better understand the separation between the BNS properties at their formation for the 3 evolutionary tracks. The standard evolutionary track has long evolution times, but not the longest, and a distribution of merger times that ranges between < 1 Myr and t_{Hubble} . The equal-mass ratio evolutionary track has short evolution times and long merger times, while the AIC evolutionary track has the longest evolution times and short merger times.

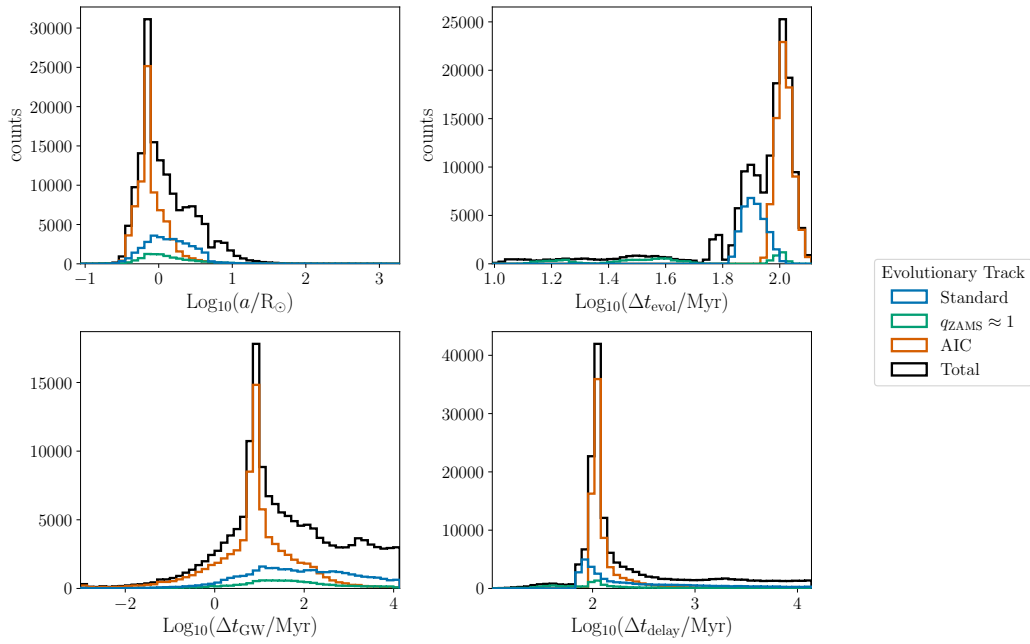


Fig. 9.12: Distribution of the properties of the population of BNS, at their formation, *i.e.* right after the secondary SN, and at metallicity $Z = 9.5 \times 10^{-5}$. We only show the BNS systems whose delay time $\Delta t_{\text{delay}} < t_{\text{Hubble}}$. In blue, we show the standard evolutionary track (Sec. 9.3.1); in green the evolutionary track with equal-mass progenitors (Sec. 9.3.2); and in orange the AIC evolutionary track (Sec. 9.3.3). In black, we show the total population. From left to right, top to bottom, the four panels show the distributions of (1) orbital separations; (2) evolution times; (3) merger times; (4) delay times, as defined in Sec. 9.4.

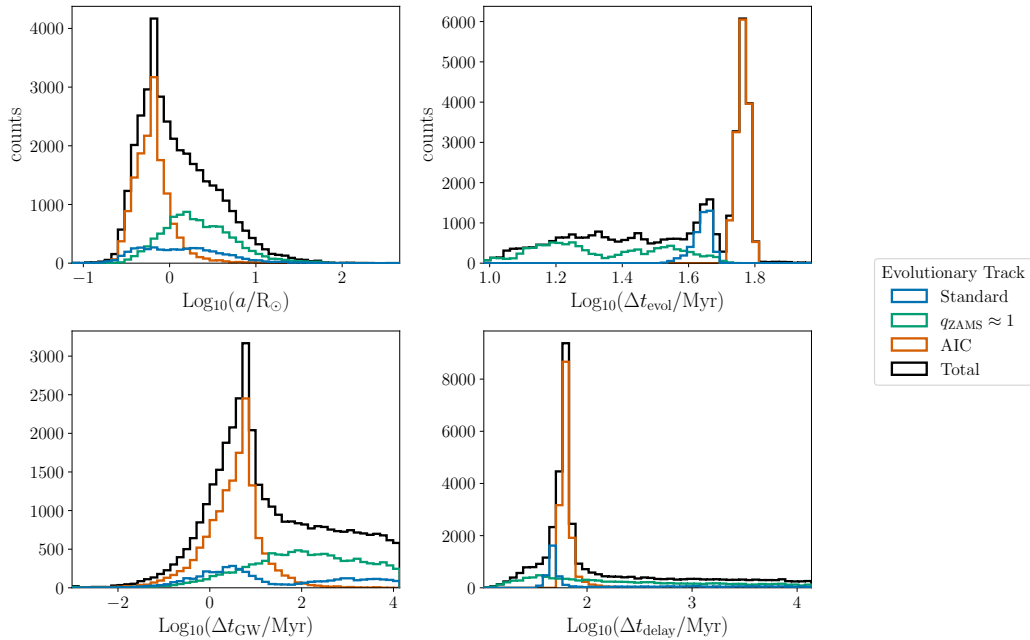


Fig. 9.13: Same as Fig. 9.12 at $Z = 9.5 \times 10^{-4}$.

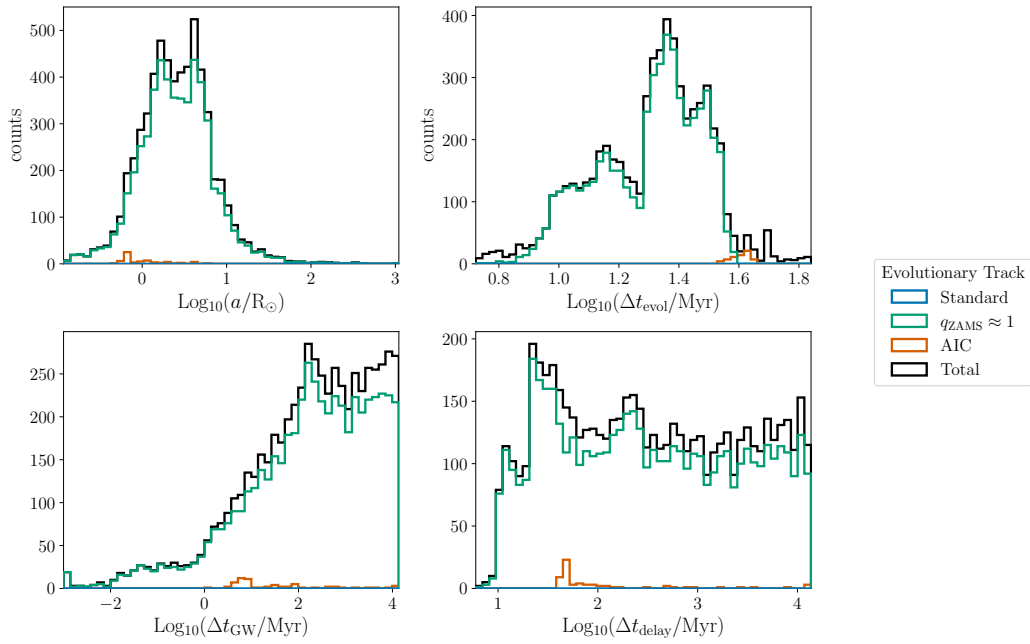


Fig. 9.14: Same as Fig. 9.12 at $Z = 1.4 \times 10^{-2}$.

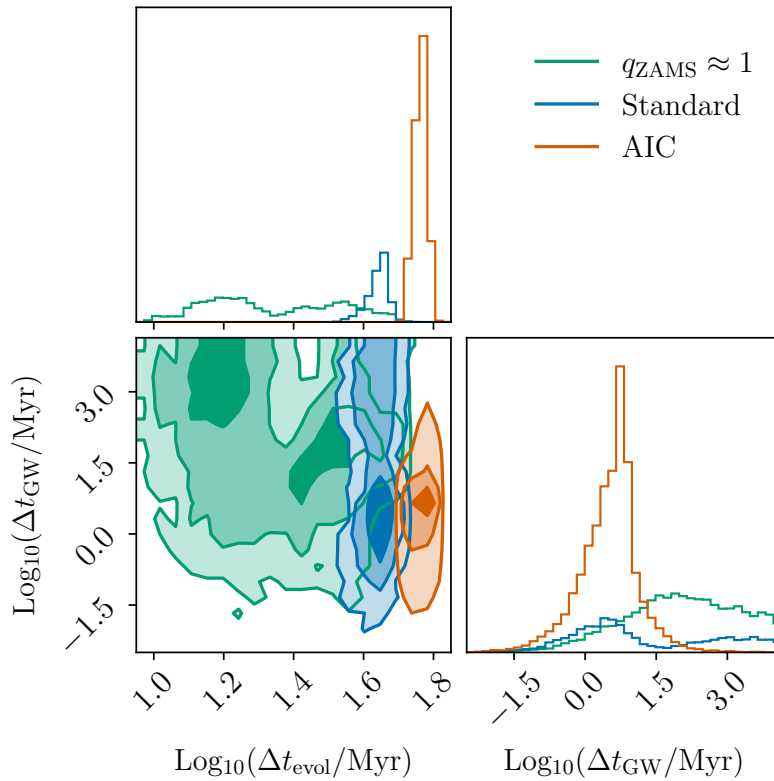


Fig. 9.15: Correlation between the formation and merger times for the 3 evolutionary tracks, at $Z = 9.5 \times 10^{-4}$. The 3 tracks are found on distinct regions of the plane, as discussed in Sec. 9.4.1. The shaded contours correspond to the 1σ , 2σ and 3σ confidence intervals.

We see that each evolutionary track leads to specific BNS properties. However, metallicity strongly impacts the population of BNSs that can be produced, as I discuss next.

9.4.2 Impact of Metallicity on the Evolutionary Tracks

Let us now discuss the impact of metallicity on each of the evolutionary tracks. I show in Figs. 9.16 – 9.18 the properties of the progenitor stars for the three evolutionary tracks, across metallicities.

A first trend that is observed for the three evolutionary track is a global decline of the total number of BNSs formed as metallicity increases. At first order, this is explained by the gradual increase of stellar winds intensities with metallicity, leading to increased mass losses by the binary. As a result, higher-metallicity systems forming BNSs have higher ZAMS masses than their lower-metallicity counterparts. Because the distribution of primary masses scales as $M^{-2.3}$ (Eq. 8.3, Kroupa 2001), there are fewer systems in the correct mass range at higher metallicities.

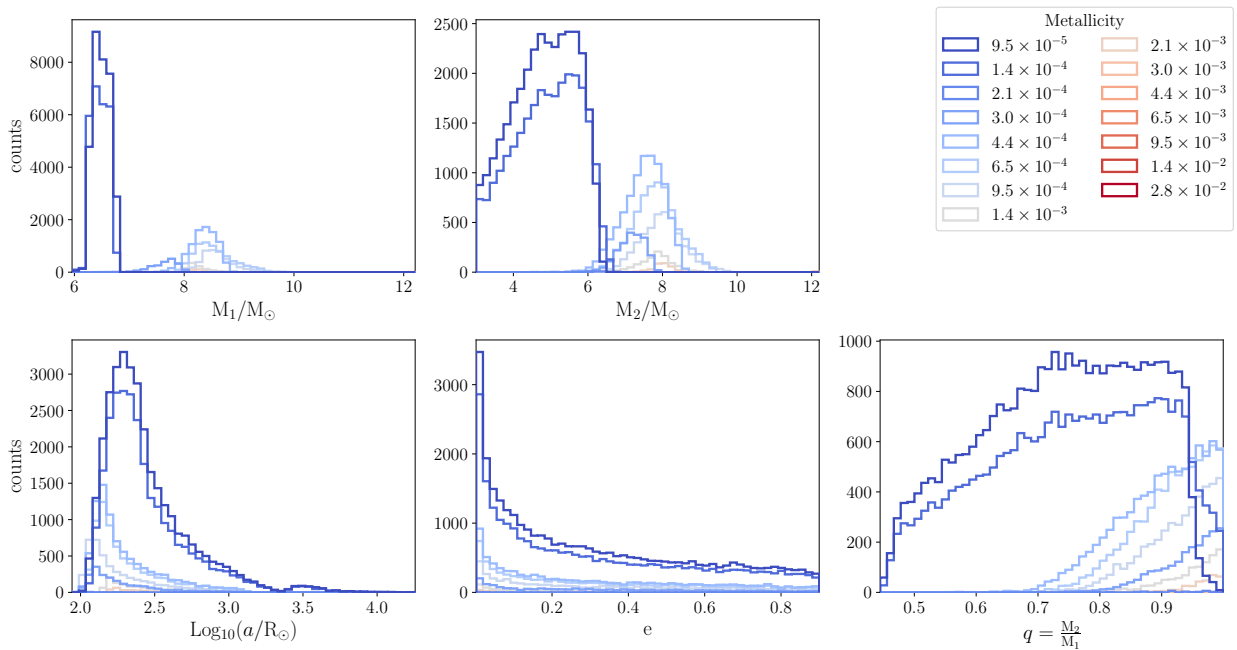


Fig. 9.16: Distribution of the properties of the population of BNS progenitors, at their formation (ZAMS) and at different metallicities for the **standard evolutionary track**. We only show the progenitors of BNS systems whose delay time $\Delta t_{\text{delay}} < t_{\text{Hubble}}$. Each color represents the population at one of the sampled metallicity values. From left to right, top to bottom, the five panels show the distributions of (1) primary masses; (2) secondary masses; (3) initial orbital separations; (4) initial orbital eccentricities; (5) initial mass ratios.

In Fig. 9.16, we see that the initial properties of the progenitor binaries transition from lower-mass progenitors with a broad distribution of mass ratios at the two lowest metallicities, to more equal and higher masses. This is the transition between the two evolutionary sequences that constitute the standard evolutionary track (see Sec. 9.3.1).

By definition, we retrieve the very peaked distribution of mass ratios $q \gtrsim 0.94$ for the equal-mass ratio evolutionary track (Fig. 9.17). The initial binary properties do not show any particular trend with metallicity.

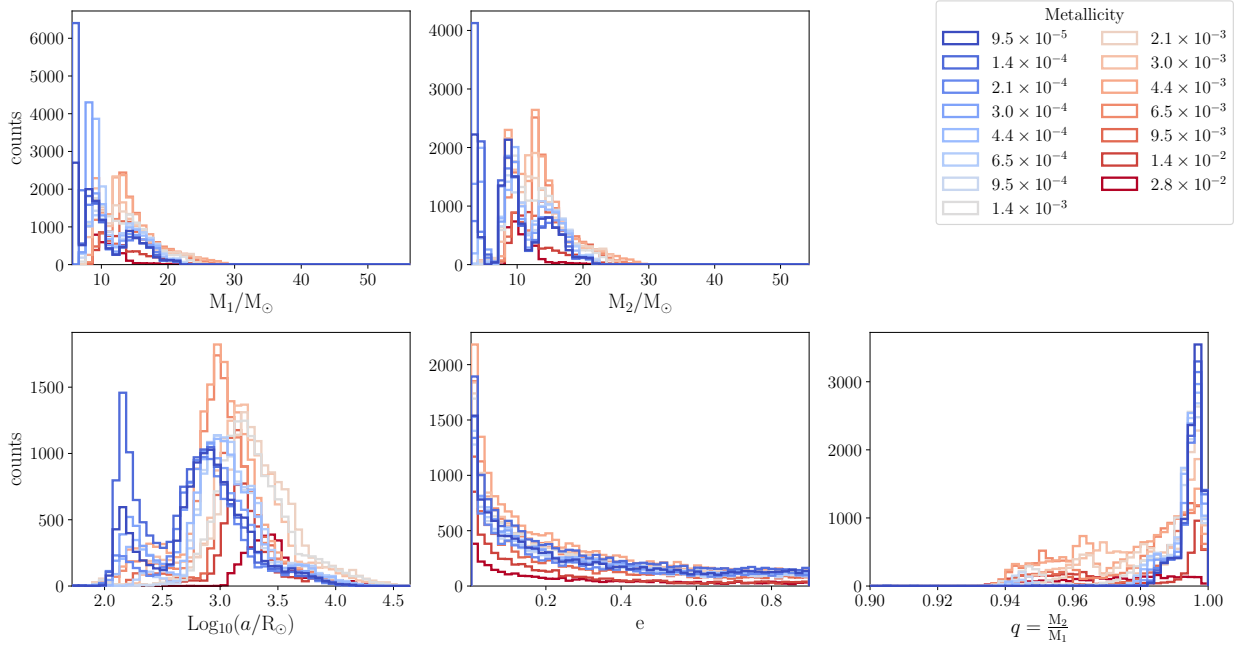


Fig. 9.17: Same as Fig. 9.16 for the **equal-mass ratio evolutionary track**. Note that the ranges of the distributions are different than in Fig. 9.16.

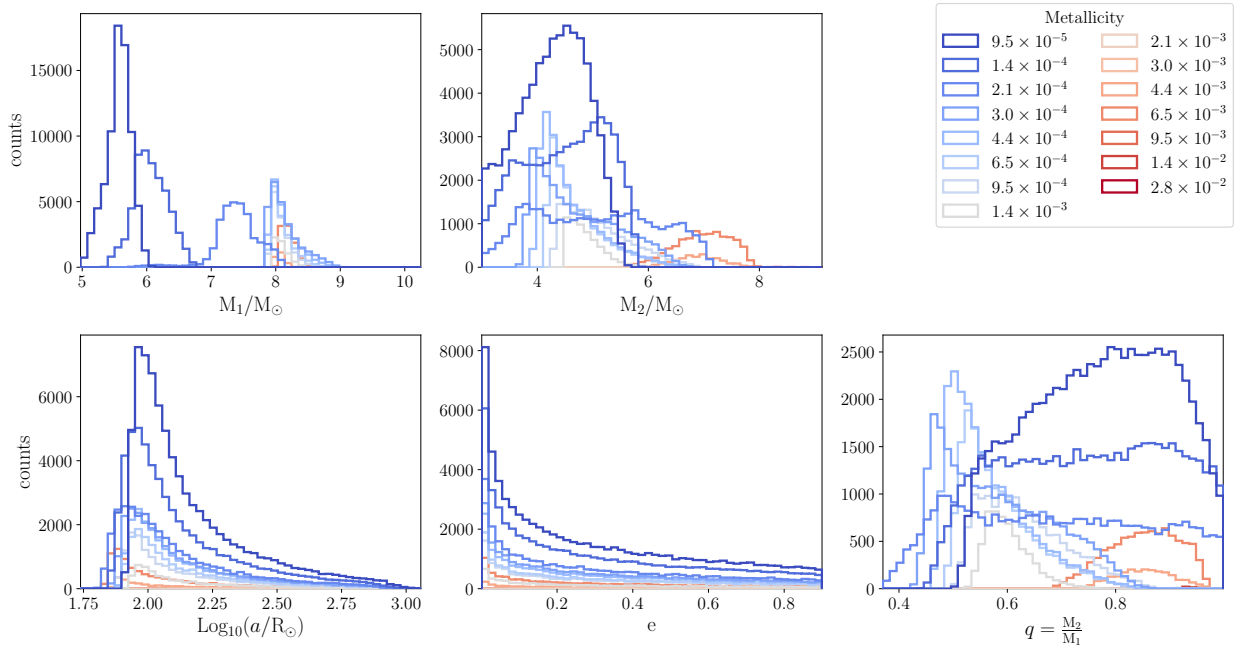


Fig. 9.18: Same as Fig. 9.16 for the **AIC evolutionary track**. Note that the ranges of the distributions are different than in Figs. 9.16 and 9.17.

For the AIC evolutionary track, there is a more complex evolution of the initial binary properties with metallicity. We observe in Fig. 9.18 that the primary mass increases with metallicity until it stalls around $8 M_\odot$. We studied this in detail and found that, at a given metallicity, if M_1 is too high, the primary directly collapses into a NS and if M_1 is too low, it collapses into a carbon-oxygen WD. The range of progenitor masses to oxygen-neon WDs that can later experience AIC is therefore

narrow. When metallicity increases, the mass lost by the primary before its core collapses also increases, thus requiring higher initial masses M_1 to produce oxygen-neon WDs. The reason this trend stops is again due to the transition between the two evolutionary sequences that compose the AIC evolutionary track (see Sec. 9.3.3). At these higher metallicities, it is this time the secondary whose mass M_2 gradually increases with metallicity. The reason is again related to the mass losses from stellar winds: the secondary initial mass must be higher at higher metallicities. We will see in Sec. 9.5 that the transition between the two evolutionary sequences produces a visible feature with two peaks in the merger rate evolution in Fig. 9.22.

As the progenitor masses required for the AIC evolutionary track to appear gradually increase with metallicity, the number of such systems therefore decreases (see again Eq. 8.3, Kroupa 2001). Combined with the very restrictive mass range of the progenitors of oxygen-neon WDs, this progressively reduces the contribution of the AIC evolutionary track to the total as metallicity increases.

I now show the evolution of the BNS properties with metallicity, for the three evolutionary tracks in Figs. 9.19 – 9.21.

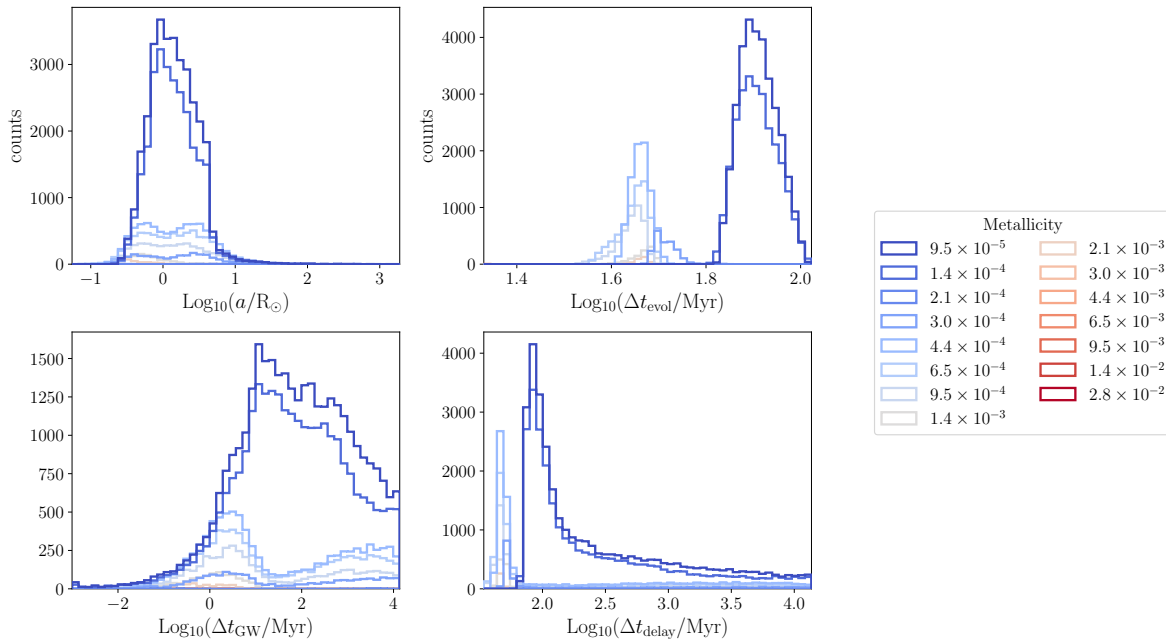


Fig. 9.19: Distribution of the properties of the population of BNS, at their formation, *i.e.* right after the secondary SN for the **standard evolutionary track**. We only show the BNS systems whose delay time $\Delta t_{\text{delay}} < t_{\text{Hubble}}$. Each color represents the population at one of the sampled metallicity values. From left to right, top to bottom, the five panels show the distributions of (1) orbital separations; (2) formation times; (3) merger times; (4) delay times, as defined in Sec. 9.4.

One major difference between the AIC evolutionary track and the other two is the distribution of merger times. In the AIC evolutionary track, the separation after the SN of the secondary is always extremely reduced after the phase of CE with the WD. After the final phases of mass transfer from the helium companion onto the WD that lead to its AIC, and the USSN of the secondary, the separation still remains extremely short in most cases, leading to a merger in typically $\lesssim 10$ Myr. This property does not evolve with redshift. The standard evolutionary track has much longer merger times at low metallicities, while for the equal-mass evolutionary track, the merger time tends to increase with metallicity.

A final trend that we observe is the general decrease in the number of successful BNS formation as metallicity increases. This is mostly due to the increased stellar wind intensities which lead

to higher progenitor masses, further in the tail of the initial mass function distribution (Eq. 8.3, Kroupa 2001). This effect is combined with the evolution of Star Formation Rate Density (SFRD) with redshift in the determination of the merger rate that I describe in Sec. 9.5. Note also that the amount of successful BNS formation among the total population is extremely small: typically one system in $10^4 - 10^6$ produces a BNS which merges within t_{Hubble} .

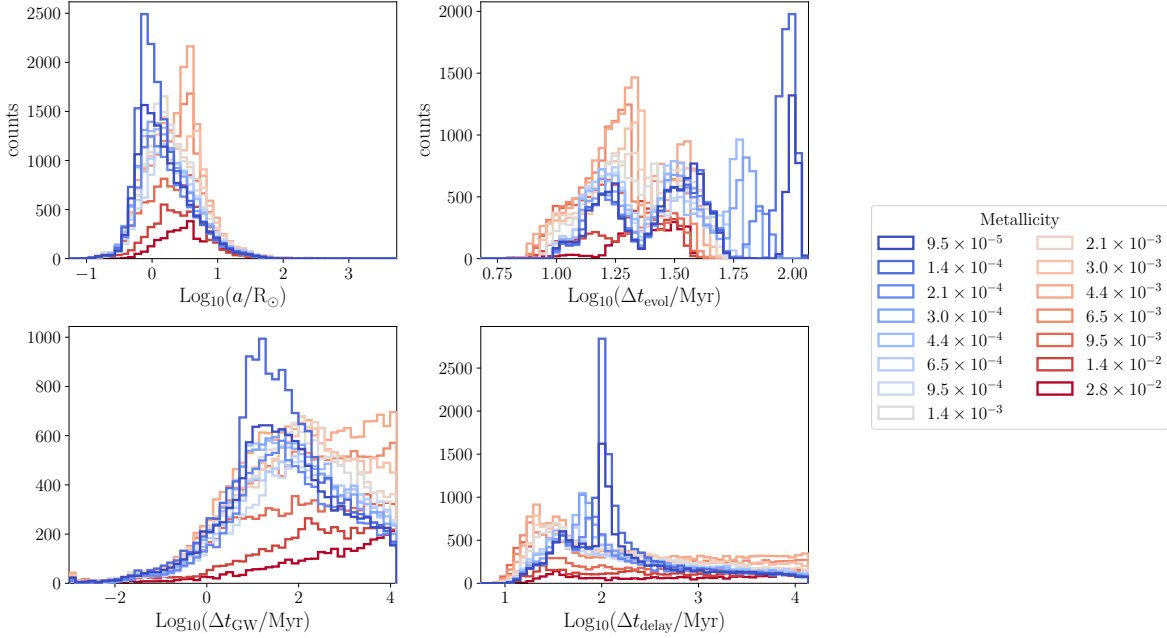


Fig. 9.20: Same as Fig. 9.19 for the equal-mass ratio evolutionary track.

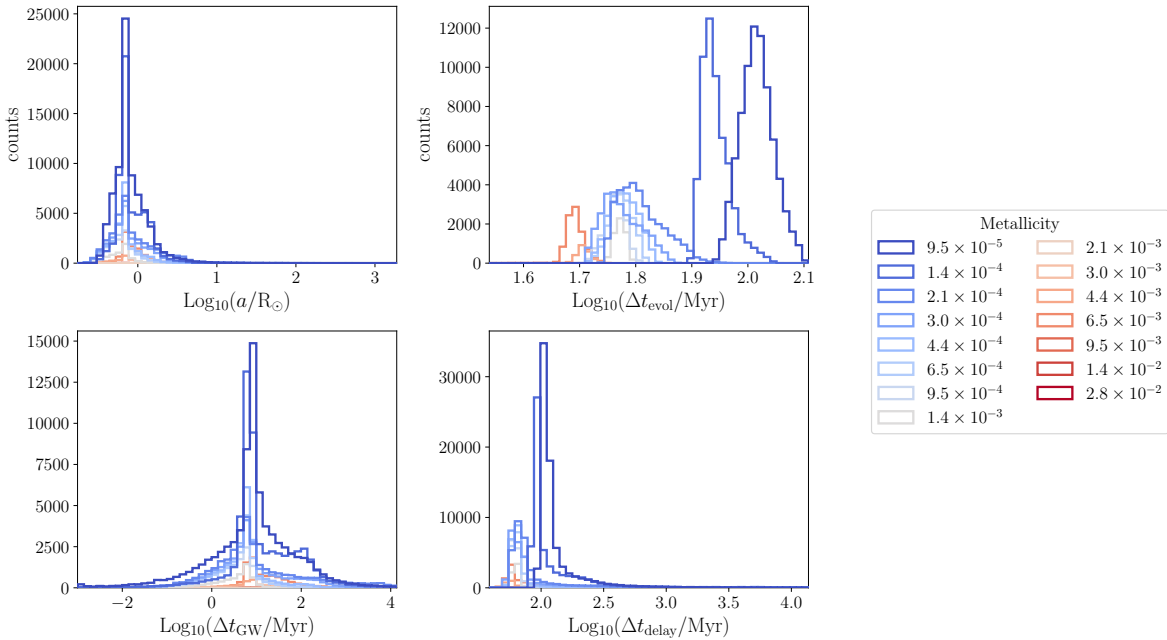


Fig. 9.21: Same as Fig. 9.19 for the AIC evolutionary track.

9.4.3 Other Possible Model Choices

During the course of this work, we explored different models for some phases of binary evolution. In particular, we looked into different values for the critical mass ratios q_{crit} , using `qcflag` (see Sec. 8.2.2 and Tab. 8.3). We find that this flag has a key consequence in the evolution of binaries we observe. When setting `qcflag`= 1 or 2, the mass transfers from helium stars are often dynamically unstable and lead to a new phase of CE, while in the model presented here (`qcflag`= 5) they are always dynamically stable. Our choice of model therefore leads to evolutionary tracks with only one CE phase, while the other have two, even sometimes three CE events.

In our model, we assume that stars are entirely disrupted during CE if the companion has no core-envelope boundary (`cemergeflag`= 1). We also made some tests by allowing such binaries to survive CE (`cemergeflag`= 0), and found that this typically adds a few additional evolutionary sequences to the total. In particular, in this alternative scenario, there is an additional AIC evolutionary sequence: 1- 1_2_3_4_7_8_9_12_13 / 2- 1_2_7_8_9_13, which dominates the population at high metallicities. In this case, a CE occurs when the primary has already formed a WD and the secondary is on the HG.

We also explored different prescriptions for the remnant masses with `remnantflag`, but did not find it to impact the evolutionary tracks as much as the previous parameters. This was expected given that this flag does not affect stellar evolution.

More generally, these comparisons showed that the model selection for some specific phases of binary stellar evolution impacts the evolutionary tracks that are represented in the population of BNS and their relative contribution. We therefore highlight that the results presented in the next section are potentially sensitive to the choice of model. Interestingly, this means that if these results can be compared to observations, they could constrain our understanding of the co-evolution of stars in binary systems.

9.5 Evolution of the Merger Rate with Redshift

9.5.1 Computing the Merger Rate Density

The method presented in this section is based on **Publication III** (Appendix E.3, [Lehoucq et al. 2023](#)). The formulae presented below are underlying all results about the predicted merger rates found in the literature. I present them here in the context of the study of evolutionary tracks, to link all notations self-consistently. They were applied in [Lehoucq et al. \(2023\)](#) (Appendix E.3) to the stochastic GW background, that I discuss below.

From the observations of BNSs – be they Galactic systems or systems detected by GWs at their merger –, it is not possible to know the metallicity of the progenitors. The populations of BNSs obtained with COSMIC across metallicities can therefore not be observationally probed directly. We need one final step to include the results of these simulations in the computation of an observable quantity: the BNS merger rate as a function of redshift or equivalently cosmic time, $\mathcal{R}_{\text{merg}}(t)$, see Eq. 9.6. Redshift and time are related by the relation

$$\frac{dt}{dz} = \frac{H_0^{-1}}{(1+z)\sqrt{\Omega_m(1+z)^3 + \Omega_\Lambda}}, \quad (9.2)$$

where $H_0 = 68 \text{ km} \cdot \text{s}^{-1} \cdot \text{Mpc}^{-1}$ is the Hubble constant, $\Omega_\Lambda = 0.69$ is the fraction of dark energy in the total Universe energy density and $\Omega_m = 0.31$ is the fraction of energy in matter (dark matter and baryonic matter). We also define the useful quantities $\Omega_b = 0.045$ the baryonic fraction of energy density and $h_0 = 0.68$ the reduced Hubble constant (dimensionless). We assume here the cosmological values of [Planck Collaboration et al. \(2020\)](#).

To compute the merger rate based on the results of our simulations, three ingredients are needed:

- **The Star Formation History (SFH).** The total number or mass of stars formed at any given redshift. Its determination has been the focus of several studies, and remains quite uncertain, especially at the highest redshifts. Much detail on the different approaches for its determination can be found in [Madau & Dickinson \(2014\)](#). Most works find a SFRD peaking at $z \approx 2$, but the exact form of its evolution is more uncertain. In this study, we use the functional form first introduced by [Springel & Hernquist \(2003\)](#) using hydrodynamical simulations:

$$\psi(z) = \nu \frac{a \exp[b(z - z_m)]}{a - b + b \exp[a(z - z_m)]}. \quad (9.3)$$

We set the values of the functional parameters following [Vangioni et al. \(2015\)](#), where they use the population of star-forming galaxies to characterise SFH. With this approach, they determine $\nu = 0.178 M_\odot \cdot \text{Mpc}^{-3} \cdot \text{yr}^{-1}$, the amplitude of the peak of SFH; $z_m = 2$, the redshift of the peak of SFH and $a = 2.37$, $b = 1.80$, where a is connected to the star formation rate density slope at $z < z_m$ and $b - a$ to the slope for $z > z_m$. Due to the current uncertainties in our understanding of the details of SFH, this ingredient adds another source of uncertainty in our predictions.

- **The metallicity-redshift relation and its dispersion.** The products of binary evolution are affected by metallicity, as we have discussed extensively through the previous chapters and in the previous sections. At the same time, the Universe is progressively enriched in chemical elements from the evolution and explosions of stars through cosmic time. The average metallicity of the Universe is therefore expected to increase as the redshift decreases. As discussed in [Lehoucq et al. \(2023\)](#), we use the formula proposed by [Belczynski et al. \(2016\)](#):

$$\bar{Z}(z) = \frac{y(1-R)}{\rho_b} \int_z^{z_{\max}} \frac{10^{0.5} \psi(z')}{H_0(1+z')\sqrt{\Omega_m(1+z')^3 + \Omega_\Lambda}} dz', \quad (9.4)$$

where, as defined in [Belczynski et al. \(2016\)](#), $R = 0.27$ is the return fraction (the mass fraction of each generation of stars that is ejected back into the interstellar medium); $y = 0.019$ is the net metal yield (the mass of new metals created and ejected into the interstellar medium by each generation of stars per unit mass locked in stars); and $\rho_b = 2.77 \cdot 10^{11} \Omega_b h_0 M_\odot \cdot \text{Mpc}^{-3}$ is the baryon density. The integration of the SFRD over the higher redshifts, weighed by the net metal yield in Eq. 9.4 determines the chemical enrichment at a given redshift z . With these values, the average metallicity at the peak of SFH is $\bar{Z}(z = 2) = 4.5 \times 10^{-3}$.

At a given redshift, the metallicity content can have a very high dispersion, due to non-homogeneous mixing in galaxies, different galactic types with more or less star formation, etc. The exact environment at the location of star formation can vary dramatically, even at a given redshift. Thus this dispersion, which is not yet constrained, influences the environments of stellar formation. For simplicity, we follow [Santoliquido et al. \(2021\)](#) and adopt a log-normal distribution of metallicities around the average metallicity at a given redshift:

$$P(Z|z) = \frac{1}{\sqrt{2\pi\sigma^2}} \exp\left(-\frac{(\log(Z/Z_\odot) - \log(\bar{Z}(z)/Z_\odot))^2}{2\sigma^2}\right), \quad (9.5)$$

with $\sigma = 0.2$. The evolution of SFRD is quite well constrained by observations, but the metallicity-redshift relation is much more uncertain (see *e.g.* [Madau & Dickinson 2014](#) and references therein). We do not discuss here the impact of our choices on the results uncertainties, which are already heavily influenced by the uncertainties on binary stellar evolution.

- **The distribution of delay times and fraction of successful BNS formation.** These two last elements are directly taken from the results of our simulations with COSMIC. Using the simulated populations at all metallicities, we determine the probability density $P(\Delta t_{\text{delay}}|Z)$, and in practice compute the merger rate density presented in Eq. 9.6 by randomly selecting

systems from the samples of binaries produced with COSMIC. The quantity $\alpha(Z)$ is the fraction of stellar mass that contributes to the population of BNSs at a given metallicity. This is also available from the simulations, since we know the total mass sampled from the Initial Mass Function (IMF), the fraction of binaries (here 0.5) and the total mass of stars producing BNSs.

With these three ingredients, we can compute the BNS merger rate (note that this formula is general to any type of merging binaries with a distribution of delay times, evolution with redshift and metallicity):

$$\mathcal{R}_{\text{merg}}(t) = \int_{Z_{\text{min}}}^{Z_{\text{max}}} \int_{t_{\text{delay,min}}}^{t_{\text{delay,max}}} \alpha(Z) \psi(t - \Delta t_{\text{delay}}) P(\Delta t_{\text{delay}}|Z) P(Z|t - \Delta t_{\text{delay}}) d\Delta t_{\text{delay}} dZ, \quad (9.6)$$

where we used Eq. 9.2 to change the redshift variable to time. The results obtained using these formulae will be discussed in Secs. 9.5.3 and 9.6, but I will first show the application of the same formalism to the computation of the stochastic GW background.

9.5.2 The Stochastic Gravitational Wave Background from Binary Neutron Star Mergers

Before resuming our study of the evolutionary tracks of BNS progenitors in the next sections, I discuss here how the population of BNSs simulated with the method presented in Sec. 9.1 and the expression of the merger rate density (Eq. 9.6) have been used to derive the contribution of BNSs to the stochastic GW background.

GW interferometers are indeed able to detect individual merger events, as described in Sec. 1.2, but they also see at all times the background signal resulting from the incoherent superposition of the signals from unresolved sources, such as Core-Collapse Supernovae (CCSNe), rotating NSs and compact object binary mergers at high redshift. This is known as the *astrophysical stochastic GW background*. There is also a *cosmological* stochastic GW background that could be produced by *e.g.* cosmological inflation, cosmic strings, primordial BHs, and first order phase transitions in the early Universe. More details on the stochastic GW background can be found in the reviews by Regimbau (2011); Christensen (2019); Renzini et al. (2022).

In **Publication III** (Appendix E.3, Lehoucq et al. 2023), we use populations of compact objects simulated with COSMIC to estimate the intensity of the stochastic GW background in the observing bands of current and future GW interferometers, in particular LIGO/Virgo and the Laser Interferometer Space Antenna (LISA, Amaro-Seoane et al. 2023). The population of BBHs used was described in Srinivasan et al. (2023), and the population of BNSs is the one described in this chapter. This article mostly discusses BBHs, since they are the dominant contributor to the stochastic GW background in the local Universe and BNSs are subdominant. The stochastic GW background from compact binary mergers suffers from large uncertainties, mainly due to the underlying uncertainties in binary stellar evolution in COSMIC, but our results indicate that some binary stellar evolution parameters which introduce a large merger rate may already be ruled out by the non-detection of the stochastic GW background in O3. As I discuss in Chapter 10, a direct follow-up of this work is to explore the astrophysical stochastic GW background for Einstein Telescope (Maggiore et al., 2020; Branchesi et al., 2023) and Cosmic Explorer (Evans et al., 2021) which is expected to be dominated by BNS mergers.

This work shows how simulated populations of BNSs with COSMIC can be used in different contexts. I now come back to the discussion on the evolutionary tracks.

9.5.3 Results for the Binary Neutron Star Merger Rate

The confirmed observation of two BNS mergers during the first three observing runs of the GW interferometers (see Chapter 3) has provided a broad constraint on the local merger rate, *i.e.* at $z \simeq 0$: $\mathcal{R}_{\text{merg}}(z = 0) = 10 - 1700 \text{ Gpc}^{-3} \cdot \text{yr}^{-1}$ (The LIGO Scientific Collaboration et al., 2021b).

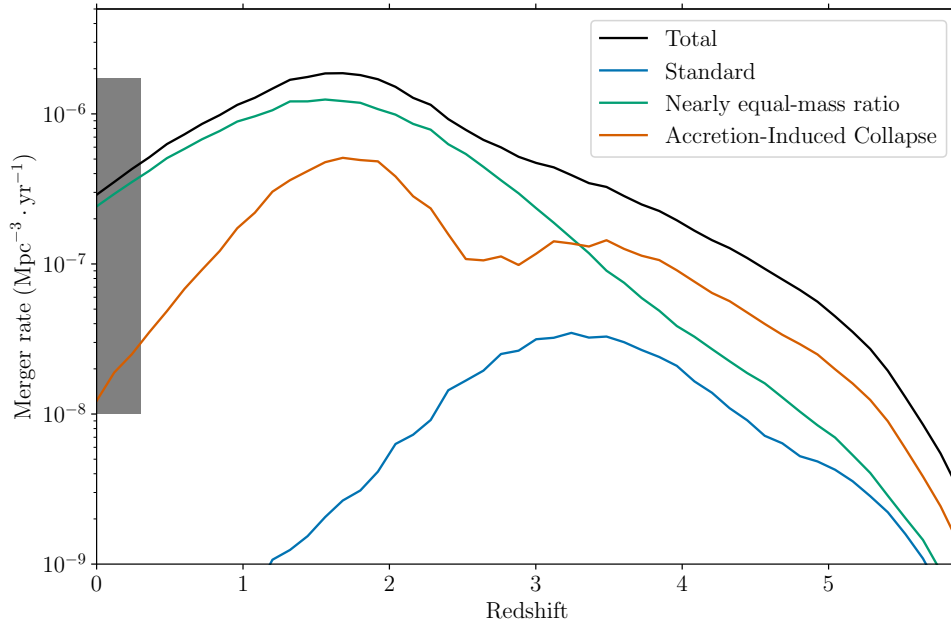


Fig. 9.22: Evolution of the merger rate (in $\text{Mpc}^{-3} \cdot \text{yr}^{-1}$) with redshift. We show the total rate in black, and the relative contributions of each evolutionary track: in blue, we show the standard evolutionary track (Sec. 9.3.1); in green the evolutionary track with equal-mass progenitors (Sec. 9.3.2); and in orange the AIC evolutionary track (Sec. 9.3.3). The relative contribution of each track to the merging population varies with redshift, with the AIC track prominent at high redshifts, and the equal-mass ratio track dominant at low redshifts. The grey box represents the constraint on the merger rate in the local Universe after the O3 observing run of LIGO/Virgo: $\mathcal{R}_{\text{merg}}(z = 0) = 10 - 1700 \text{ Gpc}^{-3} \cdot \text{yr}^{-1}$ (The LIGO Scientific Collaboration et al., 2021b). While this value is inferred at $z = 0$ given the observing range of BNS mergers for GW interferometers ($\lesssim 100 \text{ Mpc}$), we stretch the grey box up to $z = 0.3$ for visualisation purposes.

I present in Fig. 9.22 the resulting merger rate for the model discussed throughout the chapter, along with the constraint on the local merger rate from The LIGO Scientific Collaboration et al. (2021b). Our model is compatible with the observed local merger rate constraint. We focus on the contributions from each of the three evolutionary tracks. First, the standard evolutionary track contributes to a very small fraction of the merger rate. This result is in tension with other previous works focusing on BBHs, *e.g.* van den Heuvel & De Loore (1973); Tauris & van den Heuvel (2006); Belczynski et al. (2018); Vigna-Gómez et al. (2018); Neijssel et al. (2019); Broekgaarden et al. (2021); Iorio et al. (2023).

We mostly note that the evolutionary track dominating the population of merging binaries changes with redshift: at higher redshift, most mergers are produced by BNS systems formed via the AIC evolutionary track, while at lower redshift, the population we see merging in the local Universe is mostly formed by initially equal-mass stars.

The two peaks in the merger rate contribution from the AIC evolutionary track originate from the two evolutionary sequences that contribute to this track: one at low metallicities and the other at higher metallicities. This gap may simply be a numerical effect due to the treatment of stellar types in the model.

Because most merging systems at high redshift form *via* the AIC evolutionary track, they have very short merger times Δt_{GW} . The merger rate density shown in Fig. 9.22 is therefore shaped by the SFRD.

Finally, we stress that the total merger rate evolution is quite smooth and hides the diversity of progenitor evolutionary tracks that make up the BNS population. This work shows that this value alone is not enough to model the chemical enrichment of galaxies, as I discuss in the next Sec. 9.6.

9.6 Astrophysical Consequences: a Population of Short Delay Times

As shown in Fig. 9.22, our model predicts an evolution of the dominant evolutionary track with redshift. Therefore, the population observed merging today in the local Universe is different than the population of mergers at higher redshift, that could contribute to the early chemical enrichment of galaxies. In particular, the distribution of delay times of the population of BNSs that merge in the local Universe contains many systems whose delay times are of orders of Gyrs (see Fig. 9.20), while the merging binaries at higher redshift have much shorter delay times (see Fig. 9.21). Such an evolution of the distribution of delay times with redshift is not often included in analytical models and may play a role in the Universe’s chemical enrichment.

Additionally, as shown in Fig. 9.22 most mergers at high redshift occur from the AIC evolutionary track. In this evolutionary track, the first star first collapses into a WD, without CCSN. Therefore, the chemical enrichment in products of nuclear fusion is impossible, as the final fusion products such as iron are not synthesized by the primary. As a consequence, if we assume that the typical yield is the same for the entire population, this evolutionary track leads to 2 times less enrichment in nuclear fusion products (in particular iron) than the standard or the equal-mass track.

I discussed in Sec. 3.4 the observation that some low-metallicity stars ($[\text{Fe}/\text{H}] \lesssim -3$) have a significant excess of *r*-process elements, usually probed by the Europium abundance: ($[\text{Eu}/\text{Fe}] \gtrsim 1.5$). Our results are naturally compatible with this observation. As the AIC evolutionary track dominates at low metallicities, the BNS mergers typically occur close to star-formation sites due to the low migration time Δt_{GW} of these systems shown in Sec. 9.4.1. Some molecular clouds where star formation is still ongoing can therefore be enriched by these systems with short Δt_{delay} . Because they also naturally eject less products of nuclear fusion due to the intermediate collapse of the primary into a WD, the environment is prone to *r*-process enrichment, sometimes without a significant enrichment in iron. This can thus explain the observed abundance ratios.

The efficiency of BNS production is extremely low, as discussed previously. This phenomenon is therefore also expected to be quite rare among the stellar population. This is therefore in accordance with the second observational constraint: there is a large scatter in *r*-process elements abundances in low-metallicity stars. In this scenario, some sites of stellar formation host a BNS merger, while others do not. This naturally leads to a large scatter in *r*-process element abundances, assuming they are formed only in BNS mergers (see Sec. 3.4 for the discussion on energetic CCSNe).

Another observation discussed in Sec. 3.4 is the distribution of offsets of short Gamma-Ray Bursts (GRBs) in their host galaxy. It shows a large scattering, with some short GRBs close to the galactic centers, and other with large offsets. Identifying short GRBs to BNS mergers, this can be explained with a large scatter in delay times Δt_{delay} , but requires the presence of a population of short delay time binaries. This is again addressed by our model, since the AIC evolutionary track produces systems with short merger times $\Delta t_{\text{GW}} \lesssim 100$ Myr.

Interestingly, I discussed in Sec. 6.4 this population with short delay times, which is expected to be associated to more luminous GRB afterglows at Very High Energy (VHE) as they occur in higher external density environments. The two approaches discussed in this thesis therefore show complementary results on this yet elusive population.

Because most systems found with this model have very short merger times, the merger rate density peaks at $z \sim 1.7$, roughly at the time of the peak of SFH. While current GW detectors are

only sensitive to mergers occurring in the local Universe, third-generation instruments like Einstein Telescope and Cosmic Explorer are expected to be sensitive to BNS mergers up to $z \sim 2$. They can therefore help probing the evolution of the merger rate density with redshift and inform on the underlying processes of BNS formation. A merger rate density which closely follows the SFRD would for example indicate a population of BNS with short delay times. Combined with future VHE instruments such as the CTAO, they could therefore be ideal tools to study the evolutionary tracks of BNS progenitors, providing additional tests for our predictions.

Part IV

Conclusion and Perspectives

Chapter 10

Conclusion and Perspectives

Contents

10.1 Main Results of this Doctoral Thesis	186
10.2 Perspectives for Future Studies	188
10.3 General Conclusion	194

10.1 Main Results of this Doctoral Thesis

The detection of the first joint Gravitational Wave (GW) and electromagnetic transient GW 170817 has marked the passage in a new era for multi-messenger astronomy with GWs and the study of the transient sky. This detection has confirmed many of the theoretical expectations for the associated outflows and electromagnetic counterparts associated to Binary Neutron Star (BNS) mergers. A Gamma-Ray Burst (GRB) was detected ~ 1.7 s after the GW-inferred merger time, though its weak intrinsic luminosity and the jet viewing angle indicate a potentially different emitting process than in cosmological short GRBs, like the shock breakout out of the kilonova ejecta. An optical thermal kilonova was detected for ~ 30 days. It was powered by the energy deposition from the radioactive decay of unstable heavy elements produced by the r -process in this neutron-rich ejecta. A highly-relativistic jet was launched and the acceleration of electrons at the external shock induced by the jet deceleration powered a non-thermal transient, the GRB afterglow. It has been detected for more than four years, from radio to X-rays. Combined with the GW signal, these observations constitute one of the most exquisite multi-messenger observational data set for a single event. They helped refining many of the models proposed thus far, while confirming the predictions on the associated signals. The GRB afterglow of GW 170817 stood out due to its late-time peak and slow rise, which – combined with Very Long Baseline Interferometry (VLBI) observations – were the most significant signatures of an off-axis observation of a laterally-structured jet. The afterglow of GW 170817 was also observed at Very High Energy (VHE) ($h\nu \sim 1$ TeV) by H.E.S.S. but only a flux upper limit was derived. On the other hand, a few long GRB afterglows have been detected at VHE in the past years (*e.g.* GRB 190114C and GRB 221009A) and have revived the need for afterglow models including a VHE component.

GW 170817 was detected in the context of the sequence of observing runs by the GW interferometers. The gradual sensitivity improvements between the first and third observing runs (O1, O2 and O3) have allowed to detect an increasing number of compact object mergers: BNS, Neutron Star – Black Hole binary (NSBH) and Binary Black Hole (BBH). After O3, two BNS mergers were confidently reported: GW 170817 and GW 190425, but ~ 100 BBH mergers were already detected. With the fourth observing run starting at the time of writing, more detections await and therefore a more precise understanding of the local population of merging binaries is expected. Several works already model the population of compact objects mergers with different approaches. One of these approaches relies on population synthesis models, which allow to follow the simplified evolution of binary systems with short computation times. Using those, it is possible to generate mock populations of compact objects with various physical parameters, and to compare them with observations.

In this doctoral thesis, I therefore studied BNS mergers from two perspectives. I first used the detection of GW 170817 to propose a refined model of the afterglow emission which helps better characterising *individual* detections. I developed a new realistic numerical afterglow code valid from radio to VHE that includes the lessons learnt from GW 170817 and VHE afterglows. Second, I used population synthesis tools to study the *population* of merging BNSs detected with GWs. I specifically focused on the evolution of their progenitors: binary systems of massive stars.

Concerning GRB afterglows (Part II), I developed a semi-analytical model with a computationally-efficient numerical implementation allowing data fitting using Bayesian statistics as in **afterglowpy** (Ryan et al., 2020), with a specific focus on the treatment of the jet lateral structure and dynamics (Gill & Granot, 2018) and the radiation at VHE (Nakar et al., 2009). Firstly, multi-messenger detections of BNS mergers including a GW signal and the detection of the afterglow are currently limited to the local Universe due to the sensitivity limitations of current GW interferometers. Joint detections are thus likely to feature off-axis viewing angles, and accounting for the lateral structure is therefore necessary in a general case to model off-axis GRB afterglows, and specifically to reproduce the slow rise-time of the afterglow of GW 170817. Secondly, motivated by recent detections of long GRB afterglows at VHE, I extended the radiative model to account for Synchrotron Self-Compton

(SSC) diffusions of synchrotron photons on the seed electron population. This model accounts for the two regimes of diffusion, Thomson and Klein-Nishina (KN), which can also introduce modifications on the synchrotron radiation spectrum, as introduced in [Nakar et al. \(2009\)](#). I presented this model in detail in Chapter 5.

Using this afterglow model, I studied GW 170817 (**Publication I**, submitted, Appendix E.1, [Pellouin & Daigne 2023](#)), which was also observed at VHE by H.E.S.S., leading to an upper limit obtained around the peak (~ 130 days); and GRB 221009A (**Publication II**, published, Appendix E.2, [Kann et al. 2023](#)), the brightest GRB ever observed, to analyse the early near-infrared to X-rays observations in the context of the follow-up campaign of the GRANDMA collaboration. In **Publication I** (Appendix E.1), we used our model in a Bayesian framework to fit the observational data, restricting the focus to the afterglow signal only (*i.e.* not including constraints from the GW detection or VLBI observations). We found parameter values allowing for a precise fit of the synchrotron component of the spectrum, and also retrieved parameter correlations already discussed in the literature. The predicted VHE emission is however more uncertain given the absence of observational constraints, and the predicted fluxes range between 3 and 2 orders of magnitude below the H.E.S.S. upper limit. This is mostly due to a high viewing angle, and a low external density which leads to a strong KN attenuation as discussed in Chapter 6. We therefore studied the conditions under which the afterglow of GW 170817 would have been detectable with H.E.S.S. or future instruments like the CTAO ([Cherenkov Telescope Array Consortium et al., 2019](#)). We found that a smaller viewing angle or a higher external medium density increase the observed flux at the peak, while decreasing the peak time. They impact the VHE signal in different ways, as the viewing angle is a geometrical effect which does not affect the intrinsic emission and modifies the synchrotron and the SSC component in the same way. Conversely, higher external medium densities modify the jet dynamics and the radiative regimes. They also introduce variations in the synchrotron-to-SSC flux ratio. The effect of the density is however capped by the increasing efficiency of pair production at higher densities, which halts the flux increase. A consequence of this study is that mergers in higher density environments are more likely to be detected at VHE, as already suggested in the synchrotron regime by [Duque et al. \(2020\)](#), with the advantage of a better model parameter inference with VHE detections. Interestingly, mergers occurring in high-density environments could therefore trace a population of BNSs with short merger times. As discussed in Secs. 3.4 and 6.4, other indirect evidence such as the distribution of offsets of short GRBs in their host galaxy or *r*-process element abundances in low-metallicity stars suggest the existence of such a short-merger time population.

In Part III, I studied this population of short merger time binaries from a different angle ([Pellouin et al. 2023, in prep.](#)). BNSs are expected to be formed by the joint evolution of two massive progenitors in a binary system, as presented in Chapter 7. I used COSMIC ([Breivik et al., 2020](#)), a population synthesis model (see Sec. 7.3). Population synthesis allows to follow the evolution of binary systems using analytical prescriptions for the phases of single star evolution like stellar winds or Supernova (SN); and for the effects related to binarity, like mass transfers and Common Envelope (CE). Many uncertainties arise from these analytical descriptions, as presented and discussed throughout Chapter 8. We decided to use a set of physically-motivated parameters and focus on the evolutionary tracks that lead to successful BNS formation. We defined three dominant evolutionary tracks in Sec. 9.3: a standard evolution with asymmetric binaries and a phase of CE when the primary star has already collapsed in a Neutron Star (NS); a track from equal-mass ratio progenitors with a phase of CE when both stars evolve on the giant branch; and a track where the primary first collapses in an oxygen-neon White Dwarf (WD), which later collapses into a NS due to the accretion of material from its companion, in an Accretion-Induced Collapse (AIC). We studied each evolutionary track individually and in particular showed that the AIC evolutionary track produces short-separation BNSs which merge in timescales ~ 10 Myr (see Sec. 9.4). The relative contributions of each evolutionary track evolve with cosmic time. The AIC track dominates the mergers at high redshifts ($z \gtrsim 3$), while the evolutionary track with equal-mass progenitors and longer delay

times dominates the population at lower redshift ($z \lesssim 3$), as discussed in Sec. 9.5. This result has important consequences on the history of chemical enrichment of the Universe, since the AIC evolutionary channel allows the production of r -process elements from BNS mergers, while only one of the progenitors undergoes a Core-Collapse Supernova (CCSN). This could provide an explanation for the population of Galactic stars observed with high abundances of r -process elements and low abundances of the products of stellar evolution, such as iron (see Sec. 6.4). Interestingly, these systems would also be more likely to have a stronger VHE emission in their GRB afterglow, as discussed in Part II. The simulated population of BNSs was also used in **Publication III** (Appendix E.3, [Lehoucq et al. 2023](#)) to characterise the stochastic GW background from the population of BNSs.

Overall, this work provides a joint view on both individual BNS mergers that will be detected in the future, and on the global population of merging BNSs, which will also be better constrained by future observing runs of the current GW interferometers and the next generation of detectors, such as the Einstein Telescope ([Maggiore et al., 2020](#); [Branchesi et al., 2023](#)) and Cosmic Explorer ([Evans et al., 2021](#)). I discuss future follow-ups of this doctoral work in Sec. 10.2.

10.2 Perspectives for Future Studies

The work presented in this doctoral thesis paves the way to multiple future studies in a dynamic and rich observational context. I discuss hereafter some future projects. Some are direct follow-ups of the work presented here, some more median-term activities that could be conducted by future members of our group at IAP or more generally the community.

GRB 221009A: a New Afterglow Analysis using LHAASO Data at Very High Energy

I presented in Sec. 4.2 the observations of GRB 221009A and the results of the preliminary analysis of the synchrotron component of the afterglow based on early near-infrared to X-ray observations described in **Publication II** (Appendix E.2, [Kann et al. 2023](#)). Its afterglow was also monitored extensively at all wavelengths from radio to X-rays, and features some puzzling elements. The absence of detected signature of a jet break in X-ray observations up to ~ 55 days indicates that the jet was probably very narrow with a shallow lateral structure in energy, as reported by [O'Connor et al. \(2023\)](#) and also discussed in [Gill & Granot \(2023\)](#). It has also been pointed out by [Laskar et al. \(2023\)](#) that the early-time afterglow emission features potential signatures of a reverse shock emission. As shown in Sec. 4.2, our first estimates also favoured either an extremely narrow jet or conversely a jet with very large opening angle, which faces an energy budget crisis, as also discussed in [O'Connor et al. \(2023\)](#). The radio observations were published by [Laskar et al. \(2023\)](#) too late to be taken into account in our preliminary analysis, and bring new important constraints. In addition, at that time, VHE observations by LHAASO were not yet released, but have since been published in [LHAASO Collaboration et al. \(2023\)](#). In particular, ~ 64000 VHE photons were detected, and the flux peaked at the time of the peak of the prompt GRB. In this discovery article, the authors also indicate that a narrow jet may be needed to reproduce these observations. So far, it has not been attempted to fit GRB 221009A's afterglow with a structured jet model while including this VHE detection. These elements are incentives to perform a new analysis of the afterglow of GRB 221009A from a laterally-structured jet, this from radio to VHE.

Towards Even More Realistic Afterglow Models

Several aspects of the GRB afterglow modelling have been discussed, in particular in Chapter 5 (jet dynamics, jet structure, assumptions for the microphysics, ...). Currently, several physical aspects are not accounted for in our model, which will provide insights into future GRB afterglow

studies. This will be done along two main axes, related to the radiative processes and to the dynamics.

Many GRB afterglows are observed in radio. In this frequency range, synchrotron self-absorption can reduce the radiated flux and modify the spectral profile with an additional break. Another future development of the model therefore consists in including the treatment of synchrotron self-absorption at low energy that I described in Sec. 5.4.9. In the most detailed approach, synchrotron self-absorption can in principle modify the low-frequency afterglow emission and impact the SSC component. In a more simple approach, the effect of synchrotron self-absorption can be modelled with a similar treatment as for pair production.

It would also be very useful to assess the accuracy of our model in all the different regimes presented in Appendix A. Bošnjak et al. (2009) have presented a detailed radiative model in the context of the GRB prompt emission, where the evolution of electrons and photons is solved numerically including synchrotron radiation and SSC radiation in both Thomson and KN regimes, and synchrotron self-absorption and pair production. It can be used with arbitrary microphysical parameters spanning the different diffusion regimes for a detailed comparison. In particular, it appears that some of the regimes described in Appendix A feature several breaks that may not be clearly distinguishable in a detailed treatment of the radiative processes. Such a study could also lead to a refined method to determine the spectral profiles described in Sec. 5.4.6, and to better calibrate our prescription while still only using a semi-analytical treatment.

The treatment of the radiation in the slow cooling regime can also be improved. Indeed, we currently make the assumption that the accelerated electrons at the shock all radiate their energy on a dynamical timescale (see Sec. 5.4.3). While this is true in the fast cooling regime, where the radiative timescale is shorter than the dynamical timescale for all electrons ($\gamma_m > \gamma_c$), in the slow cooling regime the low-energy electrons can still contribute to the total population of accelerated electrons at the next time step and therefore alter the spectral profile. A refined treatment of the radiation in the slow cooling regime would therefore require to follow the successive populations of accelerated electrons at each time step and add up their individual contributions. This has already been introduced in Beloborodov (2005); Uhm et al. (2012); Hascoët et al. (2012a).

The reverse shock (see Sec. 5.2) is expected to contribute to the early-time light curve of some GRB afterglows, mostly in optical and radio, and may be at the origin of some of the diversity of early afterglows. The contribution of the reverse shock can be added to our model with ease, as our numerical implementation separates the computation of the dynamics of the shock from the emission in the comoving frame of each shocked region, and the final equal-arrival-time surfaces integration. The reverse shock dynamics can be modelled in several ways. In a first version, the reverse shock dynamics can be derived analytically, as shown in Sari & Piran (1999); Kobayashi (2000) and therefore implemented similarly as has already been done for the forward shock dynamics. More sophisticated methods are needed to take into account a possible radial structure of the ejecta, such as the mechanical model by Uhm & Beloborodov (2007) or the ballistic model by Genet et al. (2007). This approach has for instance been used by Uhm et al. (2012); Hascoët et al. (2014) to study the possible contribution of long-lived reverse shocks to plateaus or flares in early X-ray afterglows (Nousek et al., 2006). Another possible origin for the features observed in the early X-ray afterglow is the lateral structure from jets viewed slightly off-axis (Beniamini & Nakar, 2019; Beniamini et al., 2020a). These last two propositions can be tested with our model with the addition of the reverse shock, in a more statistical way by analysing several GRBs with X-ray plateaus.

A still open problem concerns the late-time evolution of the afterglow, and in particular the lateral expansion which impacts the jet dynamics in the mildly-relativistic regime (see Sec. 5.1). In this context, the afterglow of GW 170817 is still detected more than four years after the merger, making it one of the afterglows monitored for the longest time. Including the jet lateral expansion in our afterglow model would allow to discuss late-time properties of GRB afterglows. As discussed in Granot & Piran (2012), several prescriptions have been proposed in the past. In *afterglowpy*,

Ryan et al. (2020) use the description of Duffell & Laskar (2018), which is an extension to the models proposed in Rhoads (1999) and Granot & Piran (2012), calibrated on hydrodynamical simulations.

Another development may be relevant for the early afterglow of the brightest bursts. Beloborodov (2002) suggested that the gamma-ray photons emitted during the prompt phase can produce pairs in the ambient medium, setting it in a radial outward motion by momentum conservation. The forward shock would therefore propagate in a moving pair-enriched external medium. The net effect is a lower static-equivalent medium density, leading to a slower deceleration and therefore a longer coasting phase. This also implies that the typical Lorentz factor of accelerated electrons is lower as the dissipated energy is shared in a larger number of leptons. This could have an observable signature at early times in the optical (synchrotron) and the GeV (SSC) range (Beloborodov, 2005; Beloborodov et al., 2014; Vurm et al., 2014). This effect could also be tested with our model.

Finally, our model can be extended quite naturally to compute afterglow images and polarisation, in a similar way as proposed in Gill & Granot (2018). Images in particular can be used to track the centroid proper motion for VLBI observations of nearby off-axis afterglows, which is another interesting aspect of off-axis observations of structured jets: they provide much better constraints on the ratio θ_v/θ_c . Nakar & Piran (2021) describe an analytic estimate of this ratio depending on the width of the peak of the light curves. In a recent study, Govreen-Segal & Nakar (2023) show that the quantity $\theta_v - \theta_c$ can be constrained by the VLBI measurement of the proper motion of the centroid of the emitting region. An analytical estimate of the centroid proper motion can be included in our afterglow simulations, to model self-consistently both the afterglow light curves at several wavelengths and the VLBI constraints, as already done in the case of GW 170817 with other afterglow models by Mooley et al. (2018a, 2022); Ghirlanda et al. (2019). The equations describing the centroid displacement are closely related to several quantities already used in the calculation of the flux, and would therefore fit well in our model.

While the some proposed additions and tests are more exploratory, the inclusion of the reverse shock and synchrotron self-absorption will be required to analyse more VHE GRB afterglows in the future, as I discuss next.

Leveraging the Current and Future Diversity of Gamma-Ray Burst Afterglow Observations from Radio to Very High Energy

The sample of GRB afterglows detected at VHE is currently growing. Following the study of GRB 221009A mentioned above, we could analyse the other bursts detected at VHE. The other bursts notably include GRB 190829A (H. E. S. S. Collaboration et al., 2021), a low-luminosity GRB; and GRB 190114C (MAGIC Collaboration et al., 2019a), that I presented in Sec. 4.2 and which benefits from a remarkable multi-wavelength coverage. Most of these bursts have also been observed in radio, and several studies point towards a contribution of the reverse shock (see *e.g.* Salafia et al. 2022b; MAGIC Collaboration et al. 2019b). This justifies the priority developments of our model that I listed before. In the case of GRB 190114C, the model proposed by MAGIC Collaboration et al. (2019b) suggests the evolution of some microphysical parameters during the propagation. This study is based on the independent modelling of the afterglow spectra at different times but such an effect could be implemented in our model for the whole dynamical evolution.

In coming years, the sample of GRB afterglows with a VHE component should increase. Indeed, the CTAO (Cherenkov Telescope Array Consortium et al., 2019) will detect such afterglows with an increased sensitivity. We therefore expect to improve our understanding of VHE emission in GRB afterglows. Specifically, lifting some parameter degeneracies thanks to VHE observations (see Sec. 6.2.4) would help refining our understanding of the typical value of ζ , the fraction of electrons that are accelerated at the shock which is degenerate with other parameters such as ϵ_e in the synchrotron regime. This could be a step to better understand the details of particle acceleration in ultra-relativistic shocks and the associated radiative processes at VHE. Our model could in particular

help better constraining the VHE emission of accelerated electrons to then better constrain alternative contributions. Indeed, as presented in Sec. 4.2, some authors suggest that the VHE component may instead be produced by shock-accelerated hadrons: protons and photons interact to produce pions, which in turn decay to radiate at VHE (Asano & Mészáros, 2012); or the highest-energy protons radiate in the gamma-ray range by synchrotron, as suggested by Totani (1998). Leptonic and hadronic models are discussed in detail in Kumar & Zhang (2015). Evidence for a hadronic component in GRB afterglows would also make them good candidates for future transient neutrino detections with *e.g.* IceCube (see *e.g.* Murase & Bartos 2019).

Future GRB afterglow detections will also be made with the upcoming the Space Variable Object Monitor (SVOM) mission (Paul et al., 2011; Wei et al., 2016), to which the group at IAP is associated. Compared to Swift, SVOM aims at building a smaller sample of GRBs where most of the events are well characterised (prompt, afterglow and redshift). One important scientific objective is to have two thirds of bursts with an associated redshift, compared to one third with Swift. This will be achieved by the combination of the on-board instruments and slewing capabilities, the anti-solar pointing of the satellite allowing a fast ground-based follow-up, and a network of ground-based telescopes. In addition, the low-energy threshold (4 keV) of the X-ray instrument (ECLAIRS) will allow SVOM to explore the diversity of the GRB population in the local Universe, including soft or low-luminosity events (Arcier et al., 2020). In this context, our model could be used to perform a homogeneous analysis of these bursts and therefore better understand the intrinsic diversity of the relativistic jets associated to these events.

Finally, future multi-messenger BNS detections will of course remain events of utmost interest, and detailed modelling of the afterglow will be necessary to extract all the physical constraints. Such detections could become much more frequent with the third generation of gravitational interferometers: see, for example, the prospects offered by the Einstein Telescope in Ronchini et al. (2022).

Searching for Orphan Afterglows

With future optical instruments such as the Vera C. Rubin observatory (Ivezić et al., 2019), some GRB afterglows from off-axis jets could be detected in optical without any association to a GRB. They are known as *orphan afterglows* (see Sec. 4.1, Metzger & Berger 2012). Finding these specific transients among the millions of alerts per night from the Legacy Survey of Space and Time (LSST) is challenging, and statistical tools are being developed as part of the Fink broker to conduct this real-time analysis (Möller et al., 2021), including researchers at IAP. The numerical implementation of our model is computationally efficient, and we can use it to create a bank of light curves with varying parameters. With this bank of afterglow light curves, it is possible to grade the nightly transients depending on how well their properties fit with those of simulated GRB afterglows, either directly by using the light curves bank, or indirectly by using machine learning-based tools trained on the light curves bank. Such a template bank could also be used by follow-up collaborations such as GRANDMA to characterise orphan afterglow candidates identified by the Vera C. Rubin Observatory.

These future projects will mainly be possible thanks to the new instruments that will probe the transient sky. They will help better understand the physics of GRBs. With population synthesis, we can already follow the approach discussed in Chapter 9 to study the population of BNSs in the context of improved statistics of GW detections.

Connecting the Galactic Population of Binary Neutron Stars to the Merging Extragalactic Population

It is unclear whether the population of BNSs that we observe with GW interferometers and the population of Galactic BNSs have the same properties, and if they form *via* the same evolutionary

tracks. We can use straight-forwardly our methods for evolutionary track identification (Sec. 9.3) to probe the Galactic population of BNSs. This time, instead of filtering out systems with delay times $\Delta t_{\text{delay}} < t_{\text{Hubble}}$ to study merging binaries, we instead only keep the systems which have not merged. From a preliminary study, we find that properties of their progenitors may be different than those of the merging population. Vigna-Gómez et al. (2018) conduct a similar study but do not follow the evolution with redshift, and thus do not discuss the AIC evolutionary track. We do not expect it to contribute to the population of Galactic binaries as it produces systems with short merger times, mostly at high redshift. Interestingly, no AIC event has ever been detected so far (but there is some indirect evidence for their existence, see Wang & Liu 2020), which is expected given the relatively low amount of ejected material, leading to a faint transient, but could also be due to a low intrinsic event rate at high redshift. Our model can provide insights on the expected rate in the Milky Way.

In **Publication III** (Appendix E.3, Lehoucq et al. 2023), we explored the stochastic GW background from compact object mergers for current GW interferometers LIGO/Virgo. Third-generation interferometers such as the Einstein Telescope (ET, Maggiore et al. 2020; Branchesi et al. 2023) in Europe and the Cosmic Explorer (CE, Evans et al. 2021) in the U.S.A. are expected to detect individually BBH mergers up to $z \sim 20$ in the most favourable cases (Maggiore et al., 2020; Evans et al., 2021). Conversely, the sensitivity to BNS mergers is expected to be up to $z \sim 2$, thus leaving unresolved sources. Therefore, while the astrophysical stochastic GW background for current instruments is expected to be dominated by merging BBHs, BNSs will be the dominant contributor for third-generation instruments. The contribution to the stochastic GW background from compact objects mergers has already been studied for BBHs using extrapolations of the local merger rate and mass distribution inferred by the LIGO/Virgo interferometers (see *e.g.* Abbott et al. 2016; Jenkins et al. 2018); or analytical prescriptions with a particular focus on the BBH formation channel and the effect of metallicity (*e.g.* Dvorkin et al. 2016; Cusin et al. 2019); or using population synthesis (*e.g.* Périgois et al. 2021, 2022). However, due to the much less constraining information on the population of BNSs, there is currently less focus on the contribution of merging BNSs to the stochastic GW background. A natural follow-up of the work presented in **Publication III** (Appendix E.3, Lehoucq et al. 2023) is therefore to conduct a similar study for the third generation GW interferometers.

Improving Binary Neutron Stars Population Models with More Gravitational Wave Detections

In addition to ET and CE mentioned earlier, in the coming years, the Laser Interferometer Space Antenna (LISA, Amaro-Seoane et al. 2023) might also detect the GW signal from BNS systems. Given that it is sensitive at lower sensitivity frequencies (\sim mHz) than current interferometers (\sim 10 Hz), it will detect BNS systems with wider separations before merger. However, due to the lower amplitude of the signal at larger separations, it will only be sensitive to systems located at short distances from the Earth. This would bridge the gap between the population of Galactic binaries and the population of merging binaries and potentially inform on their differences (see *e.g.* Korol & Safarzadeh 2021).

Recently, the second BNS merger detected by the LIGO/Virgo interferometers, GW 190425 (Abbott et al., 2020a) had a total mass $\sim 3.4 M_{\odot}$ (see Sec. 3.3). This is at odds with the Galactic NSs detected electromagnetically (see Sec. 3.2), which are less massive (Farrow et al., 2019; Zhang et al., 2019). While it cannot be ruled out that one of the components of this binary is a Black Hole (BH), this would also challenge the models of BH formation which do not predict formation in such mass ranges. If we instead assume that both components of GW 190425 are NSs, such a mass discrepancy could imply that the formation mechanisms of NSs in binaries may differ than those of single NSs. For example, the first NS formed in BNS systems could experience more accretion during

its lifetime than a typical single NSs due to mass transfers from the secondary, thus gaining higher masses. Either way, we can expect a lot of progress in the future concerning the description of NS masses in binary systems, which is currently also extremely uncertain (see Sec. 8.2.5). Interestingly, as discussed by Korol & Safarzadeh (2021), LISA could also be used to find such systems.

At the time of writing, the fourth GW observing run, O4, is just starting and is expected to add new detections of BNS mergers to the current sample. In the longer-term future, ET and CE will bridge the gap between the electromagnetic detection range of GRBs and their afterglows and the GW detection range of merging BNSs, up to $z \sim 2$. This will therefore complete our understanding of the population of GRB afterglows between cosmological on-axis, and local off-axis detections. With third generation GW detectors, it will also be possible to probe the evolution of the BNS merger rate with redshift, up to $z \sim 2$. This will put much tighter constraints on the parameters of population synthesis models, in particular those describing the CE phase and SNe kicks, which are currently still extremely uncertain (dozens of studies on these parameters have been conducted in the past years, see *e.g.* Iorio et al. 2023). With these detections, we can also expect to constrain the underlying evolutionary tracks, and the putative population of short merger time BNSs, as I discuss in the next paragraph.

Further Exploring Short Merger Time Binaries

In a recent study, Dvorkin et al. (2021) propose analytical prescriptions to describe the r -process enrichment of galaxies across cosmic times. In this work, the authors assume that a given fraction of binaries form BNSs, and set a distribution of delay times $P(t) \propto 1/t$ (*e.g.* Safarzadeh & Berger 2019). We could use instead the results from our simulations with COSMIC to obtain more realistic populations of BNSs, and derive predictions for r -process enrichment. In particular, given the evolution of the dominant evolutionary tracks with redshift, we can address in more detail the question of the scatter in the observed distribution of [Eu/Fe] at low metallicities discussed in Sec. 6.4. Another approach is to use numerical simulations of galaxies to model the distribution and properties of their stellar content, and use the results of these simulations as initial conditions for the distributions of stellar binaries in COSMIC and prescriptions for the Star Formation History (SFH) (see *e.g.* van de Voort et al. 2015).

Finally, a detailed modelling of galaxy evolution combined with population synthesis can be used to describe the properties of the host galaxies of BNS mergers, as well as the distribution of offsets using the distribution of SN kicks and the galactic gravitational potential. This can in principle be used to better characterise the host galaxies of BNS mergers and be compared with the statistical properties of short GRB hosts and offset distributions. The question of the host galaxy properties has already been studied in the case of BBHs by *e.g.* Lamberts et al. (2016); Srinivasan et al. (2023) and for BNSs by *e.g.* Artale et al. (2020); Chu et al. (2022). Interestingly, this can provide statistical tools to optimise the follow-up strategy of GW detections. Depending on the volume of the error box, several hundreds or thousands of candidate host galaxies can be compatible with the location of the event. It is therefore essential to prioritize some of them for the follow-up campaign to maximize the chances of finding a kilonova transient, that may only be detectable for a few nights. Such tools can therefore be used to classify the best host candidates for a galaxy-targeted follow-up search, as also discussed in Nugent et al. (2022).

In conclusion, this doctoral work is well embedded in the current landscape of multi-messenger astrophysics and can seed many more studies, as discussed in this chapter.

10.3 General Conclusion

The doctoral work presented in this manuscript was motivated by the detection of the BNS merger GW 170817, which was a major breakthrough for multi-messenger astrophysics; and by the successive GW interferometers observing runs which start to unveil the population of compact object binaries, in particular since the third observing run in 2019. I described these foundations in Part I of this manuscript. Among the many directions that this thesis could have taken, we chose two distinct, but complementary ones. In Part II, I presented an afterglow model including a refined semi-analytical treatment of several physical properties that are vital to analyse new features of GRB afterglows: their VHE emission and the lateral structure of the decelerating jet, possibly viewed off-axis. I applied this model to predict the VHE emission of GW 170817, and studied the conditions required to observe similar events in the future. It became clear that mergers in higher density environments are good candidates for intense VHE radiation. Interestingly, such mergers in high density environments are also potential tracers of a population of short-merger time BNSs. I detailed in Part III a study of the evolutionary tracks of BNS progenitors using COSMIC, a population synthesis model. This complementary approach showed that there is a class of short-merger time binaries, dominant at high redshift, where the BNS is formed after the AIC of a WD into a NS. While being more likely to be detected at VHE, such a population of short merger times binaries also helps understanding the chaotic history of the chemical enrichment of the Universe. During this doctoral thesis, I realised that we are only at the beginning of the multi-messenger astrophysics era, and that the future will be paved with many more discoveries, especially given the large diversity of upcoming dedicated instruments, as I discussed in Part IV. Exciting times are ahead!

Bibliography

- Aartsen, M. G., Abbasi, R., Ackermann, M., et al. 2021, *Journal of Physics G Nuclear Physics*, 48, 060501
- Aartsen, M. G., Ackermann, M., Adams, J., et al. 2014, *Phys. Rev. Lett.*, 113, 101101
- Abbott, B. P., Abbott, R., Abbott, T. D., et al. 2016, *Phys. Rev. Lett.*, 116, 061102
- Abbott, B. P., Abbott, R., Abbott, T. D., et al. 2020a, *ApJ*, 892, L3
- Abbott, B. P., Abbott, R., Abbott, T. D., et al. 2019a, *Physical Review X*, 9, 031040
- Abbott, B. P., Abbott, R., Abbott, T. D., et al. 2017a, *ApJ*, 848, L13
- Abbott, B. P., Abbott, R., Abbott, T. D., et al. 2017b, *Phys. Rev. Lett.*, 119, 161101
- Abbott, B. P., Abbott, R., Abbott, T. D., et al. 2017c, *ApJ*, 848, L12
- Abbott, B. P., Abbott, R., Abbott, T. D., et al. 2017d, *Nature*, 551, 85
- Abbott, B. P., Abbott, R., Abbott, T. D., et al. 2019b, *Physical Review X*, 9, 011001
- Abbott, B. P., Abbott, R., Abbott, T. D., et al. 2018, *Phys. Rev. Lett.*, 121, 161101
- Abbott, B. P., Abbott, R., Abbott, T. D., et al. 2019c, *Phys. Rev. Lett.*, 123, 011102
- Abbott, R., Abbott, T. D., Abraham, S., et al. 2021a, *ApJ*, 915, L5
- Abbott, R., Abbott, T. D., Abraham, S., et al. 2021b, *Physical Review X*, 11, 021053
- Abbott, R., Abbott, T. D., Abraham, S., et al. 2020b, *Phys. Rev. D*, 102, 043015
- Abbott, R., Abbott, T. D., Abraham, S., et al. 2020c, *ApJ*, 896, L44
- Abbott, R., Abbott, T. D., Abraham, S., et al. 2020d, *Phys. Rev. Lett.*, 125, 101102
- Abbott, R., Abbott, T. D., Acernese, F., et al. 2016, *Phys. Rev. Lett.*, 116, 131102
- Abdalla, H., Abramowski, A., Aharonian, F., et al. 2017, *ApJ*, 850, L22
- Abdalla, H., Adam, R., Aharonian, F., et al. 2020, *ApJ*, 894, L16
- Abdalla, H., Adam, R., Aharonian, F., et al. 2019, *Nature*, 575, 464
- Abeysekara, A. U., Aguilar, J. A., Aguilar, S., et al. 2012, *Astroparticle Physics*, 35, 641
- Abt, H. A. 1983, *ARA&A*, 21, 343
- Acciari, V. A., Ansoldi, S., Antonelli, L. A., et al. 2021, *ApJ*, 908, 90

- Acernese, F., Agathos, M., Agatsuma, K., et al. 2015, *Classical and Quantum Gravity*, **32**, 024001
- Adrián-Martínez, S., Ageron, M., Aharonian, F., et al. 2016, *Journal of Physics G Nuclear Physics*, **43**, 084001
- Ageron, M., Aguilar, J. A., Al Samarai, I., et al. 2011, *Nuclear Instruments and Methods in Physics Research A*, **656**, 11
- Ajello, M., Arimoto, M., Axelsson, M., et al. 2019, *ApJ*, **878**, 52
- Aksulu, M. D., Wijers, R. A. M. J., van Eerten, H. J., & van der Horst, A. J. 2022, *MNRAS*, **511**, 2848
- Aleksić, J., Ansoldi, S., Antonelli, L. A., et al. 2016a, *Astroparticle Physics*, **72**, 76
- Aleksić, J., Ansoldi, S., Antonelli, L. A., et al. 2016b, *Astroparticle Physics*, **72**, 61
- Alexander, K. D., Berger, E., Fong, W., et al. 2017, *ApJ*, **848**, L21
- Alexander, K. D., Margutti, R., Blanchard, P. K., et al. 2018, *ApJ*, **863**, L18
- Amaro-Seoane, P., Andrews, J., Arca Sedda, M., et al. 2023, *Living Reviews in Relativity*, **26**, 2
- An, D. & Beers, T. C. 2020, *ApJ*, **897**, 39
- An, Z.-H., Antier, S., Bi, X.-Z., et al. 2023, *arXiv e-prints*, arXiv:2303.01203
- Anders, E. & Grevesse, N. 1989, *Geochim. Cosmochim. Acta*, **53**, 197
- Andrews, J. J., Farr, W. M., Kalogera, V., & Willems, B. 2015, *ApJ*, **801**, 32
- Arcier, B., Atteia, J. L., Godet, O., et al. 2020, *Ap&SS*, **365**, 185
- Artale, M. C., Mapelli, M., Bouffanais, Y., et al. 2020, *MNRAS*, **491**, 3419
- Asano, K. & Mészáros, P. 2012, *ApJ*, **757**, 115
- Ascenzi, S., Oganessian, G., Salafia, O. S., et al. 2020, *A&A*, **641**, A61
- Askar, A., Szkudlarek, M., Gondek-Rosińska, D., Giersz, M., & Bulik, T. 2017, *MNRAS*, **464**, L36
- Asplund, M., Grevesse, N., Sauval, A. J., & Scott, P. 2009, *ARA&A*, **47**, 481
- Atwood, W. B., Abdo, A. A., Ackermann, M., et al. 2009, *ApJ*, **697**, 1071
- Axford, W. I., Leer, E., & Skadron, G. 1977, in International Cosmic Ray Conference, Vol. 11, International Cosmic Ray Conference, 132
- Ayache, E. H., van Eerten, H. J., & Daigne, F. 2020, *MNRAS*, **495**, 2979
- Bailyn, C. D., Jain, R. K., Coppi, P., & Orosz, J. A. 1998, *ApJ*, **499**, 367
- Baker, T., Bellini, E., Ferreira, P. G., et al. 2017, *Phys. Rev. Lett.*, **119**, 251301
- Balasubramanian, A., Corsi, A., Mooley, K. P., et al. 2021, *ApJ*, **914**, L20
- Balasubramanian, A., Corsi, A., Mooley, K. P., et al. 2022, *ApJ*, **938**, 12
- Banerjee, S., Belczynski, K., Fryer, C. L., et al. 2020, *A&A*, **639**, A41

- Bartos, I., Brady, P., & Márka, S. 2013, *Classical and Quantum Gravity*, 30, 123001
- Bavera, S. S., Fragos, T., Zevin, M., et al. 2021, *A&A*, 647, A153
- Belczynski, K., Askar, A., Arca-Sedda, M., et al. 2018, *A&A*, 615, A91
- Belczynski, K., Bulik, T., Fryer, C. L., et al. 2010, *ApJ*, 714, 1217
- Belczynski, K., Holz, D. E., Bulik, T., & O’Shaughnessy, R. 2016, *Nature*, 534, 512
- Belczynski, K., Kalogera, V., & Bulik, T. 2002, *ApJ*, 572, 407
- Belczynski, K., Kalogera, V., Rasio, F. A., et al. 2008, *ApJS*, 174, 223
- Belczynski, K., Klencki, J., Fields, C. E., et al. 2020, *A&A*, 636, A104
- Bell, A. R. 1978, *MNRAS*, 182, 147
- Beloborodov, A. M. 2002, *ApJ*, 565, 808
- Beloborodov, A. M. 2005, *ApJ*, 627, 346
- Beloborodov, A. M. 2010, *MNRAS*, 407, 1033
- Beloborodov, A. M., Hascoët, R., & Vurm, I. 2014, *ApJ*, 788, 36
- Beniamini, P., Duque, R., Daigne, F., & Mochkovitch, R. 2020a, *MNRAS*, 492, 2847
- Beniamini, P., Gill, R., & Granot, J. 2022, *MNRAS*, 515, 555
- Beniamini, P., Granot, J., & Gill, R. 2020b, *MNRAS*, 493, 3521
- Beniamini, P., Hotokezaka, K., & Piran, T. 2016, *ApJ*, 829, L13
- Beniamini, P. & Nakar, E. 2019, *MNRAS*, 482, 5430
- Beniamini, P., Nava, L., Duran, R. B., & Piran, T. 2015, *MNRAS*, 454, 1073
- Berger, E. 2014, *ARA&A*, 52, 43
- Bethe, H. A. & Brown, G. E. 1998, *ApJ*, 506, 780
- Blanch, O., Longo, F., Berti, A., et al. 2020, GRB Coordinates Network, 29075, 1
- Blanchet, L. 2014, *Living Reviews in Relativity*, 17, 2
- Blanchet, L. & Damour, T. 1989, *Annales de L’Institut Henri Poincare Section (A) Physique Theorique*, 50, 377
- Blandford, R. D. & McKee, C. F. 1976, *Physics of Fluids*, 19, 1130
- Blandford, R. D. & Ostriker, J. P. 1978, *ApJ*, 221, L29
- Blandford, R. D. & Znajek, R. L. 1977, *MNRAS*, 179, 433
- Blondin, J. M. & Mezzacappa, A. 2007, *Nature*, 445, 58
- Boffin, H. M. J. & Jorissen, A. 1988, *A&A*, 205, 155
- Bondi, H. & Hoyle, F. 1944, *MNRAS*, 104, 273

- Bošnjak, Ž., Daigne, F., & Dubus, G. 2009, *A&A*, 498, 677
- Branchesi, M., Maggiore, M., Alonso, D., et al. 2023, *J. Cosmology Astropart. Phys.*, 2023, 068
- Bray, J. C. & Eldridge, J. J. 2016, *MNRAS*, 461, 3747
- Breivik, K., Coughlin, S., Zevin, M., et al. 2020, *ApJ*, 898, 71
- Broekgaarden, F. S., Berger, E., Neijssel, C. J., et al. 2021, *MNRAS*, 508, 5028
- Broekgaarden, F. S., Berger, E., Stevenson, S., et al. 2022, *MNRAS*, 516, 5737
- Bromberg, O., Nakar, E., Piran, T., & Sari, R. 2011, *ApJ*, 740, 100
- Bromberg, O., Nakar, E., Piran, T., & Sari, R. 2013, *ApJ*, 764, 179
- Brown, G. E. 1995, *ApJ*, 440, 270
- Buonanno, A. & Damour, T. 1999, *Phys. Rev. D*, 59, 084006
- Burbidge, E. M., Burbidge, G. R., Fowler, W. A., & Hoyle, F. 1957, *Reviews of Modern Physics*, 29, 547
- Burgay, M., D'Amico, N., Possenti, A., et al. 2003, *Nature*, 426, 531
- Burrows, A. & Hayes, J. 1996, *Phys. Rev. Lett.*, 76, 352
- Cameron, A. G. W. 1957, *PASP*, 69, 201
- Cantiello, M., Jensen, J. B., Blakeslee, J. P., et al. 2018, *ApJ*, 854, L31
- Cao, Z., della Volpe, D., Liu, S., et al. 2019, *arXiv e-prints*, arXiv:1905.02773
- Chandrasekhar, S. 1931, *ApJ*, 74, 81
- Chaty, S. 2022, *Accreting Binaries; Nature, formation, and evolution* (IOP Publishing)
- Cherenkov Telescope Array Consortium, Acharya, B. S., Agudo, I., et al. 2019, *Science with the Cherenkov Telescope Array* (World Scientific)
- Chevalier, R. A. & Li, Z.-Y. 2000, *ApJ*, 536, 195
- Christensen, N. 2019, *Reports on Progress in Physics*, 82, 016903
- Chruslinska, M., Belczynski, K., Klencki, J., & Benacquista, M. 2018, *MNRAS*, 474, 2937
- Chu, Q., Yu, S., & Lu, Y. 2022, *MNRAS*, 509, 1557
- Claeys, J. S. W., Pols, O. R., Izzard, R. G., Vink, J., & Verbunt, F. W. M. 2014, *A&A*, 563, A83
- Colbert, E. J. M. & Mushotzky, R. F. 1999, *ApJ*, 519, 89
- Côté, B., Belczynski, K., Fryer, C. L., et al. 2017, *ApJ*, 836, 230
- Côté, B., Eichler, M., Arcones, A., et al. 2019, *ApJ*, 875, 106
- Coulter, D. A., Foley, R. J., Kilpatrick, C. D., et al. 2017, *Science*, 358, 1556
- Cowperthwaite, P. S., Berger, E., Villar, V. A., et al. 2017, *ApJ*, 848, L17

- Cusin, G., Dvorkin, I., Pitrou, C., & Uzan, J.-P. 2019, *Phys. Rev. D*, 100, 063004
- Daigne, F., Bošnjak, Ž., & Dubus, G. 2011, *A&A*, 526, A110
- Daigne, F. & Mochkovitch, R. 1998, *MNRAS*, 296, 275
- Daigne, F. & Mochkovitch, R. 2002, *MNRAS*, 336, 1271
- D’Avanzo, P., Campana, S., Salafia, O. S., et al. 2018, *A&A*, 613, L1
- D’Avanzo, P., Salvaterra, R., Bernardini, M. G., et al. 2014, *MNRAS*, 442, 2342
- Davis, P. J., Kolb, U., & Knigge, C. 2012, *MNRAS*, 419, 287
- De Donder, E. & Vanbeveren, D. 2004, *New A Rev.*, 48, 861
- de Kool, M. 1990, *ApJ*, 358, 189
- De Marco, O. & Izzard, R. G. 2017, *PASA*, 34, e001
- de Sá, L. M., Bernardo, A., Bachega, R. R. A., et al. 2022, *ApJ*, 941, 130
- de Sá, L. M. d., Bernardo, A., Bachega, R. R. A., et al. 2023, *Galaxies*, 11, 19
- Derishev, E. & Piran, T. 2021, *ApJ*, 923, 135
- Derishev, E. V., Kocharovsky, V. V., & Kocharovsky, V. V. 2001, *A&A*, 372, 1071
- Dessart, L., Burrows, A., Ott, C. D., et al. 2006, *ApJ*, 644, 1063
- Dewi, J. D. M., Podsiadlowski, P., & Sena, A. 2006, *MNRAS*, 368, 1742
- di Sciacio, G. & Lhaaso Collaboration. 2016, *Nuclear and Particle Physics Proceedings*, 279-281, 166
- Dobie, D., Kaplan, D. L., Murphy, T., et al. 2018, *ApJ*, 858, L15
- Domínguez, A., Primack, J. R., Rosario, D. J., et al. 2011, *MNRAS*, 410, 2556
- Dominik, M., Belczynski, K., Fryer, C., et al. 2012, *ApJ*, 759, 52
- Drout, M. R., Piro, A. L., Shappee, B. J., et al. 2017, *Science*, 358, 1570
- Duffell, P. C. & Laskar, T. 2018, *ApJ*, 865, 94
- Duque, R., Beniamini, P., Daigne, F., & Mochkovitch, R. 2020, *A&A*, 639, A15
- Duque, R., Beniamini, P., Daigne, F., & Mochkovitch, R. 2022, *MNRAS*, 513, 951
- Duque, R., Daigne, F., & Mochkovitch, R. 2019, *A&A*, 631, A39
- Duquennoy, A. & Mayor, M. 1991, *A&A*, 248, 485
- Dvorkin, I. 2023, *IAU Symposium*, 363, 33
- Dvorkin, I., Daigne, F., Goriely, S., Vangioni, E., & Silk, J. 2021, *MNRAS*, 506, 4374
- Dvorkin, I., Vangioni, E., Silk, J., Uzan, J.-P., & Olive, K. A. 2016, *MNRAS*, 461, 3877
- Eddington, A. S. 1921, *Zeitschrift fur Physik*, 7, 351

- Eggleton, P. P. 1971, [MNRAS](#), 151, 351
- Eggleton, P. P. 1983, [ApJ](#), 268, 368
- Eichler, D., Livio, M., Piran, T., & Schramm, D. N. 1989, [Nature](#), 340, 126
- Einstein, A. 1915, [Sitzungsberichte der Königlich Preussischen Akademie der Wissenschaften](#), 844
- Einstein, A. 1916, [Annalen der Physik](#), 354, 769
- Eldridge, J. J., Izzard, R. G., & Tout, C. A. 2008, [MNRAS](#), 384, 1109
- Eldridge, J. J. & Stanway, E. R. 2016, [MNRAS](#), 462, 3302
- Eldridge, J. J., Stanway, E. R., Xiao, L., et al. 2017, [PASA](#), 34, e058
- Evans, M., Adhikari, R. X., Afle, C., et al. 2021, [arXiv e-prints](#), arXiv:2109.09882
- Evans, P. A., Cenko, S. B., Kennea, J. A., et al. 2017, [Science](#), 358, 1565
- Ezquiaga, J. M. & Zumalacárregui, M. 2017, [Phys. Rev. Lett.](#), 119, 251304
- Farah, A., Fishbach, M., Essick, R., Holz, D. E., & Galaudage, S. 2022, [ApJ](#), 931, 108
- Farrow, N., Zhu, X.-J., & Thrane, E. 2019, [ApJ](#), 876, 18
- Finke, J. D., Razzaque, S., & Dermer, C. D. 2010, [ApJ](#), 712, 238
- Finstad, D., De, S., Brown, D. A., Berger, E., & Biwer, C. M. 2018, [ApJ](#), 860, L2
- Foglizzo, T. 2002, [A&A](#), 392, 353
- Fong, W. & Berger, E. 2013, [ApJ](#), 776, 18
- Fong, W., Berger, E., Margutti, R., & Zauderer, B. A. 2015, [ApJ](#), 815, 102
- Fong, W., Blanchard, P. K., Alexander, K. D., et al. 2019, [ApJ](#), 883, L1
- Fong, W.-f., Nugent, A. E., Dong, Y., et al. 2022, [ApJ](#), 940, 56
- Foreman-Mackey, D., Farr, W., Sinha, M., et al. 2019, [The Journal of Open Source Software](#), 4, 1864
- Foreman-Mackey, D., Hogg, D. W., Lang, D., & Goodman, J. 2013, [PASP](#), 125, 306
- Fortin, F., García, F., Simaz Bunzel, A., & Chaty, S. 2023, [A&A](#), 671, A149
- Fox, D. B., Frail, D. A., Price, P. A., et al. 2005, [Nature](#), 437, 845
- Fragione, G. & Kocsis, B. 2018, [Phys. Rev. Lett.](#), 121, 161103
- Fragos, T., Andrews, J. J., Bavera, S. S., et al. 2023, [ApJS](#), 264, 45
- Fragos, T., Andrews, J. J., Ramirez-Ruiz, E., et al. 2019, [ApJ](#), 883, L45
- Franceschini, A., Rodighiero, G., & Vaccari, M. 2008, [A&A](#), 487, 837
- Fruchter, A. S., Levan, A. J., Strolger, L., et al. 2006, [Nature](#), 441, 463
- Fryer, C. L., Belczynski, K., Wiktorowicz, G., et al. 2012, [ApJ](#), 749, 91

- Fryer, C. L. & New, K. C. B. 2011, *Living Reviews in Relativity*, 14, 1
- Gaia Collaboration, Brown, A. G. A., Vallenari, A., et al. 2021, *A&A*, 649, A1
- Galama, T. J., Vreeswijk, P. M., van Paradijs, J., et al. 1998, *Nature*, 395, 670
- Galván, A., Fraija, N., & González, M. M. 2019, in International Cosmic Ray Conference, Vol. 36, 36th International Cosmic Ray Conference (ICRC2019), 681
- Gehrels, N., Chincarini, G., Giommi, P., et al. 2004, *ApJ*, 611, 1005
- Gehrels, N., Ramirez-Ruiz, E., & Fox, D. B. 2009, *ARA&A*, 47, 567
- Geller, A. M., Leigh, N. W. C., Giersz, M., Kremer, K., & Rasio, F. A. 2019, *ApJ*, 872, 165
- Genet, F., Daigne, F., & Mochkovitch, R. 2007, *MNRAS*, 381, 732
- Gezari, S. 2021, *ARA&A*, 59, 21
- Ghirlanda, G., Nava, L., Ghisellini, G., Celotti, A., & Firmani, C. 2009, *A&A*, 496, 585
- Ghirlanda, G., Salafia, O. S., Paragi, Z., et al. 2019, *Science*, 363, 968
- Ghirlanda, G., Salvaterra, R., Campana, S., et al. 2015, *A&A*, 578, A71
- Giacobbo, N. & Mapelli, M. 2018, *MNRAS*, 480, 2011
- Giacobbo, N. & Mapelli, M. 2019, *MNRAS*, 482, 2234
- Giacobbo, N. & Mapelli, M. 2020, *ApJ*, 891, 141
- Giacobbo, N., Mapelli, M., & Spera, M. 2018, *MNRAS*, 474, 2959
- Giannios, D. & Spruit, H. C. 2007, *A&A*, 469, 1
- Gill, R. & Granot, J. 2018, *MNRAS*, 478, 4128
- Gill, R. & Granot, J. 2022, *Galaxies*, 10, 74
- Gill, R. & Granot, J. 2023, *MNRAS*, 524, L78
- Gilmore, R. C., Somerville, R. S., Primack, J. R., & Domínguez, A. 2012, *MNRAS*, 422, 3189
- Goldberg, D. & Mazeh, T. 1994, *A&A*, 282, 801
- Goldberg, D., Mazeh, T., & Latham, D. W. 2003, *ApJ*, 591, 397
- Goldstein, A., Preece, R. D., Mallozzi, R. S., et al. 2013, *ApJS*, 208, 21
- Goldstein, A., Veres, P., Burns, E., et al. 2017, *ApJ*, 848, L14
- Goodman, J. 1986, *ApJ*, 308, L47
- Goriely, S., Bauswein, A., & Janka, H.-T. 2011, *ApJ*, 738, L32
- Gottlieb, O., Moseley, S., Ramirez-Aguilar, T., et al. 2022, *ApJ*, 933, L2
- Gottlieb, O., Nagakura, H., Tchekhovskoy, A., et al. 2023, *ApJ*, 951, L30
- Gottlieb, O., Nakar, E., Piran, T., & Hotokezaka, K. 2018, *MNRAS*, 479, 588

- Gould, R. J. & Schröder, G. P. 1967, *Physical Review*, 155, 1404
- Govreen-Segal, T. & Nakar, E. 2023, *MNRAS*, 524, 403
- Gräfener, G. & Hamann, W. R. 2008, *A&A*, 482, 945
- Gräfener, G., Vink, J. S., de Koter, A., & Langer, N. 2011, *A&A*, 535, A56
- Granot, J., Panaitescu, A., Kumar, P., & Woosley, S. E. 2002, *ApJ*, 570, L61
- Granot, J. & Piran, T. 2012, *MNRAS*, 421, 570
- Granot, J., Piran, T., Bromberg, O., Racusin, J. L., & Daigne, F. 2018, in *The Strongest Magnetic Fields in the Universe. Series: Space Sciences Series of ISSI*, ed. V. S. Beskin, A. Balogh, M. Falanga, M. Lyutikov, S. Mereghetti, T. Piran, & R. A. Treumann, Vol. 54 (Springer Reviews), 481–528
- Granot, J., Piran, T., & Sari, R. 1999, *ApJ*, 513, 679
- Guépin, C., Kotera, K., & Oikonomou, F. 2022, *Nature Reviews Physics*, 4, 697
- H. E. S. S. Collaboration, Abdalla, H., Aharonian, F., et al. 2021, *Science*, 372, 1081
- Haggard, D., Nynka, M., Ruan, J. J., et al. 2017, *ApJ*, 848, L25
- Hajela, A., Margutti, R., Alexander, K. D., et al. 2019, *ApJ*, 886, L17
- Hajela, A., Margutti, R., Bright, J. S., et al. 2022, *ApJ*, 927, L17
- Halevi, G. & Mösta, P. 2018, *MNRAS*, 477, 2366
- Hallinan, G., Corsi, A., Mooley, K. P., et al. 2017, *Science*, 358, 1579
- Hamann, W. R., Koesterke, L., & Wessolowski, U. 1995, *A&A*, 299, 151
- Hascoët, R., Beloborodov, A. M., Daigne, F., & Mochkovitch, R. 2017, *MNRAS*, 472, L94
- Hascoët, R., Daigne, F., & Mochkovitch, R. 2012a, *A&A*, 541, A88
- Hascoët, R., Daigne, F., & Mochkovitch, R. 2014, *MNRAS*, 442, 20
- Hascoët, R., Daigne, F., Mochkovitch, R., & Vennin, V. 2012b, *MNRAS*, 421, 525
- Haxton, W. C., Hamish Robertson, R. G., & Serenelli, A. M. 2013, *ARA&A*, 51, 21
- Heggie, D. C. 1975, *MNRAS*, 173, 729
- Hinton, J. A. & HESS Collaboration. 2004, *New A Rev.*, 48, 331
- Hirata, K., Kajita, T., Koshihara, M., et al. 1987, *Phys. Rev. Lett.*, 58, 1490
- Hjellming, M. S. & Webbink, R. F. 1987, *ApJ*, 318, 794
- Hjorth, J., Watson, D., Fynbo, J. P. U., et al. 2005, *Nature*, 437, 859
- Hobbs, G., Lorimer, D. R., Lyne, A. G., & Kramer, M. 2005, *MNRAS*, 360, 974
- Holder, J., Atkins, R. W., Badran, H. M., et al. 2006, *Astroparticle Physics*, 25, 391
- Hotokezaka, K., Kiuchi, K., Kyutoku, K., et al. 2013, *Phys. Rev. D*, 87, 024001

- Hotokezaka, K., Nakar, E., Gottlieb, O., et al. 2019, *Nature Astronomy*, **3**, 940
- Huang, Y., Hu, S., Chen, S., et al. 2022, GRB Coordinates Network, **32677**, 1
- Huang, Y.-J., Urata, Y., Huang, K., et al. 2020, *ApJ*, **897**, 69
- Hugoniot, P.-H. 1889, *Journal de l'École Polytechnique*, **58**, 1
- Hulse, R. A. & Taylor, J. H. 1975, *ApJ*, **195**, L51
- Humphreys, R. M. & Davidson, K. 1994, *PASP*, **106**, 1025
- Hurley, J. R., Pols, O. R., & Tout, C. A. 2000, *MNRAS*, **315**, 543
- Hurley, J. R., Tout, C. A., & Pols, O. R. 2002, *MNRAS*, **329**, 897
- Hurley, K., Briggs, M. S., Kippen, R. M., et al. 2011, *ApJS*, **196**, 1
- Hwang, J., Lombardi, J. C., J., Rasio, F. A., & Kalogera, V. 2015, *ApJ*, **806**, 135
- IceCube Collaboration. 2013, *Science*, **342**, 1242856
- IceCube Collaboration, Aartsen, M. G., Ackermann, M., et al. 2018, *Science*, **361**, eaat1378
- IceCube Collaboration, Abbasi, R., Ackermann, M., et al. 2022, *Science*, **378**, 538
- Iorio, G., Mapelli, M., Costa, G., et al. 2023, *MNRAS*
- Ivanova, N., Heinke, C. O., Rasio, F. A., Belczynski, K., & Fregeau, J. M. 2008, *MNRAS*, **386**, 553
- Ivanova, N., Justham, S., Chen, X., et al. 2013, *A&A Rev.*, **21**, 59
- Ivezić, Ž., Kahn, S. M., Tyson, J. A., et al. 2019, *ApJ*, **873**, 111
- Izzard, R. G. 2004, *Nucleosynthesis In Binary Stars*, PhD thesis, University of Cambridge, UK
- Izzard, R. G., Dray, L. M., Karakas, A. I., Lugaro, M., & Tout, C. A. 2006, *A&A*, **460**, 565
- Izzard, R. G., Glebbeek, E., Stancliffe, R. J., & Pols, O. R. 2009, *A&A*, **508**, 1359
- Izzard, R. G., Tout, C. A., Karakas, A. I., & Pols, O. R. 2004, *MNRAS*, **350**, 407
- Jacovich, T. E., Beniamini, P., & van der Horst, A. J. 2021, *MNRAS*, **504**, 528
- Janka, H.-T. 2017, *ApJ*, **837**, 84
- Janka, H. T. & Mueller, E. 1994, *A&A*, **290**, 496
- Jeans, J. H. 1919, *MNRAS*, **79**, 408
- Jenkins, A. C., Sakellariadou, M., Regimbau, T., & Slezak, E. 2018, *Phys. Rev. D*, **98**, 063501
- Jermyn, A. S., Bauer, E. B., Schwab, J., et al. 2023, *ApJS*, **265**, 15
- Jones, F. C. 1968, *Physical Review*, **167**, 1159
- Just, O., Bauswein, A., Ardevol Pulpillo, R., Goriely, S., & Janka, H. T. 2015, *MNRAS*, **448**, 541
- Justham, S., Podsiadlowski, P., & Han, Z. 2011, *MNRAS*, **410**, 984
- Kagra Collaboration, Akutsu, T., Ando, M., et al. 2019, *Nature Astronomy*, **3**, 35

- Kalogera, V. 1996, *ApJ*, 471, 352
- Kann, D. A., Agayeva, S., Aivazyan, V., et al. 2023, *ApJ*, 948, L12
- Kasliwal, M. M., Nakar, E., Singer, L. P., et al. 2017, *Science*, 358, 1559
- Kepler, J. 1619, *Harmonices Mundi V* (Lincii: Typis Reusnerianis)
- Kim, S., Schulze, S., Resmi, L., et al. 2017, *ApJ*, 850, L21
- Kitaura, F. S., Janka, H. T., & Hillebrandt, W. 2006, *A&A*, 450, 345
- Klebesadel, R. W., Strong, I. B., & Olson, R. A. 1973, *ApJ*, 182, L85
- Klein, O. & Nishina, T. 1929, *Zeitschrift fur Physik*, 52, 853
- Kobayashi, S. 2000, *ApJ*, 545, 807
- Kobayashi, S., Piran, T., & Sari, R. 1997, *ApJ*, 490, 92
- Kobayashi, S. & Sari, R. 2000, *ApJ*, 542, 819
- Kobulnicky, H. A. & Fryer, C. L. 2007, *ApJ*, 670, 747
- Kormendy, J. & Richstone, D. 1995, *ARA&A*, 33, 581
- Korol, V. & Safarzadeh, M. 2021, *MNRAS*, 502, 5576
- Kotera, K. & Olinto, A. V. 2011, *ARA&A*, 49, 119
- Kouveliotou, C., Meegan, C. A., Fishman, G. J., et al. 1993, *ApJ*, 413, L101
- Kouwenhoven, M. B. N., Brown, A. G. A., Goodwin, S. P., Portegies Zwart, S. F., & Kaper, L. 2009, *A&A*, 493, 979
- Kraus, A. L. & Hillenbrand, L. A. 2009, *ApJ*, 703, 1511
- Kroupa, P. 2001, *MNRAS*, 322, 231
- Kroupa, P., Tout, C. A., & Gilmore, G. 1993, *MNRAS*, 262, 545
- Kruckow, M. U., Tauris, T. M., Langer, N., Kramer, M., & Izzard, R. G. 2018, *MNRAS*, 481, 1908
- Kudritzki, R. P., Pauldrach, A., Puls, J., & Abbott, D. C. 1989, *A&A*, 219, 205
- Kudritzki, R. P. & Reimers, D. 1978, *A&A*, 70, 227
- Kumar, P. & Zhang, B. 2015, *Phys. Rep.*, 561, 1
- Lamb, G. P., Lyman, J. D., Levan, A. J., et al. 2019, *ApJ*, 870, L15
- Lamb, G. P., Tanaka, M., & Kobayashi, S. 2018, *MNRAS*, 476, 4435
- Lamberts, A. & Daigne, F. 2018, *MNRAS*, 474, 2813
- Lamberts, A., Garrison-Kimmel, S., Clausen, D. R., & Hopkins, P. F. 2016, *MNRAS*, 463, L31
- Laskar, T., Alexander, K. D., Margutti, R., et al. 2023, *ApJ*, 946, L23
- Lattimer, J. M. & Schramm, D. N. 1974, *ApJ*, 192, L145

- Lehoucq, L., Dvorkin, I., Srinivasan, R., Pellouin, C., & Lamberts, A. 2023, *MNRAS*, 526, 4378
- Lesage, S., Veres, P., Briggs, M. S., et al. 2023, *ApJ*, 952, L42
- Levan, A., Crowther, P., de Grijs, R., et al. 2016, *Space Sci. Rev.*, 202, 33
- Levan, A. J. 2018, *Gamma-Ray Bursts* (IOP Publishing)
- Levan, A. J., Lyman, J. D., Tanvir, N. R., et al. 2017, *ApJ*, 848, L28
- LHAASO Collaboration, Cao, Z., Aharonian, F., et al. 2023, *Science*, 380, 1390
- LIGO Scientific Collaboration, Aasi, J., Abbott, B. P., et al. 2015, *Classical and Quantum Gravity*, 32, 074001
- Limongi, M. & Chieffi, A. 2018, *ApJS*, 237, 13
- Lipunov, V. M., Postnov, K. A., & Prokhorov, M. E. 1996, *A&A*, 310, 489
- Lipunov, V. M., Postnov, K. A., Prokhorov, M. E., & Bogomazov, A. I. 2009, *Astronomy Reports*, 53, 915
- Lithwick, Y. & Sari, R. 2001, *ApJ*, 555, 540
- Lorentz, H. A. 1898, Koninklijke Nederlandse Akademie van Wetenschappen Proceedings Series B Physical Sciences, 1, 427
- Lorentz, H. A. 1903, Koninklijke Nederlandse Akademie van Wetenschappen Proceedings Series B Physical Sciences, 6, 809
- Lorenz, E. & MAGIC Collaboration. 2004, *New A Rev.*, 48, 339
- Lorimer, D. R. & Kramer, M. 2004, *Handbook of Pulsar Astronomy*, Vol. 4 (Cambridge University Press)
- Lyman, J. D., Lamb, G. P., Levan, A. J., et al. 2018, *Nature Astronomy*, 2, 751
- Lyman, J. D., Levan, A. J., Tanvir, N. R., et al. 2017, *MNRAS*, 467, 1795
- Madau, P. & Dickinson, M. 2014, *ARA&A*, 52, 415
- Maggiore, M., Van Den Broeck, C., Bartolo, N., et al. 2020, *J. Cosmology Astropart. Phys.*, 2020, 050
- MAGIC Collaboration, Acciari, V. A., Ansoldi, S., et al. 2019a, *Nature*, 575, 455
- MAGIC Collaboration, Acciari, V. A., Ansoldi, S., et al. 2019b, *Nature*, 575, 459
- Makhathini, S., Mooley, K. P., Brightman, M., et al. 2021, *ApJ*, 922, 154
- Mandel, I. & Broekgaarden, F. S. 2022, *Living Reviews in Relativity*, 25, 1
- Mapelli, M. 2021, in *Handbook of Gravitational Wave Astronomy* (Springer), 16
- Mapelli, M., Bouffanais, Y., Santoliquido, F., Arca Sedda, M., & Artale, M. C. 2022, *MNRAS*, 511, 5797
- Mapelli, M., Giacobbo, N., Ripamonti, E., & Spera, M. 2017, *MNRAS*, 472, 2422

- Mapelli, M., Zampieri, L., Ripamonti, E., & Bressan, A. 2013, *MNRAS*, 429, 2298
- Marcowith, A., Bret, A., Bykov, A., et al. 2016, *Reports on Progress in Physics*, 79, 046901
- Margalit, B. & Metzger, B. D. 2017, *ApJ*, 850, L19
- Margutti, R., Alexander, K. D., Xie, X., et al. 2018, *ApJ*, 856, L18
- Margutti, R., Berger, E., Fong, W., et al. 2017, *ApJ*, 848, L20
- Matsumoto, T., Nakar, E., & Piran, T. 2019, *MNRAS*, 483, 1247
- Mazeh, T., Goldberg, D., Duquennoy, A., & Mayor, M. 1992, *ApJ*, 401, 265
- McKee, C. F. & Ostriker, E. C. 2007, *ARA&A*, 45, 565
- Mei, A., Banerjee, B., Oganessian, G., et al. 2022, *Nature*, 612, 236
- Meng, X., Chen, X., & Han, Z. 2009, *MNRAS*, 395, 2103
- Mennekens, N. & Vanbeveren, D. 2014, *A&A*, 564, A134
- Meszáros, P. & Rees, M. J. 1992, *MNRAS*, 257, 29P
- Mészáros, P. & Rees, M. J. 1997, *ApJ*, 476, 232
- Metzger, B. D. 2017, *Living Reviews in Relativity*, 20, 3
- Metzger, B. D. 2019, *Living Reviews in Relativity*, 23, 1
- Metzger, B. D. & Berger, E. 2012, *ApJ*, 746, 48
- Metzger, B. D., Piro, A. L., & Quataert, E. 2009, *MNRAS*, 396, 304
- Metzger, M. R., Djorgovski, S. G., Kulkarni, S. R., et al. 1997, *Nature*, 387, 878
- Mignone, A., Plewa, T., & Bodo, G. 2005, *ApJS*, 160, 199
- Miyaji, S., Nomoto, K., Yokoi, K., & Sugimoto, D. 1980, *PASJ*, 32, 303
- Mochkovitch, R., Daigne, F., Duque, R., & Zitouni, H. 2021, *A&A*, 651, A83
- Mochkovitch, R., Hernanz, M., Isern, J., & Martin, X. 1993, *Nature*, 361, 236
- Moe, M. & Di Stefano, R. 2017, *ApJS*, 230, 15
- Möller, A., Peloton, J., Ishida, E. E. O., et al. 2021, *MNRAS*, 501, 3272
- Mooley, K. P., Anderson, J., & Lu, W. 2022, *Nature*, 610, 273
- Mooley, K. P., Deller, A. T., Gottlieb, O., et al. 2018a, *Nature*, 561, 355
- Mooley, K. P., Frail, D. A., Dobie, D., et al. 2018b, *ApJ*, 868, L11
- Mooley, K. P., Nakar, E., Hotokezaka, K., et al. 2018c, *Nature*, 554, 207
- Moss, M., Lien, A., Guiriec, S., Cenko, S. B., & Sakamoto, T. 2022, *ApJ*, 927, 157
- Murase, K. & Bartos, I. 2019, *Annual Review of Nuclear and Particle Science*, 69, 477
- Murase, K., Oikonomou, F., & Petropoulou, M. 2018, *ApJ*, 865, 124

- Murase, K., Toma, K., Yamazaki, R., & Mészáros, P. 2011, *ApJ*, 732, 77
- Murase, K., Toma, K., Yamazaki, R., Nagataki, S., & Ioka, K. 2010, *MNRAS*, 402, L54
- Nakar, E. 2007, *Phys. Rep.*, 442, 166
- Nakar, E. 2020, *Phys. Rep.*, 886, 1
- Nakar, E., Ando, S., & Sari, R. 2009, *ApJ*, 703, 675
- Nakar, E. & Piran, T. 2011, *Nature*, 478, 82
- Nakar, E. & Piran, T. 2018, *MNRAS*, 478, 407
- Nakar, E. & Piran, T. 2021, *ApJ*, 909, 114
- Nakar, E., Piran, T., & Granot, J. 2002, *ApJ*, 579, 699
- Nakar, E. & Sari, R. 2012, *ApJ*, 747, 88
- Narayan, R., Paczynski, B., & Piran, T. 1992, *ApJ*, 395, L83
- Neijssel, C. J., Vigna-Gómez, A., Stevenson, S., et al. 2019, *MNRAS*, 490, 3740
- Nelemans, G., Verbunt, F., Yungelson, L. R., & Portegies Zwart, S. F. 2000, *A&A*, 360, 1011
- Nemiroff, R. J. 1994, *Comments on Astrophysics*, 17, 189
- Nieuwenhuijzen, H. & de Jager, C. 1990, *A&A*, 231, 134
- Noda, K. & Parsons, R. D. 2022, *Galaxies*, 10, 7
- Nomoto, K. 1984, *ApJ*, 277, 791
- Nomoto, K. 1987, *ApJ*, 322, 206
- Nomoto, K. & Kondo, Y. 1991, *ApJ*, 367, L19
- Nousek, J. A., Kouveliotou, C., Grupe, D., et al. 2006, *ApJ*, 642, 389
- Nugent, A. E., Fong, W.-F., Dong, Y., et al. 2022, *ApJ*, 940, 57
- Nynka, M., Ruan, J. J., Haggard, D., & Evans, P. A. 2018, *ApJ*, 862, L19
- O'Connor, B. & Troja, E. 2022, GRB Coordinates Network, 32065, 1
- O'Connor, B., Troja, E., Ryan, G., et al. 2023, *Science Advances*, 9, eadi1405
- Oganesyan, G., Ascenzi, S., Branchesi, M., et al. 2020, *ApJ*, 893, 88
- Öpik, E. 1924, Publications of the Tartu Astrofizica Observatory, 25, 1
- Özel, F., Psaltis, D., Narayan, R., & McClintock, J. E. 2010, *ApJ*, 725, 1918
- Paciesas, W. S., Meegan, C. A., Pendleton, G. N., et al. 1999, *ApJS*, 122, 465
- Paczyński, B. 1971, *ARA&A*, 9, 183
- Paczynski, B. 1976, in Structure and Evolution of Close Binary Systems, ed. P. Eggleton, S. Mitton, & J. Whelan, Vol. 73, 75

- Paczynski, B. 1986, *ApJ*, 308, L43
- Paczyński, B. & Sienkiewicz, R. 1972, *Acta Astron.*, 22, 73
- Palmerio, J. T. & Daigne, F. 2021, *A&A*, 649, A166
- Palmerio, J. T., Vergani, S. D., Salvaterra, R., et al. 2019, *A&A*, 623, A26
- Pan, Y. C., Kilpatrick, C. D., Simon, J. D., et al. 2017, *ApJ*, 848, L30
- Panaiteanu, A. & Kumar, P. 2000, *ApJ*, 543, 66
- Paul, J., Wei, J., Basa, S., & Zhang, S.-N. 2011, *Comptes Rendus Physique*, 12, 298
- Paxton, B., Bildsten, L., Dotter, A., et al. 2011, *ApJS*, 192, 3
- Paxton, B., Cantiello, M., Arras, P., et al. 2013, *ApJS*, 208, 4
- Paxton, B., Marchant, P., Schwab, J., et al. 2015, *ApJS*, 220, 15
- Paxton, B., Schwab, J., Bauer, E. B., et al. 2018, *ApJS*, 234, 34
- Pe'er, A. 2008, *ApJ*, 682, 463
- Pellouin, C. & Daigne, F. 2023, submitted
- Pellouin, C., Dvorkin, I., & Lehoucq, L. 2023, in prep.
- Pérgois, C., Belczynski, C., Bulik, T., & Regimbau, T. 2021, *Phys. Rev. D*, 103, 043002
- Pérgois, C., Santoliquido, F., Bouffanais, Y., et al. 2022, *Phys. Rev. D*, 105, 103032
- Perri, M., Giommi, P., Capalbi, M., et al. 2005, *A&A*, 442, L1
- Peters, P. C. 1964, *Physical Review*, 136, 1224
- Pian, E., D'Avanzo, P., Benetti, S., et al. 2017, *Nature*, 551, 67
- Piran, T. 2004, *Reviews of Modern Physics*, 76, 1143
- Piran, T. & Nakar, E. 2010, *ApJ*, 718, L63
- Piro, L., Troja, E., Zhang, B., et al. 2019, *MNRAS*, 483, 1912
- Planck Collaboration, Aghanim, N., Akrami, Y., et al. 2020, *A&A*, 641, A6
- Podsiadlowski, P., Langer, N., Poelarends, A. J. T., et al. 2004, *ApJ*, 612, 1044
- Podsiadlowski, P., Rappaport, S., & Han, Z. 2003, *MNRAS*, 341, 385
- Pols, O. R., Schröder, K.-P., Hurley, J. R., Tout, C. A., & Eggleton, P. P. 1998, *MNRAS*, 298, 525
- Pols, O. R., Tout, C. A., Eggleton, P. P., & Han, Z. 1995, *MNRAS*, 274, 964
- Portegies Zwart, S. F. & Verbunt, F. 1996, *A&A*, 309, 179
- Rankine, W. J. M. 1870, *Philosophical Transactions of the Royal Society of London*, 160, 277
- Rastinejad, J. C., Gompertz, B. P., Levan, A. J., et al. 2022, *Nature*, 612, 223
- Rees, M. J. 1966, *Nature*, 211, 468

- Rees, M. J. 1988, *Nature*, **333**, 523
- Rees, M. J. & Meszaros, P. 1994, *ApJ*, **430**, L93
- Rees, M. J. & Mészáros, P. 2005, *ApJ*, **628**, 847
- Regimbau, T. 2011, *Research in Astronomy and Astrophysics*, **11**, 369
- Renzini, A. I., Goncharov, B., Jenkins, A. C., & Meyers, P. M. 2022, *Galaxies*, **10**, 34
- Renzo, M., Zapartas, E., de Mink, S. E., et al. 2019, *A&A*, **624**, A66
- Resmi, L., Schulze, S., Ishwara-Chandra, C. H., et al. 2018, *ApJ*, **867**, 57
- Rhoads, J. E. 1997, *ApJ*, **487**, L1
- Rhoads, J. E. 1999, *ApJ*, **525**, 737
- Riley, J., Agrawal, P., Barrett, J. W., et al. 2022, *ApJS*, **258**, 34
- Rodi, J. & Ubertini, P. 2023, *A&A*, **677**, L3
- Rodriguez, C. L., Chatterjee, S., & Rasio, F. A. 2016, *Phys. Rev. D*, **93**, 084029
- Rodriguez, C. L., Kremer, K., Grudić, M. Y., et al. 2020, *ApJ*, **896**, L10
- Ronchini, S., Branchesi, M., Oganessian, G., et al. 2022, *A&A*, **665**, A97
- Rosswog, S., Liebendörfer, M., Thielemann, F. K., et al. 1999, *A&A*, **341**, 499
- Ruan, J. J., Nynka, M., Haggard, D., Kalogera, V., & Evans, P. 2018a, *ApJ*, **853**, L4
- Ruan, J. J., Nynka, M., Haggard, D., Kalogera, V., & Evans, P. 2018b, *ApJ*, **859**, L16
- Ruffert, M. 1999, *A&A*, **346**, 861
- Ryan, G., van Eerten, H., Piro, L., & Troja, E. 2020, *ApJ*, **896**, 166
- Rybicki, G. B. & Lightman, A. P. 1979, *Radiative processes in astrophysics* (John Wiley & Sons)
- Safarzadeh, M. & Berger, E. 2019, *ApJ*, **878**, L12
- Saio, H. & Nomoto, K. 2004, *ApJ*, **615**, 444
- Salafia, O. S., Berti, A., Covino, S., et al. 2022a, in 37th International Cosmic Ray Conference, **944**
- Salafia, O. S., Ravasio, M. E., Yang, J., et al. 2022b, *ApJ*, **931**, L19
- Saldana-Lopez, A., Domínguez, A., Pérez-González, P. G., et al. 2021, *MNRAS*, **507**, 5144
- Salpeter, E. E. 1955, *ApJ*, **121**, 161
- Sana, H., de Mink, S. E., de Koter, A., et al. 2012, *Science*, **337**, 444
- Santoliquido, F., Mapelli, M., Giacobbo, N., Bouffanais, Y., & Artale, M. C. 2021, *MNRAS*, **502**, 4877
- Sari, R. & Esin, A. A. 2001, *ApJ*, **548**, 787
- Sari, R. & Piran, T. 1997, *MNRAS*, **287**, 110

- Sari, R. & Piran, T. 1999, *ApJ*, 520, 641
- Sari, R., Piran, T., & Narayan, R. 1998, *ApJ*, 497, L17
- Sathyaprakash, B. S. & Schutz, B. F. 2009, *Living Reviews in Relativity*, 12, 2
- Sato, Y., Murase, K., Ohira, Y., & Yamazaki, R. 2023, *MNRAS*, 522, L56
- Savchenko, V., Ferrigno, C., Kuulkers, E., et al. 2017, *ApJ*, 848, L15
- Scalo, J. M. 1986, *Fund. Cosmic Phys.*, 11, 1
- Scholberg, K. 2012, *Annual Review of Nuclear and Particle Science*, 62, 81
- Sedov, L. I. 1946, *Journal of Applied Mathematics and Mechanics*, 10, 241
- Siegel, D. M., Barnes, J., & Metzger, B. D. 2019, *Nature*, 569, 241
- Sironi, L., Keshet, U., & Lemoine, M. 2015, *Space Sci. Rev.*, 191, 519
- Smartt, S. J., Chen, T. W., Jerkstrand, A., et al. 2017, *Nature*, 551, 75
- Sokolov, V. V., Fatkhullin, T. A., Castro-Tirado, A. J., et al. 2001, *A&A*, 372, 438
- Spera, M. & Mapelli, M. 2017, *MNRAS*, 470, 4739
- Spera, M., Mapelli, M., & Bressan, A. 2015, *MNRAS*, 451, 4086
- Spera, M., Mapelli, M., Giacobbo, N., et al. 2019, *MNRAS*, 485, 889
- Springel, V. & Hernquist, L. 2003, *MNRAS*, 339, 312
- Spruit, H. C., Daigne, F., & Drenkhahn, G. 2001, *A&A*, 369, 694
- Srinivasan, R., Lamberts, A., Bizouard, M. A., Bruel, T., & Mastrogiovanni, S. 2023, *MNRAS*, 524, 60
- Stanek, K. Z., Matheson, T., Garnavich, P. M., et al. 2003, *ApJ*, 591, L17
- Stanway, E. R. & Eldridge, J. J. 2018, *MNRAS*, 479, 75
- Stevenson, S., Vigna-Gómez, A., Mandel, I., et al. 2017, *Nature Communications*, 8, 14906
- Suda, T., Katsuta, Y., Yamada, S., et al. 2008, *PASJ*, 60, 1159
- Suda, Y., Artero, M., Asano, K., et al. 2022, in 37th International Cosmic Ray Conference, 797
- Sukhbold, T., Ertl, T., Woosley, S. E., Brown, J. M., & Janka, H. T. 2016, *ApJ*, 821, 38
- Symbalisty, E. M. D., Schramm, D. N., & Wilson, J. R. 1985, *ApJ*, 291, L11
- Takahashi, K. & Ioka, K. 2021, *MNRAS*, 501, 5746
- Tamborra, I., Hanke, F., Janka, H.-T., et al. 2014, *ApJ*, 792, 96
- Tang, J., Bressan, A., Rosenfield, P., et al. 2014, *MNRAS*, 445, 4287
- Tanikawa, A., Susa, H., Yoshida, T., Trani, A. A., & Kinugawa, T. 2021, *ApJ*, 910, 30
- Tauris, T. M., Kramer, M., Freire, P. C. C., et al. 2017, *ApJ*, 846, 170

- Tauris, T. M., Langer, N., Moriya, T. J., et al. 2013, *ApJ*, 778, L23
- Tauris, T. M., Langer, N., & Podsiadlowski, P. 2015, *MNRAS*, 451, 2123
- Tauris, T. M. & van den Heuvel, E. P. J. 2006, in *Compact stellar X-ray sources*, Vol. 39 (Cambridge Astrophysics Series), 623–665
- Tavani, M., Barbiellini, G., Argan, A., et al. 2009, *A&A*, 502, 995
- Taylor, G. 1950, *Proceedings of the Royal Society of London Series A*, 201, 159
- Tchekhovskoy, A., McKinney, J. C., & Narayan, R. 2008, *MNRAS*, 388, 551
- Temmink, K. D., Pols, O. R., Justham, S., Istrate, A. G., & Toonen, S. 2023, *A&A*, 669, A45
- The LIGO Scientific Collaboration, the Virgo Collaboration, Abbott, R., et al. 2021a, *arXiv e-prints*, [arXiv:2108.01045](https://arxiv.org/abs/2108.01045)
- The LIGO Scientific Collaboration, the Virgo Collaboration, the KAGRA Collaboration, et al. 2021b, *arXiv e-prints*, [arXiv:2111.03606](https://arxiv.org/abs/2111.03606)
- Thompson, C. 1994, *MNRAS*, 270, 480
- Thorne, K. S. & Zytlow, A. N. 1975, *ApJ*, 199, L19
- Tiengo, A., Pintore, F., Vaia, B., et al. 2023, *ApJ*, 946, L30
- Toonen, S., Hamers, A., & Portegies Zwart, S. 2016, *Computational Astrophysics and Cosmology*, 3, 6
- Toonen, S., Nelemans, G., & Portegies Zwart, S. 2012, *A&A*, 546, A70
- Totani, T. 1998, *ApJ*, 502, L13
- Tout, C. A., Aarseth, S. J., Pols, O. R., & Eggleton, P. P. 1997, *MNRAS*, 291, 732
- Tout, C. A. & Eggleton, P. P. 1988, *MNRAS*, 231, 823
- Troja, E., Fryer, C. L., O'Connor, B., et al. 2022a, *Nature*, 612, 228
- Troja, E., O'Connor, B., Ryan, G., et al. 2022b, *MNRAS*, 510, 1902
- Troja, E., Piro, L., Ryan, G., et al. 2018, *MNRAS*, 478, L18
- Troja, E., Piro, L., van Eerten, H., et al. 2017, *Nature*, 551, 71
- Troja, E., van Eerten, H., Ryan, G., et al. 2019, *MNRAS*, 489, 1919
- Troja, E., van Eerten, H., Zhang, B., et al. 2020, *MNRAS*, 498, 5643
- Uhm, Z. L. & Beloborodov, A. M. 2007, *ApJ*, 665, L93
- Uhm, Z. L., Zhang, B., Hascoët, R., et al. 2012, *ApJ*, 761, 147
- van de Voort, F., Quataert, E., Hopkins, P. F., Kereš, D., & Faucher-Giguère, C.-A. 2015, *MNRAS*, 447, 140
- van den Heuvel, E. P. J. & De Loore, C. 1973, *A&A*, 25, 387
- van Eerten, H., van der Horst, A., & MacFadyen, A. 2012, *ApJ*, 749, 44

- van Eerten, H. J. & MacFadyen, A. I. 2012, [ApJ](#), 747, L30
- van Haften, L. M., Nelemans, G., Voss, R., et al. 2013, [A&A](#), 552, A69
- van Paradijs, J., Groot, P. J., Galama, T., et al. 1997, [Nature](#), 386, 686
- Vanbeveren, D., De Donder, E., Van Bever, J., Van Rensbergen, W., & De Loore, C. 1998, [New A](#), 3, 443
- Vangioni, E., Goriely, S., Daigne, F., François, P., & Belczynski, K. 2016, [MNRAS](#), 455, 17
- Vangioni, E., Olive, K. A., Prestegard, T., et al. 2015, [MNRAS](#), 447, 2575
- Vasilopoulos, G., Karavola, D., Stathopoulos, S. I., & Petropoulou, M. 2023, [MNRAS](#), 521, 1590
- Vassiliadis, E. & Wood, P. R. 1993, [ApJ](#), 413, 641
- Verbunt, F., Igoshev, A., & Cator, E. 2017, [A&A](#), 608, A57
- Vigna-Gómez, A., Neijssel, C. J., Stevenson, S., et al. 2018, [MNRAS](#), 481, 4009
- Villar, V. A., Guillochon, J., Berger, E., et al. 2017, [ApJ](#), 851, L21
- Villasenor, J. S., Lamb, D. Q., Ricker, G. R., et al. 2005, [Nature](#), 437, 855
- Vink, J. S. & de Koter, A. 2005, [A&A](#), 442, 587
- Vink, J. S., de Koter, A., & Lamers, H. J. G. L. M. 2001, [A&A](#), 369, 574
- Vink, J. S., Muijres, L. E., Anthonisse, B., et al. 2011, [A&A](#), 531, A132
- Řípa, J., Takahashi, H., Fukazawa, Y., et al. 2023, [A&A](#), 677, L2
- Vurm, I., Hascoët, R., & Beloborodov, A. M. 2014, [ApJ](#), 789, L37
- Wang, B. & Han, Z. 2010, [A&A](#), 515, A88
- Wang, B. & Liu, D. 2020, [Research in Astronomy and Astrophysics](#), 20, 135
- Wang, X.-Y., Liu, R.-Y., Zhang, H.-M., Xi, S.-Q., & Zhang, B. 2019, [ApJ](#), 884, 117
- Warren, D. C., Dainotti, M., Barkov, M. V., et al. 2022, [ApJ](#), 924, 40
- Watson, D., Hansen, C. J., Selsing, J., et al. 2019, [Nature](#), 574, 497
- Webbink, R. F. 1984, [ApJ](#), 277, 355
- Webbink, R. F. 1985, in *Interacting Binary Stars*, ed. J. E. Pringle & R. A. Wade (Cambridge Astrophysics Series, Cambridge: Cambridge University Press), 39
- Webbink, R. F. 1988, in *Astrophysics and Space Science Library*, Vol. 145, IAU Colloq. 103: The Symbiotic Phenomenon, ed. J. Mikolajewska, M. Friedjung, S. J. Kenyon, & R. Viotti, 311
- Wei, J., Cordier, B., Antier, S., et al. 2016, [arXiv e-prints](#), [arXiv:1610.06892](#)
- Wong, T.-W., Valsecchi, F., Ansari, A., et al. 2014, [ApJ](#), 790, 119
- Wongwathanarat, A., Janka, H. T., & Müller, E. 2013, [A&A](#), 552, A126
- Wongwathanarat, A., Müller, E., & Janka, H. T. 2015, [A&A](#), 577, A48

- Wood, P. R. 1990, in *From Miras to Planetary Nebulae: Which Path for Stellar Evolution?*, ed. M. O. Mennessier & A. Omont, 67
- Woods, E. & Loeb, A. 1999, *ApJ*, 523, 187
- Woosley, S. E. 1987, in *The Origin and Evolution of Neutron Stars*, ed. D. J. Helfand & J. H. Huang, Vol. 125, 255
- Woosley, S. E. 1993, *ApJ*, 405, 273
- Woosley, S. E. 2017, *ApJ*, 836, 244
- Woosley, S. E. & Heger, A. 2021, *ApJ*, 912, L31
- Yamasaki, S. & Piran, T. 2022, *MNRAS*, 512, 2142
- Yang, J., Ai, S., Zhang, B.-B., et al. 2022, *Nature*, 612, 232
- Ye, C. & Fishbach, M. 2022, *ApJ*, 937, 73
- Ye, C. S., Fong, W.-f., Kremer, K., et al. 2020, *ApJ*, 888, L10
- Yoon, S. C. & Langer, N. 2005, *A&A*, 443, 643
- Zhang, B. & Yan, H. 2011, *ApJ*, 726, 90
- Zhang, J., Yang, Y., Zhang, C., et al. 2019, *MNRAS*, 488, 5020

Appendices

Appendix A

Radiative Regimes and Corresponding Electron Distributions

In this appendix, I describe the different spectral cases corresponding to the different possible orderings between the characteristic frequencies defined in Sec. 5.4.6.

The Inverse Compton (IC) cooling impacts the distribution of electrons if $\max(\gamma_c; \tilde{\gamma}_p) < \gamma < \gamma_0$ (Eq. 5.117). As $\hat{\gamma} = \gamma_{\text{self}}^3/\gamma^2$ (Eq. 5.68), all possible cases regarding the radiative regime and the distribution of electrons can be identified in the $(\gamma_{\text{self}}; \gamma_0)$ plane shown in Fig. A.1.

As an electron of Lorentz factor γ can upscatter its own synchrotron photon only if $\gamma \leq \hat{\gamma}$, *i.e.* $\gamma \leq \gamma_{\text{self}}$, the x-axis quantifies the importance of the Klein-Nishina (KN) suppression: the lower γ_{self} (left side of the diagram), the more electrons are affected by KN effects. The y-axis quantifies the importance of IC cooling: the IC power of all electrons with $\gamma > \gamma_0$ is negligible compared to the synchrotron power. Therefore, the lower γ_0 (bottom of the diagram), the more electrons have a negligible IC cooling.

We list in Tab. A.1 (fast cooling) and A.3 (slow cooling) all these cases and provide the corresponding self-consistent solution (breaks and slopes) for the normalized distribution of electrons $f(x)$ (Eq. 5.88) and the normalized Compton parameter $h(x)$ (Eq. 5.114), as obtained following the detailed method described in Nakar et al. (2009). The break corresponding to the peak of the synchrotron spectrum is highlighted in red. We also provide in each case the expression of γ_0 obtained from the relation $Y(\gamma_c) = h(x_c)/h(x_0)$ (Eq. 5.119), as needed in the iterative procedure to determine $Y(\gamma_c)$: see Sec. 5.4.6.

The distribution of electrons is unaffected by the Synchrotron Self-Compton (SSC) cooling when $\gamma_0 < \gamma_c$ or $\gamma_c < \gamma_0 < \hat{\gamma}_{\text{m,c}}$. These two regions are shaded in orange and blue in Fig. A.1. When $\gamma_0 < \hat{\gamma}_{\text{m,c}}$ (cases F1 and S1), the IC cooling is negligible for all electrons and γ_0 is undefined. The solution is provided by the pure synchrotron case (Sec. 5.4.4). When $\hat{\gamma}_{\text{m,c}} < \gamma_0 < \gamma_c$ (cases F2 to F5 and S2 to S6), the normalized electron distribution $f(x)$ is also the same as in the pure synchrotron case but γ_0 is defined and its expression depends on the considered regime.

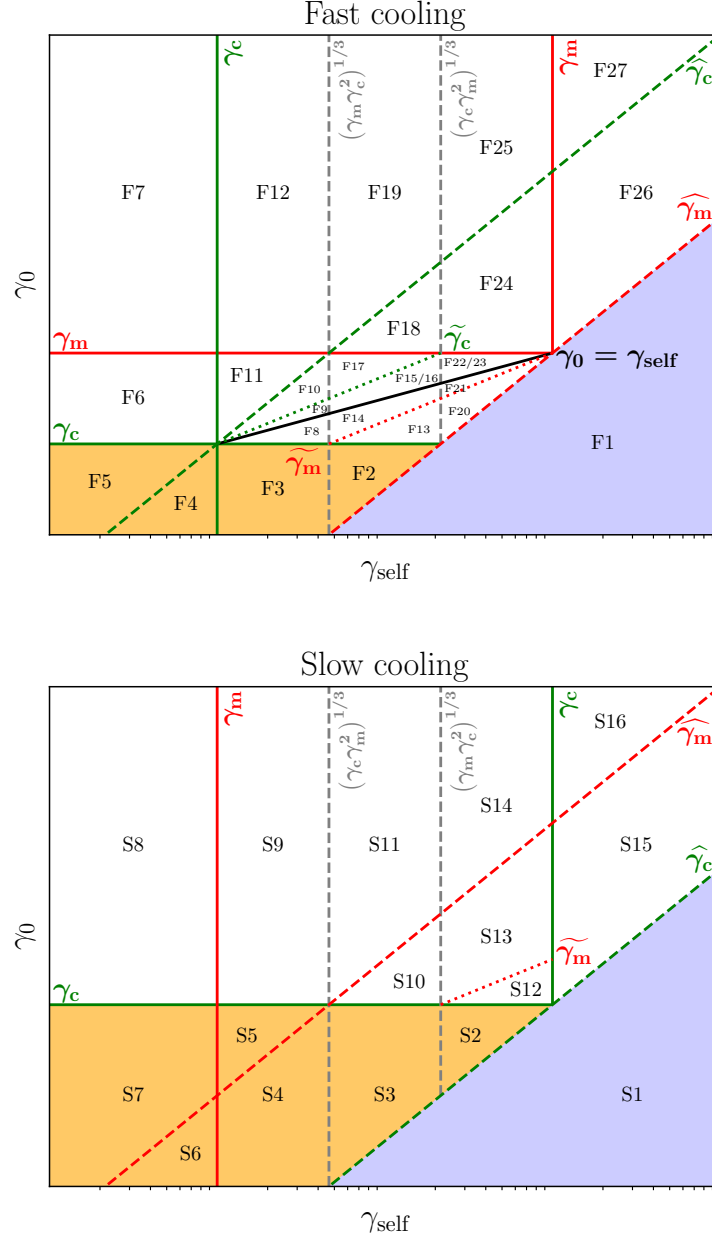


Fig. A.1: Definition of all possible cases for the radiative regime and the distribution of electrons in the plane γ_0 vs γ_{self} . The Lorentz factors γ_m and γ_c are indicated by red and green solid lines either in the fast cooling regime with $\gamma_m > \gamma_c$ (top) or in the slow cooling regime with $\gamma_m < \gamma_c$ (bottom). The black solid line in the top panel corresponds to $\gamma_0 = \gamma_{\text{self}}$. The two Lorentz factors $\hat{\gamma}_m$ (red) and $\hat{\gamma}_c$ (green) are plotted in dashed lines. In some regions, additional Lorentz factors relevant to identify the radiative regime are also plotted: $\tilde{\gamma}_m$ (red dotted line) and $\tilde{\gamma}_c$ (green dotted line). The regions where there is no impact of the SSC cooling on the distribution of electrons are shaded in orange ($\hat{\gamma}_{m,c} < \gamma_0 < \gamma_c$) and blue ($\gamma_0 < \hat{\gamma}_{m,c}$). This diagram allows to identify all possible orderings of γ_0 , γ_m , γ_c , $\hat{\gamma}_m$, $\hat{\gamma}_c$ defining all possible radiative regimes: see the text in Appendix A. The corresponding limits for γ_{self} are indicated by vertical black dashed lines.

Case F1	breaks	$\widehat{\gamma}_c$	$\widehat{\gamma}_m$	$\widehat{\gamma}_m$	$\widehat{\gamma}_c$	γ_0 undefined		
	f slopes	2		$p+1$				
	h slopes	0		$1/2$	$4/3$			
Case F2	breaks	$\widehat{\gamma}_m$	γ_0	$\widehat{\gamma}_c$	$\widehat{\gamma}_m$	$\widehat{\gamma}_c$	$\gamma_0 = \gamma_c Y_c^2$	
	f slopes			2		$p+1$		
	h slopes	0		$1/2$		$4/3$		
Case F3	breaks	$\widehat{\gamma}_m$	γ_0	$\widehat{\gamma}_c$	$\widehat{\gamma}_c$	$\widehat{\gamma}_m$	$\gamma_0 = \gamma_c Y_c^2$	
	f slopes			2		$p+1$		
	h slopes	0		$1/2$		$4/3$		
Case F4	breaks	$\widehat{\gamma}_m$	γ_0	$\widehat{\gamma}_c$	$\widehat{\gamma}_c$	$\widehat{\gamma}_m$	$\gamma_0 = \gamma_c^{8/3} \widehat{\gamma}_c^{-5/3} Y_c^2$	
	f slopes			2		$p+1$		
	h slopes	0		$1/2$		$4/3$		
Case F5	breaks	$\widehat{\gamma}_m$	$\widehat{\gamma}_c$	γ_0	$\widehat{\gamma}_c$	$\widehat{\gamma}_m$	$\gamma_0 = \gamma_c Y_c^{3/4}$	
	f slopes			2		$p+1$		
	h slopes	0	$1/2$		$4/3$			
Case F6	breaks	$\widehat{\gamma}_m$	$\widehat{\gamma}_0$	$\widehat{\gamma}_c$	γ_c	γ_0	$\widehat{\gamma}_m$	$\gamma_0 = \gamma_c Y_c^{3/4}$
	f slopes				$2/3$	2	$p+1$	
	h slopes	0	$1/2$	$7/6$		$4/3$		
Case F7	breaks	$\widehat{\gamma}_0$	$\widehat{\gamma}_m$	$\widehat{\gamma}_c$	γ_c	γ_0	$\widehat{\gamma}_m$	$\gamma_0 = \gamma_c Y_c^{3/4}$
	f slopes				$2/3$	$p-1/3$	$p+1$	
	h slopes	0	$(10-3p)/6$	$7/6$		$4/3$		
Case F8	breaks	$\widehat{\gamma}_m$	γ_c	γ_0	$\widehat{\gamma}_0$	$\widehat{\gamma}_c$	$\widehat{\gamma}_m$	$\gamma_0 = \gamma_c Y_c^2$
	f slopes		$3/2$		2		$p+1$	
	h slopes	0	$1/2$		$3/4$	$4/3$		
Case F9	breaks	$\widehat{\gamma}_m$	γ_c	$\widehat{\gamma}_0$	γ_0	$\widehat{\gamma}_0$	$\widehat{\gamma}_c$	$\gamma_0 = \gamma_c^{1/2} \widehat{\gamma}_0^{1/2} Y_c = \gamma_c^{1/4} \gamma_{\text{self}}^{3/4} Y_c^{1/2}$
	f slopes		$3/2$	1		2	$p+1$	
	h slopes	0	$1/2$		1	$3/4$	$4/3$	
Case F10	breaks	$\widehat{\gamma}_m$	$\widehat{\gamma}_0$	γ_c	γ_0	$\widehat{\gamma}_c$	$\widehat{\gamma}_m$	$\gamma_0 = \gamma_c Y_c$
	f slopes			1		2	$p+1$	
	h slopes	0	$1/2$		1	$4/3$		
Case F11	breaks	$\widehat{\gamma}_m$	$\widehat{\gamma}_0$	$\widehat{\gamma}_c$	γ_c	$\widehat{\gamma}_c$	γ_0	$\gamma_0 = \gamma_c^{3/4} \widehat{\gamma}_c^{1/4} Y_c^{3/4}$
	f slopes				1	$2/3$	2	
	h slopes	0	$1/2$	$7/6$	1	$4/3$		
Case F12	breaks	$\widehat{\gamma}_0$	$\widehat{\gamma}_m$	$\widehat{\gamma}_c$	γ_c	$\widehat{\gamma}_c$	$\widehat{\gamma}_m$	$\gamma_0 = \gamma_c^{3/4} \widehat{\gamma}_c^{1/4} Y_c^{3/4}$
	f slopes				1	$2/3$	$p-1/3$	
	h slopes	0	$(10-3p)/6$	$7/6$	1	$4/3$		
Case F13	breaks	$\widehat{\gamma}_m$	γ_c	γ_0	$\widehat{\gamma}_0$	$\widehat{\gamma}_c$	$\widehat{\gamma}_m$	$\gamma_0 = \gamma_c Y_c^2$
	f slopes		$3/2$		2		$p+1$	
	h slopes	0	$1/2$		$3/4$	$4/3$		
Case F14	breaks	$\widehat{\gamma}_m$	γ_c	γ_0	$\widehat{\gamma}_m$	$\widehat{\gamma}_c$	$\widehat{\gamma}_m$	$\gamma_0 = \gamma_c Y_c^2$
	f slopes		$3/2$	2			$p+1$	
	h slopes	0	$1/2$		$3/4$	$4/3$		
Case F15	breaks	$\widehat{\gamma}_m$	γ_c	$\widehat{\gamma}_0$	γ_0	$\widehat{\gamma}_0$	$\widehat{\gamma}_c$	$\gamma_0 = \gamma_c^{1/2} \widehat{\gamma}_0^{1/2} Y_c = \gamma_c^{1/4} \gamma_{\text{self}}^{3/4} Y_c^{1/2}$
	f slopes		$3/2$	1		2	$p+1$	
	h slopes	0	$1/2$		1	$3/4$	$4/3$	
Case F16	breaks	$\widehat{\gamma}_m$	γ_c	$\widehat{\gamma}_0$	γ_0	$\widehat{\gamma}_0$	$\widehat{\gamma}_c$	$\gamma_0 = \gamma_c^{1/2} \widehat{\gamma}_0^{1/2} Y_c = \gamma_c^{1/4} \gamma_{\text{self}}^{3/4} Y_c^{1/2}$
	f slopes		$3/2$	1		2	$p+1$	
	h slopes	0	$1/2$		1	$3/4$	$4/3$	
Case F17	breaks	$\widehat{\gamma}_m$	$\widehat{\gamma}_0$	γ_c	γ_0	$\widehat{\gamma}_c$	$\widehat{\gamma}_m$	$\gamma_0 = \gamma_c Y_c$
	f slopes			1		2	$p+1$	
	h slopes	0	$1/2$		1	$4/3$		
Case F18	breaks	$\widehat{\gamma}_0$	$\widehat{\gamma}_m$	γ_c	γ_m	γ_0	$\widehat{\gamma}_c$	$\gamma_0 = \gamma_c Y_c$
	f slopes				1	p	$p+1$	
	h slopes	0	$(3-p)/2$		1	$4/3$		
Case F19	breaks	$\widehat{\gamma}_0$	$\widehat{\gamma}_c$	$\widehat{\gamma}_m$	γ_c	γ_m	$\widehat{\gamma}_c$	$\gamma_0 = \gamma_c^{3/4} \widehat{\gamma}_c^{1/4} Y_c^{3/4}$
	f slopes				1	p	$p-1/3$	
	h slopes	0	$(10-3p)/6$	$(3-p)/2$		1	$4/3$	

Tab. A.1: Fast cooling: list of all possible radiative regimes and corresponding electron distribution. For each case, the first row of the table gives the list of breaks appearing either in the normalized electron distribution $f(x)$, *i.e.* the list of x_i , or in the normalized Compton parameter $h(x)$, *i.e.* list of relevant \widehat{x}_i , as well as all other necessary characteristic Lorentz factors to fully define the case in agreement with Fig. A.1 (blue). The break corresponding to the peak of the synchrotron spectrum is highlighted in red. The second and third rows give the slopes $-\ln f/d \ln x$ and $-\ln g/d \ln x$ for each branch. Finally, the last column gives the expression of γ_0 . Cases F24 and F25 require a specific treatment: see text.

Case F20	breaks	γ_c	$\widehat{\gamma}_m$	γ_0	$\widehat{\gamma}_0$	γ_m	$\widehat{\gamma}_m$	$\widehat{\gamma}_c$	$\gamma_0 = \widehat{\gamma}_m Y_c^2$
	f slopes	2	3/2	2	2			$p+1$	
	h slopes	0		1/2		3/4		1/2	
Case F21	breaks	γ_c	$\widehat{\gamma}_m$	γ_0	γ_m	$\widehat{\gamma}_0$	$\widehat{\gamma}_m$	$\widehat{\gamma}_c$	$\gamma_0 = \widehat{\gamma}_m Y_c^2$
	f slopes	2	3/2	2				$p+1$	
	h slopes	0		1/2		3/4		1/2	
Case F22	breaks	γ_c	$\widehat{\gamma}_m$	$\widehat{\gamma}_0$	γ_0	$\widehat{\gamma}_0$	γ_m	$\widehat{\gamma}_m$	$\gamma_0 = \widehat{\gamma}_m^{1/2} \widehat{\gamma}_0^{1/2} Y_c = \widehat{\gamma}_m^{-1/4} \gamma_{\text{self}}^{3/4} Y_c^{1/2}$
	f slopes	2	3/2	1	2	2		$p+1$	
	h slopes	0		1/2		1		3/4	
Case F23	breaks	γ_c	$\widehat{\gamma}_m$	$\widehat{\gamma}_0$	γ_0	γ_m	$\widehat{\gamma}_0$	$\widehat{\gamma}_m$	$\gamma_0 = \widehat{\gamma}_m^{1/2} \widehat{\gamma}_0^{1/2} Y_c = \widehat{\gamma}_m^{-1/4} \gamma_{\text{self}}^{3/4} Y_c^{1/2}$
	f slopes	2	3/2	1	2	2		$p+1$	
	h slopes	0		1/2		1		3/4	
Case F26	breaks	γ_c	γ_m	$\widehat{\gamma}_m$	γ_0	$\widehat{\gamma}_c$			$\gamma_0 = \widehat{\gamma}_m Y_c^2$
	f slopes	2		$p+1$	$p+1/2$	$p+1$			
	h slopes	0			1/2			4/3	
Case F27	breaks	γ_c	γ_m	$\widehat{\gamma}_m$	$\widehat{\gamma}_c$	γ_0			$\gamma_0 = \widehat{\gamma}_m^{3/8} \widehat{\gamma}_c^{5/8} Y_c^{3/4}$
	f slopes	2		$p+1$	$p+1/2$	$p-1/3$		$p+1$	
	h slopes	0			1/2			4/3	

Tab. A.2: Tab. A.1, continued.

In fast cooling regime, cases F24 and F25 require a specific treatment, as a large number of breaks can appear in the distribution (see Sec. 3.2 in Nakar et al. 2009). There are multiple possible subcases, depending on the number of breaks, that can be found iteratively. We only list below the first subcases of case F24 with breaks at $\widehat{\gamma}_m$, $\widehat{\gamma}_0$ and $\widehat{\widehat{\gamma}}_m$.

- If $\gamma_m < \gamma_0 < \min(\widehat{\gamma}_c; \widehat{\widehat{\gamma}}_m) < \widehat{\gamma}_c$:

	γ_c	$\widehat{\gamma}_0$	$\widehat{\gamma}_m$	γ_m	γ_0	$\widehat{\gamma}_m$	$\widehat{\gamma}_0$	$\widehat{\gamma}_c$
f	2	$(p+1)/2$	1	p			$p+1$	
h	0	$(3-p)/2$		1		$(5-p)/4$	1/2	4/3

- If $\gamma_m < \widehat{\gamma}_c < \gamma_0 < \widehat{\widehat{\gamma}}_m < \widehat{\gamma}_c$:

	$\widehat{\gamma}_0$	γ_c	$\widehat{\gamma}_m$	γ_m	γ_0	$\widehat{\gamma}_m$	$\widehat{\gamma}_c$
f		$(p+1)/2$	1	p		$p+1$	
h	0	$(3-p)/2$		1		$(5-p)/4$	4/3

- If $\gamma_m < \widehat{\gamma}_c < \widehat{\widehat{\gamma}}_m < \gamma_0 < \widehat{\gamma}_c$:

For $p < 13/5 = 2.6$:

	$\widehat{\gamma}_0$	$\widehat{\widehat{\gamma}}_m$	γ_c	$\widehat{\gamma}_m$	γ_m	$\widehat{\gamma}_m$	γ_0	$\widehat{\gamma}_c$
f			$(p+1)/2$	1	p		$(5p-1)/4$	$p+1$
h	0	$(13-5p)/8$	$(3-p)/2$		1		$(5-p)/4$	4/3

For $p > 13/5 = 2.6$:

	$\widehat{\widehat{\gamma}}_m$	γ_c	$\widehat{\gamma}_m$	γ_m	$\widehat{\widehat{\gamma}}_m$	γ_0	$\widehat{\gamma}_c$
f		$(p+1)/2$	1	p		$(5p-1)/4$	$p+1$
h	0	$(3-p)/2$		1		$(5-p)/4$	4/3

- etc.

The other subcases of F24 and F25 include even more breaks at $\widehat{\widehat{\widehat{\gamma}}}_m$, etc. These new breaks are gradually closer and closer, and therefore have a limited signature on the spectral shape. In addition, these extreme radiative cases correspond to physical conditions unlikely to be found in GRB afterglows.

Case S1	breaks	γ_m	γ_c	$\hat{\gamma}_c$	$\hat{\gamma}_m$	γ_0 undefined				
	f slopes	p			$p+1$					
	h slopes	0		$(3-p)/2$	$4/3$					
Case S2	breaks	γ_m	$\hat{\gamma}_c$	γ_0	γ_c	$\hat{\gamma}_m$	$\gamma_0 = \gamma_c Y_c^{2/(3-p)}$			
	f slopes			2		$p+1$				
	h slopes	0		$(3-p)/2$		$4/3$				
Case S3	breaks	$\hat{\gamma}_c$	γ_0	γ_m	γ_0	γ_c	$\hat{\gamma}_m$	$\gamma_0 = \gamma_c Y_c^{2/(3-p)}$		
	f slopes			2		$p+1$				
	h slopes	0		$(3-p)/2$		$4/3$				
Case S4	breaks	$\hat{\gamma}_c$	γ_0	γ_m	γ_0	$\hat{\gamma}_m$	γ_c	$\gamma_0 = \gamma_c^{8/(9-3p)} \hat{\gamma}_m^{(1-3p)/(9-3p)} Y_c^{2/(3-p)}$		
	f slopes				2		$p+1$			
	h slopes	0		$(3-p)/2$		$4/3$				
Case S5	breaks	$\hat{\gamma}_c$	γ_m	$\hat{\gamma}_m$	γ_0	γ_c		$\gamma_0 = \gamma_c Y_c^{3/4}$		
	f slopes				p		$p+1$			
	h slopes	0		$(3-p)/2$		$4/3$				
Case S6	breaks	$\hat{\gamma}_c$	γ_0	$\hat{\gamma}_m$	γ_m	γ_c		$\gamma_0 = \gamma_c^{8/(9-3p)} \hat{\gamma}_m^{(1-3p)/(9-3p)} Y_c^{2/(3-p)}$		
	f slopes				p		$p+1$			
	h slopes	0		$(3-p)/2$		$4/3$				
Case S7	breaks	$\hat{\gamma}_c$	$\hat{\gamma}_m$	γ_0	γ_m	γ_0	γ_c	$\gamma_0 = \gamma_c Y_c^{3/4}$		
	f slopes					p	$p+1$			
	h slopes	0		$(3-p)/2$		$4/3$				
Case S8	breaks	$\hat{\gamma}_0$	$\hat{\gamma}_c$	$\hat{\gamma}_m$	γ_m	γ_c	γ_0	$\gamma_0 = \gamma_c Y_c^{3/4}$		
	f slopes					p	$p-1/3$		$p+1$	
	h slopes	0		$(10-3p)/6$		$(3-p)/2$			$4/3$	
Case S9	breaks	$\hat{\gamma}_0$	$\hat{\gamma}_c$	γ_m	$\hat{\gamma}_m$	γ_c	γ_0	$\gamma_0 = \gamma_c Y_c^{3/4}$		
	f slopes				p		$p-1/3$		$p+1$	
	h slopes	0		$(10-3p)/6$		$(3-p)/2$			$4/3$	
Case S10 ($p < 7/3$)	breaks	$\hat{\gamma}_0$	$\hat{\gamma}_c$	γ_m	γ_c	γ_0	$\hat{\gamma}_m$	$\gamma_0 = \gamma_c Y_c^{2/(3-p)}$		
	f slopes				p		$(3p-1)/2$		$p+1$	
	h slopes	0		$(7-3p)/4$		$(3-p)/2$			$4/3$	
Case S10 ($p > 7/3$)	breaks	$\hat{\gamma}_0$	$\hat{\gamma}_c$	γ_m	γ_c	γ_0	$\hat{\gamma}_m$	$\gamma_0 = \gamma_c Y_c^{2/(3-p)}$		
	f slopes				p		$(3p-1)/2$		$p+1$	
	h slopes	0		$(3-p)/2$		$4/3$				
Case S11 ($p < 7/3$)	breaks	$\hat{\gamma}_0$	$\hat{\gamma}_m$	$\hat{\gamma}_c$	γ_m	γ_c	$\hat{\gamma}_m$	γ_0	$\gamma_0 = \hat{\gamma}_m^{(3p-1)/8} \gamma_c^{(9-3p)/8} Y_c^{3/4}$	
	f slopes					p	$(3p-1)/2$	$p-1/3$		$p+1$
	h slopes	0		$(10-3p)/6$		$(7-3p)/4$		$(3-p)/2$		$4/3$
Case S11 ($p > 7/3$)	breaks	$\hat{\gamma}_0$	$\hat{\gamma}_m$	$\hat{\gamma}_c$	γ_m	γ_c	$\hat{\gamma}_m$	γ_0	$\gamma_0 = \hat{\gamma}_m^{(3p-1)/8} \gamma_c^{(9-3p)/8} Y_c^{3/4}$	
	f slopes					p	$(3p-1)/2$	$p-1/3$		$p+1$
	h slopes	0		$(3-p)/2$		$4/3$				
Case S12 ($p < 7/3$)	breaks	γ_m	$\hat{\gamma}_0$	$\hat{\gamma}_c$	γ_c	γ_0	$\hat{\gamma}_m$	$\gamma_0 = \gamma_c Y_c^{2/(3-p)}$		
	f slopes					p	$(3p-1)/2$		$p+1$	
	h slopes	0		$(7-3p)/4$		$(3-p)/2$			$4/3$	
Case S12 ($p > 7/3$)	breaks	γ_m	$\hat{\gamma}_0$	$\hat{\gamma}_c$	γ_c	γ_0	$\hat{\gamma}_m$	$\gamma_0 = \gamma_c Y_c^{2/(3-p)}$		
	f slopes					p	$(3p-1)/2$		$p+1$	
	h slopes	0		$(3-p)/2$		$4/3$				
Case S13 ($p < 7/3$)	breaks	$\hat{\gamma}_0$	γ_m	$\hat{\gamma}_c$	γ_c	γ_0	$\hat{\gamma}_m$	$\gamma_0 = \gamma_c Y_c^{2/(3-p)}$		
	f slopes					p	$(3p-1)/2$		$p+1$	
	h slopes	0		$(7-3p)/4$		$(3-p)/2$			$4/3$	
Case S13 ($p > 7/3$)	breaks	$\hat{\gamma}_0$	γ_m	$\hat{\gamma}_c$	γ_c	γ_0	$\hat{\gamma}_m$	$\gamma_0 = \gamma_c Y_c^{2/(3-p)}$		
	f slopes					p	$(3p-1)/2$		$p+1$	
	h slopes	0		$(3-p)/2$		$4/3$				
Case S14 ($p < 7/3$)	breaks	$\hat{\gamma}_0$	$\hat{\gamma}_m$	γ_m	$\hat{\gamma}_c$	γ_c	$\hat{\gamma}_m$	γ_0	$\gamma_0 = \hat{\gamma}_m^{(3p-1)/8} \gamma_c^{(9-3p)/8} Y_c^{3/4}$	
	f slopes					p	$(3p-1)/2$	$p-1/3$		$p+1$
	h slopes	0		$(10-3p)/6$		$(7-3p)/4$		$(3-p)/2$		$4/3$
Case S14 ($p > 7/3$)	breaks	$\hat{\gamma}_0$	$\hat{\gamma}_m$	γ_m	$\hat{\gamma}_c$	γ_c	$\hat{\gamma}_m$	γ_0	$\gamma_0 = \hat{\gamma}_m^{(3p-1)/8} \gamma_c^{(9-3p)/8} Y_c^{3/4}$	
	f slopes					p	$(3p-1)/2$	$p-1/3$		$p+1$
	h slopes	0		$(3-p)/2$		$4/3$				
Case S15	breaks	γ_m	γ_c	$\hat{\gamma}_c$	γ_0	$\hat{\gamma}_m$		$\gamma_0 = \hat{\gamma}_c Y_c^{2/(3-p)}$		
	f slopes	p		$p+1$		$(3p-1)/2$			$p+1$	
	h slopes	0		$(3-p)/2$		$4/3$				
Case S16	breaks	γ_m	γ_c	$\hat{\gamma}_c$	$\hat{\gamma}_m$	γ_0		$\gamma_0 = \hat{\gamma}_m^{(3p-1)/8} \gamma_c^{(9-3p)/8} Y_c^{3/4}$		
	f slopes	p		$p+1$		$(3p-1)/2$			$p-1/3$	$p+1$
	h slopes	0		$(3-p)/2$		$4/3$				

Tab. A.3: Slow cooling: list of all possible radiative regimes and corresponding electron distribution. Same convention as in Tab. A.1.

Appendix B

Comparison between our Afterglow Model and the Model of Gill & Granot (2018)

I discuss in Sec. 5.6 how our afterglow model compares to other works in the literature, in particular the model by Gill & Granot (2018). In this appendix, I describe the difference of notation convention between our model and that in Gill & Granot (2018), and show in Fig. B.1 that our choices of normalization lead to the same results. In this comparison, we assume only synchrotron radiation at the shock and do not include Synchrotron Self-Compton (SSC) diffusions that are not accounted for in Gill & Granot (2018).

As mentioned above, our dynamics is exactly the same as that proposed by Gill & Granot (2018), but our notations slightly differ. We define $\epsilon_0(\theta)$ as the total energy per unit solid angle at a latitude θ (*i.e.* the sum of the rest mass energy of the ejected material and its kinetic energy), while Gill & Granot (2018) use $\tilde{\epsilon}_0(\theta)$ the kinetic energy of the ejected material. Both quantities are linked by

$$\tilde{\epsilon}_0(\theta) = \frac{\Gamma_0(\theta) - 1}{\Gamma_0(\theta)} \epsilon_0(\theta), \quad (\text{B.1})$$

leading to the slightly different expressions for the deceleration radius $R_{\text{dec}}(\theta)$. We define in Eq. 5.28 $R_{\text{dec}}(\theta) = \left(\frac{(3-s)\epsilon_0(\theta)}{A\Gamma_0^2(\theta)c^2} \right)^{1/(3-s)}$, while in Gill & Granot (2018),

$$\tilde{R}_{\text{dec}}(\theta) = \left(\frac{(3-s)\tilde{\epsilon}_0(\theta)}{A(\Gamma_0^2(\theta) - 1)c^2} \right)^{1/(3-s)}. \quad (\text{B.2})$$

Both expressions are therefore linked by

$$\tilde{R}_{\text{dec}}(\theta) = \left(\frac{\Gamma_0(\theta)}{\Gamma_0(\theta) + 1} \right)^{\frac{1}{3-s}} R_{\text{dec}}(\theta), \quad (\text{B.3})$$

leading to the different values for the normalized swept-up mass, related by

$$\tilde{m} = \left(\frac{R}{\tilde{R}_{\text{dec}}(\theta)} \right)^{3-s} = \frac{\Gamma_0(\theta) + 1}{\Gamma_0(\theta)} m. \quad (\text{B.4})$$

Both our model and those in Panaitescu & Kumar (2000) and Gill & Granot (2018) rely on the same expression for the energy conservation as expressed in Eq. 5.22 to determine the evolution of

$\Gamma(\theta; R)$. However, while our expression of $\Gamma(\theta; R)$ is defined in Eq. 5.29, and can also be found in Panaitescu & Kumar (2000), Gill & Granot (2018) instead define $\Gamma(\theta; R)$ by

$$\Gamma(\theta; R) = \frac{\Gamma_0(\theta) + 1}{2\tilde{m}(\theta; R)} \times \left[-1 + \sqrt{1 + 4\frac{\Gamma_0(\theta)}{\Gamma_0(\theta) + 1}\tilde{m}(\theta; R) + 4\left(\frac{\tilde{m}(\theta; R)}{\Gamma_0(\theta) + 1}\right)^2} \right]. \quad (\text{B.5})$$

With all the relations defined above, we therefore retrieve the same expression for $\Gamma(\theta; R)$. There is therefore a difference in terminology between our models, but it does not affect the definitions of $\Gamma(\theta; R)$ used in the calculations of the dynamics of the jet. In addition, we note that all these definitions coincide in the ultra-relativistic when $\Gamma_0(\theta) \gg 1$.

Regarding the radiative emission by synchrotron, the values used in Gill & Granot (2018) in our notations are given by

$$K_{P_{\max}} = 0.88 \frac{32}{3\pi} \frac{p-1}{3p-1}, \quad (\text{B.6})$$

$$K_\nu = \frac{3\pi}{8}, \quad (\text{B.7})$$

$$K_P = 0.88 \times 4 \frac{p-1}{3p-1}, \quad (\text{B.8})$$

as reported in Tab. 5.1. These values are based on a normalization of the synchrotron peak amplitude and peak frequency for the instantaneous emission of a power-law distribution of radiating electrons, that gives the correct asymptotes at low and high frequencies, as shown on Fig. 4 of Granot et al. (1999). These values are also used in Sari & Esin (2001) with $p = 2.2$. We also use these values in our model, though a possible improvement would be to calibrate them to more detailed radiative numerical simulations like the one developed in Bošnjak et al. (2009) for the Gamma-Ray Burst (GRB) prompt emission.

With these choices, our model reproduces exactly the afterglow light curves presented in Fig. 4 of Gill & Granot (2018) with the correct normalization, in the case where no SSC diffusions are accounted for, as shown in Fig.B.1.

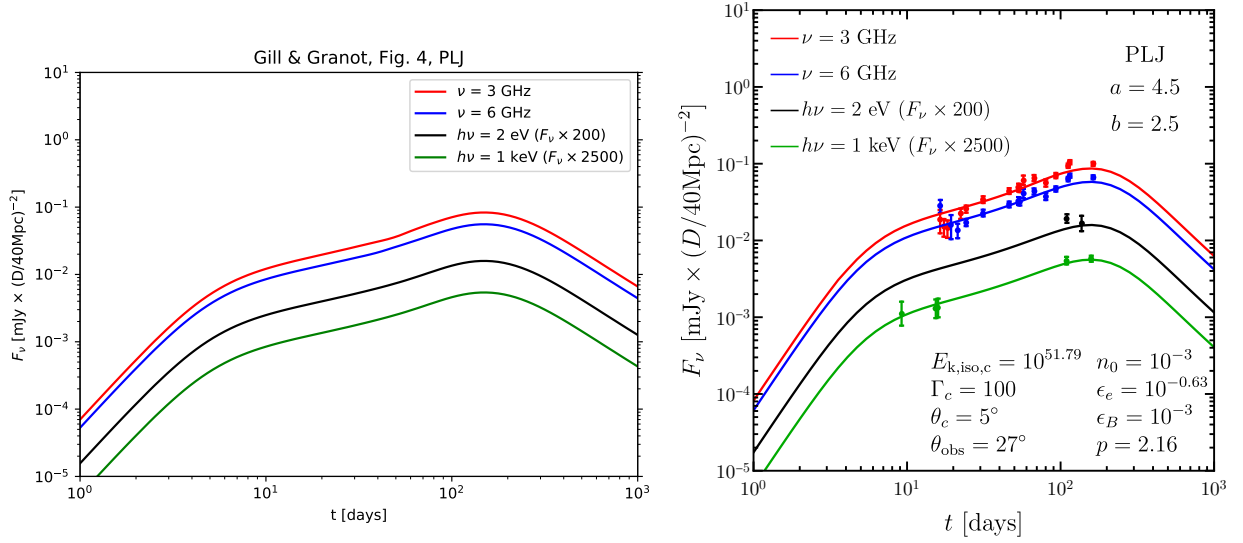


Fig. B.1: Radio, optical and X-ray light curves for a power-law jet with the lateral profile from Gill & Granot (2018) also shown in Sec. 5.1, with $a = 4.5$ and $b = 2.5$. The other parameters are shown on the bottom right corner of the right-hand side panel. **Left:** light curves obtained with our model; **Right:** figure taken from Gill & Granot (2018).

Appendix C

Derivation of the Observed Flux from a Distant Source with Relativistic Motion

In this appendix, I present the mathematical derivation of Eqs. 5.141 and 5.145, corresponding to the flux observed by a distant observer from a radiating source in relativistic motion. This calculation is an adaptation of that presented in Woods & Loeb (1999).

Some geometry

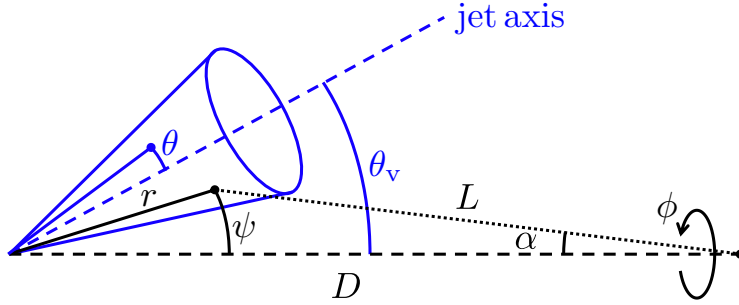


Fig. C.1: Coordinates and notations used in the calculations of the observed flux.

Let the source be located at a distance D from a distant observer. We focus here on the radiation of some emitting region located at a distance r from the source such that $r \ll D$, with spherical coordinates $(r; \psi; \phi)$, moving at a velocity βc . Let α be the angle between the emitting region and the observer, separated by a distance L . This setup is represented in Fig. C.1. Using the condition $r \ll D$ we get

$$L \approx D - r \cos \psi, \quad (\text{C.1})$$

$$\cos \alpha \approx 1 - \frac{1}{2} \left(\frac{r}{D} \right)^2 \sin^2 \psi, \quad (\text{C.2})$$

$$\sin \alpha \approx \frac{r}{D} \sin \psi, \quad (\text{C.3})$$

$$\cos(\alpha + \psi) \approx \cos \psi - \frac{r}{D} \sin^2 \psi. \quad (\text{C.4})$$

Using these relations, we can derive the expression for the change of coordinates from the observer frame $(L; \alpha; \phi)$ to the source frame $(r; \psi; \phi)$:

$$dL d\alpha d\phi = \begin{vmatrix} \frac{\partial L}{\partial r} & \frac{\partial L}{\partial \psi} \\ \frac{\partial \alpha}{\partial r} & \frac{\partial \alpha}{\partial \psi} \end{vmatrix} dr d\psi d\phi \quad (\text{C.5})$$

$$\simeq \frac{1}{|\cos \alpha|} \frac{r}{D} dr d\psi d\phi \quad (\text{C.6})$$

Observed flux

We compute the flux at an observed frequency ν_{obs} : we assume that there is no absorption or diffusion, so that the radiative transfer equation can be written

$$\frac{dI_{\nu_{\text{obs}}}}{ds} = -\alpha_{\nu_{\text{obs}}} I_{\nu_{\text{obs}}} + j_{\nu_{\text{obs}}} = j_{\nu_{\text{obs}}}. \quad (\text{C.7})$$

We integrate Eq. C.7 and get the received specific intensity at $L = 0$ at a given time \tilde{t}_{obs} :

$$I_{\nu_{\text{obs}}}(L = 0, \alpha, \phi; \tilde{t}_{\text{obs}}) = \int_{-\infty}^0 dL j_{\nu_{\text{obs}}}\left(L, \alpha, \phi; t = \tilde{t}_{\text{obs}} - \frac{L}{c}\right). \quad (\text{C.8})$$

Then, the flux is given by

$$F_{\nu_{\text{obs}}}(\tilde{t}_{\text{obs}}) = \int I_{\nu_{\text{obs}}}(L = 0, \alpha, \phi; \tilde{t}_{\text{obs}}) \cos \alpha d\Omega \quad (\text{C.9})$$

Given that the solid angle associated to direction (α, ϕ) is $d\Omega = \sin \alpha d\alpha d\phi$,

$$\begin{aligned} F_{\nu_{\text{obs}}}(\tilde{t}_{\text{obs}}) &= \int_0^{\pi/2} d\alpha \sin \alpha \int_0^{2\pi} d\phi I_{\nu_{\text{obs}}}(L = 0, \alpha, \phi; \tilde{t}_{\text{obs}}) \cos \alpha \\ &= \int_{-\infty}^0 dL \int_0^{\pi/2} d\alpha \sin \alpha \int_0^{2\pi} d\phi j_{\nu_{\text{obs}}}\left(L, \alpha, \phi; t = \tilde{t}_{\text{obs}} - \frac{L}{c}\right) \cos \alpha \\ &\approx \frac{1}{D^2} \int_0^{\infty} dr r^2 \int_0^{\pi/2} d\psi \int_0^{2\pi} d\phi \sin \psi j_{\nu_{\text{obs}}}\left(r, \psi, \phi; t = \tilde{t}_{\text{obs}} + \frac{r}{c} \cos \psi - \frac{D}{c}\right) \end{aligned} \quad (\text{C.10})$$

where we made use of the geometrical relations defined previously. For simplicity, it is useful to set a new origin for the observer time:

$$t_{\text{obs}} = \tilde{t}_{\text{obs}} - \frac{D}{c}. \quad (\text{C.11})$$

We now finally need to convert the emissivity $j_{\nu_{\text{obs}}}$ from the observer frame to emissivity $j'_{\nu'}$ the comoving frame. We define the Doppler factor

$$\mathcal{D} = \frac{1}{\Gamma(1 - \beta \cos(\alpha + \psi))} \approx \frac{1}{\Gamma(1 - \beta \cos \psi)}. \quad (\text{C.12})$$

The quantities j_{ν}/ν^2 and I_{ν}/ν^3 are Lorentz invariants and therefore transform such that

$$j_{\nu_{\text{obs}}} = \mathcal{D}^2 \times j'_{\nu'}, \quad (\text{C.13})$$

$$\nu_{\text{obs}} = \mathcal{D} \times \nu'. \quad (\text{C.14})$$

Finally, if the observer is at cosmological distance, the effect of redshift must be included. If we write D_L the luminosity distance and express

$$\nu_{\text{obs}}^z = \frac{\nu_{\text{obs}}}{1+z} = \frac{\mathcal{D}\nu'}{1+z}, \quad (\text{C.15})$$

$$t_{\text{obs}}^z = (1+z)t_{\text{obs}}, \quad (\text{C.16})$$

we finally get the expression for the observed flux density given in Eq. 5.141:

$$F_{\nu_{\text{obs}}^z}(t_{\text{obs}}^z) = \frac{1+z}{4\pi D_L^2} \int_0^{\infty} dr \int_0^{\pi} d\psi \int_0^{2\pi} d\phi r^2 \sin \psi \left[\mathcal{D}^2 4\pi j'_{\nu' = \frac{(1+z)\nu_{\text{obs}}^z}{\mathcal{D}}} \left(r, \psi, \phi; t = \frac{t_{\text{obs}}^z}{1+z} + \frac{r}{c} \cos \psi \right) \right]. \quad (\text{C.17})$$

Other expression of the observed flux

To link the definition of the observed flux from Eq. 5.141 to the quantities defined during the process of our model definition, we express $j'_{\nu'}$, the emissivity in the comoving frame, in $\text{erg} \cdot \text{s}^{-1} \cdot \text{Hz}^{-1} \cdot \text{cm}^{-3} \cdot \text{sr}^{-1}$ as a function of N_e , the number of shock-accelerated electrons per unit solid angle in $\text{electron} \cdot \text{sr}^{-1}$ (Eq. 5.148) and $p'_{\nu'}$, the radiated power per electron per unit frequency in $\text{erg} \cdot \text{s}^{-1} \cdot \text{Hz}^{-1} \cdot \text{electron}^{-1}$. We make the thin shell approximation, assuming that the radiating electrons are located at the shock front on an infinitesimal layer. At any comoving time t , the shock front is located at a radius $R(t)$ and has a Lorentz factor $\Gamma(t)$. The volume of the emitting region in the comoving frame is therefore $V' = 4\pi R^2(t)\Delta'(t)$ where the comoving infinitesimal layer is $\Delta'(t) = \Gamma(t)\Delta(t) = \frac{\Gamma(t)}{\delta(r-R(t))}$. Therefore,

$$V' = \times 4\pi R^2(t) \times \frac{\Gamma(t)}{\delta(r-R(t))}. \quad (\text{C.18})$$

Note that $\delta(r-R(t))$ has units of cm^{-1} . It follows that

$$\begin{aligned} F_{\nu_{\text{obs}}^z}(t_{\text{obs}}^z) &= \frac{1+z}{4\pi D_L^2} \int_0^\infty dr \int_0^\pi d\psi \int_0^{2\pi} d\phi r^2 \sin\psi \\ &\times \left[\mathcal{D}^2 4\pi \frac{1}{\Gamma(t)} \times \frac{1}{4\pi R^2(t)} \times \delta(r-R(t)) \times N_e(R(t)) p'_{\nu'} \left(t = \frac{t_{\text{obs}}^z}{1+z} + \frac{r}{c} \cos\psi \right) \right]. \end{aligned} \quad (\text{C.19})$$

The comoving time t , observer time t_{obs}^z and angle where the radiation originates ψ are related by

$$t = \frac{t_{\text{obs}}^z}{1+z} + \frac{r}{c} \cos\psi, \quad (\text{C.20})$$

or if we use t as our free variable:

$$\cos(\psi(t_{\text{obs}}^z; t)) = \frac{c}{R(t)} \left(t - \frac{t_{\text{obs}}^z}{1+z} \right). \quad (\text{C.21})$$

It follows that the Doppler factor \mathcal{D} is only a function of t :

$$\mathcal{D}(t_{\text{obs}}^z; t) = \frac{1}{\Gamma(t) (1 - \beta(t) \cos(\psi(t_{\text{obs}}^z; t)))}. \quad (\text{C.22})$$

From these relations, we can express

$$\begin{aligned} dt &= \beta(t) \cos\psi dt + \frac{R(t)}{c} d\cos\psi \\ d\cos\psi &= \frac{1 - \beta(t) \cos\psi}{R(t)/c} dt \\ &= \frac{c}{R(t) \Gamma(t) \mathcal{D}(t_{\text{obs}}^z; t)} dt \end{aligned} \quad (\text{C.23})$$

In addition, calculus with the Dirac δ function implies that

$$\int_{-\infty}^{+\infty} f(x) \delta(g(x)) = \sum_{x_i, g(x_i)=0} \frac{f(x_i)}{|g'(x_i)|} \quad (\text{C.24})$$

Here we solve $g(r) = r - R(t) = 0 : r = R(t)$. We note that $g(r) = r - R\left(t = \frac{t_{\text{obs}}^z}{1+z} + \frac{r}{c} \cos\psi\right)$. Then

$$\begin{aligned} g'(r) &= 1 - \frac{dR}{dt} \frac{dt}{dr} = 1 - \beta \left(t = \frac{t_{\text{obs}}^z}{1+z} + \frac{r}{c} \cos\psi \right) c \times \frac{1}{c} \cos\psi \\ g'(r) &= 1 - \beta(t) \cos\psi = \frac{1}{\Gamma(t) \mathcal{D}(t_{\text{obs}}^z; t)} \quad \text{with } t = \frac{t_{\text{obs}}^z}{1+z} + \frac{r}{c} \cos\psi. \end{aligned} \quad (\text{C.25})$$

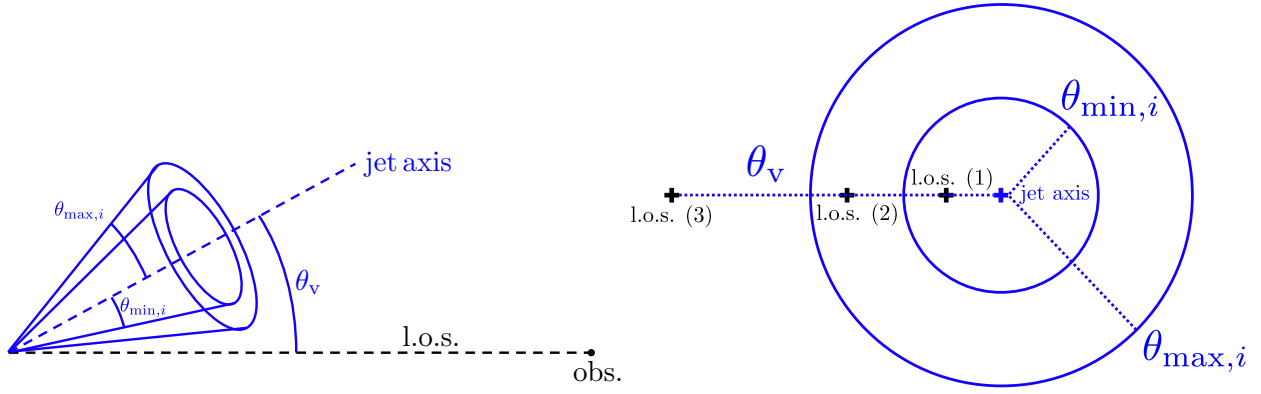


Fig. C.2: **Left:** Geometry of one component in a structured jet, defined by its minimum and maximum opening angles $\theta_{\min,i}$ and $\theta_{\max,i}$. **Right:** Same setup, this time seen from a plane perpendicular to the line of sight. The intersections of this plane with the off-axis inner and outer cones are circles. Depending on the viewing angle θ_v , three different positions of the line-of-sight with respect to the geometry of the component are possible, leading to three different expressions of $\psi_{\min,i}$ (see Eq. C.28).

Therefore, changing the variable ψ in $\cos \psi$ and solving $r = R(t)$, we get rid of the integral over r and obtain:

$$F_{\nu_{\text{obs}}^z}(t_{\text{obs}}^z) = \frac{1+z}{4\pi D_L^2} \int_{-1}^1 d \cos \psi \int_0^{2\pi} d\phi \quad (\text{C.26})$$

$$\times \left[\mathcal{D}^2(t_{\text{obs}}^z; t) \frac{1}{\Gamma(t)} \times \Gamma(t) \mathcal{D}(t_{\text{obs}}^z; t) \times N_e(R(t)) p'_{\nu'}(t) \right]_{t=\frac{t_{\text{obs}}^z}{1+z} + \frac{r}{c} \cos \psi}.$$

Now, changing the integral over ψ into an integral over t , we get

$$F_{\nu_{\text{obs}}^z}^{(i)}(t_{\text{obs}}^z) = \frac{1+z}{4\pi D_L^2} \int_{t_{\min}^{(i)}(t_{\text{obs}}^z)}^{t_{\max}^{(i)}(t_{\text{obs}}^z)} dt \int_0^{2\pi} d\phi \quad (\text{C.27})$$

$$\times \left[\frac{c}{\Gamma(t)R(t)} \mathcal{D}^2(t_{\text{obs}}^z; t) N_e(R(t)) p'_{\nu'}(t) \right]_{t=\frac{t_{\text{obs}}^z}{1+z} + \frac{r}{c} \cos \psi}.$$

In the context of a structured jet seen off-axis and whose geometry is represented in Fig. C.2 (left), its lateral structure is discretized numerically. The limits of the integral $t_{\min}^{(i)}(t_{\text{obs}}^z)$ and $t_{\max}^{(i)}(t_{\text{obs}}^z)$ are defined by the condition that $\psi_i(t_{\text{obs}}^z; t)$ under the integral can intersect the emitting region (otherwise the flux is 0), *i.e.* $\psi_{\min,i} \leq \psi_i(t_{\text{obs}}^z; t) \leq \psi_{\max,i}$, where using the illustration in Fig. C.2 (right),

$$\psi_{\min,i} = \begin{cases} \theta_{\min,i} - \theta_v & \text{if } \theta_v \leq \theta_{\min,i} \\ 0 & \text{if } \theta_{\min,i} \leq \theta_v \leq \theta_{\max,i} \\ \theta_v - \theta_{\max,i} & \text{if } \theta_{\max,i} \leq \theta_v \leq \pi/2 \end{cases}, \quad (\text{C.28})$$

and

$$\psi_{\max,i} = \theta_v + \theta_{\max,i}, \quad (\text{C.29})$$

i.e.

$$t - \frac{R_i(t)}{c} \cos(\psi_{\max,i}) \leq \frac{t_{\text{obs}}^z}{1+z} \leq t - \frac{R_i(t)}{c} \cos(\psi_{\min,i}). \quad (\text{C.30})$$

In the limit of an expanding sphere, this condition becomes

$$t - \frac{R_i(t)}{c} \leq \frac{t_{\text{obs}}^z}{1+z} \leq t + \frac{R_i(t)}{c}. \quad (\text{C.31})$$

Finally, we can simplify once more the expression of $F_{\nu_{\text{obs}}}^z$ by analytically evaluating the integral over ϕ . We use the exact analytical calculation of the geometrical term $\Delta\phi_i$ defined by $\Delta\phi_i(\theta_v; \psi) = \int_0^{2\pi} d\phi f_i(\theta_v; \psi; \phi)$, where $f_i(\theta_v; \psi; \phi) = 1$ if the direction $(\psi; \phi)$ is contained in the component i (core jet or ring) and 0 otherwise. The analytical expression of $\Delta\phi(\theta_v; \psi)$ is provided in Appendix D. With this final element, we obtain the expression of Eq. 5.145:

$$F_{\nu_{\text{obs}}}^{(i)}(t_{\text{obs}}^z) = \frac{1+z}{4\pi D_L^2} \int_{t_{\text{min}}^{(i)}(t_{\text{obs}}^z)}^{t_{\text{max}}^{(i)}(t_{\text{obs}}^z)} dt \left[\frac{c}{2\Gamma(t)R(t)} \frac{\Delta\phi_i(\theta_v; \psi; (t_{\text{obs}}^z; t))}{2\pi} \mathcal{D}^2(t_{\text{obs}}^z; t) 4\pi N_e(R(t)) p'_{\nu'}(t) \right]_{t = \frac{t_{\text{obs}}^z}{1+z} + \frac{r}{c} \cos \psi} . \quad (\text{C.32})$$

Appendix D

Intersection Between a Component of the Lateral Structure and the Line of Sight

In this appendix, I show the expressions of the geometrical term $\Delta\phi_i(\theta_v; \psi)$ (Eq. 5.145), which is defined as $\Delta\phi_i(\theta_v; \psi) = \int_0^{2\pi} d\phi f_i(\theta_v; \psi; \phi)$, where $f_i(\theta_v; \psi; \phi) = 1$ if the direction $(\psi; \phi)$ is contained in the component i (core jet or ring) and 0 otherwise. In the case of a cone, these expressions reduce to those derived in Woods & Loeb (1999). In our numerical model, these expressions allow to save one integration variable, ϕ , in the process of the calculation of the observed flux, and are therefore an important element speeding up computation time. I represent graphically the expression of $\Delta\phi_i(\theta_v; \psi)$ in all possible cases in Fig. D.1.

- If $0 \leq \theta_{\max,i} \leq 3\theta_{\min,i}$:

- If $0 \leq \theta_v \leq \frac{\theta_{\max,i} - \theta_{\min,i}}{2}$:

$$\Delta\phi_i(\theta_v; \psi) = 2 \begin{cases} \arccos\left(\frac{\cos\theta_v \cos\psi - \cos\theta_{\min,i}}{\sin\theta_v \sin\psi}\right) - 0 & \text{if } \theta_{\min} = \theta_{\min,i} - \theta_v \leq \psi \leq \theta_{\min,i} + \theta_v \\ \pi - 0 & \text{if } \theta_{\min,i} + \theta_v \leq \psi \leq \theta_{\max,i} - \theta_v \\ \pi - \arccos\left(\frac{\cos\theta_v \cos\psi - \cos\theta_{\max,i}}{\sin\theta_v \sin\psi}\right) & \text{if } \theta_{\max,i} - \theta_v \leq \psi \leq \theta_{\max} = \theta_{\max,i} + \theta_v \end{cases} \quad (\text{D.1})$$

- If $\frac{\theta_{\max,i} - \theta_{\min,i}}{2} \leq \theta_v \leq \theta_{\min,i}$:

$$\Delta\phi_i(\theta_v; \psi) = 2 \begin{cases} \arccos\left(\frac{\cos\theta_v \cos\psi - \cos\theta_{\min,i}}{\sin\theta_v \sin\psi}\right) - 0 & \text{if } \theta_{\min} = \theta_{\min,i} - \theta_v \leq \psi \leq \theta_{\max,i} - \theta_v \\ \arccos\left(\frac{\cos\theta_v \cos\psi - \cos\theta_{\min,i}}{\sin\theta_v \sin\psi}\right) - \arccos\left(\frac{\cos\theta_v \cos\psi - \cos\theta_{\max,i}}{\sin\theta_v \sin\psi}\right) & \text{if } \theta_{\max,i} - \theta_v \leq \psi \leq \theta_{\min,i} + \theta_v \\ \pi - \arccos\left(\frac{\cos\theta_v \cos\psi - \cos\theta_{\max,i}}{\sin\theta_v \sin\psi}\right) & \text{if } \theta_{\min,i} + \theta_v \leq \psi \leq \theta_{\max} = \theta_{\max,i} + \theta_v \end{cases} \quad (\text{D.2})$$

- If $\theta_{\min,i} \leq \theta_v \leq \frac{\theta_{\min,i} + \theta_{\max,i}}{2}$:

$$\Delta\phi_i(\theta_v; \psi) = 2 \begin{cases} \pi - 0 & \text{if } \theta_{\min} = 0 \leq \theta \leq \theta_v - \theta_{\min,i} \\ \arccos\left(\frac{\cos\theta_v \cos\psi - \cos\theta_{\min,i}}{\sin\theta_v \sin\psi}\right) - 0 & \text{if } \theta_v - \theta_{\min,i} \leq \psi \leq \theta_{\max,i} - \theta_v \\ \arccos\left(\frac{\cos\theta_v \cos\psi - \cos\theta_{\min,i}}{\sin\theta_v \sin\psi}\right) - \arccos\left(\frac{\cos\theta_v \cos\psi - \cos\theta_{\max,i}}{\sin\theta_v \sin\psi}\right) & \text{if } \theta_{\max,i} - \theta_v \leq \psi \leq \theta_v + \theta_{\min,i} \\ \pi - \arccos\left(\frac{\cos\theta_v \cos\psi - \cos\theta_{\max,i}}{\sin\theta_v \sin\psi}\right) & \text{if } \theta_v + \theta_{\min,i} \leq \psi \leq \theta_{\max} = \theta_{\max,i} + \theta_v \end{cases} \quad (\text{D.3})$$

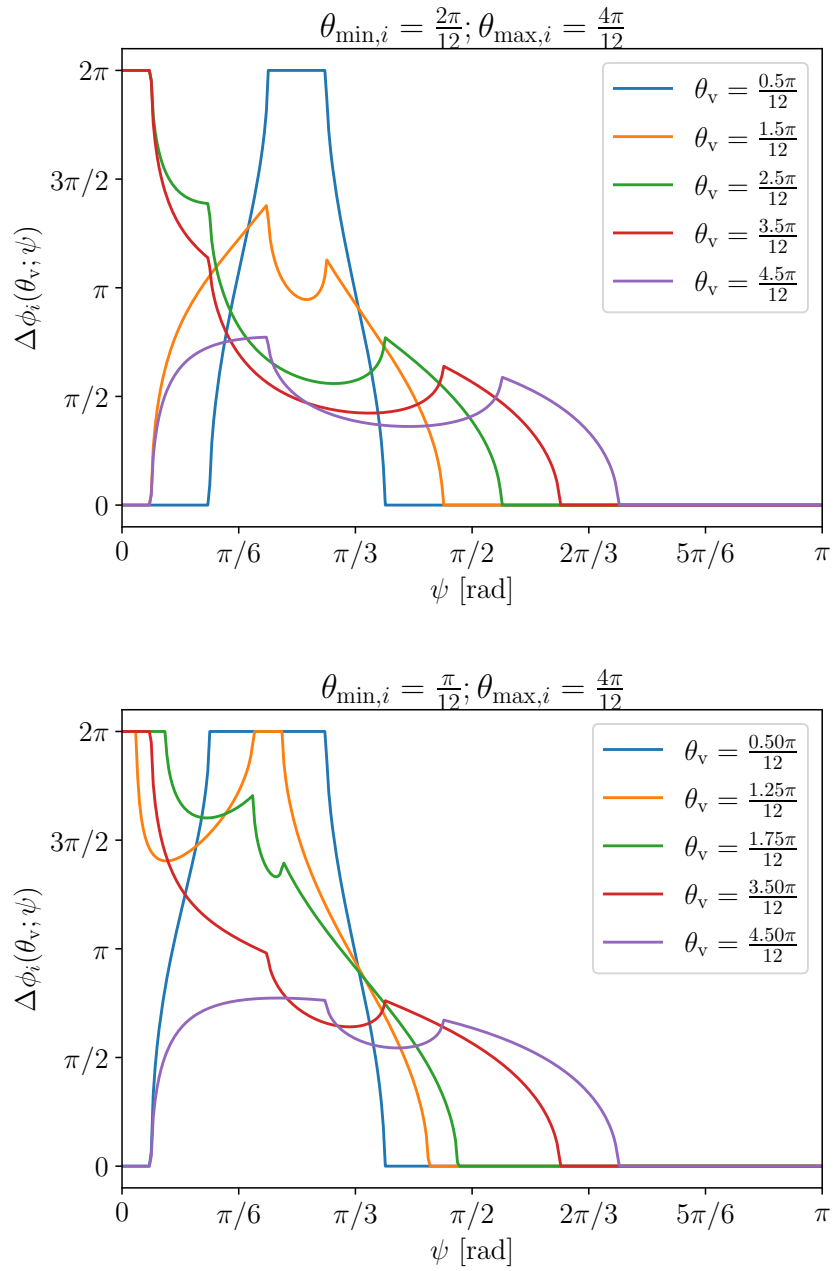


Fig. D.1: Graphical representation of $\Delta\phi_i(\theta_v; \psi)$ in all the different cases. In the top panel, $0 \leq \theta_{\max,i} \leq 3\theta_{\min,i}$, corresponding to the first 6 subcases. In the bottom panel, $0 \leq 3\theta_{\min,i} \leq \theta_{\max,i}$, corresponding to the last 6 subcases. The values of θ_v , $\theta_{\max,i}$ and $\theta_{\min,i}$ are shown on the figures.

Appendix E

Publications

The doctoral work presented in this manuscript is associated with three publications, added in this appendix.

- **Publication I**, [Pellouin & Daigne \(2023\)](#), submitted (Ap. E.1), of which I am the lead author, presents the afterglow model described in Chapter 5 and the results on the Very High Energy (VHE) emission of GW 170817 and on post-merger afterglows at VHE more generally, that are presented in Chapter 6.
- **Publication II**, [Kann et al. \(2023\)](#) (Ap. E.2) includes the analysis of the early optical and X-ray observations of GRB 221009A in the context of the follow-up campaign of this burst, discussed in Chapter 4. I am part of the group that defined the interpretation strategy, I carried the Markov Chain Monte Carlo (MCMC) exploration using my model and discussed the results together with colleagues carrying a similar exploration with `afterglowpy`. I prepared Tab. 4, Figs. 9 and 10 and contributed to write Sec. 3.4.2 and the conclusions.
- **Publication III**, [Lehoucq et al. \(2023\)](#) (Ap. E.3) discusses the stochastic Gravitational Wave (GW) background from compact objects binaries including Binary Neutron Stars (BNSs), as presented in Sec. 9.5.2. I am one of the co-authors of this article and in particular provided the simulation results used to determine the stochastic GW background from BNSs using the simulations with COSMIC discussed throughout Chapter 9.
- Finally, I am currently starting to write a fourth publication, [Pellouin et al. \(2023\)](#), to present the results on the evolutionary tracks discussed in Chapter 9.

E.1 Publication I

E.2 Publication II

E.3 Publication III

The very high energy afterglow of structured jets: GW 170817 and prospects for future detections

Clément Pellouin¹ and Frédéric Daigne¹

¹Sorbonne Université, CNRS, UMR 7095, Institut d'Astrophysique de Paris (IAP), 98 bis boulevard Arago, 75014 Paris, France; e-mails: pellouin@iap.fr; daigne@iap.fr

Received **.**.**. / Accepted **.**.**.

ABSTRACT

We present a complete numerical model of the afterglow of a laterally-structured relativistic ejecta from radio to very high energy (VHE). This includes a self-consistent calculation of the synchrotron radiation, with its maximum frequency, and of Synchrotron Self-Compton (SSC) scatterings taking into account the Klein-Nishina regime. The attenuation due to pair production is also included. This model is computationally-efficient, allowing for multi-wavelength data fitting. We use it to fit the afterglow of GW 170817 and predict its VHE emission. We find that the SSC flux at the peak was much dimmer than the upper limit from *H.E.S.S.* observations around the peak. However, we show that either a smaller viewing angle or a larger external density would make similar events detectable in the future at VHE, even above 100 Mpc with the sensitivity of the *CTA*. Large external densities are expected in the case of fast mergers, but the existence of a formation channel for such binary neutron stars is still uncertain. We highlight that VHE afterglow detections would help probing efficiently such systems.

Key words. (Stars:) Gamma-ray burst: general – (Stars:) Gamma-ray burst: individual: GW170817 – Radiation mechanisms: non-thermal – Shock waves – Stars: neutron – Stars: binaries

1. Introduction

The first detection of gravitational waves (GW) from a Binary Neutron Star (BNS) merger, GW 170817 (Abbott et al. 2017a), was followed by several electromagnetic counterparts (Abbott et al. 2017b and references therein). A short Gamma-Ray Burst (GRB), GRB 170817A, was detected ~ 1.7 s after the GW signal (Goldstein et al. 2017; Savchenko et al. 2017); a fast-decaying thermal transient in the visible/infrared range, the kilonova, was observed for ~ 10 days after the merger (see e.g. Villar et al. 2017; Tanvir et al. 2017; Cowperthwaite et al. 2017); and a non-thermal afterglow was observed from radio to X-rays for more than three years (see e.g. Balasubramanian et al. 2021; Troja et al. 2020; Hajela et al. 2019). Among the many advances made possible by this exceptional multi-messenger event, GW 170817/GRB 170817A is in particular the first direct association between a BNS merger and a short GRB and has helped to better understand the relativistic ejection associated with such events. Indeed, the study of the relativistic ejecta benefited not only from an exceptional multi-wavelength follow-up, but also from observing conditions very different from those for other short GRBs: a much smaller distance (GW 170817 was hosted in NGC 4993 at ~ 40 Mpc, Palmese et al. 2017; Cantiello et al. 2018) and a significantly off-axis observation ($32^{+10}_{-13} \pm 1.7$ deg derived from the GW signal using the accurate localization and distance of NGC 4993, Finstad et al. 2018).

The prompt short GRB is puzzling: it is extremely weak despite the short distance, but its peak energy is above 150 keV (Goldstein et al. 2017). It is very unlikely that it is produced by internal dissipation in the ultra-relativistic

core jet like in other GRBs at cosmological distance (Matsumoto et al. 2019). GRB 170817A was rather emitted in mildly-relativistic/mildly-energetic material on the line-of-sight: a promising mechanism is the shock-breakout emission when the relativistic core jet emerges from the kilonova ejecta (Bromberg et al. 2018; Gottlieb et al. 2018).

The interpretation of the afterglow is better understood. The slow rise of the light curve until its peak after $\sim 120 - 160$ days hints towards the off-axis observation of a decelerating jet surrounded by a lateral structure (see e.g. D'Avanzo et al. 2018), possibly inherited from the early interaction with the kilonova ejecta also invoked for the weak prompt emission (Gottlieb et al. 2018). The presence of a relativistic ejecta seen off-axis is confirmed by the compactness of the source and its apparent superluminal motion measured by Very Long Baseline Interferometry (VLBI) imagery (Mooley et al. 2018; Ghirlanda et al. 2019; Mooley et al. 2022). The light curve rise is dominated by the lateral structure of the relativistic ejecta, while its peak and decay are dominated by the deceleration of the ultra-relativistic core jet, which requires a kinetic energy comparable to usual values found in short GRBs (see e.g. Ghirlanda et al. 2019).

Such a lateral structure may be a common feature in GRBs due to the early propagation of the relativistic ejecta through the infalling envelope of the stellar progenitor (long GRBs) or the post-merger ejecta responsible for the kilonova emission (short GRBs) (Bromberg et al. 2011). Possible signatures of such a lateral structure in GRBs at cosmological distance viewed slightly off-axis have been recently discussed, for instance to explain the complex phenomenology observed in the early afterglow (Beniamini et al. 2020a;

Oganesyan et al. 2020; Ascenzi et al. 2020; Duque et al. 2022) or the non-standard decay of the afterglow of the extremely bright GRB 221009A (O’Connor et al. 2023; Gill & Granot 2023). Accounting for the lateral structure of the jet in afterglow models has thus become necessary not only for GW 170817 but for other cosmic GRBs as well.

Most models of The off-axis afterglow of GW 170817 only consider synchrotron emission and are therefore limited to the spectral range of observations, from radio to X-rays. However, upper limits on the flux at very high energy (VHE) were obtained by H.E.S.S. at two epochs, a few days after the merger (Abdalla et al. 2017) and around its peak (Abdalla et al. 2020). Less constraining upper limits were also obtained by *HAWC* at early times (Galván et al. 2019) and *MAGIC* around the afterglow peak (Salafia et al. 2022a). Discussing the constraints associated to these upper limits requires to include the Synchrotron Self-Compton (SSC) emission in afterglow models, i.e. the Inverse Compton (IC) scatterings of the synchrotron photons by the relativistic electrons emitting them. Indeed, recent detections of the VHE afterglow of several long GRBs¹ by *H.E.S.S.* (GRB 180720B, Abdalla et al. 2019; GRB 190829A, H. E. S. S. Collaboration et al. 2021), *MAGIC* (GRB 190114C, MAGIC Collaboration et al. 2019a,b; GRB 201216C, Blanch et al. 2020) and *LHAASO* (GRB 221009A, LHAASO Collaboration 2023) are challenging pure synchrotron afterglow models (see however H. E. S. S. Collaboration et al. 2021) and suggests the dominant contribution of a new emission process at VHE (see the discussion of possible processes at VHE by Gill & Granot 2022), most probably SSC emission, as suggested for instance by the modelling of the afterglows of GRB 190114C (MAGIC Collaboration et al. 2019b; Wang et al. 2019; Derishev & Piran 2021), GRB 190829A (Salafia et al. 2022b) or GRB 221009A (Sato et al. 2023).

While SSC emission can be efficiently computed analytically in the Thomson regime (Panaitescu & Kumar 2000; Sari & Esin 2001), several studies have pointed out the importance to also account for the Klein-Nishina (KN) attenuation at high-energy (see e.g. Nakar et al. 2009; Murase et al. 2011; Beniamini et al. 2015; Jacovich et al. 2021; Yamasaki & Piran 2022). In the KN regime, the IC power of an electron strongly depends on its Lorentz factor. This affects the cooling of the electron distribution and therefore also impacts the synchrotron spectrum (Derishev et al. 2001; Nakar et al. 2009; Bošnjak et al. 2009), which can significantly differ from the standard prediction given by Sari et al. (1998) for the pure synchrotron case.

Motivated by these recent advances in GRB afterglow studies, we propose in this paper a fully consistent model of GRB afterglow emission from a decelerating laterally-structured jet where electrons accelerated at the external forward shock radiate at all wavelengths by synchrotron emission and SSC diffusion. The treatment of SSC in the KN regime follows the approach proposed by Nakar et al. (2009), extended to account for the maximum Lorentz factor of accelerated electrons, and the attenuation at high-energy due to pair creation. The numerical implementation of the model is optimized to be computationally-efficient. This allows to use Bayesian statistics for parameter infer-

ence. We then apply this model to the multi-wavelength observations of the afterglow of GW 170817 to understand the physical constraints brought by the *H.E.S.S.* upper limits and to discuss if the detection of post-merger VHE afterglows may become possible in the future, especially in the coming era of the Cerenkov Telescope Array (CTA, see Cherenkov Telescope Array Consortium et al. 2019).

The model and its assumptions is detailed in Section 2 and then tested and compared to other afterglow models in Section 3. In Section 4 we show the results obtained when fitting GW 170817’s afterglow. We discuss the predicted VHE emission in light of the *H.E.S.S.* upper limit. We study the conditions for future post-merger detections of VHE afterglows in Section 5 and highlight that VHE emission is favored by a larger external density compared to GW 170817, which may help probing the population of fast-merging binaries, if it exists. Our conclusions are summarized in Section 6.

2. Modelling the VHE afterglow of structured jets

Our aim is to model the GRB afterglow at all wavelengths from radio bands to the TeV range. We limit ourselves to the contribution of the forward external shock propagating in the external medium and leave to a future work the extension of the model to include the reverse shock contribution at early times. Motivated by the observations of GW 170817, we rather focus here on two other aspects: the lateral structure of the jet and the detailed calculation of the inverse Compton spectral component, taking into account Klein-Nishina effects.

In this Section we describe our model: assumptions for the structure of the initial relativistic outflow (§ 2.1), dynamics of its deceleration (§ 2.2), assumptions for the acceleration of electrons and the amplification of the magnetic field at the shock front (§ 2.3), detailed calculation of the emission in the comoving frame of the shocked external medium (including synchrotron and inverse Compton components, § 2.4) and finally integration over equal-arrival time surfaces to compute the observed flux in the observer frame (light curves and spectra) (§ 2.5). Our numerical implementation of this model optimizes the computation time (typically a few seconds to compute light curves and/or spectra at different frequencies on a laptop) so that we can explore the parameter space with a Bayesian approach for data fitting, as described in Section 4. In the following, in case of ambiguity, a physical quantity q is written q without a prime in the fixed source frame, and q' with a prime in the comoving frame of the emitting material.

2.1. Relativistic outflow: geometry and structure

We consider a laterally-structured jet. The initial energy per solid angle $\epsilon_0(\theta)$ and the initial Lorentz factor $\Gamma_0(\theta)$ decrease with θ , the angle from the jet axis. We define θ_c as the opening angle of the core, i.e. the ultra-relativistic/ultra-energetic central part of the jet. We then express

$$\epsilon_0(\theta) = \epsilon_0^c \times f_a \left(\frac{\theta}{\theta_c} \right) \quad (1)$$

and

$$\Gamma_0(\theta) = 1 + (\Gamma_0^c - 1) \times g_b \left(\frac{\theta}{\theta_c} \right), \quad (2)$$

¹ Candidate VHE photons are associated at a lower level of confidence with several other bursts by *MAGIC*, including the short GRB 160821B (Acciari et al. 2021).

where ϵ_0^c is the initial energy per solid angle and Γ_0^c is the initial Lorentz factor, both on the jet axis ($\theta = 0$). f_a and g_b are the normalized profiles for the energy and Lorentz factor in the lateral structure.

Different lateral structures have been suggested in the literature, following the photometric and VLBI observations of GW 170817's GRB afterglow. In this paper, we model this afterglow assuming the power-law structure used by [Duque et al. \(2019\)](#):

$$f_a(x) = \begin{cases} 1 & \text{if } x < 1 \\ x^{-a} & \text{if } x \geq 1 \end{cases}, \quad (3)$$

$$g_b(x) = \begin{cases} 1 & \text{if } x < 1 \\ x^{-b} & \text{if } x \geq 1 \end{cases}. \quad (4)$$

This prescription allows a direct comparison with a top-hat jet ($f_a(x) = g_b(x) = 1$ for $x \leq 1$ and 0 otherwise). For comparison with other studies (see Section 3), we also considered the following possible structures:

- Power-law jet from [Gill & Granot \(2018\)](#): $f_a(x) = X^{-a}$ and $g_b(x) = X^{-b}$, with $X = \sqrt{1 + x^2}$.
- Power-law jet as defined in [afterglowpy](#), from [Ryan et al. \(2020\)](#): $f_a(x) = \left(\sqrt{1 + x^2/a}\right)^{-a}$. The model used in [afterglowpy](#) is limited to the self-similar evolution of the jet, which is independent of the initial value of the Lorentz factor. Therefore g_b is not specified in this case.
- Gaussian jet from [Gill & Granot \(2018\)](#): $f_a(x) = g_b(x) = \max\left(e^{-x^2/2}; e^{-x_{\max}^2/2}\right)$, where $x_{\max} = \theta_{\max}/\theta_c$ and θ_{\max} is defined as the angle where $\beta_{0,\min}(\theta_{\max}) = 0.01$ (by default) or any other specific value. We note that [Ryan et al. \(2020\)](#) use a similar parametrization of the lateral structure for Gaussian jets in [afterglowpy](#), with $\theta_{\max} = 90$ deg.

The initial total energy of the jet and of its core are given by

$$E_0 = 2 \int_0^{\pi/2} \epsilon_0(\theta) 2\pi \sin \theta d\theta, \quad (5)$$

$$E_0^c = 2 \int_0^{\theta_c} \epsilon_0(\theta) 2\pi \sin \theta d\theta. \quad (6)$$

The factor 2 accounts for the counter-jet. The usual isotropic-equivalent energy of the core jet equals

$$E_{0,\text{iso}}^c = \frac{E_0^c}{1 - \cos \theta_c}. \quad (7)$$

For the power-law structure considered here (Equation 3), we have $E_0^c = 4\pi\epsilon_0^c(1 - \cos \theta_c)$ and $E_{0,\text{iso}}^c = 4\pi\epsilon_0^c$.

We do not consider in this paper a possible radial structure of the outflow that may also very well be present due to the variability of the central engine. This radial structure may be at least partially smoothed out during the early propagation, *e.g.* via internal shocks ([Kobayashi et al. 1997](#); [Daigne & Mochkovitch 1998, 2000](#)) and should have more impact on the reverse shock (see *e.g.* [Uhm & Beloborodov 2007](#); [Genet et al. 2007](#)), not included in the present version of the model. Therefore $E_{0,\text{iso}}^c$, Γ_0^c , θ_c , a and b (or $\beta_{0,\min}$ for the Gaussian jet) are the only four free parameters needed

to fully describe the initial structure of the jet before the deceleration starts.

In our numerical implementation of the model, we suppress the lateral structure above the maximum angle θ_{\max} . This angle is taken as the maximum between θ_ϵ , defined as the angle up to which a fraction $(1 - \epsilon)$ of the jet energy is contained, and the viewing angle θ_v (see § 2.5). We therefore solve for θ_ϵ the equation

$$(1 - \epsilon)E_0 = 2 \int_0^{\theta_\epsilon} \epsilon_0(\theta) 2\pi \sin \theta d\theta. \quad (8)$$

We use $\epsilon = 0.01$ in the following. [Ryan et al. \(2020\)](#) introduce a similar parameter θ_W , to minimize computation time. Taking $\theta_{\max} = \max(\theta_\epsilon; \theta_v)$ allows to keep a precise calculation at early times even for very large viewing angles.

In practice, the lateral structure is discretized in $N + 1$ components, $i = 0$ being the core jet and $i = 1 \rightarrow N$ being rings at increasing angles in the lateral structure. Each component is defined by $\theta_{\min,i} \leq \theta \leq \theta_{\max,i}$ with $\theta_{\min,0} = 0$ and $\theta_{\max,0} = \theta_c$ for the core jet and $\theta_{\min,i} = \theta_{\max,i-1}$ for $i = 1 \rightarrow N$ and $\theta_{\max,N} = \theta_{\max}$. Each component is treated independently with fixed limits in latitude (no lateral spreading). The dynamics is computed such that $R_i(t) = R(\theta_i; t)$ and $\Gamma_i(t) = \Gamma(\theta_i; t)$, where $R(\theta, t)$ and $\Gamma(\theta, t)$ are given by the solution for the dynamics of the deceleration discussed below, and where $\theta_i = (\theta_{\min,i} + \theta_{\max,i})/2$ for $i \geq 1$ and $\theta_0 = 0$. We define the successive $\theta_{\min,i}$ and $\theta_{\max,i}$ such that each component carries an equal amount of energy (except for the core, $i = 0$), though a linear increase can also be chosen. Finally, we typically choose a discretization comprised of $N = 15$ components, that we find to be a good compromise between model accuracy and computational efficiency.

2.2. Dynamics of the deceleration

The structured outflow decelerates in an external medium, with an assumed density profile as a function of radius R :

$$\rho_{\text{ext}}(R) = \frac{A}{R^s}, \quad (9)$$

with $s = 0$ for a constant-density external medium as considered in the following to model the afterglow of GW 170817. In this case we write $A = n_{\text{ext}}m_p$ with n_{ext} the external medium density. We focus on the dynamics of the shocked external medium at the forward shock. It is computed assuming that (i) the dynamics of each ring of material at angle θ is independent of other angles; (ii) the lateral expansion of the outflow is negligible. These two assumptions are questionable at late times, close to the transition to the Newtonian regime ([Rhoads 1997](#)).

The Lorentz factor $\Gamma(\theta; R)$ of the shocked material at angle θ and radius R is computed in a simplified way, using energy conservation (see *e.g.* [Panaitescu & Kumar 2000](#); [Gill & Granot 2018](#)):

$$\Gamma(\theta; R) = \frac{\Gamma_0(\theta)}{2m(\theta; R)} \times \left[-1 + \sqrt{1 + 4m(\theta; R) + 4 \left(\frac{m(\theta; R)}{\Gamma_0(\theta)} \right)^2} \right], \quad (10)$$

where

$$m(\theta; R) = \frac{M_{\text{ext}}(R)}{M_{\text{ej}}(\theta)/\Gamma_0(\theta)} = \left(\frac{R}{R_{\text{dec}}(\theta)} \right)^{3-s}, \quad (11)$$

with $M_{\text{ext}}(R) = \int_0^R \rho_{\text{ext}}(R) R^2 dR$ the swept-up mass per unit solid angle and $M_{\text{ej}}(\theta) = \epsilon_0(\theta)/\Gamma_0(\theta)c^2$ the ejected mass per unit solid angle. The deceleration radius of the material at angle θ is defined by

$$R_{\text{dec}}(\theta) = \left(\frac{(3-s)\epsilon_0(\theta)}{4\Gamma_0^2(\theta)c^2} \right)^{1/(3-s)}. \quad (12)$$

For a power-law structure as defined by Equations (3–4), the deceleration radius scales as $R_{\text{dec}}(\theta) \propto \theta^{\frac{2b-a}{3-s}}$. Best fit models of the afterglow of GW 170817 usually have $2b > a$ so that the deceleration radius is larger at high latitude (see § 4.2). More generally, [Beniamini et al. \(2020b\)](#) derived the conditions for the observed afterglow light curve to have a single peak, as in the case of GW 170817. For an off-axis observation with a large viewing angle, these conditions are $\Gamma_0^c \theta_c > 1$; $2b > a/(4-s)$ (i.e. $8b > a$ for a uniform external medium); $b > -\ln \Gamma_0^c / \ln \theta_c$; and $\theta_v > \theta_c (\Gamma_0^c \theta_c)^{\frac{1}{b-1}}$.

This description allows us to characterize the early-time dynamics in the coasting phase $R \ll R_{\text{dec}}(\theta)$ where the Lorentz factor remains constant. It branches continuously to the relativistic self-similar evolution ([Blandford & McKee 1976](#)) for $R_{\text{dec}}(\theta) \ll R \ll R_N(\theta) = \Gamma_0^{\frac{2}{3-s}}(\theta)R_{\text{dec}}(\theta)$, and finally to the Sedov-Taylor phase ([Sedov 1946](#); [Taylor 1950](#)) in the non-relativistic regime for $R \gg R_N(\theta)$. For $R \gg R_{\text{dec}}(\theta)$, the self-similar evolution becomes independent of the value of the initial Lorentz factor $\Gamma_0(\theta)$.

Once the Lorentz factor $\Gamma(\theta; R)$ and the velocity $\beta(\theta; R) = \frac{\sqrt{\Gamma^2(\theta; R)-1}}{\Gamma(\theta; R)}$ are known, the corresponding time t in the source frame is given by

$$t(\theta; R) = \int_0^R \frac{dr}{\beta(\theta; r)c}. \quad (13)$$

This leads to the solution $R(\theta, t)$ and $\Gamma(\theta, t)$ used for the dynamics of each component of the structured jet.

The physical conditions in the shocked medium are easily deduced from the shock jump conditions in the strong shock regime ([Blandford & McKee 1976](#)). In the comoving frame, the mass density equals

$$\rho_*(\theta; R) = (4\Gamma(\theta; R) + 3) \rho_{\text{ext}}(R) \quad (14)$$

and the internal energy per unit mass is given by

$$\epsilon_*(\theta; R) = (\Gamma(\theta; R) - 1) c^2. \quad (15)$$

We assume here an adiabatic index of 4/3, valid as long as $\epsilon_* \gg c^2$. Finally, the timescale of the adiabatic cooling of the shocked region due to the spherical expansion is given in the comoving frame by

$$t'_{\text{dyn}}(\theta; R) = \frac{R}{\Gamma(\theta; R)\beta(\theta; R)c} = \frac{R}{c\sqrt{\Gamma^2(\theta; R)-1}}. \quad (16)$$

2.3. Accelerated electrons and amplified magnetic field

We consider a shocked region where the physical conditions in the comoving frame are given by the mass density ρ_* , internal energy per unit mass ϵ_* , and dynamical timescale t'_{dyn} (i.e. characteristic timescale of the adiabatic cooling due to the spherical expansion), and we assume that the emission is produced by non-thermal shock-accelerated electrons, that radiate in a local turbulent magnetic field amplified at the shock. In practice, we consider only the forward external shock so that in this study, ρ_* , ϵ_* and t'_{dyn} are given by equations (14–16).

We use the following standard parametrization of the microphysics at the shock: (i) a fraction ϵ_B of the internal energy is injected in the magnetic field, i.e.

$$u_B = \frac{B'^2}{8\pi} = \epsilon_B \rho_* \epsilon_*, \quad (17)$$

leading to

$$B' = \sqrt{8\pi\epsilon_B\rho_*\epsilon_*}; \quad (18)$$

(ii) a fraction ϵ_e of the internal energy is injected into non-thermal electrons, that represent a fraction ζ of all available electrons. Their number density (cm^{-3}) and energy density ($\text{erg} \cdot \text{cm}^{-3}$) in the comoving frame are therefore given respectively by

$$n_e^{\text{acc}} = \zeta \frac{\rho_*}{m_p} \quad (19)$$

and

$$u_e = \epsilon_e \rho_* \epsilon_*. \quad (20)$$

Assuming a power-law distribution at injection, with an index $-p$ and $2 < p < 3$, this leads to the following distribution of accelerated electrons (cm^{-3}):

$$n(\gamma) = (p-1) \frac{n_e^{\text{acc}}}{\gamma_m} \left(\frac{\gamma}{\gamma_m} \right)^{-p} \quad \text{for } \gamma_m \leq \gamma \leq \gamma_{\text{max}}, \quad (21)$$

where the minimum Lorentz factor at injection equals

$$\gamma_m = \frac{p-2}{p-1} \frac{\epsilon_e m_p \epsilon_*}{\zeta m_e c^2}. \quad (22)$$

As discussed later, taking into account a realistic estimate of the maximum Lorentz factor γ_{max} up to which electrons can be accelerated at the shock is important to discuss the GeV-TeV afterglow emission. This was not included in the study by [Nakar et al. \(2009\)](#) on which our calculation of the emission is based. Equations (21–22) above are obtained by assuming that the maximum Lorentz factor γ_{max} is much larger than γ_m . This is fully justified as we have typically $\gamma_{\text{max}}/\gamma_m > 10^6$ in the best fit models of GW 170817 at the peak (Section 4). The maximum electron Lorentz factor γ_{max} is evaluated by imposing that the acceleration timescale remains always shorter than the radiative and the dynamical timescales, i.e.

$$t'_{\text{acc}}(\gamma) \leq \min(t'_{\text{rad}}(\gamma); t'_{\text{dyn}}). \quad (23)$$

The acceleration timescale is written as a function of the Larmor time R'_L/c following Bohm's scaling,

$$t'_{\text{acc}}(\gamma) = K_{\text{acc}} \frac{R'_L(\gamma)}{c} = K_{\text{acc}} \frac{\gamma m_e c}{e B'}, \quad (24)$$

Reference	K_P	K_ν	$K_{P_{\max}}$
Sari et al. (1998)	1	1	1
Panaiteescu & Kumar (2000)	0.30	0.78	0.39
Sari & Esin (2001); Gill & Granot (2018)	$3.52 \frac{p-1}{3p-1}$ $\simeq 0.745$ for $p = 2.16$	$3\pi/8$ $\simeq 1.178$	$0.88 \frac{32}{3\pi} \frac{p-1}{3p-1}$ $\simeq 0.633$ for $p = 2.16$

Table 1. Values of the dimensionless parameters K_P ; K_ν and $K_{P_{\max}}$ for different afterglow models used in each reference.

where $K_{\text{acc}} \geq 1$ is a dimensionless factor. In practice, electrons at γ_{max} are usually fast cooling and the maximum electron Lorentz factor is determined by the radiative timescale, $t'_{\text{rad}}(\gamma)$. Its evaluation is non-trivial when inverse Compton scatterings are taken into account (see § 2.4). The resulting detailed calculation of γ_{max} is explained in Appendix A. In the following, we assume $K_{\text{acc}} = 1$. Our value of γ_{max} should therefore be considered as an upper limit for the true value of the maximum electron Lorentz factor.

2.4. Emissivity in the comoving frame

Our calculation of the emission from non-thermal electrons is mostly taken from Nakar et al. (2009). The population of electrons cools down by adiabatic cooling, synchrotron radiation and via Synchrotron Self-Compton (SSC) scatterings. As we are interested in the VHE afterglow emission, we include in § 2.4.7 the attenuation due to pair production, without including the emission of secondary leptons. As we focus in this paper on the afterglow of GW 170817 where the radio observations do not show any evidence for absorption, we do not include in the present version of the model the effect of synchrotron self-absorption. In this subsection, all quantities are written in the comoving frame of the considered shocked region. We therefore omit the prime to simplify the notations.

2.4.1. Synchrotron and IC radiation for a single electron

Synchrotron radiation. The synchrotron power of a single electron ($\text{erg} \cdot \text{s}^{-1}$) is given by

$$P^{\text{syn}}(\gamma) = K_1 B^2 \gamma^2, \quad (25)$$

with $K_1 = K_P \frac{\sigma_T c}{6\pi}$ and K_P a dimensionless parameter, and its synchrotron frequency equals

$$\nu_{\text{syn}}(\gamma) = K_2 B \gamma^2, \quad (26)$$

with $K_2 = K_\nu \frac{e}{2\pi m_e c}$ and K_ν a dimensionless parameter. The dimensionless parameters K_P and K_ν depend on the assumptions made on the pitch angle of electrons relative to the magnetic field lines and different values are found in afterglow models, as listed in Table 1. By default, we use the same values as Gill & Granot (2018), taken from Granot et al. (1999) where they were obtained by fitting the broken-power law approximation of the synchrotron power of a power-law distribution of electrons to the exact calculation.

The corresponding synchrotron power at frequency ν ($\text{erg} \cdot \text{s}^{-1} \cdot \text{Hz}^{-1}$) is given by

$$P_\nu^{\text{syn}}(\gamma) = P_{\text{max}} \Phi \left(\frac{\nu}{\nu_{\text{syn}}(\gamma)} \right), \quad (27)$$

with

$$P_{\text{max}} = \frac{P^{\text{syn}}(\gamma)}{\nu_{\text{syn}}(\gamma)} = \frac{K_1}{K_2} B = K_{P_{\max}} \frac{\sigma_T m_e c^2}{3e} B, \quad (28)$$

$K_{P_{\max}} = K_P/K_\nu$ and $\int_0^\infty \Phi(x) dx = 1$. In practice we adopt a simplified shape $\Phi(x) = \frac{4}{3} x^{1/3}$ for $x \leq 1$ and 0 otherwise.

Inverse Compton scatterings. The spectral number density of seed photons is n_ν^{syn} ($\text{cm}^{-3} \cdot \text{Hz}^{-1}$), assumed to result only from the synchrotron radiation of the electrons on which they also scatter (SSC). The IC power of an electron ($\text{erg} \cdot \text{s}^{-1}$) is then given by

$$P^{\text{SSC}}(\gamma) = \int_0^\infty d\nu n_\nu^{\text{syn}} \sigma_T f_{\text{KN}}(w) c \frac{4}{3} \gamma^2 g_{\text{KN}}(w) h\nu, \quad (29)$$

where $w = \gamma h\nu / m_e c^2$; and f_{KN} and g_{KN} are the KN corrections to the cross-section and to the mean energy of the scattered photon. In the Thomson regime ($w \ll 1$), the cross section is σ_T and the mean energy of scattered photons is $\frac{4}{3} \gamma^2 h\nu$ for a seed synchrotron photon of frequency ν , so that $f_{\text{KN}} = g_{\text{KN}} = 1$ for $w \ll 1$. For simplicity, we do not write explicitly in Equation (29) the dependency on the angle between the upscattered photon and the scattering electron which is discussed in Nakar et al. (2009). We assume an isotropic seed radiation field. We only account for single IC scatterings as the effects of multiple scatterings are expected to be negligible since the afterglow is produced in the optically thin regime. The Compton parameter is defined by

$$Y(\gamma) = \frac{P^{\text{SSC}}(\gamma)}{P^{\text{syn}}(\gamma)}. \quad (30)$$

This Compton parameter is constant only if all SSC scatterings occur in the Thomson regime. Here we take into account the KN regime, hence the dependence to the electron Lorentz factor. This affects not only the SSC emission but also the synchrotron component. Following Nakar et al. (2009) and keeping the same notations, we simplify the IC cross-section by assuming that scatterings are entirely suppressed in the KN regime: $f_{\text{KN}}(w) = 0$ for $w \geq 1$. Then, a synchrotron photon produced by an electron with Lorentz factor γ can only be upscattered by electrons with Lorentz factors below a certain limit $\hat{\gamma}$ to remain in the Thomson regime, i.e.

$$\hat{\gamma} = \frac{m_e c^2}{h\nu_{\text{syn}}(\gamma)} \propto \gamma^{-2}. \quad (31)$$

Note that $\hat{\gamma}$ is a decreasing function of γ : if the energy of the synchrotron photon is higher, the maximum energy of any electron on which it could be upscattered in the Thomson regime must be lower. In an equivalent way, electrons with Lorentz factor γ will only scatter photons below the energy

$$h\tilde{\nu} = m_e c^2 / \gamma. \quad (32)$$

Then it is also convenient to define $\tilde{\gamma}$ as $\nu_{\text{syn}}(\tilde{\gamma}) = \tilde{\nu}$, i.e.

$$\tilde{\gamma} = \sqrt{\gamma m_e c^2 / h \nu_{\text{syn}}(\gamma)} \propto \gamma^{-1/2}. \quad (33)$$

Electrons with a Lorentz factor γ can only scatter synchrotron photons produced by electrons with Lorentz factors below $\tilde{\gamma}$. The Lorentz factor γ_{self} is defined by

$$\gamma_{\text{self}} = \hat{\gamma}_{\text{self}} = \tilde{\gamma}_{\text{self}} = \left(\frac{m_e c^2}{h K_2 B} \right)^{1/3}. \quad (34)$$

The definition of $\tilde{\nu}$ allows to simplify the expression of the SSC power given by Equation (29):

$$P^{\text{SSC}}(\gamma) = \frac{4}{3} \sigma_{\text{TC}} \gamma^2 \int_0^{\tilde{\nu}} d\nu u_{\nu}^{\text{syn}}, \quad (35)$$

with $u_{\nu}^{\text{syn}} = n_{\nu}^{\text{syn}} \times h\nu$ the energy density of the seed synchrotron photons ($\text{erg} \cdot \text{cm}^{-3} \cdot \text{Hz}^{-1}$). Then

$$Y(\gamma) = \frac{1}{K_P} \frac{\int_0^{\tilde{\nu}} d\nu u_{\nu}^{\text{syn}}}{u_B}. \quad (36)$$

Assuming a strict suppression in the KN regime leads to a simple expression for the SSC power at frequency ν ($\text{erg} \cdot \text{s}^{-1} \cdot \text{Hz}^{-1}$) for a single electron of Lorentz factor γ :

$$P_{\nu}^{\text{SSC}}(\gamma) = \sigma_{\text{TC}} u_{\nu_{\text{seed}}=\nu/(\frac{4}{3}\gamma^2)}^{\text{syn}} \quad (37)$$

if $h\nu \leq \frac{4}{3}\gamma m_e c^2$ and 0 otherwise.

2.4.2. Radiative regime of a single electron

Following Sari et al. (1998), the first expected break in the electron distribution occurs at the critical electron Lorentz factor γ_c , defined by the condition $t_{\text{rad}}(\gamma) = t_{\text{dyn}}$, so that high-energy electrons with $\gamma \gg \gamma_c$ are radiatively efficient (fast cooling), and low-energy electrons with $\gamma \ll \gamma_c$ are mainly cooling via the adiabatic expansion and are radiatively inefficient (slow cooling). The radiative timescale is given by

$$t_{\text{rad}}(\gamma) = \frac{\gamma m_e c^2}{P_{\text{syn}}(\gamma) + P_{\text{SSC}}(\gamma)} = \frac{m_e c^2}{[1 + Y(\gamma)] K_1 B^2 \gamma}. \quad (38)$$

Then, computing self-consistently γ_c requires to solve the equation

$$\gamma_c [1 + Y(\gamma_c)] = \gamma_c^{\text{syn}} = \frac{m_e c^2}{K_1 B^2 t_{\text{dyn}}}, \quad (39)$$

where γ_c^{syn} is the value of the critical Lorentz factor obtained when only taking into account the synchrotron radiation. Our procedure to compute γ_c and $Y(\gamma_c)$ in the most general case where the SSC cooling impacts the electron distribution is discussed below in § 2.4.6.

2.4.3. Electron distribution and associated emission

Electron distribution. Following Nakar et al. (2009), we compute the time-averaged distribution of electrons $\bar{n}(\gamma)$ over the dynamical timescale t_{dyn} by keeping only the dominant term for the electron cooling: the instantaneous power of an electron is either dominated by the synchrotron and

SSC radiation ($1 + Y(\gamma)$) $P^{\text{syn}}(\gamma)$ for $\gamma > \gamma_c$ or the adiabatic cooling $\gamma m_e c^2 / t_{\text{dyn}}$ if $\gamma < \gamma_c$. This leads to

$$\bar{n}(\gamma) = \frac{n_e^{\text{acc}}}{1 + Y(\gamma)} \frac{\gamma_c^{\text{syn}}}{\gamma_m^2} \times \begin{cases} (\gamma/\gamma_m)^{-2} & \text{if } \gamma_c < \gamma < \gamma_m \\ (\gamma/\gamma_m)^{-(p+1)} & \text{if } \gamma_m < \gamma < \gamma_{\text{max}} \end{cases} \quad (40)$$

in fast cooling regime ($\gamma_m > \gamma_c$) and

$$\bar{n}(\gamma) = n_e^{\text{acc}} \frac{\gamma_c^{\text{syn}}}{\gamma_m^2} \left(\frac{\gamma_c}{\gamma_m} \right)^{-(p+1)} \times \begin{cases} (\gamma/\gamma_c)^{-p} / (1 + Y(\gamma_c)) & \text{if } \gamma_m < \gamma < \gamma_c \\ (\gamma/\gamma_c)^{-(p+1)} / (1 + Y(\gamma)) & \text{if } \gamma_c < \gamma < \gamma_{\text{max}} \end{cases} \quad (41)$$

in slow cooling regime ($\gamma_m < \gamma_c$). We define $\gamma_{m,c} = \max(\gamma_m; \gamma_c)$ and $\gamma_{c,m} = \min(\gamma_m; \gamma_c)$ so that $\gamma_{m,c} = \gamma_m$ and $\gamma_{c,m} = \gamma_c$ in fast cooling and $\gamma_{m,c} = \gamma_c$ and $\gamma_{c,m} = \gamma_m$ in slow cooling. The minimum electron Lorentz factor is therefore $\gamma_{\text{min}} = \gamma_{c,m}$. We define the corresponding synchrotron frequencies $\nu_{m,c} = \nu_{\text{syn}}(\gamma_{m,c})$ and $\nu_{c,m} = \nu_{\text{syn}}(\gamma_{c,m})$. We also always keep only the dominant term in the radiated power, i.e. $1 + Y(\gamma) \simeq 1$ if $Y(\gamma) < 1$ and $Y(\gamma)$ otherwise. As described in details in Nakar et al. (2009), the resulting distribution shows several breaks in addition to γ_m and γ_c : a break is expected at γ_0 such that $Y(\gamma_0) = 1$ and several additional breaks are possible and must be identified in an iterative way, as described in § 2.4.6.

Following Sari et al. (1998) and Nakar et al. (2009), we approximate $\bar{n}(\gamma)$ and the associated synchrotron spectrum by broken power-laws to allow for a semi-analytical calculation. Electrons Lorentz factors are normalized by $\gamma_{m,c}$, i.e. $x = \gamma/\gamma_{m,c}$, and photon frequencies by $\nu_{m,c}$, i.e. $y = \nu/\nu_{m,c}$. Hence the normalized synchrotron frequency of an electron with normalized Lorentz factor x is $y = x^2$. In the following the notations introduced for characteristic electron Lorentz factors or photon frequencies are implicitly conserved for the normalized quantities. For instance $x_{\text{self}} = \gamma_{\text{self}}/\gamma_{m,c}$, $\hat{x} = \tilde{\gamma}/\gamma_{m,c} = x_{\text{self}}^3/x^2$, $\tilde{\nu} = \tilde{\nu}/\nu_{m,c} = \hat{x}^2$, etc.

Normalized electron distribution. The electron distribution is given by

$$\bar{n}(\gamma) = \frac{1}{I_0} \frac{n_e^{\text{acc}}}{\gamma_{m,c}} f(x), \quad (42)$$

where $f(x)$ is the normalized broken power-law electron distribution with N breaks and power-law segments:

$$f(x) = \begin{cases} x^{-p_1} & \text{if } x_1 \leq x \leq x_2 \\ x_2^{p_2-p_1} x^{-p_2} & \text{if } x_2 \leq x \leq x_3 \\ x_2^{p_2-p_1} x_3^{p_3-p_2} x^{-p_3} & \text{if } x_2 \leq x \leq x_3 \\ \vdots & \vdots \\ x_2^{p_2-p_1} x_3^{p_3-p_2} \dots x_N^{p_N-p_{N-1}} x^{-p_N} & \text{if } x_N \leq x \leq x_{N+1} \end{cases} \quad (43)$$

with $x_1 = \gamma_{\text{min}}/\gamma_{m,c}$ and $x_{N+1} = \gamma_{\text{max}}/\gamma_{m,c}$. The dimensionless integral I_0 is given by

$$I_0 = \int_{x_1}^{x_{N+1}} f(x) dx, \quad (44)$$

to conserve the number of electrons: $\int_{\gamma_{\text{min}}}^{\gamma_{\text{max}}} \bar{n}(\gamma) d\gamma = n_e^{\text{acc}}$.

Normalized synchrotron spectrum. The synchrotron power per electron and per unit frequency p_ν^{syn} ($\text{erg} \cdot \text{s}^{-1} \cdot \text{Hz}^{-1} \cdot \text{electron}^{-1}$) averaged over the time scale t_{dyn} is deduced from Equation (27) using the simplified shape for Φ . This leads to a broken power-law synchrotron spectrum:

$$p_\nu^{\text{syn}} = \frac{1}{n_e^{\text{acc}}} \int_{\gamma_{\text{min}}}^{\gamma_{\text{max}}} d\gamma \bar{n}(\gamma) P_\nu^{\text{syn}}(\gamma) \quad (45)$$

$$= \frac{\gamma_{\text{m,c}}^2 m_e c^2}{\gamma_c^{\text{syn}} \nu_{\text{m,c}} t_{\text{dyn}}} \times \frac{4}{3} y^{1/3} \int_{\max(x_1; y^{1/2})}^{x_{N+1}} dx \frac{f(x)}{x^{2/3}} \\ \simeq \frac{1}{I_0} \frac{I_2}{J_0} \frac{\gamma_{\text{m,c}}^2 m_e c^2}{\gamma_c^{\text{syn}} \nu_{\text{m,c}} t_{\text{dyn}}} \times g(y), \quad (46)$$

where the normalized broken power-law spectral shape is obtained by keeping the dominant term in the integral of $f(x)/x^{2/3}$, i.e.

$$g(y) = \begin{cases} x_1^{\frac{3}{2}-p_1} y^{\frac{1}{3}} & \text{if } y < x_1^2 \\ y^{-\frac{p_1-1}{2}} & \text{if } x_1^2 < y < x_2^2 \\ x_2^{p_2-p_1} y^{-\frac{p_2-1}{2}} & \text{if } x_2^2 < y < x_3^2 \\ x_2^{p_2-p_1} x_3^{p_3-p_2} y^{-\frac{p_3-1}{2}} & \text{if } x_3^2 < y < x_4^2 \\ \vdots & \vdots \\ x_2^{p_2-p_1} x_3^{p_3-p_2} \dots x_N^{p_N-p_{N-1}} y^{-\frac{p_N-1}{2}} & \text{if } x_N^2 < y < x_{N+1}^2 \end{cases} \quad (47)$$

The dimensionless factors I_2 and J_0 are defined by

$$I_2 = \int_{x_1}^{x_{N+1}} dx x^2 f(x) \quad (48)$$

$$J_0 = \int_0^{x_{N+1}^2} dy g(y), \quad (49)$$

to ensure that the total synchrotron power per electron ($\text{erg} \cdot \text{s}^{-1} \cdot \text{electron}^{-1}$) is conserved:

$$p^{\text{syn}} = \int_0^\infty d\nu p_\nu^{\text{syn}} = \frac{I_2 \gamma_{\text{m,c}}^2 m_e c^2}{I_0 \gamma_c^{\text{syn}} t_{\text{dyn}}} \\ = \frac{1}{n_e^{\text{acc}}} \int_{\gamma_{\text{min}}}^{\gamma_{\text{max}}} d\gamma \bar{n}(\gamma) P^{\text{syn}}(\gamma). \quad (50)$$

Finally we define ν_p as the peak frequency of the synchrotron spectrum, i.e. the frequency ν where $\nu^2 p_\nu^{\text{syn}}$ is maximum. This peak frequency corresponds to synchrotron photons emitted by electrons at Lorentz factor γ_p , i.e. $\nu_p = \nu_{\text{syn}}(\gamma_p)$. We note i_p the corresponding index of the break in the normalized distributions: $x_p = x_{i_p}$ and $y_p = y_{i_p} = x_p^2$.

Normalized SSC spectrum. The SSC power per electron and per unit frequency p_ν^{SSC} ($\text{erg} \cdot \text{s}^{-1} \cdot \text{Hz}^{-1} \cdot \text{electron}^{-1}$) emitted over the timescale t_{dyn} is deduced from Equation (37) with

$$u_\nu^{\text{syn}} = n_e^{\text{acc}} p_\nu^{\text{syn}} t_{\text{dyn}}. \quad (51)$$

This leads to

$$p_\nu^{\text{SSC}} = \frac{1}{n_e^{\text{acc}}} \int_{\gamma_{\text{min}}}^{\gamma_{\text{max}}} d\gamma \bar{n}(\gamma) P_\nu^{\text{SSC}}(\gamma) \quad (52)$$

$$\simeq \frac{1}{I_0} \frac{I_2}{J_0} \frac{\tau_T}{I_0} \frac{\gamma_{\text{m,c}}^2 m_e c^2}{\gamma_c^{\text{syn}} \nu_{\text{m,c}} t_{\text{dyn}}} \times G(y), \quad (53)$$

where $\tau_T = n_e^{\text{acc}} \sigma_T c t_{\text{dyn}}$ is the Thomson optical depth and where the normalized spectral shape is given by

$$G(y) = \int_{\max\left(x_1; \frac{3}{4} \frac{h\nu_{\text{m,c}}}{\gamma_{\text{m,c}} m_e c^2} y\right)}^{x_{N+1}} dx f(x) g\left(y_{\text{seed}} = \frac{3}{4} \frac{y}{\gamma_{\text{m,c}}^2 x^2}\right). \quad (54)$$

The cutoff at $x_{\text{KN}} = \gamma_{\text{KN}}/\gamma_{\text{m,c}}$ with $\gamma_{\text{KN}} = \frac{3}{4} \frac{h\nu}{m_e c^2}$ is a direct consequence of the strict suppression assumed in the KN regime: the VHE flux due to the scatterings occurring in the KN regime are neglected. Yamasaki & Piran (2022) introduce a factor f_{KN} in their calculations to compensate this approximation, which we do not include here. The KN regime affects the high energy part of the emitted spectrum: above a photon energy $h\nu = \frac{4}{3} \gamma_{\text{min}} m_e c^2$, we have $\gamma_{\text{KN}} > \gamma_{\text{min}}$ and the SSC emission is reduced. The SSC emission is even entirely suppressed ($G(y) = 0$) at very high photon energy $h\nu > \frac{4}{3} \gamma_{\text{max}} m_e c^2$ corresponding to $\gamma_{\text{KN}} > \gamma_{\text{max}}$.

In practice, $G(y)$ is computed exactly in our numerical implementation. Note also that $J_0 \simeq 2I_2$ when only the leading term is kept in the integrals. However all dimensionless factors I_0 , I_2 and J_0 are also computed exactly in our numerical implementation, which ensures the continuity of the electron distribution and emitted spectrum at the transition from the fast to the slow cooling regime, as well as between the different possible cases in both regimes (see § 2.4.6).

2.4.4. The pure synchrotron case

The standard pure synchrotron case where the SSC emission is neglected ($Y(\gamma) = 0$ for all electrons) is fully described in Sari et al. (1998). We have $\gamma_c = \gamma_c^{\text{syn}}$ in this case. In the fast cooling regime ($\gamma_m > \gamma_c$), the normalized distributions are given by

$$f(x) = \begin{cases} x^{-2} & \text{if } x_1 < x < x_2 \\ x_2^{p-1} x^{-(p+1)} & \text{if } x_2 < x < x_3 \end{cases}, \quad (55)$$

$$g(y) = \begin{cases} x_1^{-5/3} y^{1/3} & \text{if } y < x_1^2 \\ y^{-1/2} & \text{if } x_1^2 < y < x_2^2 \\ x_2^{p-1} y^{-p/2} & \text{if } x_2^2 < y < x_3^2 \end{cases}, \quad (56)$$

with $x_1 = \gamma_c/\gamma_m$, $x_2 = 1$ and $x_3 = \gamma_{\text{max}}/\gamma_m$. In the slow cooling regime ($\gamma_m < \gamma_c$), they are given by

$$f(x) = \begin{cases} x^{-p} & \text{if } x_1 < x < x_2 \\ x_2 x^{-(p+1)} & \text{if } x_2 < x < x_3 \end{cases}, \quad (57)$$

$$g(y) = \begin{cases} x_1^{1/3-p} y^{1/3} & \text{if } y < x_1^2 \\ y^{-(p-1)/2} & \text{if } x_1^2 < y < x_2^2 \\ x_2 y^{-p/2} & \text{if } x_2^2 < y < x_3^2 \end{cases}, \quad (58)$$

with $x_1 = \gamma_m/\gamma_c$, $x_2 = 1$ and $x_3 = \gamma_{\text{max}}/\gamma_c$. Calculations using this prescription are labeled as "no SSC" in the following.

2.4.5. The SSC case in Thomson regime

If the KN regime is neglected, all IC scatterings occur in Thomson regime and the Compton parameter is the same for all electrons: $Y(\gamma) = Y^{\text{no KN}} = \text{cst}$. The corresponding solution is given by Sari & Esin (2001): the normalized distributions $f(x)$ and $g(y)$ are the same as in the

pure synchrotron case above, but the value of the critical Lorentz factor γ_c is decreased due to the IC cooling, $\gamma_c = \gamma_c^{\text{syn}} / (1 + Y^{\text{noKN}})$. Using Equations (36), (46) and (51), we get

$$Y^{\text{noKN}} (1 + Y^{\text{noKN}}) = \frac{1}{K_P} \frac{p-2}{p-1} \frac{\epsilon_e}{\epsilon_B} \frac{\gamma_{m,c}}{\gamma_{c,m}} \frac{I_2}{I_0}. \quad (59)$$

As I_2/I_0 is a function of $\gamma_c/\gamma_m = \gamma_c^{\text{syn}}/\gamma_m/(1 + Y^{\text{noKN}})$, this is an implicit equation to be solved numerically to obtain Y^{noKN} and γ_c . The limits for $(1 + Y^{\text{noKN}}) Y^{\text{noKN}}$ are $\frac{1}{K_P} \frac{\epsilon_e}{\epsilon_B}$ for $\gamma_m \gg \gamma_c$ and $\frac{1}{K_P} \frac{\epsilon_e}{\epsilon_B} \frac{1}{3-p} \left(\frac{\gamma_m}{\gamma_c^{\text{syn}}} \right)^{p-2}$ for $\gamma_m \ll \gamma_c$. Calculations using this prescription are labeled as "SSC (Thomson)" in the following.

2.4.6. Self-consistent calculation of the electron distribution and the Compton parameter in the general case

Normalized Compton parameter. In the general case where the KN suppression at high energy is included, the Compton parameter $Y(\gamma)$ is a decreasing function of the electron Lorentz factor. From Equations (36), (46) and (51), we get

$$Y(\gamma) (1 + Y(\gamma_c)) = \frac{1}{K_P} \frac{p-2}{p-1} \frac{\epsilon_e}{\epsilon_B} \frac{\gamma_{m,c}}{\gamma_{c,m}} \frac{I_2}{I_0} \frac{1}{J_0} \int_0^{\tilde{y}} dy g(y). \quad (60)$$

Note that for low Lorentz factors γ , \tilde{y} becomes very large so that, for $\tilde{y} > \nu_{\text{syn}}(\gamma_{\text{max}})$, we recover the Thomson regime, where the right-hand side of Equation (60) is formally the same as in Equation (59), even if the integrals I_0 and I_2 can be different if the normalized electron distribution $f(x)$ is different. As described in Nakar et al. (2009), when keeping only the leading term in the integral of $g(y)$, the corresponding scaling law for the Compton parameter is $Y(\gamma) = \text{cst}$ if \tilde{y} is above the peak frequency ν_p and $Y(\gamma) \propto \gamma^{-\frac{3-\tilde{p}}{2}}$ otherwise, where \tilde{p} is the slope of electron distribution in the power-law segment of the electron distribution including $\tilde{\gamma}$. This leads us to introduce a normalized Compton parameter defined by

$$Y(\gamma) (1 + Y(\gamma_c)) = \frac{1}{K_P} \frac{p-2}{p-1} \frac{\epsilon_e}{\epsilon_B} \frac{\gamma_{m,c}}{\gamma_{c,m}} \frac{I_2}{I_0} h(x), \quad (61)$$

where $h(x)$ follows this scaling and is normalized so that Equation (61) has the exact limit in the Thomson regime. This leads to

$$h(x) = \begin{cases} 1 & \text{if } x < \hat{x}_p \\ \frac{\hat{x}_p^{\frac{3-p_{i_p}-1}{2}} x^{-\frac{3-p_{i_p}-1}{2}}}{\hat{x}_p^{\frac{3-p_{i_p}-1}{2}}} & \text{if } \hat{x}_p < x < \hat{x}_{i_p-1} \\ \frac{\hat{x}_p^{\frac{3-p_{i_p}-1}{2}} \hat{x}_{i_p-1}^{\frac{p_{i_p}-1-p_{i_p}-2}{2}} x^{-\frac{3-p_{i_p}-2}{2}}}{\hat{x}_p^{\frac{3-p_{i_p}-1}{2}} \hat{x}_{i_p-1}^{\frac{p_{i_p}-1-p_{i_p}-2}{2}}} & \text{if } \hat{x}_{i_p-1} < x < \hat{x}_{i_p-2} \\ \vdots & \vdots \\ \frac{\hat{x}_p^{\frac{3-p_{i_p}-1}{2}} \hat{x}_{i_p-1}^{\frac{p_{i_p}-1-p_{i_p}-2}{2}} \dots}{\hat{x}_p^{\frac{3-p_{i_p}-1}{2}} \hat{x}_{i_p-1}^{\frac{p_{i_p}-1-p_{i_p}-2}{2}}} & \dots \\ \dots \frac{\hat{x}_2^{\frac{p_2-p_1}{2}} x^{-\frac{3-p_1}{2}}}{\dots \hat{x}_2^{\frac{p_2-p_1}{2}}} & \text{if } \hat{x}_2 < x < \hat{x}_1 \\ \frac{\hat{x}_p^{\frac{3-p_{i_p}-1}{2}} \hat{x}_{i_p-1}^{\frac{p_{i_p}-1-p_{i_p}-2}{2}} \dots}{\hat{x}_p^{\frac{3-p_{i_p}-1}{2}} \hat{x}_{i_p-1}^{\frac{p_{i_p}-1-p_{i_p}-2}{2}}} & \dots \\ \dots \frac{\hat{x}_2^{\frac{p_2-p_1}{2}} \hat{x}_1^{\frac{p_1}{2}} x^{-4/3}}{\dots \hat{x}_2^{\frac{p_2-p_1}{2}} \hat{x}_1^{\frac{p_1}{2}}} & \text{if } x > \hat{x}_1 \end{cases} \quad (62)$$

We recall that i_p is the index of the break corresponding to the peak frequency of the synchrotron spectrum. In most cases (see Appendix B) we have $i_p = 2$, leading to

$$h(x) = \begin{cases} 1 & \text{if } x < \hat{x}_2 \\ \frac{\hat{x}_2^{\frac{3-p_1}{2}} x^{-\frac{3-p_1}{2}}}{\hat{x}_2^{\frac{3-p_1}{2}}} & \text{if } \hat{x}_2 < x < \hat{x}_1 \\ \frac{\hat{x}_2^{\frac{3-p_2}{2}} \hat{x}_1^{\frac{p_1}{2}} x^{-4/3}}{\hat{x}_2^{\frac{3-p_2}{2}} \hat{x}_1^{\frac{p_1}{2}}} & \text{if } x > \hat{x}_1 \end{cases} \quad (63)$$

Self-consistent solution for the normalized electron distribution. Following Nakar et al. (2009), we define² γ_0 by $Y(\gamma_0) = 1$ and assume $1 + Y(\gamma) = Y(\gamma)$ for $\gamma < \gamma_0$ and 1 otherwise. From Equations (40) and (41), this shows that the IC cooling will only affect the electron distribution in the interval

$$\max(\gamma_c; \hat{\gamma}_p) < \gamma < \gamma_0. \quad (64)$$

Therefore the solution is entirely determined by the orderings of γ_m , γ_c , γ_0 , $\hat{\gamma}_m$ and $\hat{\gamma}_c$. All possible cases and the corresponding solutions are listed in Appendix B. In some cases, subcases are introduced as breaks can appear at $\hat{\gamma}_0$, $\hat{\gamma}_m$, $\hat{\gamma}_c$, etc. All the most relevant cases for GRB afterglows are already described in Nakar et al. (2009) along with the detailed method to obtain the corresponding solution for the electron distribution. For completeness, we list in Appendix B the additional cases allowing to fully describe the parameter space, even in regions unlikely to be explored in GRBs.

Calculation of the critical Lorentz factor γ_c . From Equation (61), we get the following equation for $Y(\gamma_c)$:

$$Y(\gamma_c) = \begin{cases} A \frac{\gamma_m}{\gamma_c^{\text{syn}}} \frac{I_2}{I_0} h(x_c) & \text{if } \gamma_m > \gamma_c \\ A \frac{\gamma_c}{\gamma_m} \frac{I_2}{I_0} h(x_c) & \text{if } \gamma_m < \gamma_c \text{ and } Y(\gamma_c) < 1 \\ \left(A \frac{\gamma_c^{\text{syn}}}{\gamma_m} \frac{I_2}{I_0} h(x_c) \right)^{1/3} & \text{if } \gamma_m < \gamma_c \text{ and } Y(\gamma_c) > 1 \end{cases} \quad (65)$$

where $A = \frac{1}{K_P} \frac{p-2}{p-1} \frac{\epsilon_e}{\epsilon_B}$ is a constant as the microphysics parameter ϵ_B , ϵ_e and p are assumed to be constant during the forward shock propagation. Note that $x_c = 1$ in the slow cooling regime $\gamma_m < \gamma_c$. A second useful relation is obtained from Equation (61) and the definition of γ_0 :

$$Y(\gamma_c) = \frac{Y(\gamma_c)}{Y(\gamma_0)} = \frac{h(x_c)}{h(x_0)}. \quad (66)$$

This leads to an iterative procedure to compute $Y(\gamma_c)$, and deduce γ_c

$$\gamma_c = \begin{cases} \gamma_c^{\text{syn}} & \text{if } Y(\gamma_c) < 1 \\ \gamma_c^{\text{syn}}/Y(\gamma_c) & \text{if } Y(\gamma_c) > 1 \end{cases} \quad (67)$$

We start by assuming $Y(\gamma_c) = Y^{\text{noKN}}$ as defined in § 2.4.5 and then iterate as follows:

1. Compute γ_c from Equation (67).

² As $Y(\gamma)$ is a decreasing function with a constant first segment, if $Y(\gamma) < 1$ for $\gamma < \max(\gamma_c; \hat{\gamma}_p)$, then $Y(\gamma) < 1$ for all values of γ and γ_0 is therefore undefined. In these cases, we retrieve the "no SSC" solution.

2. Knowing γ_m , γ_c , γ_{self} , scan the different possible cases for the ordering of γ_m , γ_c , γ_0 , $\hat{\gamma}_m$ and $\hat{\gamma}_c$ (and additional characteristic Lorentz factors for some cases) as listed in Appendix B and compute γ_0 from Equation (66), which can be analytically inverted as provided for each case in Appendix B. We stop the scan of the possible cases when the ordering of all characteristic Lorentz factors including the obtained value of γ_0 is the correct one.
3. Having identified the correct case and therefore knowing the expression of $f(x)$, compute the integrals I_0 and I_2 .
4. Compute an updated value of $Y(\gamma_c)$ from Equation (65).
5. Start a new iteration at step 1 until convergence.

We stop the procedure when the relative variation of γ_c in an iteration falls below ϵ_{tol} . We use $\epsilon_{\text{tol}} = 10^{-4}$, which is reached in most cases in less than 20 iterations. In the context of a full afterglow light curve calculation, as we expect Y to vary smoothly during the jet propagation, we use the value of $Y(\gamma_c)$ obtained at the previous step of the dynamics instead of Y^{noKN} to start the iterative procedure. Then we usually reach a convergence in only a few iterations.

Final calculation of the emission in the comoving frame. The procedure described in the previous paragraph allows not only to compute γ_c but also to identify the relevant case for the distribution of electrons and the Compton parameter (as listed in Appendix B). Therefore the functions $f(x)$, $g(x)$ and $h(x)$ are known, and the function $G(x)$ can be computed. Using Equations (46) and (53), this finally allows to compute at any frequency p_{ν}^{syn} and p_{ν}^{SSC} , the synchrotron and SSC powers per electron and per unit frequency averaged over the timescale t_{dyn} .

2.4.7. Pair production

At VHE, pair production $\gamma\gamma \rightarrow e^+e^-$ can start to contribute to the SSC flux depletion. We account for this mechanism by a simplified treatment, assuming an isotropic distribution of the low-energy seed photons, as for the SSC calculation, and approximating the cross section for pair production by a Dirac function at twice the threshold of the interaction. Then, VHE photons of frequency ν can produce pairs by interacting with low-energy photons at frequency $\nu_{\text{seed}} = 2(m_e c^2)^2 / (h^2 \nu)$ and the characteristic timescale of this interaction is given by

$$t_{\gamma\gamma}(\nu) = \frac{h}{\sigma_{\text{T}} c} \left[u_{\nu_{\text{seed}}=2\frac{(m_e c^2)^2}{h^2 \nu}} \right]^{-1}, \quad (68)$$

with $u_{\nu} = u_{\nu}^{\text{syn}} + u_{\nu}^{\text{SSC}} = n_e^{\text{acc}} (p_{\nu}^{\text{syn}} + p_{\nu}^{\text{SSC}}) t_{\text{dyn}}$, leading to

$$t_{\gamma\gamma}(\nu) = \frac{h}{\tau_{\text{T}}} \left[(p_{\nu_{\text{seed}}}^{\text{syn}} + p_{\nu_{\text{seed}}}^{\text{SSC}})_{\nu_{\text{seed}}=2\frac{(m_e c^2)^2}{h^2 \nu}} \right]^{-1}. \quad (69)$$

For very high frequencies ν , the seed photons for pair production have a low frequency and $p_{\nu_{\text{seed}}}^{\text{syn}} + p_{\nu_{\text{seed}}}^{\text{SSC}} \simeq p_{\nu_{\text{seed}}}^{\text{syn}}$. The total emitted power per electron $p_{\nu} = p_{\nu}^{\text{syn}} + p_{\nu}^{\text{SSC}}$ is then corrected by a factor $\frac{t_{\gamma\gamma}(\nu)}{t_{\text{dyn}}} (1 - e^{-t_{\text{dyn}}/t_{\gamma\gamma}(\nu)})$, which in practice only attenuates the SSC component at high frequency where $t_{\gamma\gamma}(\nu) \ll t_{\text{dyn}}$.

The implementation of the model allows to select the level of approximation for the SSC emission (synchrotron only, Thomson or full calculation) and to include or not the attenuation due to the pair production.

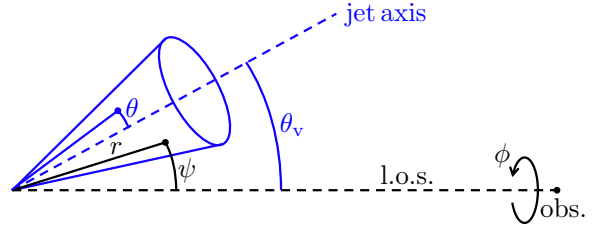


Fig. 1. Coordinates and notations used in the expression of the observed flux.

2.5. Observed flux

Once the emissivity in the comoving frame is known (§ 2.4), the flux measured by a distant observer with a viewing angle θ_v is computed by an integration over equal-arrival time surfaces, taking into account relativistic Doppler boosting and relativistic beaming, as well as the effect of cosmological redshift. This leads to the following expression of the observer frame flux density ($\text{erg} \cdot \text{s}^{-1} \cdot \text{cm}^{-2} \cdot \text{Hz}^{-1}$) measured at time t_{obs}^z and frequency ν_{obs}^z (Woods & Loeb 1999):

$$F_{\nu_{\text{obs}}^z}(t_{\text{obs}}^z) = \frac{1+z}{4\pi D_L^2} \int_0^\infty dr \int_0^\pi d\psi \int_0^{2\pi} d\phi r^2 \sin\psi \quad (70)$$

$$\times [\mathcal{D}^2(r, \psi, t) 4\pi j'_{\nu'}(r, \psi, \phi, t)]_{t=\frac{t_{\text{obs}}^z}{1+z} + \frac{r}{c} \cos\psi},$$

where we use spherical coordinates $(r; \psi; \phi)$ with the polar axis equal to the line-of-sight, ψ and ϕ the colatitude and longitude, and the jet axis in the direction $(\psi = \theta_v, \phi = 0)$ (see Figure 1), and where z and D_L are the redshift and the luminosity distance of the source. Note that the angle ψ differs from θ used in § 2.2 which is measured from the jet axis. The time t (source frame) and frequency ν' (comoving frame) are given by

$$t = \frac{t_{\text{obs}}^z}{1+z} + \frac{r}{c} \cos\psi \quad (71)$$

$$\nu' = (1+z) \frac{\nu_{\text{obs}}^z}{\mathcal{D}(r, \psi, t)}. \quad (72)$$

The Doppler factor is expressed as

$$\mathcal{D}(r, \psi, t) = \frac{1}{\Gamma(r, \psi, t) (1 - \beta(r, \psi, t) \cos\psi)} \quad (73)$$

and $j'_{\nu'}$ is the emissivity ($\text{erg} \cdot \text{cm}^{-3} \cdot \text{s}^{-1} \cdot \text{Hz}^{-1} \cdot \text{sr}^{-1}$) in the comoving frame.

In practice, following the discretization of the jet structure described in § 2.1, the observer frame flux density $F_{\nu_{\text{obs}}^z}(t_{\text{obs}}^z)$ is computed as $F_{\nu_{\text{obs}}^z}(t_{\text{obs}}^z) = \sum_{i=0}^N F_{\nu_{\text{obs}}^z}^{(i)}(t_{\text{obs}}^z)$, where $F_{\nu_{\text{obs}}^z}^{(i)}(t_{\text{obs}}^z)$ are the contributions of the core jet ($i = 0$) and lateral rings ($i = 1 \rightarrow N$). To compute each contribution, the thin shell approximation allows to reduce the double integral over r and ψ in Equation (70) to a simple integral over r , or equivalently over ψ or t . In addition, to improve the computation time, the remaining integral on ϕ is computed analytically. This leads to

$$F_{\nu_{\text{obs}}^z}^{(i)}(t_{\text{obs}}^z) = \frac{1+z}{4\pi D_L^2} \int_{t_{\text{min}}^{(i)}(t_{\text{obs}}^z)}^{t_{\text{max}}^{(i)}(t_{\text{obs}}^z)} c dt \frac{\Delta\phi_i(\theta_v; \psi_i(t_{\text{obs}}^z; t))}{2\Gamma_i(t) R_i(t)} \frac{1}{2\pi} \quad (74)$$

$$\times \mathcal{D}_i^2(t_{\text{obs}}^z; t) [4\pi N_e(R_i(t))] p_{\nu'}^{(i)}(t),$$

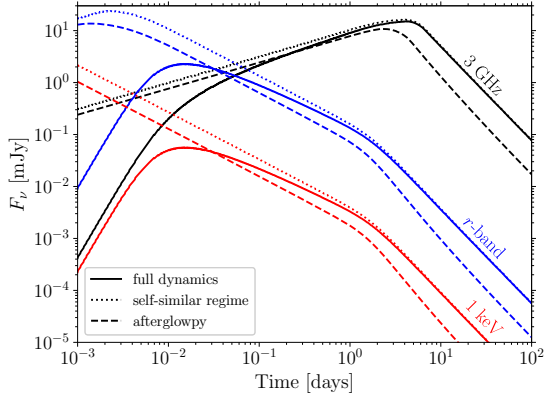


Fig. 2. Synthetic afterglow light curves of a top-hat jet viewed on-axis, in the synchrotron-only radiation regime. Solid lines show the results obtained using our model with full dynamics treatment (using Equation 10), while dotted lines follow the self-similar solution at all times. Dashed lines are obtained with **afterglowpy** without lateral expansion. The fluxes are computed in radio at 3 GHz (black), in optical in r -band at 5.06×10^{14} Hz (blue) and in X-rays at 1 keV (red). The parameters used for this figure are $E_{0,\text{iso}} = 10^{52}$ erg, $\theta_c = 4$ deg, $n_{\text{ext}} = 10^{-3} \text{ cm}^{-3}$, $\epsilon_e = 10^{-1}$, $\epsilon_B = 10^{-1}$, $p = 2.2$, $D_L = 100$ Mpc.

where

$$\cos(\psi_i(t_{\text{obs}}^z; t)) = c \frac{t - \frac{t_{\text{obs}}^z}{1+z}}{R_i(t)}, \quad (75)$$

$$D_i(t_{\text{obs}}^z; t) = \frac{1}{\Gamma_i(t) (1 - \beta_i(t) \cos \psi_i(t_{\text{obs}}^z; t))}, \quad (76)$$

$N_e(r) = \zeta M_{\text{ext}}(r)/m_p$ is the number of shock-accelerated electrons per unit solid angle, and $p_{\nu'}^{(i)}(t)$ is the power per unit frequency and per electron in the comoving frame computed in § 2.4 and evaluated at time t and comoving frequency $\nu' = (1+z)\nu_{\text{obs}}^z/D_i(t_{\text{obs}}^z; t)$.

The limits of the integral $t_{\text{min}}^{(i)}(t_{\text{obs}}^z)$ and $t_{\text{max}}^{(i)}(t_{\text{obs}}^z)$ are defined by the condition $\psi_{\text{min},i} \leq \psi_i(t_{\text{obs}}^z; t) \leq \psi_{\text{max},i}$, where

$$\psi_{\text{min},i} = \begin{cases} \theta_{\text{min},i} - \theta_v & \text{if } \theta_v \leq \theta_{\text{min},i} \\ 0 & \text{if } \theta_{\text{min},i} \leq \theta_v \leq \theta_{\text{max},i} \\ \theta_v - \theta_{\text{max},i} & \text{if } \theta_{\text{max},i} \leq \theta_v \leq \pi/2 \end{cases}, \quad (77)$$

and $\psi_{\text{max},i} = \theta_v + \theta_{\text{max},i}$, i.e.

$$t - \frac{R_i(t)}{c} \cos(\psi_{\text{max},i}) \leq \frac{t_{\text{obs}}^z}{1+z} \leq t - \frac{R_i(t)}{c} \cos(\psi_{\text{min},i}). \quad (78)$$

Finally, we use the exact analytical calculation of the geometrical term $\Delta\phi_i$ defined by $\Delta\phi_i(\theta_v; \psi) = \int_0^{2\pi} d\phi f_i(\theta_v; \psi; \phi)$, where $f_i(\theta_v; \psi; \phi) = 1$ if the direction $(\psi; \phi)$ is contained in the component i (core jet or ring) and 0 otherwise.

3. Comparison with other afterglow models

We now compare the results obtained with our model to two other models of the afterglow of a structured jet: the model presented in Gill & Granot (2018) and **afterglowpy**,

a public Python module to calculate GRB afterglow light curves and spectra, based on Ryan et al. (2020).

The first comparison is straightforward: with our default values of the normalization coefficients K_ν and K_P , the assumptions (dynamics, microphysics, radiation, calculation of observed quantities) of our model in the pure synchrotron case are exactly the same as in Gill & Granot (2018). We checked that we reproduce exactly the different cases in their Figure 4.

The case of **afterglowpy** requires a more detailed comparison as there are differences in the some treatments of the afterglow physics:

(1) Early dynamics: In **afterglowpy**, even the early-time dynamics is computed assuming the self-similar Blandford & McKee regime, i.e. $\Gamma(t; \theta) \propto E(\theta)^{1/2} n_0^{1/2} t^{-3/2}$ (see §2.1 in Ryan et al. 2020), whereas we include the coasting phase with $\Gamma \sim \text{cst}$ before a smooth transition towards the self-similar regime at the deceleration radius, as described in §2.2. Figure 2 compares for a typical set of parameters the afterglow light curves from a top-hat jet viewed on-axis in radio, optical and X-rays obtained with our model (solid line), **afterglowpy** (dashed line) and our model where the dynamics has been forced to be in the self-similar regime at all times (dotted line). This allows to check that both models with the same self-similar dynamics agree well, except for the flux normalization as discussed below, and that the model with the full dynamics converge progressively towards the same solution: following the peak at the deceleration radius (at $\sim 10^{-2}$ days in this example), the light curve obtained with the full dynamics smoothly converges towards the self-similar solution, and both light curves are identical at late times (typically after the jet break at ~ 2 days in this example). On the other hand, the self-similar approximation strongly over-estimates the fluxes until the deceleration radius and the full dynamics should always be included when considering early observations. In the case of GW 170817 discussed in the next section, the earliest detection by *Chandra* was obtained 9 days after the merger, by which time the core jet dynamics has reached the self-similar regime.

(2) Late dynamics: contrary to **afterglowpy**, the present version of our model does not include lateral expansion of the ejecta. When comparing with **afterglowpy**, we therefore deactivate this option in the latter, which leads to the excellent late-time agreement seen in Figure 2. The impact of the lateral spreading is expected to be very limited as long as the core jet is relativistic (see e.g. Woods & Loeb 1999; Granot & Piran 2012; van Eerten & MacFadyen 2012; Duffell & Laskar 2018), so that we stop the jet propagation when the core Lorentz factor reaches $\Gamma = 2$ in the simulations of GW 170817's afterglow discussed in the next section. In addition, we exclude observations after 400 days from the data set used for the afterglow fitting, which corresponds to $\Gamma \gtrsim 3-4$ for the core jet in our best fit models.

(3) Flux normalization: **afterglowpy** relies on a scaling to **boxfit** (van Eerten et al. 2012), while in our model, this normalization is derived from analytical approximations detailed in Section 2. This leads to the difference of normalization seen in Figure 2 when comparing **afterglowpy** with our model where the same self-similar dynamics is forced. The flux ratio varies between 1 and 5 at all wavelengths. When exploring a broad parameter space, varying the an-

gle, energy injection, microphysical parameters, we checked that the flux ratio never exceeds 5.

To conclude this comparison, we note that `afterglowpy` and our model (in pure synchrotron mode) have been used by [Kann et al. \(2023\)](#) for two independent Bayesian inferences of the parameters of the afterglow of GRB 221009A using the same set of early observational data and converged towards very similar solutions.

4. The VHE afterglow of GW 170817

In this Section, we present the results obtained by fitting the observations of the GRB afterglow of GW 170817, using Bayesian analysis.

4.1. Observational data

In its numerical implementation, our model allows for simultaneous, multi-wavelength modelling. We use 94 data points, from radio to X-rays between 9.2 and 380 days³, as compiled and reprocessed homogeneously by [Makhathini et al. \(2021\)](#). We also include 5 constraining early-time upper limits also reported in [Makhathini et al. \(2021\)](#), as shown in Table 2. Early-time constraints are useful to restrict the posterior models to those with a single peak in flux density, as discussed in § 2.2. All these flux measurements and upper limits are fitted simultaneously.

The likelihood that we use for our study is based on a modified χ^2 calculation to account for the upper limits:

$$\ln \mathcal{L} = -\frac{1}{2} \left[\sum_i \frac{(m_i - d_i)^2}{\sigma_i^2} + \sum_j \frac{(\max\{u_j; m_j\} - u_j)^2}{\sigma_j^2} \right], \quad (79)$$

where the first sum concerns observational data (subscripts i) while the second sum concerns upper limits (subscripts j). The quantities m_i and m_j are the model flux densities at each observing time and frequency of the observational data set; d_i is the flux density value of a detection; σ_i its associated uncertainty; u_j is a flux upper limit presented in Table 2; and σ_j is an equivalent uncertainty that we arbitrarily define as $\sigma_j = 0.2u_j$, which roughly corresponds to the typical uncertainties for the detections. Adding this element accommodates for some models whose predictions are slightly above the reported upper limit. Note that the quantity $\max\{u_j; m_j\}$ in the second term implies that it

³ Data points can be accessed on github.com/kmooley/GW170817/

Time	Frequency	Instrument	Upper limit
0.57	9.7×10^9	VLA	144
0.70	1.2×10^{18}	NuSTAR	7.3×10^{-4}
1.44	1.0×10^{10}	VLA	13.8
2.40	2.41×10^{17}	Chandra	2.3×10^{-4}
3.35	3×10^9	VLA	19

Table 2. Early-time upper limits used in the afterglow fitting. Times are given in days, frequencies in Hz, and upper limits in μJy . These flux upper limits are selected as the most constraining among all the early observations listed in the compilation by [Makhathini et al. \(2021\)](#).

behaves as a penalty added only for predicted fluxes m_j above the observed upper limits. Another option would be to force the likelihood to diverge as soon as one of the modeled fluxes is above the corresponding upper limit.

In this study, we choose not to include late-time observations after 400 days in the fits. Indeed, we expect jet lateral spreading to play a role at late times, when the shock front reaches Lorentz factors $\Gamma \lesssim 3$, by which point our model cannot accurately describe the jet dynamics. In addition, other emission sites (e.g. the kilonova afterglow, [Nakar & Piran 2011](#)) could also contribute to the observed flux at late times. Including the latest observations ([Hajela et al. 2022](#)) which were not included in the compilation by [Makhathini et al. \(2021\)](#) is also difficult: late-time data in X-rays consists of only a few photons and a correct modelling in this case should be expressed in photon counts and account for the instrumental response and low-statistics effects. The result of such an analysis is currently unclear, with an uncertain late rebrightening ([Hajela et al. 2022](#)): see discussion in [Troja et al. \(2022\)](#). Interpreting the late evolution of GW 170817's afterglow seems to require a dedicated study, and we therefore exclude this phase from the analysis presented here. Finally, we do not include the *H.E.S.S.* upper limit at the peak ([Abdalla et al. 2020](#)) as it does constrain the fit (see § 4.4).

4.2. Results from the afterglow fitting

We perform a Bayesian analysis on the GW 170817 afterglow data using the Markov Chain Monte Carlo (MCMC) algorithm of the Python suite `emcee` ([Foreman-Mackey et al. 2013, 2019](#)). We run three separate fits where the assumptions for the radiative processes in the shocked region differ:

1. "no SSC": emission is only produced by synchrotron radiation, as described in [Sari et al. \(1998\)](#) and § 2.4.4;
2. "SSC (Thomson)": SSC is taken into account assuming that all scatterings occur in Thomson regime, as described in [Sari & Esin \(2001\)](#) and § 2.4.5;
3. "SSC (with KN)": SSC is taken into account including the KN regime, as described in [Nakar et al. \(2009\)](#) and § 2.4.6.

The priors used for these three fits are identical and presented in Table 3. We use (log-)uniform priors over large intervals in order to remain as agnostic as possible. Their bounds are shown in Table 3. Additional constraints on the

Parameter	Bounds	Type
$E_{0,\text{iso}}^c$ (erg)	$10^{50} - 10^{56}$	log-uniform
θ_c (deg)	0.5 – 10	uniform
θ_v (deg)	0 – 50	uniform
n_{ext} (cm^{-3})	$10^{-6} - 10^0$	log-uniform
ϵ_B	$10^{-6} - 1$	log-uniform
ϵ_e	$10^{-4} - 1$	log-uniform
ζ	$10^{-4} - 1$	log-uniform
p	2.1 – 2.4	uniform
a	0.1 – 7	uniform
Γ_0^c	$10^1 - 10^3$	log-uniform
b	0 – 6	uniform

Table 3. Free parameters of the MCMC, their prior bounds and shape.

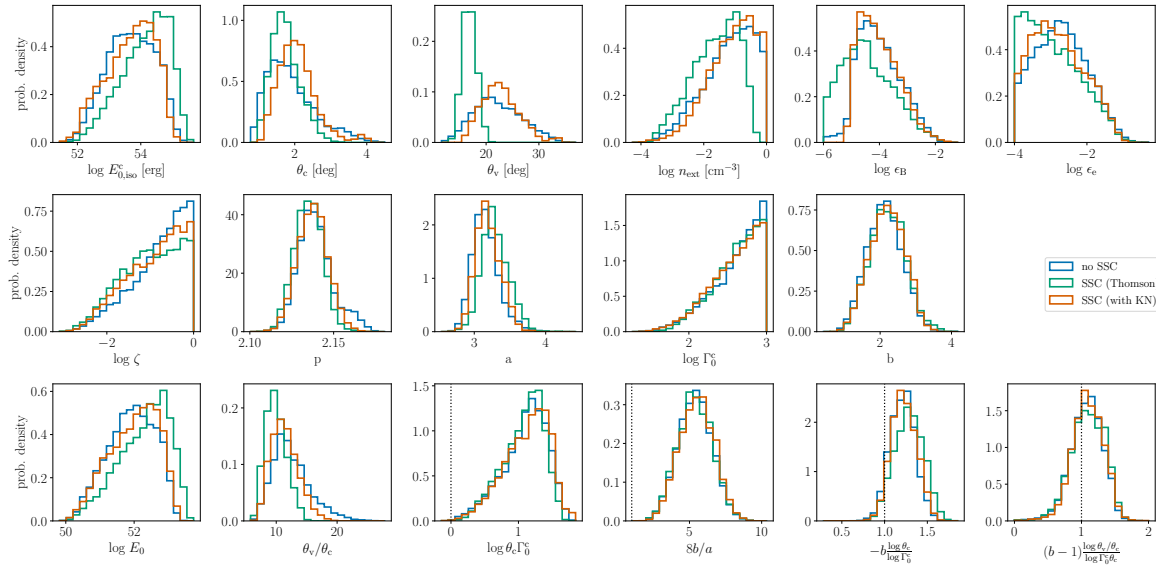


Fig. 3. Comparison of the marginalized posterior distributions for the three fits of the afterglow of GW 170817 presented in Section 4, which differ only by the treatment of the radiative processes: "no SSC" in blue; "SSC (Thomson)" in green; "SSC (with KN)" in orange. The first two rows show the inferred distributions of the model's free parameters. The last row shows the distributions of several quantities derived from these parameters: true energy of the jet E_0 (see Equation 5), ratio θ_v/θ_c , and four quantities used in the conditions for single-peaked light curves from Beniamini et al. (2020b) and described in § 2.2, $\log(\theta_v/\Gamma_0^c)$, $8b/a$, $-b \frac{\log \theta_v/\theta_c}{\log \Gamma_0^c}$ and $(b-1) \frac{\log(\theta_v/\theta_c)}{\log(\Gamma_0^c \theta_c)}$.

viewing angle can be obtained by combining the GW signal and the accurate distance and localization of the host galaxy (Finstad et al. 2018), or by combining the afterglow photometry and VLBI imagery (Govreen-Segal & Nakar 2023), and the density of the external medium can be constrained from direct observation of the host galaxy (Hallinan et al. 2017; Hajela et al. 2019). We do not include them to focus on constraints obtained from the afterglow modeling only.

For each of the three fits, we initialize 50 chains and run 10000 iterations per chain. After studying the convergence speed, we remove the first 2000 iterations for each chain and show the posterior distributions for the remaining 400000 samples of parameters.

We present the marginalized posterior distribution of the free parameters for the three fits in Figure 3, complemented by Figure C.1 in appendix, which shows the corresponding joint and marginalized posterior distributions at 3σ credibility ("corner plot"). We also show in Figure 3 the distribution of some derived quantities, the true initial kinetic energy of the ejecta E_0 as deduced from equation (5), the ratio of the viewing angle over the opening angle of the core jet θ_v/θ_c and the four conditions for single-peaked light curves described by Beniamini et al. (2020b) and in § 2.2. The three fits lead to similar distributions across the parameter space, with a few exceptions discussed in § 4.3. The median parameter values as well as their 90% credible intervals are reported in Table 4. We finally show in Table 5 the median values of the derived quantities shown in Figure 3.

Free Parameter	Model		
	no SSC	SSC (Thomson)	SSC (KN)
$\log E_{0,\text{iso}}^c$ [erg]	$53.70^{+1.21}_{-1.15}$	$54.11^{+1.14}_{-1.30}$	$53.70^{+1.12}_{-1.32}$
θ_c [°]	$1.77^{+1.12}_{-0.89}$	$1.85^{+1.28}_{-0.82}$	$2.07^{+0.83}_{-0.82}$
θ_v [°]	$21.81^{+7.69}_{-7.02}$	$17.16^{+2.50}_{-2.35}$	$22.67^{+5.94}_{-5.58}$
$\log n_{\text{ext}}$ [cm ⁻³]	$-1.09^{+1.09}_{-1.28}$	$-1.61^{+1.08}_{-1.23}$	$-1.03^{+1.03}_{-1.14}$
$\log \epsilon_B$	$-4.09^{+1.36}_{-1.01}$	$-4.43^{+1.39}_{-1.54}$	$-4.08^{+1.19}_{-0.97}$
$\log \epsilon_e$	$-2.73^{+0.99}_{-1.27}$	$-2.97^{+1.13}_{-1.03}$	$-2.81^{+1.15}_{-1.13}$
$\log \zeta$	$-0.68^{+0.68}_{-1.05}$	$-0.96^{+0.96}_{-0.96}$	$-0.81^{+0.81}_{-1.07}$
p	$2.14^{+0.02}_{-0.02}$	$2.14^{+0.01}_{-0.01}$	$2.14^{+0.01}_{-0.02}$
a	$3.14^{+0.30}_{-0.29}$	$3.34^{+0.66}_{-0.50}$	$3.19^{+0.30}_{-0.27}$
$\log \Gamma_0^c$	$2.68^{+0.32}_{-0.53}$	$2.62^{+0.49}_{-0.38}$	$2.64^{+0.51}_{-0.51}$
b	$2.13^{+0.84}_{-0.78}$	$2.20^{+1.07}_{-0.97}$	$2.24^{+0.79}_{-0.80}$

Table 4. Median posterior values for the free parameters of the three fits of the afterglow of GW 170817 presented in § 4.2. Uncertainties reported are the 90 % credible intervals of each parameter's posterior distribution.

The detailed joint posterior distributions for the "SSC (with KN)" model where emission is produced by synchrotron radiation and SSC diffusions in both Thomson and KN regimes are shown in Figure 4. In this Figure, which is representative of the results obtained with the three fits, we observe typical correlations between some of the afterglow parameters, like θ_c and θ_v , $E_{0,\text{iso}}^c$ and n_{ext} , or ϵ_e and ϵ_B . Some other parameters are anti-correlated, like $E_{0,\text{iso}}^c$ and ϵ_B , or n_{ext} and ϵ_B . Such degeneracies in the model parameters are expected when only the synchrotron component is observed (see e.g. Aksulu et al. 2022). In the case of GW 170817, the afterglow light curves can in first ap-

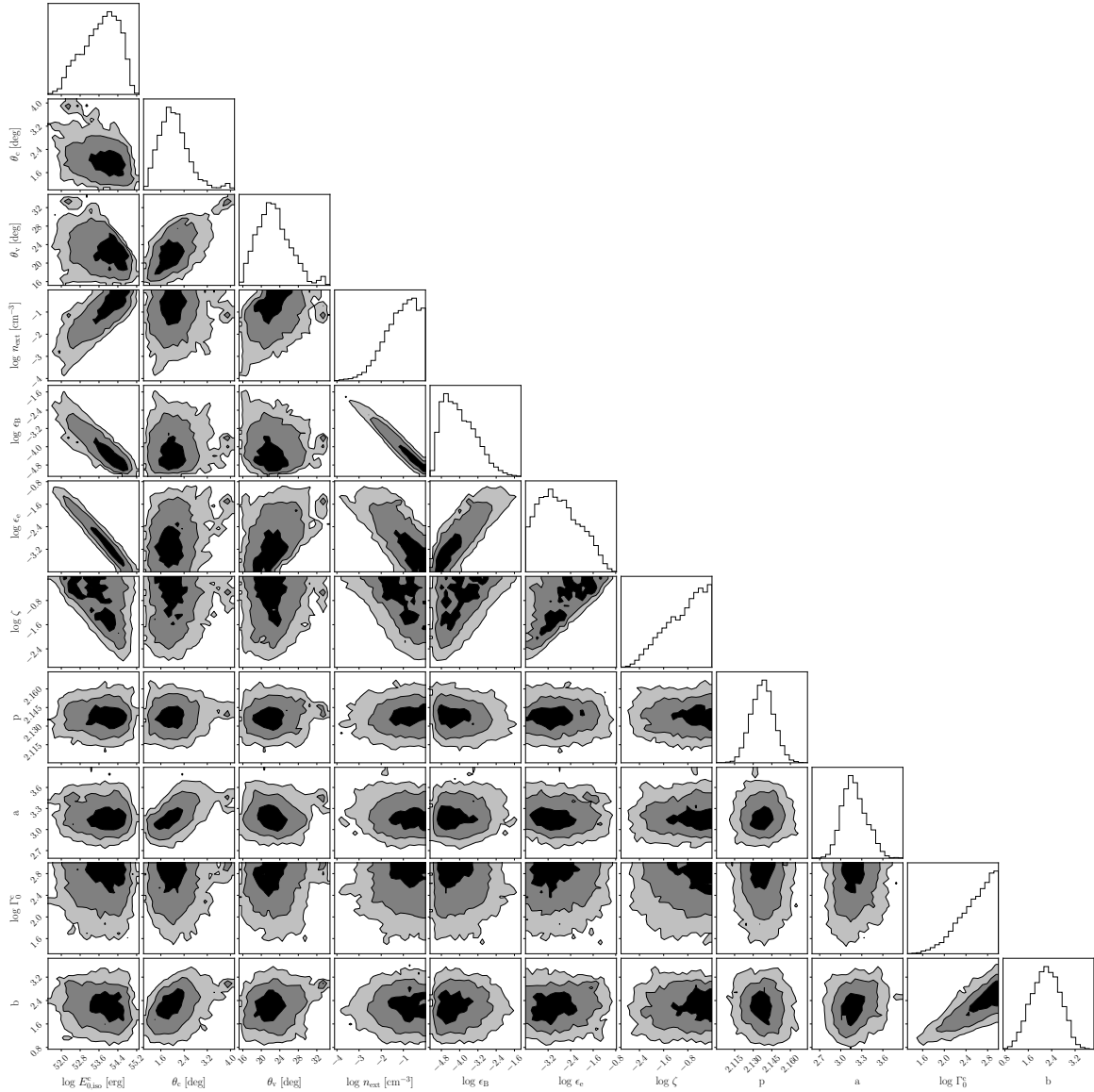


Fig. 4. Posterior joint and marginalized distributions of the model's free parameters, $E_{0,iso}^c$, θ_c , θ_v , n_{ext} , ϵ_B , ϵ_e , ζ , p , a , Γ_0^c , b , for the "SSC (with KN)" fit of the afterglow of GW 170817 presented in Section 4 which includes SSC diffusions in both Thomson and KN regimes. The priors are all uniform or log-uniform and are shown in Table 3. Fitted data includes all points until $t_{max} = 400$ days, as well as 5 early-time upper limits (see Section 4.1). The colored contours correspond to the 1σ , 2σ and 3σ confidence intervals for each parameter.

proximation be described by five quantities – its peak time, peak flux, rising and decreasing phase temporal slopes and spectral slope – which does not allow to constrain all the free parameters listed in Table 3.

As a post-processing step, we re-sample 20000 light curves at several observing frequencies (3 GHz, 1 keV and 1 TeV) and spectra at several observing times (20 days, 110 days, 400 days), where the set of parameters is directly drawn from the posterior sample, for each of the

three fits. At each observing time (for the light curves) or at each frequency (for the spectra), we then determine the 68% and 97.5% credible intervals for the distribution of predicted flux densities, that we use to draw confidence contours around the median value of the light curves and spectra. Because the posterior samples are similar between the three models, we show only the results for the most realistic case ("SSC (with KN)" model) in Figures 5 and 6

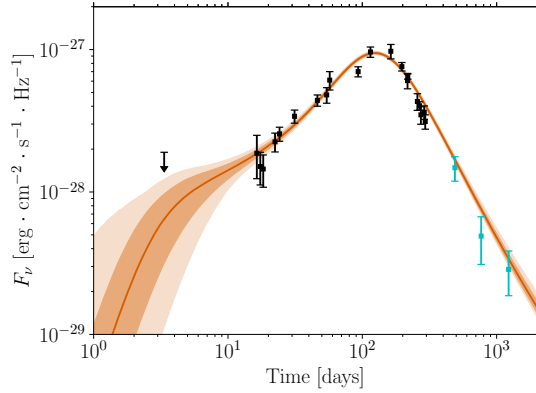


Fig. 5. Posterior distribution of the radio light curves at $\nu_{\text{obs}} = 3$ GHz for the "SSC (with KN)" fit of the afterglow of GW 170817. Solid lines represent the median value at each observing time, dark contours the 68% confidence interval and light contours the 97.5% confidence interval. Late-time observations not used in the fit are shown in blue.

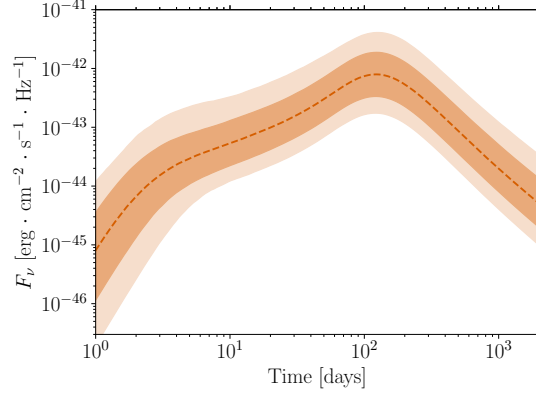


Fig. 6. Posterior distribution of the VHE light curves at $\nu_{\text{obs}} = 1$ TeV for the "SSC (with KN)" fit of the afterglow of GW 170817. Same conventions as in Figure 5. Note that this is a prediction of the model, with no observational constraint included in the fit.

(radio and VHE light curve), and in Figure 7 (spectrum at 110 days, close to the peak).

4.3. Discussion: inferred parameters

As seen in Figure 5, the afterglow of GW 170817 is very well fitted by the model. The model predicts accurately the flux at all times, with a very small dispersion. The dispersion of the predicted flux is of course larger at very early or very late times where we do not include any data point in the fit. The same quality of the model prediction is observed in the spectrum on Figure 7. The frequency $\nu_{\text{m,obs}}$ is below the data points at the lowest frequency, with some dispersion in absence of observational constraints. The critical frequency $\nu_{\text{c,obs}}$ is found to be in X-rays, at the frequency of the highest frequency data points.

The inferred values of most model parameters (Figure 3 and Table 4) are very similar to the results obtained in previous studies modelling the same afterglow with the synchrotron radiation from a decelerating structured jet (Troja et al. 2019; Lamb et al. 2019; Ghirlanda et al. 2019; Ryan et al. 2020), with some exceptions, due to different priors.

Derived quantity	Model		
	no SSC	SSC (Thomson)	SSC (KN)
$\log E_0$ [erg]	$51.95^{+1.05}_{-1.13}$	$52.41^{+1.04}_{-1.22}$	$52.07^{+1.01}_{-1.19}$
θ_v/θ_c	$11.95^{+5.29}_{-4.54}$	$9.84^{+2.80}_{-2.59}$	$11.19^{+3.58}_{-3.45}$
$\log(E_{0,\text{iso}}^c/n_{\text{ext}})$ [erg · cm ³]	$54.90^{+1.08}_{-1.18}$	$55.77^{+0.42}_{-0.43}$	$54.79^{+0.86}_{-0.85}$
$\log(\theta_c \Gamma_0^c)$	$1.15^{+0.48}_{-0.58}$	$1.12^{+0.43}_{-0.54}$	$1.17^{+0.44}_{-0.61}$
$8b/a$	$5.40^{+1.81}_{-2.05}$	$5.36^{+1.95}_{-1.94}$	$5.54^{+1.91}_{-1.96}$
$-b \log \theta_c / \log \Gamma_0^c$	$1.21^{+0.23}_{-0.25}$	$1.29^{+0.27}_{-0.28}$	$1.29^{+0.25}_{-0.22}$
$(b-1) \log(\theta_v/\theta_c) / \log(\Gamma_0^c \theta_c)$	$1.09^{+0.38}_{-0.38}$	$1.10^{+0.39}_{-0.39}$	$1.10^{+0.40}_{-0.34}$

Table 5. Median posterior values for several derived quantities for the three fits of the afterglow of GW 170817 presented in § 4.2. Uncertainties reported are the 90 % credible intervals of each quantity's posterior distribution. The four last rows correspond to the quantities appearing in the conditions for single peak light curves (§2.2).

A first difference concerns the viewing and core jet opening angles θ_v and θ_c . Even if the values inferred by the "SSC (with KN)" fit are comparable with values found in previous studies, the corresponding ratio $\theta_v/\theta_c \sim 11$ (Table 5) is on the higher end of the other predictions. Nakar & Piran (2021) give a compilation of these predictions and show that afterglow light curves can only constrain this ratio and not the two parameters independently, which is confirmed by the strong correlation observed in Figure 4. This difference is probably due to the flat and broad priors we use for these two parameters, whereas most previous studies use much stricter priors based on an external constraint, either on the viewing angle derived from GW data using the value of the Hubble constant from Planck (as in Troja et al. 2019; Ryan et al. 2020) or a constraint on the viewing angle and the core jet using VLBI imagery (as in Ghirlanda et al. 2019; Lamb et al. 2019). The marginalized distributions of θ_v and θ_c show that a restricted region of the parameter space has been explored by the MCMC chains for these parameters, as is also visible on Figure C.1.

When comparing with the results of Ryan et al. (2020), where the assumptions are the closest to those of our "no SSC" fit and where the light curves are computed using afterglowpy with which we compared our model in Section 3, we also find that our predicted values for $E_{0,\text{iso}}^c$ and n_{ext} are about one order of magnitude higher. From Figure 4, it appears that it is also an effect of our different priors for the angles. However we observe the expected strong correlation between these two parameters and the inferred ratio $E_{0,\text{iso}}^c/n_{\text{ext}} \sim 10^{55}$ erg · cm⁻³ (Table 5) is close to the value obtained by Ryan et al. (2020). Using similar priors for the angles, or including a constraint on the external density from the observation of the host galaxy (Hallinan et al. 2017; Hajela et al. 2019) would then reduce the inferred values for these two parameters. We discuss below the fact that detections in the VHE range would help to break this degeneracy and allow for a more precise determination of the energy and external density independently of such external constraints.

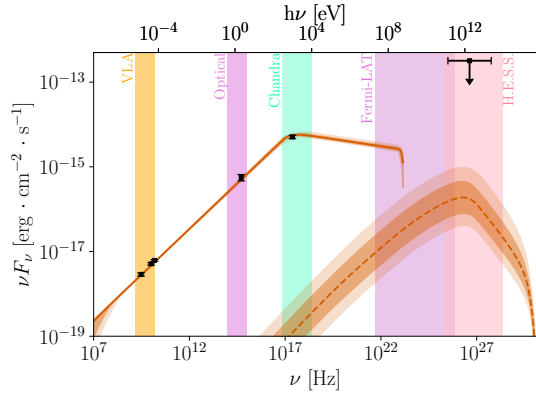


Fig. 7. Posterior distribution of the afterglow spectrum around its peak ($t_{\text{obs}} = 110$ days) for the "SSC (with KN)" fit of the afterglow of GW 170817. Data points show the multi-wavelength observations at $t_{\text{obs}} \pm 4$ days. The upper limit from *H.E.S.S.* is also indicated (Abdalla et al. 2020). The low-energy component (solid line) is produced by synchrotron radiation, while the high-energy emission (dashed line) is powered by SSC diffusions. Thick lines represent the median value at each observing frequency, dark contours the 68% confidence interval and light contours the 97.5% confidence interval. Some instrument observing spectral ranges are shown in colors.

The inferred values for the microphysics parameters ϵ_B and p are very close to those obtained in previous studies. The value of ϵ_e is slightly lower, but we also find that the median value for the fraction of accelerated electrons is ~ 0.15 , whereas this parameter is not included in past studies. Both parameters are strongly correlated, as seen in Figure 4. Overall, the values of these microphysics parameters, including ζ , are in a good agreement with the current understanding of the plasma physics at work in relativistic collisionless shocks (see e.g. Sironi et al. 2015) and comparable to values obtained for cosmological short GRBs by Fong et al. (2015). The inferred value $\zeta < 1$ leads to the question of a possible contribution to the radiation of the remaining thermal electrons (see e.g. Warren et al. 2022). Assuming $\zeta = 1$ as in previous studies is relevant in the case of GW 170817 as the observed emission is dominated by the synchrotron radiation, and the cooling break $\nu_{c,\text{obs}}$ is not detected. However these microphysics parameter impact the synchrotron and SSC components in different manners, as discussed below, and must therefore be considered to predict the VHE emission.

As shown in the second row of Figure 3 and in Table 5, the inferred values of the parameters describing the initial lateral structure of the ejecta are in good agreement with the conditions established in Beniamini et al. (2020b) and listed in §2.2 to get a single peak light curve: note that in practice, double peak light curves are not excluded a priori in our MCMC, but are disfavored thanks to the inclusion of early upper limits (Table 2). Finally, we note that the initial distribution of the Lorentz factor (Γ_0^c and b) is not well constrained, which was expected as most of the observed emission is produced in the self-similar stage of the deceleration. A correlation is observed between Γ_0^c and b . This can be explained by the fact that the lateral structure is required to reproduce the early-time slow rise of the

Parameter	"Moderate"	"Optimistic"
$E_{0,\text{iso}}^c$ [erg]	4.12×10^{52}	5.07×10^{52}
θ_c [°]	1.75	1.31
θ_v [°]	21.25	24.40
n_{ext} [cm ⁻³]	4.25×10^{-3}	1.52×10^{-2}
ϵ_B	1.61×10^{-3}	4.79×10^{-4}
ϵ_e	1.87×10^{-2}	3.54×10^{-2}
ζ	1	3.57×10^{-1}
p	2.139	2.149
a	2.98	2.95
Γ_0^c	184	164
b	2.01	1.34

Table 6. Reference cases: both sets of parameters are in the 97.5% confidence interval of the distributions inferred by the "SSC (with KN)" fit of the afterglow of GW 170817. They differ by the predicted VHE flux, which is either close to the median ("Moderate" case) or at the higher end of the confidence interval ("Optimistic" case).

light curve (Nakar & Piran 2018). Specifically, some material needs to have lower initial Lorentz factors to overcome effects of Doppler boosting out of the line of sight. With a higher core Γ_0^c , a steeper decrease in $\Gamma_0(\theta)$ is required for material at a given latitude θ to have a sufficiently low initial Lorentz factor that the observed slow rise can be reproduced, leading to higher values of b .

4.4. Discussion: the predicted VHE emission of GW 170817

We now discuss the predicted VHE emission of the afterglow of GW 170817. The predicted light curve at 1 TeV is plotted in Figure 6 and the VHE component of the spectrum at the peak of the light curve is shown in Figure 7, where is also indicated the upper limit obtained by *H.E.S.S.* (Abdalla et al. 2020). It appears that (i) the synchrotron emission extends at most up to the GeV range (due to the synchrotron burnoff limit, see Appendix A) and the VHE emission is then entirely due to the SSC process; (ii) even taking into account the dispersion, the predicted flux at 1 TeV is at least two orders of magnitude below the upper limit of 3.2×10^{-13} erg \cdot s⁻¹ \cdot cm⁻² obtained around the peak by *H.E.S.S.* (Abdalla et al. 2020), which is therefore not constraining. It is also clear when comparing Figures 5 and 6 that the dispersion of the predicted VHE flux is much larger than for the synchrotron component which is well constrained by the observations from radio to X-rays. This is also shown in the distribution of the predicted peak flux and peak time in radio and at 1 TeV in Figure 8. Note that the VHE light curve peaks a few days before the light curves from radio to X-rays, due to a different evolution of the synchrotron and SSC components. This result is due to the fact that the dependency of the SSC component on the model parameters is complex and very different from the dependencies of the synchrotron component identified by Sari et al. (1998). This also highlights the interest of detecting the VHE emission for the inference of model parameters, as some of the degeneracies visible in Figure 4 would be broken.

In the afterglow of GW 170817, the synchrotron spectrum is in slow cooling, with a spectral peak determined by the critical Lorentz factor γ_c . If IC scatterings occurred

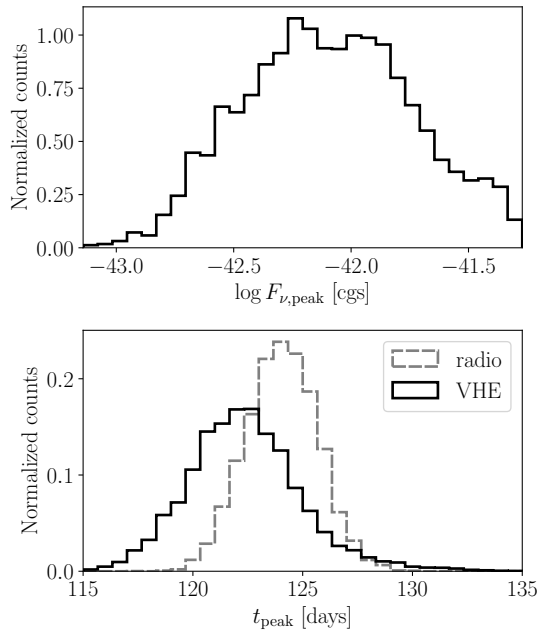


Fig. 8. Posterior distributions of the VHE peak flux density (top) and the radio (dashed grey line) and VHE (solid black line) peak times (bottom) for the "SSC (with KN)" fit of the afterglow of GW 170817.

in Thomson regime, the peak of the SSC component would be due to the diffusion of photons at ν_c by the electrons at γ_c (Sari & Esin 2001), and this peak should be intense as $\epsilon_e \gg \epsilon_B$ (see Equation 59). However, the predicted VHE emission is actually very weak because of a strong KN attenuation. To illustrate this effect, we select in Table 6 two reference sets of parameters, taken from the posterior sample. They are respectively in the 68% and 97.5% confidence intervals for the "SSC (with KN)" fit and fit perfectly well the observed light curves. The first set of parameters ("Moderate") corresponds to a predicted VHE flux which is close to the mean, whereas the second set of parameters ("Optimistic") corresponds to a predicted VHE flux on the highest end of the confidence interval: see the two predicted VHE light curves and peak spectra in Figure 9. In both cases, we selected sets of parameters having a low density, and therefore a low energy (see discussion in § 4.3).

Figure 10 shows for these two reference cases the evolution of $Y(\gamma_c)$ and $\gamma_c/\hat{\gamma}_c$ for the core jet, computing the SSC emission either by assuming that all scatterings are in Thomson regime like in the "SSC (Thomson)" fit, or by including the KN attenuation like in the "SSC (with KN)" fit. The figure shows that, in the full calculation, $\gamma_c/\hat{\gamma}_c \gg 1$ during the whole evolution, so that the scatterings of photons at ν_c by electrons at γ_c are strongly reduced by the KN regime. The Compton parameter $Y(\gamma_c)$ then remains very low. This confirms the origin of the weak VHE emission in the afterglow of GW 170817. In this regime of weak SSC emission, the synchrotron component is unaffected by the IC cooling, $\gamma_c \simeq \gamma_c^{\text{syn}}$, and this explains why the results of the "no SSC" and "SSC (with KN)" fits are so

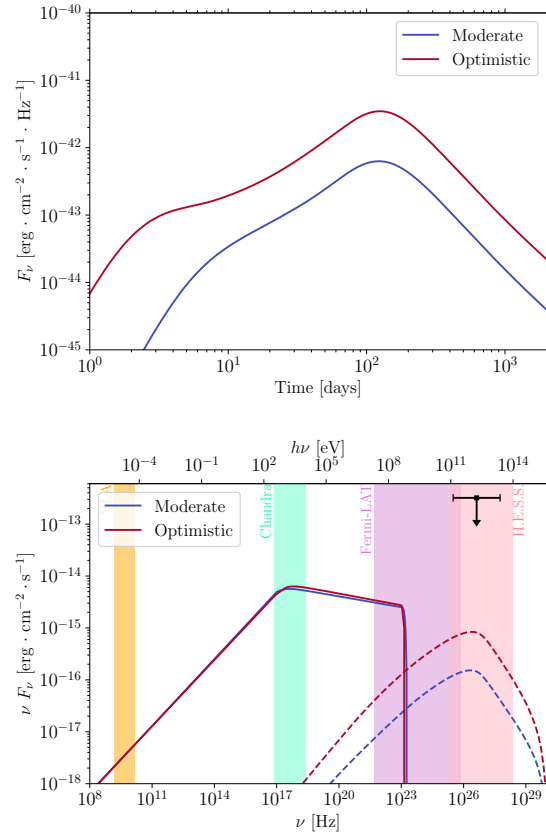


Fig. 9. VHE light curve at $h\nu_{\text{obs}} = 1$ TeV (top) and spectrum around the peak at $t_{\text{obs}} = 110$ days (bottom) for the "Moderate" (in blue) and "Optimistic" (in red) reference cases (see Table 6). Both predict similar fluxes in the synchrotron range due to the observational constraints, but differ in the SSC regime. The upper limit from *H.E.S.S.* is indicated for comparison (Abdalla et al. 2020).

close (Table 4). On the other hand, Figure 10 also shows that Y^{noKN} overestimates $Y(\gamma_c)$ in this case, leading to $Y(\gamma_c) > 1$. The critical Lorentz factor is therefore given by $\gamma_c \simeq \gamma_c^{\text{syn}}/Y(\gamma_c)$, which leads to an overestimation of γ_c^{syn} in the MCMC to maintain the cooling break above the X-ray measurements (increased $E_{0,\text{iso}}$ and lower ϵ_B). This explains the observed difference between the values of the model parameters inferred in the "SSC (Thomson)" and "SSC (with KN)" fits in Table 4. The value of $\gamma_c/\hat{\gamma}_c \gg 1$ in this case (green curves in the top panel of Figure 10) proves that the Thomson regime is not justified.

As the upper limit of *H.E.S.S.* was obtained close to the predicted peak with an already long exposure time of 53.9 hours (Abdalla et al. 2020), our prediction shows that it was unfortunately impossible to detect the VHE afterglow of GW 170817 with instruments currently available. We discuss in the next section the conditions that would make a post merger afterglow detectable at VHE in the future, especially in the context of the increased sensitivity expected with the CTA.

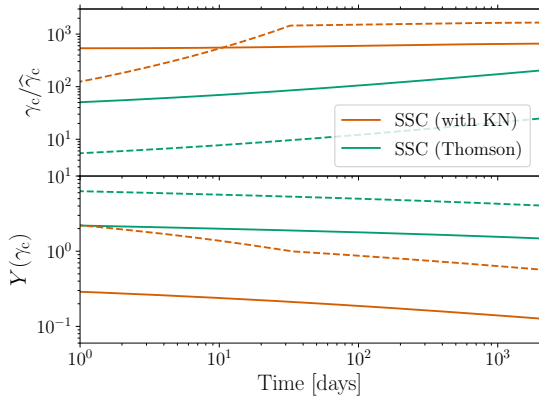


Fig. 10. Evolution of $\gamma_c/\widehat{\gamma}_c$ (top) and of the Compton parameter at γ_c , $Y(\gamma_c)$ (bottom) in the core jet. These quantities are plotted as a function of the observer time for the "Moderate" (solid line) and "Optimistic" (dashed line) references cases (see Table 6) in the "SSC (Thomson)" case (green) and in the "SSC (with KN)" case (orange).

5. Detectability of post-merger afterglows at VHE and prospects for the CTA

Even if the VHE afterglow of GW 170817 was not detectable, deeper observations of similar events can be expected in the future, in particular with the Cherenkov Telescope Array (CTA, Cherenkov Telescope Array Consortium et al. 2019). The off-axis afterglow phase is of particular interest because after a few days, full-night observations can be conducted without a significant intrinsic source flux variability over the observation time. We investigate in this section the conditions that would make such an event detectable by current instruments and the upcoming CTA. For this study, we assume a CTA detection sensitivity at 1 TeV about 6 times better than that of *H.E.S.S.*, as expected from Cherenkov Telescope Array Consortium et al. (2019). For an exposure time of ~ 50 hours as for the *H.E.S.S.* deep observations of GW 170817 (Abdalla et al. 2020), this leads to a detection sensitivity at 1 TeV of $5 \times 10^{-14} \text{ erg} \cdot \text{s}^{-1} \cdot \text{cm}^{-2}$.

A geometrical effect such as a lower viewing angle naturally increases the peak of the observed flux, and has a similar effect on the synchrotron and SSC components. In Figure 11, we show for the "Moderate" reference case the light curves (top) and spectra at the time of the 1 TeV emission peak (bottom), for gradually decreasing viewing angles. The 1 TeV light curves peak at earlier times when the viewing angle decreases, and the peak flux reaches higher values. As expected, the relative flux increase at the time of peak is similar for the synchrotron and the SSC components (Figure 11, bottom) and all light curves follow a similar long-term evolution, when the entire jet emission becomes visible to the off-axis observer. For the "Moderate" (resp. "Optimistic") reference case (Table 6), we find that a ratio $\theta_v/\theta_c \lesssim 3$ (resp. $\theta_v/\theta_c \lesssim 6$) would have made the afterglow of GW 170817 detectable by *H.E.S.S.*, provided the conditions had allowed for a very early deep observation. With the CTA, the VHE emission could have been detected up to $\theta_v/\theta_c \simeq 4$ (resp. $\theta_v/\theta_c \simeq 8$). In such a sce-

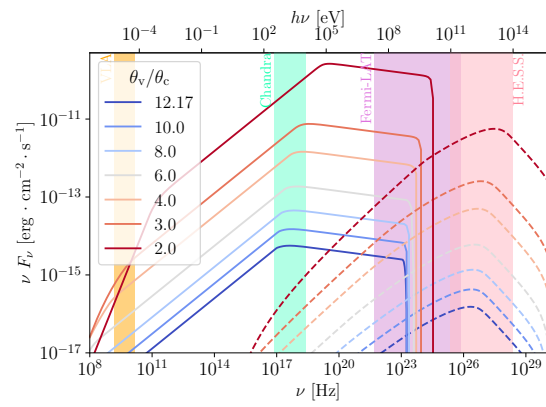
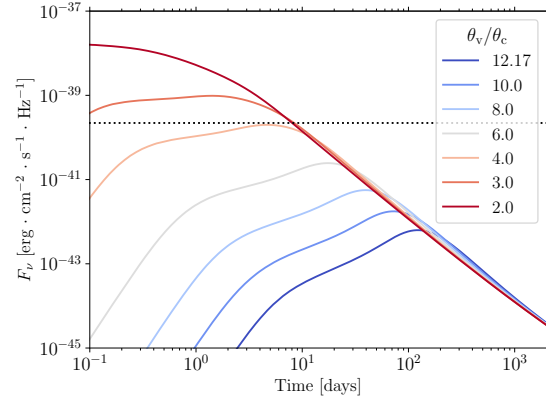


Fig. 11. Light curves at 1 TeV (top panel) and spectra at light curve peak (bottom panel) of the "Moderate" reference case (see Table 6) for varying viewing angles. The case fitting the afterglow of GW 170817 corresponds to $\theta_v/\theta_c = 12.17$. The peak times at which spectra are calculated are (in the ordering of the legend) 123, 73, 39, 17, 4.7, 1.4 and 0.06 days. The dotted line in the top panel corresponds to the assumed CTA sensitivity in Sec. 5.

nario, the emission peaks at ~ 5 days (resp. 13 days). This opens up interesting perspectives, even if the expected detection rate of nearby events at small viewing angles is low (see e.g. Duque et al. 2019; Mochkovitch et al. 2021).

Under some conditions, the predicted VHE emission could also be intrinsically brighter. As discussed in § 4.4, the VHE afterglow of GW 170817 is weak because of a strong KN attenuation ($\gamma_c/\widehat{\gamma}_c \gg 1$). The regime for the diffusions of photons at ν_c by electrons at γ_c is affected by several parameters (Nakar 2007). When the diffusions occur in the Thomson regime, the predicted scaling in the core jet is

$$\frac{\gamma_c}{\widehat{\gamma}_c} \propto \frac{1}{(1 + Y_c)^3} \frac{1}{\epsilon_B^{5/2} n_{\text{ext}}^{3/2} \epsilon_0} \quad (80)$$

Therefore, the Thomson regime is favored by a high magnetic field, a high density or a high kinetic energy. As ϵ_B is determined by plasma instabilities at the ultra-relativistic shock (Sironi et al. 2015), it should not vary much from an afterglow to another. On the other hand, the external

density and the kinetic energy may differ between mergers. We focus here on the effect of the external density, which is slightly stronger. Figure 12 shows the evolution of the afterglow emission for the "Moderate" reference case when n_{ext} increases up to $\sim 10 \text{ cm}^{-3}$, all other parameters being kept constant. A higher external density leads to an earlier peak time at higher luminosities but affects differently the synchrotron and the SSC flux: as expected the SSC process becomes more efficient and the relative SSC-to-synchrotron ratio increases. The transition from the weak SSC emission due to a strong KN attenuation described in § 4.4 to a more efficient case in Thomson regime occurs in this reference case above $n_{\text{ext}} \sim 1 \text{ cm}^{-3}$. This corresponds to the radiative regime S15 in Appendix B, with spectral breaks at $\nu_{\text{m}} < \nu_{\text{c}} < \hat{\nu}_{\text{c}} < \nu_0$. This effect can clearly be observed on the bottom panel of Figure 12, showing the observed spectrum at the peak emission. At the largest external densities, the increase of the VHE flux stalls for two reasons. Firstly, the strong SSC emission starts to affect significantly the synchrotron spectrum, which features two peaks (visible on the bottom panel of Figure 12). The cooling frequency ν_{c} at the peak also decreases, shifting the SSC peak to lower frequencies so that the flux at 1 TeV does not increase as significantly as the SSC peak flux. A second limitation, dominant at the highest densities, comes from the pair production.

Even taking into account these limitations, a higher external density clearly favors a brighter VHE emission, even if both the "Moderate" and "Optimistic" reference cases remain undetectable by H.E.S.S. or the CTA at the reference viewing angle. We conclude that post-merger VHE afterglows should become detectable in the future only under several favourable conditions, e.g. a higher external density and a slightly lower viewing angle. For instance, the "Moderate" (resp. "Optimistic") reference case with an external density $n_{\text{ext}} = 1 \text{ cm}^{-3}$ and a viewing angle $\theta_{\text{v}}/\theta_{\text{c}} = 6$ should be detectable by the CTA up to a distance of ~ 90 Mpc (resp. ~ 400 Mpc). Note however that two additional effects should be included in the "Optimistic" case and may reduce this maximum distance: (i) at 400 Mpc, the attenuation by the extragalactic background light is not negligible anymore at 1 TeV, Domínguez et al. 2011; (ii) in this case, the VHE afterglow peaks very early (~ 1 day). This would require an early follow-up which will necessarily be less deep due to a limited exposure time. It remains that detections with the CTA above 100 Mpc are possible in the "Optimistic" case. As some parameters that are naturally degenerate in an afterglow fit including only synchrotron radiation, such as n_{ext} and ϵ_{B} , have different effects on the SSC emission, such VHE detections would therefore better constrain the parameter space and allow for a better understanding of the physical conditions in the post-merger relativistic ejecta.

Another direct consequence of the impact of n_{ext} on SSC emission is that short GRB afterglows detected at VHE are more likely to originate from mergers occurring in a denser environment. Such VHE detections could therefore be unique probes to high-density media at the location of BNS mergers, which are sought clues for short merger time binaries. Fast mergers are indeed expected to occur close to their formation sites, where the external medium density is expected to be higher (see e.g. the discussion in Duque et al. 2020). Population synthesis studies have shown that the yet poorly-constrained phase of common envelope during binary stellar evolution can lead to the production of

BNS with very short initial separations that merge rapidly, as discussed by e.g. Dominik et al. (2012). Favorable kick intensities and orientations during the supernovae could also tend to shrink the initial orbital separation and increase the orbital eccentricity for part of the BNS population (Kalogera 1996). Observationally, the projected offset distribution of BNS mergers in their host galaxy seems to feature a tail below 1 half-light radius for $\sim 20\%$ of systems (Fong & Berger 2013; Berger 2014). These observations suffer from several observational biases like afterglow detection, host galaxy association and projection effects, probably leading to sample incompleteness, but give evidence for a population of fast mergers. If BNS mergers are the dominant site for r -process nucleosynthesis (see e.g. Lattimer & Schramm 1974; Goriely et al. 2011; Just et al. 2015; Côté et al. 2017), another more indirect evidence is provided by the observed large scatter of [Eu/Fe] abundances in extremely metal-poor stars (see the compilation by Suda et al. 2008), which requires fast mergers allowing the production of r -process elements when the environment is still extremely metal-poor (see e.g. Vangioni et al. 2016; Côté et al. 2019; Dvorkin et al. 2021). It has already been suggested by Duque et al. (2020) that multi-messenger observations of BNS including the detection of the afterglow will be biased in favor of high-density environment, thus allowing to probe this potential population of fast mergers. We show here that future VHE afterglow detections either following the GW detection of a BNS merger, or the detection short GRB, can also directly probe this population.

6. Conclusion

We developed a detailed model of the afterglow of a laterally-structured jet from radio to the VHE. Emission is produced in the shocked external medium behind the forward external shock and the dynamics does not include the late lateral expansion of the ejecta. Such effects, as well as the contribution of the reverse shock, will be implemented in the future. The main challenge addressed in this paper is the self-consistent calculation of the synchrotron and SSC emission while accounting for the two different IC regimes: Thomson and Klein-Nishina (KN). We based our approach on the method proposed by Nakar et al. (2009), extended to include additional effects: the maximum electron Lorentz factor γ_{max} is also computed self-consistently, leading to a realistic estimate of the high-energy cutoff of the synchrotron component, and the attenuation at high-energy due to pair production is also included. The values of γ_{c} and $Y(\gamma_{\text{c}})$, as well as the spectral regimes are determined numerically. Synchrotron self-absorption, that is relevant at low radio frequencies has not been included yet. The implementation of the model is computationally-efficient, allowing for afterglow fitting.

We used this model to fit the multi-wavelength afterglow of GW 170817, including radio to X-ray observations up to 400 days and five early-time upper limits. We inferred the model parameters using three different assumptions for the emission: pure synchrotron, synchrotron and SSC assuming that all scatterings occur in Thomson regime, and self-consistent synchrotron and SSC calculation taking into account the KN regime. We obtain excellent fits in the three cases, with similar constraints on the parameters for the pure synchrotron case and the full calculation with SSC in KN regimes, whereas the case where all scatterings are as-

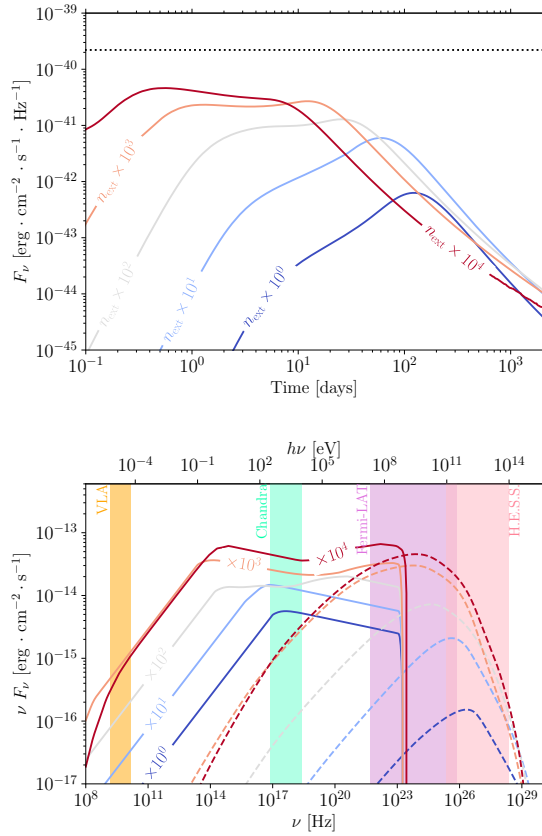


Fig. 12. Light curves at 1 TeV (top panel) and spectra at light curve peak (bottom panel) of the "Moderate" reference case (see Table 6) for varying external medium densities n_{ext} . The case fitting the afterglow of GW 170817 corresponds to $n_{\text{ext}} = 4.25 \times 10^{-3} \text{ cm}^{-3}$. Each line is labeled with the multiplication factor applied to the reference n_{ext} . The peak times at which spectra are calculated are 123, 60, 26, 12 and 0.55 days. The dotted line in the top panel corresponds to the assumed CTA sensitivity in Sec. 5.

sumed to be in the Thomson regime deviates significantly. The SSC emission in the afterglow of GW 170817 is indeed weak due to a strong KN attenuation, which confirms the need to include the self-consistent calculation of the SSC emission in the KN regime in afterglow models. The predicted VHE flux at the peak has a large dispersion but remains about two orders of magnitude below the upper limit obtained around the peak by *H.E.S.S.* This shows that the VHE afterglow of GW 170817 was undetectable by current instruments, but that future detections of similar events would break some degeneracies among the model parameters and allow better constraints on the physics of the relativistic ejecta.

We then studied how such post-merger VHE afterglows may become detectable in the future, in the context of the improved sensitivity of the CTA. Beyond the evident effect of a less off-axis viewing angle, we show that the efficiency of the SSC emission becomes larger in external media with

higher densities than GW 170817. For instance, a similar ultra-relativistic jet in a medium of density $\sim 1 \text{ cm}^{-3}$ and seen slightly less off-axis than GW 170817 may become detectable by the CTA at 100–400 Mpc.

This bias of VHE afterglow detections in favor of high-density environments offers a new probe of a possible population of fast mergers. With a short merger time, a merger should indeed occur in more central, and denser, regions of its host galaxy. Thus, future detections of such VHE afterglows would not only advance our physical understanding of relativistic jets produced after a BNS merger, but also constrain the physics of the evolution of massive binary systems.

Acknowledgements

Clément Pellouin acknowledges funding support from the Initiative Physique des Infinis (IPI), a research training program of the Idex SUPER at Sorbonne University. The authors acknowledge the Centre National d'Études Spatiales (CNES) for financial support in this research project. This work made use of the Infinity computing cluster at IAP. The authors thank K. Mooley for providing GW 170817 afterglow observation data at github.com/kmooley/GW170817/. This work made use of Python 3.8 and of the Python packages `arviz` (Kumar et al. 2019), `astropy` (Astropy Collaboration et al. 2022), `corner` (Foreman-Mackey 2016), `emcee` (Foreman-Mackey et al. 2019, 2013), `matplotlib` (Hunter 2007), `multiprocessing`, `numpy` (Harris et al. 2020), `pandas` (McKinney 2010), `scipy` (Virtanen et al. 2020).

References

- Abbott, B. P., Abbott, R., Abbott, T. D., et al. 2017a, *Phys. Rev. Lett.*, **119**, 161101
- Abbott, B. P., Abbott, R., Abbott, T. D., et al. 2017b, *ApJ*, **848**, L12
- Abdalla, H., Abramowski, A., Aharonian, F., et al. 2017, *ApJ*, **850**, L22
- Abdalla, H., Adam, R., Aharonian, F., et al. 2020, *ApJ*, **894**, L16
- Abdalla, H., Adam, R., Aharonian, F., et al. 2019, *Nature*, **575**, 464
- Acciari, V. A., Ansoldi, S., Antonelli, L. A., et al. 2021, *ApJ*, **908**, 90
- Aksulu, M. D., Wijers, R. A. M. J., van Eerten, H. J., & van der Horst, A. J. 2022, *MNRAS*, **511**, 2848
- Ascenzi, S., Oganessian, G., Salafia, O. S., et al. 2020, *A&A*, **641**, A61
- Astropy Collaboration, Price-Whelan, A. M., Lim, P. L., et al. 2022, *ApJ*, **935**, 167
- Balasubramanian, A., Corsi, A., Mooley, K. P., et al. 2021, *ApJ*, **914**, L20
- Beniamini, P., Duque, R., Daigne, F., & Mochkovitch, R. 2020a, *MNRAS*, **492**, 2847
- Beniamini, P., Granot, J., & Gill, R. 2020b, *MNRAS*, **493**, 3521
- Beniamini, P., Nava, L., Duran, R. B., & Piran, T. 2015, *MNRAS*, **454**, 1073
- Berger, E. 2014, *ARA&A*, **52**, 43
- Blanch, O., Longo, F., Berti, A., et al. 2020, GRB Coordinates Network, **29075**, 1
- Blandford, R. D. & McKee, C. F. 1976, *Physics of Fluids*, **19**, 1130
- Bošnjak, Ž., Daigne, F., & Dubus, G. 2009, *A&A*, **498**, 677
- Bromberg, O., Nakar, E., Piran, T., & Sari, R. 2011, *ApJ*, **740**, 100
- Bromberg, O., Tchekhovskoy, A., Gottlieb, O., Nakar, E., & Piran, T. 2018, *MNRAS*, **475**, 2971
- Cantiello, M., Jensen, J. B., Blakeslee, J. P., et al. 2018, *ApJ*, **854**, L31
- Cherenkov Telescope Array Consortium, Acharya, B. S., Agudo, I., et al. 2019, Science with the Cherenkov Telescope Array (World Scientific)
- Côté, B., Belczynski, K., Fryer, C. L., et al. 2017, *ApJ*, **836**, 230
- Côté, B., Eichler, M., Arcones, A., et al. 2019, *ApJ*, **875**, 106
- Cowperthwaite, P. S., Berger, E., Villar, V. A., et al. 2017, *ApJ*, **848**, L17

- Daigne, F. & Mochkovitch, R. 1998, *MNRAS*, 296, 275
- Daigne, F. & Mochkovitch, R. 2000, *A&A*, 358, 1157
- D’Avanzo, P., Campana, S., Salafia, O. S., et al. 2018, *A&A*, 613, L1
- Derishev, E. & Piran, T. 2021, *ApJ*, 923, 135
- Derishev, E. V., Kocharovskiy, V. V., & Kocharovskiy, V. V. 2001, *A&A*, 372, 1071
- Domínguez, A., Primack, J. R., Rosario, D. J., et al. 2011, *MNRAS*, 410, 2556
- Dominik, M., Belczynski, K., Fryer, C., et al. 2012, *ApJ*, 759, 52
- Duffell, P. C. & Laskar, T. 2018, *ApJ*, 865, 94
- Duque, R., Beniamini, P., Daigne, F., & Mochkovitch, R. 2020, *A&A*, 639, A15
- Duque, R., Beniamini, P., Daigne, F., & Mochkovitch, R. 2022, *MNRAS*, 513, 951
- Duque, R., Daigne, F., & Mochkovitch, R. 2019, *A&A*, 631, A39
- Dvorkin, I., Daigne, F., Goriely, S., Vangioni, E., & Silk, J. 2021, *MNRAS*, 506, 4374
- Finstad, D., De, S., Brown, D. A., Berger, E., & Biwer, C. M. 2018, *ApJ*, 860, L2
- Fong, W. & Berger, E. 2013, *ApJ*, 776, 18
- Fong, W., Berger, E., Margutti, R., & Zauderer, B. A. 2015, *ApJ*, 815, 102
- Foreman-Mackey, D. 2016, *The Journal of Open Source Software*, 1, 24
- Foreman-Mackey, D., Farr, W., Sinha, M., et al. 2019, *The Journal of Open Source Software*, 4, 1864
- Foreman-Mackey, D., Hogg, D. W., Lang, D., & Goodman, J. 2013, *PASP*, 125, 306
- Galván, A., Fraija, N., & González, M. M. 2019, in International Cosmic Ray Conference, Vol. 36, 36th International Cosmic Ray Conference (ICRC2019), 681
- Genet, F., Daigne, F., & Mochkovitch, R. 2007, *MNRAS*, 381, 732
- Ghirlanda, G., Salafia, O. S., Paragi, Z., et al. 2019, *Science*, 363, 968
- Gill, R. & Granot, J. 2018, *MNRAS*, 478, 4128
- Gill, R. & Granot, J. 2022, *Galaxies*, 10, 74
- Gill, R. & Granot, J. 2023, *MNRAS* [arXiv:2304.14331]
- Goldstein, A., Veres, P., Burns, E., et al. 2017, *ApJ*, 848, L14
- Goriely, S., Bauswein, A., & Janka, H.-T. 2011, *ApJ*, 738, L32
- Gottlieb, O., Nakar, E., Piran, T., & Hotokezaka, K. 2018, *MNRAS*, 479, 588
- Govreen-Segal, T. & Nakar, E. 2023, *MNRAS* [arXiv:2302.10211]
- Granot, J. & Piran, T. 2012, *MNRAS*, 421, 570
- Granot, J., Piran, T., & Sari, R. 1999, *ApJ*, 513, 679
- H. E. S. S. Collaboration, Abdalla, H., Aharonian, F., et al. 2021, *Science*, 372, 1081
- Hajela, A., Margutti, R., Alexander, K. D., et al. 2019, *ApJ*, 886, L17
- Hajela, A., Margutti, R., Bright, J. S., et al. 2022, *ApJ*, 927, L17
- Hallinan, G., Corsi, A., Mooley, K. P., et al. 2017, *Science*, 358, 1579
- Harris, C. R., Millman, K. J., van der Walt, S. J., et al. 2020, *Nature*, 585, 357
- Hunter, J. D. 2007, *Computing in Science and Engineering*, 9, 90
- Jacovich, T. E., Beniamini, P., & van der Horst, A. J. 2021, *MNRAS*, 504, 528
- Just, O., Bauswein, A., Ardevol Pulpillo, R., Goriely, S., & Janka, H. T. 2015, *MNRAS*, 448, 541
- Kalogera, V. 1996, *ApJ*, 471, 352
- Kann, D. A., Agayeva, S., Aivazyan, V., et al. 2023, *ApJ*, 948, L12
- Kobayashi, S., Piran, T., & Sari, R. 1997, *ApJ*, 490, 92
- Kumar, R., Carroll, C., Hartikainen, A., & Martin, O. 2019, *The Journal of Open Source Software*, 4, 1143
- Lamb, G. P., Lyman, J. D., Levan, A. J., et al. 2019, *ApJ*, 870, L15
- Lattimer, J. M. & Schramm, D. N. 1974, *ApJ*, 192, L145
- LHAASO Collaboration. 2023, arXiv e-prints, arXiv:2306.06372
- MAGIC Collaboration, Acciari, V. A., Ansoldi, S., et al. 2019a, *Nature*, 575, 455
- MAGIC Collaboration, Acciari, V. A., Ansoldi, S., et al. 2019b, *Nature*, 575, 459
- Makhathini, S., Mooley, K. P., Brightman, M., et al. 2021, *ApJ*, 922, 154
- Matsumoto, T., Nakar, E., & Piran, T. 2019, *MNRAS*, 483, 1247
- McKinney, W. 2010, in Proceedings of the 9th Python in Science Conference, ed. S. van der Walt & J. Millman, 56–61
- Mochkovitch, R., Daigne, F., Duque, R., & Zitouni, H. 2021, *A&A*, 651, A83
- Mooley, K. P., Anderson, J., & Lu, W. 2022, *Nature*, 610, 273
- Mooley, K. P., Deller, A. T., Gottlieb, O., et al. 2018, *Nature*, 561, 355
- Murase, K., Toma, K., Yamazaki, R., & Mészáros, P. 2011, *ApJ*, 732, 77
- Nakar, E. 2007, *Phys. Rep.*, 442, 166
- Nakar, E., Ando, S., & Sari, R. 2009, *ApJ*, 703, 675
- Nakar, E. & Piran, T. 2011, *Nature*, 478, 82
- Nakar, E. & Piran, T. 2018, *MNRAS*, 478, 407
- Nakar, E. & Piran, T. 2021, *ApJ*, 909, 114
- O’Connor, B., Troja, E., Ryan, G., et al. 2023, arXiv e-prints, arXiv:2302.07906
- Oganesyan, G., Ascenzi, S., Branchesi, M., et al. 2020, *ApJ*, 893, 88
- Palmese, A., Hartley, W., Tarsitano, F., et al. 2017, *ApJ*, 849, L34
- Panaitescu, A. & Kumar, P. 2000, *ApJ*, 543, 66
- Piran, T. & Nakar, E. 2010, *ApJ*, 718, L63
- Rhoads, J. E. 1997, *ApJ*, 487, L1
- Ryan, G., van Eerten, H., Piro, L., & Troja, E. 2020, *ApJ*, 896, 166
- Salafia, O. S., Berti, A., Covino, S., et al. 2022a, in 37th International Cosmic Ray Conference, 944
- Salafia, O. S., Ravasio, M. E., Yang, J., et al. 2022b, *ApJ*, 931, L19
- Sari, R. & Esin, A. A. 2001, *ApJ*, 548, 787
- Sari, R., Piran, T., & Narayan, R. 1998, *ApJ*, 497, L17
- Sato, Y., Murase, K., Ohira, Y., & Yamazaki, R. 2023, *MNRAS*, 522, L56
- Savchenko, V., Ferrigno, C., Kuulkers, E., et al. 2017, *ApJ*, 848, L15
- Sedov, L. I. 1946, *Journal of Applied Mathematics and Mechanics*, 10, 241
- Sironi, L., Keshet, U., & Lemoine, M. 2015, *Space Sci. Rev.*, 191, 519
- Suda, T., Katsuta, Y., Yamada, S., et al. 2008, *PASJ*, 60, 1159
- Tanvir, N. R., Levan, A. J., González-Fernández, C., et al. 2017, *ApJ*, 848, L27
- Taylor, G. 1950, *Proceedings of the Royal Society of London Series A*, 201, 159
- Troja, E., O’Connor, B., Ryan, G., et al. 2022, *MNRAS*, 510, 1902
- Troja, E., van Eerten, H., Ryan, G., et al. 2019, *MNRAS*, 489, 1919
- Troja, E., van Eerten, H., Zhang, B., et al. 2020, *MNRAS*, 498, 5643
- Uhm, Z. L. & Beloborodov, A. M. 2007, *ApJ*, 665, L93
- van Eerten, H., van der Horst, A., & MacFadyen, A. 2012, *ApJ*, 749, 44
- van Eerten, H. J. & MacFadyen, A. I. 2012, *ApJ*, 747, L30
- Vangioni, E., Goriely, S., Daigne, F., François, P., & Belczynski, K. 2016, *MNRAS*, 455, 17
- Villar, V. A., Guillochon, J., Berger, E., et al. 2017, *ApJ*, 851, L21
- Virtanen, P., Gommers, R., Oliphant, T. E., et al. 2020, *Nature Methods*, 17, 261
- Wang, X.-Y., Liu, R.-Y., Zhang, H.-M., Xi, S.-Q., & Zhang, B. 2019, *ApJ*, 884, 117
- Warren, D. C., Dainotti, M., Barkov, M. V., et al. 2022, *ApJ*, 924, 40
- Woods, E. & Loeb, A. 1999, *ApJ*, 523, 187
- Yamasaki, S. & Piran, T. 2022, *MNRAS*, 512, 2142

Appendix A: Maximum electron Lorentz factor and synchrotron burnoff limit

The maximum Lorentz factor γ_{\max} of accelerated electrons is defined in Section 2.3 and is reached when the acceleration timescale becomes longer than the cooling timescale, i.e.

$$t_{\text{acc}}(\gamma_{\max}) = \min(t_{\text{rad}}(\gamma_{\max}); t_{\text{dyn}}), \quad (\text{A.1})$$

where the dynamical timescale t_{dyn} and the acceleration timescale t_{acc} are defined by Equations (16) and (24). From Equations (38–39), the radiative timescale t_{rad} is given by

$$t_{\text{rad}}(\gamma) = \frac{t_{\text{dyn}}}{1 + Y(\gamma)} \frac{\gamma_{\text{c}}^{\text{syn}}}{\gamma}. \quad (\text{A.2})$$

Equation (A.1) can then be rewritten

$$\min \left[1; \frac{\gamma_{\text{c}}^{\text{syn}}}{\gamma_{\max}(1 + Y(\gamma_{\max}))} \right] = \tilde{K} \gamma_{\max}, \quad (\text{A.3})$$

with

$$\tilde{K} = K_{\text{acc}} \frac{m_{\text{e}}c}{eBt_{\text{dyn}}}. \quad (\text{A.4})$$

Then γ_{\max} is the solution of

$$\gamma_{\max}^2 [1 + Y(\gamma_{\max})] = \frac{\gamma_{\text{c}}^{\text{syn}}}{\tilde{K}} \quad (\text{A.5})$$

except in unlikely cases where electrons at γ_{\max} are slow cooling ($\gamma_{\max} < \gamma_{\text{c}}$), that lead to $\gamma_{\max} = 1/\tilde{K}$.

In the present version of the model, we assume $\gamma_{\max} \gg \gamma_{\text{m}}$ so that the calculation of γ_{c} and the identification of the radiative regime and associated normalized electron distribution $f(x)$ and Compton parameter $h(x)$ is independent of γ_{\max} (see § 2.4.6). Therefore the maximum Lorentz factor is determined once this radiative regime is identified. We follow an iterative procedure where the segments of $h(x)$ are explored successively starting from the last segment $x > \hat{x}_1$ (highest Lorentz factors):

1. We check if there is a solution of Equation (A.5) in this segment, with the usual approximation for $1 + Y$, i.e.

$$\frac{\gamma_{\text{c}}^{\text{syn}}}{\tilde{K}} = \begin{cases} \gamma_{\max}^2 & \text{if } Y(\gamma_{\max}) < 1 \\ \gamma_{\max}^2 Y(\gamma_{\max}) & \text{if } Y(\gamma_{\max}) > 1 \end{cases}, \quad (\text{A.6})$$

where $Y(\gamma_{\max})$ is computed from Equation (61), which leads to

$$Y(\gamma_{\max}) = \begin{cases} A \frac{\gamma_{\text{m}}}{\gamma_{\text{syn}}^2} \frac{I_2}{I_0} h(x_{\max}) & \text{if } \gamma_{\text{m}} > \gamma_{\text{c}} \\ A \frac{\gamma_{\text{c}}}{\gamma_{\text{m}}} \frac{I_2}{I_0} h(x_{\max}) & \text{if } \gamma_{\text{m}} < \gamma_{\text{c}} \\ & \text{and } Y(\gamma_{\max}) < 1 \\ \left(A \frac{\gamma_{\text{c}}^{\text{syn}}}{\gamma_{\text{m}}} \frac{I_2}{I_0} h(x_{\max}) \right)^{1/3} & \text{if } \gamma_{\text{m}} < \gamma_{\text{c}} \\ & \text{and } Y(\gamma_{\max}) > 1 \end{cases}. \quad (\text{A.7})$$

The pre-factor A is the same as in Equation (65).

2. If there is a solution in the considered segment, we stop the iterative procedure and keep the following value for the maximum electron Lorentz factor:
 - the solution γ_{\max} found in the segment if $\gamma_{\max} > \gamma_{\text{c}}$ (fast cooling);

- the solution $\gamma_{\max} = 1/\tilde{K}$ otherwise (slow cooling).
- 3. If there is no solution in the considered segment:
 - If the next segment is still at least partially in fast cooling regime (i.e. the upper bound is above γ_{c}), we start a new iteration at step 1. using this new segment;
 - otherwise we stop the iterative procedure and keep for γ_{\max} the slow cooling solution $\gamma_{\max} = 1/\tilde{K}$.

In most cases, the maximum electron Lorentz factor is large enough to be in fast cooling regime ($\gamma_{\max} > \gamma_{\text{c}}$ so that $t_{\text{rad}}(\gamma_{\max}) < t_{\text{dyn}}$) with a negligible IC cooling ($Y(\gamma_{\max}) < 1$). In this case, the maximum Lorentz factor

$\gamma_{\max} = \sqrt{\gamma_{\text{c}}^{\text{syn}}/\tilde{K}}$ leads to the usual synchrotron burnoff limit (see e.g. Piran & Nakar 2010) for the high-frequency cutoff of the synchrotron spectrum in the comoving frame $h\nu_{\max} = h\nu_{\text{syn}}(\gamma_{\max}) = K_2 B \gamma_{\text{c}}^{\text{syn}}/\tilde{K}$:

$$h\nu_{\max} = \frac{1}{K_{P_{\max}} \frac{3he^2}{\sigma_T m_{\text{e}}c} K_{\text{acc}}} = \frac{160 \text{ MeV}}{K_{P_{\max}} K_{\text{acc}}}. \quad (\text{A.8})$$

For the best-fit parameters of the afterglow of GW 170817 presented in Section 4, the Lorentz factor of the core jet at t_{peak} is $\Gamma \simeq 10$. The limit is thus expected at ~ 1 GeV in the observer frame, as seen in Figure 7.

Appendix B: Radiative regimes and corresponding electron distributions

The IC cooling impacts the distribution of electrons if $\max(\gamma_{\text{c}}; \hat{\gamma}_{\text{p}}) < \gamma < \gamma_0$ (Equation (64)). As $\hat{\gamma} = \gamma_{\text{self}}^3/\gamma^2$, all possible cases regarding the radiative regime and the distribution of electrons can be identified in the $(\gamma_{\text{self}}; \gamma_0)$ plane shown in Figure B.1. As an electron of Lorentz factor γ can upscatter its own synchrotron photon only if $\gamma \leq \hat{\gamma}$, i.e. $\gamma \leq \gamma_{\text{self}}$, the x-axis quantifies the importance of the KN suppression: the lower γ_{self} (left side of the diagram), the more electrons are affected by KN effects. The y-axis quantifies the importance of IC cooling: the IC power of all electrons with $\gamma > \gamma_0$ is negligible compared to the synchrotron power. Therefore, the lower γ_0 (bottom of the diagram), the more electrons have a negligible IC cooling. We list in Tables B.1 (fast cooling) and B.2 (slow cooling) all these cases and provide the corresponding self-consistent solution (breaks and slopes) for the normalized distribution of electrons $f(x)$ (Equation (43)) and the normalized Compton parameter $h(x)$ (Equation (61)), as obtained following the detailed method described in Nakar et al. (2009). The break corresponding to the peak of the synchrotron spectrum is highlighted in red. We also provide in each case the expression of γ_0 obtained from the relation $Y(\gamma_{\text{c}}) = h(x_{\text{c}})/h(x_0)$ (Equation (66)), as needed in the iterative procedure to determine $Y(\gamma_{\text{c}})$: see § 2.4.6.

The distribution of electrons is unaffected by the SSC cooling when $\gamma_0 < \gamma_{\text{c}}$ or $\gamma_{\text{c}} < \gamma_0 < \hat{\gamma}_{\text{m,c}}$. These two regions are shaded in orange and blue in Figure B.1. When $\gamma_0 < \hat{\gamma}_{\text{m,c}}$ (cases F1 and S1), the IC cooling is negligible for all electrons and γ_0 is undefined. The solution is provided by the pure synchrotron case (§2.4.4). When $\hat{\gamma}_{\text{m,c}} < \gamma_0 < \gamma_{\text{c}}$ (cases F2 to F5 and S2 to S6), the normalized electron distribution $f(x)$ is also the same as in the pure synchrotron case but γ_0 is defined and its expression depends on the considered regime.

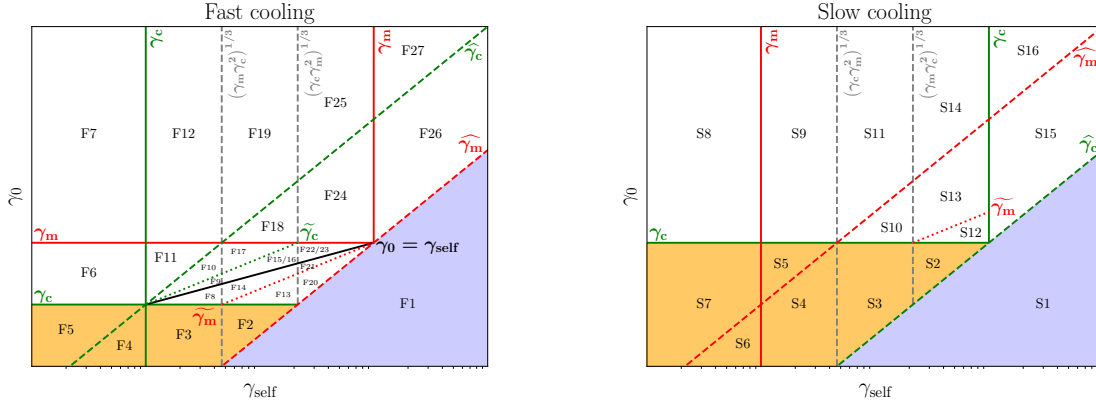


Fig. B.1. Definition of all possible cases for the radiative regime and the distribution of electrons in the plane γ_0 vs γ_{self} . The Lorentz factors γ_m and γ_c are indicated by red and green solid lines either in the fast cooling regime with $\gamma_m > \gamma_c$ (left) or in the slow cooling regime with $\gamma_m < \gamma_c$ (right). The black solid line in the left panel corresponds to $\gamma_0 = \gamma_{\text{self}}$. The two Lorentz factors $\hat{\gamma}_m$ (red) and $\hat{\gamma}_c$ (green) are plotted in dashed lines. In some regions, additional Lorentz factors relevant to identify the radiative regime are also plotted: $\tilde{\gamma}_m$ (red dotted line) and $\tilde{\gamma}_c$ (green dotted line). The regions where there is no impact of the SSC cooling on the distribution of electrons are shaded in orange ($\hat{\gamma}_{m,c} < \gamma_0 < \gamma_c$) and blue ($\gamma_0 < \hat{\gamma}_{m,c}$). This diagram allows to identify all possible orderings of γ_0 , γ_m , γ_c , $\hat{\gamma}_m$, $\hat{\gamma}_c$ defining all possible radiative regimes: see appendix B. The corresponding limits for γ_{self} are indicated by vertical black dashed lines.

In fast cooling regime, cases F24 and F25 require a specific treatment, as a large number of breaks can appear in the distribution (see section 3.2 in Nakar et al. 2009). There are multiple possible subcases, depending on the number of breaks, that can be found iteratively. We only list below the first subcases of case F24 with breaks at $\hat{\gamma}_m$, $\hat{\gamma}_0$ and $\hat{\gamma}_m$.

– If $\gamma_m < \gamma_0 < \min(\tilde{\gamma}_c; \hat{\gamma}_m) < \hat{\gamma}_c$:

	γ_c	$\hat{\gamma}_0$	$\hat{\gamma}_m$	γ_m	$\tilde{\gamma}_m$	$\tilde{\gamma}_c$
T	2	$(p+1)/2$	1	p	γ_0	$p+1$
B	0	$(3-p)/2$	1	1	$(5-p)/4$	$1/2$ $4/3$

– If $\gamma_m < \tilde{\gamma}_c < \gamma_0 < \hat{\gamma}_m < \hat{\gamma}_c$:

	$\tilde{\gamma}_0$	γ_c	$\hat{\gamma}_m$	γ_m	$\tilde{\gamma}_m$	$\tilde{\gamma}_c$
T		$(p+1)/2$	1	p	γ_0	$p+1$
B	0	$(3-p)/2$	1	1	$(5-p)/4$	$4/3$

– If $\gamma_m < \tilde{\gamma}_c < \hat{\gamma}_m < \gamma_0 < \hat{\gamma}_c$:

For $p < 13/5 = 2.6$:

	$\tilde{\gamma}_0$	$\hat{\gamma}_m$	γ_c	$\hat{\gamma}_m$	γ_m	$\tilde{\gamma}_m$	$\tilde{\gamma}_c$
T		$(p+1)/2$	1	p	γ_0	$(5p-1)/4$	$p+1$
B	0	$(13-5p)/8$	$(3-p)/2$	1	1	$(5-p)/4$	$4/3$

For $p > 13/5 = 2.6$:

	$\hat{\gamma}_m$	γ_c	$(p+1)/2$	1	γ_m	$\tilde{\gamma}_m$	$\tilde{\gamma}_c$
T		$(p+1)/2$	1	p	γ_0	$(5p-1)/4$	$p+1$
B	0	$(3-p)/2$	1	1	$(5-p)/4$	$4/3$	

– etc. The other subcases of F24 and F25 include even more breaks at $\hat{\gamma}_m$, etc. These new breaks are gradually closer and closer, and therefore have a limited signature on the spectral shape. In addition, these extreme radiative cases correspond to physical conditions unlikely to be found in GRB afterglows.

Appendix C: Posterior distributions of the three fits of the afterglow of GW 170817

Figure C.1 give the posterior joint and marginalized distributions of the model parameters for the three fits of the multi-wavelength afterglow of GW 170817 described in Section 4. The three fits use the same observational constraints

and the same priors on the free parameters, and differ only by the radiative treatment: synchrotron only ("no SSC"), synchrotron and SSC assuming that all IC scatterings occur in Thomson regime ("SSC (Thomson)"), and self-consistent calculation of synchrotron and SSC processes taking into account the KN attenuation ("SSC (with KN)"). It appears clearly that the "no SSC" and "SSC (with KN)" fits lead to similar results, whereas the parameters inferred by the "SSC (Thomson)" fit are slightly different (see also Table 4). This especially true for the viewing and core jet opening angles, but also for the kinetic energy and the external density. Note the correlations between these quantities. This difference is due to the fact that the SSC component in the afterglow of GW 170817 is very weak due to the KN attenuation, and is therefore overestimated in the "SSC (Thomson)" case: see discussion in § 4.3.

Case F1	breaks	$\hat{\gamma}_c$	$\hat{\gamma}_m$	$\hat{\gamma}_m$	$\hat{\gamma}_c$	γ_0 undefined					
	f slopes	2			$p+1$						
	h slopes	0			$1/2$					$4/3$	
Case F2	breaks	$\hat{\gamma}_m$	$\hat{\gamma}_0$	$\hat{\gamma}_c$	$\hat{\gamma}_m$	$\hat{\gamma}_c$	$\gamma_0 = \gamma_c Y_c^2$				
	f slopes			2		$p+1$					
	h slopes	0		$1/2$						$4/3$	
Case F3	breaks	$\hat{\gamma}_m$	$\hat{\gamma}_0$	$\hat{\gamma}_c$	$\hat{\gamma}_c$	$\hat{\gamma}_m$	$p+1$	$\gamma_0 = \gamma_c Y_c^2$			
	f slopes				2						
	h slopes	0		$1/2$			$4/3$				
Case F4	breaks	$\hat{\gamma}_m$	$\hat{\gamma}_0$	$\hat{\gamma}_c$	$\hat{\gamma}_c$	2	$\hat{\gamma}_m$	$p+1$	$\gamma_0 = \gamma_c^{8/3} \hat{\gamma}_c^{-5/3} Y_c^2$		
	f slopes										
	h slopes	0		$1/2$			$4/3$				
Case F5	breaks	$\hat{\gamma}_m$	$\hat{\gamma}_c$	$\hat{\gamma}_0$	$\hat{\gamma}_c$	$\hat{\gamma}_m$	$\gamma_0 = \gamma_c Y_c^{3/4}$				
	f slopes				2	$p+1$					
	h slopes	0		$1/2$						$4/3$	
Case F6	breaks	$\hat{\gamma}_m$	$\hat{\gamma}_0$	$\hat{\gamma}_c$	$\hat{\gamma}_c$	$\hat{\gamma}_0$	$\hat{\gamma}_m$	$p+1$	$\gamma_0 = \gamma_c Y_c^{3/4}$		
	f slopes					$2/3$	2				
	h slopes	0		$1/2$		$7/6$		$4/3$			
Case F7	breaks	$\hat{\gamma}_0$	$\hat{\gamma}_m$	$\hat{\gamma}_c$	$\hat{\gamma}_c$	$\hat{\gamma}_m$	$\hat{\gamma}_0$	$p+1$	$\gamma_0 = \gamma_c Y_c^{3/4}$		
	f slopes					$2/3$	$p-1/3$				
	h slopes	0		$(10-3p)/6$		$7/6$		$4/3$			
Case F8	breaks	$\hat{\gamma}_m$	$\hat{\gamma}_c$	$\hat{\gamma}_0$	$\hat{\gamma}_0$	$\hat{\gamma}_c$	$\hat{\gamma}_m$	$p+1$	$\gamma_0 = \gamma_c Y_c^2$		
	f slopes			$3/2$		2					
	h slopes	0		$1/2$		$3/4$		$4/3$			
Case F9	breaks	$\hat{\gamma}_m$	$\hat{\gamma}_c$	$\hat{\gamma}_0$	$\hat{\gamma}_0$	$\hat{\gamma}_c$	$\hat{\gamma}_m$	$p+1$	$\gamma_0 = \gamma_c^{1/2} \hat{\gamma}_c^{-1/2} Y_c = \gamma_c^{1/4} \gamma_{\text{self}}^{3/4} Y_c^{1/2}$		
	f slopes			$3/2$		1	2				
	h slopes	0		$1/2$		1		$4/3$			
Case F10	breaks	$\hat{\gamma}_m$	$\hat{\gamma}_0$	$\hat{\gamma}_c$	$\hat{\gamma}_0$	$\hat{\gamma}_c$	$\hat{\gamma}_m$	$p+1$	$\gamma_0 = \gamma_c Y_c$		
	f slopes				1	2					
	h slopes	0		$1/2$		1		$4/3$			
Case F11	breaks	$\hat{\gamma}_m$	$\hat{\gamma}_0$	$\hat{\gamma}_c$	$\hat{\gamma}_c$	$\hat{\gamma}_0$	$\hat{\gamma}_m$	$p+1$	$\gamma_0 = \gamma_c^{3/4} \hat{\gamma}_c^{1/4} Y_c^{3/4}$		
	f slopes					1	$2/3$	2			
	h slopes	0		$1/2$		$7/6$		$4/3$			
Case F12	breaks	$\hat{\gamma}_0$	$\hat{\gamma}_m$	$\hat{\gamma}_c$	$\hat{\gamma}_c$	$\hat{\gamma}_0$	$\hat{\gamma}_m$	$p+1$	$\gamma_0 = \gamma_c^{3/4} \hat{\gamma}_c^{1/4} Y_c^{3/4}$		
	f slopes					1	$2/3$	$p-1/3$			
	h slopes	0		$(10-3p)/6$		$7/6$		$4/3$			
Case F13	breaks	$\hat{\gamma}_m$	$\hat{\gamma}_c$	$\hat{\gamma}_0$	$\hat{\gamma}_0$	$\hat{\gamma}_c$	$\hat{\gamma}_m$	$p+1$	$\gamma_0 = \gamma_c Y_c^2$		
	f slopes			$3/2$		2					
	h slopes	0		$1/2$		$3/4$		$4/3$			
Case F14	breaks	$\hat{\gamma}_m$	$\hat{\gamma}_c$	$\hat{\gamma}_0$	$\hat{\gamma}_0$	$\hat{\gamma}_c$	$\hat{\gamma}_m$	$p+1$	$\gamma_0 = \gamma_c Y_c^2$		
	f slopes			$3/2$		2					
	h slopes	0		$1/2$		$3/4$		$4/3$			
Case F15	breaks	$\hat{\gamma}_m$	$\hat{\gamma}_c$	$\hat{\gamma}_0$	$\hat{\gamma}_0$	$\hat{\gamma}_c$	$\hat{\gamma}_m$	$p+1$	$\gamma_0 = \gamma_c^{1/2} \hat{\gamma}_0^{1/2} Y_c = \gamma_c^{1/4} \gamma_{\text{self}}^{3/4} Y_c^{1/2}$		
	f slopes			$3/2$		1	2				
	h slopes	0		$1/2$		1		$4/3$			
Case F16	breaks	$\hat{\gamma}_m$	$\hat{\gamma}_c$	$\hat{\gamma}_0$	$\hat{\gamma}_0$	$\hat{\gamma}_m$	$\hat{\gamma}_c$	$p+1$	$\gamma_0 = \gamma_c^{1/2} \hat{\gamma}_0^{1/2} Y_c = \gamma_c^{1/4} \gamma_{\text{self}}^{3/4} Y_c^{1/2}$		
	f slopes			$3/2$		1					
	h slopes	0		$1/2$		1		$4/3$			
Case F17	breaks	$\hat{\gamma}_m$	$\hat{\gamma}_0$	$\hat{\gamma}_c$	$\hat{\gamma}_0$	$\hat{\gamma}_c$	$\hat{\gamma}_m$	$p+1$	$\gamma_0 = \gamma_c Y_c$		
	f slopes				1	2					
	h slopes	0		$1/2$		1		$4/3$			
Case F18	breaks	$\hat{\gamma}_0$	$\hat{\gamma}_m$	$\hat{\gamma}_c$	$\hat{\gamma}_m$	$\hat{\gamma}_0$	$\hat{\gamma}_c$	$p+1$	$\gamma_0 = \gamma_c Y_c$		
	f slopes				1	p					
	h slopes	0		$(3-p)/2$		1		$4/3$			
Case F19	breaks	$\hat{\gamma}_0$	$\hat{\gamma}_c$	$\hat{\gamma}_m$	$\hat{\gamma}_c$	$\hat{\gamma}_0$	$\hat{\gamma}_m$	$p+1$	$\gamma_0 = \gamma_c^{3/4} \hat{\gamma}_c^{1/4} Y_c^{3/4}$		
	f slopes					1	p				
	h slopes	0		$(10-3p)/6$		$(3-p)/2$		$4/3$			
Case F20	breaks	$\hat{\gamma}_c$	$\hat{\gamma}_m$	$\hat{\gamma}_0$	$\hat{\gamma}_0$	$\hat{\gamma}_c$	$\hat{\gamma}_m$	$p+1$	$\gamma_0 = \hat{\gamma}_m Y_c^2$		
	f slopes			$3/2$		2					
	h slopes	0		$1/2$		$3/4$		$4/3$			
Case F21	breaks	$\hat{\gamma}_c$	$\hat{\gamma}_m$	$\hat{\gamma}_0$	$\hat{\gamma}_0$	$\hat{\gamma}_c$	$\hat{\gamma}_m$	$p+1$	$\gamma_0 = \hat{\gamma}_m Y_c^2$		
	f slopes			$3/2$		2					
	h slopes	0		$1/2$		$3/4$		$4/3$			
Case F22	breaks	$\hat{\gamma}_c$	$\hat{\gamma}_m$	$\hat{\gamma}_0$	$\hat{\gamma}_0$	$\hat{\gamma}_c$	$\hat{\gamma}_m$	$p+1$	$\gamma_0 = \hat{\gamma}_m^{1/2} \hat{\gamma}_0^{1/2} Y_c = \hat{\gamma}_m^{1/4} \gamma_{\text{self}}^{3/4} Y_c^{1/2}$		
	f slopes			$3/2$		1	2				
	h slopes	0		$1/2$		1		$4/3$			
Case F23	breaks	$\hat{\gamma}_c$	$\hat{\gamma}_m$	$\hat{\gamma}_0$	$\hat{\gamma}_0$	$\hat{\gamma}_c$	$\hat{\gamma}_m$	$p+1$	$\gamma_0 = \hat{\gamma}_m^{1/2} \hat{\gamma}_0^{1/2} Y_c = \hat{\gamma}_m^{1/4} \gamma_{\text{self}}^{3/4} Y_c^{1/2}$		
	f slopes			$3/2$		1	2				
	h slopes	0		$1/2$		1		$4/3$			
Case F26	breaks	$\hat{\gamma}_c$	$\hat{\gamma}_m$	$\hat{\gamma}_0$	$\hat{\gamma}_0$	$\hat{\gamma}_c$	$\hat{\gamma}_m$	$p+1$	$\gamma_0 = \hat{\gamma}_m Y_c^2$		
	f slopes			$p+1$		$p+1/2$					
	h slopes	0				$1/2$		$4/3$			
Case F27	breaks	$\hat{\gamma}_c$	$\hat{\gamma}_m$	$\hat{\gamma}_0$	$\hat{\gamma}_0$	$\hat{\gamma}_c$	$\hat{\gamma}_m$	$p+1$	$\gamma_0 = \hat{\gamma}_m^{3/8} \hat{\gamma}_c^{5/8} Y_c^{3/4}$		
	f slopes			$p+1$		$p-1/3$					
	h slopes	0		$1/2$		$4/3$					

Table B.1. Fast cooling: list of all possible radiative regimes and corresponding electron distribution. For each case, the first row of the table gives the list of breaks appearing either in the normalized electron distribution $f(x)$, i.e. the list of x_i , or in the normalized Compton parameter $h(x)$, i.e. list of relevant \hat{x}_i , as well as all other necessary characteristic Lorentz factors to fully define the case in agreement with figure B.1 (blue). The break corresponding to the peak of the synchrotron spectrum is highlighted in red. The second and third rows give the slopes $-d \ln f / d \ln x$ and $-d \ln g / d \ln x$ for each branch. Finally, the last column gives the expression of γ_0 . Cases F24 and F25 require a specific treatment: see text in appendix B.

Case S1	breaks	$\hat{\gamma}_m$	$\hat{\gamma}_c$	$\hat{\gamma}_c$	$\hat{\gamma}_m$	γ_0 undefined		
	f slopes	p	$p+1$	$(3-p)/2$	$4/3$			
	h slopes	0						
Case S2	breaks	$\hat{\gamma}_m$	$\hat{\gamma}_c$	2	$\hat{\gamma}_c$	$\hat{\gamma}_m$	$\gamma_0 = \gamma_c Y_c^{2/(3-p)}$	
	f slopes	p	$p+1$	$(3-p)/2$	$4/3$			
	h slopes	0						
Case S3	breaks	$\hat{\gamma}_c$	$\hat{\gamma}_c$	$\hat{\gamma}_m$	$\hat{\gamma}_c$	$\hat{\gamma}_m$	$\gamma_0 = \gamma_c Y_c^{2/(3-p)}$	
	f slopes	2	$p+1$	$(3-p)/2$	$4/3$			
	h slopes	0						
Case S4	breaks	$\hat{\gamma}_c$	$\hat{\gamma}_c$	$\hat{\gamma}_m$	2	$\hat{\gamma}_m$	$\hat{\gamma}_c$	$\gamma_0 = \gamma_c^{8/(9-3p)} \hat{\gamma}_m^{(1-3p)/(9-3p)} Y_c^{2/(3-p)}$
	f slopes	$p+1$	$(3-p)/2$	$4/3$				
	h slopes	0						
Case S5	breaks	$\hat{\gamma}_c$	$\hat{\gamma}_m$	$\hat{\gamma}_m$	$\hat{\gamma}_c$	$p+1$	$\gamma_0 = \gamma_c Y_c^{3/4}$	
	f slopes	p	$4/3$	$p+1$				
	h slopes	0	$(3-p)/2$					
Case S6	breaks	$\hat{\gamma}_c$	$\hat{\gamma}_c$	$\hat{\gamma}_m$	$\hat{\gamma}_c$	$p+1$	$\gamma_0 = \gamma_c^{8/(9-3p)} \hat{\gamma}_m^{(1-3p)/(9-3p)} Y_c^{2/(3-p)}$	
	f slopes	p	$4/3$	$p+1$				
	h slopes	0	$(3-p)/2$					
Case S7	breaks	$\hat{\gamma}_c$	$\hat{\gamma}_m$	$\hat{\gamma}_c$	$\hat{\gamma}_m$	$\hat{\gamma}_c$	$\gamma_0 = \gamma_c Y_c^{3/4}$	
	f slopes	p	$p+1$	$4/3$				
	h slopes	0	$(3-p)/2$					
Case S8	breaks	$\hat{\gamma}_0$	$\hat{\gamma}_c$	$\hat{\gamma}_m$	$\hat{\gamma}_c$	$\hat{\gamma}_c$	$\hat{\gamma}_0$	$\gamma_0 = \gamma_c Y_c^{3/4}$
	f slopes	$p-1/3$	$p+1$	$4/3$				
	h slopes	0	$(10-3p)/6$	$(3-p)/2$				
Case S9	breaks	$\hat{\gamma}_0$	$\hat{\gamma}_c$	$\hat{\gamma}_m$	$\hat{\gamma}_c$	$\hat{\gamma}_c$	$\hat{\gamma}_0$	$\gamma_0 = \gamma_c Y_c^{3/4}$
	f slopes	$p-1/3$	$p+1$	$4/3$				
	h slopes	0	$(10-3p)/6$	$(3-p)/2$				
Case S10 ($p < 7/3$)	breaks	$\hat{\gamma}_0$	$\hat{\gamma}_c$	$\hat{\gamma}_m$	$\hat{\gamma}_c$	$\hat{\gamma}_c$	$\hat{\gamma}_0$	$\gamma_0 = \gamma_c Y_c^{2/(3-p)}$
	f slopes	p	$(3p-1)/2$	$p+1$				
	h slopes	0	$(7-3p)/4$	$(3-p)/2$	$4/3$			
Case S10 ($p > 7/3$)	breaks	$\hat{\gamma}_0$	$\hat{\gamma}_c$	$\hat{\gamma}_m$	$\hat{\gamma}_c$	$\hat{\gamma}_m$	$\gamma_0 = \gamma_c Y_c^{2/(3-p)}$	
	f slopes	p	$(3p-1)/2$	$p+1$				
	h slopes	0	$(3-p)/2$	$4/3$				
Case S11 ($p < 7/3$)	breaks	$\hat{\gamma}_0$	$\hat{\gamma}_m$	$\hat{\gamma}_c$	$\hat{\gamma}_c$	$\hat{\gamma}_m$	$\hat{\gamma}_c$	$\gamma_0 = \hat{\gamma}_m^{(3p-1)/8} \gamma_c^{(9-3p)/8} Y_c^{3/4}$
	f slopes	p	$(3p-1)/2$	$p-1/3$	$p+1$			
	h slopes	0	$(10-3p)/6$	$(7-3p)/4$	$(3-p)/2$	$4/3$		
Case S11 ($p > 7/3$)	breaks	$\hat{\gamma}_0$	$\hat{\gamma}_m$	$\hat{\gamma}_c$	$\hat{\gamma}_c$	$\hat{\gamma}_m$	$\hat{\gamma}_0$	$\gamma_0 = \hat{\gamma}_m^{(3p-1)/8} \gamma_c^{(9-3p)/8} Y_c^{3/4}$
	f slopes	p	$(3p-1)/2$	$p-1/3$	$p+1$			
	h slopes	0	$(3-p)/2$	$4/3$				
Case S12 ($p < 7/3$)	breaks	$\hat{\gamma}_m$	$\hat{\gamma}_c$	$\hat{\gamma}_c$	$\hat{\gamma}_c$	$\hat{\gamma}_m$	$\gamma_0 = \gamma_c Y_c^{2/(3-p)}$	
	f breaks	p	$(3p-1)/2$	$p+1$				
	h breaks	0	$(7-3p)/4$	$(3-p)/2$	$4/3$			
Case S12 ($p > 7/3$)	breaks	$\hat{\gamma}_m$	$\hat{\gamma}_c$	$\hat{\gamma}_c$	$\hat{\gamma}_c$	$\hat{\gamma}_m$	$\gamma_0 = \gamma_c Y_c^{2/(3-p)}$	
	f breaks	p	$(3p-1)/2$	$p+1$				
	h breaks	0	$(3-p)/2$	$4/3$				
Case S13 ($p < 7/3$)	breaks	$\hat{\gamma}_0$	$\hat{\gamma}_m$	$\hat{\gamma}_c$	$\hat{\gamma}_c$	$\hat{\gamma}_m$	$\gamma_0 = \gamma_c Y_c^{2/(3-p)}$	
	f slope	p	$(3p-1)/2$	$p+1$				
	h slope	0	$(7-3p)/4$	$(3-p)/2$	$4/3$			
Case S13 ($p > 7/3$)	breaks	$\hat{\gamma}_0$	$\hat{\gamma}_m$	$\hat{\gamma}_c$	$\hat{\gamma}_c$	$\hat{\gamma}_m$	$\gamma_0 = \gamma_c Y_c^{2/(3-p)}$	
	f slope	p	$(3p-1)/2$	$p+1$				
	h slope	0	$(3-p)/2$	$4/3$				
Case S14 ($p < 7/3$)	breaks	$\hat{\gamma}_0$	$\hat{\gamma}_m$	$\hat{\gamma}_c$	$\hat{\gamma}_c$	$\hat{\gamma}_m$	$\hat{\gamma}_0$	$\gamma_0 = \hat{\gamma}_m^{(3p-1)/8} \gamma_c^{(9-3p)/8} Y_c^{3/4}$
	f slopes	$p-1/3$	$p+1$	$4/3$				
	h slopes	0	$(10-3p)/6$	$(7-3p)/4$	$(3-p)/2$			
Case S14 ($p > 7/3$)	breaks	$\hat{\gamma}_0$	$\hat{\gamma}_m$	$\hat{\gamma}_c$	$\hat{\gamma}_c$	$\hat{\gamma}_m$	$\hat{\gamma}_0$	$\gamma_0 = \hat{\gamma}_m^{(3p-1)/8} \gamma_c^{(9-3p)/8} Y_c^{3/4}$
	f slopes	p	$(3p-1)/2$	$p-1/3$	$p+1$			
	h slopes	0	$(3-p)/2$	$4/3$				
Case S15	breaks	$\hat{\gamma}_m$	$\hat{\gamma}_c$	$\hat{\gamma}_c$	$\hat{\gamma}_c$	$\hat{\gamma}_m$	$\gamma_0 = \gamma_c Y_c^{2/(3-p)}$	
	f slopes	p	$p+1$	$(3p-1)/2$	$p+1$			
	h slopes	0	$(3-p)/2$	$4/3$				
Case S16	breaks	$\hat{\gamma}_m$	$\hat{\gamma}_c$	$\hat{\gamma}_c$	$\hat{\gamma}_m$	$\hat{\gamma}_c$	$\gamma_0 = \hat{\gamma}_m^{(3p-1)/8} \gamma_c^{(9-3p)/8} Y_c^{3/4}$	
	f slopes	p	$p+1$	$(3p-1)/2$	$p-1/3$	$p+1$		
	h slopes	0	$(3-p)/2$	$4/3$				

Table B.2. Slow cooling: list of all possible radiative regimes and corresponding electron distribution. Same convention as in table B.1.

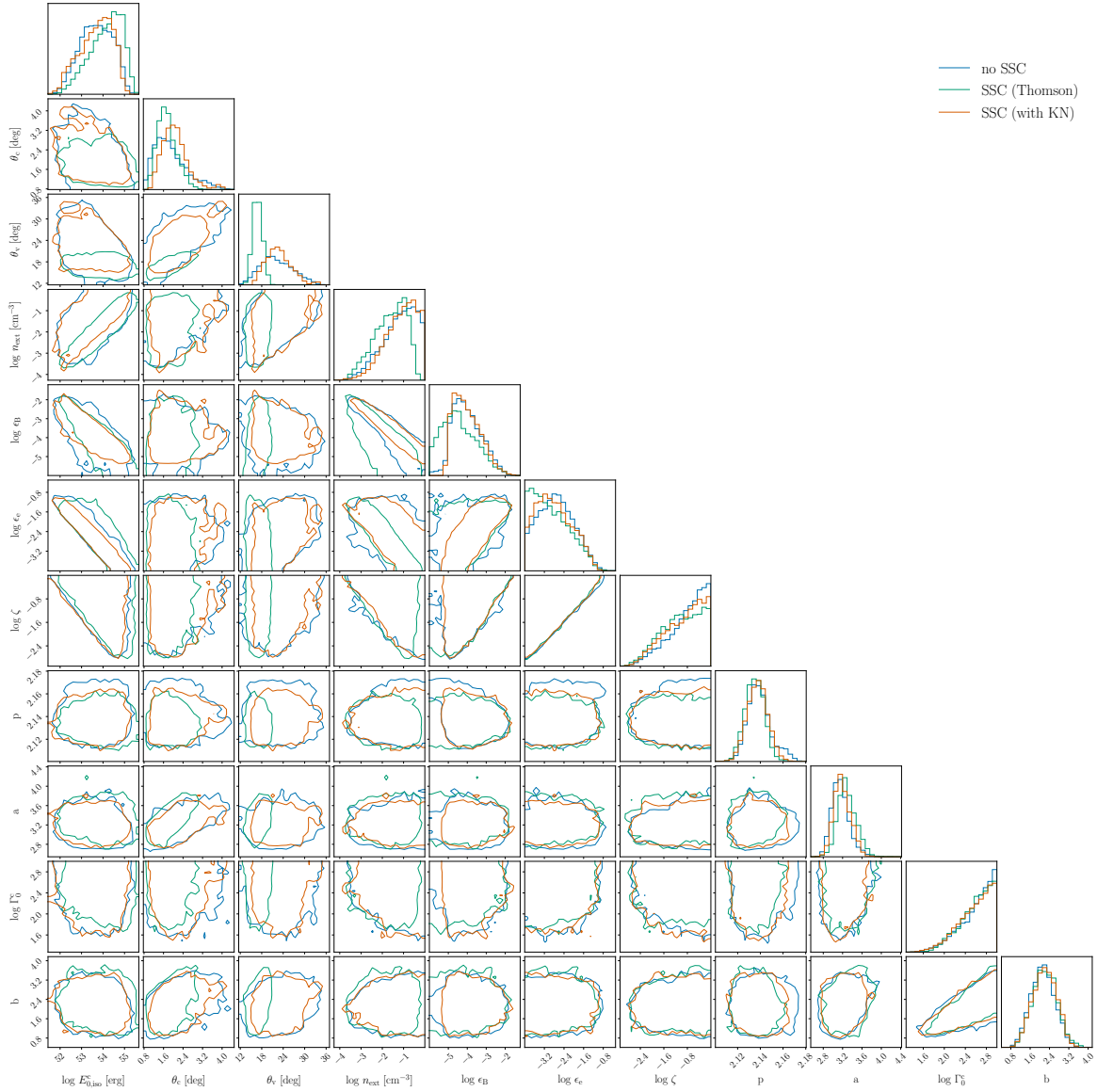


Fig. C.1. Posterior joint and marginalized distributions of the model's free parameters, $E_{0,iso}^c$, θ_c , θ_v , n_{ext} , ϵ_B , ϵ_e , ζ , p , a , Γ_0^c , b for the three fits of the afterglow of GW 170817 presented in section 4, which differ only by the treatment of the radiative processes: in blue, no SSC diffusions are taken into account ("no SSC"); in green, SSC diffusions are assumed to be only in the Thomson regime ("SSC (Thomson)"); in orange, the SSC diffusion is depleted at high energy in the Klein-Nishina regime ("SSC (with KN)"). The colored contours correspond to the 3σ confidence intervals for each model and each parameter.



GRANDMA and HXMT Observations of GRB 221009A: The Standard Luminosity Afterglow of a Hyperluminous Gamma-Ray Burst—In Gedenken an David Alexander Kann

D. A. Kann¹, S. Agayeva², V. Aivazyan^{3,4}, S. Alishov², C. M. Andrade⁵, S. Antier⁶, A. Baransky⁷, P. Bendjoya⁸, Z. Benkhaldoun⁹, S. Beradze^{3,4}, D. Berezin^{10,11}, M. Boër⁶, E. Broens¹², S. Brunier⁸, M. Bulla^{13,14,15}, O. Burkhonov¹⁶, E. Burns¹⁷, Y. Chen¹⁸, Y. P. Chen¹⁸, M. Conti¹⁹, M. W. Coughlin⁵, W. W. Cui¹⁸, F. Daigne²⁰, B. Delaveau²¹, H. A. R. Devillepoix²², T. Dietrich^{23,24}, D. Dornic²⁵, F. Dubois^{26,27}, J.-G. Ducoin²⁰, E. Durand²¹, P.-A. Duverne²⁸, H.-B. Eggenstein²⁹, S. Ehgamberdiev^{16,30}, A. Fouad³¹, M. Freeberg³², D. Froebrich³³, M. Y. Ge¹⁸, S. Gervasoni⁶, V. Godunova^{10,11}, P. Gokuldass³⁴, E. Gurbanov², D. W. Han¹⁸, E. Hasanov², P. Hello³⁵, T. Husenot-Desenonges³⁵, R. Inasaridze^{3,4}, A. Iskandar³⁶, N. Ismailov², A. Janati⁹, T. Jegou du Laz³⁵, S. M. Jia¹⁸, S. Karpov³⁷, A. Kaecouch³⁸, R. W. Kiendrebeogo^{5,6,39}, A. Klotz^{40,41}, R. Kneip⁴², N. Kochiashvili³, N. Kunert²³, A. Letic²¹, S. Leonini¹⁹, C. K. Li¹⁸, W. Li¹⁸, X. B. Li¹⁸, J. Y. Liao¹⁸, L. Logie^{26,27}, F. J. Lu¹⁸, J. Mao^{43,44,45}, D. Marchais⁴⁶, R. Ménard⁴⁷, D. Morris⁴⁸, R. Natsvlishvili³, V. Nedora²⁴, K. Noonan⁴⁸, K. Noysena⁴⁹, N. B. Orange⁵⁰, P. T. H. Pang^{51,52}, H. W. Peng⁵³, C. Pellouin²⁰, J. Peloton³⁵, T. Pradier⁵⁴, O. Pyshna⁷, Y. Rajabov¹⁶, S. Rau^{26,27}, C. Rinner⁹, J.-P. Rivet⁸, F. D. Romanov⁵⁵, P. Rosi¹⁹, V. A. Rupchandani^{56,57}, M. Serrau⁵⁸, A. Shokry³¹, A. Simon^{59,60}, K. Smith⁴⁸, O. Sokoliuk^{7,10}, M. Soliman⁶¹, L. M. Song¹⁸, A. Takey³¹, Y. Tillyayev^{16,30}, L. M. Tinjaca Ramirez¹⁹, I. Tosta e Melo⁶², D. Turpin⁶³, A. de Ugarte Postigo⁶, S. Vanaverbeke^{26,27}, V. Vasilenko^{59,60}, D. Vernet⁶⁴, Z. Vidadı², C. Wang⁶⁵, J. Wang¹⁸, L. T. Wang³⁶, X. F. Wang^{53,66}, S. L. Xiong¹⁸, Y. P. Xu¹⁸, W. C. Xue¹⁸, X. Zeng⁶⁷, S. N. Zhang¹⁸, H. S. Zhao¹⁸, and X. F. Zhao¹⁸

¹ Hessian Research Cluster ELEMENTS, Giersch Science Center, Max-von-Laue-Straße 12, Goethe University Frankfurt, Campus Riedberg, D-60438 Frankfurt am Main, Germany; grandma-1@in2p3.fr

² N. Tusi Shamakhy Astrophysical Observatory, Azerbaijan National Academy of Sciences, settl.Y. Mammadaliyev, AZ 5626, Shamakhy, Azerbaijan

³ E. Kharadze Georgian National Astrophysical Observatory, Mt. Kanobili, Abastumani, 0301, Adigeni, Georgia

⁴ Samtskhe-Javakheti State University, Rustaveli Str. 113, Akhaltsikhe, 0080, Georgia

⁵ School of Physics and Astronomy, University of Minnesota, Minneapolis, MN 55455, USA

⁶ Artemis, Observatoire de la Côte d'Azur, Université Côte d'Azur, Boulevard de l'Observatoire, F-06304 Nice, France

⁷ Astronomical Observatory of Taras Shevchenko National University of Kyiv, Observatorna Str. 3, Kyiv, 04053, Ukraine

⁸ Université Côte d'Azur, Observatoire de la Côte d'Azur, CNRS UMR 7293 Laboratoire Lagrange, F 06108 Nice, France

⁹ Oukaïmeden Observatory, High Energy Physics and Astrophysics Laboratory, FSSM, Cadi Ayyad University, Av. Prince My Abdellah, BP 2390 Marrakesh, Morocco

¹⁰ Main Astronomical Observatory of National Academy of Sciences of Ukraine, 27 Acad. Zabolotnoho Str., Kyiv, 03143, Ukraine

¹¹ ICAMER Observatory, National Academy of Sciences of Ukraine, 27 Acad. Zabolotnoho Str., 03143 Kyiv, Ukraine

¹² Vereniging Voor Sterrenkunde, Balen-Neetlaan 18A, B-2400, Mol, Belgium

¹³ Department of Physics and Earth Science, University of Ferrara, via Saragat 1, I-44122 Ferrara, Italy

¹⁴ INFN, Sezione di Ferrara, via Saragat 1, I-44122 Ferrara, Italy

¹⁵ INAF, Osservatorio Astronomico d'Abruzzo, via Mentore Maggini snc, I-64100 Teramo, Italy

¹⁶ Ulugh Beg Astronomical Institute, Uzbekistan Academy of Sciences, Astronomy Str. 33, Tashkent 100052, Uzbekistan

¹⁷ Department of Physics & Astronomy, Louisiana State University, Baton Rouge, LA 70803, USA

¹⁸ Key Laboratory of Particle Astrophysics, Institute of High Energy Physics, Chinese Academy of Sciences, Beijing 100049, People's Republic of China
xiongs1@ihep.ac.cn

¹⁹ Montarrenti Observatory, S.S. 73 Ponente, I-53018 Sovicille, Siena, Italy

²⁰ Sorbonne Université, CNRS, UMR 7095, Institut d'Astrophysique de Paris, 98 bis bd Arago, F-75014 Paris, France

²¹ Institut Polytechnique des Sciences Avancées IPSA, 63 bis Boulevard de Brandebourg, F-94200 Ivry-sur-Seine, France

²² Space Science & Technology Centre, School of Earth and Planetary Sciences, Curtin University, GPO Box U1987, Perth, WA 6845, Australia

²³ Institute for Physics and Astronomy, University of Potsdam, Haus 28, Karl-Liebknecht-Str. 24/25, D-14476 Potsdam, Germany

²⁴ Max Planck Institute for Gravitational Physics (Albert Einstein Institute), Am Mühlenberg 1, D-14476 Potsdam, Germany

²⁵ CPPM, Aix Marseille Univ, CNRS/IN2P3, CPPM, Marseille, France

²⁶ AstroLAB IRIS, Provinciaal Domein "De Palingbeek", Verbrandemolenstraat 5, B-8902 Zillebeke, Ieper, Belgium

²⁷ Vereniging Voor Sterrenkunde (VVS), Oostmeers 122 C, B-8000 Brugge, Belgium

²⁸ Université Paris Cité, CNRS, Astroparticule et Cosmologie, F-75013 Paris, France

²⁹ Volkssternwarte Paderborn, Im Schlosspark 13, D-33104 Paderborn, Germany

³⁰ National University of Uzbekistan, 4 University Str., Tashkent 100174, Uzbekistan

³¹ National Research Institute of Astronomy and Geophysics (NRIAG), 1 El-marsad St., 11421 Helwan, Cairo, Egypt

³² KNC, AAVSO, Hidden Valley Observatory (HVO), Colfax, WI, USA; iTelescope, New Mexico Skies Observatory, Mayhill, NM, USA

³³ School of Physics and Astronomy, University of Kent, Canterbury CT2 7NH, UK

³⁴ Department of Aerospace, Physics, and Space Sciences, Florida Institute of Technology, Melbourne, FL 32901, USA

³⁵ IJCLab, Univ Paris-Saclay, CNRS/IN2P3, Orsay, France

³⁶ Xinjiang Astronomical Observatory (XAO), Chinese Academy of Sciences, Urumqi, 830011, People's Republic of China

³⁷ CEICO, Institute of Physics of the Czech Academy of Sciences, Na Slovance 1999/2, CZ-182 21, Praha, Czech Republic

³⁸ Oukaïmeden Observatory, Cadi Ayyad University, High Atlas Observatory, Morocco

³⁹ Laboratoire de Physique et de Chimie de l'Environnement, Université Joseph KI-ZERBO, Ouagadougou, Burkina Faso

⁴⁰ IRAP, Université de Toulouse, CNRS, UPS, 14 Avenue Edouard Belin, F-31400 Toulouse, France

⁴¹ Université Paul Sabatier Toulouse III, Université de Toulouse, 118 Route de Narbonne, F-31400 Toulouse, France

⁴² K26 / Contern Observatory (private obs.), 1, beim Schmilberbour, 5316 Contern, Luxembourg

⁴³ Yunnan Observatories, Chinese Academy of Sciences, 650011 Kunming, Yunnan Province, People's Republic of China

⁴⁴ Center for Astronomical Mega-Science, Chinese Academy of Sciences, 20A Datun Road, Chaoyang District, 100012 Beijing, People's Republic of China

- ⁴⁵ Key Laboratory for the Structure and Evolution of Celestial Objects, Chinese Academy of Sciences, 650011 Kunming, People's Republic of China
- ⁴⁶ Observatoire du Crous des Gats, F-31550 Cintegabelle, France
- ⁴⁷ Club d'astronomie Mont-Tremblant, 545 Chemin Saint-Bernard, Mont-Tremblant, QC, J8E 1S8, Canada
- ⁴⁸ University of the Virgin Islands, United States Virgin Islands 00802, USA
- ⁴⁹ National Astronomical Research Institute of Thailand (Public Organization), 260, Moo 4, T. Donkaew, A. Mae Rim, Chiang Mai, 50180, Thailand
- ⁵⁰ OrangeWave Innovative Science, LLC, Moncks Corner, SC 29461, USA
- ⁵¹ Nikhef, Science Park 105, 1098 XG Amsterdam, The Netherlands
- ⁵² Institute for Gravitational and Subatomic Physics (GRASP), Utrecht University, Princetonplein 1, 3584 CC Utrecht, The Netherlands
- ⁵³ Physics Department, Tsinghua University, Beijing, 100084, People's Republic of China
- ⁵⁴ Université de Strasbourg, CNRS, IPHC UMR 7178, F-67000 Strasbourg, France
- ⁵⁵ AAVSO Observer; Pobedy Street, House 7, Flat 60, Yuzhno-Morskoy, Nakhodka, Primorsky Krai 692954, Russia
- ⁵⁶ Brown University, Providence, RI 02912, USA
- ⁵⁷ American University of Sharjah, Sharjah, UAE
- ⁵⁸ Société Astronomique de France, Observatoire de Dauban, F-04150 Banon, France
- ⁵⁹ Astronomy and Space Physics Department, Taras Shevchenko National University of Kyiv, Glushkova Ave., 4, Kyiv, 03022, Ukraine
- ⁶⁰ National Center Junior Academy of Sciences of Ukraine, Dehtiarivska St. 38-44, Kyiv, 04119, Ukraine
- ⁶¹ Department of Astronomy and Meteorology, Faculty of Science, Al-Azhar University, 11884 Nasr City, Cairo, Egypt
- ⁶² INFN, Laboratori Nazionali del Sud, I-95125 Catania, Italy
- ⁶³ Université Paris-Saclay, Université Paris Cité, CEA, CNRS, AIM, F-91191, Gif-sur-Yvette, France
- ⁶⁴ Observatoire de la Côte d'Azur, CNRS, UMS Galilée, France
- ⁶⁵ National Astronomical Observatories, Chinese Academy of Sciences, Beijing 100012, People's Republic of China
- ⁶⁶ Beijing Planetarium, Beijing Academy of Science and Technology, Beijing, 100044, People's Republic of China
- ⁶⁷ Center for Astronomy and Space Sciences, China Three Gorges University, Yichang 443000, People's Republic of China
- Received 2023 February 13; revised 2023 March 26; accepted 2023 March 26; published 2023 May 9

Abstract

Object GRB 221009A is the brightest gamma-ray burst (GRB) detected in more than 50 yr of study. In this paper, we present observations in the X-ray and optical domains obtained by the GRANDMA Collaboration and the Insight Collaboration. We study the optical afterglow with empirical fitting using the GRANDMA+HXMT-LE data sets augmented with data from the literature up to 60 days. We then model numerically using a Bayesian approach, and we find that the GRB afterglow, extinguished by a large dust column, is most likely behind a combination of a large Milky Way dust column and moderate low-metallicity dust in the host galaxy. Using the GRANDMA+HXMT-LE+XRT data set, we find that the simplest model, where the observed afterglow is produced by synchrotron radiation at the forward external shock during the deceleration of a top-hat relativistic jet by a uniform medium, fits the multiwavelength observations only moderately well, with a tension between the observed temporal and spectral evolution. This tension is confirmed when using the augmented data set. We find that the consideration of a jet structure (Gaussian or power law), the inclusion of synchrotron self-Compton emission, or the presence of an underlying supernova do not improve the predictions. Placed in the global context of GRB optical afterglows, we find that the afterglow of GRB 221009A is luminous but not extraordinarily so, highlighting that some aspects of this GRB do not deviate from the global known sample despite its extreme energetics and the peculiar afterglow evolution.

Unified Astronomy Thesaurus concepts: [Optical astronomy \(1776\)](#); [Optical telescopes \(1174\)](#); [Interstellar dust extinction \(837\)](#); [Gamma-ray bursters \(1878\)](#); [Astronomy data modeling \(1859\)](#)

1. Introduction

Gamma-ray bursts (GRBs) are among the most energetic phenomena detected in the universe. They release extreme amounts of energy in soft gamma rays, up to $1 M_{\odot}$ assuming isotropic emission (Kulkarni et al. 1999; Atteia et al. 2017), and can also be exceedingly luminous in the optical domain (Akerlof et al. 1999; Boër et al. 2006; Kann et al. 2007; Racusin et al. 2008; Bloom et al. 2009; Jin et al. 2023).

The GRBs exhibit durations⁶⁸ from milliseconds up to several hours (e.g., Thöne et al. 2011; Gendre et al. 2013; Levan et al. 2014b). They have been historically divided

(Mazets et al. 1981; Kouveliotou et al. 1993) into two classes based on their duration and spectral hardness.

So-called “short/hard GRBs” have durations of a few seconds or less and a harder spectrum with respect to their isotropic energy release (e.g., Minaev & Pozanenko 2020; Agüí Fernández et al. 2023). They have been linked to gravitational waves (Abbott et al. 2017a, 2017b, 2017c; Goldstein et al. 2017), and their progenitors are supposed to be mainly coalescing compact objects such as binary neutron stars or neutron star–black hole binary systems (for reviews, see Nakar 2007; Berger 2014). The general short/hard paradigm has been called into question, especially with the long-duration event GRB 211211A (Rastinejad et al. 2022; Troja et al. 2022; Yang et al. 2022), which has been claimed to be associated with kilonova emission, a hallmark of compact binary mergers.

Conversely, so-called “long/soft GRBs” generally have durations greater than a few seconds and a softer spectrum, and their origin is most likely related to the core collapse of rapidly rotating massive stars (Woosley 1993; Mösta et al. 2015). Similar to the case of short GRBs, the long/soft paradigm has been called into question by GRB 200826A, a subsecond GRB clearly associated

⁶⁸ Usually measured as T_{90} , denoting the time span during which 90% of the emission, from 5% to 95%, is accumulated. The T_{90} durations are detector-dependent and can include gamma-ray tail emission in bright bursts.

with supernova (SN) emission (Zhang et al. 2021; Ahumada et al. 2021; Rossi et al. 2022). For reviews of long GRBs and their connection to stripped-envelope SN explosions, see Gehrels et al. (2009), Hjorth & Bloom (2012), and Cano et al. (2017).

The luminosity of GRB afterglows (in the X-ray to optical/near-infrared, NIR, energy range) is moderately correlated with the isotropic prompt emission (mostly gamma-ray) energy release E_{iso} (Gehrels et al. 2008; Nysewander et al. 2009; Kann et al. 2010, 2011), so very luminous GRBs usually have more luminous afterglows, and of course, a low distance also implies a brighter afterglow that can be more easily followed up. A combination of these two features therefore usually yields the richest data sets for any electromagnetic study. Two examples of such well-studied, nearby bright GRBs are GRBs 030329 and 130427A. The first occurred at $z = 0.16867 \pm 0.00001$ (Thöne et al. 2007) and is to this day the GRB afterglow with the most optical/NIR observations. It yielded data for a wide range of studies of the prompt emission, afterglow evolution and polarization, and associated SN 2003dh (Matheson et al. 2003; Stanek et al. 2003; Hjorth et al. 2003; Greiner et al. 2003; Lipkin et al. 2004; Vanderspek et al. 2004). The second, GRB 130427A, is the first known nearby GRB ($z = 0.3399 \pm 0.0002$; Selsing et al. 2019) that exhibited an E_{iso} in the range of “cosmological” GRBs at $z \gtrsim 1$. There is also a rich observational data set for this event, stretching from trigger time to nearly 100 Ms (e.g., Levan et al. 2014a; Melandri et al. 2014; Perley et al. 2014; van der Horst et al. 2014; Vestrand et al. 2014; Ackermann et al. 2014; Maselli et al. 2014; De Pasquale et al. 2016).

In this paper, we report observations by the GRANDMA collaboration and its partners of the paragon of nearby bright GRBs, GRB 221009A, by far the brightest GRB observed to date.

On 2022 October 9 at 14:10:17 UT, the Burst Alert Telescope (BAT; Barthelmy et al. 2005) on board the Neil Gehrels Swift Observatory satellite (hereafter Swift; Gehrels et al. 2004) triggered and located a new, X-ray bright transient denoted as Swift J1913.1+1946 (triggers 1126853 and 1126854; Dichiaro et al. 2022a, 2022b). Swift immediately slewed to the position, and its narrow-field instruments, the X-Ray Telescope (XRT; Burrows et al. 2005) and the Ultraviolet/Optical Telescope (UVOT; Roming et al. 2005), discovered a transient that was very bright in X-rays (>800 counts s^{-1}) and moderately bright in the optical (unfiltered finding chart, white = 16.63 ± 0.14 mag). The optical detection was somewhat remarkable, as the transient lies in the Galactic plane, and extinction along the line of sight is very high, $E_{(B-V)} = 1.32$ mag/ $A_V = 4.1$ mag (Schlafly & Finkbeiner 2011, hereafter SF11). It was furthermore reported that the source was also detected more than 10 minutes earlier by the Gas Slit Camera of the MAXI X-ray detector on board the International Space Station (Negoro et al. 2022; Kobayashi et al. 2022; Williams et al. 2023). Overall, this is in agreement with a new Galactic transient.

About 6.5 hr after the Swift trigger, it was reported by Kennea et al. (2022b) that this source might be a GRB, GRB 221009A, as both the Gamma-Ray Burst Monitor (GBM; Meegan et al. 2009) and the Large Area Telescope (LAT; Atwood et al. 2009) of the Fermi observatory (GLAST Facility Science Team et al. 1999) triggered on a GRB⁶⁹ localized to the same sky position at 13:16:59.99 UT, which we henceforth

use as trigger time T_0 . This event turned out to be extraordinarily bright (Veres et al. 2022)—not just the brightest event ever detected by GBM, but the brightest ever detected.

The event begins with a moderately bright precursor, followed by ≈ 180 s of quiescence before the main phase starts. The first peak, ≈ 20 s long, would already place GRB 221009A among the brightest GRBs ever detected, exceeding all but a handful of GBM/Konus detections. This peak is followed by two ultrabright peaks and finally a fourth, less bright but longer peak that fades into a high-energy afterglow at ≈ 600 s. The extreme fluence led to a saturation of all sensitive gamma-ray detectors, such as Fermi GBM (Lesage et al. 2022), Fermi LAT (Omodei et al. 2022a, 2022b; Bissaldi et al. 2022; Pillera et al. 2022), Konus-Wind (Frederiks et al. 2022, 2023), Insight-HXMT/HE (Tan et al. 2022; Ge et al. 2022), AGILE/MCAL+AC (Ursi et al. 2022), and INTEGRAL SPI/ACS (Gotz et al. 2022).

This saturation leads to preliminary analyses reporting only lower limits on the true fluence. INTEGRAL SPI/ACS (Gotz et al. 2022) analysis found 1.3×10^{-2} erg cm^{-2} , Fermi GBM found $(2.912 \pm 0.001) \times 10^{-2}$ erg cm^{-2} and peak flux 2385 ± 3 photons $\text{s}^{-1} \text{cm}^{-2}$ (Lesage et al. 2022), Konus-Wind reported 5.2×10^{-2} erg cm^{-2} (Frederiks et al. 2022), and Kann & Agui Fernandez (2022) estimated $\approx 9 \times 10^{-2}$ erg cm^{-2} . Even these preliminary estimates show that GRB 221009A exceeded GRB 130427A in fluence by a factor of at least 10. Recently, Frederiks et al. (2023) presented the full Konus-Wind analysis, which yields a fluence more than twice as high as that derived by Kann & Agui Fernandez (2022), leading to an isotropic energy release $E_{\text{iso}} > 10^{55}$ erg, twice as high as the previous record holder.

Several smaller orbital detectors were not saturated, stemming from size, environment, or off-axis detection, such as detectors on Insight (the low-energy, LE, telescope and the particle monitors; Ge et al. 2022), SATech-01/GECAM-C HEBS (Liu et al. 2022), GRBAlpha (Ripa et al. 2022, 2023), STPSat-6/SIRI-2 (Mitchell et al. 2022), and SRG/ART-XC (Lapshov et al. 2022; Frederiks et al. 2023).

Optical spectroscopy of the transient showed it to indeed be a GRB afterglow, with a redshift $z = 0.151$ measured in both absorption and emission (de Ugarte Postigo et al. 2022; Castro-Tirado et al. 2022; Izzo et al. 2022; Malesani et al. 2023), making it even closer than GRB 030329. Such an event is ultrarare; e.g., Atteia (2022) estimated it to occur only once every half-millennium. Williams et al. (2023), O’Connor et al. (2023), and Malesani et al. (2023) also discussed the rate of events, finding estimates of the same order. Using the significantly higher fluence from Frederiks et al. (2023), Burns et al. (2023) derived an even more extreme value, finding a repetition rate of once every $\approx 10,000$ yr, a once-in-all-human-civilization event.

The GRB showed very strong very high energy (VHE) emission, with an ≈ 400 GeV photon detected by Fermi LAT (Xia et al. 2022a, 2022b), a highly significant detection by AGILE/GRID (Piano et al. 2022), photons of ≈ 10 GeV seen more than 2 weeks after the GRB by DAMPE (Duan et al. 2022), the spectacular detection by LHAASO of thousands of VHE photons up to 18 TeV (Huang et al. 2022), and potentially even a 250 TeV photon detected by Carpet-2 (Dzhappuev et al. 2022).

The burst caused a sudden ionospheric disturbance (Schnoor et al. 2022; Guha & Nicholson 2022; Hayes & Gallagher 2022;

⁶⁹ The initial GBM trigger notice was distributed, but a problem with automated data processing prevented any additional real-time classification/localization messages from being sent to the ground.

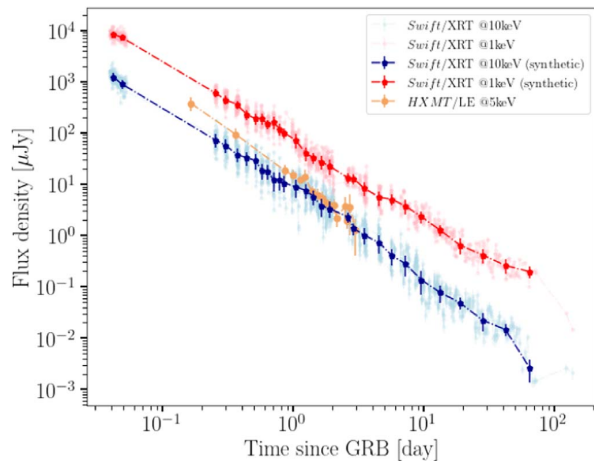


Figure 1. Unabsorbed X-ray light curve of GRB 221009A detected by the Swift/XRT (given at 10 keV in blue and 1 keV in red) and HXMT/LE (orange) instruments. The light curves were corrected for Galactic and intrinsic N_{H} column density absorption estimated from the late-time Swift/XRT spectrum analysis (https://www.swift.ac.uk/xrt_spectra/01126853/). In dark blue and red, we show the synthetic Swift/XRT light curve that we finally used in our afterglow modeling analysis; see Sections 3.4.2 and 3.4.1.

Pal et al. 2023). There were no detected neutrinos associated with GRB 221009A, however (Ai & Gao 2023; IceCube Collaboration 2022; KM3NeT Collaboration 2022). The gravitational-wave detectors were off or not sensitive enough to achieve any detection (Pannarale 2022).

The Global Rapid Advanced Network for Multi-messenger Addicts (GRANDMA; Antier et al. 2020a, 2020b; Aivazyan et al. 2022) is a collaboration of ground-based facilities dedicated to time-domain astronomy and focused on electromagnetic follow-up of gravitational-wave candidates and other transients, such as GRBs. Its network contains 36 telescopes from 30 observatories, 42 institutions, and groups from 18 countries.⁷⁰ The network has access to wide field-of-view (FoV) telescopes ($[\text{FoV}] > 1 \text{ deg}^2$) located on three continents and remote and robotic telescopes with narrower FoVs.

Here we present the analysis of the afterglow emission of GRB 221009A with different model approaches. All results are obtained using the Fermi GBM trigger time of October 9 13:16:59.99 UT. In Section 2, we present the observational data we use in the paper, the photometric methods we use, and a discussion of the extinction selection. In Section 3, we present our methods to analyze the afterglow light curves using empirical light-curve fitting and two Bayesian inference analyses. We then present our results to investigate which astrophysical scenarios and processes best describe the data. In Section 4, we present our conclusions.

2. Observational Data

2.1. Swift XRT and HXMT/LE Afterglow Data

The Swift XRT started to observe the field of GRB 221009A right after BAT triggered on the afterglow, about 56 minutes after the Fermi/GBM trigger time. The X-ray light curve (0.3–10 keV) of GRB 221009A was collected from the UK Swift Science Data Centre⁷¹ at the University of Leicester

(Evans et al. 2007, 2009). We made direct use of the Burst Analyser light curve given in janskys at the 10 keV central frequencies (Evans et al. 2010). Due to the large number of data points in the Swift XRT light curve, we could not use it directly for the Markov Chain Monte Carlo (MCMC) analysis without overweighting the X-ray data. We therefore constructed a synthetic light curve of the Swift XRT data (both at 1 and 10 keV). Assuming a power-law spectrum within the Swift XRT passband (as found by the Swift spectral analysis⁷²), the 1 keV band is constructed using an extrapolation of the 10 keV flux density curve at the times when the photon index could be derived from the Swift burst analyzer hardness ratio analysis. We separated the observations in both bands into 29 time windows, fitting a Gaussian to the flux distribution of the observations in each time window. Its median value and standard deviation are used as the measure and error of the synthetic curve. The obtained synthetic light curve is presented in Figure 1.

The Insight-HXMT/LE X-ray telescope (Zhang et al. 2020) detected the afterglow emission of GRB 221009A at late times from about 9.8 hr to 3 days after the Fermi/GBM trigger time, including two scanning observations (P050124003601 and P050124003701) and 20 pointing observations ranging from P051435500101 to P051435500401 with a total good time interval of 24 ks. The first two points are obtained by the spectral fitting of two scanning observations. The spectrum is obtained from the data when the target appears in the FoV. Unlike the pointing observations, the background is not obtained by the background model but from a region with no bright source in the FoV. Moreover, the instrumental response is calculated with the target track in the FoV and the point-spread function (PSF) of the Insight-HXMT/LE collimator. For the pointing observations, we use the Insight-HXMT data analysis software HXMTDAS v2.05⁷³ to extract the light curves, spectra, and background following the recommended procedure of the Insight-HXMT data reduction for HXMT-LE analysis. For both the scanning and pointing observations, the spectra of Insight-HXMT/LE in the 1.5–10 keV range are fitted by an absorbed power law, i.e., $\text{tbabs}^* \text{power}$ in XSPEC. The HXMT/LE X-ray afterglow is shown in comparison to the Swift/XRT measurements in Figure 1.

The HXMT/LE flux measurements are not corrected for the dust echo scattering (see, for example, Negro et al. 2023; Tiengo et al. 2023; Williams et al. 2023), since Insight-HXMT is a collimated telescope with a large FoV, e.g., $1^\circ \times 4^\circ$. It is thus not possible to easily remove the dust echo scattering flux contribution. However, to evaluate the apparent flux increase caused by the dust-scattering echoes, we employed a similar procedure to the one adopted on the NICER data (Williams et al. 2023). As the dust scattering only dominates at energies below 4 keV, we first restricted the energy range to 4–8 keV. As a mild change of the spectral shape is observed during our Insight-HXMT observations (Williams et al. 2023), we used the spectral model of Swift/XRT with a fixed Galactic/intrinsic N_{H} and photon index ($\Gamma = 1.8$) to fit the spectra. For the first several pointing data, the derived unabsorbed fluxes above the 1.5–10 keV energy range are then consistent with the interpolated fluxes of Swift/XRT at the same times, which are about 10% lower than the uncorrected/dust echo-included

⁷⁰ <https://grandma.ijclab.in2p3.fr>

⁷¹ <https://www.swift.ac.uk/>

⁷² https://www.swift.ac.uk/xrt_spectra/01126853/

⁷³ <http://hxmtweb.ihep.ac.cn/>

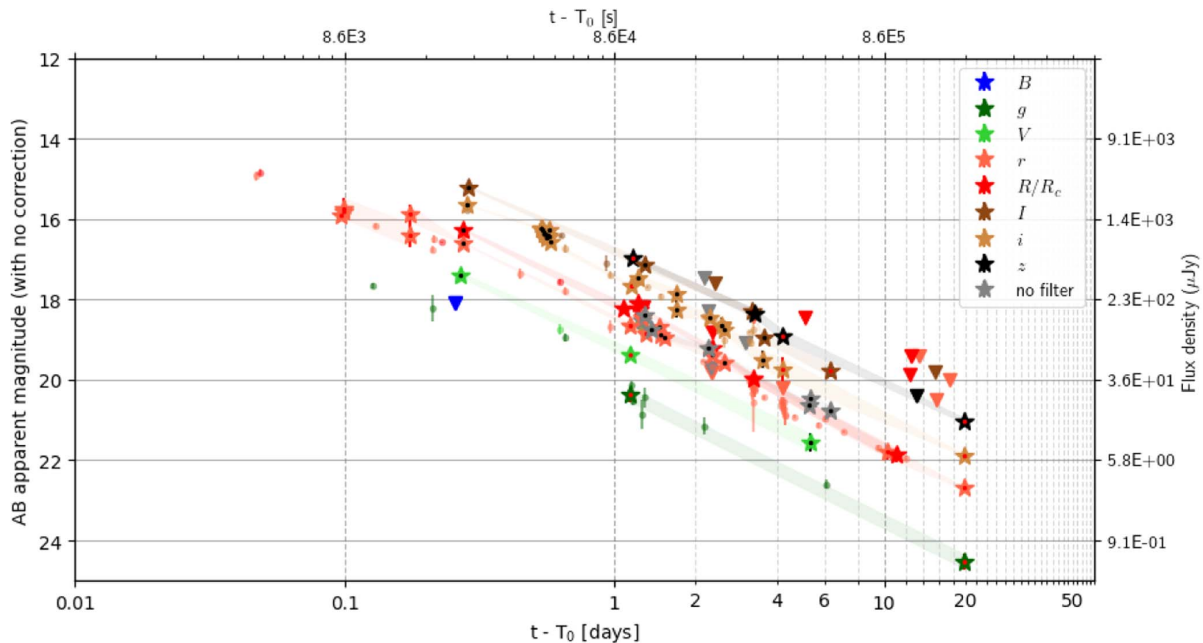


Figure 2. The optical afterglow of GRB 221009A was observed using the $g'r'R_C'i'z'$ filters and without a filter, with data points shown in the observer frame. The selected optical GCN data we use are represented by dots, and the GRANDMA data measurements and upper limits are indicated by larger stars and downward-pointing triangles (see Appendix). The red points within the stars indicate measurements made by professional observers, while black points represent observations made by KNC observers. Only magnitude measurements with at least a 3σ detection significance are included (the upper limits being given at 5σ significance), with uncertainty regions shown as shading. The measurements are not corrected for any extinction.

fluxes. However, for the last several pointing data, the combination of the low count rate of the source and the high background level prevents us from correcting the fluxes caused by dust-scattering echoes. To keep all HXMT fluxes produced in the same way, only the uncorrected dust echo scattering fluxes are given for all of the data of LE. Therefore, these fluxes are systematically brighter (about 10%) than those derived from Swift/XRT at early (<0.5 day) times. We also notice that the flux difference between Insight-HXMT/LE and Swift/XRT narrows as time goes, which could be due to the fading of the dust-scattering echoes.

2.2. Optical Observations during the GRB Prompt Emission

We used the images taken from two sites managed by the Desert Fireball Network (Towner et al. 2020) at Mundrabilla (lon. = $127^{\circ}8486$ E, lat. = $31^{\circ}8356$ S, altitude = 84 m) and at Raw War Road (lon. = $125^{\circ}7503$ E, lat. = $29^{\circ}7422$ S, altitude = 215 m), Western Australia. The acquisition device consists of a Nikon D810 (color CFA matrix) set at 3200 ISO with Samyang 8 mm F/3.5 optics. This provides images covering the full sky. Images have 27 s exposure times taken every 30 s for the entire night. At the prompt time, the GRB is located at elevations of 15° and 17° above the local horizons of Mundrabilla and Raw War Road, respectively. The sky at Mundrabilla was partially covered by thin clouds, and there was bright moonlight. Weather and elevation conditions were better at Raw War Road. We analyzed the archive images taken between $t_{\text{GRB}} - 30$ s and $t_{\text{GRB}} + 500$ s. There is no detection at the position of the GRB to a limiting magnitude of 3.8 mag in the green filter (which is roughly compatible with Johnson V) at Raw War Road. The limits are shallower at Mundrabilla. Times and magnitudes in the AB system are reported corrected

and uncorrected for extinction in the Appendix. No other contemporaneous observations have been reported, so to our knowledge, these are unique.

2.3. Optical Post-GRB Observations

Our first observation of the GRB within GRANDMA was obtained with the TAROT-Réunion telescope (TRE) at 2022-10-9T15:34:41 UTC (2:20 hr after T_0) thanks to its automated program following GRBs. Although GRANDMA was not conducting an observational campaign at the time of the event, at the request of A. de Ugarte Postigo, the GRANDMA network was activated to observe about 1 day post-trigger time; at this point, we provided the network the Swift UVOT coordinates (Dichiara et al. 2022b). The first target-of-opportunity image requested by GRANDMA was taken by the 60 cm telescope from Maidanak ~ 90 minutes after the notification at 2022-10-10T14:56:43 UTC (1.08 day after the GBM trigger) with the R_C filter. Our last observations were made by the Canada-France-Hawaii Telescope (CFHT) equipped with Megacam at 2022-10-29T06:32 (19 days, 17 hr post- T_0). In total, we collected about 80 images (usually consisting of stacks of short exposures) from 15 GRANDMA partner telescopes. In successive order, we provide here the midtime of the first observation relative to T_0 for each telescope and the filters used during the whole campaign: D810 (before and during the prompt emission in the V band) at the Mundrabilla and Raw War Road observatories, TAROT-Réunion (0.0972 day without filter) near Les Makes Observatory, UBAl-ST60 (1.0813 days in R_C) at Maidanak Observatory, KAO (1.1368 days in $g'r'i'z'$) at Kottamia Observatory, ShAOT60 (1.1465 days in VR_C) at Shamakhy Observatory, AZT-8 (1.2274 days in R_C) at Lisnyky Observatory, HAO (1.2563 days without filter) at Oukaimenden Observatory, MOSS (1.2722 days

without filter) at Oukaimenden Observatory, C2PU-Omicron (1.3077 days in r') at Calern Observatory, SNOVA (2.1535 days without filter) at Nanshan Observatory, T70 (2.2424 days in I_C) at Abastumani Observatory, UBAI-AZT22 (11.1313 days in R_C) at Maidanak Observatory, VIRT (12.4567 days in $R_C I_C$) at Etelman Observatory, and CFHT-Megacam (19.6945 days in $g'r'i'z'$) at Maunakea Observatory. Our preliminary analysis of the GRANDMA observations was reported by Rajabov et al. (2022), where we reported observations from UBAI-ST60, KAO, Lisnyky-AZT-8, MOSS, C2PU-Omicron, and SNOVA. In general, the sensitivity of the observations at the earliest epochs was reduced by the full Moon.

In addition to the professional network, GRANDMA activated its *Kilonova-Catcher* (KNC) citizen science program for further observations. Our web portal was used to provide the coordinates of the Swift UVOT source. Some amateur astronomers participating in the program observed the source by their own volition and distributed their own reports to the astronomical community (Romanov 2022a, 2022b, 2022c; Broens 2022; Aguerre et al. 2022). They also transferred their images to our web portal to allow us to perform our own image reduction and analysis. In total, more than 250 images were uploaded to our web portal. Here we provide a list of the names of the telescopes (see Tables 5 and 6 for the images selected for photometric analysis): a Celestron C11-Edge telescope, iT11 and iT21 iTelescopes, the IRIS 0.68 m telescope, the Celestron EdgeHD14, the 12" MEADE telescope at the RIT Observatory, the C11 Dauban MSXD Telescope, the 0.53 m Ritchey–Chrétien telescope of Montarrenti Observatory, the OMEGON200F5 Newton telescope, a Newton SW 200/1000 telescope, a Newton 250 f/4 telescope, a Celestron 11 ATLAS telescope, the T-CAT telescope at the Crous des Gats Observatory, the iT24 iTelescope of the Sierra Remote Observatory and the 0.61 m Dall–Kirkham telescope of Burke–Gaffney Observatory, the 0.28 m Mol SCT, the LCO 0.4 m telescope at the McDonald Observatory, a Celestron C11 Millery telescope, and the Planewave CDK-14 telescope at the Contern Observatory. The observations started 0.25 to ~ 6 days after the trigger time, predominantly in Johnson–Cousins and Sloan filter sets but also with other filters, such as Lumen or Bayer sensors.

The GRANDMA observations are listed in Tables 5 and 6 and shown in Figure 2. The former reports the midtime (in ISO format with post-trigger delay) and extinction-corrected brightness (in AB magnitudes) of the observations, while the latter includes the uncorrected magnitudes and references to selected online GCN reports (see [public observational reports](#); individual GCNs are cited in the table). The midtime is calculated as the weighted average of the observation start time and the number of exposures. The number of exposures is also provided. Our method for calculating magnitudes is described in the following section, and images that did not meet our criteria are labeled as “VETO.” In the [Appendix](#), the reference catalogs and stars used by external teams for comparison are also included unless not specified in the GCN reports. When the information is not provided by the online GCN report, we mark it as “–.”

2.4. Photometric Methods

We required all GRANDMA images to be preprocessed by the telescope teams with bias or dark subtraction and flat-fielding. We reject a few images from amateur astronomers

where these corrections were not performed. Some teams uploaded their images with their own astrometric calibration, but for most images, the astrometric calibration is obtained directly from the Astrometry.net website. Then, two methods are used to measure the magnitude on the template-subtracted images (see below): STDPipe and MUPHOTEN. For both of these methods, we use techniques to blindly search for new detections within the Swift UVOT error localization (Dichiara et al. 2022b), but we can also force photometry at the GRB 221009A afterglow coordinates we fixed to R.A. = 288.2646558, decl. = 19.7733650 (Atri et al. 2022).

STDPipe—The Simple Transient Detection Pipeline STDPipe (Karpov 2021) is a set of Python libraries aimed at performing astrometry, photometry, and transient detection tasks on optical images. To do so, it uses several external algorithms, such as SEXTRACTOR (Bertin & Arnouts 1996) for the source extraction, catalog cross-matching tools using the CDS Xmatch service developed at the Strasbourg Astronomical Observatory (Boch et al. 2012; Pineau et al. 2020), the HOTPANTS code (Becker 2015) for image subtraction tasks, and the PHOTUTILS⁷⁴ Astropy package (Bradley et al. 2021) to perform photometric calibration and measurements. More details about the STDPipe software architecture can be found in the git documentation.⁷⁵ In order to increase the signal-to-noise ratio (S/N) of some KNC images where the GRB afterglow was barely visible, we resampled and coadded individual frames using the SWARP software (Bertin 2010). Our final set of science images was subtracted with Pan-STARRS DR1 (PS1) catalog (Chambers et al. 2016) images downloaded from the CDS HIPS2FITS service (Boch et al. 2020) and rescaled to each image pixel scale. Forced aperture photometry was then applied at the GRB afterglow position in the residual images in order to limit the flux contribution from the very nearby stars. Due to the heterogeneity of the KNC instruments, we had a wide pixel scale distribution in our images. Therefore, the aperture radius was fixed per image to the average FWHM of stars detected at $S/N > 5$ by SEXTRACTOR in the image field. Depending on the photometric system used by KNC astronomers, the photometric calibration was done with the stars in the image field either using the native photometric bands ($g'r'i'z'$) of the PS1 catalog or by converting them into the Johnson–Cousins $BVR_C I_C$ system using the transformation described by Pancino et al. (2022). The photometric model for the calibrated magnitudes, mag_{cal} , is defined following the method described in Karpov (2021),

$$mag_{cal} = -2.5 \log_{10}(\text{ADU}) + ZP(x, y) + C \times (B - V), \quad (1)$$

where ADU is the star flux measured by the detector, ZP is the spatially varying zero-point function, and C is a color-correction term to take into account the color distribution of the PS1 calibration stars. The ZP distribution is estimated by performing an iterative weighted linear least-squares fit to match the photometric model given in Equation (1) to the cataloged magnitudes. The 3σ outliers to our photometric model were iteratively rejected (sigma clipping). The statistical errors on the ZP distribution were then propagated to the magnitude errors. Additional systematic errors due to the magnitude system conversion are also taken into account and can affect our measured magnitude up to 0.1 mag at maximum,

⁷⁴ <https://github.com/astropy/photutils>

⁷⁵ <https://github.com/karpov-sv/stdpipe>

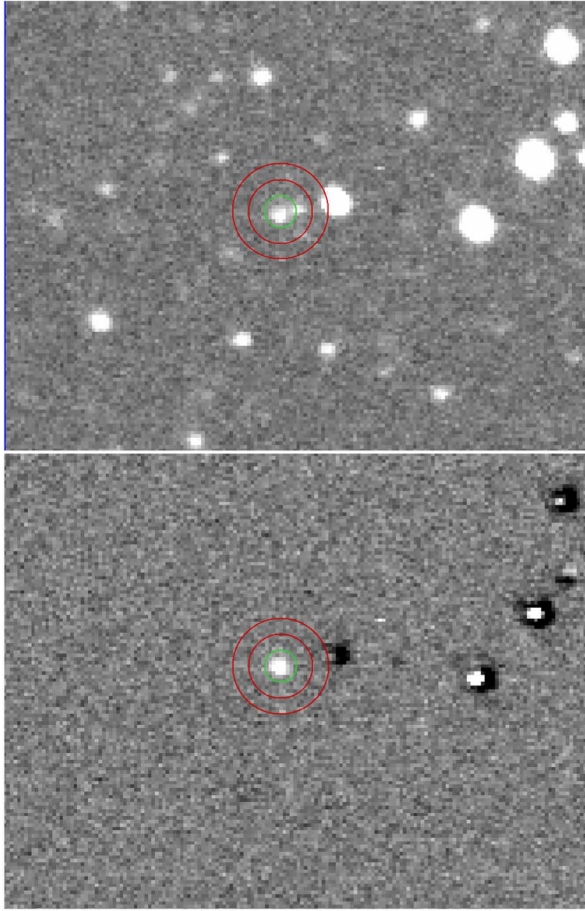


Figure 3. Top panel: 60 s exposure I_C of GRB 221009A taken on the 0.61 m Dall–Kirkham458 telescope of the Burke–Gaffney Observatory ~ 0.5 day after the Fermi GBM trigger time. Bottom panel: corresponding difference image using a PS1 template image downloaded from the CDS HIPS2FITS service. The optical afterglow is well detected in the residual image and cleaned of any nearby star contribution. The aperture radii (the flux aperture in green and the background flux annulus in red) used to compute the photometric measurement are also shown in both images.

depending on the source brightness. Our KNC photometric results are shown in Tables 5 and 6. As an illustration, we show in Figure 3 one of the analyzed KNC images according to the method described above.

MUPHOTEN—MUPHOTEN⁷⁶ is a Python-based software dedicated to the photometry of transients observed by heterogeneous instruments developed for the analysis of GRANDMA images (Duverne et al. 2022). Similarly to STDPipe, it uses Python libraries like PHOTUTILS (Bradley et al. 2021) and external algorithms like SEXTRACTOR (Bertin & Arnouts 1996) and HOTPANTS (Becker 2015). The MUPHOTEN software was utilized for the analysis of all GRANDMA images and a portion of the KNC images. We first construct a template image by mosaicking PS1 archive images and matching the image FoV, and we use HOTPANTS to subtract the template from the image. We do this to limit the contamination from nearby objects in an FoV that is crowded

due to its proximity to the Galactic plane. However, for a limited number of images, the template subtraction was unsuccessful due to nonconvergence with HOTPANTS. Nevertheless, these images had adequate resolution to clearly distinguish the transient from neighboring sources, so they were retained for further analysis. The background is estimated using the method of SEXTRACTOR in a mesh of 150×150 pixels by default (smaller grids were applied for images with rapidly varying backgrounds). The background and its standard deviation are interpolated to each pixel of the image and subtracted to obtain the final result. Sources are detected by identifying clusters of at least five neighboring pixels that exceed a threshold of 2σ above the background.

Next, we conducted isophotal photometry on all detected sources, measuring the flux and its corresponding error (obtained by integrating the squared flux error, computed by PHOTUTILS as background variation plus gain-adjusted Poisson noise, over the same elliptical aperture). The sources were cross-matched with the PS1 catalog, yielding the PS1 magnitudes of the matched sources in the corresponding filter. For images taken with Johnson–Cousins filters, we transformed the PS1 magnitudes to the observed filters using the conversion equations from Kostov & Bonev (2018). Unfiltered images were treated as if they were taken with the Cousins R_C filter and were processed using the same conversion equations. We construct a calibration scale by fitting the instrumental and PS1 magnitudes using a first-order polynomial fit with iterative clipping of outliers (3σ away from the fit). We then compute calibrated magnitudes for all detected sources, sort them by distance to expected transient coordinates, and consider a source a detection if its coordinates match within 5 pixels. We also compute the photometric error for each source, adding contributions from the flux error measured above and the calibration uncertainties. Due to crowding in the Galactic plane, we checked for neighboring objects affecting the automatically computed apertures, reducing them if necessary. Forced photometry using circular apertures of default radius 1.5 times the average FWHM of stars in the image was performed at the GRB coordinates in the absence of direct detection. This was calculated using the PSFEX software (Bertin 2011). Plotting circular apertures of increasing radius (1–10 pixels) and their corresponding measured fluxes, we could check whether the default aperture collected all of the transient flux and not neighboring sources and manually correct its coordinates and radius when needed.

Finally, MUPHOTEN assesses the sensitivity of the image with upper-limit estimations. In MUPHOTEN, upper limits are computed as global properties of the whole studied image. The default method outlined in Duverne et al. (2022) calculates the success rate of recovering PS1 objects based on 0.2 mag intervals and selects the faintest interval where more than 10% of the PS1 objects in the FoV are detected in the image. In the case of images where there is a high detection rate up until the limit of the Pan-STARRS catalog, an alternative method defines the upper limit as the magnitude of the faintest source detected with an $S/N > 5$.

2.5. Extinction Selection

Unfortunately for optical studies, the brightest GRB ever detected lies behind significant extinction near the Galactic plane ($b = 4^\circ.32$). Following the maps of SF11, the line of sight at the “reference pixel” lies behind $E_{(B-V)} = 1.32 \text{ mag}/A_V$

⁷⁶ <https://gitlab.in2p3.fr/icare/MUPHOTEN>

= 4.1 mag. However, at Galactic latitudes $|b| < 5^\circ$, the maps of Schlegel et al. (1998, which those of SF11 are based on) are known to be unreliable and may overestimate the extinction (Popowski et al. 2003, and references therein).

Rowles & Froebrich (2009, hereafter RF09) presented a method of determining extinction toward the Galactic plane using NIR color excess determinations based on Two Micron All Sky Survey (2MASS) observations, following earlier work from Froebrich et al. (2005) based on stellar counts. Using their extinction calculator⁷⁷ and the position of the GRB, we find a significantly lower extinction using the 100NN (nearest neighbor; see RF09 for details) result (which has the highest S/N) of $A_V = 2.195$ mag. Using the classical Milky Way (MW) extinction curve of Cardelli et al. (1989, hereafter CCM89), this translates into $E_{(B-V)} = 0.709$ mag. The extinction maps of RF09 show that extinction toward this region of the MW is smooth and quite homogeneous for several degrees around (and not high in the context of the potential extinction toward the MW); the nearest pronounced molecular clouds with significantly higher extinction lie closer to the plane in the neighboring constellation Vulpecula, about 5° away. Therefore, we deem the use of the extinction curve of CCM89 to be valid.

The method of RF09 only extends⁷⁸ to 2–3 kpc. There is evidence for additional dust screens at larger distances, however. Swift XRT observations reveal expanding rings in the X-rays (Tiengo et al. 2022) arising from scattering on distant dust curtains. These authors reported the discovery of nine dust rings and derived the distances, with the most distant one lying at 3635 ± 36 pc, potentially already beyond the detection range of the RF09 method. Observations with IXPE (Negro et al. 2023) confirm the most distant dust ring found by Swift at 3.75 ± 0.0375 kpc and report an even more distant dust curtain at 14.41 ± 0.865 kpc. Recently, Vasilopoulos et al. (2023) reported a detailed analysis of Swift XRT data and also found evidence for dust out to 15 kpc (see Williams et al. 2023 for further analysis), and XMM-Newton analysis of a total of 20 dust rings presented by Tiengo et al. (2023) detects an even further dust curtain at ≈ 18.6 kpc.

The Galactic disk exhibits a warp (e.g., Hou & Han 2014, and references therein). The map derived by Hou & Han (2014, their Figure 16) shows that at the Galactic longitude of GRB 221009A ($l = 52^\circ 96'$), H II regions indeed extend up to several hundred parsecs “above” the Galactic plane. For the Galactic latitude of GRB 221009A ($b = 4^\circ 32'$), the sight line lies ≈ 1100 pc above the plane at a distance of 14.4 kpc, beyond the H II regions mapped by Hou & Han (2014). However, this does not rule out the existence of cold dust curtains that high above the Galactic disk, which would contribute extra extinction beyond the RF09 measurement. We therefore conclude that the true extinction value along the line of sight to GRB 221009A lies in the interval of $A_V = 2.2\text{--}4.1$ mag and will discuss both extreme values.

3. Multiwavelength Analysis of the Afterglow

To analyze the afterglow light curve, we use data from multiple sources: our own GRANDMA and KNC data, selected GCN data (see Appendix), and data published in Williams et al. (2023), Shrestha et al. (2023), Laskar et al. (2023),

⁷⁷ https://astro.kent.ac.uk/~df/query_input.html

⁷⁸ Neckel & Klare (1980) gave a value of $A_V = 3.3$ mag along this sight line out to 3 kpc.

Levan et al. (2023), and O’Connor et al. (2023). We especially note that we use the Hubble Space Telescope data from Levan et al. (2023), where the host-galaxy contribution has been subtracted using `galfit`. The NIR observations are taken from Durbak et al. (2022), D’Avanzo et al. (2022), Huber et al. (2022), Ferro et al. (2022), and O’Connor et al. (2023), as well as the James Webb Space Telescope (JWST) MIR F560W data point (Levan et al. 2023).

3.1. Empirical Light-curve Analysis

With the exception of our shallow upper limits from Mundrabilla and Raw War Road, no optical observations have been reported before the Swift trigger.

The first observations, consisting of Swift UVOT data from Williams et al. (2023) and Laskar et al. (2023) and obtained via automatic analysis,⁷⁹ as well as some ground-based observations (Belkin et al. 2022c; Xu et al. 2022), are found to decay more steeply than following the observations (see Appendix) and also lie above the back-extrapolation of those data. This indicates an extra component in the light curve, potentially the tail end of a reverse-shock flash. The extreme intensity of the GRB makes it potentially possible that the early transient was extremely bright.

Fitting a joint multiband fit to the data, which assumes achromatic evolution and leaves only the normalization of each band as an independent parameter, we derive a first decay slope of $\alpha_{\text{steep}} = 1.32 \pm 0.34$ (we define $F_\nu \propto t^{-\alpha} \nu^{-\beta}$), significantly steeper than the later decay observed in the range ~ 0.09 day $< t < 0.59$ day but quite shallow for a reverse-shock flash (Sari & Piran 1999; Kobayashi 2000). As the baseline is short, it is possible we are seeing the transition from the early steeply decaying component to the later shallower light-curve decay, and the decay at even earlier times might have been steeper and more in accordance with a reverse-shock flash. Extrapolating this slope backward to the peak of the brightest gamma-ray flare of the prompt emission, at ≈ 220 s post-trigger, we find $R_{\text{AB}} \approx 11$ mag ($R_{\text{AB}} \approx 7.6$ mag when corrected for SF11 extinction). This value is far fainter than our Mundrabilla/Raw War Road exposures probe. A steeper decay (see as mentioned earlier in the paragraph) or an additional component directly associated with the prompt emission cannot be ruled out but would still be unlikely to be bright enough to be detected by our shallow all-sky observations.

Data at > 0.09 day can be fit with a smoothly broken power law, with parameters of prebreak slope α_1 , postbreak slope α_2 , break time t_b in days, and break smoothness n . The very last data points at $\gtrsim 30$ days show a flattening that may result from the host galaxy becoming dominant; we exclude these data points from the analysis. We see no direct evidence of an SN component in the late light curve,⁸⁰ in agreement with Shrestha et al. (2023), similar to the case of GRB 030329 (e.g., Kann et al. 2006), and therefore also do not include such a component in the fit. A dedicated search will need well-calibrated late-time data. In general, the data show dispersion, leading to a large χ^2 .

⁷⁹ https://swift.gsfc.nasa.gov/uvot_tdrss/1126853/index.html

⁸⁰ Note that data presenting evidence of a photometric SN rise (Belkin et al. 2022a, 2022b) were taken under inclement conditions and are likely the result of blending with nearby sources and are therefore too bright (A. Pozanenko, private communication). However, Fulton et al. (2023) assumed an intrinsic optical decay slope identical to the X-ray slope and interpreted the shallower decay as a rising luminous SN component.

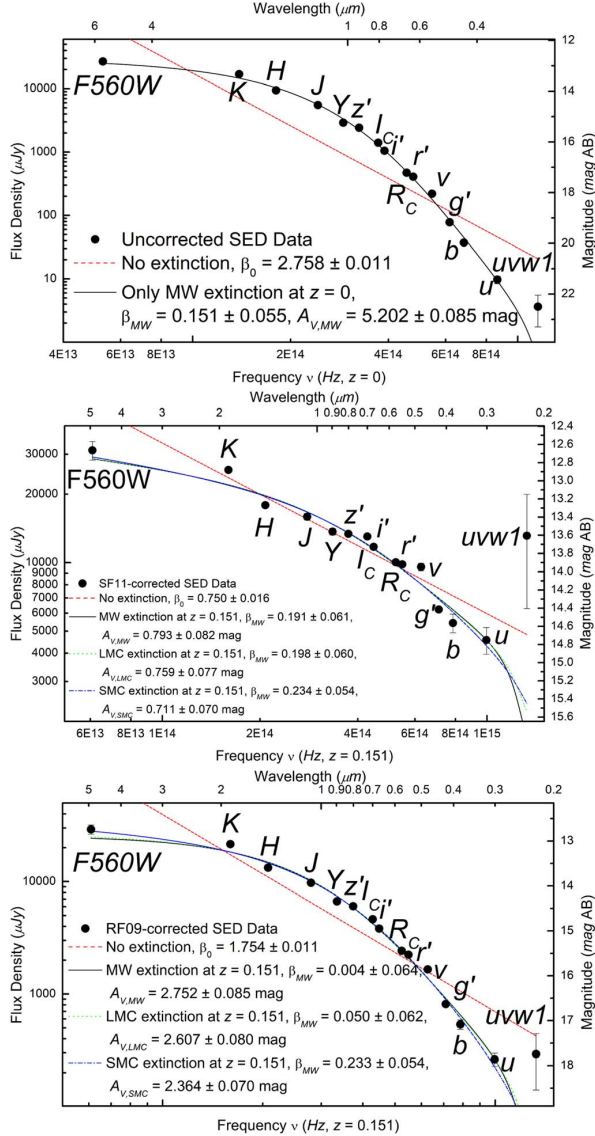


Figure 4. Analysis of the SED. Top panel: fit to the uncorrected SED with an MW extinction model at $z = 0$, i.e., assuming no additional host-galaxy extinction. The fit is generally in agreement with the data, with the *uvw1* data point being brighter than the model. Middle panel: fit to the SED after correcting it for SF11 foreground extinction and shifting it to $z = 0.151$. The correction leads to significant scatter, with the *uvw1* now being clearly brighter than any fit, even one without additional host-galaxy extinction. The three extinction laws cannot be discerned from each other, but the potential bright *uvw1* emission makes the SMC law the preferred one. There is still significant curvature, which implies additional significant host-galaxy extinction. Bottom panel: same as the middle panel but with RF09 foreground extinction. The SED remains very red, and very high host extinction is implied. Again, SMC extinction leads to the most physical solution, but all dust laws are in conflict with the bluest Swift UVOT detection.

This fit results in $\alpha_1 = 0.722 \pm 0.012$ and $\alpha_2 = 1.437 \pm 0.003$, with $\sim t_b = 0.6$ and a sharp break $n = 100$ fixed. Note that the errors of the fitted parameters are only statistical and do not include the systematic uncertainties ($\sim 10\%$) due to the intercalibration of the different photometric bands. Therefore, they are simply presented for diagnostic purposes. This

steepening was also reported by D’Avanzo et al. (2022), who found $\alpha_1 \approx 0.8$, $\alpha_2 \approx 1.6$, and $t_b \approx 0.98$ day based on a significantly smaller data set. Shrestha et al. (2023) found $\alpha_1 = 0.64$, $\alpha_2 = 1.44$ in r' and $\alpha_1 = 0.81$, $\alpha_2 = 1.46$ in i' , similar to our result. Williams et al. (2023), using only Swift UVOT data, found $\alpha_{1,O} = 0.98^{+0.05}_{-0.11}$, $\alpha_{2,O} = 1.31^{+0.07}_{-0.05}$, and $t_{\text{break},O} = 0.255^{+0.197}_{-0.127}$ day, in agreement with our results within 2σ . They pointed out that this decay is clearly slower than that of the X-rays (see below) but very unlikely to be influenced by a host or SN component.

Swift XRT observations (initially reported in Kennea et al. 2022a; Tohuvavohu et al. 2022, but these reports are based on the Swift trigger time) as given in the XRT repository (Evans et al. 2007, 2009) show the light curve⁸¹ to have multiple shallow breaks (see also Williams et al. 2023, who cautioned that especially during the WT mode observation, the dust-scattering rings can influence the light curve stemming from the atypical background around the afterglow PSF), but within the first ≈ 10 days, the decay slope is $\alpha_X \approx 1.5$ – 1.6 , similar to but steeper than our optical result. In their detailed analysis, Williams et al. (2023) found $\alpha_{1,X} = 1.498 \pm 0.004$, $\alpha_{2,X} = 1.672 \pm 0.008$, and $t_{\text{break},X} = 0.914^{+0.127}_{-0.116}$ day. Insight-HXMT observations (Ge et al. 2022; see also An et al. 2023) also yielded a somewhat steeper slope, $\alpha_X \approx 1.66$. NICER observations also found $\alpha_X \approx 1.6$ (Iwakiri et al. 2022). The significantly shallower decay phase in the optical ($\alpha_O \approx 0.83$), as well as the earlier break at $t_b \approx 0.6$ day, are not seen in X-rays at all. The optical light curve also shows a much stronger break with $\Delta\alpha_O = 0.617 \pm 0.013$ versus $\Delta\alpha_X = 0.174 \pm 0.009$.

3.2. Analysis of the Spectral Energy Distribution

The normalizations derived from the joint multiband fit described in Section 3.1 yield a spectral energy distribution (SED), a very low resolution “spectrum” of the afterglow that is nonetheless valuable to study the dust properties along the line of sight. The fit assumes achromaticity, i.e., no spectral evolution, and is therefore based on all data involved in the fit. Except for scaling, the SED is identical at any time point covered by the fit; the specific values are measured at break time. While our data do not indicate an obvious spectral evolution, such a break is hard to constrain due to the challenge of building an empirical model that describes the data well.

We fit the SED both without extinction (a simple power law) and with MW and Large (LMC) and Small Magellanic Cloud (SMC) dust following the parameterization by Pei (1992). These fits are performed after correction for Galactic extinction, and we study both the RF09 and SF11 models. The derived SED shows scatter, especially the z' band deviating and being too faint. The field is not covered by the Sloan Digital Sky Survey (SDSS; e.g., Almeida et al. 2023, and references therein); however, many telescopes use filters that are close to the SDSS system. There are offsets to the Pan-STARRS system, which was used for calibration in most cases. Following the Pan-STARRS to SDSS conversion of Tonry et al. (2012), we find $g'_{\text{PS1}} - g'_{\text{SDSS}} = -0.26$, $r'_{\text{PS1}} - r'_{\text{SDSS}} = 0.02$, $i'_{\text{PS1}} - i'_{\text{SDSS}} = 0.03$, and $z'_{\text{PS1}} - z'_{\text{SDSS}} = 0.13$ mag, i.e., small changes for r'/i' but more significant changes to g' and z' . As we are unable to examine each measurement individually for more precise color terms, we just apply these offsets to the

⁸¹ https://www.swift.ac.uk/xrt_live_cat/01126853/

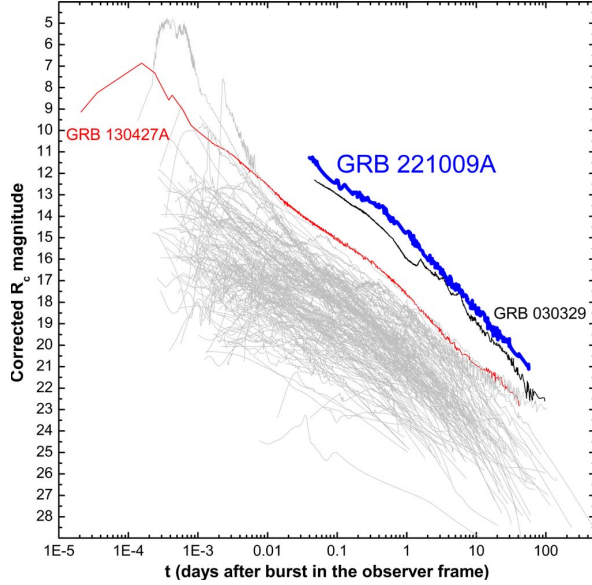


Figure 5. Afterglow light curve of GRB 221009A in the context of a large sample of GRB afterglows (Kann et al. 2006, 2010, 2011, 2023a, 2023b, in preparation). These data have been corrected for Galactic extinction along each individual line of sight and, if possible, for the host-galaxy and SN contribution. For the GRB 221009A afterglow, we show the result for SF11 Galactic extinction. We highlight the afterglows of two other GRBs, namely, that of the much less energetic but similarly distant GRB 030329 and that of the well-studied, ultrabright GRB 130427A, which had been the closest highly energetic (“cosmological”) GRB so far. Assuming the higher extinction correction, the afterglow of GRB 221009A is seen to be the brightest that has ever been detected, even brighter than the afterglow of GRB 030329—however, by only a small margin.

four data points in the SED, which leads to a marked reduction in scatter and χ^2 . However, scatter still remains, with especially the H band being fainter than the models and the K band being brighter. The precise light-curve fit leads these normalizations to have small errors, causing large χ^2 values that are not formally acceptable even for fits that generally model the SEDs well. The source of this scatter is less easy to understand than for the light-curve data points themselves; e.g., in the case of the H and K bands, most data points are from the final analyses presented in refereed papers (e.g., O’Connor et al. 2023), and the few GCN points have larger errors and do not disagree with the fit curves. Furthermore, these data span a long time period, e.g., from 0.23 to 25.4 days for H and 4.4 to 25.4 days for K . This would imply that all data from multiple sources are systematically offset in the same manner. As we have no immediate solution to this issue, we will continue to work with these results despite the fits being formally rejected, noting that the scatter is approximately symmetric around the SED fit curves and not due to a clear discrepancy between the model fit and data (as is the case for the fits without extinction, which disregard the curvature of the SEDs).

3.2.1. Pure MW Extinction

We first study the SED without applying any MW foreground correction and taking the data at $z=0$. The SED is very steep and shows evidence for curvature (see Figure 4, top panel). A simple power-law fit yields a spectral slope

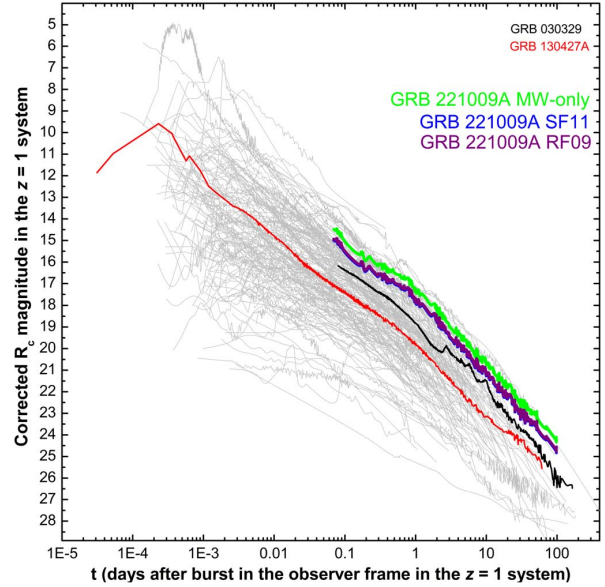


Figure 6. Same as Figure 5, but now all afterglows are in the $z=1$ system. This means that the afterglow magnitudes have been additionally corrected for host-galaxy extinction, and all of them have been shifted to $z=1$, taking the individual spectral slopes β and cosmological k -correction into account. We again highlight the afterglows of the bright nearby GRBs 030329 and 130427 and three solutions for GRB 221009A: the pure MW solution, SF11 MW extinction, and RF09 MW extinction, along with the respective host-galaxy solutions. All yield similar brightness, with the SF11 and RF09 results essentially overlapping (offset by only 0.05 mag), and the afterglow is seen to be among the more luminous ones detected so far. We note that the late afterglow of GRB 221009A is not corrected for a potential SN contribution; therefore, the luminosity may be overestimated.

$\beta_0 = 2.758 \pm 0.011$. This is clearly not a good model; we find $\chi^2 = 8102$ for 13 degrees of freedom (d.o.f.).

Applying MW dust to the SED yields a highly significant improvement ($\chi^2 = 142.8$ for 12 d.o.f.; this number of d.o.f. is identical for all extinction fits), and we derive $\beta = 0.323 \pm 0.086$, $A_{V,\text{Gal}} = 5.202 \pm 0.085$ mag ($E_{(B-V)} = 1.69 \pm 0.03$ mag). This value exceeds the SF11 correction by over a magnitude and can indicate one of three things: even the SF11 result does not encompass the entirety of the MW foreground extinction, there is additional significant host-galaxy extinction along the line of sight, or there is a combination of both. The detection of the NaI doublet at the redshift of the host galaxy (de Ugarte Postigo et al. 2022; Malesani et al. 2023) indicates that there must be some amount of host-galaxy extinction. However, we note that the free fit already yields an intrinsic spectral slope lying in the typical range found for GRB afterglows, $\beta \sim 0.2\text{--}1.2$ (Kann et al. 2010).

3.2.2. SF11 Extinction

We next correct the SED for SF11 MW extinction and study the pure host extinction at $z=0.151$. After this correction, the spectral slope is obviously much flatter than before ($\beta_{0,\text{SF11}} = 0.750 \pm 0.016$, $\chi^2 = 207$ for 13 d.o.f.); however, the SED shows remaining significant curvature, as well as scatter (see Figure 4, middle panel), with the $uvw1$ band especially deviating. We caution that this color is derived using only two r'/R_C -band GCN points, which yields additional uncertainty beyond the fact that it is only a 2σ excess above the

background and thus barely a confident detection. If real, the $uvw1$ -band detection (Williams et al. 2023) coincides with the 2175 Å bump feature for LMC and MW dust in the host-galaxy rest frame, indicating that the host-galaxy extinction law is most likely similar to SMC dust, which lacks this feature almost completely. Mathematically, the different results cannot be distinguished ($\chi^2 = 128, 125, \text{ and } 116$ for MW, LMC, and SMC dust, respectively; see also Williams et al. 2023), but SMC dust yields the overall most logical result, with an intrinsic spectral slope very close to the MW-only fit ($\beta_{\text{SF11,SMC}} = 0.234 \pm 0.054$) and moderately high additional host-frame extinction ($A_{V,\text{SF11,SMC}} = 0.711 \pm 0.070$ mag, $E_{(B-V)} = 0.243 \pm 0.024$ mag). In terms of the intrinsic spectral slope, our results are in good agreement with those of Levan et al. (2023), who gave several results in the slope range of $\beta = 0.3\text{--}0.4$, but especially a broadband fit using JWST and Gran Telescopio Canarias spectra, as well as NOEMA submillimeter data that yield $\beta = 0.362$. They attributed most extinction to the MW and found only very small host-galaxy extinction. Modeling these data together with XRT, they found evidence for a spectral break between the optical and X-ray bands but not for a spectral break within the optical/NIR regime itself. Using only Swift UVOT data, Williams et al. (2023) derived higher values; correcting for the higher foreground extinction given by Schlegel et al. (1998) and using an intrinsic slope of $\beta = 0.7$, they found $E_{(B-V)} = 0.51 \pm 0.03$ mag for SMC dust.

3.2.3. RF09 Extinction

Finally, for the lowest assumed MW extinction, that of RF09, we find a combination of “moderately high” MW extinction and “moderately high” host-galaxy extinction. The SED after RF09 correction is still very steep (see Figure 4, bottom panel; we find $\beta_{0,\text{SF11}} = 1.754 \pm 0.011$, $\chi^2 = 2300$). Again, the three dust models yield similar goodness-of-fit values ($\chi^2 = 161, 152, \text{ and } 123$ for MW, LMC, and SMC dust, respectively), but in this case, the very flat intrinsic spectral slopes $\beta \approx 0.0\text{--}0.1$ additionally speak against MW and LMC dust being the correct solution. The SMC dust results in $\beta_{\text{RF09,SMC}} = 0.233 \pm 0.054$, $A_{V,\text{RF09,SMC}} = 2.364 \pm 0.070$ mag. Even this result is not in agreement with the $uvw1$ detection, however.

Overall, while there is no strong evidence for one or another foreground extinction, the most logical solution is SF11 foreground extinction with additional moderately high SMC extinction in the host galaxy. High host-galaxy extinction such as in the RF09 case is also not supported by the relatively small equivalent width of the Na doublet at the host redshift (Malesani et al. 2023). In general, given the poor performance of the fits, it seems like the extinction law is different from the three canonical functions used above, or the spectrum cannot be approximated as a power law; however, for the sake of the analysis, for both foreground-extinction scenarios, we corrected our data for Galactic and host-galaxy extinction. During this step, we accounted for the systematic uncertainties of our extinction estimate in each band, adding them to the photometric errors. These fully corrected data sets are shown in the Appendix.

3.3. The Afterglow of GRB 221009A in a Global Context: Luminous but Not Intrinsically Extraordinary

With knowledge of the intrinsic extinction and the redshift and using the method first presented in Kann et al. (2006), we are able to place the optical/NIR afterglow of GRB 221009A in the context of a large sample of GRB afterglows. The sample is compiled from Kann et al. (2006, 2010, 2011). These afterglows have been corrected for individual Galactic foreground extinction, host-galaxy contribution (where known), and SN contribution at late times (where applicable).

The otherwise as-observed light curves are shown in Figure 5. We highlight the afterglows of the two exceptional GRBs mentioned in the Introduction. One is the nearby but only moderately energetic GRB 030329, whose afterglow (e.g., Lipkin et al. 2004; Kann et al. 2006) remains the most well observed up to the present day and is seen to be brighter than all other afterglows in the sample at any given time. The other is the afterglow of the extremely bright GRB 130427A (e.g., Perley et al. 2014; Vestrand et al. 2014, Kann et al. 2023a, 2023b, in preparation), also among the brightest observed GRB afterglows and energetically more similar to GRB 221009A.

The placement of the afterglow of GRB 221009A depends on the MW foreground-extinction correction. From our three models, we display the SF11 solution here, which is usually the standard correction for extinction in other cases. If we used the MW-only solution, the resultant afterglow would be even brighter, whereas it would be magnitudes fainter with the RF09 solution, but as pointed out, this solution is unlikely. For SF11, we see that the observed afterglow is even brighter than that of GRB 030329 at all times (albeit usually by not more than 1 mag)—potentially, yet another record that GRB 221009A holds. Williams et al. (2023) reported that the observed afterglow of GRB 221009A is by far the brightest X-ray afterglow and the brightest UVOT afterglow (after extinction correction) ever detected.

A better afterglow comparison can be achieved if we correct for both the distance (temporally and in terms of luminosity, we choose to place all afterglows at $z = 1$ and present them in the observer frame) and any intrinsic (host-galaxy) extinction. If the latter value is high, it can hide extremely luminous GRB afterglows from initially looking extraordinary (e.g., GRB 080607; Perley et al. 2011). The results are shown in Figure 6. It can now be seen that the afterglow of GRB 130427A is only of medium brightness, and that of GRB 030329, while brighter, is also well within the sample of known afterglows. The same is true for the afterglow of GRB 221009A. The three foreground-extinction solutions yield similar results now, as high foreground extinction implies low additional host-galaxy extinction (MW-only; SF11), while the lower RF09 foreground extinction is mostly compensated for by necessary high intrinsic extinction. Indeed, the degeneracy between the foreground and host-galaxy extinction, which stems from the very low redshift of the event, leads the completely corrected light curves for the SF11 and RF09 extinction to almost overlap; the offset is only 0.05 mag. This motivates us to only use the SF11 solution for numerical modeling (see Sections 3.4.1 and 3.4.2). The afterglow of GRB 221009A is clearly among the more luminous detected so far, but it is not egregious. Only at late times does the unbroken decay lead it to become exceptional, but we caution that these observations are not corrected for host-galaxy and SN contribution and are

therefore to be taken with caution (see Fulton et al. 2023 for the potential SN contribution, but see also Shrestha et al. 2023).

Quantitatively, we determine the $z=1$ mag of a sample of 170 GRB afterglow light curves, including that of GRB 221009A, where not every afterglow has measurements at the chosen time (however, the GRB 221009A afterglow does). As times, we chose 0.07, 0.5, 1, 5, 10, and 20 days. For these times, the comparison sample encompasses 140, 144, 130, 78, 52, and 34 other afterglows, respectively. We find that the afterglow of GRB 221009A is brighter than 83.6%, 86.1%, 83.8%, 87.2%, 88.5%, and 85.3% of all other afterglows, respectively. More generally, it is brighter than 80%–90%, which supports our claim that it is not exceptional in the way the prompt emission energetics are. However, it is extraordinary indeed in one aspect. As an example, at 1 day after trigger (12 hr in the rest frame), there are 20 afterglows found to be brighter than that of GRB 221009A, but none of these lie at $z < 1.4$, and 15 lie at $z > 2$. In all time slices, the single afterglow at $z < 1$ found to be brighter (at 0.5 and 2 days but not 1 day) is that of GRB 110715A at $z = 0.8225$ (Sánchez-Ramírez et al. 2017; Kann et al. 2023a, 2023b, in preparation).

Overall, despite its extreme energetics, the optical/NIR afterglow of GRB 221009A is not intrinsically extraordinary compared to the global sample of known afterglows, a phenomenon also seen for other highly energetic GRBs like GRB 990123 (Kann et al. 2010). Williams et al. (2023) reached similar conclusions for both the UVOT and the X-ray afterglow, and Laskar et al. (2023) showed that this is true as well for the radio afterglow.

3.4. Properties of the GRB Afterglow from Bayesian Inference

We analyzed our data in the framework of the standard afterglow model, where the observed emission is dominated by the synchrotron radiation from shock-accelerated electrons at the forward external shock due to the deceleration of a relativistic jet by the ambient medium (assumed here to be uniform). We explored the allowed parameter space of this model with a Bayesian approach using the constraints provided by two distinct data sets. Both data sets include X-ray data from the Swift/XRT instrument (at 1 and 10 keV), following the procedure outlined in Section 2.1 and downsampling the data to avoid our Bayesian inference runs being entirely dominated by X-ray observations. These data were combined with HXMT-LE data at 5 keV. We then combine the Swift XRT and HXMT X-ray data with two different optical data sets. (i) GRANDMA data points in the optical and NIR (presented in Sections 2.2 and 2.3) are simply completed in the u band by early Swift UVOT points. We denote this set as “GRANDMA.” (ii) We enrich the “GRANDMA” data with the same observations collected in the literature as already used in the introduction of Section 3. This full data set has the advantage of including J , H , K , and F560W in our analysis, increasing the existing optical data, and extending the observations up to nearly 60 days. We denote this set as “Extended.” Both sets are corrected for extinction using the SF11 assumption for the foreground extinction; see Section 3.2. We made the choice not to take into account any radio data, as only a subset was publicly available at the time of the publication of the article (e.g., data from Laskar et al. 2023 were not yet available). For these two multiwavelength data sets and both Bayesian inferences presented below, we use the same parameter space and priors, presented in Table 1, except

for the initial Lorentz factor Γ_0 , which is needed only in the second model including the coasting phase. The luminosity distance to the source is fixed to $D_L = 742$ Mpc, corresponding to a redshift $z = 0.151$ for a flat cosmology with $H_0 = 67.7 \text{ km s}^{-1} \text{ Mpc}^{-1}$ and $\Omega_m = 0.307$ (Planck Collaboration et al. 2016).

3.4.1. Bayesian Inference Using NMMA: Investigation of the Jet Structure and SN Contribution

As a further framework to interpret GRB 221009A, we use the Nuclear physics and Multi-Messenger Astronomy framework NMMA (Dietrich et al. 2020; Pang et al. 2022),⁸² which allows us to perform joint Bayesian inference of multi-messenger events containing gravitational waves, kilonovae, SNe, and GRB afterglows. We have analyzed both the GRANDMA and Extended data sets with NMMA.

For this work, we follow Kunert et al. (2023) and first employ the top-hat jet structure (with on-axis assumption and a free case) with the semianalytic code `afterglowpy` (van Eerten et al. 2010; Ryan et al. 2020).⁸³ In this model, the dynamics of the relativistic ejecta propagating through the interstellar medium are treated under the thin-shell approximation, and the angular structure is introduced by dissecting the blast wave into angular elements, each of which is evolved independently, including lateral expansion. Magnetic field amplification, electron acceleration, and the synchrotron emission from the forward shock are treated according to the analytical prescriptions of Sari et al. (1998). The observed radiation is computed by performing equal-time arrival surface integration. It is important to note that the model does not account for the presence of the reverse shock or the early coasting phase and does not include inverse Compton radiation. This limits its applicability to the early afterglow of very bright GRBs.

While we find a more steeply decaying emission component at early times, it is unclear whether it can be attributed to the reverse-shock emission (Laskar et al. 2023).

The advantage of the NMMA framework is the possibility of comparing different astrophysical scenarios and models in a straightforward way. As a starting point, we compare different jet structures. In addition to the top-hat jet, we also employed Gaussian and power-law jets. The Gaussian jet features an angular dependence $E(\theta_{\text{obs}}) \propto \exp(-\theta_{\text{obs}}^2/(2\theta_c^2))$ for $\theta_{\text{obs}} \leq \theta_w$, with θ_w being an additional free parameter. The power-law jet features an angular dependence $E(\theta_{\text{obs}}) \propto (1 + (\theta_{\text{obs}}/\theta_c)^2/b)^{-b/2}$ for $\theta_{\text{obs}} \leq \theta_w$, with θ_w and b being additional parameters.

We present our best-fit light curves for the SF11 extinction with different jet structures assumed in Figure 7, which shows the GRANDMA data (see Figure 12 in the Appendix for the Extended data).

We find that the observational data are only moderately well fit by the model. While the r -band light curve is reasonably well recovered, the predicted light curves at higher frequencies, especially in X-rays, cannot reproduce the observed evolution.

We present the corresponding source parameters, namely, the inclination angle θ_{obs} , isotropic energy E_0 , interstellar medium density n_{ISM} , half-opening angle of the jet core θ_{core} , and microphysical parameters $\{p, \epsilon_e, \epsilon_B, \zeta\}$ (the power-law

⁸² <https://github.com/nuclear-multimessenger-astronomy/nmma>

⁸³ The nested sampling algorithm implemented in PYMULTINEST (Buchner 2016) is used.

Table 1
NMMA: Parameters and Prior Bounds Employed in Our Bayesian Inferences

Parameter	Bounds	Prior	Top Hat		Top Hat On-axis		Gaussian		Power Law	
			GRANDMA	Extended	GRANDMA	Extended	GRANDMA	Extended	GRANDMA	Extended
Isotropic afterglow energy E_0 (erg)	$[10^{50}, 10^{58}]$	Log uniform	$10^{54.16^{+0.71}_{-0.45}}$	$10^{54.71^{+0.91}_{-0.80}}$	$10^{54.15^{+0.52}_{-0.45}}$	$10^{54.51^{+0.52}_{-0.57}}$	$10^{54.62^{+1.18}_{-0.81}}$	$10^{55.27^{+1.20}_{-1.10}}$	$10^{54.17^{+1.15}_{-0.68}}$	$10^{55.13^{+1.22}_{-1.05}}$
Ambient medium's density n_{ism} (cm^{-3})	$[10^{-6}, 10^3]$	Log uniform	$10^{2.61^{+0.39}_{-0.70}}$	$10^{2.60^{+0.40}_{-0.63}}$	$10^{2.61^{+0.39}_{-0.49}}$	$10^{2.51^{+0.49}_{-0.51}}$	$10^{2.27^{+0.73}_{-1.14}}$	$10^{2.48^{+0.52}_{-0.82}}$	$10^{+2.39^{+0.61}_{-1.04}}$	$10^{-2.51^{+0.49}_{-0.76}}$
Energy fraction in electrons ϵ_e	$[10^{-4}, 1]$	Log uniform	$10^{-0.38^{+0.38}_{-0.70}}$	$10^{-0.96^{+0.66}_{-0.81}}$	$10^{-0.41^{+0.41}_{-0.47}}$	$10^{-0.68^{+0.49}_{-0.51}}$	$10^{-0.85^{+0.78}_{-1.09}}$	$10^{-1.39^{+0.98}_{-1.08}}$	$10^{-0.75^{+0.67}_{-1.07}}$	$10^{-1.27^{+0.93}_{-1.09}}$
Energy fraction in magnetic field ϵ_B	$[10^{-9}, 1]$	Log uniform	$10^{-6.54^{+0.62}_{-0.49}}$	$10^{-6.59^{+0.64}_{-0.56}}$	$10^{-6.56^{+0.49}_{-0.42}}$	$10^{-6.83^{+0.55}_{-0.49}}$	$10^{-6.46^{+1.02}_{-0.86}}$	$10^{-6.71^{+0.84}_{-0.71}}$	$10^{-6.50^{+0.90}_{-0.80}}$	$10^{-6.69^{+0.79}_{-0.70}}$
Electron distribution power-law index p	[2, 3]	Uniform	$2.49^{+0.04}_{-0.04}$	$2.39^{+0.03}_{-0.03}$	$2.52^{+0.04}_{-0.04}$	$2.53^{+0.03}_{-0.03}$	$2.49^{+0.04}_{-0.05}$	$2.40^{+0.03}_{-0.03}$	$2.49^{+0.04}_{-0.04}$	$2.40^{+0.03}_{-0.03}$
Fraction of accelerated electrons ζ	$[10^{-4}, 1]$	Log uniform	$10^{-0.63^{+0.45}_{-0.67}}$	$10^{-0.39^{+0.39}_{-0.62}}$	$10^{-0.44^{+0.44}_{-0.47}}$	$10^{-0.47^{+0.47}_{-0.52}}$	$10^{-0.85^{+0.78}_{-1.09}}$	$10^{-0.52^{+0.52}_{-0.83}}$	$10^{-0.75^{+0.67}_{-1.07}}$	$10^{-0.47^{+0.67}_{-0.80}}$
Viewing angle θ_{obs} (deg)	[0, 30]	Uniform	$21.45^{+4.79}_{-5.56}$	$17.14^{+4.82}_{-4.50}$	0	0	$13.98^{+5.75}_{-5.54}$	$12.32^{+4.87}_{-5.04}$	$15.36^{+7.33}_{-6.31}$	$13.19^{+5.34}_{-5.45}$
Jet core's opening angle θ_{core} (deg)	[0.1, 30]	Uniform	$24.91^{+5.09}_{-5.50}$	$23.68^{+6.31}_{-5.42}$	$28.85^{+1.15}_{-2.37}$	$29.58^{+0.42}_{-0.98}$	$27.65^{+2.35}_{-4.17}$	$27.85^{+2.15}_{-4.02}$	$27.29^{+2.71}_{-4.80}$	$27.56^{+2.44}_{-4.00}$
"Wing" truncation angle θ_{wing} (deg)	[0.1, 30]	Uniform	$16.65^{+6.81}_{-6.83}$	$17.51^{+7.01}_{-7.19}$	$18.33^{+8.99}_{-7.17}$	$18.70^{+7.49}_{-7.54}$
Power-law structure index b	[0.1, 7]	Uniform	$2.42^{+3.62}_{-2.32}$	$2.64^{+3.41}_{-2.54}$
Angle ratio $\theta_{\text{obs}}/\theta_{\text{core}}$	[1/300, 300]	...	$0.866^{+0.05}_{-0.06}$	$0.725^{+0.04}_{-0.04}$	0	0	$0.515^{+0.212}_{-0.189}$	$0.454^{+0.165}_{-0.192}$	$0.573^{+0.304}_{-0.232}$	$0.491^{+0.180}_{-0.218}$

Note. We report median posterior values at 90% credibility from simulations that were run with different jet structures using SF11 extinction data for analysis (GRANDMA and Extended); see Section 3.4.1 and Figures 12 and 13.

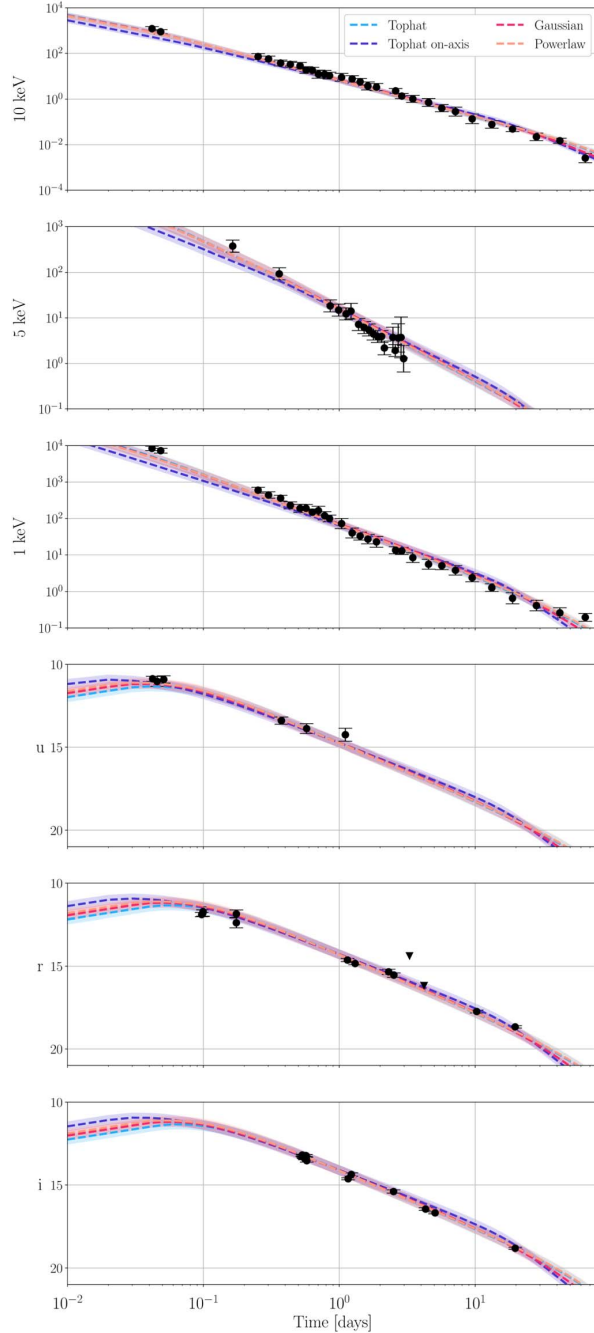


Figure 7. The NMMA observational data (GRANDMA data) and best-fit light curves of selected filters for the NMMA analysis using the SF11 extinction and the four employed jet structures. The X-ray bands are shown in microjanskys, and the rest of the bands are shown in AB magnitude.

index of the electron energy distribution, the fraction of energy in electrons, the fraction of energy in the magnetic field, and the fraction of electrons accelerated, respectively), using the four different jet structure models in Figure 8, which uses the GRANDMA data (see Appendix for the Extended data); each simulation uses 2048 live points for the nested sampling. The full posteriors can be found in Table 1.

Table 2
The log Bayes Factor between Different Models

	Extended Data	GRANDMA Data
Top hat $\theta_{\text{obs}} \leq 0$ vs. $\theta_{\text{obs}} = 0$	71.26 ± 0.14	30.66 ± 0.13
Top hat vs. Gaussian	4.29 ± 0.14	3.86 ± 0.14
Top hat vs. power law	3.53 ± 0.14	3.19 ± 0.14

Note. For both the Extended and GRANDMA data, the top-hat model without an on-axis assumption is preferred.

Table 3
The $\chi^2/\text{d.o.f.}$ of Different Models for NMMA

	Extended Data	GRANDMA Data
Top hat $\theta_{\text{obs}} \leq 0$	0.551	0.496
Top hat $\theta_{\text{obs}} = 0$	0.882	0.972
Gaussian	0.561	0.542
Power law	0.555	0.520

Most surprising in our analysis might be the relatively large jet opening angle (the viewing angle being near the edge but still within the jet), which might be hard to explain given the high isotropic energy release of the GRB. For the top hat on-axis (i.e., $\theta_{\text{obs}} = 0$), the light curve seems dimmer than expected for the X-ray data, which drives the analysis to prefer larger viewing angles. Although a larger viewing is preferred, the relation of $\theta_{\text{obs}} < \theta_{\text{core}}$ is clearly observed in the posterior of the angle ratio $\theta_{\text{obs}}/\theta_{\text{core}}$ (in Table 1), which is attributed to the absence of the jet break in the present data. We also provide the log Bayes Factors in Table 2 and the $\chi^2/\text{d.o.f.}$ for these fits in Table 3.

Finally, following the study of Fulton et al. (2023), we investigate the possibility of an SN connected to GRB 221009A. For modeling the SN, we use the nugent-hyper model from `sncosmo` (Levan et al. 2005) with a shift in the absolute magnitude, S_{max} , as the main free parameter. We vary this free parameter within $S_{\text{max}} \in [-30 \text{ mag}, 30 \text{ mag}]$. The nugent-hyper model is a template constructed from observations of SN 1998bw (Galama et al. 1998). Within our analysis, we find that in our runs combining the GRB top-hat jet afterglow with an SN component, the $\chi^2/\text{d.o.f.}$ are very similar to the pure top-hat jet model (0.551 and 0.548 for Extended data and 0.496 and 0.503 for GRANDMA data). Due to the size of the parameter space, the log Bayes factor prefers the simpler top-hat jet model, 0.542 ± 0.140 for the Extended data and 0.540 ± 0.136 for the GRANDMA data (see Table 2). Hence, there is no strong evidence for or against the presence of an SN contribution consistent with the nugent-hyper model combined with the models used in our analysis (see, for instance, Fulton et al. 2023 for another interpretation).

3.4.2. Refining the Physics in the Top-hat Jet Model

The poor quality of the fits obtained in Section 3.4.1 is a clear indication of tension between the observed temporal and spectral slopes, as suggested by other authors, e.g., Laskar et al. (2023), Sato et al. (2023), and O'Connor et al. (2023). We also note that some of the parameters obtained and presented in Figures 8 and 13 are at odds with typical GRB afterglow parameters. Perhaps the most striking is the very large jet opening angle. It is constrained to $\theta_{\text{core}} \gtrsim 15^\circ$, while typical

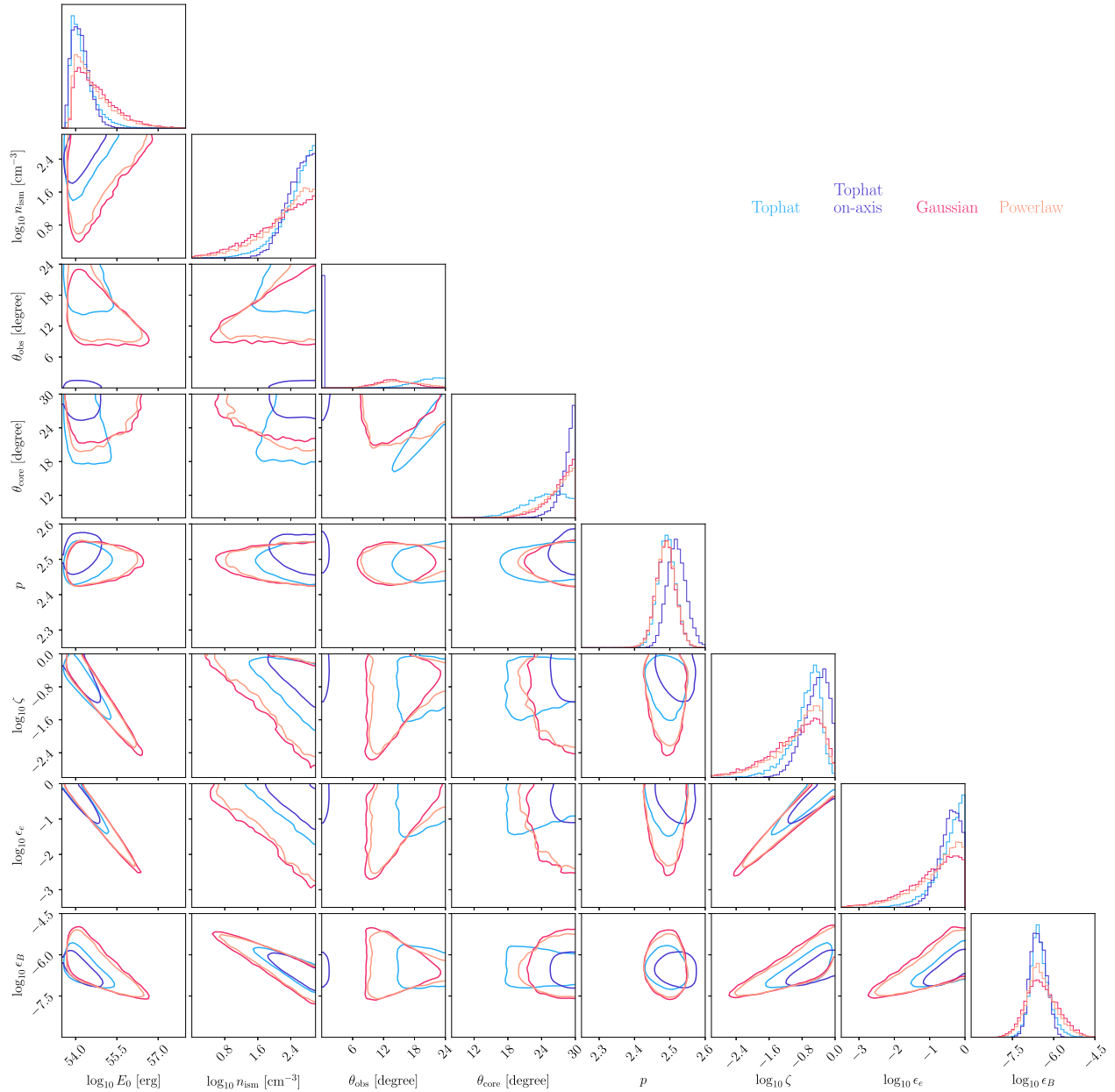


Figure 8. The NMMA posterior distribution (shown are 90% confidence intervals) for our selected data sets when using different jet models of afterglow analyzing the GRANDMA data.

jets have opening angles $\theta_{\text{core}} \simeq (2.5 \pm 1.0)$ (Wang et al. 2018).

The afterglow model, which is used by NMMA despite already being a refined implementation of the external shock afterglow model (Ryan et al. 2020), suffers from some limitations. The dynamics of the jet deceleration is assumed to be in the self-similar regime at all times, which can lead to flux overestimates at very early times when the jet is still in the coasting phase. We also note that synchrotron self-Compton (SSC) scattering is not accounted for; this could be important in the case of GRB 221009A, where some very high energy photons observed may hint toward strong SSC emission.

To further validate the previous analysis, we also model the afterglow data of GRB 221009A using the afterglow model from C. Pellouin & F. Daigne (2023, in preparation), which not only includes synchrotron radiation but also computes the SSC radiation, taking into account both the Thomson and Klein-Nishina regimes with a treatment following Nakar et al. (2009). This model also accounts for the jet lateral structure at any viewing angle and includes the treatment of the coasting phase of the jet propagation, which can induce differences at early times. A detailed description of this afterglow model will be provided in C. Pellouin & F. Daigne (2023, in preparation). However, an analysis with the best-fit parameters shows that it

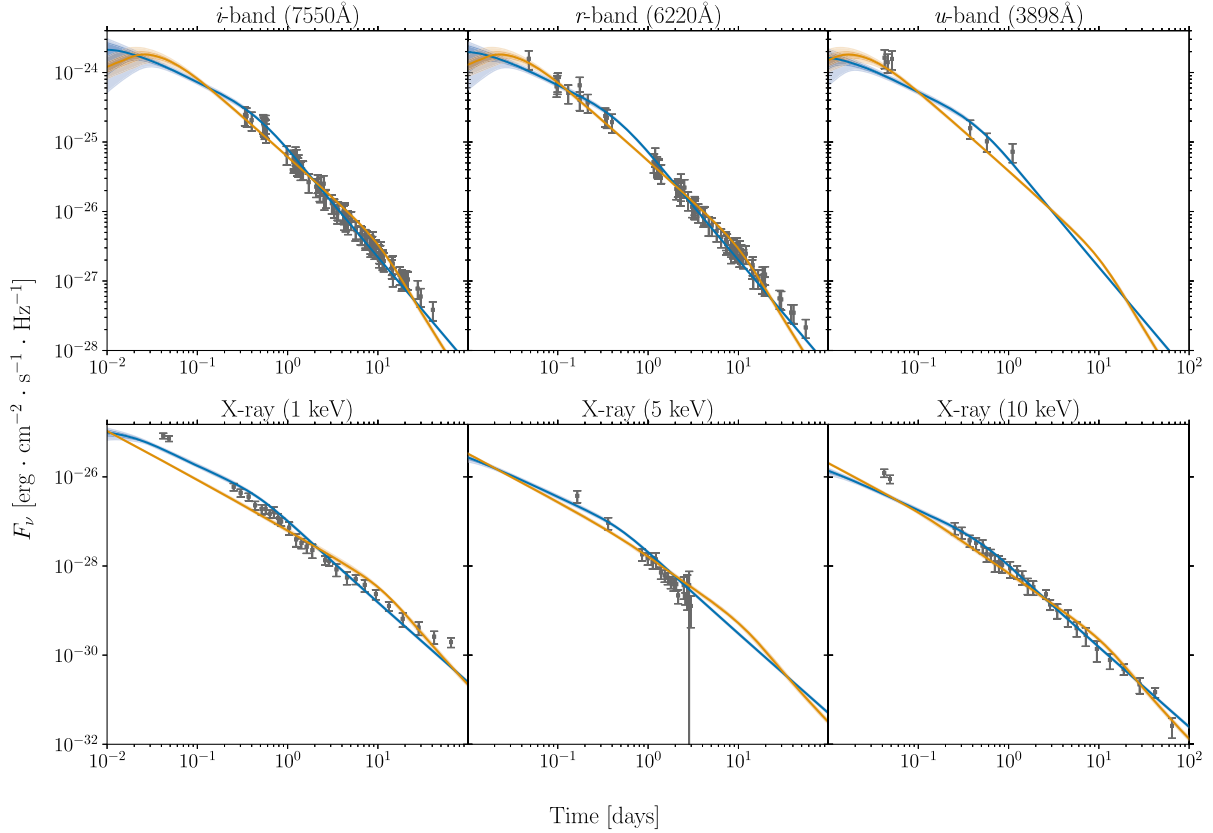


Figure 9. Bayesian inference presented in Section 3.4.2. Shown are the predicted light curves for the two classes of parameters reported in Figure 10 and found using a top-hat model with a fixed observing angle $\theta_{\text{obs}} = 0^\circ$ and assuming only synchrotron radiation. Observing frequencies or energies are shown on top of each panel, and the fitted observational data are displayed in gray. Blue curves show the model with a low θ_{core} and $p \sim 2$. Orange curves show the model with a high θ_{core} .

Table 4
Bayesian Inference Presented in Section 3.4.2: Parameters and Prior Bounds Employed in Our Bayesian Inferences

Parameter	Symbol	Bounds	Prior	Posterior	
				Low θ_{core}	High θ_{core}
Isotropic afterglow energy (erg)	E_0	$[10^{50}, 10^{58}]$	Log uniform	$10^{57.01+0.99}_{-1.16}$	$10^{53.58+0.09}_{-0.08}$
Opening angle of the core of the jet (deg)	θ_{core}	$[0.1, 30]$	Uniform	$0.39^{+0.13}_{-0.11}$	$28.47^{+1.52}_{-1.18}$
Density of the ambient medium (cm^{-3})	n_{ism}	$[10^{-6}, 10^3]$	Log uniform	$10^{-4.23+1.36}_{-1.51}$	$10^{2.98+0.02}_{-0.04}$
Fraction of the energy that generates the magnetic field	ϵ_B	$[10^{-9}, 1]$	Log uniform	$10^{-1.93+1.39}_{-1.17}$	$10^{-6.59+0.11}_{-0.10}$
Fraction of the energy that accelerates the electrons	ϵ_e	$[10^{-4}, 1]$	Log uniform	$10^{-2.22+1.33}_{-1.16}$	$10^{-0.02+0.02}_{-0.05}$
Fraction of electrons accelerated at the shock	ζ	$[10^{-4}, 1]$	Log uniform	$10^{-1.10+1.10}_{-1.25}$	$10^{-0.04+0.04}_{-0.06}$
Electron population Lorentz factor injection index	p	$[2, 3]$	Uniform	$2.003^{+0.005}_{-0.003}$	$2.43^{+0.03}_{-0.02}$
Initial Lorentz factor	Γ_0	$[10^1, 10^3]$	Log uniform	$10^{2.96+0.04}_{-0.07}$	$10^{2.94+0.06}_{-0.11}$

Note. We report median posterior values at 90% credibility from simulations that were run with a top-hat jet structure with a fixed observing angle $\theta_{\text{obs}} = 0^\circ$ assuming synchrotron radiation. We fit the extended data set presented in Section 3.4. These results are discussed in Section 3.4.2 and Figures 9 and 10.

does not impact the light curves after the first time observed by Swift XRT, at 3618 s in this case.

We used an MCMC routine to infer the physical parameters for the afterglow using the data set presented at the beginning of Section 3.4. When performing the χ^2 computation, we inflate the errors to avoid any overfitting of points with artificially small errors using $\max\{\text{flux error}; 0.3 \times \text{flux}\}$. We initialize 100 independent chains and run them over 20,000

iterations; we remove chains that get stuck in a high- χ^2 region of the parameter space, as they are not true solutions.

Our first analysis uses a simplified model, where only synchrotron radiation powers the afterglow emission, for comparison with the analysis presented in Section 3.4.1. For the top-hat jet with a fixed viewing angle $\theta_{\text{obs}} = 0^\circ$, the posterior samples converge toward parameter values that are very similar to those presented in Section 3.4.1 when fitting

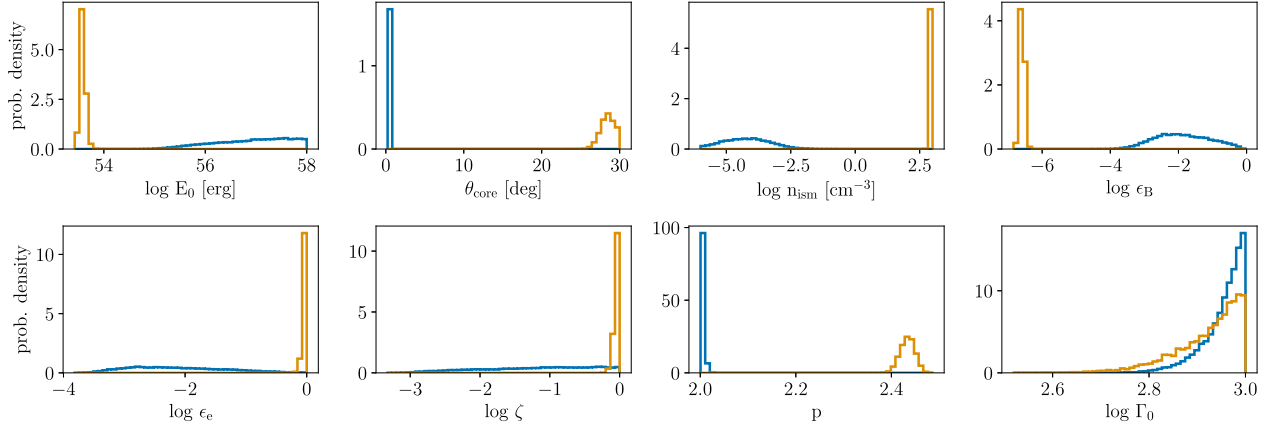


Figure 10. Bayesian inference presented in Section 3.4.2. Shown is a marginalized posterior distribution of the free parameters best fitting the extended data with an on-axis observation of a top-hat jet radiating via synchrotron only, as presented in Section 3.4.2. In blue, we show marginalized distributions for the model that features a low θ_{core} and $p \sim 2$, not found with NMMA. In orange, we show marginalized distributions for the model with a high θ_{core} , similar to what is found with NMMA. The median values and 90% confidence intervals can be found in Table 4.

both the GRANDMA and extended data. Those values are listed in Table 4, and the results are presented in Figure 9. Our analysis with this independent model confirms the relatively poor quality of the best fit. However, when fitting the extended data set, another solution emerges in the MCMC posteriors with this model; this fit has a lower χ^2 but still leads to a best fit of poor quality. Contrary to NMMA using *afterglowpy*, the model does not include the lateral expansion of the jet at late times, which leads to an alternative scenario with an early jet break with a shallow post-jet break decay slope. This solution implies a small core jet opening angle $\theta_{\text{core}} \lesssim 0.7^\circ$ and an electron slope very close to 2. Both solutions to the model appear on an equal number of MCMC chains (44 each) and therefore correspond to two local minima for the χ^2 distribution, with similar weight. When isolating both solutions, we observe the usual parameter correlations (e.g., $E_{0,\text{iso}}$ and n_{ism} or between ϵ_B , ϵ_e , and ζ). For better readability, we show in Figure 10 only the marginalized posterior distribution for the eight free parameters of the model and split the two classes of models into two colors. In blue, we show marginalized posterior distributions for this new model (with a low θ_{core} and $p \lesssim 2.02$), and in orange, we show marginalized posterior distributions for the model with a large θ_{core} , similar to what is found in Section 3.4.1. The median values and 90% confidence intervals are reported in Table 4 for the two models.

We investigate these two types of models and show in Figure 9 the light curves obtained with the two posterior samples of parameters. The light curves are computed in three optical/UV bands (*i*, 755 nm; *r*, 622 nm; and *u*, 389.8 nm) and three X-ray bands (1 and 10 keV with XRT observations and 5 keV with HXMT observations). All of the fitted observations are shown in gray.

Using Figure 9, we see that though both classes of models are able to broadly reproduce the multiwavelength observations, they both fail to reproduce the observed features accurately. The models with high θ_{core} , also found with NMMA and shown in orange, accurately fit the optical but fail to reproduce the observed X-ray temporal slope. They also feature a jet break at $t \sim 8$ days, which is not observed in the data. Conversely, the models with low θ_{core} , though slightly favored statistically ($\chi^2 = 600$ for the latter model, $\chi^2 = 950$ for the

former with the same d.o.f.), also pose major interpretation challenges. The temporal decay in X-rays is also not in line with X-ray observations, and the very high E_0 values that are found (between 10^{55} and 10^{58} erg) imply a very low prompt efficiency, given a prompt energy $E_{\gamma,\text{iso}} \sim 10^{55}$ erg (An et al. 2023).

While the true energy in the jet ranges between 10^{51} and 5×10^{53} erg due to the very narrow jet opening angles $\theta_{\text{core}} \lesssim 0.7^\circ$, the posterior distribution of the prompt efficiency peaks at 10^{-4} , which seems very low for most prompt emission models, especially considering the bright luminosity of the prompt emission of GRB 221009A. However, this posterior distribution shows a tail toward larger values, reaching 10^{-1} , which are more physically plausible. The physical relevance of this scenario is also questionable regarding the jet dynamics, as at least a moderate lateral expansion should be expected.

As a final verification, we also computed the predicted light curves at radio frequencies and compared them with observations reported in Laskar et al. (2023) and O’Connor et al. (2023). With both classes of models, our predictions overestimate the flux compared to the observations. We therefore conclude that while these parameters do correspond to the best fits of the extended data set using a top-hat jet model with a fixed observing angle $\theta_{\text{obs}} = 0^\circ$ and assuming only synchrotron radiation, they do not provide satisfactory predictions given other constraints found in the literature, motivating a deeper analysis. When accounting for SSC scattering in the model, we ran the models with a narrow θ_{core} . We also tested models with a free observing angle and found similar results to those presented in Section 3.4.1; this model is preferred, but the typical values found for the parameters are close to those found with the fixed observation angle. Therefore, our analysis shows that even in a more realistic description, including the coasting phase and the SSC radiation, the standard top-hat jet afterglow model is in tension with the observed data. We note that for free observing angles, the MCMC chains do not favor a narrow θ_{core} anymore. Finally, we also study the impact of the jet structure; our findings are similar to those presented in Section 3.4.1. We also performed our analysis with only the GRANDMA data set and found similar values as those found with NMMA, but in this case, the MCMC chains also do not find

the very narrow θ_{core} models. We leave to a future study the investigation of more advanced models regarding, for instance, the jet structure of the external medium density.

4. Discussion and Conclusion

In this work, the properties of the GRB 221009A afterglow are studied using a multiwavelength data set presenting data from optical observations from ground-based telescopes or the GRANDMA/KNC network and the LE X-ray telescope on board the Insight-HXMT satellite. The X-ray observations were made 9.8 hr to 3 days after the trigger time, while the ultraviolet, optical, and NIR sky was covered from the prompt emission (shallow limits from all-sky cameras) and then (with narrow-field instruments) from 2.2 hr after the trigger time to about 20 days. The GRANDMA network involved more than 30 telescopes, including both professional and amateur telescopes, and collected more than 200 images for this GRB. This is one of the few GRB afterglows that has been observed extensively by amateur astronomers. The measurements with the deepest limiting magnitudes reach $m_{\text{lim}} = 24.6$ mag in the g' band with a professional telescope (CFHT) and $m_{\text{lim}} = 21.5$ mag in the V band with an amateur telescope, demonstrating the potential for citizen contributions to time-domain astrophysical science. We also collected prompt observations of the GRB in the optical (between T_0 and T_0+500 s) by cameras managed by the Desert Fireball Network, but no optical flash was detected in the V band (down to a limiting magnitude of 3.8 mag). We furthermore collect public data from the XRT telescope on board the Swift satellite, with the first observation having been taken about 1 hr after the GRB trigger time. Two specially tuned photometric pipelines, STDPipe and MUPHOTEN, are used to analyze the GRB afterglow data. The observations are calibrated using stars from the PS1 catalog, with slightly different results being obtained for Johnson–Cousins filters between the two pipelines. For this reason, only a subset of data with good quality and consistent results has been selected for analysis.

In this paper, we tackle the challenge of determining the significant extinction correction, as the GRB lies behind the Galactic plane. To correct for this, we employ two different techniques. First, we use the SF11 maps, which may overestimate the extinction. Second, we use the RF09 maps, which utilize NIR color excess determinations based on 2MASS observations. This method results in a significantly lower extinction value (but is only valid out to 2–3 kpc) compared to the SF11 value. Taking into account the existence of dust at larger distances determined by X-ray measurements of dust rings (Negro et al. 2023; Williams et al. 2023; Vasilopoulos et al. 2023), we proceed to discuss the reliability of these measurements and conduct our follow-up analysis using both correction methods for comparison.

Empirical analysis of the light curve shows it to be composed of three power-law sections (steep, shallow, and steep), with the first section only covered by a short data baseline. The data after ~ 0.1 day show a clear break and a relatively shallow postbreak slope with no further indication of a jet break, which would usually lead to a decay slope $\alpha \gtrsim 2$. The light-curve analysis yields an SED, which we fit with three solutions for the foreground/host-galaxy extinction, including one under the assumption that the entire extinction is foreground. All extinction models yield viable solutions; in combination with spectroscopic evidence for small-to-moderate

host-galaxy extinction, we prefer the combination of SF11 foreground correction and about half a magnitude of SMC-type host-galaxy extinction. Using these values, we are able to compare the optical afterglow to a global sample and find it to be luminous but not excessively so, in contrast to the extreme isotropic energy release of the prompt emission, a result also found for the X-ray afterglow (Williams et al. 2023).

We analyzed our observations in the framework of the standard GRB afterglow model; in this model, the observed flux is dominated by synchrotron radiation from shock-accelerated electrons at the forward external shock due to the deceleration of the GRB relativistic jet by the ambient medium (Sari et al. 1998). We limited our study to the case of a uniform medium. We performed Bayesian inference using two multi-wavelength data sets, the first composed of our own GRANDMA data complemented by X-ray data (Swift XRT and HXMT-LE) and the second extended with additional optical and NIR measurements collected from the literature; see Section 3.4. This Bayesian inference was done using NMMA (Dietrich et al. 2020; Pang et al. 2022) employing the semianalytic code `afterglowpy` for afterglow light-curve modeling (Ryan et al. 2020) and was complemented with an independent Bayesian inference based on the model by C. Pellouin & F. Daigne (2023, in preparation) to test the impact of more realistic physics for the jet dynamics; this model accounts for both the early coasting phase and the emission by including the SSC emission with a full treatment in the Thomson and Klein–Nishina regimes. We started with the simplest version of the standard GRB afterglow model, i.e., a top-hat jet seen exactly on-axis. Both independent pipelines converged to similar solutions, with a best fit that yields poor fits to some of the observations. This analysis confirms a tension between the standard afterglow model and the observed spectral and temporal evolution, as suggested by Laskar et al. (2023), based on the closure relations. The smoother transitions, rather than sharp breaks, observed in such a detailed model only moderately improve the predicted light curves. In particular, the high-frequency light curves, especially in X-rays, are not well reproduced, and the late-time radio flux is overpredicted. In addition, we note that this best fit yields an unexpectedly large opening angle for such a bright GRB and a very dense external medium. We explored several additional effects: free viewing angle, lateral structure of the jet (power law or Gaussian), early coasting phase, SSC radiation, or underlying SN component. None of these models that include more realistic physics leads to better fits. We therefore conclude that the modeling of the GRB 221009A afterglow will require going beyond the most standard afterglow model by, for instance, considering more complex jet structure, external density, or the contribution of the reverse shock, as also suggested by Laskar et al. (2023) and O'Connor et al. (2023).

Object GRB 221009A is an absolutely unique event, representing not just the nearest extremely energetic GRB but potentially also the most energetic GRB ever detected. These two factors combined make it by far the brightest GRB ever seen, at the very least a once-in-a-lifetime event and probably even a millennial one. To have such an event occur when we have a fleet of satellites in space able to detect gamma rays and the ground- and space-based capabilities to determine the distance and follow up the afterglow evolution in detail, even by amateur astronomers, is fortuitous indeed. It is unlikely that

a chance like this will come again in the coming decades or even centuries, making this an event to be remembered through the ages.

The GRANDMA consortium thanks the amateur participants of the Kilonova-Catcher program and observers from GRANDMA. GRANDMA thanks the paper writing team managed by D.A.K. The Kilonova-Catcher program is supported by the IdEx Université de Paris Cité ANR-18-IDEX-0001. The GRANDMA collaboration thanks G. Parent, E. Maris, F. Bayard, O. Aguerre, and M. Richmond for their observations. This project has received financial support from the CNRS through the MITI interdisciplinary programs. We thank Mathias Schultheis for fruitful discussions regarding extinction selection. D.A.K. acknowledges the support by the State of Hessen within the Research Cluster ELEMENTS (Project ID 500/10.006). S.A. acknowledges the financial support of the Programme National Hautes Energies (PNHE) and Crédits Scientifiques Incitatifs dUCA 2023. M.W.C. acknowledges support from National Science Foundation grant Nos. PHY-2010970 and OAC-2117997. C.A. and M.W.C. were supported by the Preparing for Astrophysics with LSST Program, funded by the Heising Simons Foundation through grant 2021-2975 and administered by Las Cumbres Observatory. J.-G.D. is supported by a research grant from the Ile-de-France Region within the framework of the Domaine d'Intérêt Majeur-Astro physique et Conditions d'Apparition de la Vie (DIM-ACAV). This work has made use of the Infinity Cluster hosted by Institut d'Astrophysique de Paris. C.P. acknowledges funding support from the Initiative Physique des Infinis (IPI), a research training program of the Idex SUPER at Sorbonne Université. The Egyptian team acknowledges support from the

Science, Technology & Innovation Funding Authority (STDF) under grant No. 45779. S.K. is supported by the European Structural and Investment Fund and the Czech Ministry of Education, Youth and Sports (project CoGraDS—CZ.02.1.01/0.0/0.0/15_003/0000437). J.M. is supported by the NSFC 11673062 and Oversea Talent Program of Yunnan Province. The Insight-HXMT team acknowledges support from the National Key R&D Program of China (2021YFA0718500) and the National Natural Science Foundation of China under grant Nos. U1838201 and U1838202. J. Mao is supported by the National Natural Science Foundation of China 11673062 and Yunnan Revitalization Talent Support Program (YunLin Scholar Award).

Appendix

In the appendix, Figure 11 displays the optical light curves of GRB 221009A in various bands, as analyzed in the section on “Empirical light curve analysis”. These light curves have been corrected for the SF11 galactic extinction using both GRANDMA data and common literature sources. Each empirical light curve is composed by three power-law sections. To complement this analysis, Figure 12 presents the results of the NMMA analysis, which utilized the light curves from Figure 11 and compared the best-fit light curves using different types of jet structures. Figure 13 shows the physical properties of the GRB using the data from Figure 11. For additional context, Table 5 lists all the measurements contributed by the GRANDMA collaboration that were used in constructing Figure 11. Moreover, Table 6 provides the results available in the Gamma-Ray coordination network, augmenting the information available in Table 5.

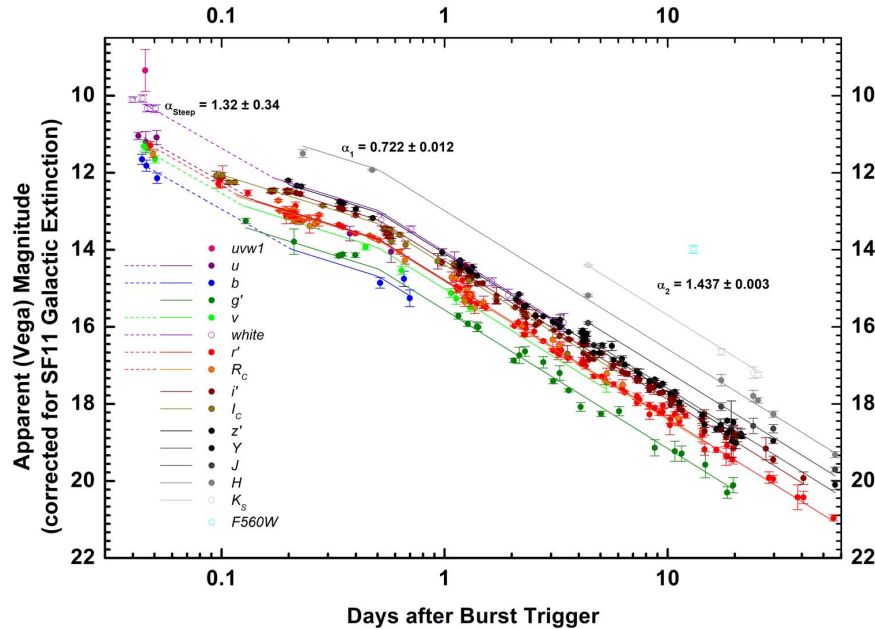


Figure 11. The UVOIR light curve of GRB 221009A (see Section 3.1). The magnitudes, expressed in the Vega system, are corrected for the SF11 galactic extinction. The break slope is at ~ 0.6 day post-GRB trigger time between α_1 and α_2 .

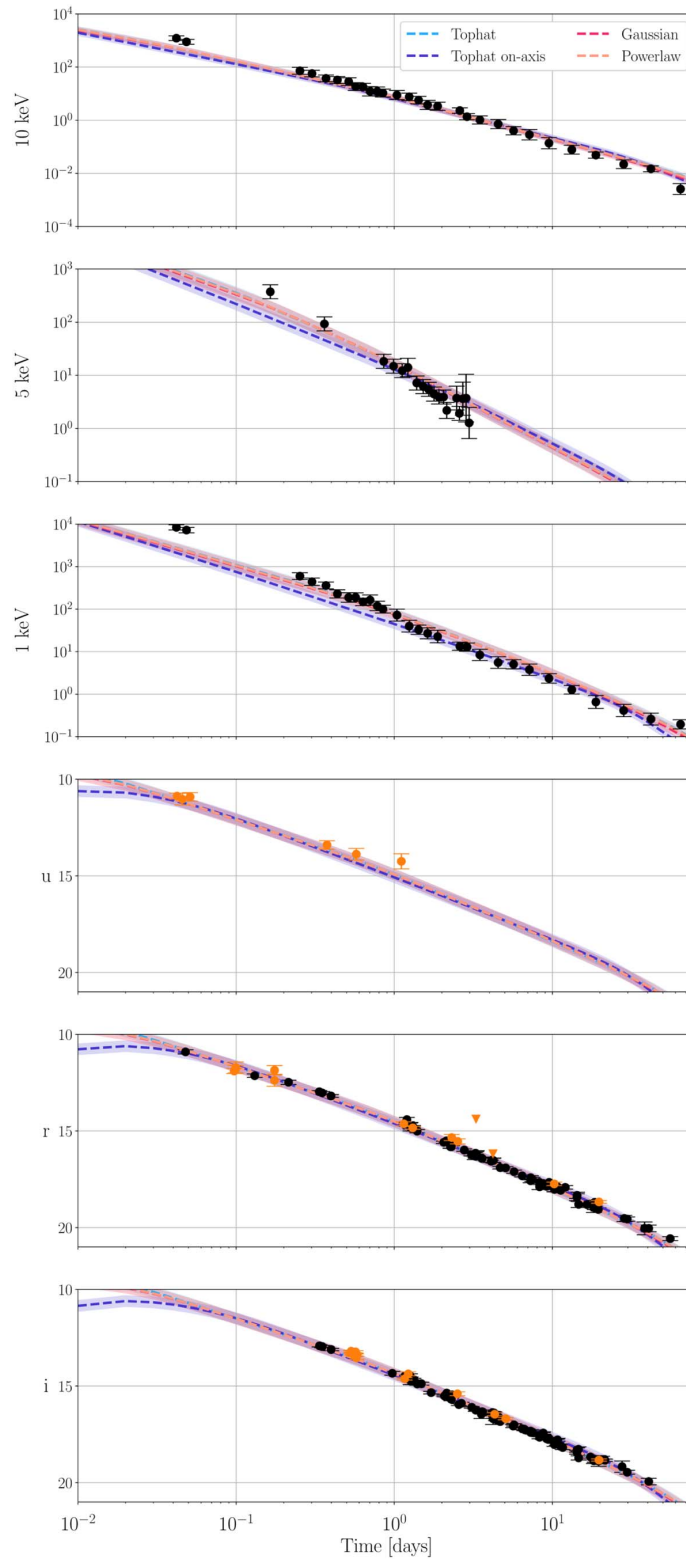


Figure 12. The NMMA observational data (Extended data) and best-fit light curves of selected filters for the NMMA analysis using the SF11 extinction and the four employed jet structures. The X-ray bands are shown in microjanskys, and the rest of the bands are shown in AB magnitude. In the optical band, the GRANDMA data points are shown in orange.

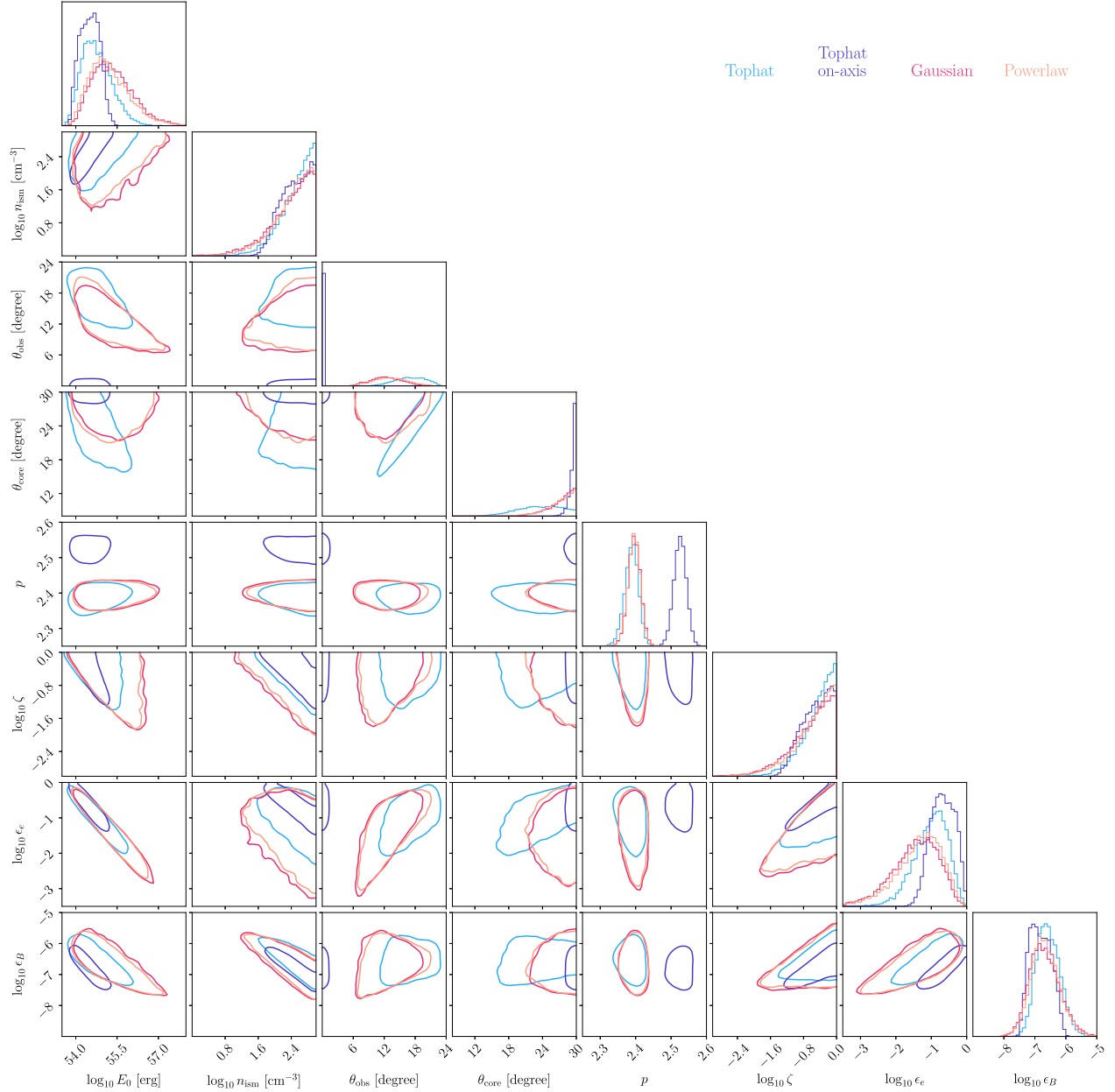


Figure 13. The NMMA posterior distribution (90% confidence intervals) for our selected data sets when using different jet models of afterglow analyzing the Extended data.

Table 5
Data Used for the Numerical Data Analysis Sections (Sections 3.4.1 and 3.4.2)

Delay		Filter	SF11		RF09		Observatory
(day)	(s)		Magnitude	Upper Limit	Magnitude	Upper Limit	
0.0423	3.657×10^3	<i>u</i>	10.87 ± 0.15	...	10.65 ± 0.35	...	Swift UVOT
0.0457	3.949×10^3	<i>u</i>	$11.03 \pm 0.30^*$...	10.77 ± 0.44	...	Swift UVOT
0.0511	4.416×10^3	<i>u</i>	10.91 ± 0.22	...	10.75 ± 0.39	...	Swift UVOT
0.3755	3.244×10^4	<i>u</i>	13.40 ± 0.22	Swift UVOT
0.5751	4.969×10^4	<i>u</i>	13.88 ± 0.30	Swift UVOT
1.1084	9.576×10^4	<i>u</i>	14.25 ± 0.39	Swift UVOT

Table 5
(Continued)

Delay		Filter	SF11		RF09		Observatory
(day)	(s)		Magnitude	Upper Limit	Magnitude	Upper Limit	
0.2572	2.222×10^4	<i>B</i>	...	11.76	...	11.69	KNC-SCT-0.28
1.1368	9.822×10^4	<i>g'</i>	14.81 ± 0.21	...	14.70 ± 0.31	...	KAO
19.6945	1.702×10^6	<i>g'</i>	18.95 ± 0.22	...	18.84 ± 0.31	...	CFHT-Megacam
-0.0010	-90	<i>V</i>	...	-2.79	...	-2.9	Mundrabilla
-0.0007	-60	<i>V</i>	...	-2.79	...	-2.9	Mundrabilla
-0.0003	-30	<i>V</i>	...	-0.99	...	-1.1	Raw War Road
0.0000	0	<i>V</i>	...	-0.99	...	-1.1	Raw War Road
0.0004	30	<i>V</i>	...	-0.99	...	-1.1	Raw War Road
0.0007	60	<i>V</i>	...	-0.99	...	-1.1	Raw War Road
0.0011	90	<i>V</i>	...	-0.99	...	-1.1	Raw War Road
0.0014	120	<i>V</i>	...	-0.99	...	-1.1	Raw War Road
0.0017	150	<i>V</i>	...	-0.99	...	-1.1	Raw War Road
0.0021	180	<i>V</i>	...	-0.99	...	-1.1	Raw War Road
0.0024	210	<i>V</i>	...	-0.99	...	-1.1	Raw War Road
0.0031	270	<i>V</i>	...	-0.99	...	-1.1	Raw War Road
0.0035	300	<i>V</i>	...	-0.99	...	-1.1	Raw War Road
0.0042	360	<i>V</i>	...	-0.99	...	-1.1	Raw War Road
0.0045	390	<i>V</i>	...	-0.99	...	-1.1	Raw War Road
0.2677	2.313×10^4	<i>V</i>	12.60 ± 0.10	...	12.50 ± 0.22	...	KNC-SCT-0.28
1.1465	9.906×10^4	<i>V</i>	14.57 ± 0.16	...	14.47 ± 0.26	...	ShAO
1.2606	1.089×10^5	<i>V</i>	...	13.90	...	13.80	KNC-SCT-0.28
0.0972	8.40×10^3	<i>r'</i>	11.90 ± 0.13	...	11.79 ± 0.21	...	TRE
0.0993	8.58×10^3	<i>r'</i>	11.80 ± 0.19	...	11.69 ± 0.25	...	TRE
0.0995	8.60×10^3	<i>r'</i>	11.72 ± 0.29	...	11.61 ± 0.33	...	TRE
0.1748	1.510×10^4	<i>r'</i>	12.38 ± 0.31	...	12.27 ± 0.35	...	TRE
0.1750	1.512×10^4	<i>r'</i>	11.86 ± 0.24	...	11.75 ± 0.29	...	TRE
1.1489	9.926×10^4	<i>r'</i>	14.63 ± 0.10	...	14.52 ± 0.19	...	KAO
1.3077	1.130×10^5	<i>r'</i>	14.84 ± 0.07	...	14.73 ± 0.18	...	C2PU/Omicron
2.3083	1.994×10^5	<i>r'</i>	15.34 ± 0.16	...	15.23 ± 0.23	...	KNC-Parent
2.5206	2.178×10^5	<i>r'</i>	15.54 ± 0.13	...	15.43 ± 0.21	...	KNC-LCO/McDO-0.4 m
3.2874	2.840×10^5	<i>r'</i>	...	14.38	...	14.27	KNC-C11-ATLAS
4.2097	3.637×10^5	<i>r'</i>	...	16.18	...	16.07	KAO
10.2667	8.870×10^5	<i>r'</i>	17.74 ± 0.09	...	17.63 ± 0.19	...	C2PU/Omicron
19.6965	1.702×10^6	<i>r'</i>	18.67 ± 0.07	...	18.56 ± 0.18	...	CFHT/MegaCam
0.2736	2.364×10^4	<i>R_C</i>	12.41 ± 0.07	...	12.34 ± 0.18	...	KNC-SCT-0.28
1.0813	9.342×10^4	<i>R_C</i>	14.36 ± 0.15	...	14.29 ± 0.22	...	UBAI-ST60
1.2274	1.060×10^5	<i>R_C</i>	14.25 ± 0.10	...	14.18 ± 0.19	...	Lisnyky-AZT-8
1.2365	1.068×10^5	<i>R_C</i>	14.39 ± 0.10	...	14.32 ± 0.19	...	Lisnyky-AZT-8
1.2755	1.102×10^5	<i>R_C</i>	...	14.30	...	14.23	KNC-SCT-0.28
2.2956	1.983×10^5	<i>R_C</i>	...	14.91	...	14.84	KNC-SCT-0.28
2.3042	1.991×10^5	<i>R_C</i>	15.37 ± 0.10	...	15.30 ± 0.19	...	Lisnyky-AZT-8
3.2868	2.840×10^5	<i>R_C</i>	16.13 ± 0.12	...	16.06 ± 0.20	...	Lisnyky-AZT-8
5.0674	4.378×10^5	<i>R_C</i>	...	14.61	...	14.54	UBAI-ST60
11.1313	9.617×10^5	<i>R_C</i>	18.01 ± 0.19	...	17.94 ± 0.25	...	UBAI-AZT22
12.4567	1.076×10^6	<i>R_C</i>	...	16.02	...	15.95	VIRT
0.5333	4.608×10^4	<i>i'</i>	13.20 ± 0.06	...	13.13 ± 0.14	...	KNC-BGO
0.5372	4.641×10^4	<i>i'</i>	13.21 ± 0.06	...	13.14 ± 0.14	...	KNC-BGO
0.5411	4.675×10^4	<i>i'</i>	13.24 ± 0.06	...	13.17 ± 0.14	...	KNC-BGO
0.5450	4.709×10^4	<i>i'</i>	13.30 ± 0.06	...	13.23 ± 0.14	...	KNC-BGO
0.5489	4.742×10^4	<i>i'</i>	13.34 ± 0.07	...	13.27 ± 0.15	...	KNC-BGO
0.5527	4.775×10^4	<i>i'</i>	13.33 ± 0.06	...	13.26 ± 0.14	...	KNC-BGO
0.5572	4.814×10^4	<i>i'</i>	13.42 ± 0.06	...	13.35 ± 0.14	...	KNC-BGO
0.5611	4.848×10^4	<i>i'</i>	13.40 ± 0.06	...	13.33 ± 0.14	...	KNC-BGO
0.5650	4.882×10^4	<i>i'</i>	13.37 ± 0.07	...	13.30 ± 0.15	...	KNC-BGO
0.5689	4.915×10^4	<i>i'</i>	13.23 ± 0.06	...	13.16 ± 0.14	...	KNC-BGO
0.5727	4.948×10^4	<i>i'</i>	13.40 ± 0.07	...	13.33 ± 0.15	...	KNC-BGO
0.5766	4.982×10^4	<i>i'</i>	13.54 ± 0.08	...	13.47 ± 0.15	...	KNC-BGO
1.1625	1.004×10^5	<i>i'</i>	14.63 ± 0.06	...	14.56 ± 0.14	...	KAO
1.2255	1.059×10^5	<i>i'</i>	14.37 ± 0.10	...	14.30 ± 0.16	...	KNC-IRIS

Table 5
(Continued)

Delay		Filter	SF11		RF09		Observatory
(day)	(s)		Magnitude	Upper Limit	Magnitude	Upper Limit	
2.5092	2.168×10^5	i'	15.40 ± 0.10	...	15.33 ± 0.16	...	KNC-BGO
3.5534	3.070×10^5	i'	16.46 ± 0.22	...	16.39 ± 0.26	...	KNC-BGO
4.2108	3.638×10^5	i'	16.69 ± 0.30	...	16.62 ± 0.33	...	KAO
19.7097	1.703×10^6	i'	18.83 ± 0.06	...	18.76 ± 0.14	...	CFHT/MegaCam
0.2887	2.494×10^4	I_C	12.40 ± 0.06	...	12.21 ± 0.13	...	KNC-SCT-0.28
1.2902	1.115×10^5	I_C	14.31 ± 0.14	...	14.12 ± 0.18	...	KNC-SCT-0.28
2.3509	2.031×10^5	I_C	...	14.79	...	14.60	KNC-SCT-0.28
6.3104	5.452×10^5	I_C	16.96 ± 0.17	...	16.77 ± 0.21	...	Lisnyky-AZT-8
15.4848	1.338×10^6	I_C	...	16.98	...	16.79	VIRT
1.1745	1.015×10^5	z'	14.80 ± 0.07	...	14.70 ± 0.11	...	KAO
4.217	3.643×10^5	z'	16.73 ± 0.16	...	16.63 ± 0.19	...	KAO
13.184	1.139×10^6	z'	...	18.23	...	18.13	KAO
19.7308	1.705×10^6	z'	18.84 ± 0.09	...	18.74 ± 0.12	...	CFHT/MegaCam

Delay		X-ray Filter Central Frequency	Flux (Jy)	Flux Error (Jy)	Observatory
(day)	(s)				
0.1644	1.420×10^4	5 keV	3.74×10^{-4}	7.49×10^{-5}	HXMT/LE
0.3617	3.125×10^4	5 keV	9.32×10^{-5}	2.06×10^{-5}	HXMT/LE
0.8580	7.413×10^4	5 keV	1.83×10^{-5}	3.66×10^{-6}	HXMT/LE
0.9896	8.550×10^4	5 keV	1.49×10^{-5}	2.99×10^{-6}	HXMT/LE
1.1223	9.697×10^4	5 keV	1.23×10^{-5}	2.45×10^{-6}	HXMT/LE
1.2192	1.053×10^5	5 keV	1.41×10^{-5}	5.53×10^{-6}	HXMT/LE
1.3864	1.198×10^5	5 keV	7.18×10^{-6}	1.44×10^{-6}	HXMT/LE
1.5256	1.318×10^5	5 keV	6.17×10^{-6}	1.23×10^{-6}	HXMT/LE
1.6526	1.428×10^5	5 keV	5.45×10^{-6}	1.09×10^{-6}	HXMT/LE
1.7844	1.542×10^5	5 keV	4.44×10^{-6}	8.87×10^{-7}	HXMT/LE
1.9157	1.655×10^5	5 keV	3.91×10^{-6}	7.82×10^{-7}	HXMT/LE
2.0485	1.770×10^5	5 keV	3.91×10^{-6}	8.87×10^{-7}	HXMT/LE
2.1473	1.855×10^5	5 keV	2.19×10^{-6}	7.59×10^{-7}	HXMT/LE
2.4809	2.143×10^5	5 keV	3.73×10^{-6}	1.93×10^{-6}	HXMT/LE
2.5822	2.231×10^5	5 keV	1.92×10^{-6}	3.84×10^{-7}	HXMT/LE
2.7138	2.345×10^5	5 keV	3.64×10^{-6}	2.62×10^{-6}	HXMT/LE
2.8464	2.459×10^5	5 keV	3.73×10^{-6}	3.83×10^{-6}	HXMT/LE
2.9744	2.570×10^5	5 keV	1.27×10^{-6}	8.57×10^{-7}	HXMT/LE
0.0419	0.362×10^4	10 keV	1.23×10^{-3}	2.51×10^{-4}	Swift XRT
0.0486	0.420×10^4	10 keV	8.95×10^{-4}	1.88×10^{-4}	Swift XRT
0.2529	2.185×10^4	10 keV	7.23×10^{-5}	2.14×10^{-5}	Swift XRT
0.3018	2.608×10^4	10 keV	5.71×10^{-5}	1.64×10^{-5}	Swift XRT
0.3701	3.197×10^4	10 keV	3.76×10^{-5}	1.10×10^{-5}	Swift XRT
0.4365	3.771×10^4	10 keV	3.29×10^{-5}	9.87×10^{-6}	Swift XRT
0.5145	4.445×10^4	10 keV	2.87×10^{-5}	9.62×10^{-6}	Swift XRT
0.5698	4.923×10^4	10 keV	1.85×10^{-5}	6.31×10^{-6}	Swift XRT
0.6348	5.484×10^4	10 keV	1.80×10^{-5}	5.48×10^{-6}	Swift XRT
0.7026	6.070×10^4	10 keV	1.22×10^{-5}	4.97×10^{-6}	Swift XRT
0.7808	6.746×10^4	10 keV	1.22×10^{-5}	4.72×10^{-6}	Swift XRT
0.8481	7.327×10^4	10 keV	1.06×10^{-5}	3.63×10^{-6}	Swift XRT
1.0395	8.982×10^4	10 keV	8.91×10^{-6}	3.54×10^{-6}	Swift XRT
1.2431	1.074×10^5	10 keV	7.61×10^{-6}	2.45×10^{-6}	Swift XRT
1.4247	1.231×10^5	10 keV	5.73×10^{-6}	1.91×10^{-6}	Swift XRT
1.6254	1.404×10^5	10 keV	3.77×10^{-6}	1.48×10^{-6}	Swift XRT
1.8796	1.624×10^5	10 keV	3.36×10^{-6}	1.17×10^{-6}	Swift XRT
2.5980	2.245×10^5	10 keV	2.32×10^{-6}	5.38×10^{-7}	Swift XRT
2.8842	2.492×10^5	10 keV	1.37×10^{-6}	3.63×10^{-7}	Swift XRT
3.4783	3.005×10^5	10 keV	1.02×10^{-6}	3.60×10^{-7}	Swift XRT
4.5403	3.923×10^5	10 keV	7.20×10^{-7}	2.87×10^{-7}	Swift XRT
5.6807	4.908×10^5	10 keV	4.04×10^{-7}	1.46×10^{-7}	Swift XRT
7.1565	6.183×10^5	10 keV	2.85×10^{-7}	1.28×10^{-7}	Swift XRT
9.5104	8.217×10^5	10 keV	1.37×10^{-7}	6.70×10^{-8}	Swift XRT
13.260	1.146×10^6	10 keV	7.76×10^{-8}	2.97×10^{-8}	Swift XRT

Table 5
(Continued)

Delay		X-ray Filter Central Frequency	Flux (Jy)	Flux Error (Jy)	Observatory
(day)	(s)				
18.832	1.627×10^6	10 keV	4.86×10^{-8}	1.31×10^{-8}	Swift XRT
28.236	2.440×10^6	10 keV	2.21×10^{-8}	8.34×10^{-9}	Swift XRT
41.971	3.626×10^6	10 keV	1.48×10^{-8}	3.81×10^{-9}	Swift XRT
64.598	5.581×10^6	10 keV	2.59×10^{-9}	1.23×10^{-9}	Swift XRT
0.0419	0.362×10^4	1 keV	8.36×10^{-3}	1.16×10^{-3}	Swift XRT
0.0486	0.420×10^4	1 keV	7.25×10^{-3}	1.04×10^{-3}	Swift XRT
0.2529	2.185×10^4	1 keV	5.98×10^{-4}	1.12×10^{-4}	Swift XRT
0.3018	2.608×10^4	1 keV	4.39×10^{-4}	8.75×10^{-5}	Swift XRT
0.3701	3.197×10^4	1 keV	3.59×10^{-4}	6.76×10^{-5}	Swift XRT
0.4365	3.771×10^4	1 keV	2.30×10^{-4}	5.15×10^{-5}	Swift XRT
0.5145	4.445×10^4	1 keV	1.89×10^{-4}	4.82×10^{-5}	Swift XRT
0.5698	4.923×10^4	1 keV	1.91×10^{-4}	4.60×10^{-5}	Swift XRT
0.6348	5.484×10^4	1 keV	1.49×10^{-4}	3.07×10^{-5}	Swift XRT
0.7026	6.070×10^4	1 keV	1.65×10^{-4}	4.62×10^{-5}	Swift XRT
0.7808	6.746×10^4	1 keV	1.19×10^{-4}	3.07×10^{-5}	Swift XRT
0.8481	7.327×10^4	1 keV	9.98×10^{-5}	2.10×10^{-5}	Swift XRT
1.0395	8.982×10^4	1 keV	7.24×10^{-5}	2.33×10^{-5}	Swift XRT
1.2431	1.074×10^5	1 keV	3.96×10^{-5}	1.23×10^{-5}	Swift XRT
1.4247	1.231×10^5	1 keV	3.28×10^{-5}	8.30×10^{-6}	Swift XRT
1.6254	1.404×10^5	1 keV	2.71×10^{-5}	7.93×10^{-6}	Swift XRT
1.8796	1.624×10^5	1 keV	2.28×10^{-5}	7.84×10^{-6}	Swift XRT
2.5980	2.245×10^5	1 keV	1.35×10^{-5}	2.94×10^{-6}	Swift XRT
2.8842	2.492×10^5	1 keV	1.28×10^{-5}	2.86×10^{-6}	Swift XRT
3.4783	3.005×10^5	1 keV	8.41×10^{-6}	2.59×10^{-6}	Swift XRT
4.5403	3.923×10^5	1 keV	5.56×10^{-6}	1.75×10^{-6}	Swift XRT
5.6807	4.908×10^5	1 keV	5.08×10^{-6}	1.24×10^{-6}	Swift XRT
7.1565	6.183×10^5	1 keV	3.77×10^{-6}	1.16×10^{-6}	Swift XRT
9.5104	8.217×10^5	1 keV	2.34×10^{-6}	5.99×10^{-7}	Swift XRT
13.260	1.146×10^6	1 keV	1.27×10^{-6}	2.92×10^{-7}	Swift XRT
18.832	1.627×10^6	1 keV	6.52×10^{-7}	2.28×10^{-7}	Swift XRT
28.236	2.440×10^6	1 keV	4.15×10^{-7}	1.38×10^{-7}	Swift XRT
41.971	3.626×10^6	1 keV	2.59×10^{-7}	8.25×10^{-8}	Swift XRT
64.598	5.581×10^6	1 keV	1.96×10^{-7}	4.82×10^{-8}	Swift XRT

Note. Swift data have been converted from the Vega system to the AB system. Data are given fully extinction-corrected for either SF11 MW foreground extinction (described in Section 3.2) or RF09^a and the corresponding SMC extinction in the host galaxy (Section 3.2).

^a This does not include updated measurements provided after 2022 February 5.

Table 6
The GRANDMA and GCN Optical Observations of GRB 221009A

T_{start} UT (1)	T_{mid} (days)		Filter (3)	Exposure (4)	Magnitude (5)	U.L. (6)	Telescope (7)	Reference (8)	Analysis Method (9)
	MJD (2)	$T - T_{\text{GRB}}$							
2022-10-09T18:06:27	59,861.7545	0.2010	u'	6×60 s	...	17.9 (3σ)	MeerLICHT	de Wet & Groot (2022)	...
2022-10-10T05:00	59,862.2083	0.6549	u'	6×60 s	Nickel-1 m	Vidal et al. (2022)	...
2022-10-09T19:19:51	59,861.8107	0.2572	B	5×180 s	...	18.1 (5σ)	KNC-SCT-0.28	Broens (2022) and this work	STDPipe
2022-10-10T04:21	59,862.1812	0.6278	B	5×60 s	...	19.7	LOAO-1 m	Paek et al. (2022)	...
2022-10-09T16:21	59,861.6812	0.1278	g'	200 s	17.66 ± 0.07	...	GIT	Kumar et al. (2022)	...
2022-10-09T18:21	59,861.7646	0.2111	g'	6×60 s	18.22 ± 0.33	...	MeerLICHT	de Wet & Groot (2022)	...
2022-10-10T05:00	59,862.2083	0.6549	g'	300 s	18.96 ± 0.1	...	Nickel-1 m	Vidal et al. (2022)	...

Table 6
(Continued)

T_{start} UT (1)	T_{mid} (days)		Filter (3)	Exposure (4)	Magnitude (5)	U.L. (6)	Telescope (7)	Reference (8)	Analysis Method (9)
	MJD (2)	$T-T_{\text{GRB}}$							
2022-10-10T11:39	59,862.4854	0.932	g'	8340 s	...	18.3	MITSuME	Sasada et al. (2022)	...
2022-10-10T12:25	59,862.5174	0.9639	g'	2×150 s	...	18.3 (3σ)	SLT-40	Chen et al. (2022)	...
2022-10-10T16:34	59,862.6903	1.1368	g'	2×120 s	20.38 ± 0.19	19.9 (3σ)	KAO	This work	MUPHOTEN
2022-10-10T16:56	59,862.7056	1.1521	g'	600 s	20.13 ± 0.08	...	RTT-150	Bikmaev et al. (2022a)	...
2022-10-10T17:16	59,862.7194	1.166	g'	15×30 s	20.53 ± 0.1	21.0 (3σ)	AZT-20	Belkin et al. (2022a)	...
2022-10-10T19:40	59,862.8194	1.266	g'	3×100 s	20.87 ± 0.36	...	LCOGT	Strausbaugh (2022a)	...
2022-10-10T20:17	59,862.8451	1.2917	g'	600 s	20.44 ± 0.25	...	RTT-150	Bikmaev et al. (2022a)	...
2022-10-11T17:10	59,863.7153	2.1618	g'	600 s	21.15 ± 0.21	...	RTT-150	Bikmaev et al. (2022a)	...
2022-10-12T02:40	59,864.1111	2.5577	g'	23.0	LBTO	Shrestha et al. (2022)	...
2022-10-12T03:34	59,864.1486	2.5952	g'	3×300 s	...	22.3	LCOGT	Strausbaugh (2022b)	...
2022-10-15T15:44	59,867.6556	6.1021	g'	30×60 s	22.6 ± 0.12	23.4 (3σ)	AZT-20	Belkin et al. (2022a)	...
2022-10-29T05:57	59,881.2479	19.6945	g'	3×300 s	24.52 ± 0.2	26.1	CFHT-Megacam	This work	MUPHOTEN
2022-10-09T13:15:29	59,861.5524	-0.0010	V	27 s	-	2.0	Mundrabilla	This work	Section 2.2
2022-10-09T13:15:59	59,861.5528	-0.0007	V	27 s	...	2.0	Mundrabilla	This work	Section 2.2
2022-10-09T13:16:30	59,861.5531	-0.0003	V	27 s	...	3.8	Raw War Road	This work	Section 2.2
2022-10-09T13:17:00	59,861.5535	0.0000	V	27 s	...	3.8	Raw War Road	This work	Section 2.2
2022-10-09T13:17:30	59,861.5538	0.0004	V	27 s	...	3.8	Raw War Road	This work	Section 2.2
2022-10-09T13:18:00	59,861.5542	0.0007	V	27 s	...	3.8	Raw War Road	This work	Section 2.2
2022-10-09T13:18:30	59,861.5545	0.0011	V	27 s	...	3.8	Raw War Road	This work	Section 2.2
2022-10-09T13:19:00	59,861.5549	0.0014	V	27 s	...	3.8	Raw War Road	This work	Section 2.2
2022-10-09T13:19:30	59,861.5552	0.0017	V	27 s	...	3.8	Raw War Road	This work	Section 2.2
2022-10-09T13:20:00	59,861.5556	0.0021	V	27 s	...	3.8	Raw War Road	This work	Section 2.2
2022-10-09T13:20:30	59,861.5559	0.0024	V	27 s	...	3.8	Raw War Road	This work	Section 2.2
2022-10-09T13:21:30	59,861.5566	0.0031	V	27 s	...	3.8	Raw War Road	This work	Section 2.2
2022-10-09T13:22:00	59,861.5569	0.0035	V	27 s	...	3.8	Raw War Road	This work	Section 2.2
2022-10-09T13:23:00	59,861.5576	0.0042	V	27 s	...	3.8	Raw War Road	This work	Section 2.2
2022-10-09T13:23:30	59,861.5580	0.0045	V	27 s	...	3.8	Raw War Road	This work	Section 2.2
2022-10-09T19:35:00	59,861.82118	0.2677	V	5×180 s	17.39 ± 0.08	18.3 (5σ)	KNC-SCT-0.28	Broens (2022) and this work	MUPHOTEN
2022-10-10T04:23	59,862.1826	0.6292	V	5×60 s	18.74 ± 0.13	19.5	LOAO-1 m	Paek et al. (2022)	...
2022-10-10T16:48	59,862.7	1.1465	V	25×120 s	19.36 ± 0.15	19.5	ShAOT60	This work	STDPipe
	59,862.8141	1.2606	V	11×180 s	...	18.7 (5σ)	KNC-SCT-0.28	This work	MUPHOTEN

Table 6
(Continued)

T_{start} UT (1)	T_{mid} (days)		Filter (3)	Exposure (4)	Magnitude (5)	U.L. (6)	Telescope (7)	Reference (8)	Analysis Method (9)
	MJD (2)	$T-T_{\text{GRB}}$							
2022-10-10T19:16									
2022-10-14T20:13	59,866.8768	5.3233	V	180×32 s	21.55 ± 0.24	$21.2 (5\sigma)$	KNC-T-CAT	This work	STDPipe
2022-10-09T19:51	59,861.8271	0.2736	R_C	5×180 s	16.26 ± 0.05	$17.9 (5\sigma)$	KNC-SCT-0.28	Broens (2022) and this work	MUPHOTEN
2022-10-10T11:39	59,862.4854	0.932	R_C	60 s	...	17.0	MITSuME	Sasada et al. (2022)	...
2022-10-10T14:56	59,862.6347	1.0813	R_C	6×180 s	18.21 ± 0.14	18.5	UBAI-ST60	This work	MUPHOTEN
2022-10-10T15:53	59,862.6774	1.124	R_C	15×90 s	ShAOT60	This work	VETO
2022-10-10T18:32	59,862.7809	1.2274	R_C	25×30 s	18.1 ± 0.08	19.3	Lisnyky-AZT-8	This work	MUPHOTEN
2022-10-10T18:45	59,862.7899	1.2365	R_C	25×30 s	18.24 ± 0.08	19.1	Lisnyky-AZT-8	This work	MUPHOTEN
2022-10-10T19:43:14	59,862.8290	1.2755	R_C	7×180 s	...	$18.2 (5\sigma)$	KNC-SCT-0.28	This work	MUPHOTEN
2022-10-11T19:52:44	59,863.8292	2.2956	R_C	20×180 s	...	$18.8 (5\sigma)$	KNC-SCT-0.28	Broens (2022) and this work	MUPHOTEN
2022-10-11T18:44	59,863.8576	2.3042	R_C	111×60 s	19.22 ± 0.08	20.5	Lisnyky-AZT-8	This work	MUPHOTEN
2022-10-12T14:24	59,864.6139	3.0604	R_C	5×240 s	UBAI-ST60	This work	VETO
2022-10-12T19:40	59,864.8403	3.2868	R_C	30×60 s	19.98 ± 0.11	20.1	Lisnyky-AZT-8	This work	MUPHOTEN
2022-10-14T14:10	59,866.6208	5.0674	R_C	11×240 s	...	18.5	UBAI-ST60	This work	MUPHOTEN
2022-10-21T22:58	59,874.0102	12.4567	R_C	460×10 s	...	19.9	VIRT	This work	MUPHOTEN
2022-10-22T03:34:20	59,874.1697	12.6162	R_C	6×600 s	...	$19.4 (5\sigma)$	KNC-iT11	This work	STDPipe
2022-10-09T14:25	59,861.6007	0.0472	r'	...	14.93 ± 0.1	...	NEXT	Xu et al. (2022)	...
2022-10-09T14:27	59,861.6021	0.0486	r'	120 s	14.84 ± 0.09	20.8	Mondy	Belkin et al. (2022c)	...
2022-10-09T15:36	59,861.6507	0.0972	r'	180 s	15.92 ± 0.12	16.5	TRE	This work	STDPipe and MUPHOTEN
2022-10-09T15:39	59,861.6528	0.0993	r'	180 s	15.82 ± 0.18	16.7	TRE	This work	STDPipe and MUPHOTEN
2022-10-09T15:40	59,861.6530	0.0995	r'	180 s	15.74 ± 0.28	16.1	TRE	This work	STDPipe and MUPHOTEN
2022-10-09T16:25	59,861.684	0.1306	r'	200 s	16.16 ± 0.07	...	GIT	Kumar et al. (2022)	...
2022-10-09T17:28	59,861.7283	0.1748	r'	180 s	16.4 ± 0.3	16.3	TRE	This work	STDPipe and MUPHOTEN
2022-10-09T17:29	59,861.7285	0.1750	r'	180 s	15.88 ± 0.23	16.3	TRE	This work	STDPipe and MUPHOTEN
2022-10-09T18:25	59,861.7674	0.2139	r'	...	16.5 ± 0.1	...	NEXT	Xu et al. (2022)	...
2022-10-09T18:23	59,861.766	0.2125	r'	6×60 s	16.76 ± 0.08	...	MeerLICHT	de Wet (2022)	...
2022-10-09T18:49	59,861.784	0.2306	r'	90 s	16.57 ± 0.02	...	OSN-0.9	Hu et al. (2022)	...
2022-10-09T23:58	59,861.9986	0.4452	r'	...	17.36 ± 0.12	...	REM	Brivio et al. (2022)	...
2022-10-10T04:25	59,862.184	0.6306	r'	60×5 s	17.55 ± 0.06	19.8	LOAO-1 m	Paek et al. (2022)	...
2022-10-10T05:00	59,862.2083	0.6549	r'	300 s	17.8 ± 0.1	...	Nickel-1 m	Vidal et al. (2022)	...

Table 6
(Continued)

T_{start} UT (1)	T_{mid} (days)		Filter (3)	Exposure (4)	Magnitude (5)	U.L. (6)	Telescope (7)	Reference (8)	Analysis Method (9)
	MJD (2)	$T-T_{\text{GRB}}$							
2022-10-10T12:25	59,862.5174	0.9639	r'	2×150 s	18.67 ± 0.16	...	SLT-40	Chen et al. (2022)	...
2022-10-10T16:33	59,862.7023	1.1489	r'	11×100 s	18.65 ± 0.08	20.9	KAO	This work	MUPHOTEN
2022-10-10T17:06	59,862.7125	1.159	r'	600 s	18.65 ± 0.02	...	RTT-150	Bikmaev et al. (2022a)	...
2022-10-10T17:14	59,862.7181	1.1646	r'	18×30 s	18.64 ± 0.03	$20.8 (3\sigma)$	AZT-20	Kim et al. (2022)	...
2022-10-10T19:26	59,862.8097	1.2563	r'	2×300 s	18.74 ± 0.12	...	RC-80	Vinko et al. (2022)	...
2022-10-10T19:40	59,862.8194	1.266	r'	3×100 s	18.8 ± 0.21	...	LCOGT	Strausbaugh (2022a)	...
2022-10-10T20:30	59,862.8611	1.3077	r'	2×300 s	18.86 ± 0.04	20.5	C2PU/Omicron	This work	STDPipe and MUPHOTEN
2022-10-10T20:50	59,862.8681	1.3146	r'	600 s	18.81 ± 0.05	...	RTT-150	Bikmaev et al. (2022a)	...
2022-10-11T00:15	59,863.0444	1.4909	r'	16×360 s	18.89 ± 0.06	$20.4 (5\sigma)$	KNC-C14/Ste-Sophie	This work	STDPipe
2022-10-11T00:58	59,863.0846	1.5312	r'	59×120 s	18.93 ± 0.09	$19.8 (5\sigma)$	KNC-C11-FREE	This work	STDPipe
2022-10-11T16:37	59,863.6924	2.1389	r'	600 s	19.53 ± 0.04	...	RTT-150	Bikmaev et al. (2022a)	...
2022-10-11T20:41	59,863.8617	2.3083	r'	...	19.36 ± 0.15	$19.8 (5\sigma)$	KNC-Parent	This work	STDPipe
2022-10-11T20:44	59,863.8639	2.3104	r'	600 s	19.67 ± 0.11	...	RTT-150	Bikmaev et al. (2022a)	...
2022-10-12T01:36	59,864.1041	2.5506	r'	31×180 s	19.56 ± 0.12	$20.2 (5\sigma)$	KNC-LCO/McDO-0.4m	This work	STDPipe
2022-10-12T03:34	59,864.1486	2.5952	r'	3×300 s	...	21.4	LCOGT	Strausbaugh (2022b)	...
2022-10-12T17:05	59,864.7118	3.1583	r'	600 s	20.03 ± 0.06	...	RTT-150	Bikmaev et al. (2022a)	...
2022-10-12T17:38	59,864.7347	3.1813	r'	600 s	19.97 ± 0.08	...	RTT-150	Bikmaev et al. (2022a)	...
2022-10-12T18:10	59,864.7569	3.2035	r'	600 s	20.07 ± 0.19	...	RTT-150	Bikmaev et al. (2022a)	...
2022-10-12T18:42	59,864.7792	3.2257	r'	600 s	20.32 ± 0.17	...	RTT-150	Bikmaev et al. (2022a)	...
2022-10-12T19:15	59,864.8409	3.2874	r'	30×120 s	...	18.4	KNC-C11-ATLAS	This work	STDPipe
2022-10-12T19:46	59,864.8236	3.2702	r'	600 s	20.17 ± 0.12	...	RTT-150	Bikmaev et al. (2022a)	...
2022-10-12T19:40	59,864.8194	3.266	r'	1800 s	20.23 ± 0.09	...	OHP	Schneider et al. (2022)	...
2022-10-12T20:18	59,864.8458	3.2924	r'	300 s	20.58 ± 0.7	...	RC-80	Vinko et al. (2022)	...
2022-10-12T20:25	59,864.8507	3.2972	r'	600 s	20.26 ± 0.16	...	RTT-150	Bikmaev et al. (2022a)	...
2022-10-12T20:57	59,864.8729	3.3195	r'	600 s	20.24 ± 0.19	...	RTT-150	Bikmaev et al. (2022a)	...
2022-10-13T03:09	59,865.1312	3.5778	r'	...	20.44 ± 0.05	...	LDT	O'Connor et al. (2022a)	...
2022-10-13T17:37	59,865.7632	4.2097	r'	21×120 s	...	20.2	KAO	This work	MUPHOTEN
2022-10-13T16:53	59,865.7035	4.15	r'	600 s	20.53 ± 0.09	...	RTT-150	Bikmaev et al. (2022b)	...
2022-10-13T17:25	59,865.7257	4.1722	r'	600 s	20.63 ± 0.09	...	RTT-150	Bikmaev et al. (2022b)	...
2022-10-13T17:58	59,865.7486	4.1952	r'	600 s	20.71 ± 0.15	...	RTT-150	Bikmaev et al. (2022b)	...
	59,865.7708	4.2174	r'	600 s	20.54 ± 0.1	...	RTT-150		...

Table 6
(Continued)

T_{start} UT (1)	T_{mid} (days)		Filter (3)	Exposure (4)	Magnitude (5)	U.L. (6)	Telescope (7)	Reference (8)	Analysis Method (9)
	MJD (2)	$T-T_{\text{GRB}}$							
2022-10-13T18:30								Bikmaev et al. (2022b)	
2022-10-13T19:02	59,865.7931	4.2396	r'	600 s	20.55 ± 0.12	...	RTT-150	Bikmaev et al. (2022b)	...
2022-10-13T19:35	59,865.816	4.2625	r'	600 s	20.74 ± 0.16	...	RTT-150	Bikmaev et al. (2022b)	...
2022-10-13T20:08	59,865.8389	4.2854	r'	600 s	20.9 ± 0.23	...	RTT-150	Bikmaev et al. (2022b)	...
2022-10-13T20:43	59,865.8632	4.3097	r'	600 s	20.86 ± 0.27	...	RTT-150	Bikmaev et al. (2022b)	...
2022-10-14T05:27	59,866.2271	4.6736	r'	...	20.92 ± 0.05	...	Pan-STARRS	Huber et al. (2022)	...
2022-10-15T14:40	59,867.6111	6.0577	r'	30×60 s	20.96 ± 0.05	$22.9 (3\sigma)$	AZT-20	Belkin et al. (2022a)	...
2022-10-15T06:34	59,867.2736	5.7202	r'	...	21.13 ± 0.06	...	Faulkes	Shrestha et al. (2022)	...
2022-10-16T14:41	59,868.6118	7.0583	r'	200×25 s	21.3 ± 0.04	...	DFOT	Gupta et al. (2022)	...
2022-10-19T02:05	59,871.0868	9.5333	r'	...	21.68 ± 0.07	...	LDT	O'Connor et al. (2022b)	...
2022-10-19T18:26	59,871.8201	10.2667	r'	4×300 s	21.8 ± 0.07	21.9	C2PU/Omicron	This work	STDPipe and MUPHOTEN
2022-10-20T16:11	59,872.6847	11.1313	r'	3×300 s	21.86 ± 0.18	21.8	UBAI-AZT22	This work	MUPHOTEN
2022-10-21T14:33	59,873.6062	12.0528	r'	30×60 s	21.94 ± 0.07	$23.9 (3\sigma)$	AZT-20	Belkin et al. (2022b)	...
2022-10-23T00:59:10	59,875.0757	13.5222	r'	31×180 s	...	$19.4 (5\sigma)$	KNC-C11-FREE	This work	STDPipe
2022-10-25T01:59:52	59,877.1045	15.5510	r'	6×600 s	...	$20.5 (5\sigma)$	KNC-iT11	This work	STDPipe
2022-10-27T00:45:41	59,879.0501	17.4967	r'	26×120 s	...	$20.0 (5\sigma)$	KNC-C11-FREE	This work	STDPipe
2022-10-29T05:50	59,881.25	19.6965	r'	2×300 s	22.69 ± 0.05	25.5	CFHT-Megacam	This work	STDPipe and MUPHOTEN
2022-10-09T18:26:56	59,861.7687	0.2152	i'	6×60 s	15.58 ± 0.03	...	MeerLICHT	de Wet & Groot (2022)	...
2022-10-10T02:04:32	59,862.0868	0.5333	i'	300 s	16.24 ± 0.05	$17.9 (5\sigma)$	KNC-BGO	This work	STDPipe
2022-10-10T02:10:06	59,862.0907	0.5372	i'	300 s	16.25 ± 0.05	$17.9 (5\sigma)$	KNC-BGO	This work	STDPipe
2022-10-10T02:15:41	59,862.0945	0.5411	i'	300 s	16.28 ± 0.05	$17.9 (5\sigma)$	KNC-BGO	This work	STDPipe
2022-10-10T02:21:15	59,862.0984	0.5450	i'	300 s	16.34 ± 0.05	$17.9 (5\sigma)$	KNC-BGO	This work	STDPipe
2022-10-10T02:26:50	59,862.1023	0.5489	i'	300 s	16.38 ± 0.06	$17.8 (5\sigma)$	KNC-BGO	This work	STDPipe
2022-10-10T02:32:25	59,862.1062	0.5527	i'	300 s	16.37 ± 0.05	$17.9 (5\sigma)$	KNC-BGO	This work	STDPipe
2022-10-10T02:38:55	59,862.1107	0.5572	i'	300 s	16.46 ± 0.05	$18.0 (5\sigma)$	KNC-BGO	This work	STDPipe
2022-10-10T02:44:29	59,862.1107	0.5611	i'	300 s	16.44 ± 0.05	$17.9 (5\sigma)$	KNC-BGO	This work	STDPipe
2022-10-10T02:50:04	59,862.1184	0.5650	i'	300 s	16.41 ± 0.06	$17.9 (5\sigma)$	KNC-BGO	This work	STDPipe
2022-10-10T02:55:39	59,862.1223	0.5689	i'	300 s	16.27 ± 0.05	$17.8 (5\sigma)$	KNC-BGO	This work	STDPipe
2022-10-10T03:01:14	59,862.1262	0.5727	i'	300 s	16.44 ± 0.06	$17.8 (5\sigma)$	KNC-BGO	This work	STDPipe
2022-10-10T03:06:48	59,862.1301	0.5766	i'	300 s	16.58 ± 0.07	$17.8 (5\sigma)$	KNC-BGO	This work	STDPipe
	59,862.1847	0.6313	i'	60×5 s	16.41 ± 0.05	19.56	LOAO-1 m	Paek et al. (2022)	...

Table 6
(Continued)

T_{start} UT (1)	T_{mid} (days)		Filter (3)	Exposure (4)	Magnitude (5)	U.L. (6)	Telescope (7)	Reference (8)	Analysis Method (9)
	MJD (2)	$T-T_{\text{GRB}}$							
2022-10-10T04:26									
2022-10-10T12:25	59,862.5174	0.9639	<i>i'</i>	2×150 s	17.38 ± 0.09	...	SLT-40	Chen et al. (2022)	...
2022-10-10T16:59	59,862.716	1.1625	<i>i'</i>	9×80 s	17.67 ± 0.05	20.7	KAO	This work	MUPHOTEN
2022-10-10T17:23	59,862.7243	1.1708	<i>i'</i>	15×30 s	17.58 ± 0.01	$20.7 (3\sigma)$	AZT-20	Belkin et al. (2022a)	...
2022-10-10T17:17	59,862.7201	1.1667	<i>i'</i>	600 s	17.52 ± 0.01	...	RTT-150	Bikmaev et al. (2022a)	...
2022-10-10T18:20:07	59,862.7938	1.2255	<i>i'</i>	14×180 s	17.47 ± 0.09	$17.6 (5\sigma)$	KNC-IRIS	This work	STDPipe
2022-10-10T19:26	59,862.8097	1.2563	<i>i'</i>	2×300 s	17.5 ± 0.12	...	RC-80	Vinko et al. (2022)	...
2022-10-10T21:01	59,862.8757	1.3222	<i>i'</i>	600 s	17.69 ± 0.02	...	RTT-150	Bikmaev et al. (2022a)	...
2022-10-11T06:07:28	59,863.2569	1.7035	<i>i'</i>	300 s	17.85 ± 0.13	$18.1 (5\sigma)$	KNC-iT24	This work	STDPipe
2022-10-11T06:12:57	59,863.2607	1.7072	<i>i'</i>	300 s	18.24 ± 0.22	$18.2 (5\sigma)$	KNC-iT24	This work	STDPipe
2022-10-11T00:54	59,863.0375	1.484	<i>i'</i>	...	17.92 ± 0.06	...	BlackGEM	Groot et al. (2022)	...
2022-10-11T16:48	59,863.7	2.1465	<i>i'</i>	600 s	18.4 ± 0.02	...	RTT-150	Bikmaev et al. (2022a)	...
2022-10-11T18:46:47	59,863.8193	2.2659	<i>i'</i>	199×32 s	18.64 ± 0.21	$18.7 (5\sigma)$	KNC-EHEA-200F5	This work	STDPipe
2022-10-11T20:56	59,863.8722	2.3188	<i>i'</i>	600 s	18.49 ± 0.04	...	RTT-150	Bikmaev et al. (2022a)	...
2022-10-12T00:58:02	59,864.0626	2.5092	<i>i'</i>	11×300 s	18.44 ± 0.09	$19.0 (5\sigma)$	KNC-BGO	This work	STDPipe
2022-10-12T02:07:18	59,864.1083	2.5548	<i>i'</i>	11×300 s	18.74 ± 0.13	$19.3 (5\sigma)$	KNC-C11-FREE	This work	STDPipe
2022-10-12T02:40	59,864.1111	2.5577	<i>i'</i>	...	19.0 ± 0.2	...	LBTO	Shresta et al. (2022)	...
2022-10-12T03:34	59,864.1486	2.5952	<i>i'</i>	3×300 s	...	20.5	LCOGT	Strausbaugh (2022b)	...
2022-10-12T16:54	59,864.7042	3.1507	<i>i'</i>	600 s	18.82 ± 0.03	...	RTT-150	Bikmaev et al. (2022a)	...
2022-10-12T17:27	59,864.7271	3.1736	<i>i'</i>	600 s	19.02 ± 0.07	...	RTT-150	Bikmaev et al. (2022a)	...
2022-10-12T17:59	59,864.7493	3.1958	<i>i'</i>	600 s	19.09 ± 0.1	...	RTT-150	Bikmaev et al. (2022a)	...
2022-10-12T18:31	59,864.7715	3.2181	<i>i'</i>	600 s	18.95 ± 0.07	...	RTT-150	Bikmaev et al. (2022a)	...
2022-10-12T19:03	59,864.7938	3.2403	<i>i'</i>	600 s	18.93 ± 0.04	...	RTT-150	Bikmaev et al. (2022a)	...
2022-10-12T19:36	59,864.8167	3.2632	<i>i'</i>	600 s	18.93 ± 0.04	...	RTT-150	Bikmaev et al. (2022a)	...
2022-10-12T19:40	59,864.8194	3.266	<i>i'</i>	3×600 s	18.91 ± 0.11	...	OHP	Schneider et al. (2022)	...
2022-10-12T20:08	59,864.8389	3.2854	<i>i'</i>	600 s	18.92 ± 0.04	...	RTT-150	Bikmaev et al. (2022a)	...
2022-10-12T20:18	59,864.8458	3.2924	<i>i'</i>	300 s	18.74 ± 0.18	...	RC-80	Vinko et al. (2022)	...
2022-10-13T02:36:45	59,865.1069	3.5534	<i>i'</i>	12×300 s	19.50 ± 0.22	$19.4 (5\sigma)$	KNC-BGO	This work	STDPipe
2022-10-13T02:24:22	59,865.1149	3.5614	<i>i'</i>	20×120 s	...	$18.7 (5\sigma)$	KNC-iT11	This work	STDPipe
2022-10-13T03:09	59,865.1312	3.5778	<i>i'</i>	...	19.37 ± 0.05	...	LDT	O'Connor et al. (2022a)	...
	59,865.7111	4.1577	<i>i'</i>	600 s	19.51 ± 0.06	...	RTT-150		...

Table 6
(Continued)

T_{start} UT (1)	T_{mid} (days)		Filter (3)	Exposure (4)	Magnitude (5)	U.L. (6)	Telescope (7)	Reference (8)	Analysis Method (9)
	MJD (2)	$T-T_{\text{GRB}}$							
2022-10-13T17:04								Bikmaev et al. (2022b)	
2022-10-13T17:36	59,865.7333	4.1799	i'	600 s	19.41 ± 0.05	...	RTT-150	Bikmaev et al. (2022b)	...
2022-10-13T18:09	59,865.7562	4.2028	i'	600 s	19.52 ± 0.05	...	RTT-150	Bikmaev et al. (2022b)	...
2022-10-13T17:42	59,865.7642	4.2108	i'	21×110 s	19.73 ± 0.3	20.3	KAO	This work	MUPHOTEN
2022-10-13T18:41	59,865.7785	4.225	i'	600 s	19.44 ± 0.04	...	RTT-150	Bikmaev et al. (2022b)	...
2022-10-13T19:13	59,865.8007	4.2472	i'	600 s	19.45 ± 0.05	...	RTT-150	Bikmaev et al. (2022b)	...
2022-10-13T19:46	59,865.8236	4.2702	i'	600 s	19.43 ± 0.05	...	RTT-150	Bikmaev et al. (2022b)	...
2022-10-13T20:18	59,865.8458	4.2924	i'	600 s	19.48 ± 0.06	...	RTT-150	Bikmaev et al. (2022b)	...
2022-10-13T20:53	59,865.8701	4.3167	i'	600 s	19.5 ± 0.07	...	RTT-150	Bikmaev et al. (2022b)	...
2022-10-14T00:04	59,866.0028	4.4493	i'	...	19.89 ± 0.05	...	VLT	Izzo et al. (2022)	...
2022-10-14T00:40	59,866.0278	4.4743	i'	7×60 s	19.8 ± 0.5	...	GMOS	Rastinejad & Fong (2022)	...
2022-10-15T06:34	59,867.2736	5.7202	i'	...	20.01 ± 0.05	...	Faulkes	Shrestha et al. (2022)	...
2022-10-15T14:11	59,867.591	6.0375	i'	30×60 s	20.0 ± 0.04	$23.2 (3\sigma)$	AZT-20	Belkin et al. (2022a)	...
2022-10-19T02:05	59,871.0868	9.5333	i'	...	20.72 ± 0.05	...	LDT	O'Connor et al. (2022b)	...
2022-10-21T15:04	59,873.6278	12.0743	i'	30×60 s	20.72 ± 0.11	$23.3 (3\sigma)$	AZT-20	Belkin et al. (2022b)	...
2022-10-29T06:09	59,881.2632	19.7097	i'	2×300 s	21.87 ± 0.05	24.5	CFHT-Megacam	This work	STDPipe and MUPHOTEN
2022-10-09T20:05:19	59,861.8422	0.2887	I_C	5×180 s	15.21 ± 0.04	$17.0 (5\sigma)$	KNC-SCT-0.28	This work	MUPHOTEN
2022-10-10T05:00	59,862.2083	0.6549	I_C	300 s	16.74 ± 0.1	...	Nickel-1 m	Vidal et al. (2022)	...
2022-10-10T11:39	59,862.4854	0.932	I_C	8340 s	17.1 ± 0.2	...	MITSuME	Sasada et al. (2022)	...
2022-10-10T20:04:25	59,862.8436	1.2902	I_C	7×180 s	17.12 ± 0.13	$17.0 (5\sigma)$	KNC-SCT-0.28	This work	MUPHOTEN
2022-10-11T18:14	59,863.7958	2.2424	I_C	52×60 s	AbAO-T70	This work	VETO
2022-10-11T21:06:16	59,863.9043	2.3509	I_C	24×180 s	...	$17.6 (5\sigma)$	KNC-SCT-0.28	This work	MUPHOTEN
2022-10-12T18:11	59,864.7889	3.2354	I_C	45×60 s	Lisnyky-AZT-8	This work	VETO
2022-10-13T01:49:56	59,865.1248	3.5713	I_C	23×300 s	18.95 ± 0.12	$19.7 (5\sigma)$	KNC-C11-FREE	This work	STDPipe
2022-10-15T18:44	59,867.8639	6.3104	I_C	120×60 s	19.77 ± 0.17	19.0	Lisnyky-AZT-8	This work	MUPHOTEN
2022-10-24T23:01	59,877.0383	15.4848	I_C	685×10 s	...	19.8	VIRT	This work	MUPHOTEN
2022-10-09T18:29	59,861.7701	0.2167	z'	6×60 s	14.89 ± 0.03	...	MeerLICHT	de Wet & Groot (2022)	...
2022-10-10T12:25	59,862.5174	0.9639	z'	2×150 s	16.6 ± 0.09	...	SLT-40	Chen et al. (2022)	...
2022-10-10T17:26	59,862.7264	1.1729	z'	15×30 s	16.87 ± 0.05	19.8	AZT-20	Belkin et al. (2022a)	...
2022-10-10T17:28	59,862.7278	1.1743	z'	600 s	16.81 ± 0.01	...	RTT-150	Bikmaev et al. (2022a)	...

Table 6
(Continued)

T_{start} UT (1)	T_{mid} (days)		Filter (3)	Exposure (4)	Magnitude (5)	U.L. (6)	Telescope (7)	Reference (8)	Analysis Method (9)
	MJD (2)	$T-T_{\text{GRB}}$							
2022-10-10T17:15	59,862.728	1.1745	z'	10×80 s	16.97 ± 0.06	20.3	KAO	This work	MUPHOTEN
2022-10-10T21:13	59,862.884	1.3306	z'	600 s	16.99 ± 0.01	...	RTT-150	Bikmaev et al. (2022a)	...
2022-10-11T00:50	59,863.0347	1.4813	z'	...	16.92 ± 0.05	...	BlackGEM	Groot et al. (2022)	...
2022-10-11T16:59	59,863.7076	2.1542	z'	600 s	17.69 ± 0.02	...	RTT-150	Bikmaev et al. (2022a)	...
2022-10-11T21:07	59,863.8799	2.3264	z'	600 s	17.72 ± 0.03	...	RTT-150	Bikmaev et al. (2022a)	...
2022-10-12T02:40	59,864.1111	2.5577	z'	...	18.26 ± 0.01	...	LBTO	Shresta et al. (2022)	...
2022-10-12T14:34	59,864.6092	3.0557	z'	...	18.40 ± 0.11	...	GMG-Lijiang	Mao et al. (2022)	...
2022-10-12T17:16	59,864.7194	3.166	z'	600 s	18.2 ± 0.04	...	RTT-150	Bikmaev et al. (2022a)	...
2022-10-12T17:48	59,864.7417	3.1882	z'	600 s	18.19 ± 0.05	...	RTT-150	Bikmaev et al. (2022a)	...
2022-10-12T18:21	59,864.7646	3.2111	z'	600 s	18.4 ± 0.08	...	RTT-150	Bikmaev et al. (2022a)	...
2022-10-12T18:53	59,864.7868	3.2333	z'	600 s	18.26 ± 0.03	...	RTT-150	Bikmaev et al. (2022a)	...
2022-10-12T19:25	59,864.809	3.2556	z'	600 s	18.23 ± 0.03	...	RTT-150	Bikmaev et al. (2022a)	...
2022-10-12T19:40	59,864.8194	3.266	z'	2100 s	18.35 ± 0.13	...	OHP	Schneider et al. (2022)	STDPipe
2022-10-12T19:57	59,864.8312	3.2778	z'	600 s	18.23 ± 0.04	...	RTT-150	Bikmaev et al. (2022a)	...
2022-10-12T20:35	59,864.8576	3.3042	z'	600 s	18.3 ± 0.04	...	RTT-150	Bikmaev et al. (2022b)	...
2022-10-12T21:08	59,864.8806	3.3271	z'	600 s	18.18 ± 0.04	...	RTT-150	Bikmaev et al. (2022b)	...
2022-10-13T17:15	59,865.7188	4.1653	z'	600 s	18.63 ± 0.05	...	RTT-150	Bikmaev et al. (2022b)	...
2022-10-13T17:47	59,865.741	4.1875	z'	600 s	18.76 ± 0.05	...	RTT-150	Bikmaev et al. (2022b)	...
2022-10-13T18:19	59,865.7632	4.2097	z'	600 s	18.69 ± 0.04	...	RTT-150	Bikmaev et al. (2022b)	...
2022-10-13T17:51	59,865.7705	4.217	z'	21×110 s	18.90 ± 0.16	19.8	KAO	This work	MUPHOTEN
2022-10-13T18:52	59,865.7861	4.2327	z'	600 s	18.75 ± 0.04	...	RTT-150	Bikmaev et al. (2022b)	...
2022-10-13T19:24	59,865.8083	4.2549	z'	600 s	18.74 ± 0.05	...	RTT-150	Bikmaev et al. (2022b)	...
2022-10-13T19:57	59,865.8312	4.2778	z'	600 s	18.83 ± 0.05	...	RTT-150	Bikmaev et al. (2022b)	...
2022-10-13T20:32	59,865.8556	4.3021	z'	600 s	18.74 ± 0.05	...	RTT-150	Bikmaev et al. (2022b)	...
2022-10-13T21:06	59,865.8792	4.3257	z'	600 s	18.71 ± 0.06	...	RTT-150	Bikmaev et al. (2022b)	...
2022-10-14T12:12	59,866.5106	4.9571	z'	...	19.21 ± 0.12	...	GMG-Lijiang	Mao et al. (2022)	...
2022-10-15T06:34	59,867.2736	5.7202	z'	...	19.39 ± 0.05	...	Faulkes	Shrestha et al. (2022)	...
2022-10-15T16:08	59,867.6722	6.1188	z'	15×60 s	19.31 ± 0.08	$21.0 (3\sigma)$	AZT-20	Belkin et al. (2022a)	...
2022-10-22T16:22	59,874.7375	13.184	z'	20×240 s	...	20.4	KAO	This work	MUPHOTEN
2022-10-29T06:32	59,881.2843	19.7308	z'	4×260 s	21.01 ± 0.08	24.0	CFHT-Megacam	This work	MUPHOTEN
	59,861.6458	0.0924	Clear	180 s	15.5 ± 0.1	...	SCT	Odeh (2022)	...






Table 6
(Continued)


T_{start} UT (1)	T_{mid} (days)		Filter (3)	Exposure (4)	Magnitude (5)	U.L. (6)	Telescope (7)	Reference (8)	Analysis Method (9)
	MJD (2)	$T-T_{\text{GRB}}$							
2022-10-09T15:30									
2022-10-09T15:49	59,861.659	0.1056	Clear	180 s	15.6 ± 0.1	...	SCT	Odeh (2022)	...
2022-10-09T17:14	59,861.7181	0.1646	Clear	180 s	15.9 ± 0.1	...	SCT	Odeh (2022)	...
2022-10-09T18:44	59,861.7806	0.2271	Clear	60 s	16.21 ± 0.11	...	BOOTES-2	Hu et al. (2022)	...
2022-10-10T19:29	59,862.8257	1.2722	Clear	20×60 s	18.52 ± 0.06	19.5	MOSS	This work	MUPHOTEN
2022-10-10T19:31	59,862.8490	1.2955	<i>L</i>	34×180 s	18.38 ± 0.25	$20.2 (3\sigma)$	KNC-HAO	This work	MUPHOTEN
2022-10-10T21:48:00	59,862.9188	1.3652	CR	10×180 s	18.76 ± 0.14	$19.2 (5\sigma)$	KNC-MSXD	This work	STDPipe
2022-10-11T16:33	59,863.7069	2.1535	Clear	10×150 s	...	17.5	SNOVA	This work	MUPHOTEN
2022-10-11T18:29:21	59,863.7707	2.2172	CR	2×30 s	...	$18.3 (5\sigma)$	KNC-Montarrenti	This work	STDPipe
2022-10-11T18:24:14	59,863.7825	2.2290	CR	15×180 s	19.22 ± 0.08	20.3	KNC-MSXD	This work	STDPipe
2022-10-11T18:27:11	59,863.8203	2.2668	<i>L</i>	3×2960 s	...	$19.7 (5\sigma)$	KNC-COK26	This work	STDPipe
2022-10-12T13:56	59,864.5979	3.0445	Clear	10×150 s	...	19.1	SNOVA	This work	MUPHOTEN
2022-10-14T18:17:29	59,866.7944	5.2409	CR	31×180 s	20.63 ± 0.11	$21.3 (5\sigma)$	KNC-MSXD	This work	STDPipe
2022-10-14T20:13:33	59,866.8768	5.3233	CR	180×32 s	20.46 ± 0.14	$21.0 (5\sigma)$	KNC-T-CAT	This work	STDPipe
2022-10-15T19:17:26	59,867.8329	6.2795	CR	28×180 s	20.75 ± 0.13	$21.3 (5\sigma)$	KNC-MSXD	This work	STDPipe

Note. In column (2), the T_{mid} time is the delay between the beginning of the observation and the Fermi GBM GRB trigger time (2022-10-9T13:16:59.99) in days. In column (5), magnitudes are given in the AB system and not corrected for Galactic and host-galaxy dust extinction. In column (9), the VETO tag refers to GRANDMA data that were not analyzed due to the bad quality of the images.

ORCID iDs

D. A. Kann  <https://orcid.org/0000-0003-2902-3583>
S. Agayeva  <https://orcid.org/0009-0007-3673-8997>
C. M. Andrade  <https://orcid.org/0009-0004-9687-3275>
S. Antier  <https://orcid.org/0000-0002-7686-3334>
A. Baransky  <https://orcid.org/0000-0002-9808-1990>
P. Bendjoya  <https://orcid.org/0000-0002-4278-1437>
Z. Benkhaldoun  <https://orcid.org/0000-0001-6285-9847>
S. Beradze  <https://orcid.org/0000-0002-8291-2817>
M. Boër  <https://orcid.org/0000-0001-9157-4349>
E. Broens  <https://orcid.org/0000-0003-1523-4478>
M. Bulla  <https://orcid.org/0000-0002-8255-5127>
O. Burkhonov  <https://orcid.org/0000-0003-1169-6763>
E. Burns  <https://orcid.org/0000-0002-2942-3379>
M. W. Coughlin  <https://orcid.org/0000-0002-8262-2924>
H. A. R. Devillepoix  <https://orcid.org/0000-0001-9226-1870>
T. Dietrich  <https://orcid.org/0000-0003-2374-307X>
D. Dornic  <https://orcid.org/0000-0001-5729-1468>
H.-B. Eggenstein  <https://orcid.org/0000-0001-5296-7035>
S. Ehgamberdiev  <https://orcid.org/0000-0001-9730-3769>
M. Freeberg  <https://orcid.org/0009-0005-4287-7198>

D. Froebrich  <https://orcid.org/0000-0003-4734-3345>
M. Y. Ge  <https://orcid.org/0000-0002-2749-6638>
V. Godunova  <https://orcid.org/0000-0001-7668-7994>
T. Hussenot-Desenonges  <https://orcid.org/0009-0009-2434-432X>
R. Inasaridze  <https://orcid.org/0000-0002-6653-0915>
N. Ismailov  <https://orcid.org/0000-0002-5307-4295>
S. M. Jia  <https://orcid.org/0000-0002-5203-8321>
S. Karpov  <https://orcid.org/0000-0003-0035-651X>
R. W. Kiendrebeogo  <https://orcid.org/0000-0002-9108-5059>
A. Klotz  <https://orcid.org/0000-0002-2652-0069>
N. Kochiashvili  <https://orcid.org/0000-0001-5249-4354>
J. Mao  <https://orcid.org/0000-0002-7077-7195>
D. Marchais  <https://orcid.org/0009-0004-2563-0399>
K. Noysena  <https://orcid.org/0000-0001-9109-8311>
N. B. Orange  <https://orcid.org/0000-0001-6866-1436>
P. T. H. Pang  <https://orcid.org/0000-0001-7041-3239>
C. Pellouin  <https://orcid.org/0000-0001-9489-783X>
J. Peloton  <https://orcid.org/0000-0002-8560-4449>
T. Pradier  <https://orcid.org/0000-0001-5501-0060>

Y. Rajabov  <https://orcid.org/0000-0001-9878-9553>
 J.-P. Rivet  <https://orcid.org/0000-0002-0289-5851>
 F. D. Romanov  <https://orcid.org/0000-0002-5268-7735>
 A. Simon  <https://orcid.org/0000-0003-0404-5559>
 L. M. Song  <https://orcid.org/0000-0003-0274-3396>
 A. Takey  <https://orcid.org/0000-0003-1423-5516>
 Y. Tillayev  <https://orcid.org/0000-0002-2861-1343>
 D. Turpin  <https://orcid.org/0000-0003-1835-1522>
 A. de Ugarte Postigo  <https://orcid.org/0000-0001-7717-5085>
 S. Vanaverbeke  <https://orcid.org/0000-0003-0231-2676>
 V. Vasylenko  <https://orcid.org/0000-0001-8864-2363>
 Z. Vidadi  <https://orcid.org/0009-0002-3591-0568>
 X. F. Wang  <https://orcid.org/0000-0002-7334-2357>
 S. L. Xiong  <https://orcid.org/0000-0002-4771-7653>

References

- Abbott, B. P., Abbott, R., Abbott, T. D., et al. 2017a, *PhRvL*, **119**, 161101
 Abbott, B. P., Abbott, R., Abbott, T. D., et al. 2017b, *ApJL*, **848**, L12
 Abbott, B. P., Abbott, R., Abbott, T. D., et al. 2017c, *ApJL*, **848**, L13
 Ackermann, M., Ajello, M., Asano, K., et al. 2014, *Sci*, **343**, 42
 Aguerre, O., Bayard, F., Broens, E., et al. 2022, *GCN*, **32934**, 1
 Agüí Fernández, J. F., Thöne, C. C., Kann, D. A., et al. 2023, *MNRAS*, **520**, 613
 Ahumada, T., Singer, L. P., Anand, S., et al. 2021, *NatAs*, **5**, 917
 Ai, S., & Gao, H. 2023, *ApJ*, **944**, 115
 Aivazyan, V., Almualla, M., Antier, S., et al. 2022, *MNRAS*, **515**, 6007
 Akerlof, C., Balsano, R., Barthelmy, S., et al. 1999, *Natur*, **398**, 400
 Almeida, A., Anderson, S. F., Argudo-Fernández, M., et al. 2023, arXiv:2301.07688
 An, Z.-H., Antier, S., Bi, X.-Z., et al. 2023, arXiv:2303.01203
 Antier, S., Agayeva, S., Aivazyan, V., et al. 2020a, *MNRAS*, **492**, 3904
 Antier, S., Agayeva, S., Almualla, M., et al. 2020b, *MNRAS*, **497**, 5518
 Atri, P., An, T., Giroletti, M., et al. 2022, *GCN*, **32907**, 1
 Atteia, J. L. 2022, *GCN*, **32793**, 1
 Atteia, J. L., Heussaff, V., Dezalay, J. P., et al. 2017, *ApJ*, **837**, 119
 Atwood, W. B., Abdo, A. A., Ackermann, M., et al. 2009, *ApJ*, **697**, 1071
 Barthelmy, S. D., Barbier, L. M., Cummings, J. R., et al. 2005, *SSRv*, **120**, 143
 Becker, A. 2015, HOTPANTS: High Order Transform of PSF ANd Template Subtraction, Astrophysics Source Code Library, ascl:1504.004
 Belkin, S., Kim, V., Pozanenko, A., et al. 2022a, *GCN*, **32769**, 1
 Belkin, S., Moskvitin, A., Kim, V., et al. 2022b, *GCN*, **32818**, 1
 Belkin, S., Pozanenko, A., Klunko, E., Pankov, N. & GRB IKI FuN 2022c, *GCN*, **32645**, 1
 Berger, E. 2014, *ARA&A*, **52**, 43
 Bertin, E. 2010, Warp: Resampling and Co-adding FITS Images Together, Astrophysics Source Code Library, ascl:1010.068
 Bertin, E., & Arnouts, S. 1996, *A&AS*, **117**, 393
 Bertin, E. 2011, in ASP Conf. Ser. 442, Astronomical Data Analysis Software and Systems XX, ed. I. N. Evans et al. (San Francisco, CA: ASP), **435**
 Bikmaev, I., Khamitov, I., Irtuganov, E., et al. 2022a, *GCN*, **32743**, 1
 Bikmaev, I., Khamitov, I., Irtuganov, E., et al. 2022b, *GCN*, **32752**, 1
 Bissaldi, E., Omodei, N., Kerr, M. & Fermi-LAT Team 2022, *GCN*, **32637**, 1
 Bloom, J. S., Perley, D. A., Li, W., et al. 2009, *ApJ*, **691**, 723
 Boch, T., Fernique, P., Bonnarel, F., et al. 2020, in ASP Conf. Ser. 527, Astronomical Society of the Pacific Conference Series, ed. R. Pizzo et al. (San Francisco, CA: ASP), **121**
 Boch, T., Pineau, F., & Derriere, S. 2012, in ASP Conf. Ser. 461, Astronomical Data Analysis Software and Systems XXI, ed. P. Ballester, D. Egret, & N. P. F. Lorente (San Francisco, CA: ASP), **291**
 Boër, M., Atteia, J. L., Damerdjij, Y., et al. 2006, *ApJL*, **638**, L71
 Bradley, L., Sipiöcz, B., Robitaille, T., et al. 2021, *astropy/photutils*: v1.1.0, Zenodo, doi:10.5281/zenodo.4624996
 Brivio, R., Ferro, M., D'Avanzo, P., et al. 2022, *GCN*, **32652**, 1
 Broens, E. 2022, *GCN*, **32640**, 1
 Buchner, J. 2016, PyMultiNest: Python interface for MultiNest, Astrophysics Source Code Library, record ascl:1606.005
 Burns, E., Svinkin, D., Fenimore, E., et al. 2023, *ApJ*, **946**, L31
 Burrows, D. N., Hill, J. E., Nousek, J. A., et al. 2005, *SSRv*, **120**, 165
 Cano, Z., Wang, S.-Q., Dai, Z.-G., & Wu, X.-F. 2017, *AdAst*, **2017**, 8929054
 Cardelli, J. A., Clayton, G. C., & Mathis, J. S. 1989, *ApJ*, **345**, 245
 Castro-Tirado, A. J., Sanchez-Ramirez, R., Hu, Y. D., et al. 2022, *GCN*, **32686**, 1
 Chambers, K. C., Magnier, E. A., Metcalfe, N., et al. 2016, arXiv:1612.05560
 Chen, T. W., Malesani, D. B., Yang, S., et al. 2022, *GCN*, **32667**, 1
 D'Avanzo, P., Ferro, M., Brivio, R., et al. 2022, *GCN*, **32755**, 1
 De Pasquale, M., Page, M. J., Kann, D. A., et al. 2016, *MNRAS*, **462**, 1111
 de Ugarte Postigo, A., Izzo, L., Pugliese, G., et al. 2022, *GCN*, **32648**, 1
 de Wet, S. 2022, *GCN*, **32944**, 1
 de Wet, S., & Groot, P. J. 2022, *GCN*, **32646**, 1
 Dichiaro, S., Gropp, J. D., Kennea, J. A., et al. 2022a, *ATel*, **15650**
 Dichiaro, S., Gropp, J. D., Kennea, J. A., et al. 2022b, *GCN*, **32632**, 1
 Dietrich, T., Coughlin, M. W., Pang, P. T. H., et al. 2020, *Sci*, **370**, 1450
 Duan, K.-K., Xu, Z.-L., Shen, Z.-Q., et al. 2022, *GCN*, **32973**, 1
 Durbak, J. M., Kutuyev, A. S., Andreoni, I., et al. 2022, *GCN*, **32654**, 1
 Duverne, P. A., Antier, S., Basa, S., et al. 2022, *PASP*, **134**, 114504
 Dzhanpuev, D. D., Afashokov, Y. Z., Dzaparova, I. M., et al. 2022, *ATel*, **15669**
 Evans, P. A., Beardmore, A. P., Page, K. L., et al. 2007, *A&A*, **469**, 379
 Evans, P. A., Beardmore, A. P., Page, K. L., et al. 2009, *MNRAS*, **397**, 1177
 Evans, P. A., Willingale, R., Osborne, J. P., et al. 2010, *A&A*, **519**, A102
 Ferro, M., Brivio, R., D'Avanzo, P., et al. 2022, *GCN*, **32804**, 1
 Frederiks, D., Lysenko, A., Ridnaia, A., et al. 2022, *GCN*, **32668**, 1
 Frederiks, D., Svinkin, D., Lysenko, A. L., et al. 2023, arXiv:2302.13383
 Froebich, D., Ray, T. P., Murphy, G. C., & Scholz, A. 2005, *A&A*, **432**, L67
 Fulton, M. D., Smartt, S. J., Rhodes, L., et al. 2023, *ApJL*, **946**, L22
 Galama, T. J., Vreeswijk, P. M., van Paradijs, J., et al. 1998, *Natur*, **395**, 670
 Ge, M. Y., Chen, Y. P., Liao, J. Y., et al. 2022, *ATel*, **15703**
 Gehrels, N., Barthelmy, S. D., Burrows, D. N., et al. 2008, *ApJ*, **689**, 1161
 Gehrels, N., Chincarini, G., Giommi, P., et al. 2004, *ApJ*, **611**, 1005
 Gehrels, N., Ramirez-Ruiz, E., & Fox, D. B. 2009, *ARA&A*, **47**, 567
 Gendre, B., Stratta, G., Atteia, J. L., et al. 2013, *ApJ*, **766**, 30
 GLAST Facility Science Team, Gehrels, N., & Michelson, P. 1999, *Aph*, **11**, 277
 Goldstein, A., Veres, P., Burns, E., et al. 2017, *ApJL*, **848**, L14
 Gotz, D., Mereghetti, S., Savchenko, V., et al. 2022, *GCN*, **32660**, 1
 Greiner, J., Klose, S., Reinsch, K., et al. 2003, *Natur*, **426**, 157
 Groot, P. J., Vreeswijk, P. M., Ter Horst, R., et al. 2022, *GCN*, **32678**, 1
 Guha, A., & Nicholson, P. 2022, *GCN*, **32745**, 1
 Gupta, R., Ror, A. K., Pandey, S. B., et al. 2022, *GCN*, **32811**, 1
 Hayes, L. A., & Gallagher, P. T. 2022, *RNAAS*, **6**, 222
 Hjorth, J., & Bloom, J. S. 2012, Chapter 9 in *Gamma-Ray Bursts* (Cambridge: Cambridge Univ. Press), 169
 Hjorth, J., Sollerman, J., Møller, P., et al. 2003, *Natur*, **423**, 847
 Hou, L. G., & Han, J. L. 2014, *A&A*, **569**, A125
 Hu, Y. D., Casanova, V., Fernandez-Garcia, E., et al. 2022, *GCN*, **32644**, 1
 Huang, Y., Hu, S., Chen, S., et al. 2022, *GCN*, **32677**, 1
 Huber, M., Schultz, A., Chambers, K. C., et al. 2022, *GCN*, **32758**, 1
 IceCube Collaboration 2022, *GCN*, **32665**, 1
 Iwakiri, W., Jaisawal, G. K., Younes, G., et al. 2022, *GCN*, **32694**, 1
 Izzo, L., Saccardi, A., Fynbo, J. P. U., et al. 2022, *GCN*, **32765**, 1
 Jin, Z.-P., Zhou, H., Wang, Y., et al. 2023, arXiv:2301.02407
 Kann, D. A., & Agui Fernandez, J. F. 2022, *GCN*, **32762**, 1
 Kann, D. A., Klose, S., & Zeh, A. 2006, *ApJ*, **641**, 993
 Kann, D. A., Klose, S., Zhang, B., et al. 2010, *ApJ*, **720**, 1513
 Kann, D. A., Klose, S., Zhang, B., et al. 2011, *ApJ*, **734**, 96
 Kann, D. A., Masetti, N., & Klose, S. 2007, *AJ*, **133**, 1187
 Karpov, S. 2021, STDPipe: Simple Transient Detection Pipeline, Astrophysics Source Code Library, ascl:2112.006
 Kennea, J. A., Tohuvavohu, A., Osborne, J. P., et al. 2022a, *GCN*, **32651**, 1
 Kennea, J. A., Williams, M. & Swift Team 2022b, *GCN*, **32635**, 1
 Kim, V., Krugov, M., Pozanenko, A., et al. 2022, *GCN*, **32670**, 1
 KM3NeT Collaboration 2022, *GCN*, **32741**, 1
 Kobayashi, K., Negoro, H., Nakajima, M., et al. 2022, *GCN*, **32756**, 1
 Kobayashi, S. 2000, *ApJ*, **545**, 807
 Kostov, A., & Bonev, T. 2018, *BlgAJ*, **28**, 3
 Kouveliotou, C., Meegan, C. A., Fishman, G. J., et al. 1993, *ApJL*, **413**, L101
 Kulkarni, S. R., Djorgovski, S. G., Odewahn, S. C., et al. 1999, *Natur*, **398**, 389
 Kumar, H., Swain, V., Waratkar, G., et al. 2022, *GCN*, **32662**, 1
 Kunert, N., Antier, S., Nedora, V., et al. 2023, arXiv:2301.02049
 Lapshov, I., Molkov, S., Mereminsky, I., et al. 2022, *GCN*, **32663**, 1
 Laskar, T., Alexander, K. D., Margutti, R., et al. 2023, *ApJL*, **946**, L23
 Lesage, S., Veres, P., Roberts, O. J., et al. 2022, *GCN*, **32642**, 1
 Levan, A., Nugent, P., Fruchter, A., et al. 2005, *ApJ*, **624**, 880
 Levan, A. J., Lamb, G. P., Schneider, B., et al. 2023, arXiv:2302.07761
 Levan, A. J., Tanvir, N. R., Fruchter, A. S., et al. 2014a, *ApJ*, **792**, 115
 Levan, A. J., Tanvir, N. R., Starling, R. L. C., et al. 2014b, *ApJ*, **781**, 13
 Lipkin, Y. M., Ofek, E. O., Gal-Yam, A., et al. 2004, *ApJ*, **606**, 381
 Liu, J. C., Zhang, Y. Q., Xiong, S. L., et al. 2022, *GCN*, **32751**, 1

- Malesani, D. B., Levan, A. J., Izzo, L., et al. 2023, arXiv:2302.07891
- Mao, J., Lu, K. X., Zhao, X. H., & Bai, J. M. 2022, GCN, 32727, 1
- Maselli, A., Melandri, A., Nava, L., et al. 2014, *Sci*, 343, 48
- Matheson, T., Garnavich, P. M., Stanek, K. Z., et al. 2003, *ApJ*, 599, 394
- Mazets, E. P., Golenetskii, S. V., Ilinskii, V. N., et al. 1981, *Ap&SS*, 80, 3
- Meegan, C., Lichti, G., Bhat, P. N., et al. 2009, *ApJ*, 702, 791
- Melandri, A., Pian, E., D'Elia, V., et al. 2014, *A&A*, 567, A29
- Minaev, P. Y., & Pozanenko, A. S. 2020, *MNRAS*, 492, 2020
- Mitchell, L. J., Philips, B. F., & Johnson, W. N. 2022, GCN, 32746, 1
- Mösta, P., Ott, C. D., Radice, D., et al. 2015, *Natur*, 528, 376
- Nakar, E. 2007, *PhR*, 442, 166
- Nakar, E., Ando, S., & Sari, R. 2009, *ApJ*, 703, 675
- Neckel, T., & Klare, G. 1980, *A&AS*, 42, 251
- Negoro, H., Nakajima, M., Kobayashi, K., et al. 2022, ATel, 15651
- Negro, M., Di Lalla, N., Omodei, N., et al. 2023, *ApJ*, 946, L21
- Nysewander, M., Fruchter, A. S., & Pe'er, A. 2009, *ApJ*, 701, 824
- O'Connor, B., Cenko, S. B., Troja, E., et al. 2022a, GCN, 32739, 1
- O'Connor, B., Cenko, S. B., Troja, E., et al. 2022b, GCN, 32799, 1
- O'Connor, B., Troja, E., Ryan, G., et al. 2023, arXiv:2302.07906
- Odeh, M. 2022, GCN, 32649, 1
- Omodei, N., Bruel, P., Bregeon, J., et al. 2022a, GCN, 32760, 1
- Omodei, N., Bruel, P., Bregeon, J., et al. 2022b, GCN, 32916, 1
- Paek, G. S. H., Im, M., Urata, Y., & Sung, H.-I. 2022, GCN, 32659, 1
- Pal, S., Hobar, Y., Shvets, A., et al. 2023, *Atmos*, 14, 217
- Pancino, E., Marrese, P. M., Marinoni, S., et al. 2022, *A&A*, 664, A109
- Pang, P. T. H., Dietrich, T., Coughlin, M. W., et al. 2022, arXiv:2205.08513
- Pannarale, F. 2022, GCN, 32877, 1
- Pei, Y. C. 1992, *ApJ*, 395, 130
- Perley, D. A., Cenko, S. B., Corsi, A., et al. 2014, *ApJ*, 781, 37
- Perley, D. A., Morgan, A. N., Updike, A., et al. 2011, *AJ*, 141, 36
- Piano, G., Verrecchia, F., Bulgarelli, A., et al. 2022, GCN, 32657, 1
- Pillera, R., Bissaldi, E., Omodei, N., et al. 2022, GCN, 32658, 1
- Pineau, F.-X., Boch, T., Aerrière, S., & Schaaff, A. 2020, in ASP Conf. Ser. 522, *Astronomical Data Analysis Software and Systems XXVII*, ed. P. Ballester et al. (San Francisco, CA: ASP), 125
- Planck Collaboration, Ade, P. A. R., Aghanim, N., et al. 2016, *A&A*, 594, A13
- Popowski, P., Cook, K. H., & Becker, A. C. 2003, *AJ*, 126, 2910
- Racusin, J. L., Karpov, S. V., Sokolowski, M., et al. 2008, *Natur*, 455, 183
- Rajabov, Y., Sadibekova, T., Tillayev, Y., et al. 2022, GCN, 32795, 1
- Rastinejad, J., & Fong, W. 2022, GCN, 32749, 1
- Rastinejad, J. C., Gompertz, B. P., Levan, A. J., et al. 2022, *Natur*, 612, 223
- Ripa, J., Pal, A., Werner, N., et al. 2022, GCN, 32685, 1
- Ripa, J., Takahashi, H., Fukazawa, Y., et al. 2023, arXiv:2302.10047
- Romanov, F. 2022a, arXiv:2212.12543
- Romanov, F. D. 2022b, GCN, 32664, 1
- Romanov, F. D. 2022c, GCN, 32679, 1
- Roming, P. W. A., Kennedy, T. E., Mason, K. O., et al. 2005, *SSRv*, 120, 95
- Rossi, A., Rothberg, B., Palazzi, E., et al. 2022, *ApJ*, 932, 1
- Rowles, J., & Froeblich, D. 2009, *MNRAS*, 395, 1640
- Ryan, G., van Eerten, H., Piro, L., & Troja, E. 2020, *ApJ*, 896, 166
- Sánchez-Ramírez, R., Hancock, P. J., Jóhannesson, G., et al. 2017, *MNRAS*, 464, 4624
- Sari, R., & Piran, T. 1999, *ApJ*, 520, 641
- Sari, R., Piran, T., & Narayan, R. 1998, *ApJL*, 497, L17
- Sasada, M., Imai, Y., Murata, K. L., et al. 2022, GCN, 32730, 1
- Sato, Y., Obayashi, K., Theodore Zhang, B., et al. 2023, *JHEAp*, 37, 51
- Schlafly, E. F., & Finkbeiner, D. P. 2011, *ApJ*, 737, 103
- Schlegel, D. J., Finkbeiner, D. P., & Davis, M. 1998, *ApJ*, 500, 525
- Schneider, B., Adami, C., Le Floc'h, E., et al. 2022, GCN, 32753, 1
- Schnoor, P. W., Nicholson, P., & Welch, D. L. 2022, GCN, 32744, 1
- Selsing, J., Malesani, D., Goldoni, P., et al. 2019, *A&A*, 623, A92
- Shrestha, M., Sand, D., Alexander, K. D., et al. 2022, GCN, 32759, 1
- Shrestha, M., Bostroem, K., Sand, D., et al. 2022, GCN, 32771, 1
- Shrestha, M., Sand, D. J., Alexander, K. D., et al. 2023, *ApJL*, 946, L25
- Stanek, K. Z., Matheson, T., Garnavich, P. M., et al. 2003, *ApJL*, 591, L17
- Strausbaugh, R. 2022a, GCN, 32693, 1
- Strausbaugh, R. 2022b, GCN, 32738, 1
- Tan, W. J., Li, C. K., Ge, M. Y., et al. 2022, ATel, 15660
- Thöne, C. C., de Ugarte Postigo, A., Fryer, C. L., et al. 2011, *Natur*, 480, 72
- Thöne, C. C., Greiner, J., Savaglio, S., & Jehin, E. 2007, *ApJ*, 671, 628
- Tiengo, A., Pintore, F., Mereghetti, S., Salvaterra, R. & a larger Collaboration 2022, GCN, 32680, 1
- Tiengo, A., Pintore, F., Vaia, B., et al. 2023, arXiv:2302.11518
- Tohuvavohu, A., Aeadmore, A. P., Osborne, J. P., et al. 2022, GCN, 32671, 1
- Tonry, J. L., Stubbs, C. W., Lykke, K. R., et al. 2012, *ApJ*, 750, 99
- Towner, M. C., Cupak, M., Deshayes, J., et al. 2020, *PASA*, 37, e008
- Troja, E., Fryer, C. L., O'Connor, B., et al. 2022, *Natur*, 612, 228
- Ursi, A., Panebianco, G., Pittori, C., et al. 2022, GCN, 32650, 1
- van der Horst, A. J., Paragi, Z., de Bruyn, A. G., et al. 2014, *MNRAS*, 444, 3151
- van Eerten, H., Leventis, K., Meliani, Z., Wijers, R., & Keppens, R. 2010, *MNRAS*, 403, 300
- Vanderspek, R., Sakamoto, T., Barraud, C., et al. 2004, *ApJ*, 617, 1251
- Vasilopoulos, G., Karavola, D., Stathopoulos, S. I., & Petropoulou, M. 2023, *MNRAS*, 521, 1590
- Veres, P., Burns, E., Bissaldi, E., et al. 2022, GCN, 32636, 1
- Vestrand, W. T., Wren, J. A., Panaitescu, A., et al. 2014, *Sci*, 343, 38
- Vidal, E., Zheng, W., Filippenko, A. V. & KAIT GRB team 2022, GCN, 32669, 1
- Vinko, J., Bodi, A., Pal, A., et al. 2022, GCN, 32709, 1
- Wang, X.-G., Zhang, B., Liang, E.-W., et al. 2018, *ApJ*, 859, 160
- Williams, M. A., Kennea, J. A., Dichiaro, S., et al. 2023, *ApJL*, 946, L24
- Woodsley, S. E. 1993, *ApJ*, 405, 273
- Xia, Z.-Q., Wang, Y., Yuan, Q., & Fan, Y.-Z. 2022a, GCN, 32748, 1
- Xia, Z.-Q., Wang, Y., Yuan, Q., & Fan, Y.-Z. 2022b, arXiv:2210.13052
- Xu, D., Jiang, S. Q., Fu, S. Y., et al. 2022, GCN, 32647, 1
- Yang, J., Ai, S., Zhang, B.-B., et al. 2022, *Natur*, 612, 232
- Zhang, B. B., Liu, Z. K., Peng, Z. K., et al. 2021, *NatAs*, 5, 911
- Zhang, S.-N., Li, T., Lu, F., et al. 2020, *SCPMA*, 63, 249502

Astrophysical uncertainties in the gravitational-wave background from stellar-mass compact binary mergers

Léonard Lehoucq¹,^{*} Irina Dvorkin,¹^{*} Rahul Srinivasan^{2,3},^{*} Clément Pellouin¹ and Astrid Lamberts^{2,3}

¹*Institut d'Astrophysique de Paris, Sorbonne Université and CNRS, UMR 7095, 98 bis bd Arago, F-75014 Paris, France*

²*Observatoire de la Côte d'Azur, Université Côte d'Azur, CNRS, Lagrange, F-P789+P5 Nice France*

³*Observatoire de la Côte d'Azur, Université Côte d'Azur, CNRS, ARTEMIS, F-P789+P5 Nice France*

Accepted 2023 September 18. Received 2023 September 18; in original form 2023 June 19

ABSTRACT

We investigate the stochastic gravitational-wave background (SGWB) produced by merging binary black holes (BBHs) and binary neutron stars (BNSs) in the frequency ranges of Laser Interferometer Gravitational-Wave Observatory (LIGO)/Virgo/Kagra and *Laser Interferometer Space Antenna* (*LISA*). We develop three analytical models, which are calibrated to the measured local merger rates, and complement them with three population synthesis models based on the *COSMIC* code. We discuss the uncertainties, focusing on the impact of the BBH mass distribution, the effect of the metallicity of the progenitor stars, and the time delay distribution between star formation and compact binary merger. We also explore the effect of uncertainties in binary stellar evolution on the background. For BBHs, our analytical models predict Ω_{GW} in the range $[4 \times 10^{-10}$ to $1 \times 10^{-9}]$ (25 Hz) and $[1 \times 10^{-12}$ to $4 \times 10^{-12}]$ (3 mHz), and between $[2 \times 10^{-10}$ to $2 \times 10^{-9}]$ (25 Hz) and $[7 \times 10^{-13}$ to $7 \times 10^{-12}]$ (3 mHz) for our population synthesis models. This background is unlikely to be detected during the LIGO/Virgo/Kagra O4 run, but could be detectable with *LISA*. We predict about 10 BBH and no BNS mergers that could be individually detectable by *LISA* for a period of observation of 4 yr. Our study provides new insights into the population of compact binaries and the main sources of uncertainty in the astrophysical SGWB.

Key words: gravitational waves – black hole mergers – neutron star mergers.

1 INTRODUCTION

Gravitational waves (GWs) have emerged as a promising tool for exploring our Universe (Abbott et al. 2016a). In recent years, ground-based detectors such as the Laser Interferometer Gravitational-Wave Observatory (LIGO) and Virgo have detected GWs from compact binary (CB) mergers. To date, a total number of 90 CB mergers with an inferred probability of astrophysical origin of $p_{\text{astro}} > 0.5$ have been detected (Abbott et al. 2019a, 2021a, b, c, 2023). These observations have already provided valuable information about black hole (BH) and neutron star (NS) populations, in particular they have permitted to refine stellar population models that predict the formation and merger rates of CBs (e.g. Baibhav et al. 2019; Mapelli et al. 2019; Kimball et al. 2021; Zevin et al. 2021; Broekgaarden et al. 2022; van Son et al. 2022; Srinivasan et al. 2023).

In addition to these resolved signals from individual binary mergers, the incoherent superposition of unresolved sources creates an astrophysical stochastic GW background (SGWB). This signal, if detected, contains crucial information about high-redshift CB mergers. Moreover, other astrophysical and cosmological sources could contribute to the SGWB, including core-collapse supernovae, rotating NSs, primordial BHs, cosmological inflation, cosmic strings,

and first-order phase transitions in the early Universe (see Regimbau 2011; Caprini & Figueroa 2018; Christensen 2019; Renzini et al. 2022, for extensive reviews).

The *Laser Interferometer Space Antenna* (*LISA*), a space-based interferometer to be launched in the next decade, aims to detect new classes of GW sources at mHz frequencies. One of the primary objectives of *LISA* is to detect a cosmological SGWB, which could, for example, be produced by phase transitions in the primordial Universe or by cosmic strings (Caprini & Figueroa 2018; Auclair et al. 2023). Most cosmological backgrounds are expected to be significantly lower in magnitude than the astrophysical one; however, some realistic cases rooted in particle physics, such as cosmic strings, predict signals that can be orders of magnitude larger (Auclair et al. 2020). None the less, investigating the properties of the astrophysical background is crucial in order to prepare the detection strategies of the cosmological signal (Chen, Huang & Huang 2019; Cusin et al. 2020; Zhao & Lu 2021; Liang et al. 2022).

The investigation of the SGWB is an active field of research, both theoretically and observationally. Data collected by the LIGO and Virgo observatories during the first three observational runs have been used to search for this background in the $\mathcal{O}(10)$ – $\mathcal{O}(100)$ Hz range, but so far only upper limits have been inferred (Abbott et al. 2017, 2018a, b, 2019b, 2021d, e). The most stringent upper limit provided by the LIGO/Virgo collaboration in Abbott et al. (2021d) is $\Omega_{\text{GW}} \leq 3.4 \times 10^{-9}$ at 25 Hz for a power-law background with a

* E-mail: lehoucq@iap.fr (LL); dvorkin@iap.fr (ID)

spectral index of $2/3$ (consistent with expectations for CB mergers). This limit is very likely to improve with the next observing runs of LVK and, in the more distant future, with 3G detectors (Einstein Telescope and Cosmic Explorer; Maggiore et al. 2020; Evans et al. 2021).

Models of SGWB from stellar-mass CBs have been studied in recent years with different methods, in particular using extrapolations of the local observed merger rate and BH mass distribution (e.g. Abbott et al. 2016b; Jenkins et al. 2018; Lewicki & Vaskonen 2021; Mukherjee & Silk 2021; Babak et al. 2023), analytical descriptions of BH formation and evolution via different channels, and including the effects of the metallicity of progenitor stars (e.g. Dvorkin et al. 2016; Nakazato, Niino & Sago 2016; Cusin et al. 2019; Mangiagli et al. 2019) as well as detailed population synthesis models (e.g. Périgois et al. 2021, 2022).

In this article, we explore the SGWB from binary BHs (BBHs) and binary NSs (BNSs), with a focus on the frequency ranges accessible to LIGO/Virgo and *LISA* and using both analytical and population synthesis models. We note that the recent work of Babak et al. (2023) has also addressed the SGWB from stellar-mass binaries in the *LISA* band. Our results, while using different astrophysical models, are in agreement with their conclusions, as we show below. Our goal here is to estimate the main sources of uncertainty stemming from astrophysical modelling and estimate the prospects of detection with LIGO/Virgo and *LISA*.

The structure of the article is as follows: Section 2 details all the ingredients we use to model the BBH and BNS populations, including mass, redshift, time delay, and metallicity distributions. Section 3 establishes our population synthesis models based on the COSMIC code (Breivik et al. 2020). Section 4 presents the calculation of the SGWB in the LIGO/Virgo and *LISA* frequency bands. Section 5 discusses the possibility for *LISA* to detect individually some of these sources. Finally, we discuss our results and their implications for future work in Section 6.

Throughout this article, we use the following cosmological parameters: $h_0 = H_0/H_{100} = 0.68$, where $H_{100} = 100 \text{ km s}^{-1} \text{ Mpc}^{-1}$, $\Omega_\Lambda = 0.69$, and $\Omega_m = 0.31$ (Planck Collaboration VI 2020).

2 MODELLING THE BBH AND BNS POPULATIONS

This section describes all the components of our analytical modelling of the BBH and BNS populations. We leave the description of the population synthesis models to Section 3.

Each CB is represented by a set of six parameters: the masses M_1 and M_2 of the binary components (described in Section 2.1), the merger redshift of the CB (detailed in Section 2.2), its sky position represented by the right ascension α and the declination δ , and finally the orbital inclination angle θ . These three angles are drawn uniformly from the interval $[0, 2\pi]$ for α , and from $[-1, 1]$ for $\cos \delta$ and $\cos \theta$. We regroup as λ five parameters: $\lambda = \{M_1, M_2, \alpha, \delta, \theta\}$.

The spins χ_1 and χ_2 of the binary components are assumed to be zero as their effect is subdominant for the total energy in GWs emitted in the inspiralling phase (Zhou et al. 2023).

We assume that all CBs have circularized their orbits prior to entering the final phase of the inspiral. We note that while this assumption holds in the LIGO/Virgo band, this is not necessarily the case for *LISA*. Indeed, in some dynamical formation channels CBs enter the *LISA* band while still retaining some eccentricity (see, for example, Breivik et al. 2016).

2.1 Mass distributions

2.1.1 Black hole binaries

We introduce the following probability distributions to describe the masses of the binary components: $P(M_1)$ for the mass of the primary and $P(q)$ for the mass ratio $q = M_1/M_2$. In order to model these distributions, we use the LVK analysis of the third Gravitational-Wave Transient Catalog (GWTC-3; Abbott et al. 2023), based on the 69 confident BBH events that have a false alarm rate below 1 yr^{-1} .

We have chosen to use mainly their POWERLAW + PEAK (PL + P) model, as it provides the highest Bayes factor among the models considered in the catalogue. We also discuss the impact of choosing other mass distributions, such as their POWERLAW (PL) and BROKEN POWERLAW (BPL) models. These models are described in the appendix of Abbott et al. (2023).

In the PL + P model (Talbot & Thrane 2018), the distribution of the primary mass M_1 has two components: a power law between m_{\min} and m_{\max} , and a Gaussian peak with mean μ_m and width σ_m . The parameter λ_{peak} determines the fraction of the BBH systems that are contained in the Gaussian peak. The full list of parameters and their best-fitting values are given in Abbott et al. (2023).

The $m_{\max} \sim 80 M_\odot$ cut-off is motivated by the pair-instability supernova (PISN) phenomenon. PISNe are thought to occur in very massive ($m_{\text{ZAMS}} \gtrsim 130 M_\odot$) and low-metallicity ($Z \lesssim 0.1 Z_\odot$) stars (Fryer, Woosley & Heger 2001; Umeda & Nomoto 2002), in which electron–positron pair creation leads to a thermonuclear runaway that completely disrupts the star, leaving no remnant (Fryer et al. 2001; Woosley & Heger 2021). Previous calculations have suggested that this effect may create a mass gap in the BH mass distribution in the range of 50–130 M_\odot (Woosley & Heger 2021). The existence of this mass gap has been challenged by recent LIGO/Virgo observations that show BBH merging within the gap (Abbott et al. 2020a, d).

The Gaussian peak at $\mu_m \sim 35 M_\odot$ could be explained by a similar phenomenon, but in less massive stars. In this case, the pair instability is not strong enough to completely disrupt the star, but can still lead to a transient regime where the star ejects matter to regain stability in a pulsating manner until its core eventually collapses (Fowler & Hoyle 1964; Umeda & Nomoto 2002). This pulsating PISN (PPISN) leaves a remnant BH, which is, however, less massive than it would have been in the absence of the pulsating mechanism.

Finally, the secondary mass M_2 is calculated from the mass ratio q , which has a probability density that is a power law with a smoothed cut at m_{\min} (Abbott et al. 2023).

2.1.2 Neutron star binaries

The mass distribution of BNSs is obtained from Galactic observations and assumed to be valid at all redshifts. As per the study conducted by Farrow, Zhu & Thrane (2019), this distribution can be accurately represented by a Gaussian with a mean of 1.33 M_\odot and a standard deviation of 0.09 M_\odot . We note that both NSs in the binary system are assumed to follow this mass distribution. The mass distribution of BNSs is not a critical parameter in this study as it is highly concentrated around a single value close to the Tolman–Oppenheimer–Volkoff limit, although this value is somewhat uncertain as it depends on the equation of state (Lattimer & Prakash 2016; Özel & Freire 2016; Abbott et al. 2018c).

It is important to note that the mass distribution of BNSs detected through GWs may differ from those observed in the Galaxy. This effect could indeed explain the observation of the BNS merger GW190425 (Abbott et al. 2020b; Romero-Shaw et al. 2020), whose

total mass is much larger than that of Galactic binaries. Additionally, the recent observation of GW190814 seems to have provided evidence for a BH–NS merger with a NS much heavier than typical Galactic NSs (Abbott et al. 2020c).

2.2 Redshift distributions

To compute the merger rate of CBs, we first use the star formation rate (SFR) ψ , as given in Vangioni et al. (2015) using a fit to observed data:

$$\psi(z) = v \frac{a \exp[b(z - z_m)]}{a - b + b \exp[a(z - z_m)]}, \quad (1)$$

with $v = 0.178 M_\odot \text{ Mpc}^{-3} \text{ yr}^{-1}$, $a = 2.37$, $b = 1.80$, and $z_m = 2$.

We assume that the merger rate follows the SFR with some delay (t_d), which represents the time between the formation of the stellar progenitors and the merger of the CBs. We also consider the metallicity Z , which plays a key role in the evolution of the binary and thus affects the merger rate, as detailed in Section 2.4. Thus, we can write the merger rate as

$$R_{\text{merg}}(t) = \int_0^{Z_{\text{max}}} \int_{t_{d,\text{min}}}^{t_{d,\text{max}}} \alpha(Z) \psi(t - t_d) P(t_d|Z) P(Z|t - t_d) dt_d dZ, \quad (2)$$

where α is the efficiency (in M_\odot^{-1}) of forming CBs that merge within the age of the Universe. Although the general redshift dependence of this efficiency is not known, we can use the local merger rate of BBHs and BNSs measured by LIGO/Virgo (Abbott et al. 2023) to constrain its value, as described below in Section 2.5. Lastly, we take $Z_{\text{max}} = Z_\odot = 0.014$, $t_{d,\text{max}} = t_{\text{Hubble}} = 13.8 \text{ Gyr}$, and $t_{d,\text{min}} = 10 \text{ Myr}$.

Note that the time variable t in equation (2) is connected to the redshift z in equation (1) by

$$\frac{dt}{dz} = \frac{H_0^{-1}}{(1+z)\sqrt{\Omega_m(1+z)^3 + \Omega_\Lambda}}. \quad (3)$$

In the following sections, we discuss each component of equation (2).

2.3 Time delay distributions

The time delay t_d between the formation of the stellar progenitors and the merger of the CBs can depend on their formation channel. It is usually assumed that the distribution of time delays is represented by a power-law probability function (e.g. Chruslinska et al. 2018, see the discussion in Section 2). In equation (2), we consider the possible dependence of t_d on the metallicity of the progenitor stars, which plays an important role in the formation of CB through its influence on the strength of the stellar winds. These processes are taken into account in population synthesis codes, which we discuss below.

In the following, we consider analytical models in which t_d does not depend on metallicity. Specifically, in the BASELINE model all time delays are taken to be zero, so that the CB merger rate follows the SFR, while in the BASELINE_DELAYS model the time delays are described by the probability distribution:

$$P(t_d) \propto t_d^{-1}. \quad (4)$$

This functional form closely follows the results of population synthesis codes, as seen in Fig. 1 below. This power law is restricted between 10 Myr and the Hubble time t_{Hubble} .

Note that in both the BASELINE and the BASELINE_DELAYS model, the efficiency α in equation (2) is chosen to be constant.

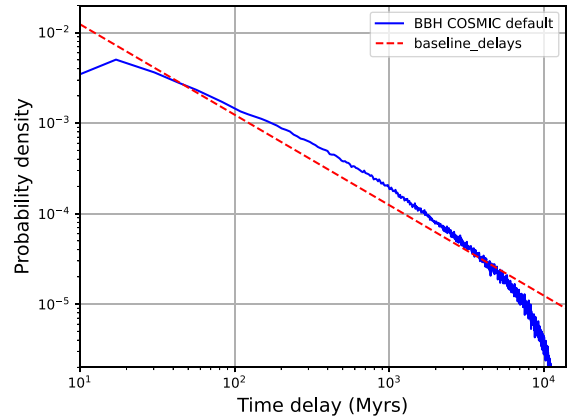


Figure 1. Time delay probability density integrated over all metallicities for our analytical BASELINE_DELAYS model and our COSMIC simulation with the default parameters. The power-law time delay model adopted in our analytical prescriptions provides a good description of the detailed COSMIC model.

2.4 Metallicity distributions

Metallicity affects the formation and evolution of BBHs in several ways. First, higher metallicity can result in more efficient stellar winds, which can decrease the final masses of the progenitor stars and affect the properties of the BBHs formed (Chruslinska, Nelemans & Belczynski 2019; Neijssel et al. 2019). Secondly, metallicity can impact the efficiency of mass transfer phases during binary star evolution (like the common envelope phase), which can result in less efficient mergers and a lower probability of forming BBHs (Neijssel et al. 2019). Finally, metallicity influences the properties of supernovae that produce BHs through fallback (Wong et al. 2014). In low-metallicity environments, the explosion mechanism is more likely to be asymmetric, leading to a larger fraction of BHs that receive a natal kick and thus breaking the binary. Additionally, the amount of mass ejected during a supernova is lower in low-metallicity environments, leading to the formation of more massive BHs (Belczynski et al. 2010; Spera, Mapelli & Bressan 2015).

Metallicity evolves with cosmic time as stars form and then enrich their surroundings with metals both during and at the end of their lifetimes. However, the metallicity distribution in the Universe is not homogeneous, with a large dispersion at any given redshift between various galaxies and even within individual galaxies. In our analytical models, at a given redshift we none the less use averaged quantities over the entire galactic population.

We take the metallicity evolution model from Belczynski et al. (2016):

$$\bar{Z}(z) = \frac{y(1-R)}{\rho_b} \int_z^{z_{\text{max}}} \frac{10^{0.5} \psi(z')}{H_0(1+z')\sqrt{\Omega_m(1+z')^3 + \Omega_\Lambda}} dz', \quad (5)$$

where $R = 0.27$ is the return fraction (the mass fraction of each generation of stars that is ejected back into the interstellar medium), $y = 0.019$ is the net metal yield (the mass of new metals created and ejected into the interstellar medium by each generation of stars per unit mass locked in stars), and $\rho_b = 2.77 \times 10^{11} \Omega_b h_0 M_\odot \text{ Mpc}^{-3}$ is the baryon density, with $\Omega_b = 0.045$.

We also include a dispersion in metallicity at any given redshift. Assuming for simplicity that this dispersion is lognormal (Santoliquido et al. 2021), we obtain the following probability distribution of

metallicity Z at redshift z :

$$P(Z|z) = \frac{1}{\sqrt{2\pi}\sigma^2} \exp\left(-\frac{(\log(Z/Z_\odot) - \log(\bar{Z}(z)/Z_\odot))^2}{2\sigma^2}\right), \quad (6)$$

with $\sigma = 0.2$. The probability $P(Z|t - t_d)$ that we use in equation (2) is then obtained using the redshift–time mapping of equation (3).

If we make the assumption that the probability $P(t_d|Z)$ in equation (2) does not depend on the metallicity, for example if it is a power law as considered in Section 2.3, then we can factorize the two integrals in the merger rate equation to obtain

$$R_{\text{merg}}(t) = \int_{t_{d,\text{min}}}^{t_{d,\text{max}}} \psi(t - t_d) P(t_d) dt_d \times f_Z(t - t_d), \quad (7)$$

with the merging fraction $f_Z(z(t))$:

$$f_Z(z(t)) = \int_0^{Z_{\text{max}}} \alpha(Z) P(Z|z) dZ. \quad (8)$$

We assume that no BHs could be formed by a progenitor star with a metallicity above 10 per cent of the solar one. This cut is inspired by population synthesis results (see e.g. Santoliquido et al. 2021; Srinivasan et al. 2023). As a result, under our assumptions, α is a step function centred on $Z_{\text{cut}} = 0.1 Z_\odot$. Then $f_Z(z)$ is a step-like function with a cut-off around $z = 4.5$. The cut-off is sharpened with the decrease of σ in equation (6).

These metallicity effects are taken into account in our METALLICITY CUT model. Specifically, we use equation (7) to calculate the merger rate with the metallicity distribution given in equation (6) and the time delay distribution from equation (4). Note that for this model the time delay distribution is the same as for the BASELINE_DELAYS model, but the efficiency of forming CBs now depends on redshift.

2.5 Local rates and astrophysical uncertainty

In our analytical models, we do not know a priori the general redshift dependence of the efficiency α in equation (2). However, we can constrain its value by using the local merger rate obtained from the GWTC-3 catalogue by LIGO/Virgo (Abbott et al. 2023). That is, we take α constant in order that locally, the merger rate given in equation (2) matches the value measured by LIGO/Virgo.

For BBHs, we use the rate provided by the *PP* model in GWTC-3, which is $R_{\text{BBH}}(z = 0.2) = 28.3^{+13.9}_{-9.1} \text{ yr}^{-1} \text{ Gpc}^{-3}$. This rate is given for $z = 0.2$ since it corresponds to the redshift where the uncertainty is minimal. For BNSs, we use the rate provided by the *PDB* (*pair*) model in GWTC-3, which is $R_{\text{BNS}}(z = 0) = 44^{+96}_{-34} \text{ yr}^{-1} \text{ Gpc}^{-3}$. The uncertainties quoted for these values correspond to 90 per cent confidence intervals.

Note that, in our analytical models, we have assumed that the relevant quantities, such as the SFR, metallicity, time delay, mass, and redshift distribution, have already been averaged over the mass distribution of the host galaxies. This implies that the host galaxy dependence has been accounted for by taking an average over all possible hosts. This simplifies the analysis by eliminating the need to integrate the merger rate over the host galaxy mass distribution. However, we do not make this assumption for our BBH population synthesis model, as we detail in the next section.

3 POPULATION SYNTHESIS MODELS

We supplement the analytical models described above with a set of population synthesis models that rely on a more realistic description

Table 1. Summary of our three analytical models and three population synthesis models. The PL + P BBH mass distribution is taken from Abbott et al. (2023). The \emptyset symbol means that the model does not take into account the related parameter.

Model name	BBH mass dist.	Time delay dist.	Metallicity
BASELINE	PL + P	\emptyset	\emptyset
BASELINE_DELAYS	PL + P	Power law, equation (4)	\emptyset
METALLICITY CUT	PL + P	Power law, equation (4)	Equations (7) and (8)
COSMIC	Three models: DEFAULT, PESSIMISTIC, and OPTIMISTIC. They have different sets of parameters (described in Section 3) that change the stellar evolution.		

of stellar evolution. We follow the prescription of Srinivasan et al. (2023) to produce an astrophysical population of BBHs that merge by the present day. We account for the SFR through cosmic time as a function of progenitor environment properties (metallicity and galaxy mass) and the efficiency of BBH formation from binary stars. The former is adopted from the default SFR of Srinivasan et al. (2023) that models the mass–metallicity relation based on the metallicity calibration of Kobulnicky & Kewley (2004) and extrapolated to high redshift based on the fit provided by Ma et al. (2016). The latter is obtained using a rapid binary population synthesis code, COSMIC (v3.4.0; Breivik et al. 2020), which simulates the binary evolution of stars that ultimately form merging BBHs. These binary simulations are based on parametric models of single-star evolution and their binary interactions. We adopt the default binary evolution parameters shown in bold in table 1 of Srinivasan et al. (2023) to generate a population of merging BBHs, BBH COSMIC DEFAULT.

Uncertainties in modelling the SFR and binary evolution result in a large variance in the predicted merger rate. Therefore, we explore models with a pessimistic and optimistic merger rate in comparison to the BBH COSMIC DEFAULT, termed BBH COSMIC PESSIMISTIC and BBH COSMIC OPTIMISTIC, respectively. BBH COSMIC PESSIMISTIC differs from the default model in two aspects: a different critical mass ratio model of the onset of unstable mass transfer ($q_{\text{cfl}} = 4$ as per COSMIC documentation¹ and a different common-envelope efficiency $\alpha = 0.1$). Likewise, BBH COSMIC OPTIMISTIC varies in the description of the common envelope phase ($\lambda_{\text{bdaf}} = 0$ and $\alpha = 0.2$ as per COSMIC documentation). The present-day merger rates of our PESSIMISTIC, DEFAULT, and OPTIMISTIC models are 15, 120, and 590 $\text{Gpc}^{-3} \text{ yr}^{-1}$, respectively.

For the BNSs, we take the DEFAULT COSMIC parameters of Srinivasan et al. (2023). To compute the merger rate, we use equation (2) with SFR and metallicity distribution $P(Z|z)$ provided, respectively, in equations (1) and (6). We use 15 log-uniform metallicity bins between 4.4×10^{-4} and 2.8×10^{-1} . The mass efficiency $\alpha(Z)$ and the time delay distribution $P(t_d|Z)$ are calculated from our COSMIC results.

All of our models are summarized in Table 1. Analytical models (BASELINE, BASELINE_DELAYS, and METALLICITY CUT) are easy to calibrate and to use because of their small number of parameters. Each new analytical model adds a physical process (time delay, metallicity) that refines the model and makes it more realistic. None the less, these analytical models are not detailed enough and cannot capture some aspects of BBH and BNS formation. That is why we choose to compare them with more realistic models based on the population synthesis code COSMIC, as outlined above. This code describes better the physical processes at play during stellar

¹<https://cosmic-popsynth.github.io/>

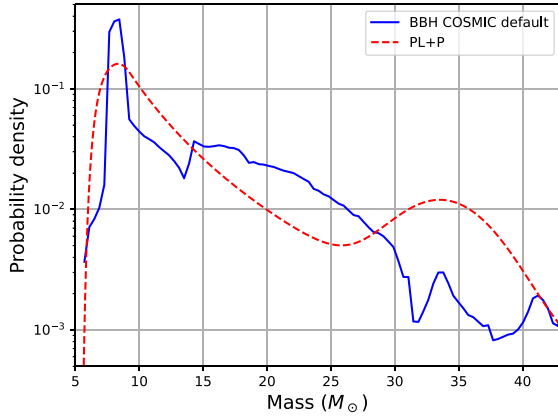


Figure 2. The distribution of the primary mass M_1 for the PL + P model from the GWTC-3 catalogue and our COSMIC simulations with default parameters. The peak at around $M_1 \sim 10 M_\odot$ as well as the power-law-like behaviour are similar in both models. Note, however, the differences at high masses, at $M_1 \gtrsim 30 M_\odot$.

evolution, taking into account several physical effects (common envelope phase, kick velocity, etc.; see Breivik et al. 2020) and it is in this sense more realistic. On the other hand, population synthesis codes have numerous parameters that are difficult to constrain (see Mandel & Broekgaarden 2022, for a recent review). Looking at observables produced by a set of COSMIC parameters (for example, BBH merger rate and stochastic backgrounds) and comparing them to observations could help us to calibrate COSMIC parameters. In practice, there are currently not enough observational constraints to overcome the degeneracies between various COSMIC parameters. In this work, we are not attempting to calibrate COSMIC parameters, rather we use specific sets of parameters that represent well the range of variability of COSMIC.

In Fig. 2, we show the BBH primary mass distribution of the PL + P model and the one resulting from our default COSMIC model. The COSMIC distribution has a more pronounced peak at low masses around $8 M_\odot$ and presents an overdensity centred around $22 M_\odot$ but does not have any peak around $34 M_\odot$ contrary to the PL + P model.

Fig. 1 compares the time delay probability density integrated over all metallicities in our analytical BASELINE_DELAYS model and our default COSMIC model. The distribution from COSMIC is very close to a power law but with a turn over at very short time delays.

We compare the merger rate of BBHs in our models in Fig. 3. As expected, since there is no time delay between formation and merger, the shape of the BASELINE merger rate is close to the SFR (see equation 1) and peaks at around $R_{\text{merg}}(z = 2) \sim 1.5 \times 10^7$ events $\text{yr}^{-1} \text{Mpc}^{-3}$.

We also observe that for $z > 0.2$ the BASELINE_DELAYS merger rate is always below the BASELINE model. The reason is that the inclusion of time delays shifts the entire BASELINE merger rate curve to lower redshifts. Then this shifted curve needs to be renormalized to be in accordance with the local LIGO/Virgo observations at $z = 0.2$, as described in Section 2.5. This procedure then results in a merger rate that is below the BASELINE model at all redshifts above $z = 0.2$.

The merger rate in the METALLICITY CUT model is slightly lower than the BASELINE one at small redshifts ($z < 2$), but significantly higher at larger redshifts ($z > 2$). This is due to the fact that the effect of metallicity is to reduce the fraction of massive stars that can collapse into BHs. At lower redshifts, stars tend to have higher

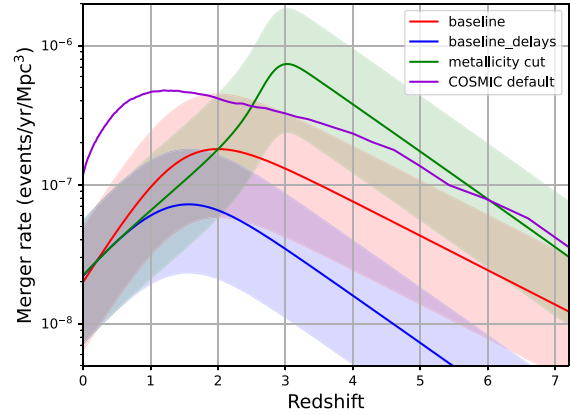


Figure 3. The merger rate of BBHs calculated with our main models. The uncertainties in this figure come from the 90 percent confidence interval on the merger rate at $z = 0.2$ from the GWTC-3 catalogue. We assume the uncertainty to be the same at every redshift.

metallicity, resulting in fewer stars collapsing into BHs. Conversely, at higher redshifts, stars tend to have lower metallicity, leading to a larger fraction of stars collapsing into BHs. The asymmetry of this trend around the BASELINE model results predominantly from the renormalization of the merger rate at low redshifts ($z = 0.2$).

Finally, the merger rate from the COSMIC DEFAULT model is significantly higher than our other models and peaks at lower redshift around $z = 1$. This model predicts a merger rate at $z = 0.2$, which is outside the 90 per cent confidence interval computed in the GWTC-3 catalogue (Abbott et al. 2023). This implies that the default set of parameters from Srinivasan et al. (2023) does not describe the observed merger rate of BBHs. Note that this difference in merger rate can be also due to our model for star formation and metallicity evolution.

In this study, we choose to explore the range of uncertainties due to COSMIC parameters rather than trying to find the best parameter set. For this reason, we include also two other sets (PESSIMISTIC and OPTIMISTIC in Table 1) from the same study that represent well the range of variability of COSMIC models. The former set has a merger rate at $z = 0.2$ that is in accordance with GWTC-3, while the latter provides an upper bound on the merger rate that COSMIC can predict.

4 CALCULATION OF THE SGWB FROM BBH AND BNS

The total dimensionless energy density of GWs Ω_{GW} , per logarithmic unit of frequency and in unit of the critical density of the Universe ρ_c , is expressed as

$$\Omega_{\text{GW}} = \frac{1}{\rho_c} \frac{d\rho_{\text{GW}}}{d \ln f}, \quad (9)$$

with $d\rho_{\text{GW}}$ the energy density of the GWs in the frequency interval $[f, f + df]$.

We can write the background from BBH or BNS mergers as

$$\Omega_{\text{GW}}(f) = \frac{f}{\rho_c c^2 H_0} \int_0^{z_{\text{max}}} \int_{\lambda} \frac{R_{\text{merg}}(z, \lambda) \frac{dE_{\text{GW}}(f_s)}{df_s} P(\lambda)}{(1+z) \sqrt{\Omega_M(1+z)^3 + \Omega_\Lambda}} d\lambda dz, \quad (10)$$

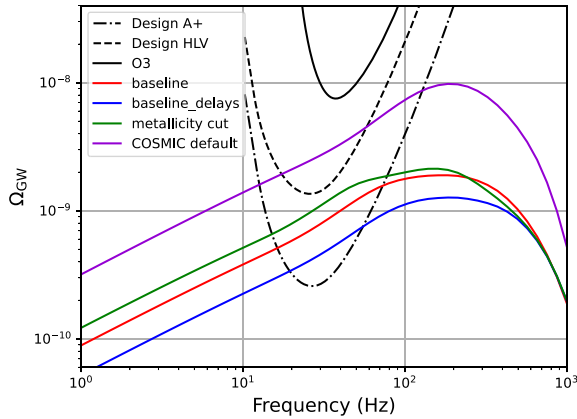


Figure 4. In coloured lines, the SGWB from BBHs calculated with our main models (see Table 1); in black lines, the LIGO/Virgo SGWB sensitivity. There is a factor of 3 variability in the background predicted by our analytical models. The prediction obtained using COSMIC DEFAULT significantly exceeds the analytical models, mainly due to its higher merger rate (see Fig. 3).

with f the observed frequency, $f_s = f(1+z)$ the frequency emitted at the source, R_{merg} the CB merger rate, $dE_{\text{GW}}(f_s)/df_s$ the energy spectrum emitted by each CB, and $P(\lambda)$ the probability distribution of the parameters of the CB, summarized as λ .

We used the phenomenological expression given in Périgois et al. (2021) for the energy spectrum emitted by each CB. The coefficients of this expression are obtained by matching post-Newtonian and numerical relativity waveforms (see Appendix A and Ajith et al. 2011).

4.1 LIGO/Virgo and LISA sensitivity to an SGWB

We use the LIGO/Virgo sensitivity curves to an SGWB given by the LIGO/Virgo/Kagra collaboration (Abbott et al. 2023). For LISA, we use an analytical approximation for the sensitivity curve for a point-like source given in Robson, Cornish & Liu (2019) to calculate the power-law integrated sensitivity to an SGWB.

We define the latter to be the limit at which the signal-to-noise ratio (SNR) for detecting a signal is equal to 5, assuming an observation time of $T_{\text{obs}} = 4$ yr. A reasonable frequency range to calculate the sensitivity of LISA is between 10^{-1} and 10^2 mHz. To compute the power-law integrated sensitivity curve, we use the method proposed by Thrane & Romano (2013).

5 STELLAR-MASS CB MERGERS DETECTABLE BY LISA

Even though the mergers of stellar-mass BHs do not emit their maximum intensity in the LISA band, it could be possible to detect these systems individually with LISA. In fact, LISA is not well suited to detect stellar-mass BBH and BNS because its sensibility is in the mHz regime. None the less, by accumulating the signal over multiple periods, the SNR can be increased and pass beyond the detection threshold. We estimate the expected number of individual detections N_{LISA} with LISA for a mission duration of $T_{\text{obs}} = 4$ yr using the method described in Gerosa et al. (2019):

$$N_{\text{LISA}} = \int_z \int_{\lambda} P(\lambda) R_{\text{merg}}(z) \frac{dV_c}{dz} \frac{1}{1+z} \Delta(\lambda, z) dz d\lambda. \quad (11)$$

The quantity $\Delta(\lambda, z)$ provides an estimate of the time window in which a merging CB is visible by LISA with SNR above a threshold value SNR_{thr} . We chose $\text{SNR}_{\text{thr}} = 8$ since the source parameters were shown to be well constrained in this case (Buscicchio et al. 2021), although we note that lower values can be considered for sources observable with ground-based detectors (Wong et al. 2018).

We need to remove these sources from the background, since they are individually detected. Removing these sources will lower the background, thus some new sources could become individually detectable since the background contributes to the overall noise budget. As a result, Δ in equation (11) is likely to increase with the decrease of the background. Therefore, we need to recompute N_{LISA} and eventually repeat this process until we reach convergence. In practice, this iterative process is not necessary, indeed in our case N_{LISA} is of the order of magnitude of 10 for the BBHs and 0 for the BNSs (see the results in Section 6 below). Thus, detectable stellar-mass sources have a negligible contribution to the SGWB for LISA.

6 RESULTS

In this section, we present and analyse the results of the various models for the SGWB from BBH and BNS sources, in both the LISA and LIGO/Virgo frequency ranges. The main results are summarized in Fig. 4 and Table 2, which provides the SGWB values at 3 mHz and 25 Hz, which are the reference frequencies, respectively, for LISA and LIGO/Virgo. All of our models are consistent with the upper limit from LVC O3 observations, but only the COSMIC model predicts an SGWB strong enough to be confidently detected with design LIGO/Virgo sensitivity.

Compared to the BASELINE model, the BASELINE_DELAYS takes into account the time delay of the CB mergers, leading to a decrease in the SGWB by a factor of 1.7 across all frequencies. Indeed, as we showed

Table 2. Values of the SGWB in Fig. 4 and the number of the individually detected BBH mergers with LISA with an SNR of at least 8 for a 4 yr observation run. $N_{\text{LISA}} \sim 10$ for all of our analytical models. The error bars on the background from analytical models come from the 90 percent confidence interval on the merger rate at $z = 0.2$ (GWTC-3 catalogue), on which these models are calibrated. Error bars cannot be provided for population synthesis-based models, but in Fig. 5 and in the text we discuss their range of uncertainty.

Models	BASELINE	BASELINE_DELAYS	Z CUT	COSMIC
(25 Hz) $\Omega_{\text{GW}} \times 10^{10}$	$6.83^{+3.35}_{-2.20}$	$3.90^{+1.96}_{-1.28}$	$9.42^{+4.63}_{-3.03}$	24.11
(3 mHz) $\Omega_{\text{GW}} \times 10^{12}$	$1.89^{+0.93}_{-0.61}$	$1.10^{+0.54}_{-0.35}$	$2.61^{+1.28}_{-0.84}$	6.75
N_{LISA}	6^{+3}_{-2}	7^{+3}_{-2}	7^{+3}_{-2}	19

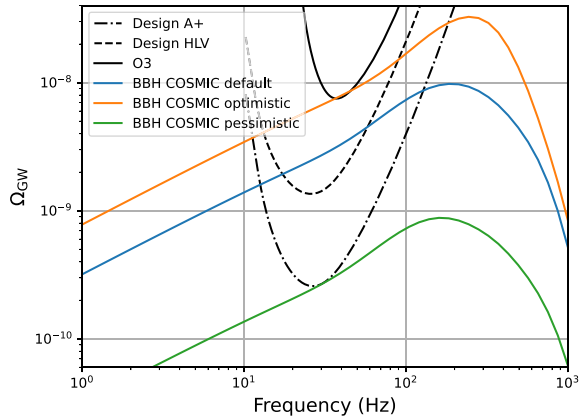


Figure 5. The SGWB from BBHs, based on the results of our COSMIC simulations discussed in Section 3. There is a variation of one order of magnitude between our models. The COSMIC OPTIMISTIC model seems to be already excluded by observation, since no background has been detected during O3.

in Section 3, the BASELINE_DELAYS merger rate is lower compared to the BASELINE at all redshifts, resulting in a lower background since the other parameters in equation (10) remain unchanged for both of these models.

The METALLICITY CUT model includes the effect of metallicity, resulting in an amplitude increase by a factor of 1.4 and a shift of the peak towards lower frequencies. These effects can be explained by the combination of two effects. First, as shown in Section 3, the METALLICITY CUT merger rate is higher than the BASELINE one for most of the redshift range, thus the corresponding background is higher. Secondly, as can be seen in Fig. 3, the merger rate for the METALLICITY CUT model peaks close to $z = 3$. As a result, the GW frequencies of the background for this model are more redshifted.

Note that a second bump is observed in the METALLICITY CUT merger rate around 50 Hz. As we show below, this feature is due to the peak in the PL + P mass distribution.

The SGWB obtained for the COSMIC model is higher than that for the other models, and so upcoming observations in run O4 are expected to have sufficient sensitivity to either detect or place strong constraints on this model. It is important to mention that the peak around 200 Hz in the COSMIC model appears to be more prominent than in other cases. This is due to the mass distribution produced by the COSMIC simulation, which peaks at lower masses than the distribution presented in GWTC-3 (Abbott et al. 2023), as shown in Fig. 1.

Fig. 5 compares the results of the three different COSMIC runs described in Section 3. We choose these runs because they illustrate well the range of uncertainty of binary population synthesis models. It can be seen that changing the stellar evolution parameters of the COSMIC code leads to a variation of one order of magnitude in the resulting background, from the O3 limits to the design sensitivity. Therefore, the range predicted by the COSMIC models studied in this paper will be probed in the near future. In fact, the OPTIMISTIC model appears to be already excluded by observations, as no background has been detected during O3. Thus, this also excludes the merger rate predicted by this model. The upcoming O4 run is expected to constrain even more these parameters.

In Fig. 6, we set the model to be METALLICITY CUT, and we examine the impact of the mass distribution model on the background. The

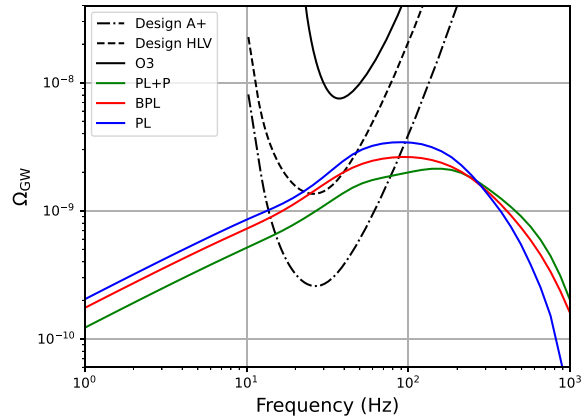


Figure 6. The SGWB for BBH mass distribution models described in Abbott et al. (2023) and the METALLICITY CUT model. Varying the mass distribution results in a factor of 2 difference of the SGWB.

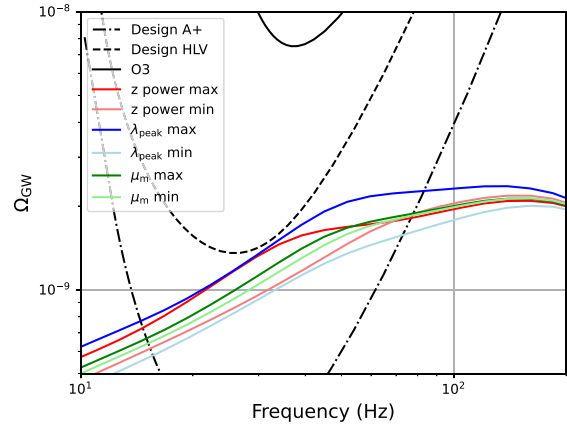


Figure 7. The variation of the SGWB from BBHs due to uncertainties on the PL + P mass distribution. Each coloured curve represents the predicted background by our METALLICITY CUT model with each time a different value for one parameter of the PL + P distribution. The uncertainty on the amplitude of the Gaussian peak of the PL + P model results in the most significant variation on the background.

PL + P distribution results in a broad peak with two distinguishable bumps around 50 and 200 Hz, which are a result of the two peaks in this mass distribution (around 5 and 35 M_{\odot}). On the other hand, the PL model gives only one peak around 100 Hz and a bit higher background overall. The BPL model is intermediate between the two, with a lower background but a wider peak. Upcoming O4 observations have the potential to constrain the parameters of the mass distribution models and thus the resulting background.

Fixing the mass model to be PL + P, we now study the impact of the main parameters of this mass distribution on the resulting background. To this end, we vary the amplitude (λ_{peak}) and the position (μ_m) of the Gaussian peak in the mass distribution. These values are set to their maximum and minimum of the 90 per cent credibility interval, and the resulting backgrounds are compared in Fig. 7.

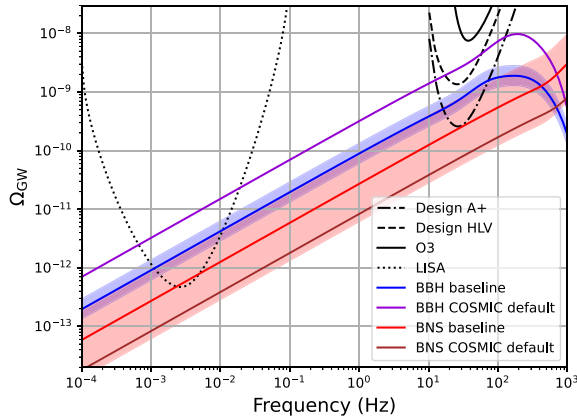


Figure 8. The SGWB from both BBHs and BNSs in the frequency range of *LISA* and LIGO/Virgo. The analytical and population synthesis models for the BNS background are compatible, within the error bars of the former, contrary to their predictions for the BBH.

Table 3. Our predictions for the SGWB in LIGO/Virgo and *LISA* frequency bands, comparing the BASELINE and default COSMIC models.

Models	BBH		BNS	
	BASELINE	COSMIC	BASELINE	COSMIC
(25 Hz) $\Omega_{\text{GW}} \times 10^{10}$	6.83	24.11	2.07	1.60
(3 mHz) $\Omega_{\text{GW}} \times 10^{12}$	1.89	6.75	0.52	0.40

We also investigate the impact of varying μ_m with redshift by taking $\mu_m \propto (1+z)^{0.5}$ (*‘z power max’* in Fig. 7) or $\mu_m \propto (1+z)^{-0.5}$ (*‘z power min’*). Indeed, μ_m may vary with the redshift since, as we discuss in Section 2.1, the Gaussian peak in the mass distribution could be the result of PPSiNE and the efficiency of this phenomenon depends on the metallicity (and so on the redshift).

The uncertainty in the amplitude of the bump results in the most significant variations of the SGWB. When set to its minimum, the bump around 50 Hz is almost imperceptible. The uncertainty in the absolute position of μ_m results in only minor variations in the background. However, assuming a strong redshift dependence moves the bump from 35 (*‘z power max’*) to 75 Hz (*‘z power min’*).

Note that the bump in the background around 200 Hz does not change. This confirms that the secondary bump around 50 Hz is indeed due to the peak around $35 M_{\odot}$ in the PL + P mass distribution. Furthermore, this secondary bump is the closest part of the SGWB to the minimum sensitivity of LIGO/Virgo and thus could be one of the first features of the SGWB to be detected.

In Fig. 8 and Table 3, we compare the backgrounds due to BBH and BNS mergers for the BASELINE and the DEFAULT COSMIC models. The uncertainty bands for the BASELINE model are based on the 90 per cent credibility interval of the local merger rate measurement by LIGO/Virgo, as reported in Abbott et al. (2023), and are consistent with the recent results reported in Babak et al. (2023). Our results show that the default parameters of COSMIC are not in agreement with the simple analytical model for the BBH background (this is not so surprising since the merger rates predicted by these models are perceptibly different, see Fig. 3). However, this is not the case for the BNS background. It is important to note that the uncertainty for the BNS case is very high given that LIGO/Virgo have only detected two BNS mergers to date. The fourth run of LIGO/Virgo is expected

to detect a few additional BNS mergers (Colombo et al. 2022), which will result in a more constrained local merger rate. Finally, our results suggest that the BNS background is likely subdominant to the BBH contribution, consistent with previous studies.

7 CONCLUSION

We investigated the SGWB produced by several population models of BBHs and BNSs in the frequency ranges of LIGO/Virgo and *LISA*. We developed three analytical models, namely BASELINE, BASELINE_DELAYS, and METALLICITY CUT, and complemented them with a set of population synthesis models based on the COSMIC code. Our BASELINE model assumes a merger rate that follows the SFR with zero delay times, while the BASELINE_DELAYS model takes into account the time delay between the formation of the stellar progenitors and the merger of the CBs. The METALLICITY CUT model includes also the effect of metallicity on the efficiency of producing CBs.

We specifically focused on the mass distribution of CBs in our models. For BBHs, we used mainly the PL + P mass distribution from GWTC-3 and investigated some other distributions from the same catalogue. For BNSs, we used the mass distribution obtained from Galactic observations, assumed to be valid at all redshifts.

To complement our analytical models, we investigated three models for the BBH population based on the population synthesis code COSMIC, which differ by the set of parameters used to describe the stellar physics, namely OPTIMISTIC, PESSIMISTIC, and DEFAULT. The mass distribution predicted by the COSMIC models differs from the PL + P model, but the time delay distribution was consistent with a simple power law as used in our analytical description. For BNSs, we used only one COSMIC simulation with the DEFAULT set of parameters.

For BBHs, our analytical models predict Ω_{GW} in the range $[4 \times 10^{-10}$ to $1 \times 10^{-9}]$ at 25 Hz and $[1 \times 10^{-12}$ to $4 \times 10^{-12}]$ at 3 mHz, where the range of our predicted values corresponds to the uncertainty in the physical assumptions of our models. These backgrounds could be detectable by *LISA* with a period of observation of 4 yr, but they are unlikely to be detected during the upcoming LIGO/Virgo/Kagra O4 run. However, the O4 run can help to constrain the parameters of our models.

Our analytical models are calibrated to the observed merger rate at $z = 0.2$. Thus, the uncertainty in this measurement can lead to a possible variation of about a factor of 1.5 for BBHs and 2 for BNSs in the predicted background.

We also investigated the impact of the mass distribution of BBHs on the background, which could vary by a factor of 2 by varying the mass distribution model within the confidence limits of the GWTC-3 population analysis. Additionally, we found that the uncertainties of the Gaussian peak of the PL + P mass distribution are dominated by the uncertainty in the amplitude of this peak and could lead to a factor of 1.5 variation in the SGWB. We also discussed the possibility that the position of this peak depends on redshift, but more constraints on the amplitude are needed in order to explore this potential effect. Indeed, our results suggest that the main source of uncertainty is the amplitude of the peak, while its redshift dependence has a negligible impact on the amplitude of the SGWB.

The SGWB predicted by our three COSMIC models varies between $[2 \times 10^{-10}$ to $2 \times 10^{-9}]$ (25 Hz) and $[7 \times 10^{-13}$ to $7 \times 10^{-12}]$ (3 mHz). This range, which is larger than the uncertainty due to the measurement error of the local merger rate, corresponds to the uncertainties in the physics of massive stellar binaries (Srinivasan

et al. 2023). The OPTIMISTIC COSMIC model appears to be excluded by observations, as no background has been detected during O3. However, the upcoming O4 run will likely help us constrain the parameters of the stellar model.

Finally, all of our models predict an $O(10)$ number of BBHs and no BNSs that could be individually detectable by *LISA* for a period of observation of 4 yr.

While we have explored some uncertainties in the SGWB from CBs, several important effects were not included and could lead to further variations in the predicted SGWB. First, we assumed that all binaries are circularized; however, including eccentricity and precession in the waveforms might have an important effect on the SGWB amplitude (Zhao & Lu 2021).

More importantly, in this study we considered only the isolated binary formation scenario for BBHs, while the properties of the observed BBH population suggest that some sources could be formed through the dynamical channel, in particular hierarchical mergers in dense stellar environments. The mass and redshift distributions of this population are expected to be quite different and lead to a different component of the SGWB (Pérgois et al. 2022). The remnants of Pop III stars, which could have higher merger rates at higher redshifts, could also have an important contribution to the SGWB (Dvorkin et al. 2016; Hartwig et al. 2016; Martinovic et al. 2022). These contributions and their associated uncertainties will be studied in future work.

ACKNOWLEDGEMENTS

This work was supported by the Programme National des Hautes Energies of CNRS/INSU with INP and IN2P3, co-funded by CEA and CNES. We thank Cyril Pitrou and Jean-Philippe Uzan for their very useful comments and all the interesting discussions we had together. CP acknowledges funding support from the Initiative Physique des Infinis (IPI), a research training programme of the IDEX SUPER at Sorbonne Université. RS and AL acknowledge support from the graduate and research school EUR SPECTRUM. This work made use of the Infinity computing cluster at IAP.

DATA AVAILABILITY

The data underlying this article will be shared on reasonable request to the corresponding author.

REFERENCES

Abbott B. P. et al., 2016a, *Phys. Rev. Lett.*, 116, 061102
 Abbott B. P. et al., 2016b, *Phys. Rev. Lett.*, 116, 131102
 Abbott B. P. et al., 2017, *Phys. Rev. Lett.*, 118, 121101
 Abbott B. P. et al., 2018a, *Phys. Rev. Lett.*, 120, 091101
 Abbott B. P. et al., 2018b, *Phys. Rev. Lett.*, 120, 201102
 Abbott B. P. et al., 2018c, *Phys. Rev. Lett.*, 121, 161101
 Abbott B. P. et al., 2019a, *Phys. Rev. X*, 9, 031040
 Abbott B. P. et al., 2019b, *Phys. Rev. D*, 100, 061101
 Abbott R. et al., 2020a, *Phys. Rev. Lett.*, 125, 101102
 Abbott R. et al., 2020b, *ApJ*, 892, L3
 Abbott R. et al., 2020c, *ApJ*, 896, L44
 Abbott R. et al., 2020d, *ApJ*, 900, L13
 Abbott R. et al., 2021a, preprint (arXiv:2108.01045)
 Abbott R. et al., 2021b, preprint (arXiv:2111.03606)
 Abbott R. et al., 2021c, *Phys. Rev. X*, 11, 021053
 Abbott R. et al., 2021d, *Phys. Rev. D*, 104, 022004
 Abbott R. et al., 2021e, *Phys. Rev. D*, 104, 022005
 Abbott R. et al., 2023, *Phys. Rev. X*, 13, 011048

Ajith P. et al., 2008, *Phys. Rev. D*, 77, 104017
 Ajith P. et al., 2011, *Phys. Rev. Lett.*, 106, 241101
 Auclair P. et al., 2020, *J. Cosmol. Astropart. Phys.*, 2020, 034
 Auclair P. et al., 2023, *Living Rev. Relativ.*, 26, 5
 Babak S. et al., 2023, *J. Cosmol. Astropart. Phys.*, 2023, 034
 Baibhav V., Berti E., Gerosa D., Mapelli M., Giacobbo N., Bouffanais Y., Di Carlo U. N., 2019, *Phys. Rev. D*, 100, 064060
 Belczynski K., Dominik M., Bulik T., O’Shaughnessy R., Fryer C., Holz D. E., 2010, *ApJ*, 715, L138
 Belczynski K., Holz D. E., Bulik T., O’Shaughnessy R., 2016, *Nature*, 534, 512
 Breivik K., Rodriguez C. L., Larson S. L., Kalogera V., Rasio F. A., 2016, *ApJ*, 830, L18
 Breivik K. et al., 2020, *ApJ*, 898, 71
 Broekgaarden F. S. et al., 2022, *MNRAS*, 516, 5737
 Busicchio R., Klein A., Roebber E., Moore C. J., Gerosa D., Finch E., Vecchio A., 2021, *Phys. Rev. D*, 104, 044065
 Caprini C., Figueroa D. G., 2018, *Class. Quantum Gravity*, 35, 163001
 Chen Z.-C., Huang F., Huang Q.-G., 2019, *ApJ*, 871, 97
 Christensen N., 2019, *Rep. Prog. Phys.*, 82, 016903
 Chruslinska M., Belczynski K., Klencik J., Benacquista M., 2018, *MNRAS*, 474, 2937
 Chruslinska M., Nelemans G., Belczynski K., 2019, *MNRAS*, 482, 5012
 Colombo A., Salafia O. S., Gabrielli F., Ghirlanda G., Giacomazzo B., Perego A., Colpi M., 2022, *ApJ*, 937, 79
 Cusin G., Dvorkin I., Pitrou C., Uzan J.-P., 2019, *Phys. Rev. D*, 100, 063004
 Cusin G., Dvorkin I., Pitrou C., Uzan J.-P., 2020, *MNRAS*, 493, L1
 Dvorkin I., Vangioni E., Silk J., Uzan J.-P., Olive K. A., 2016, *MNRAS*, 461, 3877
 Evans M. et al., 2021, preprint (arXiv:2109.09882)
 Farrow N., Zhu X.-J., Thrane E., 2019, *ApJ*, 876, 18
 Fowler W. A., Hoyle F., 1964, *ApJS*, 9, 201
 Fryer C. L., Woosley S. E., Heger A., 2001, *ApJ*, 550, 372
 Gerosa D., Ma S., Wong K. W. K., Berti E., O’Shaughnessy R., Chen Y., Belczynski K., 2019, *Phys. Rev. D*, 99, 103004
 Hartwig T., Volonteri M., Bromm V., Klessen R. S., Barausse E., Magg M., Stacy A., 2016, *MNRAS*, 460, L74
 Jenkins A. C., Sakellariadou M., Regimbau T., Slezak E., 2018, *Phys. Rev. D*, 98, 063501
 Kimball C. et al., 2021, *ApJ*, 915, L35
 Kobulnicky H. A., Kewley L. J., 2004, *ApJ*, 617, 240
 Lattimer J. M., Prakash M., 2016, *Phys. Rep.*, 621, 127
 Lewicki M., Vaskonen V., 2021, preprint (arXiv:2111.05847)
 Liang Z.-C., Hu Y.-M., Jiang Y., Cheng J., Zhang J.-d., Mei J., 2022, *Phys. Rev. D*, 105, 022001
 Ma X., Hopkins P. F., Faucher-Giguère C.-A., Zolman N., Muratov A. L., Kereš D., Quataert E., 2016, *MNRAS*, 456, 2140
 Maggiore M. et al., 2020, *J. Cosmol. Astropart. Phys.*, 2020, 050
 Mandel I., Broekgaarden F. S., 2022, *Living Rev. Relativ.*, 25, 1
 Mangiagli A., Bonetti M., Sesana A., Colpi M., 2019, *ApJ*, 883, L27
 Mapelli M., Giacobbo N., Santoliquido F., Artale M. C., 2019, *MNRAS*, 487, 2
 Martinovic K., Pérgois C., Regimbau T., Sakellariadou M., 2022, *ApJ*, 940, 29
 Mukherjee S., Silk J., 2021, *MNRAS*, 506, 3977
 Nakazato K., Niino Y., Sago N., 2016, *ApJ*, 832, 146
 Neijssel C. J. et al., 2019, *MNRAS*, 490, 3740
 Özel F., Freire P., 2016, *ARA&A*, 54, 401
 Pérgois C., Belczynski C., Bulik T., Regimbau T., 2021, *Phys. Rev. D*, 103, 043002
 Pérgois C., Santoliquido F., Bouffanais Y., Di Carlo U. N., Giacobbo N., Rastello S., Mapelli M., Regimbau T., 2022, *Phys. Rev. D*, 105, 103032
 Planck Collaboration VI, 2020, *A&A*, 641, A6
 Regimbau T., 2011, *Res. Astron. Astrophys.*, 11, 369
 Renzini A. I., Goncharov B., Jenkins A. C., Meyers P. M., 2022, *Galaxies*, 10, 34
 Robson T., Cornish N. J., Liu C., 2019, *Class. Quantum Gravity*, 36, 105011

- Romero-Shaw I. M., Farrow N., Stevenson S., Thrane E., Zhu X.-J., 2020, *MNRAS*, 496, L64
- Santoliquido F., Mapelli M., Giacobbo N., Bouffanais Y., Artale M. C., 2021, *MNRAS*, 502, 4877
- Spera M., Mapelli M., Bressan A., 2015, *MNRAS*, 451, 4086
- Srinivasan R., Lamberts A., Bizouard M. A., Bruel T., Mastrogiovanni S., 2023, *MNRAS*, 524, 60
- Talbot C., Thrane E., 2018, *ApJ*, 856, 173
- Thrane E., Romano J. D., 2013, *Phys. Rev. D*, 88, 124032
- Umeda H., Nomoto K., 2002, *ApJ*, 565, 385
- van Son L. A. C. et al., 2022, *ApJ*, 931, 17
- Vangioni E., Olive K. A., Prestegard T., Silk J., Petitjean P., Mandie V., 2015, *MNRAS*, 447, 2575
- Wong T.-W., Fryer C. L., Ellinger C. I., Rockefeller G., Kalogera V., 2014, preprint (arXiv:1401.3032)
- Wong K. W. K., Kovetz E. D., Cutler C., Berti E., 2018, *Phys. Rev. Lett.*, 121, 251102
- Woosley S. E., Heger A., 2021, *ApJ*, 912, L31
- Zevin M. et al., 2021, *ApJ*, 910, 152
- Zhao Y., Lu Y., 2021, *MNRAS*, 500, 1421
- Zhou B., Reali L., Berti E., Çalıřkan M., Creque-Sarbinowski C., Kamionkowski M., Sathyaprakash B. S., 2023, *Phys. Rev. D*, 108, 064040

APPENDIX

The energy loss of a binary system by gravitational radiation is expressed according to the three phases of the coalescence, the inspiralling phase (for $f_s < f_{\text{merg}}$), the coalescence phase (for $f_{\text{merg}} \leq f_s < f_{\text{ring}}$), and finally the ringdown phase, i.e. the relaxation phase (for $f_{\text{ring}} \leq f_s < f_{\text{cut}}$). It is therefore expressed as (Ajith et al. 2008)

$$\frac{dE_{\text{GW}}(f_s)}{df_s} = \frac{dE_{\text{GW}}^{\text{Newton}}(f_s)}{df_s} \times \begin{cases} (1 + \sum_2^3 \alpha_i v^i)^2 & \text{for } f_s < f_{\text{merg}}, \\ f_s w_m (1 + \sum_1^2 \epsilon_i v^i)^2 & \text{for } f_{\text{merg}} \leq f_s < f_{\text{ring}}, \\ f_s^{1/3} w_r \mathcal{L}^2(f_s, f_{\text{ring}}, \sigma) & \text{for } f_{\text{ring}} \leq f_s < f_{\text{cut}}, \end{cases}$$

where

- (i) $\frac{dE_{\text{GW}}^{\text{Newton}}(f_s)}{df_s} = \frac{5}{12} (G\pi)^{2/3} \mathcal{M}_c^{5/3} F_\theta f_s^{-1/3}$,
- (ii) $F_\theta = \frac{(1 + \cos^2 \theta)^2}{4} + \cos^2 \theta$,
- (iii) $v = \frac{(\pi G M f_s)^{1/3}}{c}$, and
- (iv) $\mathcal{L}(f, f_{\text{ring}}, \sigma) = \frac{\sigma}{2\pi[(f - f_{\text{ring}})^2 + 0.24\sigma^2]}$, w_m , and w_r are the continuity coefficients.

The coefficients α_i and ϵ_i are given in Ajith et al. (2008); with our null assumption for the spin ($\chi = 0$), they can be written as $\epsilon_1 = -1.8897$, $\epsilon_2 = 1.6557$, $\alpha_2 = -\frac{323}{224} + \frac{451}{168}\eta$, and $\alpha_3 = 0$, with $\eta = \frac{M_1 M_2}{M^2}$.

The phase transition frequencies f_{merg} , f_{ring} , f_{cut} , and σ are calculated as (Ajith et al. 2008)

$$\frac{\pi G M}{c^3} \mu_k = \mu_k^0 \text{ with } \mu_k = (f_{\text{merg}}, f_{\text{ring}}, f_{\text{cut}}, \sigma),$$

where the coefficients μ_k^0 are given in table I of Ajith et al. (2011); for $\chi = 0$, we get the following:

μ_k	μ_k^0
f_{merg}	0.066
f_{ring}	0.185
f_{cut}	0.3236
σ	0.925

This paper has been typeset from a $\text{\TeX}/\text{\LaTeX}$ file prepared by the author.

